Chapter 5: Global Carbon and other Biogeochemical Cycles and Feedbacks

Coordinating Lead Authors:
Josep G. Canadell (Australia), Pedro M.S. Monteiro (South Africa)

Lead Authors:
Marcos Costa (Brazil), Leticia Cotrim da Cunha (Brazil), Peter Cox (UK), Alexey V. Eliseev (Russia), Stephanie Henson (UK), Masao Ishii (Japan), Samuel Jaccard (Switzerland), Charles Koven (USA), Annalea Lohila (Finland), Prabir Patra (Japan/India), Shilong Piao (China), Joeri Rogelj (Austria/Belgium), Stephen Sympungani (Zambia), Sönke Zaehle (Germany), Kirsten Zickfeld (Canada/Germany)

Contributing Authors:
Georgii Alexandrov (Russia), Govindasamy Bala (India/USA), Lena Boysen (Germany), Long Cao (China), Naveen Chandra (Japan), Philippe Ciais (France), Sergey N. Denisov (Russia), Frank Dentener (EU, Netherlands), Piers Forster (UK), Pierre Friedlingstein (UK), Weiwei Fu (China/USA), Véronique Garçon (France), Bettina Gier (Germany), Nathan Gillett (Canada), Luke Gregor (South Africa/Switzerland), Robert Jackson (USA), Vanessa Haverd (Australia), Jian He (USA), Forrest Hoffman (USA), Tatiana Ilyina (Germany), Chris Jones (UK), David Keller (USA/Germany), Xin Lan (USA), Charlotte Laufkötter (Switzerland), Andrew Lenton (Australia), Spencer Liddicoat (UK), Laura Lorenzoni (USA), Nicole Lovenduski (USA), Andrew MacDougall (Canada), Damon Matthews (Canada), Malte Meinshausen (Germany/Australia), Igor Mokhov (Russia), Vaishali Naik (USA), Intan Nurhati (Indonesia), Glen Peters (Norway), Julia Pongratz (Germany), Benjamin Poulter (USA), Ann Stavert (Australia), Parvadha Suntharalingham (UK), Kaoru Tachiiri (Japan), Rona Thompson (Norway), Hanqin Tian (USA), Jocelyn Turnbull (New Zealand), Xuhui Wang (China), Phil Williamson (UK)

Chapter Scientist:
Alice D. Lebehot (South Africa/France)

Review Editors:
Victor Brovkin (Germany/Russia), Richard Feely (USA), Jose Lara Lara (Mexico)

Date of Draft:
02/03/2020

Notes:
TSU compiled version

Executive Summary

Increasing accumulation of greenhouse gases (GHGs) in the atmosphere affects the Earth's radiative properties leading to global warming and other changes in the climate system. It is unequivocal that the main driver of changes in atmospheric GHG concentrations since the pre-industrial period is the direct emission of GHGs from human activities. However, the accumulation of GHGs in the atmosphere is determined by the balance of human GHG emissions and biogeochemical source-sink dynamics. This chapter assesses how biogeochemical processes affect the variability and trends of GHGs in the atmosphere. It identifies biogeochemical feedbacks that have led, or could lead to, a future acceleration, slowdown or abrupt transition in the rate of GHG accumulation in the atmosphere, and therefore, of climate change and its impacts. The chapter also assesses the remaining carbon budget for mitigating global warming, and large-scale consequences of carbon dioxide removal and solar radiation modification on biogeochemical cycles.

The human perturbation of the carbon and biogeochemical cycles

Global mean concentrations for GHGs (CO_2, CH_4 and N_2O) in 2018 correspond to an increase of about 46%, 157%, and 23% above pre-industrial levels. Current atmospheric concentrations of the three GHGs are higher than at any point in the last 800,000 years, and in 2018 reached 407 ppm of CO_2, 1859 ppb for CH_4, and 331 ppb for N_2O (*very high confidence*)**.** Current CO_2 concentrations are also unprecedented in the last 2 million years (*high confidence*). There have been times in Earth's history when CO_2 concentrations were much higher than at present, but multiple lines of evidence show with *medium confidence* that the rate at which CO_2 increased in the atmosphere during the Industrial Era has been at least 10 times higher than at any other time during the last 66 million years. This speed of change characterises the unprecedented nature of the current anthropogenic perturbation. {5.1.1, Figures 5.1, 5.2, Chapter 2 Section 2.2.3}

For global warming of no more than 2ºC, paleo records do not provide strong support for abrupt changes in the carbon cycle (*low confidence*). In response to climate forcing, paleoclimate records show changes of a magnitude larger than 100 ppm in atmospheric CO_2 over several millennia and abrupt smaller changes of about 10 ppm over centuries. However, the annual CO_2 emissions rates from any of these paleo changes are one order of magnitude slower than the contemporary perturbation from anthropogenic emissions suggesting caution when using the paleo record as an analogue for contemporary and future carbon-climate feedbacks. {Figure 5.2, 5.1.3.3}

Contemporary Trends of Greenhouse Gases

It is unequivocal that the increase of CO_2, CH_4, and N_2O in the atmosphere over the Industrial Era is the result of human activities. Multiple lines of evidence using atmospheric gradients, isotopes, and inventory data show that the atmospheric growth in GHGs since the beginning of the Industrial Era is due to the direct emissions from human activities (*high confidence*). During the last measured decade, average annual anthropogenic emissions of CO_2, CH_4, and N_2O, reached the highest levels in human history at 11.8 ± 0.8 PgC yr^{-1} (2009–2018), 348–392 Tg CH_4 yr^{-1} (2018–2017), and 4.2–11.4 TgN yr^{-1} (2007–2016), respectively (*high confidence*). {5.2.1.1, Figure 5.4, 5.2.2.1, 5.2.3.1}.

The fate of the carbon emitted from human activities during the decade of 2009–2018 (decadal average 11.0 PgC yr^{-1}) was: 44% accumulated in the atmosphere (4.9 ± 0.02 PgC yr^{-1}), 23% was taken up by the ocean (2.5 ± 0.6 PgC yr^{-1}) and 29% was removed by terrestrial ecosystems (3.5 ± 0.7 PgC yr^{-1}) (*high confidence*). The sum of these quantities has an imbalance of 0.4 PgC suggesting an underestimation of the sinks, or an overestimation of the emissions, or combination of both. Of the total anthropogenic CO_2 emissions, the combustion of fossil fuels was responsible for about 81–91% and the remaining from land use, land use change (e.g., deforestation, degradation, or peat drainage). {Table 5.1, 5.2.1.2, 5.2.1.5}

It is unequivocal that the ocean and land uptake of CO_2 have continued to grow as anthropogenic CO_2 emissions have increased over the past six decades. There is however *high confidence* that the combined rates of CO_2 removal by oceans and land per unit of excess anthropogenic CO_2 in the atmosphere has declined. Interannual and decadal variability of the ocean and land sinks indicate that these sinks are

sensitive to climate conditions and therefore to be sensitive to climate change (*high confidence*). {5.2.1.1, 5.2.1.3.1, 5.2.1.4.2, Figures 5.5, 5.8, 5.9, 5.11}.

Atmospheric CH_4 resumed its long-term growth trend in 2007 at an average rate of 7.1 ± 2.7 ppb yr^{-1} for the last decade (2009–2018), a growth rate that increased over the last measured 5-year period (2014–2018) (*high confidence*). The multi-decadal growth trend in atmospheric CH_4 is *very likely* dominated by anthropogenic activities, and there is *medium confidence* that the growth since 2007 is largely driven by emissions from fossil fuels and livestock for food production. The multi-year variability is predominantly driven by El Niño Southern Oscillation cycles during which biomass burning and wetland emissions play an important role. {5.2.2}

The growth rate of atmospheric N_2O has increased by 0.80 ± 0.07 ppb yr^{-1} since the 1990s, predominantly driven by the global increase in emissions from the expansion and intensification of agriculture (*high confidence*). Agricultural N_2O emissions have increased by about 80% since the early 1900s, and by 30% since the 1980s. There is *high confidence* that increased use of nitrogen fertiliser and manure contributed to about 70% of the increase during the 1980–2016 period (*high confidence*). {5.2.3}

Ocean Acidification and Ocean de-Oxygenation

Ocean Acidification is strengthening as a result of the ocean continuing to take up 23 ± 6% of the global anthropogenic CO_2 emissions (*high confidence*). This uptake is driving changes in seawater chemistry that results in the decrease of pH and associated reductions in the level of calcium carbonate minerals that form skeletons or shells of a variety of marine organisms. These trends of ocean acidification are becoming clearer globally with a very likely range of 0.017 to 0.027 decrease in pH units per decade since the late 1980s in the ocean surface layer (*high confidence*). Ocean acidification is spreading downward into the ocean interior over time, having already reached depths surpassing 2000 meters. {Figure 5.20, Figure 5.21, 5.3.2, 5.3.3}

Future Projections of Carbon Feedbacks on Climate Change

Oceanic and terrestrial carbon sinks will continue to grow due to increased atmospheric concentrations of CO_2 but emerging feedbacks will weaken those sinks (*high confidence*). It is *very likely* that the global ocean sink will stop taking up more CO_2 from the second part of the century under any emission scenario, at a level varying from about 4 to 6 PgC yr^{-1}. It is *very likely* that the land carbon sink will decline from mid-century onwards under high-emissions scenarios, but there is *low confidence* that the land will switch from being a sink to a source. Despite the wide range of model responses, the overall uncertainty in projections of atmospheric CO_2 by 2100 is dominated by uncertainties in emissions pathways rather than uncertainties in carbon-climate feedbacks. {5.4}

Paleo records indicate that carbon uptake from living organisms in the ocean is sensitive to climate and directly decreases the CO_2 ocean sink in periods of increased warming *(medium confidence).* Thus, future warming is expected to reduce carbon uptake by living organisms, with an overall decline in the ocean carbon uptake. The processes driving future changes in the magnitude and efficiency of this process remains *uncertain*. {5.4.4.2}

Additional radiative forcing arising from climate-CH_4 and climate-N_2O feedbacks at multidecadal to centennial timescales will be small (<10%) compared to the forcing from the direct anthropogenic GHG emissions in the 21st century (*medium to high confidence*). There is a large uncertainty about the magnitude and timing of the responses of each individual process involved. {5.4.7}

There is *high confidence* that thawing terrestrial permafrost will lead to carbon release, but the timing, magnitude and the relative roles of CO_2 versus CH_4 as feedback processes are known with *low confidence*. An ensemble of models project feedbacks due to CO_2 release from permafrost of 20 ± 13 PgC per degree of global warming by 2100. However, the incomplete representation of important processes such as abrupt thaw, combined with weak observational constraints, only allow *low confidence* in both the

magnitude of these estimates and in how linearly proportional this feedback is to the amount of global warming. Because of water-saturated soils and a lack of oxygen in thawing permafrost regions, part of the carbon is released as CH_4, which leads to the combined radiative forcing being larger than from if there were CO_2 emissions only. {5.4.3, 5.4.8}

The response of biogeochemical cycles to human-forcing may be abrupt at regional scales, and irreversible on decadal to century timescales (*high confidence*). The probability of crossing regional thresholds (e.g., forest dieback) increases with climate change, but there is no one particular threshold of global warming or atmospheric CO_2 identified in Earth system model projections. There is *medium confidence* that carbon-climate feedbacks can have a discernible effect on global atmospheric GHG concentrations, but do not lead to runaway changes over the next 100 years. Large uncertainties remain on the possibility of additional feedbacks not represented in many current models (e.g., fires) which could lead to departures from the current modelled trajectories. {5.4.8}

Carbon Budgets to Climate Stabilisation

Medium evidence with high agreement underpins the near linear relationship during the 21st century between cumulative CO_2 emissions and maximum global mean temperature increase caused by CO_2 for the range of temperatures included in the Paris Agreement (*medium confidence*). This relationship implies that halting global warming requires global net anthropogenic CO_2 emissions to become zero, and no significant warming occurs afterwards. The ratio between cumulative CO_2 emissions and the global surface air temperature increase they cause is assessed to be in the likely in the 1.0–2.2°C per 1000 PgC range (*high confidence*). This is slightly narrower than the 0.8–2.5°C per 1000 PgC assessment of AR5 due to a better integration of different lines of evidence. Additional Earth system feedbacks that operate on century timescales, such as permafrost thawing, have the potential to weaken the linearity of cumulative carbon-climate relationship. This could result in potentially higher warming, further warming after net zero CO_2 emissions are reached, or a path dependency of warming as a function of cumulative emissions of CO_2 (*low confidence)* {5.5.1}

There is *high confidence* that mitigation requirements for limiting warming to specific levels can be quantified using a carbon budget that relates cumulative CO_2 emissions to global mean temperature increase. Since pre-industrial times (1850), a total of 2,363 Gt (645 ±65 PgC) of anthropogenic CO_2 has been emitted. The remaining carbon budgets starting from the year 2020 for limiting warming to 1.5°C, 1.7°C, and 2.0°C with a probability of at least 66% are 310 $GtCO_2$, 570 $GtCO_2$, 960 $GtCO_2$, respectively. For a probability of at least 50%, the budgets for the same temperature targets are 390 $GtCO_2$, 690 $GtCO_2$, 1140 $GtCO_2$. Since AR5, estimates have been updated with methodological improvements, resulting in larger, yet consistent estimates. Starting from 2018 global CO_2 emissions of 42 $GtCO_2$ (11.5 ±0.9 PgC) and following a linear downward trajectory from today onwards, the values for a 50% probability of limiting warming to 1.5°C, 1.7°C or 2°C correspond to reaching net zero in about 20, 35, and 55 years, respectively. If a specific remaining carbon budget is exceeded, carbon dioxide removal will be required to return warming to a certain temperature level. {5.5.2, 5.6}

There is *medium confidence* that several factors, including estimates of historical warming, future emissions from thawing permafrost, and variations in projected non-CO_2 warming, affect the precise value of carbon budgets but do not change the need for global CO_2 emissions to decline to net zero to halt global warming. Geophysical uncertainties related to the climate response to non-CO_2 emissions and the transient temperature response to cumulative CO_2 emissions distribution result in an uncertainty of at least ±300 $GtCO_2$. Uncertainties in the level of historical warming result in a ±450 $GtCO_2$ uncertainty, and estimates may vary by ±250 $GtCO_2$ depending on median the amount of warming caused by past and future non-CO_2 emissions. The combined effect of all additional Earth system feedbacks – included in the estimates of the remaining carbon budget – is assessed to result in a reduction of the remaining carbon budget of about 135 $GtCO_2$ per °C of additional warming relative to the recent past (2010–2019, with a 1-sigma range of a ±135 $GtCO_2$). The release of CO_2 from thawing permafrost alone is estimated to be responsible for about 75 $GtCO_2$ (±50 $GtCO_2$, 1-sigma range) per degree of additional warming of this overall range. Due to limited studies, the assessment of the size of these contributions has *very low confidence.* Despite the large

uncertainties surrounding the understanding and quantification of the impact of these processes, they represent identified additional risk factors that scale with additional warming and mostly increase the challenge of limiting warming to specific temperature thresholds. {5.4, 5.5.2}

Biogeochemical implications of Carbon Dioxide Removal and Solar Radiation Modification

There is *high confidence* that land- and ocean-based Carbon Dioxide Removal (CDR) methods have the potential to sequester CO_2 from the atmosphere. However, a given amount of CO_2 sequestered by CDR results in a smaller amount of CO_2 reduction in the atmosphere due to the redistribution of CO_2 between carbon pools (e.g., degassing from the ocean) and Earth system feedbacks (*medium confidence*). The effectiveness of CDR, defined as the reduction in atmospheric CO_2 per unit CO_2 sequestered, is largely independent of the magnitude and rate of CDR but varies strongly with the background atmospheric CO_2 concentration from which CDR is applied (*medium confidence*). Due to asymmetries in the climate-carbon cycle response, CO_2 emissions are more effective at raising atmospheric CO_2 than CO_2 removals are at lowering atmospheric CO_2, particularly for large emissions/removals (>100 PgC). This asymmetry implies that an extra amount of CDR is required to offset a positive emission of a given magnitude (*low confidence*). {5.6.2.1, Figures 5.32, 5.34, 5.36}

The climate-carbon cycle response to the removal of CO_2 from the atmosphere (negative emissions) is not always equal and opposite to the response to positive emissions (*medium confidence*). Model simulations show a symmetric response of the carbon cycle for pulse emissions and removals of ±100 PgC, but the response becomes increasingly asymmetric for higher pulse emissions and removals. The asymmetry originates largely from state-dependencies and nonlinearities in the ocean and will require proportionally larger removal efforts as the reliance on CDR methods increases. {Figure 5.32, 5.6.2.1}

The sequestration potential of many land- and ocean-based CDR methods is weakened by associated Earth system feedbacks by decreasing either the land or ocean carbon uptake or through impacts on climate (*medium confidence*). CDR methods can have positive or negative biogeochemical (e.g., non-CO_2 emissions) and biophysical side-effects (e.g., changes in hydrology or surface reflectivity) (*high confidence*) and other side-effects related to water, food and biodiversity (*high confidence*). The level of confidence in the direction and magnitude of multiple side effects of CDR methods varies from *low* to *medium* and is often project and region specific. {5.6.2.2}

Solar Radiation Modification (SRM) is *likely* to reduce the atmospheric CO_2 concentration by enhancing global land and ocean sinks. SRM acts to cool the planet relative to unmitigated climate change, which reduces plant and soil respiration, and also reduces the negative impacts of warming on ocean carbon uptake (*medium confidence*). SRM will not counteract ocean acidification. The rapid termination of SRM, if required, would cause rapid increase in global warming with return of positive and negative effects on carbon sinks (*low confidence*) {5.6.3}

5.1 Introduction and the Paleo Context

Changes in the abundance of greenhouse gases (GHGs) in the atmosphere play a large role in determining the Earth's radiative properties and its climate (see Chapters 2 and 7). Since 1950, the increase in atmospheric GHG has been the dominant cause of the human-induced climate change (see Section 3.3). While the main driver of changes in atmospheric GHGs over the past 200 years is the direct emissions from human activities, the net accumulation of GHGs in the atmosphere is also controlled by biogeochemical source-sink dynamics that exchange quantities between multiple carbon reservoirs on land, oceans and atmosphere. For instance, the combustion of fossil fuels and land use change for the period 1750–2018 have released an estimated 675 ± 80 PgC (1 PgC = 10^{15} g of carbon) to the atmosphere of which less than half remains in the atmosphere today (Friedlingstein et al., 2019). This underscores the large role of terrestrial and ocean carbon dioxide (CO_2) sinks in regulating the concentration of atmospheric CO_2 (Ballantyne et al., 2012; Li et al., 2016b; Le Quéré et al., 2018a; Gruber et al., 2019a;).

The biogeochemical controls of GHGs is a central motivation for this chapter, which identifies biogeochemical feedbacks that have led or could lead to a future acceleration, slowdown or abrupt transitions in the rate of GHG accumulation in the atmosphere, and therefore of climate change. Other motivations are to constrain better the remaining carbon budgets for climate stabilization in light of the above, and the responses of the carbon cycle to atmospheric CO_2 removal which is embedded in many of the mitigations scenarios to achieve the goals of the Paris Agreement.

The chapter covers three dominant GHGs in the human perturbation of the Earth's radiation budget for which high quality records exist: carbon dioxide (CO_2), methane (CH_4) and nitrous oxide (N_2O).

Section 5.1 (this section) provides the time context on how unique current and future scenarios of GHG atmospheric concentrations and growth rates are in the Earth's history. It also introduces the main processes involved in GHGs-climate feedbacks followed by an assessment of what can be learned from the paleo record towards a better understanding of contemporary and future GHG-climate dynamics and their response to different mitigation trajectories.

Section 5.2 covers the historical (<200 years) and contemporary (1959-2018, as well as more recent time periods) state of the carbon cycle and other biogeochemical cycles, including the global budgets of CO_2, CH_4, and N_2O. This period represents the Industrial Era (since c.f. 1750) and the section particularly emphasises the last 60-year period for which high-resolution observations are available. Significant advances have taken place since IPCC AR5, particularly in constraining the annual to decadal variability of the ocean and land carbon sinks and what that reveals about the sensitivity of carbon pools to current and future climate changes. There are also new isotopic and other data constraints on the causes of the observed CH_4 trends over the past two decades, and a significantly more comprehensive and better constrained global N_2O budget than in previous assessments.

Section 5.3 covers the uptake of CO_2 by the oceans that leads to ocean acidification, including the paleo, historical and future trends in ocean acidification, with consequences for biogeochemical cycles and marine life. The impacts on marine life are assessed in AR6-WG II. The section also assesses the trend in de-oxygenation of the oceans due to warming, increased stratification of the surface ocean and slowing of the meridional overturning circulation, which affects the ventilation of the ocean interior, the biological carbon pump, and pH in the ocean interior. Growing hypoxia zones (i.e., low O_2 zones) in the tropical and sub-tropical oceans linked to changing ventilation are also significant sources of N_2O emissions as well as important influences on Eastern Boundary Upwelling systems where they can amplify ocean acidification and the production of CH_4 and N_2O.

Section 5.4 covers the future projections of biogeochemical cycles and their feedbacks to the climate system fully utilizing the database the Coupled Model Intercomparison Project Phase 6 (CMIP6). Since AR5, Earth system models have made progress towards including more complex carbon cycle and associated biogeochemical processes that enable exploring a range of possible future carbon-climate feedbacks and their impacts in the climate system. Uncertainties and the limits of our models to predict future dynamics for

GHG emissions trajectories are covered. The section also assesses new understanding on processes involved in carbon-climate feedbacks and the possibility for rapid and abrupt changes brought about non-linear dynamics.

Section 5.5 covers the development of the total and remaining carbon budgets to climate stabilisation targets and the associated transient climate response to cumulative CO_2 emissions. These advances were based on the finding that the excess global warming compared to the pre-industrial time was quasi linearly related with the historical cumulative CO_2 emissions. The section shows the progress made since the AR5 and the 1.5°C Special Report (IPCC, 2018a), particularly on key components required to estimate the remaining carbon budget. These components include the transient response to cumulative emissions of CO_2, the zero emission commitment, the projected non-CO_2 warming, and the unrepresented Earth system feedbacks.

Section 5.6 assesses the biogeochemical implications of Carbon Dioxide Removal (CDR, also known as negative emissions) and Solar Radiation Modification (SRM). CDR seeks to directly reverse the effects of GHGs emissions by removing CO_2 from the atmosphere either directly or by enhancing terrestrial, marine or geological carbon sinks. SRM attempts to offset the climate effects of GHGs emissions, by intentional manipulation of planetary solar absorption to counter climate change. The potential capacity to delivery atmospheric reductions and the socio-economic feasibility of such options are assessed in detail in IPCC AR6 WGIII.

Finally, Section 5.7 highlights the knowledge gaps that emerged from this assessment, which would have strengthened the assessment reported in this chapter had those gaps not existed. These are important research areas for the future. Please refer to Figure 5.0 for the Chapter 5 overview.

[START FIGURE 5.0 HERE]

Figure 5.0: Chapter overview figure. [Placeholder: This Figure numbering will be changed to 5.1 for the FGD]

[END FIGURE 5.0 HERE]

5.1.1 Time context of the human perturbation of biogeochemical cycles

Measurements in air samples extracted from bubbles and clathrate crystals in ice cores and collected from the ambient atmosphere show that concentrations of three dominant well-mixed GHGs, CO_2, CH_4 and N_2O, began to rapidly increase at the onset of the Industrial Era around 1750 (Figure 5.1). Tabulated global mixing ratios of all well mixed GHGs, including CO2, CH4, and N2O, from 1750-2018 are provided in Annex V.

Atmospheric concentrations of the three GHGs reached 405 ppm for CO_2, 1850 ppb for CH_4, and 330 ppb for N_2O in 2017. These concentrations correspond to 46%, 156%, and 22% increase above pre-industrial levels, respectively (Section 5.2). Using CO_2, CH_4, and N_2O proxy-data from ice cores, it can be established with *high confidence* that current concentrations of the three GHGs are the highest in the last 800,000 years (Figure 5.1), and also unprecedented in more than 2 million years for CO_2 concentrations (*high confidence*, Martínez-Botí et al., 2015b), see Annex II for data sources).

[START FIGURE 5.1 HERE]

Figure 5.1: Atmospheric concentrations of CO_2, CH_4 and N_2O in air bubbles and clathrate crystals in ice cores, dated period from 800,000 BCE to 1990 CE (note the variable x-axis range and tick mark intervals for the 3 columns). Ice core data is over-plotted by atmospheric observations from 1958 to present for CO_2, from 1984 for CH_4 and from 1994 for N_2O. The linear growth rates for different time periods (800,000–0 BCE, 0–1900 CE and 1900–2017 CE) are given in each panel. For the BCE period, mean rise and fall rates are calculated for the individual slopes between the peaks and troughs, which are given in the panels in left

column. The data for BCE period are used from the Vostok, EPICA, Dome C and WAIS ice cores (Petit et al., 1999; Monnin, 2001; Pépin et al., 2001; Raynaud et al., 2005; Siegenthaler et al., 2005; Loulergue et al., 2008; Lüthi et al., 2008; Schilt et al., 2010a). The data after 0–yr CE are taken mainly from Law Dome ice core analysis (MacFarling Meure et al., 2006). The surface observations for all species are taken from NOAA cooperative research network (Dlugokencky and Tans, 2019), where ALT, MLO and SPO stand for Alert (Canada), Mauna Loa Observatory, and South Pole Observatory, respectively. BCE = Before Current Era, CE = Current Era.

[END FIGURE 5.1 HERE]

Further back in time (see Cross-Chapter Box 2.1), CO_2 concentrations reached much higher levels than present day. Possibly the best studied interval in the past that provides some level of comparison with the current anthropogenic increase in CO_2 emissions relates to the Paleocene-Eocene Thermal Maximum (PETM), 55.8 Myr ago. Atmospheric CO_2 concentrations increased from about 800 to about 2200 ppm (not shown in Figure 5.2a) in 4–20 kyr as a result of pulsed release of geological carbon to the ocean–atmosphere system (Zeebe et al., 2016; Gutjahr et al., 2017; Turner, 2018).

The PETM was also associated with pronounced, widespread ocean acidification, with surface ocean pH transiently decreasing by 0.15–0.30 units (Penman et al., 2014; Gutjahr et al., 2017; Babila et al., 2018) with large consequences for many terrestrial and marine ecosystems (McInerney and Wing, 2011). These observations highlight that the rate of CO_2 emissions is crucial in determining the severity of adverse consequences to ocean systems such as ocean acidification (caused by the absorption of CO_2) and de-oxygenation (associated with warming ocean temperatures). [Placeholder: Discussion of pH being the metric for growth rates]

Multiple lines of evidence show that the rates of CO_2 emissions to the atmosphere during the Industrial Era have been by at least a factor of 10 higher than at any other time of the last 66 million years (*medium confidence*) (Zeebe and Zachos, 2013; Zeebe et al., 2016) showing the unprecedented pace of change of the current anthropogenic perturbation (Figure 5.2, Chapter 2).

The last ~50 million years have been characterised by a gradual decline in atmospheric CO_2 levels at a rate of ~16 ppm Myr^{-1} (Foster et al., 2017; Gutjahr et al., 2017). The most recent time interval when atmospheric CO_2 concentration was as high as 1000 ppm (i.e., similar to the end-of 21st century projection for the high-end emission scenario RCP8.5) was around 33.5 million years ago, prior to the Eocene-Oligocene transition (Zhang et al., 2013; Anagnostou et al., 2016). Atmospheric CO_2 levels then reached a critical low threshold (1000–750 ppm, (DeConto et al., 2008)) that was necessary to develop regional ice-sheets on Antarctica.

The most recent interval characterised by atmospheric CO_2 levels similar to modern (i.e. 400–450 ppm) was the mid-to-late Pliocene (3–3.3 Myr, (Martínez-Botí et al., 2015a)) after which atmospheric CO_2 concentration declined gradually at a rate of 40 ppm Myr^{-1}, allowing for major advances in Northern Hemisphere ice sheets, 2.7 Myr ago (Sigman et al., 2004; DeConto et al., 2008).

During the period 800,000–1 BCE, periodic oscillations in GHG concentrations are forced by orbital modulation as per the Milankovich theory, reinforced by feedbacks internal to the Earth climate system. Concentrations of CO_2 during that time period oscillated cyclically between 160–180 ppm and 300 ppm (Lüthi et al., 2008) (Figure 5.1). During the last deglaciation, growth rates of CO_2 concentrations peaked at 0.12 ppm yr^{-1} (Marcott et al., 2014), 6 times smaller when compared to the average growth rate of CO_2 emissions for the 20th Century (0.71 ppm yr^{-1} (Joos and Spahni, 2008)), and 20 times smaller when compared with the growth rate of 2.3 ppm yr^{-1} for the last decade (2009–2018) (Dlugokencky and Tans, 2019). The rise and decline rates for each of the glacial and interglacial peaks suggests that both the high concentrations at present and the growth rates of atmospheric accumulation of CO_2, CH_4, and N_2O in the past century are unprecedented relative to the past 800 kyr.

For the period with the highest resolution of paleo and atmospheric records, data show growth rates of atmospheric CO_2 were about 100 times faster *(medium confidence)* during the period of 1900–2017

compared to that during the period of 0–1900 (Figure 5.1).

The acceleration in the GHGs atmospheric growth over the past century is consistent with the intensification of industrial and agricultural activities. However, beyond a causal relationship, there are multiple lines of independent evidence that make the relationship between growth of excess GHGs and human activities *virtually certain* (see Sections 5.2.1.1, 5.2.2.1, 5.2.3.1).

[START FIGURE 5.2 HERE]

Figure 5.2: CO_2 concentrations (a) and growth rates (b) for the past 60 million years to 2100 using RCP2.6 and RCP8.5. Concentrations data as in Figure 5.1 and data prior to 800 Kyr from (Foster et al., 2017). Inserts in (b) shows growth rates at the scale of the sampling resolution.

[END FIGURE 5.2 HERE]

5.1.2 The Physical and Biogeochemical Processes in Carbon-Climate feedbacks

The influence of anthropogenic CO_2 emissions and emission scenarios on the carbon – climate system is primarily driving the ocean and terrestrial sinks as major negative feedbacks (β) that determine the atmospheric CO_2 levels, that then drive climate feedbacks through radiative forcing (γ) (Figure 5.3) (Friedlingstein et al., 2006; Jones et al., 2013b). Biogeochemical feedbacks follow as an outcome of both carbon and climate forcing on the physics and the biogeochemical processes of the ocean and terrestrial carbon cycles (Figure 5.3) (Ciais et al., 2013). Together, these carbon–climate feedbacks can then amplify or suppress climate change by altering the rate at which CO_2 builds up in the atmosphere through changes in the land and ocean sinks (Figure 5.3) (Jones et al., 2013b; Raupach et al., 2014; Williams et al., 2019). These changes depend on the, often non-linear, interaction of the drivers (CO_2 and climate) and processes in the ocean and land as well as the emission scenarios (Figure 5.3; Sections 5.4 and 5.6) (Raupach et al., 2014; Schwinger et al., 2014; Williams et al., 2019). There is *high confidence* that carbon – climate feedbacks and their century scale evolution may then play a critical role in two linked climate metrics that have significant climate and policy implications: 1) the fraction of anthropogenic CO_2 emissions that remains in the atmosphere, the so called airborne fraction of CO_2 (AF) (Figure 5.3, Section 5.2.1.1, Figure 5.5, FAQ 5.1), and 2) the quasi-linear trend characteristic of the transient temperature response to cumulative CO_2 emissions (TCRE) (MacDougall, 2016; Williams et al., 2016; Section 5.5) and other GHGs (CH_4 and N_2O). This chapter assesses the implications of these issues from a carbon cycle processes perspective (Figure 5.3) in Sections 5.2 (historical and contemporary), 5.3 (changing carbonate chemistry), 5.4 (future projections), 5.5 (remaining carbon budget) and 5.6 (response to CDR).

The airborne fraction is an important constraint for adjustments in carbon-climate feedbacks and reflects the partitioning of CO_2 emissions between reservoirs by the negative feedbacks on land (29%), oceans (24%), which dominate in the historical period (Figure 5.3) (Friedlingstein et al., 2019). During the period 1959–2018, the airborne fraction has largely followed the growth in anthropogenic CO_2 emissions with a mean of 44% and a large interannual variability (Ballantyne et al., 2012; Ciais et al., 2019; Friedlingstein et al., 2019; Section 5.2.1.5; Table 5.1). The negative feedback to CO_2 concentrations is associated with its impact on the air-sea and air-land CO_2 exchange through strengthening of pCO_2 gradients as well as the internal processes that enhance uptake: the CO_2 fertilisation effect on gross primary production and the buffering capacity of the ocean (Section 5.4.1–5.4.4).

Positive and negative climate and carbon feedbacks involve 1) fast processes on land and oceans at time scales from minutes to years such as photosynthesis, soil respiration, and net primary production, shallow ocean physics, air-sea fluxes, and 2) slower processes taking decades to millennia such as changing ocean buffering capacity, ocean ventilation, vegetation dynamics and peat formation and decomposition (Figure 5.3) (Ciais et al., 2013; Forzieri et al., 2017; Williams et al., 2019). Depending on the particular combination of driver process and response dynamics, they behave as positive or negative feedbacks that amplify or

dampen the magnitude and rates of climate change (Cox et al., 2000; Friedlingstein et al., 2003, 2006; Hauck and Völker, 2015; Williams et al., 2019) (black and magenta arrows in Figure 5.3; Section 5.2.1.5; Table 5.1).

Carbon cycle feedbacks co-exist with climate (heat and moisture) feedbacks, which together drive contemporary (Section 5.2) and future (Section 5.4) carbon-climate feedbacks (Williams et al., 2019). The excess heat generated by radiative forcing from an increasing concentration of atmospheric CO_2 and other GHGs is itself partitioned into the ocean (>90%) and the residual balance partitioned between atmospheric, terrestrial and ice melting (blue arrows: Figure 5.3; Chapter 7; Frölicher et al., 2015). The combined effect of these two large scale negative feedbacks of CO_2 and heat are reflected in the TCRE (Section 5.5; Chapter 7), which points to a quasi-linear and quasi-emission-path independent relationship between cumulative emissions of CO_2 and global warming. which is used as the basis to estimate the remaining carbon budget (Section 5.5) (MacDougall and Friedlingstein, 2015). This climate metric maybe related to carbon and climate feedbacks processes but there is still *low confidence* on the relative roles and importance of the ocean and terrestrial carbon processes on TCRE variability and uncertainty on decadal to centennial time scales (Jones and Friedlingstein, submitted; Katavouta et al., 2018, 2019; MacDougall, 2016; MacDougall et al., 2017; Williams et al., 2017a) (Section 5.5; Chapter 7; Chapter 9).

[START FIGURE 5.3 HERE]

Figure 5.3: Schematic summarizing the key compartments, processes and pathways that govern historical and future carbon concentration and carbon–climate feedbacks through both terrestrial and ocean systems. Central to this is the influence of both carbon (dotted arrows) and climate (dashed arrows) feedbacks on the evolution of the GHG burden in the atmosphere and the airborne fraction of anthropogenic CO_2, which drives the Earth's energy imbalance that is partitioned between the ocean (93%) and the terrestrial residual (7%). The ocean dominates the heat feedback in respect of the excess heat from increasing atmospheric CO_2. The airborne fraction that drives this historical climate forcing (about 44%) is largely regulated by the negative feedback of ocean (22%) and terrestrial (29%) sinks that partition anthropogenic CO_2 (black arrows) in ocean and terrestrial domains (magenta) and result in negative feedbacks (magenta)(partition excludes the estimated imbalance of 0.5 PgC: see Table 5.1). Positive feedback processes (purple arrows) although mostly weak in the historical period, are *likely* to strengthen in the coming decades and are influenced by both carbon and climate forcing simultaneously (purple). Additional biosphere processes have been included that have an, as yet uncertain feedback bias, especially at regional and global scales (brown arrows). Although this schematic is built around CO_2, the dominant GHG, some of the same processes also influence the fluxes of CH_4 and N_2O from the terrestrial and ocean systems. Those are noted as they contribute to the total radiative forcing.

[END FIGURE 5.3 HERE]

The combined effects of climate and CO_2 concentration feedbacks on the global carbon cycle are projected by Earth system models to modify both the processes and natural reservoirs of carbon on a regional and global scale that may result in feedbacks (purple arrows in Figure 5.3) that could weaken the major terrestrial and ocean sinks and disrupt both the airborne fraction and TCRE on those time scales.

5.1.3 Paleo trends and feedbacks

Paleoclimatic records extend beyond the variability of recent decadal climate oscillations and provide an independent perspective on feedbacks between climate and carbon cycle dynamics. These past changes tended to be slower than the current anthropogenic ones, so they cannot provide a direct comparison. Nonetheless, they can help appraise sensitivities and point toward potentially dominant mechanisms of change.

Polar ice cores represent the only climatic archives from which past greenhouse concentrations can be directly measured. Major GHGs, methane (CH_4), nitrous oxide (N_2O) and carbon dioxide (CO_2) generally co-vary, on both orbital and millennial timescales (Schilt et al., 2010b), with consistently higher atmospheric concentrations during warm intervals of the past, suggesting a strong sensitivity to climate (Figure 5.1). Detailed investigations using rapidly accumulating ice cores reveal that temperature rise preceded the increase in atmospheric GHG concentrations, indicating that greenhouse forcing amplified subtle, orbitally driven climate change (Shakun et al., 2012) (*high confidence*). Although orbitally induced warming may have kickstarted the last glacial termination, global surface temperature reconstructions support a correlation with atmospheric partial pressure of CO_2 (pCO_2) with greenhouse forcing leading global warming (Shakun et al., 2012; Marcott et al., 2014) (*high confidence*). The centennial-scale lag of global temperature behind CO_2 is consistent with the thermal inertia of the climate system associated with ocean heat uptake/release and ice sheet dynamics. Atmospheric growth rates inferred for the three major greenhouse gases, CH_4, N_2O and CO_2, were consistently one order of magnitude lower than their respective anthropogenic growth rates (Figure 5.1) for the time period spanning historical to geological timescales (*medium confidence*).

Major pre-industrial sources of CH_4 include wetlands (including subglacial environments), biomass burning and methane hydrates (clathrates) (Bock et al., 2010, 2017; Lamarche-Gagnon et al., 2019). Stable isotope analyses on CH_4 extracted from Antarctic ice cores, suggest that CH_4 emissions were predominantly associated with boreal and tropical wetlands as well as biomass burning across the last glacial termination (Bock et al., 2017) (*high confidence*), yet a detailed source apportionment remains inconclusive. Changes in these sources were steered by variations in temperatures and precipitation as modulated by insolation, local sea-level changes and monsoon intensity (Bock et al., 2017). Geological emissions, related to the destabilization of fossil CH_4 hydrates buried in continental margins and boreal permafrost as a result of sudden warming appear negligible (Bock et al., 2017; Petrenko et al., 2017) (*medium confidence*).

Pre-industrial atmospheric N_2O emissions were regulated by microbial production in marine and terrestrial environments as well as by photochemical removal in the stratosphere (Schilt et al., 2014; Fischer et al., 2019). N_2O is produced through nitrification and denitrification processes on land and in the ocean, with nitrification dominating in marine environments (Battaglia and Joos, 2018b). Stable isotope analysis on N_2O extracted from Antarctic and Greenland ice reveal that marine and terrestrial emissions increased by 0.7 ± 0.3 and 1.7 ± 0.3 TgN, respectively, across the last glacial termination (Fischer et al., 2019) (*medium confidence*). During abrupt northern hemisphere warmings, terrestrial emissions responded rapidly to the northward displacement of the inter tropical convergence zone (ITCZ) associated with the resumption of the Atlantic Meridional Overturning Circulation (Fischer et al., 2019). About 90% of these step increases occurred rapidly, possibly in less than 200 years (Fischer et al., 2019). In contrast, marine emissions increased more gradually, modulated by global ocean circulation reorganisation.

Atmospheric CO_2 concentrations are regulated by rapid exchange with terrestrial and surface ocean carbon reservoirs. The dominant process controlling atmospheric CO_2 concentrations on millennial to orbital timescales involves exchange with the voluminous deep ocean reservoir (Schmitt et al., 2012; Bauska et al., 2016; Jaccard et al., 2016; Rae et al., 2018). Stable carbon isotope measurement on CO_2 covering the transition from the last ice age to the Holocene highlight that the reconstructed CO_2 rise was primarily related to the release of CO_2 from the ocean interior and rapid oxidation of organic carbon on land (Bauska et al., 2016; Schmitt et al., 2012) (*medium confidence*) (Section 5.1.1).

CH_4 and N_2O contribute approximately equally to the change in radiative forcing across the last glacial cycle, but their relative contribution is of secondary importance compared to the radiative forcing of CO_2, which alone represents more than 80% of the total change in radiative forcing across the last glacial termination (Schilt et al., 2014; Köhler et al., 2017)

5.1.3.1 Glacial-interglacial changes

The high-resolution Antarctic ice core record covering the past 800,000 years provides an important archive to explore the carbon-climate feedbacks prior to human perturbations (Brovkin et al., 2016). Modelling work

suggests that the carbon cycle contributed to globalise and amplify changes in orbital forcing, which are pacing glacial-interglacial climate oscillations (Ganopolski and Brovkin, 2017), with ocean biogeochemistry and physics, terrestrial vegetation, peatland and permafrost all playing a role in modulating the concentration of atmospheric GHGs prior the Industrial Era.

Under the generally colder glacial climate, characterised by atmospheric CO_2 concentrations 90 ± 10 ppm (–190 ± 20 GtC) lower than pre-industrial levels (280 ppm) (Lüthi et al., 2008), interactions between climate and the global carbon cycle were arguably different.

During past ice ages, a generally colder climate, associated with a weaker hydrological cycle contributed to a substantial decline of the land biosphere carbon inventory, in particular in boreal peatlands (Treat et al., 2019). Early estimates assessing the glacial decrease in the terrestrial biosphere C stock vary widely, yet, recent, and arguably more realistic calculations cluster around 300–600 PgC (Ciais et al., 2012; Peterson et al., 2014; Menviel et al., 2017), possibly 850 PgC when accounting for ocean-sediment interactions and burial (Jeltsch-Thömmes et al., 2019) (*medium confidence*), a considerable contraction when compared to the modern land biosphere stock (4000 GtC). The large uncertainty reflects a yet limited understanding on how glacially perturbed nutrient fluxes and soil dynamics as well as largely exposed shelf areas in the tropics as a result of lowered sea-level altered carbon inventories.

Vegetation regrowth and increased precipitation in wetland regions associated with the mid-deglacial Northern Hemisphere warming (referred to as the Bølling/Allerød warm interval, 14.7–12.7 kyr BP), in particular in the (sub)tropics, accounts for large increases in both CH_4 and N_2O emissions to the atmosphere (Schilt et al., 2014; Bock et al., 2017). Rapid warming of high northern latitudes has also been proposed to have destabilised permafrost, potentially liberating vast quantities of labile organic carbon to the atmosphere (Köhler et al., 2014; Crichton et al., 2016; Winterfeld et al., 2018).

Recent estimates suggest deep-sea CO_2 storage during the last ice age exceeded modern values by as much as 750–950 PgC (Skinner et al., 2015; Buchanan et al., 2016; Anderson et al., 2019; Jacobel et al., 2020) (*medium confidence*), sufficient to balance the removal of carbon from the atmosphere and the terrestrial biosphere reservoirs combined. A combination of increased CO_2 solubility associated with generally colder oceanic temperatures, increased oceanic residence time of CO_2 (Skinner et al., 2017), altered oceanic alkalinity (Yu et al., 2010a; Cartapanis et al., 2018; Hoogakker et al., 2018); and a generally more efficient marine biological carbon pump (Galbraith and Jaccard, 2015; Galbraith and Skinner, 2020; Yu et al., 2019) conspired to partition CO_2 into the ocean interior (Anderson et al., 2019) (*medium confidence*). Glacial atmospheric CO_2 concentrations were kept to a temporally consistent lower level of 190 ± 7 ppm, as a result of CO_2 limitation of photosynthesis, either directly or via CO_2-limitation on N_2 fixation (Galbraith and Eggleston, 2017).

The gradual increase in atmospheric CO_2 from the last ice age into the Holocene was punctuated by three sudden, sub-millennial 10–15 ppm increments (Marcott et al., 2014). The early deglacial release of remineralised carbon from the ocean abyss coincides with the resumption of the Southern Ocean overturning circulation and the concomitant reduction in the efficiency of the marine biological carbon pump, associated, in part, with dwindling Fe fertilization (Skinner et al., 2010; Ferrari et al., 2014; Martinez-Garcia et al., 2014; Gottschalk et al., 2016; Jaccard et al., 2016; Rae et al., 2018) (*medium confidence*). The two subsequent pulses, centred 14.8 and 12.9 kyr ago, are associated with enhanced air-sea gas exchange in the Southern Ocean and rapid oxidation of land carbon owing to the resumption of AMOC and associated southward migration of the ITCZ (Bauska et al., 2016; Marcott et al., 2014). Enhanced mid-ocean ridge magmatism and/or hydrothermal activity modulated by sea-level rise has recently been hypothesised to have contributed to the deglacial CO_2 rise (Crowley et al., 2015; Lund et al., 2016; Huybers and Langmuir, 2017; Stott et al., 2019b). While geological carbon release may have affected the ocean's radiocarbon budget (Ronge et al., 2016; Rafter et al., 2019; Stott et al., 2019a), it remains yet unclear whether mantle CO_2 degassing contributed substantially to the deglacial CO_2 rise (Roth and Joos, 2012) (*low confidence*).

The deglacial increase in Atlantic overturning contributed to transfer the locus of remineralised carbon to intermediate depths (Schmittner and Galbraith, 2008; Jaccard and Galbraith, 2012), which contributed to

reduce subsurface dissolved oxygen concentrations thereby substantially increasing marine N_2O emissions (Schilt et al., 2014; Fischer et al., 2019). However, details in the simulated response of the marine carbon cycle and atmospheric CO_2 concentrations to changes in ocean circulation depend to a large degree on model parametrization (Gottschalk et al., 2019).

Simulation of Earth Models of Intermediate Complexity with coupled glacial-interglacial climate and the carbon cycle were able to reproduce first-order changes in the atmospheric CO_2 content for the first time (Brovkin et al., 2012; Ganopolski and Brovkin, 2017). The most important processes accounting for the full deglacial CO_2 amplitude in the model include solubility changes, changes in oceanic circulation and marine inorganic carbonate chemistry. The impact of the terrestrial carbon cycle, variable volcanic outgassing, and the temperature dependence on the oceanic remineralization length scale contribute less than 15 ppm CO_2 between the glacial and interglacial parts of the cycles.

5.1.3.2 Holocene changes

The pre-industrial Holocene (11.7 kyr–1750) was characterised by relatively stable global climate conditions, despite changes in the seasonal and latitudinal distributions of incoming solar radiation. The Early Holocene (11.7–5 kyr) warmth is followed by about 0.7°C cooling through the middle to late Holocene (<5 ka), culminating in the coolest temperatures of the Holocene during the Little Ice Age, about 200 years ago. This cooling could be associated with about 2°C change in the North Atlantic, possibly linked to a slow-down of the Atlantic meridional overturning circulation, although recent paleoceanographic evidence report stable and vigorous Atlantic circulation throughout the Holocene (Hoffmann et al., 2018; Lippold et al., 2019). Parallel increase in Southern Ocean circulation and upwelling intensity (Studer et al., 2018), possibly promoted by stronger westerly winds (Saunders et al., 2018), could account for the 20 μatm increase in atmospheric pCO_2 reported for the pre-industrial Holocene.

Peat reservoirs have gradually increased over the Holocene, resulting in long-term sequestration of carbon (Frolking and Roulet, 2007; Nichols and Peteet, 2019). Rates were higher under relatively high temperatures during the early and middle Holocene than for the cooler late Holocene (Loisel et al., 2014; Stocker et al., 2017) as a result of rapid peat growth during times of ice-sheet retreat and strong seasonality, contributing to maintain Holocene atmospheric CO_2 concentrations changes within limited bounds. Recent stock estimates suggest that northern peatlands could have sequestered between 545−1055 GtC during the Holocene (Nichols and Peteet, 2019) (*low confidence*). Increased methanogenesis in tropical wetlands during the early Holocene contributed only marginally to the atmospheric CH_4 inventory (Zheng et al., 2019). Stable carbon isotope values measured on CO_2 extracted from Antarctic ice are consistent with a parallel uptake of carbon by the land biosphere and carbon release from the ocean as a result of enhanced outgassing and carbonate compensation (Elsig et al., 2009; Menviel and Joos, 2012).

5.1.3.3 Past to understand the future

The geological record of past climate variability offers a unique opportunity to document how Earth system processes and feedbacks operated beyond the instrumental record and are fundamental to our ability to adequately project future climate and environmental change. These records have provided key insights in the processes involved in past dynamics of biogeochemical cycles and in the development of understanding and modelling capability.

Paleoclimatic reconstructions reveal profound ecosystem disturbances associated with pulsed CO_2 emissions to the ocean and atmosphere reservoirs in the geologic past, with multiple instances of rapid increases of 10 to 15 ppm of CO_2 in less than two centuries during the last glacial termination (Marcott et al., 2014). Importantly, the CO_2 emission rates from paleo records show to be one order of magnitude slower that the current anthropogenic change (Figure 5.1) (*medium confidence*) raising concerns about future ecological changes on land and related to ocean acidification (Gattuso et al., 2015) and ocean de-oxygenation (Gruber, 2011).

A recent observation-based synthesis of past intervals with temperatures within the range of projected future warming suggest that for warming of no more than 2°C there is low probability of crossing a tipping-point in the climate system leading to large, unpredictable changes in the state of the system (Fischer et al., 2018) (*medium confidence*). This synthesis reveals however, that substantial regional impact can occur, in particular in high-latitude environments, which were more severely affected by warming owing to polar amplification.

5.2 Historical Trends, Variability and Budgets of CO_2, CH_4, and N_2O

This section assesses the trends and variability in atmospheric accumulation of the three main GHGs-CO_2, CH_4 and N_2O, its ocean and terrestrial sources and sinks as well as their budget during the historical period (1750–2018). Emphasis is placed on the more recent contemporary period (1959–2018) where understanding is increasingly better constrained by atmospheric, ocean and land observations. The section also assesses our increasing understanding of the anthropogenic forcing and processes driving the trends, as well as how variability at the seasonal to decadal scales provide insights on the mechanism governing long term trends and emerging biogeochemical-climate feedbacks as well as their regional characteristics.

5.2.1 CO_2: Trends, Variability and Budget

5.2.1.1 Atmosphere

Atmospheric CO_2 concentration measurements in remote (background) locations began in 1957 at the South Pole Observatory (SPO), and in 1958 at Mauna Loa Observatory (MLO), Hawaii, USA (Keeling, 1960) (Figure 5.4a). Since then, measurements have been extended to multiple locations around the world (Bacastow et al., 1980; Conway et al., 1994; Nakazawa et al., 1997). Annual mean CO_2 growth rates are observed to be 1.56 ± 0.18 ppm yr^{-1} (average and range from 1-σ standard deviation of annual values) over the 59 years of atmospheric measurements (1959–2018), with the rate of CO_2 accumulation almost tripling from an average of 0.82 ± 0.28 ppm yr^{-1} during the 1960s to 2.30 ± 0.07 ppm yr^{-1} during the most recent decade of 2009–2018 (Dlugokencky and Tans, 2019). The oscillation in monthly-mean growth rates (Figure 5.4b; lines) show close relationship with the El Niño Southern Oscillation (ENSO) cycle (Figure 5.4b; shaded) due to the changes in terrestrial and ocean CO_2 sources and sinks on the Earth's surface (see also Section 5.2.1.4).

Atmospheric measurements at very high accuracy and time resolution are critical for understanding the natural and anthropogenic processes that influence the atmospheric CO_2 trends and variability. There are now multiple lines of evidence that makes unequivocal the dominant role of human activities in the growth of atmospheric CO_2. 1) The seasonal variation at MLO is observed due to the predominant role of the terrestrial biosphere uptake of CO_2 in the northern hemispheric during summer and release in winter. The systematic increase in the difference between MLO and SPO is caused primarily by continuous increase in emissions due to fossil fuel combustion by the industrialised nations which are largely in the northern hemisphere (Figure 5.4a). 2) Measurements of the stable carbon isotope ($\delta^{13}C$) show more negative values with time because both coal and oil extracted from geological storage are depleted in $\delta^{13}C$ (Ishidoya et al., 2012;) (Figure 5.4c). 3) Measurements of the ratio $\delta(O_2/N_2)$ show a declining trend because for every molecule of carbon burned one molecule of oxygen (O_2) is consumed (Keeling et al., 2017) (Figure 5.4d). 4) Since the AR5, an additional strong line of evidence for fossil fuel emissions causing CO_2 increase comes from the measurements of radiocarbon (^{14}C) at Wellington, New Zealand (Turnbull et al., 2017) and other sites around the world (Levin et al., 2010; Graven et al., 2017), which show a long-term decrease in the $^{14}C/^{12}C$ ratio. Fossil fuels are devoid of ^{14}C and therefore fossil fuel CO_2 additions decrease the atmospheric $^{14}C/^{12}C$ ratio (Suess, 1955). The naturally occurring ^{14}C abundance (background) in the atmosphere was strongly perturbed by nuclear bomb tests in the 1940s through 1960s that nearly doubled atmospheric ^{14}C and $^{14}C/^{12}C$ ratio in the 1960s; the high levels gradually decreased to return close to background $^{14}C/^{12}C$ ratios in 2015. A combination of the available atmospheric ^{14}C observations and modelling have

demonstrated that in the 1960s and 1970s, the decrease was largely due to uptake of the excess ^{14}C into the ocean interior, but in recent years dilution by the large fossil fuel emission rate has been the primary driver of ongoing $^{14}C/^{12}C$ ratio decreases. Exchange with the land biosphere and both natural cosmogenic and anthropogenic nuclear industry production of ^{14}C lead to modest increases in $^{14}C/^{12}C$ ratio that are outweighed by the decreases from ocean and fossil fuel processes (Levin et al., 2010).

[START FIGURE 5.4 HERE]

Figure 5.4: Time series of CO_2 concentrations and related measurements in ambient air (a: concentration time series and MLO-SPO difference, b: growth rates, c: ^{14}C and ^{13}C isotopes, and d: O_2/N_2 ratio). The data for Mauna Loa Observatory (MLO) and South Pole Observatory (SPO) are taken from the Scripps Institution of Oceanography (SIO)/University of California, San Diego (Keeling et al., 2001) except for the $\Delta^{14}C$-CO_2 (panel c, left y-axis). The global mean CO_2 and growth rate are taken from NOAA cooperative network (as in Chapter 2). The $\delta(O_2/N2)$ are expressed in per meg units (= $(FF/M)\times10^6$, where FF = moles of O_2 consumed by fossil-fuel burning, M = 3.706×10^{19}, total number of O_2 molecules in the atmosphere; http://scrippso2.ucsd.edu/units-and-terms). The $^{14}CO_2$ time series at Wellington, New Zealand (BHD) is provided by GNS Science and NIWA (Turnbull et al., 2017). The multivariate ENSO index (MEI) is shown as the shaded background in panel (b).

[END FIGURE 5.4 HERE]

The evolution of atmospheric CO_2 over the past six decades has shown a largely unchanged airborne fraction, the fraction of anthropogenic emissions that have accumulated in the atmosphere, of 44% (Figure 5.5; Ballantyne et al., 2012; Gruber et al., 2019a; P. Ciais et al., 2019). That suggests that the land and ocean CO_2 sinks have continued to grow at a rate consistent with the growth rate of anthropogenic CO_2 emissions, albeit with large inter-annual and sub-decadal variability dominated by the land sinks (Figure 5.5).

Since AR5, new research has proposed the use of the sink rate as an observable diagnostic to understand the trends in land and ocean sinks in response to its major driver (the atmospheric excess of CO_2 since pre-industrial times), compared to the airborne fraction, which relates sinks to CO_2 (Raupach et al., 2014; Bennedsen et al., 2019). The sink rate is defined as the combined ocean and land sink flux per unit excess of CO_2 above pre-industrial levels (Raupach et al., 2014). This research confirms the lack of trend in the airborne fraction since 1959 but shows a declining sink rate that suggests that the combined ocean and land sinks are not growing as fast as the growth in atmospheric CO_2 (*medium confidence*) (Figure 5.5; (Raupach et al., 2014; Bennedsen et al., 2019). The processes behind the sink rate decline are the sink responses to climate change and the non-linear response to increased atmospheric CO_2 (see Sections 5.2.1.3 and 5.2.1.4). The *medium confidence* stems from the fact that both the airborne fraction and the sink rate are also influenced by the slower-than-exponential CO_2 emissions, major climate modes (e.g., El Niño Southern Oscillation), and volcanic eruptions (Gloor et al., 2010) (Frölicher et al., 2013; Raupach et al., 2014). In conclusion, both ocean and land CO_2 sinks have grown and continuous to growth with the rising of atmospheric CO_2 and consistent with anthropogenic emissions, but the growth of the combined ocean and land sink has been slower than the accumulation of anthropogenic CO_2 in the atmosphere (*medium confidence*). The large inter-annual variability of both diagnostics (airborne fraction and sink rate) along with the high uncertainty in the land use change CO2 emissions makes difficult to detect trends.

[START FIGURE 5.5 HERE]

Figure 5.5: Airborne fraction and anthropogenic (fossil fuel and land use change) CO_2 emissions. Data as in carbon budget (Section 5.2.1.5).

[END FIGURE 5.5 HERE]

5.2.1.2 Anthropogenic CO_2 Emissions

There are two anthropogenic sources of CO_2 emissions, fossil fuels and the net flux from land use change (Friedlingstein et al., 2019), noting the different definitions used in scientific and inventory studies (Grassi et al., 2018).

Fossil CO_2 emissions include the combustion of coal, oil and gas covering all sectors of the economy (domestic, transport and industrial use), the production of cement, and industrial processes such as the production of chemicals and fertilisers (Figure 5.6a). Fossil CO_2 emissions are estimated by combining activity data and emission factors, with different levels of methodological complexity (tiers) or approaches (e.g., IPCC Guidelines for National Greenhouse Gas Inventories). There are several organisations that provide estimates of fossil CO_2 emissions (e.g., UNFCC, IEA, GCP, EDGAR, CEDS, BP), with each dataset having slightly different system boundaries, methods, activity data, and emissions factors. Datasets cover different time periods, which can dictate the datasets and methods that are used for a particular application. The data reported in this report is updated annually (Friedlingstein et al., 2019), and uses multiple data sources to maximises temporal coverage 1750-2016 (CDIAC) extended to 2018 (BP) and overwritten with national inventory reports for Annex I countries (UNFCCC) and cement (Andrew, 2019). The uncertainty in global fossil CO_2 emissions is estimated to be ±5% (1 standard deviation) (Friedlingstein et al., 2019).

Fossil CO_2 emissions have grown continuously since the beginning of the Industrial Era (Figure 5.6) with short intermissions due to global economic crises or social instability (Peters et al., 2012; Friedlingstein et al., 2019). Fossil CO_2 emissions reached 9.5 ± 0.5 PgC yr^{-1} during the most recent decade (2009–2018) and were responsible for 86% of all anthropogenic CO_2 emissions. As of 2018, fossil CO_2 emissions were estimated at 10.0 ± 0.5 PgC yr^{-1} in 2018 (Friedlingstein et al., 2019). Fossil CO_2 emissions grew at 0.9% per year in the 1990s, increasing to 3.2% per year in the 2000s, and back to 0.9% from 2010–2018. Since AR5, fossil CO_2 emissions showed a period with little or no growth between 2014 and 2016 (Jackson et al., 2016), but have since returned to growth with 1.5% in 2017 and 2.1% in 2018. The slower growth between 2014 and 2016 was largely due to coincidental reductions in CO_2 emissions from coal use in the US and China The stronger growth in emissions in the 2000s was due to a rapid expansion of coal use, driven by growth China. The growth in coal ended in 2012, and since then coal use has remained flat while oil and gas use have continued to grow strongly, with gas use the dominant driver of CO_2 emissions since 2012 (Friedlingstein et al., 2019). Process CO_2 emissions from cement (clinker) production are around 4% of total fossil CO_2 emissions, and continue to grow steadily despite more rapid growth in the 2000s. These results are robust across the different fossil CO_2 emission datasets, despite minor differences in levels and rates as expected given the reported uncertainties.

[START FIGURE 5.6 HERE]

Figure 5.6: Global anthropogenic CO_2 emissions: A) Historical trends of anthropogenic CO_2 emission for the period 1870 to 2016. Data sources: (Boden et al., 2017; IEA, 2017; Andrew, 2018; BP, 2018; Le Quéré et al., 2018a). B) The net land use change CO_2 flux (PgC yr^{-1}) as estimated by two bookkeeping models and 16 dynamic global vegetation models (DGVM) for the global annual carbon budget 2018 (Le Quéré et al., 2018a). The two bookkeeping models are from Hansis et al., 2015 and Houghton and Nassikas, 2017 both updated to 2018; their average is used as to determine the net land use change flux in the annual global carbon budget. The DGVM estimates are the result of differencing a simulation with and one without land use changes run under observed historical climate and CO_2, following the Trendy v7 protocol; they are used to provide an uncertainty range to the bookkeeping estimates (Friedlingstein et al., 2019). All estimates are unsmoothed annual data. Note that the estimates differ in process comprehensiveness of the models and in definition of flux components included in the net land use change flux.

[END FIGURE 5.6 HERE]

The net carbon flux from land use and land use change, including management interventions such as forestry, consists of gross sources (e.g. loss of biomass and soil carbon in clearing, biomass burning) and

gross sinks (e.g. CO_2 uptake in forest re-growing after harvesting or agricultural abandonment). The net flux from land use change relates to direct human interference with the terrestrial vegetation, as opposed to the natural carbon fluxes occurring due to interannual variability or trends in environmental conditions (in particular climate, CO_2, nutrient deposition) (Houghton, 2013). However, synergistic effects of land use change and environmental changes emerge. They have been identified since AR5 as a key reason for the large discrepancies between model estimates of the net land use change flux, explaining up to 50% of differences (Pongratz et al., 2014; Stocker and Joos, 2015). Another reason for discrepancies relates to natural fluxes being considered as part of the net land use change flux when occurring on managed land under the United Nations Framework Convention on Climate Change (UNFCCC), while they are considered part of the natural terrestrial sink in global vegetation models (Grassi et al., 2018). Also, evidence emerged that the net land use change flux might have been underestimated (which would imply an underestimation of the land sink to meet the observation-based net land-atmosphere exchange), as Dynamic Global Vegetation Models (DGVMs) have included anthropogenic land cover change, but often ignore land management practices (Pongratz et al., 2018). Sensitivity studies find that practices such as wood and crop harvesting increase land use emissions (Arneth et al., 2017) and explain about half of the cumulative loss in aboveground biomass (Erb et al., 2018). However, individual practices such as fire suppression may also create carbon sinks (Andela et al., 2017; Arora and Melton, 2018).

Industrial Era of land use change estimates have been updated routinely in the annual budgets of the Global Carbon Project using bookkeeping models combined with uncertainty estimates from DGVMs (Le Quéré et al., 2018a). The two bookkeeping models applied (Hansis et al., 2015; Houghton and Nassikas, 2017) combine changes in land use areas with observation-based, biome-level carbon densities and response curves for biomass decay and regrowth.to quantify the net land use change flux. For the decade 2008–2017 emissions averaged to 1.5 PgC yr^{-1} with an assigned uncertainty of ±0.7 PgC yr^{-1} (Le Quéré et al., 2018a). A general upward trend since 1850 is halted or reversed during the second part of the 20th Century (Figure 5.6b), but trends differ since the 1980s related, amongst other, to Hansis et al. (2015) and the DGVMs using a different land use forcing than Houghton and Nassikas, (2017). A trend from generally lower to higher emission estimates as compared to bookkeeping estimates is expected from the DGVMs run under transient environmental conditions as they include the loss of additional sink capacity, meaning that the sink capacity of the biosphere is reduced by decreasing the residence time of carbon by transforming forests to agricultural areas (Gitz and Ciais, 2003); this loss of additional sink capacity is growing with atmospheric CO_2 (Figure 5.6).

Cumulative (pre-industrial and Industrial Era) losses by land use activities since the start of agriculture and forestry have been estimated based on global compilations of carbon stocks for soils as 116 PgC (Sanderman et al., 2018), with about 70 PgC of this occurring prior to 1750, and for vegetation as 447 (375–525) PgC (Erb et al., 2018). Subtracting the post-1750 net land use change flux from Table 5.1 from the combined cumulative soil and vegetation losses yields pre-1750 emissions of 328 (161–501) assuming error ranges are independent). For the latter, a share of 353 (310–395) PgC from prior to 1800 has indirectly been suggested as the difference between net biosphere flux and terrestrial sink estimates, which is compatible with ice-core records due to a low airborne fraction of anthropogenic emissions in pre-industrial times. An Earth system model considering natural slow carbon cycle processes – release of CO_2 during formation of coral reefs and CO_2 uptake during peat accumulation – in addition to land use emissions supports the view that anthropogenic emissions are needed in the last 3 ka to explain the CO_2 increase seen in ice-core record (Kleinen et al., 2016), but upper-end assumptions about the extent of agricultural expansion before 1850 CE are found incompatible with the carbon budget thereafter (Stocker et al., 2017). Overall, the CO_2 increase measured from ice-cores between the early Holocene and the beginning of the Industrial Era is still plagued by large uncertainties (Brovkin et al., 2016; Ruddiman et al., 2016).

Uncertainties related to current estimates of the net land use change flux are still large (Figure 5.6b). Carbon fluxes inferred from atmospheric inversions have been used to constrain the temporal evolution of the net land use change flux (Piao et al., 2018a). However, inversion products measure the net land-atmosphere fluxes, including fossil-fuel emissions and natural and anthropogenic biosphere fluxes. The biospheric fluxes estimated by inversions still show large differences, explained to some extent by the choice of fossil-fuel data subtracted from the net surface CO_2 fluxes (Gaubert et al., 2019). Moreover, inversions cannot resolve

natural and anthropogenic fluxes, so they can provide estimates of the net land use change flux only for regions where the fluxes due to natural environmental changes are known with confidence. Still, inversions can be used as references against which modelled datasets can be compared, allowing to identify regional hot-spots of uncertainty and the underlying causes (Bastos et al., submitted). The latter constraint also applies to satellite-based estimates of biomass changes. Satellite-based biomass observations in combination with information on remotely-sensed land cover change are used for independent quantifications of land-use-related carbon fluxes in particular for the tropics, but differ from bookkeeping and DGVM modelling in excluding legacy emissions from pre-satellite-era land use change, and neglecting soil carbon changes, and often focus on gross deforestation, not regrowth (SRCCL Chapter 2 - Section 2.3.1.2.2, [Placeholder: Authors to add reference link]).

5.2.1.3 Ocean CO_2 Fluxes and Storage: Historical and Contemporary Trends and Variability

Since AR5 three major advances have had a decisive impact on the levels of confidence of the trends and the variability of both air-sea fluxes of CO_2 and its storage in the ocean interior. These are 1) the new observations and observational-based products for decadal variability in ocean uptake fluxes and ocean storage, 2) the observational-based product changes in amplitude of the seasonal cycle of surface ocean pCO_2 (the partial pressure of CO_2 expressed in µatm) in response to changing ocean carbonate chemistry, and 3) spatially-resolved pCO_2 seasonal climatologies for the global coastal ocean (Gruber et al., 2019a; (Rödenbeck et al., 2015; Landschützer et al., 2016, 2018); Laruelle et al., 2017). These advances were made possible by the simultaneous global coordination of observations and data quality control through the Surface Ocean CO_2 Atlas (SOCAT) and Lamont-Doherty Earth Observatory (LDEO) as well as the rapid adoption of a large variety of interpolation techniques for the surface layer and their inter-comparison to constrain uncertainties and biases (Rödenbeck et al., 2015; Bakker et al., 2016; Landschützer et al., 2016; McKinley et al., 2017; Gregor et al., 2019; Gruber et al., 2019a).

Advances in the multiple methods of interpolating surface ocean pCO_2 observations provide a *medium to high confidence* in the air-sea fluxes of CO_2 over most of the ocean (Rödenbeck et al., 2015; Landschützer et al., 2016; Gregor et al., 2019). However, there is *low confidence* in those fluxes for important regions such as the Southern Ocean, the Arctic, South Pacific as well as coastal oceans (Laruelle et al., 2017; Gregor et al., 2019; Gruber et al., 2019b); while these regions remain temporally and spatially under sampled the development and deployment of carbon and biogeochemically enabled Argo autonomous floats is starting to close those gaps (Williams et al., 2017a; Gray et al., 2018; Claustre et al., 2020).

Similarly, for anthropogenic carbon storage in the ocean interior (i.e. below the mixed layer) the Global Ocean Ship-based Hydrographic Investigations Programme (GO-SHIP) coupled to the Global Ocean Data Analysis Project for Carbon (GLODAPv2) were central to supporting the advances in characterising changes to the storage in the ocean interior by generating a new consistent, quality-controlled, global dataset, allowing the decadal variability in ocean carbon storage to be quantified (Lauvset et al., 2016; Olsen et al., 2016; Clement and Gruber, 2018; Gruber et al., 2019a). There is *high confidence* that a significant advance since AR5 and SROCC is the improved characterization of the variability of the ocean CO_2 storage trends in space and time, which has notable decadal and regional scale variability (Tanhua et al., 2017; Gruber et al., 2019a) (SROCC Chapters 3 and 5).

Since it is also unequivocal that anthropogenic CO_2 taken up from the atmosphere into the ocean surface layer is further transported into the ocean interior through ocean ventilation processes including vertical mixing, diffusion, subduction and meridional overturning circulations (Sallée et al., 2012; Nakano et al., 2015; Bopp et al., 2015; Iudicone et al., 2016; Toyama et al., 2017), the trends as well as the spatial and temporal variability were assessed in an integrated way for both the air-sea flux and storage of anthropogenic CO_2.

5.2.1.3.1 Ocean Fluxes and Storage of Anthropogenic CO_2: Global Multi-Decadal Trends

Estimates of the global CO_2 ocean sink for the contemporary period have been derived from forced Global

Ocean Biogeochemistry Models (GOBMS), which simulate ocean circulation and biogeochemistry for recent decades by forcing the models with various atmospheric reanalysis products (Aumont and Bopp, 2006; Doney et al., 2009; Le Quéré et al., 2010, 2018b; Lenton et al., 2013; Schwinger et al., 2016; McKinley et al., 2017; Hauck et al., 2018; Berthet et al., 2019; Friedlingstein et al., 2019). The ocean-atmosphere CO_2 flux reconstructions from GOBMs span 1959–2018, and are updated every year for the Global Carbon Budget (Friedlingstein et al., 2019). These GOBM reconstructions demonstrate with *high confidence* that the global ocean carbon sink has grown over the past six decades, but also reveal a slowdown in the sink in the 1990s, consistent with that found from the observationally based products (Figure 5.7a). It is unequivocal that, notwithstanding decadal variability, the mean contemporary ocean uptake, in this report also referred to as the ocean sink, of CO_2 continues to grow from 1 ± 0.6 PgC yr^{-1} to 2.5 ± 0.6 PgC yr^{-1} from the 1960–1969 to 2009–2018 decades in response to growing anthropogenic CO_2 emissions (Figure 5.7a) (Friedlingstein et al., 2019; Chapter 5 Table 5.1; SROCC Chapters 5 (Section 5.2.2.3) and 3). This corresponds to a multidecadal mean (1960–2018) uptake fraction of $24 \pm 5\%$ of total CO_2 emissions (Friedlingstein et al., 2019; Table 5.1). The confidence level of this assessment is supported by the convergence of the magnitudes of decadal means of the ocean uptake of CO_2 calculated from 6 quasi-independent methods (Figure 5.7b; Appendix 5.1). These robust constraints show that the contemporary ocean uptake flux has increased from 1.82 ± 0.39 in 1990–1999 to 2.34 ± 0.16 in 2000–2009 and 2.55 ± 0.08 in 2009–2018, in close agreement with the GOBMs models (Figure 5.7a) (Friedlingstein et al., 2019). However, variability in globally-integrated flux from the GOBMs is on average lower than that of observationally-based and inverse modelled products; this is characterised by both regional differences and biases in the variability of sea surface pCO_2, which can influence the trends and the climate sensitivity in GOBM and ESMs (Kessler and Tjiputra, 2016; Mongwe et al., 2016, 2018; McKinley et al., 2017; Goris et al., 2018; DeVries et al., 2019; Gregor et al., 2019; Lebehot et al., 2019) (Figure 5.7a). There is *medium to high confidence* that this growing ocean CO_2 sink is also beginning to drive observable large scale changes to ocean carbonate chemistry that are reducing the carbonate buffering capacity of the ocean, changing the seasonal cycle of surface ocean pCO_2 and intensifying ocean acidification (Section 5.3.2; SROCC 5.2.2.3.2) (Bates et al., 2014; Landschützer et al., 2018; Sutton et al., 2016). Though the effect of these changes on carbon - climate feedbacks and the airborne fraction of anthropogenic CO_2 in the contemporary period is still small, it is *very likely* that these changing mechanisms will drive future weakening of the ocean CO_2 sink under low-medium mitigation scenarios (Hauck and Völker, 2015; Sasse et al., 2015). There is *medium confidence* on the absolute magnitudes of ocean CO_2 uptake fluxes calculated from empirical interpolation methods as well as atmospheric inversions due to uncertainties in contribution of the river flux and especially its regional contributions (McKinley et al., 2017; Ward et al., 2017; Resplandy et al., 2018; Gruber et al., 2019a).

[START FIGURE 5.7 HERE]

Figure 5.7: (a): Temporal evolution of the globally-integrated sea-air CO_2 flux as reconstructed by (grey/black) ocean physical and biogeochemical models forced with observed atmospheric history (Doney et al., 2009; Buitenhuis et al., 2010; Schwinger et al., 2016; Hauck et al., 2018; Berthet et al., 2019), and (blue) observationally-based products that represent spatial and temporal variability in the flux from sparse observations of surface ocean pCO_2 (Rödenbeck et al., 2013; Iida et al., 2015; Zeng et al., 2015; Landschützer et al., 2016; Denvil-Sommer et al., 2019; Gregor et al., 2019). Thick lines represent the multi-model mean. Observationally-based products have been corrected differences in spatial coverage, as in (McKinley et al., submitted). (b): Mean decadal constraints for global ocean air-sea CO_2 fluxes using quasi-independent lines of evidence or methods for the period 1990–2018 (See supporting table Appendix 5.1 for magnitudes, uncertainties and published sources). (References as above but including: (Rödenbeck et al., 2003; Chevallier et al., 2005; Keeling and Manning, 2014; Aumont et al., 2015; Jones et al., 2015; DeVries et al., 2017; Law et al., 2017; Saeki and Patra, 2017; Gregor et al., 2018; Friedlingstein et al., 2019; Gruber et al., 2019a; Liu et al., 2019a; Mauritsen et al., 2019; Tohjima et al., 2019). The fluxes from both empirical models and atmospheric inversions have been corrected for the river fluxes (0.78 PgC yr^{-1}) based on the estimate from Resplandy et al. (2018).

[END FIGURE 5.7 HERE]

The total increase of CO_2 stored in the ocean interior (net anthropogenic and natural CO_2 uptake and storage changes has been evaluated as 140 ± 22 (±2σ) PgC in the year 2007, that is 28 ± 5% of total anthropogenic CO_2 emissions (Gruber et al., 2019a). As reported in SROCC (Section 5.2.2.3.1), the ocean CO_2 inventory has increased by 29 ± 5 PgC (26 ± 5%) between1994 and 2007 with a mean annual storage rate of 2.2 ± 0.4 PgC yr^{-1}, which corresponds closely to the global mean ocean-atmosphere flux estimate of 2.1 ± 0.6 PgC yr^{-1}, in proportion to the atmospheric CO_2 increases of 31 ± 1% for the same period (Gruber et al., 2019a) (Table 5.1). There is *high confidence* that most of the increase in the ocean CO_2 inventory between 1994 and 2007 is found in the Southern Hemisphere mid-latitudes associated with CO_2 transport through Mode and Intermediate Waters, in the North Atlantic through deep-water formation, and in the shallow overturning circulation of the western North Pacific mid-latitudes (Tanhua et al., 2017; DeVries et al., 2019; Gruber et al., 2019a) (Figure 5.8b).

5.2.1.3.2 Ocean Fluxes and Storage of Anthropogenic CO_2: Global and Regional Variability

The most important advance from ocean CO_2 observations-based products since AR5 was an increase in the confidence level of assessing the regional to global characteristics of interannual variability for both air-sea and storage fluxes (Gruber et al., 2019b, 2019a) (Figure 5.8a,b). Observations-based products have provided important new constraints into the regional characteristics of variability of ocean uptake (Figure 5.8a) and storage of anthropogenic CO_2 (Figure 5.8b). There is *high confidence* that the ocean uptake of both natural and anthropogenic CO_2 is dominated by the mid to high latitude oceans, particularly the Southern Ocean because of its area and the North Atlantic because of its intensity (Figure 5.8a). There is *high confidence* that in both cases these are regions associated with the formation of water masses that sink and carry the anthropogenic CO_2 into storage in the ocean interior in the sub-tropical regions on time scales of decades to centuries (Figure 5.8b) (Gruber et al., 2019a). In contrast, ocean emissions of natural CO_2 are dominated by the tropical Pacific Ocean and the upwelling of Circumpolar Deep Water in the Southern Ocean and there is *medium confidence* that they account for decadal variability in air-sea CO2 fluxes (Figure 5.8a) (Gruber et al., 2019b, 2019a; SROCC Chapters 3 and 5). This improved characterization of regional ocean CO_2 air-sea fluxes and storage fluxes provides greater confidence by also explaining how regions may amplify or reduce the temporal variability of the ocean uptake of CO_2 (McKinley et al., 2017; Gregor et al., 2019; Gruber et al., 2019b, 2019a).

[START FIGURE 5.8 HERE]

Figure 5.8: A comparative assessment of the spatial characteristics of the mean multi-decadal (1994–2007) (a) ocean air-sea CO_2 fluxes derived from the ensemble observation-based product CSIR-ML6 (Gregor et al., 2019) using SOCATv5 observational data set (Bakker et al., 2016). Black contours characterise the biomes defined by Fay and McKinley, (2014) and adjusted by Gregor et al. (2019) and (b) the storage fluxes of CO_2 in the ocean (Gruber et al., 2019a).

[END FIGURE 5.8 HERE]

Globally, the mid-to-high latitude oceans account for most of the storage, which is also reflected by the comparable fluxes (Figure 5.8b). In the Indian and Pacific sectors of the Southern Ocean and in the North Atlantic, the increase in the CO_2 inventory from 1994 to 2007 was about 20% smaller than expected from the atmospheric CO_2 increase during the same time period and the anthropogenic CO_2 inventory in 1994 (Sabine, 2004; Gruber et al., 2019b). This is attributable to the impact of change in the meridional overturning circulation on the transport of anthropogenic CO_2 into the ocean interior associated with regional climate variability (DeVries et al., 2019; Pérez et al., 2013; Wanninkhof et al., 2010; Section 9.2.3.1).

5.2.1.3.3 Ocean Fluxes and Storage of Anthropogenic CO_2: Global and Regional Temporal Variability

Since AR5 advances in global ocean CO_2 flux products have strengthened the confidence of the assessment of interannual trends of air-sea CO_2 fluxes through improved resolution of the temporal characteristics of variability: seasonal, interannual and decadal variability of the global ocean CO_2 sink both in respect of air-

sea fluxes and storage (Figure 5.9); (Landschützer et al., 2014, 2015; Rödenbeck et al., 2014; McKinley et al., 2017; Le Quéré et al., 2018b; Friedlingstein et al., 2019; Gregor et al., 2019). This has also highlighted, which regions of the ocean account for most of the mean global variability and its sensitive to climate change as well as strengthening the rigour of ocean and Earth system model evaluation (Gregor et al., 2019; Gruber et al., 2019b). The interannual-decadal variability in mean monthly CO_2 fluxes (1990–2016) highlights the strong regional contrasts in ocean outgassing (Tropics) and ingassing (mid-to-high latitudes) (Figure 5.9). The global invigoration of ocean CO_2 uptake (2002–2016) was dominated by the strengthening of the mid and high latitudes sinks particularly in the Southern Ocean (Figure 5.9d,e). This provides *medium confidence* that the global interannual-decadal variability is *likely* measurably influenced by the Southern Ocean and its sensitivity to carbon concentration and climate forcing (Gruber et al., 2019a). However, the magnitude of the temporal variability may be significantly influenced by the data sparseness in the Southern Ocean and other parts of the ocean reducing its confidence level to *medium-low* (Gloege et al., submitted). There is moreover *low confidence* in the attribution of the drivers of interannual variability both in respect of observations-based products (Landschützer et al., 2014; Rödenbeck et al., 2014; Gregor et al., 2019; Gruber et al., 2019a) and models (Lebehot et al., 2019; McKinley et al., submitted; Mongwe et al., 2016, 2018).

[START FIGURE 5.9 HERE]

Figure 5.9: A comparative assessment of the contribution made by 5 regional ocean biomes (b-f) to the temporal variability and empirical model spread characteristics of the global air-sea CO_2 fluxes for the period 1990–2016 using both the ensemble observation-based product CSIR-ML6 (Gregor et al., 2019) using SOCATv5 observational data set (Bakker et al., 2016) and an atmospheric inversion model (Friedlingstein et al., 2019).

[END FIGURE 5.9 HERE]

There is *medium confidence* that during the decade after the mid-2000s the increase in the ocean CO_2 inventory was re-invigorated (DeVries et al., 2017, 2019). Globally, an ocean carbon cycle model coupled with an ocean inverse model constrained by observations showed that decadal-scale enhancement in the upper ocean overturning circulation drove a weakened ocean CO_2 sink in the 1990s due to increased natural CO_2 outgassing, but it reversed in the 2000s leading to the strengthening of the ocean CO_2 sink (DeVries et al., 2017). In the North Atlantic, a low rate of anthropogenic CO_2 storage at 1.9 ± 0.4 PgC per decade during the time period of 1989–2003 increased to 4.4 ± 0.9 PgC per decade during 2003–2014 (Woosley et al., 2016). In the Pacific, the rate of anthropogenic CO_2 storage also increased from 8.8 ± 1.1 PgC during 1995–2005 to 11.7 ± 1.1 PgC during 2005–2015 (Carter et al., 2019). However, in the Subantarctic Mode Water of the Atlantic sector of the Southern Ocean, the storage rate of the anthropogenic CO_2 was rather lower after 2005 than before (Tanhua et al., 2017; SROCC Chapter 5). There is *medium confidence* that these changes have been predominantly ascribed to the change in ocean circulation in addition to the increase in the atmospheric CO_2 concentration (DeVries et al., 2017; Gruber et al., 2019a).

5.2.1.4 Terrestrial Carbon Dioxide: Historical and Contemporary Variability and Trends

5.2.1.4.1 Trend in land-atmosphere CO_2 exchange

The global net land CO_2 sink has been strengthening (*high confidence*) over the past six decades (Ciais et al., 2019; Le Quéré et al., 2018a; Sarmiento et al., 2010). Based on the residual resulting from the mass balance budget with fossil fuel emissions minus atmospheric CO_2 growth rate and ocean CO_2 sink, the global net land CO_2 sink increased from 0.3 ± 0.5 PgC yr^{-1} during the 1960s to 2.1 ± 0.7 PgC yr^{-1} during the last decade (2008–2017) (Le Quéré et al., 2018a). Increasing global net land CO_2 sink since 1980s (Figure 5.10) were consistently suggested both by atmospheric inversions (e.g. Peylin et al., 2013) and DGVMs (e.g. Sitch et al., 2015). The northern hemisphere contributes more to increasing net land CO_2 sink than the southern hemisphere (Ciais et al., 2019). Attributing increased net land CO_2 sink to finer regional scale remain challenging. Although inversions using total column CO_2 retrievals from satellites become available since

AR5 as an additional approach to constrain regional land-atmosphere CO_2 exchange, these regional estimates are still largely uncertain(Houweling et al., 2015; Reuter et al., 2017; Palmer et al., 2019).

Carbon uptake by vegetation photosynthesis exerts a first-order control over net land CO_2 sink. Several lines of evidence show enhanced vegetation photosynthesis (*medium to high confidence*) over the past decades (Figure 5.10), including increasing satellite-derived vegetation greenness (e.g. Mao et al., 2016; Zhu et al., 2016; see Chapter 2), observation-driven inference of increasing photosynthesis CO_2 uptake based on enhanced water use efficiency and evapotranspiration (Cheng et al., 2017), change in atmospheric concentration of carbonyl sulphide (Campbell et al., 2017), enlarging seasonal CO_2 amplitude (Forkel et al., 2016; Graven et al., 2013; Piao et al., 2018b) and DGVM simulated increase of vegetation photosynthesis (Anav et al., 2015). DGVMs can reproduce the significant increase of seasonal CO_2 amplitude at boreal (north of 50°N) stations since 1980s (Forkel et al., 2016; Piao et al., 2018b), but not the seasonal CO_2 amplitude change since 1960s (Graven et al., 2013; Thomas et al., 2016).

Increasing strength of global net land CO_2 sink since 1980s is mainly driven by the fertilisation effect from rising atmospheric CO_2 concentrations (*medium to high confidence*) (e.g. Fernández-Martínez et al., 2019; O'Sullivan et al., 2019; Schimel et al., 2015; Sitch et al., 2015). Increasing nitrogen deposition (de Vries et al., 2009; Devaraju et al., 2016; Huntzinger et al., 2017) or the synergy between increasing nitrogen deposition and atmospheric CO_2 concentration (O'Sullivan et al., 2019) could have also contributed to the increased global net land CO_2 sink. The contribution of climate change to changes of the global net land CO_2 sink is so divergent that even the signs of the effects are not the same across DGVMs (Keenan et al., 2016; Huntzinger et al., 2017).

Although increasing burned area observed over some regions, such as western United States (Holden et al., 2018), interior Alaska (Veraverbeke et al., 2017) and southern Africa (Andela and Van Der Werf, 2014) due to warmer temperature and reduced precipitation regionally, as well as increasing frequency of lightning (Jolly et al., 2015; Bowman et al., 2017; Veraverbeke et al., 2017; Holden et al., 2018; Turco et al., 2018), Satellite observations reveal a declining trend of global burned area over past two decades (*medium confidence*) (Andela et al., 2017; Earl and Simmonds, 2018; Forkel et al., 2019b). This declining trend is primarily driven by fire management and suppression (Andela et al., 2017), which, at global scale, outweigh the climate-driven change of burned area (Forkel et al., 2019a). The reduced global burned area leads to lower fire emission of CO_2 (Giglio et al., 2013; Arora and Melton, 2018), which could have contributed to increasing global net land CO_2 sink (*low confidence*) (Arora and Melton, 2018). The lower fire emissions could also lead to lower concentration of fire-induced O_3 and aerosol, which have divergent indirect impacts on vegetation carbon uptake (Yue and Unger, 2018). Since the sensitivity of vegetation carbon uptake to O_3 concentration is highly uncertain (see Chapter 6), the net effects of reduced fire emissions of CO_2 and air pollution on net land CO_2 sink remain unclear.

Evidence also emerges that lower land use change emission (Hansis et al., 2015; Houghton and Nassikas, 2017; Kondo et al., 2018; Piao et al., 2018a), largely from reduced deforestation, afforestation and regrowth, could have contributed to acceleration of global net land CO_2 sink since late 1990s (*low to medium confidence*) (Piao et al., 2018a), though other mechanisms explaining acceleration of land CO_2 sink were also proposed, such as acceleration of photosynthesis (Keenan et al., 2016) or reduced respiration (Ballantyne et al., 2017).

While substantial progresses were made since AR5 on attributing change of global net land CO_2 sink, sizeable uncertainties remain due to challenges in reconciling evidences from the scale of the experiments to that of the globe (Fatichi et al., 2019) and from large spatial and inter-model differences in the dominant driving factors affecting the net land CO_2 sink (Huntzinger et al., 2017; Fernández-Martínez et al., 2019), as well as model deficiency in process representations. As a major gap identified, nutrient dynamics have now been incorporated in about half of the Trendy DGVMs (see Le Quéré et al., 2018a for model characteristics) and growing number of Earth system models. The representations of carbon-nitrogen interactions vary greatly among models, leading to large uncertainties in the response of ecosystem carbon uptake to higher atmospheric CO_2 (Walker et al., 2015; Zaehle et al., 2014; see Section 5.4.1). Fire modules have been incorporated into 10 of 16 Trendy DGVMs (Le Quéré et al., 2018a) and inter-compared by the other group

of DGVMs (Forkel et al., 2019b). There are also growing DGVM developments to include management practices (Pongratz et al., 2018b) and the dynamics of secondary forest regrowth (Pugh et al., 2019), though models still show biases over intensively managed ecosystems, such as croplands and managed forests (Guanter et al., 2014; Zhu et al., 2016; Thurner et al., 2017). Processes that do not manifest themselves in the past decades but may become tipping elements to land carbon cycle in future (e.g. permafrost, see Section 5.4) have also attracted growing attentions since AR5. Several DGVMs have developed more detailed representation of permafrost carbon cycle process (Koven et al., 2015a; Burke et al., 2017a; Guimberteau et al., 2018), though the sensitivity of permafrost carbon storage to climate change remains largely uncertain (Schurer et al., 2015; McGuire et al., 2016, 2018). Growing numbers and varieties of Earth observations are being jointly used for contesting models, which have the potential to further help identify key processes missing or mechanisms poorly represented in current generation of DGVMs (e.g. Collier et al., 2018).

[START FIGURE 5.10 HERE]

Figure 5.10: Change of net land CO_2 sink, Normalised Difference Vegetation Index (NDVI) and net primary production (NPP) during 1980–2017. **a**. Residual net land CO_2 sink is estimated from the global CO_2 mass balance with fossil fuel emission minus atmospheric CO_2 growth rate and ocean sink. Inversions indicate the net land CO_2 sink estimated by an ensemble of four atmospheric inversions (Le Quéré et al., 2018a). DGVMs indicate the mean net land CO_2 sink estimated by 16 Dynamic Global Vegetation Models driven by climate change, rising atmospheric CO_2, land use change and nitrogen deposition change (for carbon-nitrogen models). The positive CO_2 sink indicates net CO_2 uptake from the atmosphere. **b**. The anomaly of global area-weighted NDVI observed by AVHRR and MODIS satellite sensors. AVHRR data are available during 1982–2016 and MODIS data are available during 2000–2016. **c**. NPP based on the two satellite-based datasets having the temporal coverage of 1982–2011 for AVHRR NPP (Kolby Smith et al., 2016) and 2000-2014 for MODIS NPP (Zhao and Running, 2010). NPP from DGVMs is the ensemble mean global NPP estimated by the same 16 DGVMs that provide the net land CO_2 sink estimates. Shaded area indicates 1–σ inter-model spread except for atmospheric inversions, whose ranges were used due to limited number of models.

[END FIGURE 5.10 HERE]

5.2.1.4.2 Interannual variability in land-atmosphere CO_2 exchange

Interannual variability is a temporal component in addition to variability on seasonal, decadal and even longer time scales. AR5 concluded with substantial evidence that interannual variability of atmospheric CO_2 growth rate is dominated by tropical land ecosystems. Since AR5, studies from process carbon cycle models and atmospheric inversions further suggested that semi-arid ecosystems over the tropics have larger contribution to interannual variability in global land-atmosphere CO_2 exchange than moist tropical forest ecosystems (*low to medium confidence*) (Poulter et al., 2014; Ahlstrom et al., 2015; Zhang et al., 2018; Piao et al., 2019). A major advancement since AR5 is new satellite measurements that constrain the variability of the tropical land carbon balance, including satellite column CO_2 measurements that provided estimates at continental scale for recent years' El Niño-induced anomalous land-atmosphere CO_2 exchange (e.g. Liu et al., 2017; Palmer et al., 2019) and L-band vegetation optical depths that provided since 2010 tropical above-ground biomass carbon stock changes (Fan et al., 2019).

Mechanisms driving interannual variability of the carbon cycle could illustrate whether and how much the carbon cycle might accelerate or slow down climate warming, with particular interests on the highly responsive tropical carbon cycle to interannual climate anomalies (e.g. Cox et al., 2013a; Fang et al., 2017; Humphrey et al., 2018; Jung et al., 2017a; Malhi et al., 2018; Wang et al., 2014; see Section 5.4). The carbon cycle responses to climatic variations have been proposed as metrics for evaluating DGVMs, who, for example, can reproduce the sensitivity of global residual net land CO_2 sink to interannual temperature variations (γIAV) within its observational uncertainties (Piao et al., 2013; Huntzinger et al., 2017). Atmospheric inversions, satellite observations and DGVMs consistently report that warmer and drier conditions, particularly during El Niño events, reduce the tropical net land CO_2 sink (e.g. Bastos et al., 2018; Malhi et al., 2018; Rödenbeck et al., 2018; Wang et al., 2016). The interannual anomalies of atmospheric

CO_2 growth rate, resulting mostly from variations in tropical land-atmosphere CO_2 exchange, are more closely correlated with tropical temperature anomalies than with tropical precipitation anomalies (Figure 5.11; Wang et al., 2013, 2014). Anomalies of terrestrial water storage (TWS) were also found to correlate significantly with atmospheric CO_2 growth rate (Humphrey et al., 2018), but tropical TWS anomalies are not independent from tropical temperature/precipitation anomalies (e.g. Gloor et al., 2018; Piao et al., 2019). The response of atmospheric CO_2 growth rate to tropical temperature anomalies varies by two-folds depending on the study period and temperature data used (e.g. Cox et al., 2013a; Humphrey et al., 2018; Jung et al., 2017a; Rödenbeck et al., 2018; Wang et al., 2013, 2014). Because the response of atmospheric CO_2 growth rate to tropical temperature anomalies is regulated by tropical moisture conditions (Wang et al., 2014), and anomalies of temperature and moisture indices significantly correlated over the tropics (Jung et al., 2017; Humphrey et al., 2018), distinguishing the relative contribution of interannual variability of temperature and moisture to that of tropical net land CO_2 sink remain challenging.

[START FIGURE 5.11 HERE]

Figure 5.11: Interannual variation in detrended anomalies of net land CO_2 sink and land surface air temperature (T) at the globe or at the latitudinal bands during 1980–2017, and corresponding correlation coefficient between net land CO_2 sink anomalies and temperature anomalies. Net land CO_2 sink is estimated by four atmospheric inversions (blue) and fifteen Dynamic Global Vegetation Models (DGVMs) (green), respectively (Le Quéré et al., 2018a). Solid blue and green lines show model mean detrended anomalies of net land CO_2 sink. The ensemble mean of DGVMs is bounded by the 1–σ inter-model spread in each large latitude band (North 30°N–90°N, Tropics 30°S–30°N, South 90°S–30°S) and the globe. The ensemble mean of atmospheric inversions is bounded by model spread. For each latitudinal band, the anomalies of net land CO_2 sink and temperature (orange) were obtained by removing the long-term trend and seasonal cycle. 12-month running mean was taken to reduce high-frequency noise. Years on the horizontal axis indicate January of this year as the sixth month in the moving 12-month window. The bars in the right panels show correlation coefficients between net land CO_2 sink anomalies and temperature anomalies for each region. Two asterisks indicate $P<0.01$, and one indicates $P<0.05$. Grey shaded area shows the intensity of El Niño Southern Oscillation (ENSO) as defined by the multivariate ENSO index (MEI). Two volcanic eruptions (El Chichón eruption and Pinatubo eruption) are indicated with light blue dashed lines. Temperature data are from Climatic Research Unit (CRU), University of East Anglia (Harris et al., 2014).

[END FIGURE 5.11 HERE]

5.2.1.5 CO_2 budget

The global CO_2 budget (Figure 5.12, Table 5.1) refers to the perturbation of the carbon budget since the beginning of the Industrial era, circa 1750. The human perturbation prior to the Industrial Era is considered to be small based on the small changes in atmospheric CO_2 concentration. The budget, based on the annual assessment by the Global Carbon Project (Friedlingstein et al., 2019), is constructed using independent estimates of all major flux components: fossil fuel and industry emissions (E_{FF}), land use change emissions (E_{LUC}), the growth rate of CO_2 in the atmosphere (G_{Atm}), and the ocean (S_{Ocean}) and land (S_{Land}) CO_2 sinks. An imbalance term (B_{Imb}) is required to ensure mass balance of the source and sinks that have been independently estimated: $E_{FF} + E_{LUC} = G_{Atm} + S_{Ocean} + S_{Land.} + B_{Imb.}$

Fossil fuels and land use change together emitted 10.9 ± 1.1 PgC yr^{-1} during the decade of 2009–2018. The equivalent amount was distributed between accumulation in the atmosphere (44%, 4.9 ± 0.02 PgC yr^{-1}), the ocean (23%, 2.5 ± 0.6 PgC yr^{-1}) and land (29%, 3.2 ± 0.6 PgC yr^{-1}) (Table 5.1). The budget imbalance of 0.4 $PgCy^{-1}$is within the uncertainties of the other terms.

Over the Industrial Era (1750–2018), the cumulative CO_2 fossil fuel and industry emissions were 440 ± 20 PgC, and emission from land use change was 235 ± 75 PgC (Friedlingstein et al., 2019). The equivalent total (675 ± 80 PgC) was distributed between the atmosphere (41%, 275 ± 5 PgC), oceans (25%, 170 ± 20 PgC) and land (33%, 220 ± 50 PgC) (Table 5.1).

This budget does not explicitly account for source/sink dynamics due to carbon cycling in the land–ocean aquatic continuum comprising freshwaters, estuaries, and coastal areas. While some estimates suggest that natural and anthropogenic transfers of carbon from soils to freshwater systems are significant (0.78–5.1 PgC yr^{-1}, (Drake et al., 2018; Resplandy et al., 2018)) and increasing in response to human activity, an almost equivalent flux is returned to the atmosphere via outgassing in lakes, rivers and estuaries (Regnier et al., 2013). Thus, the net export of carbon from the terrestrial domain to the open oceans is relatively small (0.65 PgC yr^{-1}, *medium confidence* (Regnier et al., 2013)) relative to either the land or ocean sinks and their uncertainty. Accounting for the land-ocean continuum carbon dynamics reduces the size of the of land sink (Regnier et al., 2013).

[START FIGURE 5.12 HERE]

Figure 5.12: The global carbon cycle. Blue arrows represent annual carbon exchange fluxes (in PgC yr^{-1}) associated with the natural carbon cycle estimated for the time prior to the Industrial Era, around 1750. Pink arrows represent anthropogenic fluxes averaged over the period 2008–2017. The rate of carbon accumulation in the atmosphere is equal to net land-use change emissions plus fossil fuel emissions, minus land and ocean sinks (plus a small budget imbalance, Table 5.1). Numbers in white circles represent pre-industrial carbon stocks in PgC. Fossil fuel reserves are those stocks that are currently recoverable using commercially viable existing technologies. Numbers in dashed circles represent anthropogenic changes to these stocks (cumulative anthropogenic fluxes) since 1750. Anthropogenic net fluxes are reproduced from (Friedlingstein et al., 2019) The relative change of *Gross photosynthesis* since pre-industrial times is estimated as the range of observation-based of 31 ± 3 % (Campbell et al., 2017) and land-model of 19 ± 12% (Sitch et al., 2015) estimates. This is used to estimate the pre-industrial *Gross photosynthesis*, assuming a present-day range of 116–175 PgC yr^{-1} (Joiner et al., 2018). The corresponding emissions by *Total respiration and fire* are those required to match the *Net land flux*, exclusive of net land-use change emissions which are accounted for separately. The cumulative change of anthropogenic carbon in the terrestrial reservoir is the sum of carbon cumulatively lost by net land use change emissions, and net carbon accumulated since 1750 in response to environmental drivers (warming, rising CO_2, nitrogen deposition) (Le Quéré et al., 2018a).The change in *Ocean-atmosphere gas exchange* (red arrows of ocean atmosphere gas exchange) is estimated from the difference in atmospheric partial pressure of CO_2 since 1750 (Sarmiento and Gruber, 2006). Individual gross fluxes and their changes since the beginning of the Industrial Era have typical uncertainties of more than 20%, while their differences (*Net ocean flux*) are determined from independent measurements with a much higher accuracy. Therefore, to achieve an overall balance, the values of the more uncertain gross fluxes have been adjusted so that their difference matches the and *Net ocean flux* estimate. The sediment storage is a sum of 150 PgC of the organic carbon in the mixed layer (Emerson and Hedges, 1988) and 1600 PgC of the deep-sea $CaCO_3$ sediments available to neutralise fossil fuel CO_2 (Archer et al., 1998). Note that the mass balance of the two ocean carbon stocks *Surface ocean* and *Intermediate and deep ocean* includes a yearly accumulation of anthropogenic carbon (not shown). Fossil fuel reserves are from (BGR, 2017). Permafrost region stores are from (Hugelius et al., 2014; Strauss et al., 2017) and soil carbon stocks outside of permafrost region from (Batjes, 2016; Jackson et al., 2017) Biomass stocks (range of seven estimates) are from (Erb et al., 2018). Fluxes from volcanic eruptions, rock weathering (removal of atmospheric CO_2 in weathering reactions and chemical weathering of C contained in rocks) export of carbon from soils to rivers, burial of carbon in freshwater lakes and reservoirs, estuaries and coastal ecosystems, and transport of carbon by rivers to the open ocean are all assumed to be pre-industrial fluxes and are sourced from (Regnier et al., 2013).

[END FIGURE 5.12 HERE]

[START TABLE 5.1 HERE]

Table 5.1: Global anthropogenic CO_2 budget accumulated since the Industrial Revolution (onset in 1750) and averaged over the 1980s, 1990s, 2000s, as well as the recent decade from 2008. By convention, a negative ocean or land to atmosphere CO_2 flux is equivalent to a gain of carbon by these reservoirs. The table does not include natural exchanges (e.g., rivers, weathering) between reservoirs. Uncertainties represent the 68% confidence interval. All numbers are reproduced from (Friedlingstein et al., 2019)

	1750–2018 Cumulative (PgC)	1980–1989 Mean Annual Growth Rate (PgC yr^{-1})	1990–1999 Mean Annual Growth Rate (PgC yr^{-1})	2000–2009 Mean Annual Growth Rate (PgC yr^{-1})	2009–2018 Mean Annual Growth Rate (PgC yr^{-1})
Emissions					
Fossil fuel combustion and cement production	440 ± 20	5.5 ± 0.3	6.4 ± 0.3	7.8 ± 0.4	9.5 ± 0.5
Net land use change	235 ± 190	1.2 ± 0.7	1.3 ± 0.7	1.4 ± 0.8	1.5 ± 0.7
Total Emissions		6.7 ± 0.8	7.7 ± 0.8	9.2 ± 0.8	11.0 ± 0.8
Partition					
Atmospheric increase	275 ± 5	3.4 ± 0.02	3.1 ± 0.02	4.0 ± 0.02	4.9 ± 0.02
Ocean sink[c]	170 ± 20	1.7 ± 0.6	2.0 ± 0.6	-2.1 ± 0.5	2.5 ± 0.6
Terrestrial sink	220 ± 50	1.8 ± 0.5	2.4 ± 0.4	-2.7 ± 0.7	3.2 ± 0.6
Budget imbalance	10	-0.2	0.3	0.3	0.4

[END TABLE 5.1 HERE]

5.2.2 CH_4: Trends, Variability and Budget

The CH_4 variability in atmosphere is mainly a result of net balance between Earth's surface emissions and chemical losses in atmosphere. Atmospheric transport only redistributes the CH_4 variability signal to different parts of the Earth's atmosphere. The time scales relevant to CH_4 process studies range between hourly to monthly and for the budget estimations that are predominantly monthly to annual (Figure 6.1). The average atmospheric burden of CH_4 is about 5001 ± 54 Tg, with an emission and loss of about 543 ± 18 Tg yr^{-1} and 522 ± 8 Tg yr^{-1} during 2007–2016 (1Tg = 10^{12}g; 1–σ standard deviation for the interannual variations is shown as the range). The budgets are consistent with median value of CH_4 steady-state chemical lifetime of 9.6 years (Saunois et al., 2019). About 90% of CH_4 are lost in the troposphere by reaction with hydroxyl (OH) radicals and 6% by bacterial soil oxidation, and the rest is transported through the stratosphere-troposphere exchange into the stratosphere where CH_4 is lost by chemical reactions with OH, excited state oxygen (O^1D), atomic chlorine (Cl) (Patra et al., 2016; Saunois et al., 2016). Methane has significant emissions from both natural and anthropogenic origins, but a clear demarcation of their nature is difficult because of the use and conversions of natural ecosystem for human purposes. Methane sources, however, can also be divided into thermogenic, biogenic or pyrogenic processes. The greatest natural sources are wetlands, freshwaters and coastal oceans, while the largest anthropogenic emissions are due to ruminant farming and manure treatment, waste treatment (including landfills), rice cultivation and fossil fuels (Saunois et al., 2016; details in Section 5.2.2.5, Table 5.2). In the past two centuries, CH_4 emissions have nearly doubled and persistently exceeded the losses (*virtually certain*), thereby increasing the atmospheric abundance (Dalsøren et al., 2016; Ferretti et al., 2005; Ghosh et al., 2015). Since the cause of renewed CH_4 growth rate in the late 2000s has been debated highly in the recent literatures, the SRCCL (2019) has conducted as assessment with a focus on mainly the land processes. A wholesome assessment is done in this report by accounting for all source sector for emissions and atmospheric loss budgets (Cross-Chapter Box 5.1). Both the bottom-up and top-down estimations of the emissions and sinks are discussed (as in AR5). The bottom-up estimations are based on empirical upscaling of point measurements, emission inventories and dynamical model simulations, while the top-down estimations referred to those are constrained by atmospheric measurements and models.

5.2.2.1 Atmosphere

During the period with direct measurements of CH_4 in the atmosphere beginning in the 1970s (Figure 5.13), the increase rate was most rapid at the rate of 18 ± 4 ppb yr^{-1} during 1977–1986 (Rice et al., 2016). The rapid CH_4 growth was observed following the green revolution for increased crop-production and fast pace of industrialisation, because that period experienced rapid increases in CH_4 emissions from ruminant animals, landfills, coal mining, oil and gas industry, and rice cultivation (Ferretti et al., 2005; Ghosh et al., 2015; Janssens–Maenhout et al., 2017). Due to increases in oil prices in the early 1980s, emissions from gas flaring

declined significantly (Stern and Kaufmann, 1996). This is *likely* to explain the first reduction in CH_4 growth rates during 1985–1990 (Steele et al., 1992; Chandra et al., 2019). The causes of the temporary pause in CH_4 growth rate in the late 1990s and persistence through 2006 are often linked with the changes in emission or loss (Dlugokencky, 2003). CH_4 growth rates were about 6 ± 4 ppb yr^{-1} and 0.5 ± 3 ppb yr^{-1} during the 1990s and 2000–2006, respectively. Recent studies suggest a decrease in wetland emissions due to a lower surface temperature under the Mt Pinatubo aerosols in 1991 triggered further reduction in CH_4 growth rate (Bândă et al., 2016; Chandra et al., submitted). The cause of the renewed high CH_4 growth rate of about 7 ppb yr^{-1} since 2007 is highly debated even today (Dlugokencky et al., 2011; Nisbet et al., 2019), with studies conflicting on the relative contribution of thermogenic, pyrogenic and biogenic emissions (see Cross-Chapter Box 5.1). However, an increasing contribution from biogenic emissions is evidenced from reversal of $\delta^{13}C$ trend to lighter values post 2007; the opposite of that lasted for prior 200 years.

[START FIGURE 5.13 HERE]

Figure 5.13: Time series of CH_4 dry-air mole fraction (in ppb; panel a), growth rate (ppb yr^{-1}; panel b) and $\delta^{13}C$ (panel c) from selected site networks operated by NOAA (www.esrl.noaa.gov/gmd/ccgg/trends_ch4/), AGAGE (https://agage.mit.edu/data/agage-data) and PDX (Portland State University; (Rice et al., 2016)). To maintain clarity, data from many other measurement networks are not included here. Global mean values of XCH_4 (total-column), retrieved from radiation spectra measured by the Greenhouse gases Observation SATellite (GOSAT; www.gosat.nies.go.jp/en/recent-global-ch4.html) are shown in panels a and b. Cape Grim Observatory (CGO) and Trinidad Head (THD) data are taken from the AGAGE network, NOAA global and northern hemispheric (NH) means for $\delta^{13}C$ are calculated from 10 and 6 sites, respectively. The PDX data adjusted to NH (period: 1977–1996) are merged with THD (period: 1997–2018) for CH_4 concentration and growth rate analysis, and PDX and NOAA NH means of $\delta^{13}C$ data are used for joint interpretation of long-term trends analysis. The multivariate ENSO index (MEI) is shown in panel b (the shading indicates the period and strength of the El Nino).

[END FIGURE 5.13 HERE]

5.2.2.2 Anthropogenic CH_4 emissions

The gradient between CH_4 at Cape Grim, Australia (41°S) and Trinidad Head, USA (41°N), and theirs with the global mean CH4 strongly suggest the dominance of anthropogenic emissions (Figure 5.13), because the loss rate of CH_4 in troposphere should be equal due to parity in hemispheric mean OH concentration (Patra et al., 2014). CH_4 emissions from fossil fuels mainly originate from coal, gas, and oil emissions during their excavation, pumping, transport and use (Table 5.2.). Coal mining contributes to about 35% of the total CH_4 emissions from fossil fuels. Top-down estimates of fossil fuel emissions (101 Tg yr^{-1}) are slightly smaller than bottom-up estimates (113 Tg yr^{-1}) during 2010–2017. Both top–down and bottom–up methods suggest that emissions in 2008–2012 have increased from 2002–2006, with the BU method showing a larger increase (17 Tg yr^{-1}) than top–down (7 Tg yr^{-1}) (Patra et al., 2016; Saunois et al., 2016), which can be largely explained by the uncertainties in fugitive emissions from Chinese coal mines (Peng et al., 2016). Emissions from the China's coal mines are likely to have continued growing, as suggested by top-down estimations (Saunois et al., 2019; Chandra et al., 2019; Miller et al., 2019). The latest edition of the Emissions Database for Global Atmospheric Research (EDGAR, v4.3.2; Janssens-Maenhout et al., 2019) is in better agreement with the top-down estimates for the period 2007–2012 but a faster emission increase still persists between 2003–2007 in EDGARv4.3.2. By applying a box model on atmospheric CH_4 and $\delta^{13}C$ data for the period 2001–2014, global total methane emissions from fossil fuels are suggested to be 40 to 95% greater than mean value of 95 Tg yr^{-1} during 1990-1999 (Table 5.2), and further that the fossil fuel emission have decreased monotonically by about 25 Tg yr^{-1} between the period 1985–2002 and 2003–2013 (Schwietzke et al., 2016). The apportionment of multiple CH_4 source sectors using spatially aggregated atmospheric $\delta^{13}C$ data remained underdetermined to infer the global total emissions from fossil fuel industry, biomass burning, agriculture (Rice et al., 2016; Schaefer et al., 2016; Schwietzke et al., 2016; Worden et al., 2017; Thompson et al., 2018).

In the agriculture and waste sector, livestock production has the largest emissions (117 Tg yr^{-1} in 2010–2017) which are dominated by enteric fermentation (105 Tg yr^{-1}), while manure emissions are only about 10% of the total (EDGAR, v4.3.2). Methane is formed during the storage of manure, when anoxic conditions are developed (Hristov et al., 2013). The livestock emissions have been continuously increasing since 2000 from about 100 ± 1-Sigma Tg yr^{-1} to 119 ± 1-Sigma Tg yr^{-1} in 2017 [[Placeholder: complete the 1-sigma values]](EDGAR, v4.3.2; Janssens-Maenhout et al., 2019; Statistics division. Food and Agriculture Organisation of the United Nations, 2018; Wolf et al. 2017). Anthropogenic ruminant emissions are caused by CH_4 production in livestock rumens (cattle, goats, sheep) and are affected by the type, amount and quality of feeds, energy consumption, animal size, health and growth rate, production rate, and temperature (Broucek, 2014; Williams et al., 2015). Waste management and landfills produced 65 Tg CH_4 yr^{-1} in 2010-2017 (Saunois et al., 2019), and the emissions have been, with *high confidence,* steadily increasing since 1970's (EDGAR, v4.3.2; Janssens-Maenhout et al., 2019).

Emissions from rice cultivation tended to decrease from about 42 Tg yr^{-1} in the 1980s to about 33 Tg yr^{-1} in 2003 but have increased gradually by about 20% between 2003 and 2012 as per EDGARv4.3.2 (*low agreement, limited evidence*). Emissions are partly affected by climate, elevated CO_2 in atmosphere and site-specific soil C content, but can, to a large extent, be controlled by modifying management-related factors such as organic amendments, water management (from intermittent irrigation to continuous flooding), use of inorganic and organic fertilisers, and rice cultivars (Feng et al., 2013; Jiang et al., 2017; Liu et al., 2017b; Oo et al., 2018; Yang et al., 2018).

Biomass burning and biofuel consumption (include both natural and anthropogenic processes), causing an emission of at least 24 Tg CH_4 yr^{-1} constitute up to about 8% of global anthropogenic CH_4 emissions (*likely*). Wildfires comprise a small natural CH_4 source globally, with 3 Tg yr^{-1} being liberated into the atmosphere. The satellite observed burned area anomaly provided critical information for estimation of open biomass burning, which showed tight link with the natural climate variability, for example ENSO and explained a large part of the interannual variability in atmospheric CH_4 (Patra et al., 2016; Saunois et al., 2017; van der Werf et al., 2017). CH_4 emissions from open biomass burning show a decreasing trend during past two decades mainly due to reduction in Savanna, grassland and shrubland fires (van der Werf et al., 2017; Worden et al., 2017). There is recent evidence from the tropics that fire occurrence is non-linearly related to the precipitation, implying that severe droughts will increase CH_4 emissions from fires, particularly from the degraded peatlands (Field et al., 2016).

[START TABLE 5.2 HERE]

Table 5.2: Sources and sinks of CH_4 for the 4 recent decades from bottom–up and top-down estimations (in Tg yr^{-1}). The data are updated from Saunois et al. (2016), Kirschke et al. (2013) and references therein (e.g., Etiope et al., 2019; FAOSTAT, 2018; Herrero et al., 2016; Hristov, et al., 2013; Janssens-Maenhout et al., 2019; Poulter et al., 2017; Van Der Werf et al., 2017; Wik et al., 2016; Wolf et al., 2017). Note that the most top-down estimations cannot distinguish between various source sectors due to limited observations of molecular CH_4 and measurements of carbon and hydrogen isotopes in the atmosphere.

Global methane budget								
	1980-1989		1990-1999		2000-2009		2008-2017	
Tg CH4/yr	Top-Down	Bottom-Up	Top-Down	Bottom-Up	Top-Down	Bottom-Up	Top-Down	Bottom-Up
SOURCES								
Natural sources	203 (150-267)	355 (244-466)	182 (230-465)	336 (230-456)	214 (176-243)	369 (245-485)	215 (176-248)	371 (245-488)
Wetlands	167 (115-231)	225 (183-266)	150 (144-160)	206 (169-265)	180 (153-196)	147 (102-179)	178 (155-200)	149 (102-182)
Other Sources	35 (35-36)	130 (61-200)	32 (23-37)	130 (61-200)	35 (21-47)	222 (143-306)	37 (21-50)	222 (143-306)
Freshwater (lakes and rivers)		40 (8-73)				159 (117-212)		
Wild animals		15 (15-15)				2 (1-3)		
Termites		11 (2-11)				9 (3-15)		
Wildfires		3 (1-3)				*		
Permafrost (excl. lakes and wetlands)		1 (0-1)				1 (0-1)		
Geological (inc. Oceans)		54 (33-75)				45 (18-65)		
Other oceanic (inc. hydrates)		6 (2-9)				6 (4-10)		
Permafrost (excl. lakes and wetlands)		1 (0-1)				1 (0-1)		
Anthropogenic sources	348 (305-383)	308 (292-323)	372 (290-453)	313 (281-347)	331 (310-346)	334 (325-357)	357 (334-375)	366 (348-392)
Agriculture & Waste	208 (187-220)	185 (172-197)	239 (180-30)	188 (177-196)	202 (173-219)	192 (178-206)	219 (175-239)	206 (191-223)
Enteric fermentation & Manure		85 (81-90)		87 (82-91)		104 (93-109)		111 (106-116)
Landfills & waste		55 (50-60)		65 (63-68)		60 (55-63)		65 (60-69)
Rice		45 (41-47)		35 (32-27)		28 (23-34)		30 (25-38)
Fossil fuels	94 (75-108)	89 (89-89)	95 (84-107)	84 (66-96)	100 (70-149)	110 (93-129)	109 (79-168)	127 (111-154)
Coal		27 (27-27)		24 (19-28)		31 (24-42)		42 (29-60)
Oil and gas		61 (61-61)		58 (46-67)		73 (59-85)		79 (66-92)
Transport		1 (1-1)		1 (1-1)		4 (1-11)		4 (1-12)
Industry		1 (1-1)		1 (1-1)		2 (0-6)		3 (0-7)
Biomass burning & biofuels	46 (43-55)	34 (31-37)	38 (26-45)	42 (38-45)	29 (23-35)	32 (25-46)	30 (22-36)	30 (26-40)
Biomass burning						19 (15-32)		17 (14-26)
Biofuels						12 (9-14)		12 (10-14)
SINKS								
Total chemical loss	490 (450-533)	539 (411-671)	525 (491-554)	571 (521-621)	505 (459-516)	595 (489-749)	518 (474-532)	595 (489-749)
Tropospheric OH		468 (382-567)		479 (457-501)		553 (476-677)		553 (476-677)
Stratospheric loss		46 (16-67)		67 (51-83)		31 (12-37)		31 (12-37)
Tropospheric Cl		25 (13-37)		25 (13-37)		11 (1-35)		11 (1-35)
Soil uptake	21 (10-27)	28 (9-47)	27 (27-27)	28 (9-47)	34 (27-41)	30 (11-49)	38 (27-45)	30 (11-49)
Sum of sources	551 (500-592)	663 (536-789)	554 (529-596)	649 (511-569)	545 (522-559)	703 (570-842)	572 (538-593)	745 (600-893)
Sum of sinks	511 (460-559)	539 (420-718)	542 (518-579)	596 (530-668)	540 (486-556)	625 (500-798)	556 (501-574)	625 (500-798)
Imbalance	30 (16-40)		12 (7-17)		5 (11-36)		16	
Atmospheric growth rate (ppb yr-1)	12 ±6		6 ±8		2.1 ±0.3		6.6 ±0.3	

* Value not reported in Saunois 2019 to avoid potential double counting with satelite-based biomass burning products

[END TABLE 5.2 HERE]

5.2.2.3 Land biospheric emissions and sinks

Freshwater wetlands are the single largest global natural source of CH_4 into the atmosphere, accounting for about 30% of the total CH_4 source (*medium agreement, robust evidence*). Bottom-up and top-down estimates for 2010–2017 are 183 and 166 Tg CH_4 yr^{-1}, respectively, with a top-down uncertainty range of 125–204 Tg CH_4 yr^{-1} (updated from (Saunois et al., 2016)). The large uncertainties stem from challenges in mapping wetland area and temporal dynamics, and in scaling methane production, transport, and consumption processes, that are measured with small chambers or flux towers, to landscape estimates (Pham-Duc et al., 2017). Both the top-down and bottom-up estimates presented in Saunois et al. (2017) indicate little increase in wetland CH_4 emissions during the last three decades but are slightly smaller than in AR5 as the new wetland maps and ecosystem model simulations are available (Poulter et al., work in prog.). It is *likely* that the bulk of the post–2006 increase in atmospheric CH_4 concentration should be attributed to sources from animal farming and coal mining as the two major sectors. The evidence from land-surface models, emission inventories, isotopic $^{13}CH_4$ data and inverse modelling together suggested that sources other than wetlands are mainly responsible for the increase from 2002–2006 to 2008–2012 (Janssens-Maenhout et al., 2019; Patra et al., 2016; Poulter et al., 2017; Schaefer et al., 2016). The biogenic methane fluxes due to enteric fermentation, waste and manure management are also depleted in ^{13}C, relative to the ambient air.

Trees contribute to CH_4 emissions by producing it in photochemical reactions in the living parts, by conducting CH_4 from soil into the atmosphere and by the methanogenesis taking place in the stem (Covey and Megonigal, 2019). Although direct production of a marked amount of CH_4 by vegetation is considered *uncertain* and *unlikely*, there is emerging evidence of the role of trees in transporting and conducting CH_4 from soils into the atmosphere, which may further widen the gap between the bottom-up and top-down estimates in the global budget, particularly needing a reassessment of emissions in the tropics and in forested wetlands of temperate region (Pangala et al., 2017; Jeffrey et al., 2019; Welch et al., 2019).

Microbial methane uptake by soil comprises about 5% of the total atmospheric chemical CH_4 sink (Table 5.2). Since AR5, the estimate of global methane loss by microbial oxidation in upland soils has not changed significantly, the bottom-up value equalling 30 Tg yr^{-1} for 2000–2009 and 2008–2017 (Saunois et al., 2019). Evidence of both increasing (Yu et al., 2017) and decreasing (Ni and Groffman, 2018) soil microbial uptake during recent decades, due to higher temperature and higher precipitation, respectively, have emerged from experimental and modelling studies, but they do not allow making an assessment.

5.2.2.4 Ocean and inland emissions and sinks

Coastal oceans, fjords and mud volcanos are the major source of CH_4 in marine environment but measurement of CH_4 fluxes are sparse. However, there is an increasing amount of evidence of CH_4 seepage from the Arctic shelf, possibly triggered by the loss of geological storage due to warming and thawing of permafrost and hydrate decomposition (Shakhova et al., 2010, 2017). These emissions are estimated to be 2–9 Tg yr^{-1} (Table 5.2), and although they are *likely* to increase in a warmer world, the current flux is *likely* to be a mix of pre-industrial and climate change-driven fluxes. All geological sources, including the coastal oceans and fjords, around the world are estimated to emit CH_4 in the range of 35–76 Tg yr^{-1} (Etiope et al., 2019). There is evidence that the ventilation of geological CH_4 is *likely* to be smaller than 15 Tg yr^{-1} (Petrenko et al., 2017). A lower geological CH_4 ventilation will reduce the gap between top-down and bottom-up estimations (Table 5.2).

Inland water (lakes, rivers, streams, ponds, estuaries) emissions are proportionally the largest source of uncertainty in the CH_4 budget. Since AR5, the cumulative estimate of inland water CH_4 source has been revised from 8–73 Tg yr^{-1} to 60–180 Tg yr^{-1} with the availability of more observational data and improved areal estimates (Bastviken et al. 2011; Deemer et al. 2016; Stanley et al. 2016; DelSontro et al. 2018; Saunois et al., 2019). A large spatial and temporal variation in lake and river CH_4 fluxes (Natchimuthu et al., 2017; Wik et al., 2016; Crawford et al., 2017) and uncertainties in global area of them (Allen and Pavelsky, 2018), together with a relatively small number of observations, varying measurement and upscaling methods and lack of appropriate process models (Saunois et al., 2019) make the bottom-up CH_4 emission estimate uncertain with *high confidence*. Accordingly, there is no clear accounting of inland waters in top-down budgets, which is the main reason for the large gap in bottom-up and top-down estimates of "other sources" in the CH_4 budget (Table 5.2). Despite recent progress in separating wetlands from inland waters, there is double accounting in the bottom-up estimates of their emissions (*medium confidence*) (Thornton et al., 2016). Although there is evidence that human impact and climate warming both increase the inland water CH_4 emissions (Beaulieu et al., 2019), the increase in the decadal emissions since AR5 rather reflect improvements in the estimate (*medium confidence)*, such as reduced double counting and new upscaling approaches than an increasing trend in the actual emissions (Saunois et al., 2019). New studies, since the AR5, suggest that the reservoir and estuary emissions contribute up to 13 and 7 Tg yr^{-1}, respectively (Borges and Abril, 2011; Deemer et al., 2016).

5.2.2.5 CH_4 budget

A summary of top-down and bottom-up estimations of CH_4 emissions and sinks for the period 2010–2017 are depicted in Figure 5.14 (details in Table 5.2). Since AR5, the uncertainty in sectorial emissions have reduced significantly, except for the emissions from freshwaters (60–180 Tg yr^{-1}). Presently freshwater emissions are not considered in the top-down model simulations. The decadal mean CH_4 burden increase has been about 42, 17, 6 and 20 Tg yr^{-1} in the 1980s, 1990s, 2000s and 2010s (*virtually certain*), respectively, as can be estimated from observed atmospheric increase. It is *very likely* that the inter-decadal differences in CH_4 growth rate is driven by changes in emissions rather than the OH variability. Variability in OH is very uncertain and is *likely* to be of some importance at interannual or shorter time scales (Chapter 6 and Cross-Chapter Box 5.1).

[START FIGURE 5.14 HERE]

Figure 5.14: Schematic diagram of major sources and sinks of CH_4 for the decade 2010–2017 (in Tg CH_4). Values and data sources as in Table 5.2.

[END FIGURE 5.14 HERE]

[START CROSS-CHAPTER BOX 5.1 HERE]

Cross-Chapter Box 5.1: Drivers of atmospheric methane changes during 1980–2019

Contributors:
Josep G. Canadell (Australia), Frank Dentener (EU, Netherlands), Xin Lan (USA), Vaishali Naik (USA), Prabir K. Patra (Japan/India)

Atmospheric methane (CH_4) growth rate varied widely over the past three decades. The mean growth rate decreased from 15 ± 5 ppb yr^{-1} in the 1980s to 0.48 ± 3.2 ppb yr^{-1} during 2000–2006 (the so-called quasi-equilibrium phase) and returned to an average rate of 7.1 ± 2.7 ppb yr^{-1} in the past decade (2009–2018) (based on data in Figure 5.12). Atmospheric CH_4 grew sharply (9.1 ± 2.4 ppb yr^{-1}) over the last five years (2014–2018), a period that included a prolonged El Niño condition covering 2014–2015. During the prolonged El Niño conditions covering 2014-2015 CH_4 growth rates were high, as occurred also during previous El Niño events (Figure 5.12b). Because of large uncertainties in both the emissions and sinks of CH_4, it has been challenging to quantify accurately the methane budget and ascribe reasons for the growth over the past decade. To address greenhouse gas mitigation, it is critical to know if changes are related to emissions from human activities or from natural processes responding to changing climate. Due to these uncertainties, projections of atmospheric methane considered in AR5 and the IPCC 1.5°C Special Report (IPCC, 2018b) did not anticipate this renewed growth after a period of stabilisation (Ciais et al., 2013; Rogelj et al., 2018). A sustained growth of CH_4 at rates similar to those observed over the past decade contribute to decadal scale climate change and weaken countries' ability to meet the Paris agreement goal of keeping global average temperature increase well below 2°C (Nisbet et al., 2019).

Cross-Chapter Box 5.1 Figure 1 shows the decadal CH_4 budget derived from the Global Carbon Project (GCP)-CH_4 synthesis for 1980s, 1990s and 2000s (Kirschke et al., 2013), and for 2010–2017 (Saunois et al., 2019). The sources and sinks as estimated from top-down (T-D; atmospheric observation inversions) and bottom-up (B-U; process-based models for land surface emissions and global chemistry-climate models driven by anthropogenic emission inventories) studies are shown. Natural sources include emissions from natural wetlands, lakes and rivers, land-based geologic, wild animals, termites, wildfires, permafrost soils, and oceans (offshore geologic and hydrates). Anthropogenic sources include emissions from enteric fermentation and manure, landfills, waste and waste water, rice cultivation, coal mining, oil and gas industry, biomass and biofuel burning. The top-down total sink determined from global mass balance, includes loss due to reactions with hydroxyl (OH), atomic Cl, and O^1D, and oxidation by bacteria in aerobic soils.

[START CROSS-CHAPTER BOX 5.1, FIGURE 1 HERE]

Cross-Chapter Box 5.1, Figure 1: Methane budget estimates for four decades from top-down (darker colour, left; labelled T-D) and bottom-up (lighter colour, right; labelled B-U) analyses (plotted on the left y axis). Sources are positive and sinks are negative. The black line (plotted on the right y axis) represents observed global monthly mean atmospheric CH_4 in dry-air mole fractions for 1983–2019 (www.esrl.noaa.gov/gmd/ccgg/trends_ch4; Dlugokencky et al. 2019). The bottom-up total sinks are inferred from global mass balance, that is source minus growth in atmospheric CH_4 abundance, and are given as the numbers under the top x-axis for different decades.

[END CROSS-CHAPTER BOX 5.1, FIGURE 1 HERE]

Since AR5, many studies have discussed the role of different source categories in explaining the increase in CH_4 growth rate since 2007 and a coincident decrease of $\delta^{13}C–CH_4$ and $\delta D–CH_4$ isotopes (ref. Figure 5.12; Rice et al., 2016). Both ^{13}C and D are enriched in mass-weighted average source signatures for CH_4 emissions from thermogenic sources (e.g., coal mining, oil and gas industry) and pyrogenic (biomass burning) sources, and depleted in biogenic (e.g., wetlands, rice paddies, enteric fermentation, landfill and waste) sources. Proposed hypotheses for CH_4 growth (2007–2017) vary from a concurrent decrease in thermogenic and an increase in wetland and other biogenic emissions (Nisbet et al., 2016; Schwietzke et al., 2016), emissions increase from agriculture in the tropics (Schaefer et al., 2016), a concurrent reduction in pyrogenic and increase in thermogenic emissions (Worden et al., 2017) or emission increase from biogenic sources and a slower increase in emissions from thermogenic sources compared to inventory emissions (Chandra et al., submitted; Patra et al., 2016; Saunois et al., 2017b; Thompson et al., 2018a). The decrease (1985–2000) in ethane (C_2H_6), the 2nd most abundant hydrocarbon after CH_4 in the remote atmosphere, suggests that decreasing emissions from venting and flaring of natural gas in oil fields have reduced the CH_4 growth rates in the 1980s/1990s (Simpson et al., 2012).

A few studies have emphasised the role of chemical destruction by OH, the primary sink of methane, in driving changes in the growth of atmospheric methane abundance, in particular after 2006. Box-model atmospheric inversions suggest declining OH after 2006 contributes to renewed methane growth (Rigby et al., 2017; Turner et al., 2017), however, when uncertainties inherent in such box modelling approaches are accounted for, no systematic decline in global mean OH is simulated for the post-2006 period (Naus et al., 2019). Studies applying three-dimensional atmospheric inversion (McNorton et al., 2018), simple multi-species inversion (Thompson et al., 2018) as well as empirical method using a variety of observational constraints based on OH chemistry (Nicely et al., 2018) do not find trends in OH large enough to play a role in methane changes post-2006. On the contrary, global chemistry-climate models based on fundamental principles of atmospheric chemistry and known emission trends of precursors simulate an increasing trend in OH (more than 8%) over the past three decades with small (< 3%) interannual variability (Dalsøren et al., 2016; Stevenson et al., 2019; Zhao et al., 2019) (see Section 6.2.3). While OH is important for maintaining the balance between methane source and sink, it is not the primary driver of the renewed rise in atmospheric methane since 2007 (*medium confidence*).

Methane emissions derived by inversion models using their best OH estimates (Turner et al., 2017), sharply increase by up to about 30 Tg yr^{-1} (or 6%) from 1990-1994 to 2000-2004 and decrease afterwards. The sharp increase in the late 1990s and decrease throughout the period of 2004-2012 is inconsistent with anthropogenic inventory emissions estimated for farmed animals, the fossil fuel industry and distribution, and waste management (e.g., Janssens-Maenhout et al., 2019). However, a more consistent picture emerges for the regional trends of emission rates from high-resolution inverse modelling, where observations from individual sites are utilised to optimise subcontinental scale CH_4 emissions (Cross-Chapter Box 5.1 Figure 2). Because the emissions are derived at monthly or shorter time scales, the effect of OH inter-annual variability does not strongly influence the determination of regional emission trends. CH_4 lifetime in any latitude band is one year or longer, and its global mean lifetime is about 9.6 years; both much longer than the mixing timescales of regional emissions within one hemisphere (~weeks). Cross-Chapter Box 5.1 Figure 2 suggests that progress toward atmospheric CH_4 quasi-equilibrium was primarily driven by reductions in emissions in Europe, Russia and Temperate North America over 1988–2000. In the global totals, emissions equalled loss in the early 2000s. The recent growth since 2006 is driven by increasing emissions from East Asia (1997–2016), West Asia (2005–2016), Brazil (1988–2016), temperate North America (2010–2016), Northern Africa (2015–2016). A recent study using a variety of sensitivity simulations by changing OH, provides further evidence for strong link between the total emission variability and CH_4 growth rate at inter-decadal time periods, and only minor role of OH on the interannual CH_4 variability (Chandra et al., submitted).

[START CROSS-CHAPTER BOX 5.1, FIGURE 2 HERE]

Cross-Chapter Box 5.1, Figure 2: Anomalies in regional CH_4 emissions during 1988–2016, and a representative CH_4 emission map are shown. Results for 2000–2016 are shown for 6 inversion models that participated in GCP-CH_4 budget assessment (Saunois et al., 2019), and results for 1988–1999 are available from only one inversion using 19 sites only (Chandra et al., submitted). A long-term mean value, as indicated within each panel separately for the GCP average and MIROC4-19 sites, is subtracted from the annual-mean time series for the calculation of anomalies for each region.

[END CROSS-CHAPTER BOX 5.1, FIGURE 2 HERE]

There is evidence from emission inventories at country level and regional scale inverse modelling that CH_4 growth rate variability during the 1980s through the 2010s is closely linked to anthropogenic activities (*likely, medium agreement*). Isotopic composition observations and inventory data suggest that both fossil fuels and agriculture are *likely* playing a role in the resumed CH_4 growth and trends since 2007. Shorter-term variability is predominantly driven by the El Niño Southern Oscillation, and *very likely* associated with emissions from wetland and biomass burning, and loss due to OH. By synthesising all available information regionally from a priori (bottom-up) emissions and inverse modelling (top-down observation constraints), the capacity to track "changes" in natural and anthropogenic emissions has been improved since the AR5. Inventory data suggest increases in emissions from East Asia and Temperate North America are primarily of industrial origin, while the emission increase from West Asia, Southeast Asia and Brazil are driven by the agricultural sectors. For segregating regional sources types by top-down methods denser surface observation networks for more number of species and remote sensing observations in an improved modelling framework will be critical by the time of global stocktake (Pandey et al., 2019).

[END CROSS-CHAPTER BOX 5.1 HERE]

5.2.3 N_2O: Trends, Variability and Budget

Changes in the atmospheric abundance of nitrous oxide (N_2O) result largely from the balance of the net N_2O sources on land and ocean, and the photochemical destruction of N_2O in the stratosphere. In land, freshwater systems and oceans, N_2O is primarily produced during the remineralisation of organic matter via the primary processes of nitrification and denitrification (Butterbach-Bahl et al., 2013; Voss et al., 2013). The net N_2O production is, amongst others, highly sensitive to local temperature, oxygen concentrations, pH and the concentrations of ammonium and nitrate, causing strong variability of N_2O emissions in time and space. Since AR5, improved understanding the N_2O sources allows for a more comprehensive assessement of the global N_2O. The human perturbation of the natural nitrogen cycle through the use of articial fertiliser and manure, as well as N deposition resulting from land-based agriculture and fossil fuel burning have been the largest driver of the increase in atmospheric N_2O of 30.1 ppb (10%) between 1980 and 2018 (*robust evidence, high confidence*). The rise of tropospheric N_2O is of concern, not only because of its contribution to the anthropogenic radiative forcing (see Chapter 7), but also because of the importance of N_2O in stratospheric ozone loss (Ravishankara et al., 2009; Fleming et al., 2011).

5.2.3.1 Atmosphere

The present-day level of tropospheric abundance N_2O, of 331.2 ± 0.6 ppb (parts per billion) for 2018, is 23% higher than pre-industrial levels of 270 ± 3.4 ppb (Figure 5.15) (MacFarling Meure et al., 2006; Prinn et al., 2016; Elkins et al., 2018)) (*robust evidence, high agreement*). Since the late 1990s, atmospheric measurements with high accuracy and density show an average tropospheric growth rate of 0.80 ± 0.07 ppb yr^{-1} (mean and interannual standard deviation for 1999 to 2018, Figure 5.15a). The growth rate exhibits large interannual variations and shows an increase of nearly 20% between the decade 1999 to 2008 and the most

recent decade (2009 to 2018; 0.93 ± 0.14 ppb yr^{-1}) (Elkins et al., 2018)). The growth rate in 2009–2018 is also higher than during 1970–2000 of 0.6–0.8 ppb yr^{-1} (Ishijima et al., 2007) and the thirty-year period prior to 2011 (0.73 ± 0.03 ppb yr^{-1}), as reported by AR5. In the tropics and sub-tropics, inter-annual variations in the atmospheric growth rate are negatively correlated with the multivariate ENSO index (MEI) and associated anomalies in land and ocean fluxes (Ishijima et al., 2009; Thompson et al., 2013) (Figure 5.15, and Section 5.2.3.3, 5.2.3.4). In the mid to high latitudes of both hemispheres, inter-annual variations in the seasonal minima of N_2O abundance are correlated with anomalies in the winter-spring temperature of the lower stratosphere (Nevison et al., 2011). This suggests that inter-annual variations in the stratosphere to troposphere air mass transport, coupled with the stratospheric depletion of N_2O, contribute to the inter-annual variability of tropospheric N_2O in the mid to high latitudes. However, the quantitative understanding of the processes influencing the inter-annual variations of natural N_2O emissions and tropospheric abundance is poor.

Combined firn ice air and atmospheric measurements show that the $^{15}N/^{14}N$ isotope ratio (*robust evidence, high confidence*), as well as the 15N site preference (*limited evidence, low confidence*), in N_2O has changed since 1940 (Figure 5.15b, c) (Ishijima et al., 2007; Park et al., 2012; Prokopiou et al., 2017), whereas they were relatively constant in the pre-industrial period (Prokopiou et al., 2018). This change indicates that the N-substrate available for (de-)nitrification, and the relative contribution of nitrification to the global N_2O source have increased. Both of these phenomena are associated with increased fertiliser use in agriculture (Davidson, 2009; Zaehle et al., 2011; Park et al., 2012; Prokopiou et al., 2018).

[START FIGURE 5.15 HERE]

Figure 5.15: (a) Atmospheric N_2O abundance (parts per billion, ppb) and growth rate (ppb yr^{-1}), (b) δ15N of atmospheric N_2O, and (c) alpha-site $^{15}N–N_2O$, based on direct atmospheric measurements in the AGAGE and NOAA (Prinn et al., 2000, 2016; Hall et al., 2007; Elkins et al., 2018) networks, archived air samples from Cape Grim, Australia (Park et al., 2012), and firn air from NGRIP Greenland and H72 Antarctica (Ishijima et al., 2007), Law Dome Antarctica (Park et al., 2012), and NEEM Greenland (Prokopiou et al., 2017). Grey shading in (a) are times of positive values of the multivariate ENSO index, indicating El Niño conditions (Wolter and Timlin, 1998).

[END FIGURE 5.15 HERE]

5.2.3.2 Anthropogenic N_2O emissions

Agriculture is the largest anthropogenic source of N_2O emissions and emits 3.8 (2.5–5.8) TgN yr^{-1} (average 2007–2016), owing to the widespread use of nitrogen fertiliser and manure on cropland and pasture, manure management and aquaculture (Table 5.3 (Tian et al., submitted, b)). Agricultural N_2O emissions have increased by approximately 80% since the early 1900s (Davidson, 2009), and by more than 45% since the 1980s (*robust evidence, high agreement*) (Figure 5.16). During 1980–2016, increased use of nitrogen fertiliser and manure in agriculture contributed to about 70% of the increase, with further contributions by manure application in pasture/range/paddock and manure management. Although N_2O emissions from aquaculture are amongst the fastest rising contributors of N_2O emissions, their overall magnitude is still small in the overall N_2O budget (Tian et al., submitted, b). Estimates of agricultural emissions are either based on empirical emission factors (De Klein et al., 2006; Smith et al., 2012a; Tubiello et al., 2013; Janssens-Maenhout et al., 2019) or process-based modelling (Tian et al., 2019). As discussed in SRCCL, both approaches are subject to large uncertainties regarding the extrapolation of data in space and time and the ability to account adequately for the heterogeneity in environmental factors affecting emissions (Shcherbak et al., 2014; Zhou et al., 2015; Gerber et al., 2016; Wagner-Riddle et al., 2017).

[START FIGURE 5.16 HERE]

Figure 5.16: Decadal mean N_2O emissions for 2007–2016 based on the N_2O Model Intercomparison Project (NMIP)

ensemble of terrestrial biosphere models (Tian et al., 2019) and three ocean biogeochemical models (Landolfi et al., 2017; Battaglia and Joos, 2018a; Buitenhuis et al., 2018), as well as the change in N_2O emissions from terrestrial soils (natural and agriculture) simulated from the (Tian et al., 2019). The effect of anthropogenic nitrogen additions (atmospheric deposition, manure addition, fertiliser use and land-use) is evaluated against the background flux driven by changes in atmospheric CO_2 concentration, and climate change.

[END FIGURE 5.16 HERE]

The principal non-agricultural anthropogenic sources of N_2O are industry, specifically chemical processing, and the combustion of fossil fuels. Industrial emissions of N_2O mainly due to nitric and adipic acid production have decreased since the wide-spread installation of abatement technologies in the 1990s (Pérez-Ramírez et al., 2003; Lee et al., 2011; Janssens-Maenhout et al., 2019). However, contributions from fossil fuel combustion emissions by stationary sources, such as power plants, as well as smaller emissions from mobile sources (e.g. road transport and aviation) have resulted in near-constant industry and fossil fuel related emissions in the 1980s and 1990s (Wiesen et al., 1994, 1996; Heland and Schäfer, 1998; Graham et al., 2009; Bouwman et al., 2013). Two inventories suggest increases in emissions from industry and fossil fuel use in East Asia, South Asia, and Africa during 2000-2016 while emissions in Europe and North America decreased, resulting in an estimated global increase from 0.9 (0.8–1.0) TgN yr^{-1} to 1.0 (0.8–1.1) TgN yr^{-1} during 2000–2016 (*moderate evidence, medium agreement*) (Tian et al., submitted, a).

Biomass burning from crop residue burning, grassland, savannah and forest fires, as well as biomass burnt in household stoves, releases N_2O during the combustion of organic matter. Updated inventories since AR5 result in a lower range of the decadal mean emissions of 0.6 (0.5–0.8) TgN yr^{-1} (Tian et al., submitted, a). However, there is substantial interannual variability reflecting the variability in global fire activity (van der Werf et al., 2017). The attribution of grassland, savannah or forest fires to natural or anthropogenic origins is uncertain, preventing a separation of the biomass burning source into natural and anthropogenic. Wastewater N_2O emissions, including those from domestic and industrial sources are estimated to have increased from 0.2 (0.1–0.3) TgN yr^{-1} to 0.3 (0.2–0.5) TgN yr^{-1} between the 1980s and 2007–2016 (Tian et al., submitted, a).

5.2.3.3 Emissions from Ocean, Inland water bodies and Estuaries

Since AR5, new estimates of the global ocean N_2O source derived from ocean biogeochemistry models are 3.4 (2.5–4.3) TgN yr^{-1} for the period 2007-2016, and slightly lower than some of the earlier empirically based-methods (Bianchi et al., 2012; Manizza et al., 2012; Suntharalingam et al., 2012; Martinez-Rey et al., 2015; Landolfi et al., 2017; Battaglia and Joos, 2018b; Buitenhuis et al., 2018). Reduced upwelling in the eastern tropical Pacific during El Niño conditions reduces the ocean N_2O source and thereby contributes to the interannual variability of the ocean N_2O source (Nevison et al., 2007; Ji et al., 2019).

In the oxic ocean (> 97% of ocean volume), nitrification is believed to be the primary N_2O source (Freing et al., 2012). In sub-oxic ocean zones (see Section 5.3), where denitrification prevails, higher N_2O yields and turnover rates make these regions potentially significant sources of N_2O (Arévalo-Martínez et al., 2015; Babbin et al., 2015; Ji et al., 2015). The relative proportion of ocean N_2O from oxygen-minimum zones is *highly uncertain* (Zamora et al., 2012). Estimates derived from in-situ sampling, particularly in the eastern tropical Pacific, suggest significant fluxes from these regions, and potentially up to 50% of the global ocean source (Codispoti, 2010; Arévalo-Martínez et al., 2015; Babbin et al., 2015). However, recent global-scale analyses estimate lower contributions (4 to 7%, Battaglia and Joos, 2018; Buitenhuis et al., 2018). Further investigation is required to reconcile these estimates and provide improved constraints on the N_2O source from low-oxygen zones.

Atmospheric deposition of anthropogenic N on oceans can stimulate marine productivity and influence ocean emissions of N_2O. Recent ocean model analyses suggest a relatively modest global potential impact of 0.01–0.32 TgN yr^{-1} (pre-industrial to present-day) equivalent to 0.5–3.3% of the global ocean N_2O source (Suntharalingam et al., 2012; Jickells et al., 2017; Landolfi et al., 2017). However, larger proportionate

impacts are predicted in nitrogen-limited coastal and inland waters down-wind of continental pollution outflow, such as the Northern Indian Ocean (Jickells et al., 2017; Suntharalingam et al., 2019).

N_2O processes in coastal upwelling zones are only poorly represented in global estimates of marine N_2O emissions (Kock et al., 2016), but may account for and additional 0.2 to 0.6 TgN yr^{-1} of the global ocean source (Seitzinger et al., 2000; Nevison et al., 2004). Inland waters are generally sources of N_2O as a result of nitrification and denitrification of dissolved inorganic nitrogen, however, they can serve as N2O sinks in specific conditions (Webb et al., 2019). Since AR5, improved emission factors including their spatio-temporal scaling, and consideration of transport within the aquatic system allow to better constrain these emissions and separate these into natural and anthropogenic emissions (Hu et al., 2016; Maavara et al., 2019; Murray et al., 2015; Tian et al., submitted, a). The attribution to inland water N_2O emissions to anthropogenic sources leads to the increased anthropogenic share of the global N_2O source compared to AR5. As indirect consequence of agricultural nitrogen-use and waste-water treatment, the anthropogenic emissions from inland waters have increased by about a quarter (0.1 TgN yr^{-1}) between the 1980s and 2007–2016.

5.2.3.4 Emissions and sinks in non-agricultural land

Soils are the largest natural source of N_2O, arising from nitrogen processing associated with nitrification and denitrification (Butterbach-Bahl et al., 2013; Snider et al., 2015). Under some conditions, soils can also act as a net sink of N_2O, but this effect is small compared to the overall source (Schlesinger, 2013). Since AR5, improved global process-based models (Tian et al., 2019) suggest a present-day source of 6.7 (5.3–8.1) TgN yr^{-1} from non-agricultural soils during the period 2007–2016 that is consistent with independent inventory-based methods (Winiwarter et al., 2018; Janssens-Maenhout et al., 2019). The largest source of natural terrestrial N_2O emissions is in the tropics, 4.3 TgN yr^{-1} for 23.5°N–23.5°S during the period 1980–2016 (Tian et al., 2019). Reduction in precipitation in the tropics and sub-tropics associated with El Niño conditions may lead to reduced tropical N_2O emissions from land (Werner et al., 2007). Model simulations do not suggest a trend over this time, but do not account for increased N_2O emissions from tropical peatlands due to land-use change (Hadi et al., 2000).

Despite remaining uncertainties in process-based models with respect to their ability to accurately capture the complicated responses of terrestrial N_2O emissions to rain pulses, freeze-thaw cycles and the net consequences of elevated levels of CO_2 (Tian et al., 2019), this progress allows to separate the natural background emissions from trends induced by the effect of atmospheric N deposition, land-use, climate and atmospheric CO_2 change. Models and inventory-based methods suggest that increased N deposition has enhanced terrestrial N_2O emissions by 0.8 (0.4–1.4 TgN yr^{-1}) relative to pre-industrial times, and by 0.2 (0.1–0.2) TgN yr^{-1} between the 1980s and 2007–2016 (*limited evidence, moderate agreement*). This estimate is at the high end of the range reported in AR5. Model projections further suggest that global warming has been associated with an increase in soil N_2O emissions of 0.8 (0.3–1.3) TgN yr^{-1} since pre-industrial times, of which about half occurred since the 1980s (*limited evidence, moderate agreement* (Tian et al., submitted b). As discussed in SRCCL, land-use change significantly alters the N_2O emissions through emission pulses following conversions and changes in the area of intact ecosystems (Tian et al., submitted, b).

5.2.3.5 N_2O budget

[START FIGURE 5.17 HERE]

Figure 5.17: Global nitrous oxide (N_2O) budget for the period 2007–2016. Annual nitrous oxide fluxes (TgN_2O–N yr^{-1}), as described in Table 5.3, and the atmospheric nitrous oxide pools (TgN_2O–N)

[END FIGURE 5.17 HERE]

The N_2O budget derived from the synthesis of empirical and process-based bottom-up sources in Sections 5.2.3.2- 5.2.3.4 yield a global N_2O source of 17.0 (12.2–23.5) TgN yr^{-1} for the years 2007–2016 (Figure 5.17, Table 5.3). This estimate is comparable to AR5, but the uncertainty range has been reduced primarily due to improved estimates of the ocean and anthropogenic N_2O sources. Improved budget estimates now cover the time period 1980–2016 and allow to assess with *high confidence* that anthropogenic emissions from agricultural nitrogen use, industry and other indirect effects have increased by 1.7 (1.0–2.7) TgN yr^{-1} between the 1980s and 2007–2016 and were thereby the primary cause of the increase in the total N_2O source. In 2007–2016, anthropogenic emissions contributed about 40% (7.3; uncertainty range: 4.2–11.4 TgN yr^{-1}) to the total N_2O source.

Since AR5, improvements in the capacity to estimate N_2O sources from atmospheric N_2O measurements by inverting models of atmospheric transport provides new and independent estimates to constrain the global N_2O budget. This new top-down estimate of 16.9 (15.9–17.7) TgN yr^{-1} is remarkably consistent with the bottom-up global N_2O budget for the same period (Saikawa et al., 2014; Thompson et al., 2019; Tian et al., submitted, a). Based on the observed growth rate of atmospheric N_2O and simulations of the atmospheric loss of N_2O, the inversions suggest an increase in global emissions between the 2000s and 2007–2016 of 1.0 (1.4–1.7) TgN yr^{-1}, which is larger than the increase based on bottom-up estimates for the same period. The increase is primarily caused by changes in land-based emissions (90%), in particular in East Asia (26%) (Thompson et al., 2019). Notably, the split between land and ocean sources based on atmospheric inversions is less well constrained, yielding 11.3 (10.2–13.2) TgN yr^{-1} and 5.7 (3.4–7.2) TgN yr^{-1} for land and ocean, respectively.

The revised estimate of the mean atmospheric lifetime of N_2O (116 ± 9 years) with has a small negative feedback of the N_2O lifetime to increasing atmospheric N_2O resulting in a slightly lower residence time (109 ± 10 years) of N_2O perturbations (Prather et al., 2015) is lower than assessed by AR5 (118–131 years), The dominant N_2O loss occurs through photolysis and oxidation by O(1D) radicals in the stratosphere and amounts to approximately 13.1 (12.4–13.6) TgN yr^{-1} (Minschwaner et al., 1993; Prather et al., 2015; Tian et al., submitted, a). The imbalance between the sum of N_2O sources and atmospheric loss results in an increase in atmospheric N_2O abundance 4.5 (4.3–4.6) TgN yr^{-1} as determined from the atmospheric growth rate for 2007–2016. The long atmospheric lifetime of N_2O implies that it will take more than a century before atmospheric abundances stabilise after the stabilisation of global emissions.

[START TABLE 5.3 HERE]

Table 5.3: Global N_2O budget (units TgN yr^{-1}), derived from a compilation of inventories, bottom-up models, as well as atmospheric inversions as described in (Tian et al., submitted, a)

	AR6 1980–1989	AR6 1990–1999	AR6 2000–2009	AR6 (2007–2016)	AR5 (2006)
Bottom-up budget					
Anthropogenic Sources					
Fossil Fuel combustion and Industry	0.9 (0.8–1.1)	0.9 (0.9–1.0)	0.9 (0.8–1.0)	1.0 (0.8–1.1)	0.7 (0.2–1.8)
Agriculture (incl. Aquaculture)[b]	2.6 (1.8–4.1)	3.0 (2.1–4.8)	3.4 (2.3–5.2)	3.8 (2.5–5.8)	4.1 (1.7–4.8)
Biomass and biofuel burning[c]	0.7 (0.7–0.7)	0.7 (0.6–0.8)	0.6 (0.6–0.6)	0.6 (0.5–0.8)	0.7 (0.2–1.0)
Wastewater[d]	0.2 (0.1–0.3)	0.3 (0.2–0.4)	0.3 (0.2–0.4)	0.3 (0.2–0.5)	0.2 (0.1–0.3)
Inland water, estuaries, coastal zones	0.4 (0.2–0.5)	0.4 (0.2–0.5)	0.4 (0.2–0.6)	0.5 (0.2–0.7)	
Atmospheric N deposition on ocean[f]	0.1 (0.1–0.2)	0.1 (0.1–0.2)	0.1 (0.1–0.2)	0.1 (0.1–0.2)	0.2 (0.1–0.4)
Atmospheric N deposition on land[e]	0.6 (0.3–1.2)	0.7 (0.4–1.4)	0.7 (0.4–1.3)	0.8 (0.4–1.4)	0.4 (0.3–0.9)

Other indirect effects from CO_2, climate and land-use change	0.1 (-0.4–0.7)	0.1 (-0.5–0.7)	0.2 (-0.4–0.9)	0.2 (-0.6–1.1)	
Total Anthropogenic	**5.6 (3.6–8.7)**	**6.2 (3.9–9.6)**	**6.7 (4.1–10.3)**	**7.3 (4.2–11.4)**	**6.3 (2.6–9.2)**
Natural Sources and Sinks					
Rivers, estuaries, and coastal zones[g]	0.3 (0.3–0.4)	0.3 (0.3–0.4)	0.3 (0.3–0.4)	0.3 (0.3–0.4)	0.6 (0.1–2.9)
Oceans[h]	3.6 (3.0–4.4)	3.5 (2.8–4.4)	3.5 (2.7–4.3)	3.4 (2.5–4.3)	3.8 (1.8–9.4)
Soils under natural vegetation[e]	5.6 (4.9–6.6)	5.6 (4.9–6.5)	5.6 (5.0–6.5)	5.6 (4.9–6.5)	6.6 (3.3–9.0)
Atmospheric chemistry[i]	0.4 (0.2–1.2)	0.4 (0.2–1.2)	0.4 (0.2–1.2)	0.4 (0.2–1.2)	0.6 (0.3–1.2)
Surface sink[k]	-0.01 (-0.3–0)	-0.01 (-0.3–0)	-0.01 (-0.3–0)	-0.01 (-0.3–0)	-0.01 (-1–0)
Total natural	**9.9 (8.5–12.2)**	**9.8 (8.3–12.1)**	**9.8 (8.2–12.0)**	**9.7 (8.0–12.0)**	**11.6 (5.5–23.5)**
Total bottom-up source	**15.5 (12.1–20.9)**	**15.9 (12.2–21.7)**	**16.4 (12.3–22.4)**	**17.0 (12.2–23.5)**	**17.9 (8.1–30.7)**
Observed growth rate[l]			**3.7 (3.7–3.7)**	**4.5 (4.3–4.6)**	**3.6 (3.5–3.8)**
Inferred stratospheric sink			**12.9 (12.2-13.5)**	**13.1 (12.4–13.6)**	14.3 (4.3–28.7)
Atmospheric inversion[n]					
Atmospheric loss			12.1 (11.4–13.3)	12.4 (11.7–13.3)	
Total source			15.9 (15.1–16.9)	16.9 (15.9–17.7)	
Imbalance			3.6 (2.2–5.7)	4.2 (2.4–6.4)	

[END TABLE 5.3 HERE]

5.2.4 The relative importance of CO_2, CH_4, and N_2O

The total influence of anthropogenic GHGs on the Earth's radiative balance and further consequences needs to be understood as the combined effect of those gases, and the three most important were discussed separately in the previous sections. This section compares the balance of the sources and sinks of the three gases and their regional net flux contributions to the radiative forcing. GHGs include spatially heterogenous gases such as ozone or shorter lives species, and well mixed gases (e.g., CO_2, CH_4, N_2O) with both anthropogenic sources and sinks, and the other category produced entirely by industrial processes, also called synthetic gases (e.g., perfluoro-compounds, chlorofluorocarbons, HCFCs, HFCs). Chapter 6 discusses the spatial heterogeneity of atmospheric species and shows it is proportional to their chemical lifetime (Figure 6.1). CH_4, which has a lifetime of about 9.6 years, considered a short-lived pollutant but are well mixed in the troposphere to play significant role in global radiative forcing. Figure 5.18 shows that CO_2 in atmosphere is by far the single most important GHG, with greater increase of its radiative forcing since the 1960s (see also Figure 2.9). For the period 2007–2016, the relative contribution to the total radiative forcing was 65% for CO_2, 17% for CH_4, 6% for N_2O, and 11% synthetic gases (Chapter 7).

[START FIGURE 5.18 HERE]

Figure 5.18: Effective Radiative forcing by long-lived GHGs since 1900 (values relative to 1750, as a reference of the pre-industrial Era). All data are taken from Chapter 7 Annex 7.A.1 (simplified from Figure 2.10).

[END FIGURE 5.18 HERE]

It is well-known that the atmospheric abundance of the GHGs are proportional to the emissions-loss budget in the Earth's environment, and thus the international efforts are on to mitigate emissions of the GHGs for limiting the global warming. There are multiple metrics to evaluate the relative importance of the three GHGs emissions, for the global atmospheric radiation budget (Chapter 7, section 7.6). Two of them are used in Figure 5.19: The Global Temperature Potential (GTP) and the Global Warming Potential (GWP) are the most commonly used metrics (Chapter 7). The GTP provides information to reach an end goal temperature (e.g., the climate goals of the Paris Agreement), GWP at various time scales provides relevant information on the warming path (and therefore impacts) along the way to an end temperature goal. Each metric, GWP, GTP or others discussed in Chapter 7-Box 7.3, provides information on different aspects of the GHGs impacts on radiative forcing.

For most developed nations in North America, Europe, East Asia and West Asia, total net CO_2 flux overwhelm s the emissions for CH_4 and N_2O for all metric used for comparing emissions (*high confidence*). The high importance of CH_4 to the global climate is dwarfed when GTP is chosen over GWP over a 100-year time horizon, especially for the South Asia, Southeast Asia, Brazil, Tropical America regions. Because N_2O has chemical lifetime of 120 years, its GWP and GTP weighted emissions are not very different over the 100-year time horizon. Both the boreal regions in America and Russia are total net sinks of CO_2, while close to flux neutrality is observed for Southern Africa, Australia and New Zealand. Persistent emission of CO_2 is observed for Tropical and South America regions, Northern Africa and Southeast Asia (*medium confidence*). This analysis suggests that the pathways to reaching the goal of Paris Agreement depend on the management of non-CO_2 greenhouse gases.

[START FIGURE 5.19 HERE]

Figure 5.19: Regional attribution of global fluxes of CO_2, CH_4 and N_2O derived from their concentrations, measured globally. The fluxes include anthropogenic sources and sinks, and natural fluxes that result from responses to anthropogenic GHGs and climate forcing (feedbacks) as in the three budgets shown in Sections 5.2.1.5, 5.2.2.5, and 5.2.3.5. The CH_4 and N_2O emissions are weighted by their global warming potential (GWP) and global temperature-change potential (GTP) over 100-year and 50-year time horizon (GTP and GWP values from Table 7.2). Fluxes are shown as the mean from of the inverse models as available from the global carbon project (Le Quéré et al., 2018a; Saunois et al., 2019; Thompson et al., 2019b).

[END FIGURE 5.19 HERE]

5.3 Ocean Acidification and De-oxygenation

5.3.1 Introduction and paleo-context

The surface ocean absorbs up to a quarter of all anthropogenic CO_2 emissions mainly through physical-chemical processes (Hofmann et al., 2011a; Le Quéré et al., 2018a). Once dissolved in seawater, CO_2 reacts with water and forms carbonic acid, that in turns dissociates, leading to a decrease in the concentration of carbonate (CO_3^{-2}) ions, and increasing both bicarbonate (HCO_3^-) and hydrogen H^+ ions concentration, which increases the water acidity (Doney et al., 2009). Although the societal concern for this problem is relatively recent (about the last 20 years), the physical-chemical basis for the ocean absorption (sink) of atmospheric CO_2 has been discussed much earlier by Revelle and Suess (1957). There is *robust evidence* that the increased H^+ ions concentration in the surface ocean has reduced seawater pH (Ciais et al., 2013; IPCC, 2019) (Chapter 2, Section 2.3.4.1), although there is *low agreement* on the effects of ocean acidification on marine organisms (Hofmann et al., 2011b; Browman, 2016; IPCC, 2019).

There is *high confidence* that the upper ocean (0–700 m depth) heat content is increasing (IPCC, 2019) (Chapter 9; Chapter 2 Section 2.3.3.1) due to increasing GHG concentrations in the atmosphere, strengthening upper water column stratification. Ocean warming decreases the solubility of dissolved oxygen in seawater, and there is *medium confidence* that it contributes to about 15% of the oxygen decrease in the oceans, especially in surface waters (Helm et al., 2011; Schmidtko et al., 2017; Breitburg et al., 2018;

Oschlies et al., 2018) (SROCC, Chapter 5 Section 5.3.1). Stratification reduces the ventilation flux into the ocean interior, contributing to most of the remaining ocean de-oxygenation (Schmidtko et al., 2017; Breitburg et al., 2018) (Chapter 3, Section 3.6.2). Since AR5 in 2013 and SROCC (Bindoff et al., 2019), other ocean modelling and observation-based studies have projected a general decline in the total dissolved oxygen content in the ocean, such as 2% loss (4.8 ± 2.1 Pmoles O_2) since 1960 to present (Schmidtko et al., 2017) (Chapter 2, Section 2.3.4.2).

De-oxygenation may enhance the emissions of nitrous oxide, especially from oxygen minimum zones or hypoxic coastal areas (Breitburg et al., 2018; Oschlies et al., 2018). The coupled effects of acidification on de-oxygenation occur at the level of marine organism metabolism, as the excess CO_2 dissolved in the oceans may lead to respiratory stress and reduction of thermal tolerance by organisms (*medium confidence*) (Gruber, 2011; IPCC, 2019; Kawahata et al., 2019) (SROCC Chapter 5).

5.3.1.1 Paleocene-Eocene Thermal Maximum (PETM)

The Paleocene-Eocene Thermal Maximum (PETM) was an episode of global warming possibly exceeding 4–8°C (McInerney and Wing, 2011; Dunkley Jones et al., 2013) (Chapter 2) that occurred 55.8 Myr ago. The PETM involved a large pulse of (isotopically light) CO_2 released into the ocean-atmosphere system within 5–20 kyrs (Turner, 2018) and was associated with profound perturbations of the global carbon cycle. Model estimates of the total amount of carbon released during the PETM vary from around 3000 PgC to more than 10,000 PgC (*low confidence)*, with methane hydrates, volcanic emissions, terrestrial and/or marine organic carbon, or some combination thereof, as the probable source of carbon (Zeebe et al., 2009; Cui et al., 2011; Gutjahr et al., 2017). The estimated carbon input is similar to the RCP8.5 extension scenario, although CO_2 release rates during the PETM were about an order of magnitude slower than today (i.e. 0.5–1.1 PgC yr^{-1}; (Panchuk et al., 2008; Zeebe et al., 2016)) (*low confidence*). Carbon emissions related to hydrate/permafrost destabilisation and fossil carbon oxidation may have acted as positive feedbacks (Lunt et al., 2011; Armstrong McKay and Lenton, 2018; Lyons et al., 2019), as the inferred increase in atmospheric CO_2 can only account for approximately half of the reported warming (Zeebe et al., 2009). The PETM thus provides a test for our understanding of the ocean's response to the rapid invasion of carbon (and heat).

In response to carbon emissions during the PETM, observationally-constrained model simulations report an increase in atmospheric CO_2 concentrations ranging from about 800 ppm to a peak value of >2000 ppm (Gutjahr et al., 2017) (*low confidence*). As a result, the PETM was associated with a negative surface ocean pH excursion ranging from 0.15 to 0.30 units (Gutjahr et al., 2017; Penman et al., 2014; Babila et al., 2018) (*medium confidence*). It was also accompanied by a rapid (<10 kyrs) shallowing of the carbonate saturation horizon, resulting in the widespread dissolution of sedimentary carbonate, followed by a gradual (100 kyrs) recovery (Zachos, 2005; Bralower et al., 2018). The remarkable similarity among sedimentary records spanning a wide range of ecosystems suggests that the perturbation in the ocean carbonate saturation was likely globally uniform (Babila et al., 2018) and directly resulted from elevated atmospheric CO_2 levels. The degree of acidification is similar to the 0.4 pH unit decrease projected for the end of the 21st century under RCP8.5 (Gattuso et al., 2015) and likely occurred at one order of magnitude slower than the current rate of ocean acidification (Zeebe et al., 2016) (*low confidence*).

This event was characterised by widespread detrimental ecological consequences (McInerney and Wing, 2011; Honisch et al., 2012). Continental shelf ecosystems (Ridgwell and Schmidt, 2010; McInerney and Wing, 2011) and planktonic communities (including both phyto- and zooplankton) show reductions in diversity (Robinson, 2011). For calcifiers residing deeper in the ocean, the impact of the PETM was much more detrimental, with a major extinction affecting 30–50% of the benthic foraminifera species, globally (Thomas, 2007). It is not yet established, however, whether the mass mortality affecting benthic organisms was related to a decrease in oxygenation (see below), bottom ocean warming and/or carbonate undersaturation (Thomas, 2007; Ridgwell and Schmidt, 2010).

Recent model outputs as well as geochemical data reveal widespread ocean de-oxygenation during the PETM (Dickson et al., 2012; Winguth et al., 2012), with parts of the ocean potentially becoming drastically

oxygen-depleted (anoxia) (Yao et al., 2018). De-oxygenation affected the surface ocean globally (including the Arctic Ocean (Sluijs et al., 2006), due to vertical and lateral expansion of oxygen minimum zones (OMZs) (Zhou et al., 2014) that resulted from warming and related changes in ocean stratification as well as the oxidation of methane hydrates (Pälike et al., 2014). Expansion of OMZs may have stimulated N_2O production through water-column denitrification (Junium et al., 2018). The degree to which N_2O production impacted PETM warming has not yet been established.

The feedbacks associated with recovery from the PETM are uncertain, with hypotheses that include drawdown associated with silicate weathering (Zachos, 2005), rapid regrowth of terrestrial and marine organic carbon stocks (Bowen and Zachos, 2010; Gutjahr et al., 2017).

5.3.1.2 Last deglaciation (18–11 kyr ago)

The last deglaciation is the best documented climatic transition in the past associated with a substantial atmospheric CO_2 rise ranging from 190 to 265 ppm (equivalent to 160 PgC) between 17.8 to 11.6 kyr ago (Marcott et al., 2014). The amplitude of the deglacial CO_2 rise is thus on the order of magnitude of the increase undergone since the Industrial Revolution. The increase in atmospheric CO_2 was punctuated by three abrupt 10–15 ppm increments within less than two hundred years, associated with the rapid transfer of CO_2 previously sequestered in the ocean interior and rapid oxidation of terrestrial carbon (Köhler et al., 2014; Bauska et al., 2016). Emission rates during these transient events remained lower than 0.5 PgC yr^{-1} (Marcott et al., 2014).

Boron isotope data suggest a 0.15–0.05 unit decrease in sea-surface pH (Hönisch and Hemming, 2005; Henehan et al., 2013) across the deglacial transition (*medium confidence*), an average rate of decline of about 0.002 units per century compared with the current rate of more than 0.1 units per century (Bopp et al., 2013; Gattuso et al., 2015). Planktonic foraminiferal shell weights decreased by 40% to 50% (Barker, 2002), and coccolith mass decreased by about 25% (Beaufort et al., 2011) across the last glacial termination.

Geochemical and micropaleontological evidence suggest that intermediate-depth OMZs almost totally vanished during the last glacial maximum (Jaccard et al., 2014). On the other hand, the deep (>1500 m) ocean became depleted in O_2 (concentrations were possibly lower than 50 μmol kg^{-1}) (*medium confidence*) globally (Jaccard and Galbraith, 2012; Hoogakker et al., 2015, 2018; Gottschalk et al., 2016; Anderson et al., 2019) as a combined result of sluggish ventilation of the ocean subsurface (Gottschalk et al., 2016; Skinner et al., 2017) and a generally more efficient marine biological carbon pump (Buchanan et al., 2016; Yamamoto et al., 2019). This highlights the contribution of apparent oxygen utilization (AOU), which overcompensated changes in temperature-dependent O_2 solubility (Jaccard et al., 2014; Bopp et al., 2017).

During the deglaciation, deep ocean ventilation increased as Antarctic bottom water (Skinner et al., 2010; Gottschalk et al., 2016; Jaccard et al., 2016) and subsequently North Atlantic deep water (McManus et al., 2004; Lippold et al., 2016) circulation resumed, transferring previously sequestered remineralised carbon from the ocean interior to the upper ocean and eventually the atmosphere (Galbraith and Jaccard, 2015), contributing to the deglacial CO_2 rise. Intermediate depths lost oxygen as a result of sluggish ventilation and increasing temperatures (decreasing saturation) as the world emerged from the last ice age. OMZs underwent a large volumetric increase at the beginning of the Bølling-Allerød (B/A), a northern-hemisphere wide warming event, 14.7 kyr ago (Jaccard and Galbraith, 2012; Praetorius et al., 2015) with deleterious consequences for benthic ecosystems (e.g. Moffitt et al., 2015). These observations suggest that the rate of warming imposes a direct control on the degree of ocean de-oxygenation, implying a high sensitivity of OMZ expansion to warming (Praetorius et al., 2015).

The expansion of OMZs contributed to a widespread increase in water column denitrification (Galbraith and Kienast, 2013), which contributed to substantially enhance marine N_2O emissions (Schilt et al., 2014; Fischer et al., 2019). Nitrogen stable isotope measurements on N_2O extracted from ice cores suggest that approximately one third (on the order of 0.7 ± 0.3 TgN yr^{-1}) of the deglacial increase in N_2O emissions relates to oceanic sources (Schilt et al., 2014; Fischer et al., 2019).

5.3.2 Historical trends and spatial characteristics in the upper ocean

5.3.2.1 Observations of ocean acidification over the past decades

SROCC indicated with *very high confidence* that the ocean has undergone increasing acidification globally in response to ocean CO_2 uptake. It was concluded that the pH in open ocean surface water was declining by a *very likely* range of 0.017 to 0.027 pH units per decade since the late 1980s. Since SROCC, continued observations of seawater carbonate chemistry at ocean time-series stations and compiled shipboard studies providing temporally resolved datasets have further documented the pH decline for each ocean domain (Figure 5.20).

In the subtropical ocean, pH has been decreasing at rates ranging 0.016 to 0.020 pH unit per decade for the last decades, that is about 4% increase in hydrogen ion concentration ($[H^+]$) per decade, and the saturation level of calcium carbonate mineral aragonite has been declining at rates ranging 0.084 to 0.120 per decade (*medium confidence*) (González-Dávila et al., 2010; Ishii et al., 2011; Bates et al., 2014; Takahashi et al., 2014; Ono et al., 2019). These rates are consistent with the range of values expected from the transient equilibration with increasing atmospheric CO_2 concentrations (Bates et al., 2014; Ono et al., 2019). A speed-up of pH decrease tracking the acceleration of atmospheric CO_2 increase has also been detected from a quasi-time-series record of ocean surface CO_2 measurements in the western North Pacific covering the past thirty-five years (Ono et al., 2019). In the tropical Pacific, central and eastern upwelling zones exhibit a pH trend of –0.018 to –0.026 per decade from 1997 to 2011 due to increased upwelling of CO_2-rich sub-surface waters in addition to anthropogenic CO_2 uptake (Sutton et al., 2014). Decrease of pH was relatively slower (–0.013 ± 0.001 per decade from 1985 to 2017) in the western Pacific warm pool that accommodates a highly diverse range of coral reef habitats (Ishii et al., submitted; Ono et al., 2019). The rate of $[H^+]$ increase in this region is 20% lower than in the subtropics and is attributable to the shallow overturning circulation that transports anthropogenic CO_2 from the extra-tropics at time scales of a decade, and thus dampens the $[H^+]$ increase in the tropics (Ishii et al., submitted).

In subpolar to polar oceans and in near-shore environments, the range and uncertainty in pH decline is larger than in subtropical regions (–0.002 to –0.026 pH unit per decade), reflecting the complex interplay between physical and biological forcing mechanisms, which can be further augmented by local processes in near-shore region (Section 5.3.4) (Midorikawa et al., 2012; Bates et al., 2014; Takahashi et al., 2014; Fay et al., 2014; Lauvset et al., 2015; Wakita et al., 2017; Merlivat et al., 2018). Nevertheless, the trend of acidification has been recognised with *high confidence* at most observed sites except one coastal site off the Antarctic Peninsula where biological productivity increased along substantial changes in temperature and sea ice dynamics (Brown et al., 2019). In the Arctic Ocean, the lack of CO_2 time-series long enough to make a robust analysis of ocean acidification prevents drawing robust conclusions. However, calcium carbonate saturation level is generally low, and undersaturation of aragonite has been reported in response to large freshwater inputs due to the recent extensive melting of sea ice and river discharges (*high confidence*) (Bates et al., 2009; Chierici and Fransson, 2009; Yamamoto-Kawai et al., 2009; Azetsu-Scott et al., 2010; Robbins et al., 2013) as well as to the degradation of terrestrial organic matter (Semiletov et al., 2016; Anderson et al., 2017) (see SROCC Section 3.2.1.2.4).

[START FIGURE 5.20 HERE]

Figure 5.20: Annual mean pH distributions in the year 2017 evaluated from surface pCO_2^{sea} (Iida et al., 2015) and total alkalinity (Lee et al., 2006; Takatani et al., 2014), and time-series of pH in surface layer at various sites of the oceans showing the trends of ocean acidification (Dore et al., 2009; González-Dávila et al., 2010; Midorikawa et al., 2010; Ishii et al., 2011; Bates et al., 2014).

[END FIGURE 5.20 HERE]

5.3.2.2 Reconstructed centennial ocean acidification trends

Ocean pH time series reconstructed based on coral boron isotopic ratio ($\delta^{11}B$) records evidence a prominent ocean acidification trend since mid-20th century (*high confidence*) underlying strong imprints of internal climate variability (*high confidence*). A majority of coral $\delta^{11}B$ data have been generated from the western Pacific regions with a few from the Atlantic Ocean. Biweekly resolution paleo-pH records show monsoonal variation of about 0.5 pH unit in the South China Sea (Liu et al., 2015). Interannual ocean pH variability in the range of 0.07–0.16 pH unit characterise SW Pacific corals that are attributed to ENSO (Wu et al., 2018) and river runoff (D'Olivo et al., 2015). Decadal (10, 22 and 48-year) ocean pH variations in the southwest Pacific have been linked to the Interdecadal Pacific Oscillation, causing up to 0.30 in ocean pH changes in the Great Barrier Reef (Pelejero, 2005; Wei et al., 2009) but weaker (about 0.08 pH unit) in the open ocean setting (Wu et al., 2018). Decadal variation in the South China Sea of 0.10–0.20 ocean pH changes also have been associated with the variation in the East Asian Monsoon (Liu et al., 2015; Wei et al., 2015),as a weakening of the Asian Winter Monsoon leads to sluggish water circulation within the reefs, building up CO_2 due to calcification and respiration. Since the beginning of the Industrial Period in the mid-19th century, coral $\delta^{11}B$-derived ocean pH has decreased by 0.06–0.24 pH unit in the South China Sea (Liu et al., 2015; Wei et al., 2015) and 0.12 pH unit in the southwest Pacific (Wu et al., 2018). A distinct feature of coral $\delta^{11}B$ records is ocean acidification trends since the mid-20th century albeit having wide-range values. The trends are 0.12–0.40 pH unit in the Great Barrier Reef (Wei et al., 2009; D'Olivo et al., 2015), 0.05–0.08 pH unit in the northwest Pacific (Shinjo et al., 2013) and 0.04–0.09 pH unit in the Atlantic Ocean (Goodkin et al., 2015; Fowell et al., 2018) since the mid-20th century. Concurrent coral carbon isotopic ($\delta^{13}C$) measurements infer the ocean uptake of anthropogenic CO_2 from the combustion of fossil fuel characterised based on the isotopically depleted $\delta^{13}C$ of fossil fuels. Western Pacific coral records show depleted $\delta^{13}C$ trends since the late 19th century that are more prominent since the mid-20th century (*high confidence*) (Pelejero, 2005; Wei et al., 2009; Shinjo et al., 2013; Liu et al., 2015; Kubota et al., 2017; Wu et al., 2018). Overall, many of the records show a highly oscillating seawater pH, in most instances a depleted $\delta^{11}B$ trend in recent decades that is indicative of anthropogenic ocean acidification (*medium confidence*). Further work is needed to better calibrate and constrain the use of this paleo-pH proxy in different tropical coral species.

5.3.3 Ocean interior change

5.3.3.1 Ocean memory – acidification in the ocean interior

Anthropogenic CO_2 taken up into the ocean surface layer propagates deeper into the ocean (see Section 5.2.1.3.2), causing ocean acidification in the interior of the ocean (*very high confidence*). The net change in metabolic CO_2 release by marine organisms (remineralisation of organic matter) is also regulating seawater pH (*high confidence*), accompanying the removal of dissolved oxygen in proportion to the change in CO_2 (Gruber, 2011; Mora et al., 2013; Gattuso et al., 2015; Chen et al., 2017; Breitburg et al., 2018; Levin, 2018; Robinson, 2019) (Section 5.3.3.2).

The extent of acidification due to anthropogenic CO_2 invasion tends to diminish with depth although it has been amplified over time (*very high confidence*) (Figure 5.21) (Lauvset et al., submitted) (see Section 5.2.1.3.2). The depth at which the progression of acidification has been detected so far varies by region largely connecting with the structure of the three-dimensional ocean circulation. It is deeper in the subpolar North Atlantic (Perez et al., 2018) and mid-latitudinal zones in both hemispheres, and is shallower in the tropics (Murata and Saito, 2012; Ríos et al., 2015; Carter et al., 2017) and in the Southern Ocean with significant pH decrease on the Antarctic continental shelf (Hauck et al., 2010; Williams et al., 2015). In the subpolar North Atlantic, the trend of acidification has been observed during the time period of 1991–2016 even at 3000 m depth with the shoaling of aragonite saturation horizon ($\Omega_{arag}<1$) at a rate of 10–15 m per year to 2250 m (Perez et al., 2018).

[START FIGURE 5.21 HERE]

Figure 5.21: Vertical sections of the changes in (a) pH and (b) Ω_{arag} between the years 1800 and 2002 due to anthropogenic CO_2 invasion (colour) and of their contemporary values in 2002 (contour line) in the Arctic, Atlantic, Southern, Pacific and Indian Oceans (left to right) (Lauvset et al., submitted).

[END FIGURE 5.21 HERE]

At 30°S–40°S in the South Atlantic, a distinct pH decrease that reached –0.029 ± 0.014 pH unit within two decades has been observed at 1000 m for the interval 1993–2013 (Ríos et al., 2015). This large decrease in pH is attributable to increased organic matter remineralisation promoted by a general weakening of ocean ventilation as well as anthropogenic CO_2 invasion into the Antarctic intermediate water. A significant reinforcement of acidification as a result of increased remineralisation is also evident in the broad range of the intermediate water in the North Pacific (*high confidence*) (Byrne et al., 2010; Carter et al., 2017; Chu et al., 2016; Dore et al., 2009; Lauvset et al., submitted). Since a decline in dissolved oxygen has occurred persistently in the past several decades (*medium confidence*) (–4.0 μmol kg^{-1} per decade at maximum) in time-series measurements in the intermediate water of the western North Pacific (Takatani et al., 2012; Sasano et al., 2015, 2018), the reinforcement of acidification by increased organic matter remineralisation is also thought to have been occurring persistently (*medium confidence*). By contrast, in the North Pacific Subtropical Mode Water (at the depth of about 200–300 m), a large decadal variability in pH and aragonite saturation level with amplitudes of about 0.02 and about 0.1 have been observed superimposed on the secular trend of decrease due to anthropogenic CO_2 invasion (Oka et al., 2019). This is associated with the variability in the impact of remineralisation driven by the approximately 50% variation in the formation volume of the mode water that is forced remotely by the Pacific Decadal Oscillation (Qiu et al., 2014; Oka et al., 2015).

5.3.3.2 De-oxygenation and its implications for GHGs

The rate of oxygen decrease in the ocean interior exhibits large variability in space, depth and time. However, as summarised in SROCC (Section 5.2.2.4), there is a growing consensus that the open ocean is losing oxygen by a *very likely* range of 0.5–3.3% between 1970–2010 from the ocean surface to 1000 m (*medium confidence*) (Helm et al., 2011; Ito et al., 2017; Schmidtko et al., 2017). Substantial changes in thermocline oxygen concentrations have been observed (Deutsch et al., 2014; Hahn et al., 2017) but attribution to different forcing agents such as anthropogenic warming, internal climate variability or a combination of both (i.e., changing internal variability in a warming world) is challenging (Oschlies et al., 2018). Climate models confirm the decline and predict continuing and accelerating ocean de-oxygenation (Bopp et al., 2013). However, current models do not reproduce observed patterns for oxygen changes in the ocean's tropical thermocline and generally simulate only about half the oceanic oxygen loss inferred from observations (Oschlies et al., 2018).

In hypoxic and oxygen-depleted waters, microbial processes of denitrification and anammox (anaerobic ammonium oxydation) (Kuypers et al., 2005; Codispoti, 2007; Gruber and Galloway, 2008) deplete available nitrogen to primary producers and thus, when upwelled waters reach the photic zone, primary production becomes nitrogen-limited and CO_2 from deeper water masses is emitted to the atmosphere (Tyrrell and Lucas, 2002). However, in other oceanic regions, increased water-column stratification due to warming may reduce the amount of N_2O reaching the surface and decrease N_2O flux to the atmosphere. Landolfi et al. (2017) suggest that by 2100, under the RCP8.5 scenario, total N_2O production may have declined by 5% and N_2O emissions be reduced by 24% due to decrease in organic matter export and anthropogenic driven changes in ocean circulation and atmospheric N_2O concentrations (*low confidence*).

The areas with relatively rapid oxygen decrease and its large impact include regions of lowest oxygen, known as oxygen minimum zones (OMZs), found in the tropical oceans, where oxygen content is decreasing at a rate of 0.9 to 3.4 μmol kg^{-1} per decade in the thermocline for the past five decades (Stramma et al.,

2008). Low oxygen, low pH and shallow aragonite saturation horizons in the OMZ of the eastern boundary upwelling regions co-occur, affecting ecosystem structure (Chavez et al., 2008) and function in the water column, including the presently unbalanced nitrogen cycle (Paulmier and Ruiz-Pino, 2009) (*high confidence*). The coupling between upwelling, productivity, and oxygen depletion feeds back to biological productivity and the role of these regions as sinks or sources of climate active gases. When OMZ waters upwell and impinge on the euphotic zone, they release significant quantities of greenhouse gases, including CO_2, N_2O (1.27–2.12 TgN_2O yr^{-1}), and CH_4 (0.27–0.38 $TgCH_4$ yr^{-1}) to the atmosphere, exacerbating global warming (Naqvi et al., 2010; Kock et al., 2012; Arévalo-Martínez et al., 2015; Babbin et al., 2015a; Farías et al., 2015). According to modelling projections of oceanic N_2O emissions in 2100 under RCP8.5 emission scenario, the expansion of OMZs could thus increase N_2O production, associated primarily to denitrification, and partly compensate for the decrease in global ocean N_2O emissions from 2005 to 2100 (*low confidence*) (Martinez-Rey et al., 2015). It is yet unclear whether N_2O production from bacterial nitrification increases exponentially or linearly with decreasing oxygen and whether a threshold oxygen value exists below which net N_2O production switches to N_2O consumption (Babbin et al., 2015b; Trimmer et al., 2016; Landolfi et al., 2017). Furthermore, the correlation between N_2O and oxygen varies with microorganisms present, nutrient concentrations, and other environmental variables (Voss et al., 2013).

5.3.3.3 Future projections for ocean acidification

Ocean acidification is projected to continue *unequivocally* as atmospheric CO_2 levels continue to rise. Earth system models under the same concentration pathways scenario show similar change in the surface ocean in the period to 2100, primarily determined by atmospheric CO_2 concentration and regional carbonate chemistry (Hurd et al., 2018), thereby bringing limited update since SROCC. The Arctic Ocean is an exception due to freshwater input from rivers and sea-ice melt, as well as circulation changes, which leads to a faster rate of change than in other regions (Qi et al., 2017), that continues through to 2100 (Hurd et al., 2018) (*high confidence*).

Earth system models project significant and irreversible changes that start to occur in polar regions within the next 15 years, as surface waters begin to become seasonally undersaturated with respect to aragonite. This is *very likely* to occur in Southern Ocean surface waters by 2030 under all concentration pathways except very low RCP2.6 (Sasse et al., 2015; Hauri et al., 2016; Negrete-García et al., 2019). The extent, timing and persistence of ocean acidification are thought to be very sensitive to the scenarios and ocean circulation (Negrete-García et al., 2019). The area of the Southern Ocean that experiences aragonite undersaturation, for at least one month per year, by 2100 were calculated to vary from negligible (less than 2%) under RCP2.6 to about 30% for RCP4.5 and more than 95% for RCP8.5 (Sasse et al., 2015) (*medium confidence*). These long term projections are modulated at interannual timescales by large-scale climate modes (Ríos et al., 2015), such as the representation of the El Niño Southern Oscillation and the Southern Annular Mode in models (Conrad and Lovenduski, 2015).

As atmospheric CO_2 levels continue to rise, the seasonal cycle of ocean acidification is *very likely* to continue to be modulated. Overall a decrease in pH seasonality is anticipated globally, but in contrast, seasonality of hydrogen ion concentration ($[H^+]$) increases. For instance, the amplitude of pH seasonality will decrease by 12 to 20% across 90% confidence interval and that of $[H^+]$ will increase by 71 to 90% over 21st century under RCP 8.5. However, the aragonite saturation state shows a reduction in all basins except for the subtropical gyres, which show an amplification of the seasonal cycle due to warming under high emissions scenarios (Kwiatkowski and Orr, 2018). The magnitude of these changes, however, will be sensitive to the future concentration pathway followed and highlights the interplay between warming and ocean chemistry in future projections.

At regional scale, these changes are modulated by local variability due to a range of processes that includes circulation, temperature changes, carbon cycling, carbonate chemistry and the structure of the marine ecosystem (*high confidence*). As current model projections do not resolve these fine-scale temporal and spatial variability and processes, this suggests that current projections may not fully capture the chemical changes that the marine environment will experience in the future (Takeshita et al., 2015; Turi et al., 2016).

As atmospheric CO_2 concentrations rather than emissions often drive models used to project future changes, important carbon-climate feedbacks (more positive than negative) have been overlooked, which will directly impact the rates of ocean acidification suggesting changes possibly occurring more quickly than currently modelled (Matear and Lenton, 2018; Zhang et al., 2018a). Equally, feedbacks of the marine ecosystem on ocean chemistry have also been overlooked, and while the magnitude and sign of many of these feedbacks are still poorly known, nevertheless studies that explore these feedbacks suggest a potentially very significant and long-lasting impact (Matear and Lenton, 2014) (*medium confidence*).

5.3.3.4 Reversal of ocean acidification by CDR

Reversing the increase in atmospheric CO_2 concentrations will reverse ocean acidification at the sea surface but will not result in rapid amelioration of ocean acidification in the deeper ocean (Section 5.3.3.1). The ocean's uptake of atmospheric CO_2 will start to decrease if atmospheric CO_2 decreases, and the ocean will gradually become a source, rather than sink, of CO_2 (Mathesius et al., 2015; Tokarska and Zickfeld, 2015). However, because of the long timescales of the ocean turnover that transfers CO_2 from the upper to the deep ocean, excess carbon will continue to accumulate in the deep ocean even after a decrease in atmospheric CO_2 (*high confidence*) (Cao et al., 2014; Mathesius et al., 2015; Tokarska and Zickfeld, 2015).

In model simulations with a strong increase in atmospheric CO_2 and a subsequent decrease to pre-industrial levels, surface pH returns to its pre-industrial value in about 100 years after atmospheric CO_2 returns to pre-industrial levels (Cao et al., 2014). The global ocean mean pH, however, does not reverse when atmospheric CO_2 returns to pre-industrial levels, remaining about 0.1 units lower than its pre-industrial value, even 200 years after atmospheric CO_2 returns to pre-industrial levels (Mathesius et al., 2015; Section 5.3.3.1). Even with a probably unfeasible CO_2 extraction rate of 25 PgC yr^{-1}, global ocean pH does not return to pre-industrial levels by 2700 (Mathesius et al., 2015).

The slow timescales of ocean circulation result in an inability to restore the mean ocean pH to pre-industrial levels even with an aggressive atmospheric CO_2 removal rate. Even with reversal of the atmospheric CO_2 increase, CO_2 emissions leave a long-term legacy in ocean acidification, and are therefore irreversible at multi-human generational scales (*high confidence*).

5.3.4 Coastal ocean acidification and de-oxygenation

5.3.4.1 Drivers

Strong spatial and temporal variability characterise the coastal ocean marine carbonate system, thus surface pCO_2^{sea}, pH, and sea-air CO_2 fluxes (*high agreement*, *robust evidence*). Although some exceptions exist, typically, inner seas, bays and estuaries are saturated with CO_2, regardless of the region (i.e. tropical, temperate, polar) because heterotrophic respiration of organic matter from basin drainage prevails over photosynthesis. Additionally, highly populated coastal areas receive large amounts of organic matter from domestic and industrial sewage (Chen and Borges, 2009). On the contrary, continental shelves, excluding estuaries and near-shore areas, act as CO_2 sinks at a rate of about 0.2 ± 0.02 PgC yr^{-1} (Laruelle et al., 2014; Roobaert et al., 2019) or a sink yield of 0.7 molC m^{-2} yr^{-1}, considering ice-free areas only. Under scenarios of concomitant increasing atmospheric CO_2 and eutrophication, such ecosystems would be more vulnerable to ecological and biogeochemical changes, impacting local economic activities. Nevertheless, there is *medium agreement (medium evidence)* that coastal and shelf seas acidification, whether induced by the increasing atmospheric CO_2 or by enhancement of eutrophication, has negative effects on specific groups of marine organisms (Dupont et al., 2010), especially when combined with other stressors such as temperature and increased availability of potentially toxic metallic ions such as arsenic and copper (Millero et al., 2009; Boyd et al., 2015; Breitburg et al., 2018).

5.3.4.2 Spatial characteristics

The coastal ocean, including bays and estuaries, is highly heterogenous due to the complex interplay between physical, biogeochemical and anthropogenic factors (Gattuso et al., 1998; Chen and Borges, 2009; Dürr et al., 2011; Laruelle et al., 2014; McCormack et al., 2016). This heterogeneity also affects the degree of local seawater buffering, and thus the responses of these ecosystems to increasing atmospheric CO_2, and ocean acidification and de-oxygenation (Duarte et al., 2013; Regnier et al., 2013; Laruelle et al., 2018; Carstensen and Duarte, 2019).

Upwelling coastal areas such as the California current system in the north-western USA (Pacific coast) are naturally exposed to intrusions of deep waters displaying low-pH, high-CO_2 conditions from remineralization (respiration) processes (Feely et al., 2008, 2010, 2018; Chan et al., 2019; Lilly et al., 2019). Studies combining in situ data and models predict for this area an expansion and intensification of these deep water intrusions (Hauri et al., 2013; Feely et al., 2016). Eastern boundary upwelling systems under the influence of river inputs (freshwater, organic matter) such as in the southwestern Chilean coast display stronger influence of riverine organic matter respiration on surface pCO_2^{sea} supersaturation and consequent lower pH (Vargas et al., 2016). Both Pacific upwelling coastal regions display seasonality in subsurface waters aragonite undersaturation *likely* as a consequence of the interplay between respiration and intrusion of upwelling waters (Feely et al., 2008, 2010, 2016, 2018; Hauri et al., 2013; Vargas et al., 2016; Chan et al., 2019; Lilly et al., 2019).

Northern hemisphere, temperate, non-upwelling coastal areas display a trend in decreasing seawater pH, mainly attributed to the combined effects of eutrophication and decreasing seawater buffering capacity (*high agreement*, *medium evidence*). Areas such as the eastern USA (Atlantic coast) present a north-south decreasing gradient of pH and aragonite saturation state (Sutton et al., 2016; Fennel et al., 2019). Local conditions of low alkalinity and total inorganic carbon concentration in coastal areas, such as within Chesapeake Bay, combined to an open ocean signal of acidification, lead to a lower ecosystem buffering capacity along the decreasing salinity gradient from the ocean to the inner estuary (Cai et al., 2017). Other estuaries along the NE USA coast present a significant positive correlation between pH and dissolved oxygen, where lower pH waters (i.e. pH ≈ 7.00) are found in hypoxic areas (Wallace et al., 2014). (Rheuban et al., 2019) empirical model suggests that for these estuaries, aragonite saturation is controlled by nitrogen loading, reinforcing that eutrophication is the main driver for estuarine acidification for non-upwelling areas. Further south along the USA Atlantic coast, Robbins and Lisle, (2018) reviewed available estuarine data from 1980 to 2008. For this region, the authors found an overall trend of decreasing pH, ranging from 7.3 to 5.0 10^{-4} pH units yr^{-1}, which are lower than the present ocean acidification trends in open ocean areas (Section 5.3.2). Model results predict a concomitant increase in bottom waters acidification and de-oxygenation in the northern shelf of the Gulf of Mexico with increasing eutrophication, implying that this situation could be managed with regulation of the riverine input of nutrients (Laurent et al., 2017). Model studies also suggest that, for this area, the decrease in pH since the beginning of the Industrial Era is due to the effects of eutrophication and ocean acidification combined with a decrease in the local seawater buffering capacity (Cai et al., 2011).

The tropical southwestern Atlantic coastal areas are heterogenous and highly affected by the large river nutrient and organic matter inputs (e.g. Amazon, Orinoco rivers; Araujo et al., 2014, 2019), or mainly exhibit lower than average ocean surface water pH as a result of heavy eutrophication (Noriega et al., 2013; Noriega and Araujo, 2014). Nevertheless, heavy eutrophication induces net atmospheric CO_2 absorption in tropical, shallow and vertically stratified ecosystems in spite of the presence of bottom water acidification and hypoxia, driven by autochthonous primary production (Cotovicz Jr. et al., 2015; Cotovicz et al., 2018). In addition to that, coastal sub-surface waters with pH values lower than average open ocean surface (i.e. about 8.0) are also found close to wastewater effluents, where microbial respiration lowers water pH (Wallace et al., 2014; Cotovicz Jr. et al., 2015; Fennel and Testa, 2019; Lowe et al., 2019). Cai et al. (2011) showed through observations, that the CO_2 production from the decomposition of organic matter in temperate to subtropical eutrophic coastal areas (off the Mississippi and Changjiang rivers) has already increased acidification levels in adjacent subsurface waters.

Despite the increasing availability of pH and other marine carbonate parameters datasets for the coastal oceans, it is important to highlight that there may be a high level of uncertainty in the data. In these portion of the oceans, physical-chemical parameters have a higher variability compared to open ocean areas, including marine carbonate system, and are thus poorly constrained (Feely et al., 2008; Duarte et al., 2013; Sutton et al., 2016; Robbins and Lisle, 2018). Additionally, for pH data, there is a concern for the variety of methods used, especially regarding the calibration of instruments (glass electrodes) and the potential measurement values drift within time (McLaughlin et al., 2017; Robbins and Lisle, 2018; Carstensen and Duarte, 2019).

Spatial distribution of hypoxic coastal areas is highly heterogeneous, but more severe hypoxia or anoxia may occur more often in highly populated coastal areas, or in regions where local water circulation, water column stratification and wind patterns lead to an accumulation of organic matter (*high agreement, medium evidence*) (Ciais et al., 2013; Rabalais et al., 2014; Breitburg et al., 2018) (SROCC Chapter 5). The signal for de-oxygenation trends is thus heterogeneous and can be only assessed by making available coastal water quality surveys, many times not obtainable in the peer-reviewed literature.

The Baltic Sea is the largest regional sea where hypoxia is reported to happen before the 1950s (Carstensen et al., 2014; Rabalais et al., 2014; Łukawska-Matuszewska et al., 2019). The frequency and volume of seawater inflow from North Sea into the Baltic Sea decreased after 1950, leading to an expansion of hypoxic areas from 40,000 to 60,000 km² in combination with increasing eutrophication (Carstensen et al., 2014). Chesapeake Bay, a densely populated coastal ecosystem on the North American east coast, displays summer hypoxia with large interannual variation (Li et al., 2016b). Wang et al. (2017) showed, using the sedimentary record from the present back to 1850, that the oxygen minimum zone off southern California in the Pacific Ocean has become more intense since the 1990s, with high interannual variability due to the Southern Oscillation. The East China Sea is one of the largest coastal oxygen-depleted areas in the world, where observed summer hypoxia has been related to increasing inputs of riverine nutrients (Chen et al., 2007). Recently, Qian et al. (2017) have shown that regional seawater circulation processes (i.e. non local) also play a role in the intensity of East China Sea summer hypoxia. On the north-western Atlantic shelf, (Claret et al., 2018) in a combined observation and model approach show that the observed shelf de-oxygenation trends are related to changes (retreat) in the Labrador Current circulation patterns.

Shelf waters in the Arabian Sea display seasonal hypoxia driven by the summer monsoon upwelling (Madhupratap et al., 1996). A comparison of observational data from the late 1950s with a modern time-series does not show an increase in hypoxia in this area (Gupta et al., 2016). Djakovac et al. (2015) have analysed a 40-year time-series and concluded that changes in regional circulation in the Adriatic Sea alleviated the local strong summer/autumn bottom hypoxia events in its eastern portion while on the north-western Adriatic Sea, the decrease in nutrient and freshwater inputs lead to present less severe hypoxic conditions when compared to the 1970s and 1980s.

5.4 Biogeochemical Feedbacks on Climate Change

This section covers biogeochemical feedbacks on climate change, which represent one of the largest sources of uncertainty in projections of climate change. The relevant processes are discussed, prior to discussing the simulation and projection of the carbon cycle in Earth system models, emergent constraints on future projections, non-CO_2 feedbacks, and possible biogeochemical tipping points.

5.4.1 Direct CO_2 effect on land carbon uptake

AR5 assessed, with *high confidence,* that increased atmospheric CO_2 will lead to increased land carbon uptake, but by an uncertain amount. Our understanding of the various biological processes, which affect the strength of the CO_2 fertilisation effect on photosynthesis and carbon storage in vegetation and soils, in particular the limitations imposed by nitrogen availability, has developed since AR5. CMIP6 ESMs continue to suggest that CO_2 fertilisation of photosynthesis acts as an important negative feedback on anthropogenic

climate change, by reducing the rate at which CO_2 accumulates in the atmosphere (*high confidence*). An increasing number of CMIP6 ESMs account for nutrient cycles. These models suggest that nutrient availability will limit the CO_2 fertilisation effect (*high confidence*). The magnitude of both the direct CO_2 effect on land carbon uptake, and its limitation by nutrients, remains uncertain.

AR5 and SRCCL concluded with *high confidence* that rising atmospheric CO_2 increases leaf-level photosynthesis (e.g. Ainsworth and Long, 2005). This effect is represented in all ESMs. New studies since AR5 add evidence that the leaf-level CO_2 fertilisation is modulated by acclimation of photosynthesis to long-term CO_2 exposure, growth temperature, seasonal drought, and nutrient availability, but these effects are not yet routinely represented in ESMs (Smith and Dukes, 2013; Baig et al., 2015; Kelly et al., 2016; Norby et al., 2016). New syntheses since AR5 corroborate that the long-term effect of elevated CO_2 on plant growth and ecosystem carbon storage is generally positive (*high confidence*), but is modulated by temperature, water and nutrient availability (Reich et al., 2014; Obermeier et al., 2017; Hovenden et al., 2019; Song et al., 2019). Plant carbon allocation, changes in plant community composition, disturbance, and natural plant mortality are important processes affecting the magnitude of the response, but are currently poorly represented in models (De Kauwe et al., 2014; Reich et al., 2018; Walker et al., 2019), and thus contribute to uncertainty in ESM projections (Arora et al. submitted). Despite advances in the regional coverage of experiments, observations of the CO_2 fertilisation effect are still scarce, in particular from outside the temperate zone (Song et al., 2019).

Field studies with elevated CO_2 have demonstrated that the initial stimulation of above-ground growth may decline if insufficient nutrients such as nitrogen or phosphorus are available (Finzi et al., 2007; Norby et al., 2010; Hungate et al., 2013; Reich and Hobbie, 2013; Talhelm et al., 2014; Terrer et al., 2018). Although the scale mismatch and the abrupt nature of the perturbation make direct comparisons difficult, model-data syntheses have demonstrated that the ability to capture the observed long-term effect of elevated CO_2 depends on the ability of models to predict the effect of vegetation on soil biogeochemistry (Zaehle et al., 2014; Koven et al., 2015; Medlyn et al., 2015; Walker et al., 2015). Meta-analyses of CO_2 manipulation experiments point to accelerated turnover of soil organic matter (van Groenigen et al., 2017) as a result of increased below-ground carbon allocation by plants (Song et al., 2019), and increased root exudation or mycorrhizal activity due to enhanced plant nutrient requirements under elevated CO_2 (Drake et al., 2011; Terrer et al., 2016; Meier et al., 2017). These effects are not considered in most ESMs. Consistent with expectations from these observations, one global model that includes these processes suggests reduced accumulation of carbon in soils, but increased vegetation carbon storage in response to elevated CO_2, relative to a model that does not (Sulman et al., 2019).

Understanding the effects of phosphorus limitation in large parts of the tropical zone and Australia (Vitousek et al., 2010; Grandy et al., 2013) is less well developed. The first free-air CO_2 enrichment experiment in a phosphorus-limited mature forest ecosystem did not find an increase in biomass growth despite increases in photosynthesis after three years of CO_2 exposure (Jiang et al., submitted). Models accounting for the effects of P availability, in addition to N, generally show an even stronger reduction of the response of ecosystem carbon storage to elevated CO_2. Insufficient data and uncertainties in the process formulation cause large uncertainty in the magnitude of this effect (Medlyn et al., 2016; Fleischer et al., 2019).

As discussed by AR5 and SRCCL, multiple lines of evidence suggest that the ratio of plant CO_2 uptake to water loss (plant water-use efficiency) has increased in near proportionality to atmospheric CO_2 (*high confidence*), at a rate that generally consistent with ESMs, despite notable spread in the different observations that so far remain partially unexplained (De Kauwe et al., 2013; Frank et al., 2015; van der Sleen et al., 2015; Brienen et al., 2017; Keeling et al., 2017; Knauer et al., 2017; Mastrotheodoros et al., 2017; Lavergne et al., 2019). The available tree ring records do not suggest that increased water-use efficiency is always associated with increased tree growth (Franks et al., 2013; van der Sleen et al., 2015), but models and observations suggest that higher water-use efficiency may lead to increased vegetation cover or carbon storage in drier environments (Farrior et al., 2015; Ukkola et al., 2016). The effects of altered plant water-use efficiency on the water-cycle and biophysical feedbacks in the climate system are discussed in Sections 8.2.3.1 and 11.5.5.

Consistent with AR5, the CO_2 fertilisation effect is the dominant cause for the projected increase in land carbon uptake between 1860 and 2100 in ESMs (Figure 5.28; Table 5.5) (Arora et al. submitted). In the CMIP6 ensemble, the increase of land carbon storage due to CO_2 fertilisation is a global phenomenon but is strongest in the tropics (Figure 5.26). The resulting increase of productivity is a key driver of increases in vegetation and soil carbon storage. However, consistent with earlier findings (Todd-Brown et al., 2013; Friend et al., 2014; Hajima et al., 2014), processes affecting vegetation carbon-use efficiency and turnover such as allocation changes, mortality, and vegetation structural changes, as well as the pre-industrial soil carbon turnover time, also play an important role (Arora et al. submitted).

As a major advance since AR5, 6 out of 11 models in the C^4MIP-CMIP6 ensemble account for nitrogen cycle dynamics over land (Table 5.4). On average, these models exhibit a 25–30% lower CO_2 fertilisation effect on land carbon storage, compared to models that do not (Table 5.5). The only model in the C^4MIP-CMIP6 ensemble that explicitly represents the effect of P availability on plant growth suggests the lowest C storage in response to increasing CO_2. The lower CO_2 effect due to nutrient availability is generally consistent with analyses of the implicit nutrient limitation in CMIP5 simulations (Wieder et al., 2015; Zaehle et al., 2015) and independent assessments by stand-alone land models (Zaehle et al., 2010; Wårlind et al., 2014; Zhang et al., 2014; Goll et al., 2017; Meyerholt et al., 2020). The magnitude of nutrient feedbacks in these models is poorly constrained by observations, owing to the limited geographic distribution of available observations and the uncertain scaling of results obtained from manipulation experiment to transient system dynamics (Liu et al., 2019; Wieder et al., 2019; Meyerholt et al., 2020, Davies-Barnard et al., submitted).

5.4.2 Direct CO_2 effects on ocean carbon uptake

Undersaturation and supersaturation of CO_2 in the surface layer of the ocean, as quantified by the difference in the partial pressure of CO_2 between in the air that is in air-sea equilibrium with surface seawater (pCO_2^{sea}) and in the overlying atmosphere (pCO_2^{air}), gives rise to a net CO_2 transfer across the air-sea interface until the partial pressure of carbon dioxide in the surface water equals that in the atmosphere ($pCO_2^{sea} = pCO_2^{air}$). As a result, an increase in atmospheric CO_2 concentration due to anthropogenic emissions drives a net CO_2 uptake by the ocean. However, the CO_2 that dissolves in seawater reduces the CO_2 buffering capacity of seawater, which reduces the efficiency of the ocean carbon sink under high atmospheric CO_2 (*very high confidence*). Historically, the ocean is thought to have absorbed 28 ± 5% of total anthropogenic CO_2 emissions between the beginning of the industrial revolution and the mid-2000s (Gruber et al., 2019a) (Section 5.2.1.3.3). During years of 1994–2007, the ocean continued to absorb essentially the same ratio (26 ± 5%) of anthropogenic CO_2 emissions (*medium confidence*), even though atmospheric CO_2 emissions continued to grow (see Section 5.2.1.3.3). However, as reported in AR5 (see Section 6.4.2 of AR5), there is a broad agreement among ESMs that the fraction of anthropogenic CO_2 emissions taken-up by the ocean will decrease significantly in the future if the increase of CO_2 continues in the atmosphere (Arora et al., 2013) (*very likely*). For the historical/RCP8.5 scenario, it is projected that the annual oceanic CO_2 uptake will stop growing after approximately 2070 and thus the fraction of oceanic CO_2 uptake will decrease from 32% in the 1990s to 23% on average over the 21st century (Jones et al., 2013b; Kessler and Tjiputra, 2016; Wang et al., 2016a). This decrease is predominantly attributable to the reduced CO_2 buffering capacity of seawater (Katavouta et al., 2018), but with contributions due to changes in physical and biological drivers under climate change (see Sections 5.2.1.3.2, 5.4.4).

The reduced CO_2 buffering capacity and the increased impact of warming on pCO_2^{sea} amplify the seasonal variation of pCO_2^{sea} and thereby that of air-sea CO_2 flux (*high confidence*). These trends since mid-1940s have been simulated by an ocean carbon model for the North Pacific (Rodgers et al., 2008) and verified at the global scale by an observation-based data product in which the rate of increase in the winter-to-summer pCO_2^{sea} difference has been quantified to be 2.2 ± 0.4 µatm per decade for 1982–2015 poleward of 10º latitude (Landschützer et al., 2018). According to one ESM, the increase of the seasonal variation of pCO_2^{sea} will show its maximum in the subtropics of each ocean basin in summer, with the increase in ($pCO_2^{sea} - pCO_2^{air}$) reaching 3 µatm per decade between 1990 and 2030 (Schlunegger et al., 2019). On the other hand, biological CO_2 assimilation increases in importance for CO_2 uptake in the Southern Ocean in summer, because the lower buffering capacity results in a larger draw-down of pCO_2^{sea}, even if biological productivity

remains unchanged (Hauck et al., 2015). Changes in seawater carbonate chemistry due to cumulative CO_2 uptake are also *likely* to amplify the seasonal cycle of surface-water hydrogen ion concentration (+81 ± 16%) while attenuating that of pH by 16 ± 7%, on average, during the 21st century (Kwiatkowski et al., 2018; see also Chapter 5.3.2). Depending on the seasons and regions, it may exacerbate or ameliorate the impacts of ocean acidification on marine organisms (Section 5.3).

Ocean acidification is considered to reduce the calcification rate of marine organisms (e.g. Kroeker et al., 2013) (*high confidence*). This can form a negative feedback on atmospheric CO_2 levels by increasing the CO_2 buffering capacity of seawater. However, the predicted sensitivity of atmospheric CO_2 is fairly small; under RCP8.5, the decrease in $CaCO_3$ production and dissolution due to increasing ocean acidification are predicted to result in a small negative feedback on atmospheric CO_2 of –2 to –11 ppm by 2100 (Gangstø et al., 2011). However, different model parameterisations for the CO_2-calcification feedback result in widely diverging estimates of the feedback magnitude, which range from –1 ppm to –125 ppm (part of this spread is also due to use of different forcing scenarios) (Heinze, 2004; Ridgwell et al., 2007; Hofmann and Schellnhuber, 2009; Zhang and Cao, 2016). The magnitude of the negative feedback effect will also depend on the parameterisation of the ballast effect on export fluxes of organic carbon, which acts to counteract the negative calcification response to increased CO_2 (Barker et al., 2003).

5.4.3 Climate effect on land carbon uptake

AR5 assessed, with *medium confidence*, that future climate change will decrease land carbon uptake relative to the case with constant climate, but with a poorly-constrained magnitude. CMIP6 ESMs continue to project that a warming climate, in isolation from the physiological effects of CO_2, will lead to global-scale losses of carbon from vegetation and soils, due to a variety of factors, which include: reduced photosynthetic uptake, particularly in tropical ecosystems, due to temperature and water stresses; elevated rates of plant (autotrophic) respiration with higher temperatures; changes to plant mortality and disturbance rates; and increases to heterotrophic respiration rates with warmer temperatures. ESMs also indicate areas of carbon gain that offset some of these losses due to processes that include: longer growing seasons in colder climates and increased nutrient availability from mineralisation of organic matter that accompanies elevated decomposition rates. Uncertainty in the magnitude and geographic pattern of these feedbacks remain *high*, but it is *likely* that terrestrial ecosystem responses to climate change will act as a positive feedback that will enhance global warming. However, the net effect of CO_2-induced climate change, which is a result of the compensating effects of CO_2-fertilisation (Section 5.4.1), and warming-induced increases in plant and soil respiration and disturbance, is expected to be a net increase in global land carbon storage on timescales out to 2100 (*high confidence*).

5.4.3.1 Plant Physiology

Plant productivity is highly dependent on local climate. In cold environments, warming has generally led to an earlier onset of the growing season, and with it an increase in early-season vegetation productivity (e.g. Forkel et al., 2016). However, this trend is affected by adverse effects of climate variability, and other emerging limitations on vegetation production by water, energy and nutrients, which may gradually reduce the effects of warming (Piao et al., 2017; Buermann et al., 2018).

In tropical and temperate environments, high temperatures are observed to correlate with reduced photosynthetic rates (e.g. Pau et al., 2018), suggesting that further warming may reduce vegetation productivity. A key question is whether the observed relationships are due to the exceedance of temperature thresholds in photosynthetic biochemistry itself, or to higher vapour pressure deficit accompanying high temperatures. Observations and models suggest that the vapour pressure deficit effects are stronger than direct temperature effects on enzyme activities, and that acclimation of photosynthetic optimal temperature may mitigate productivity losses of tropical forests under climate change (Kattge and Knorr, 2007; Lloyd and Farquhar, 2008; Tan et al., 2017), though it is also possible that warming may lead to exceedance of temperature optima for photosynthesis (Huang et al., 2019). Since AR5, some ESMs have begun to include

these acclimation responses, both in photosynthesis (Smith et al., 2015; Lombardozzi et al., 2015; Mercado et al., 2018) as well as in autotrophic respiration (Huntingford et al., 2017). Further research since AR5 has shown that observed variation in photosynthetic temperature optima reflects acclimation within the lifespans of individual plants, rather than reflecting local adaptation (Kumarathunge et al., 2019), thus emphasizing the importance of representing thermal acclimation of plant physiology under transient climate change.

Since AR5, research has been conducted to understand better the effect of variability in water availability on plant production and net land carbon uptake. Much of the local scale year-to-year variability in global vegetation production and net carbon uptake is associated with interannual variability in total and seasonal precipitation and therefore the extent of drought (see also Section 8.4.2.7). In particular, semi-arid regions with substantial variability in interannual rainfall appear to be an important driver of the global interannual variability of productivity (Ahlstrom et al., 2015; Jung et al., 2017). ENSO-related occurrence of drought in the Amazon basin is a further large contributor to interannual variability in carbon exchange. Analyses of offline land models show that they underestimate the correlation between terrestrial water storage and carbon fluxes (Humphrey et al., 2018), thus suggesting a corresponding bias in fully-coupled ESMs.

5.4.3.2 Fire and Disturbance

Increasing fire frequency and severity with global warming is possible in several regions, including Arctic and boreal ecosystems (Mack et al., 2011; Gauthier et al., 2015), Mediterranean-type ecosystems (Turco et al., 2014; Jin et al., 2015), degraded tropical forests (Aragão et al., 2018), and tropical forest-savanna transition zones (Lehmann et al., 2014), which may thus release carbon to act as a climate change feedback. The potential for such increases is based on the fundamental mechanism of increased fire danger in a warmed climate (Abatzoglou et al., 2019) but is complicated by both ecosystem responses to fire (Hurteau et al., 2019) and changes to land and fire management practices. As in CMIP5, fire processes are included in some but not all CMIP6 ESMs. Of the models that do include prognostic fire, while they roughly agree with observations on present-day burned area, they disagree with each other on historical trends and drivers of burned area (Teckentrup et al., 2019), and they disagree with observations that show a decline in global burned area over the period of satellite observations (Andela et al., 2017). There is limited evidence and *low confidence* for a positive feedback mechanism between fire emissions and climate change based on model simulations and reconstructions based on charcoal and methane carbon isotope records (Arneth et al., 2010; Eliseev et al., 2014; Harrison et al., 2018); these estimates are included in Figure 5.28.

Changes to climate may also drive changes to vegetation composition and ecosystem carbon storage, with particular vulnerability of forest dieback-type biome shifts in tropical forests (Cox et al., 2004; Jones et al., 2009; Brando et al., 2014; Le Page et al., 2017; Zemp et al., 2017) and temperate and boreal zones (Joos et al., 2001; Lucht et al., 2006; Scheffer et al., 2012; Lasslop et al., 2016). AR5 assessed that large-scale loss of tropical forests due to climate change is *unlikely*. Newer ecosystem modelling approaches that include a greater degree of ecosystem heterogeneity and diversity show a reduced sensitivity of such forest dieback-type changes (Levine et al., 2016; Sakschewski et al., 2016), supporting this prior assessment. However, observations of tropical forests also show that changes to mortality rates within tropical forests may reduce carbon storage due to changing carbon turnover in vegetation (Brienen et al., 2015). Globally, vegetation dynamics may act as a centennial-timescale carbon sink, as expansion of boreal forest may act to offset tropical losses (Pugh et al., 2018). In addition to changes in vegetation biogeography, an ensemble of land models that include ecological processes such as forest demography suggest that changes to mortality may be a more important driver of carbon dynamics than changes to productivity (Friend et al., 2014). CMIP6 models, under idealised warming, show a smaller change to vegetation carbon than to soil carbon, unlike their response to CO_2, which is dominated by vegetation. However, the majority of CMIP6 ESMs do not allow for such dynamic vegetation processes, and instead impose a fixed biogeography of plant functional types (Arora et al., submitted), and, like the CMIP5 models, a static representation of vegetation carbon turnover (Koven et al., 2015a). Thus, while it is unlikely that large-scale losses of tropical forests may substantially drive carbon feedbacks, the confidence in the ability of ESMs to represent such vegetation shifts is low.

5.4.3.3 Soils and Permafrost

The majority of terrestrial ecosystem carbon resides in soils, where it is cycled back to the atmosphere by decomposers. Changes to soil carbon stocks in response to global change have long been considered a likely and potentially strong positive feedback (Cox et al., 2000). Since the AR5, there have been important changes to our understanding of soil carbon dynamics, and thus the strength of feedbacks from soils. These are: (1) an increased recognition of the role of high latitude soils in storing large amounts of potentially decomposable soil carbon, and an increased focus on modelling these dynamics in ESMs; (2) a shift in the understanding of the causes responsible for soil carbon persistence on long timescales, away from earlier theories governed mainly by the intrinsic chemical recalcitrance of soil organic matter to a view of soil organic matter persistence as governed by complex ecological dynamics of the decomposer community interacting with soil organic matter and mineral assemblages (Schmidt et al., 2011; Luo et al., 2016).

In the CMIP5 ESMs, soils represented a significant contributor to both the carbon-concentration ('beta', negative feedback) and carbon-climate ('gamma', positive feedback) feedbacks. The CMIP5 models show a large inter-model ensemble spread for carbon stock changes that determine the soil contributions to these feedbacks, and also show a large spread in the current soil carbon stocks predicted by the models (Todd-Brown et al., 2013). Soil contributions to both feedbacks can often be traced to changes in plant carbon inputs to soils, which then result in changing soil carbon stocks. Changes to the lifetime of carbon in the soil, in response to elevated decomposition rates under global warming, were relatively small in the CMIP5 ESMs (Koven et al., 2015a). This may be an artefact of the lack of permafrost carbon representation in any of the models. Changes to soil decomposition rates due to interactions between elevated productivity under elevated CO_2 and changing decomposer dynamics were also not included in any of the models (Guenet et al., 2018). Isotopic constraints furthermore suggest that CMIP5 ESMs systematically overestimated the transient sensitivity of soil ^{14}C responses to atmospheric ^{14}C changes, implying that the models respond too quickly to changes in either inputs or turnover times and that both feedbacks may thus be weaker than currently projected (He et al., 2016). Using natural gradients of soil carbon turnover as a constraint on long-term responses to warming suggests that the CMIP5 ESMs may systematically underestimate the temperature sensitivity at high latitudes, and may overestimate the temperature sensitivity in the tropics (Koven et al., 2017; Wieder et al., 2018). Such spatial gradients may also be used as an emergent constraint on ESM-predicted long-term carbon losses due to warming, suggesting a range of such losses of –182 ± 46 PgC globally at 2ºC warming (Varney et al., submitted).

For CMIP6, two ESMs includes permafrost carbon cycle dynamics, which changes the sign of the carbon-climate feedback from the high latitudes from a weak sink with warming to a strong source of carbon with warming (Schneider von Deimling et al., 2012; Burke et al., 2013; Koven et al., 2015c; Gasser et al., 2018; Kleinen and Brovkin, 2018). This response arises from the enormous stocks of carbon stored in high latitude soils (1300 ± 200 PgC) (Hugelius et al., 2014), which are highly decomposable upon thaw (Schädel et al., 2014). Experimental warming treatments that thaw permafrost demonstrate a high potential for ecosystem carbon losses with warming (Schuur et al., 2009). Interactions between permafrost C and N cycles under warming weaken but do not completely offset feedback (Koven et al., 2015b). The range of model estimates of the magnitude of this feedback remains large (McGuire et al., 2016), and SROCC assessed with *medium confidence* that the permafrost region would contribute tens to hundreds of PgC to the atmosphere by 2100 under an RCP8.5 scenario. As the majority of CMIP6 models do not include permafrost C feedbacks, they are represented separately in Figure 5.28, and included in remaining carbon budget calculations in Section 5.6, based on published estimates. Further, most models that do include permafrost carbon dynamics still do not consider fine-scale processes such as thermokarst and ice-wedge polygon degradation; those that do suggest these processes may further accelerate and amplify permafrost carbon loss (Nitzbon et al. *c*; Schneider von Deimling et al., 2015; Turetsky et al., in press, a). Permafrost CO_2 feedbacks act as a positive feedback to climate change (*high confidence*) of 20 ± 13 PgC $^{o}C^{-1}$ (*low confidence*). Models suggest that the permafrost carbon feedbacks act at timescales slower (by decades) than other carbon-climate feedbacks, but there is *low confidence* in the timing of feedbacks or the degree of linearity of permafrost CO_2 feedbacks as a function of global temperature change.

Soil microbial dynamics shift in response to temperature, giving rise to complex longer-term trophic effects

that are more complex than the short-term sensitivity of decomposition to temperature. Such responses are observed in response to long-term warming experiments (Melillo et al., 2017). Complex responses show no clear pattern in meta-analyses of soil responses to warming, partially due to inability to separate decomposition from productivity changes (van Gestel et al., 2018). These microbial dynamics also operate in response to changes in productivity (Sulman et al., 2014; van Groenigen et al., 2017). While most CMIP6 ESMs do not include microbial dynamics, simplified global soil models that do include such dynamics show greater uncertainty in projections of soil C changes, despite agreeing more closely with current observations, than the linear models used in most ESMs (Wieder et al., 2013).

In nutrient limited ecosystems, prolonged soil warming can induce a fertilisation effect through increased decomposition, which increases nutrient availability and thereby vegetation productivity (Melillo et al., 2011). Models that include this process tend to show a weaker carbon-climate feedback than those that do not (Thornton et al., 2009; Zaehle et al., 2010; Wårlind et al., 2014; Meyerholt et al., submitted). In CMIP6, 6 out of 11 ESMs include a representation of the nitrogen cycle, and the mean of those models predicts a weaker carbon-climate feedback than the overall ensemble mean. These models only partly account for the interactions of nutrient effects with other processes such as shift of vegetation zones under climate changes (Sakaguchi et al., 2016) leading to either changes in species composition or changes in plant tissue nutrient to carbon ratios (Thomas et al., 2015; Achat et al., 2016; Du et al., 2019).

5.4.4 Climate effects on ocean carbon uptake

5.4.4.1 Physical drivers of ocean carbon uptake

The cumulative ocean CO_2 uptake is projected to decrease by 20–44 PgC by year 2100 under the RCP8.5 scenario due to climate-driven perturbations to the natural carbon cycle (Bernardello et al., 2014; Randerson et al., 2015). The heat and anthropogenic CO_2 storage in the ocean show a common broad-scale pattern of change (Frölicher et al., 2015) as ocean warming tends to reduce CO_2 uptake from the atmosphere. Changing buoyancy fluxes, due to increased heat uptake by the ocean and altered freshwater input patterns, also lead to circulation-driven changes in carbon storage, which decrease global CO_2 uptake and redistribute ocean carbon, with higher concentration at high latitudes and increased vertical gradients in low latitude regions (Bernardello et al., 2014; Ito et al., 2015). Ocean warming reduces the solubility of CO_2 and increases stratification, which limits air-sea CO_2 exchange (Section 5.2.1.3.1; Section 9.2.1.4) (Matsumoto et al., 2010). Coupled climate models demonstrate a resultant positive climate-carbon cycle feedback (*high confidence*). On centennial timescales, CO_2 uptake and storage is strengthened in the Southern Ocean due to intensified winds (Ito et al., 2015). On millennial timescales, weakening deep ocean circulation reduces the downward transport of CO_2 from the surface to the deep ocean in high latitudes resulting in decreased CO_2 uptake (Yamamoto et al., 2018). At the same time in low latitudes, weaker equatorial upwelling reduces upward transport of CO_2 therefore enhancing CO_2 uptake (Yamamoto et al., 2018). The warming of the ocean and circulation changes in a high-CO_2 world also explain in part the lowering of the oceanic CO_2 uptake fraction.

Sea-ice processes may also affect the air-sea CO_2 exchange, although there is *low confidence* in the direction of change. During sea-ice growth, seawater total alkalinity (TA) and dissolved inorganic carbon (DIC) are concentrated in the brine and hence brine rejection during sea-ice melt increases the underlying DIC and TA (Søren et al., 2011). In regions of net export of sea ice, the polar mixed layer may become enriched in brine-associated TA and DIC, driving a sea-ice induced flux of CO_2 to the atmosphere (Grimm et al., 2016). Alternatively, brine may sink below the mixed layer and so drive CO_2 uptake (Rysgaard et al., 2013). However, this sea-ice induced uptake is a small fraction of net regional oceanic CO_2 uptake: about 1% in the Arctic and 5% in the Antarctic under the RCP4.5 warming scenario (Grimm et al., 2016).

5.4.4.2 Biological drivers of ocean carbon uptake

Ocean carbon uptake mediated by biological factors begins with oceanic primary production (PP), which

uses aqueous CO_2, thereby driving a decrease in surface ocean pCO_2 which may result in a net ocean uptake of atmospheric CO_2. However, in order for the organic carbon arising from primary production to contribute to net ocean carbon uptake, the organic material has to be transferred into the deep ocean via either physical or biological processes; this is referred to as the 'soft tissue pump' or 'biological carbon pump'. In the modern ocean, the ocean's biological carbon pump is a major factor in determining the air-sea partitioning of CO_2 (Kwon et al., 2009). The biological carbon pump currently stores on the order of 3000 PgC, lowering atmospheric CO_2 by hundreds of ppm (Parekh et al., 2006).

Changes in the efficiency of the biological carbon pump have modulated climate variability in the past, with the net impact on climate depending on the timescales over which ocean circulation returns the biologically sequestered carbon to the surface (Sigman et al., 2010). Nutrient inventories may have been higher during the last glacial maximum (*medium confidence*; Mahowald et al., 1999; Wallmann et al., 2016; Somes et al., 2017), but it remains to be determined whether global primary production increased in parallel. However, evidence suggests that the biological carbon pump was more efficient at sequestering carbon in the ocean interior (Galbraith and Jaccard, 2015; Anderson et al., 2019)(Galbraith and Skinner, 2020) as a result of generally colder temperatures slowing bacterial respiration rates (Kwon et al., 2009) (*medium confidence*). Deeper remineralisation coupled with a more isolated deep ocean (Skinner et al., 2017; Rae et al., 2018) retained CO_2 in the ocean interior, reducing atmospheric CO_2 concentrations (*high confidence*). During the last glacial termination the efficiency of the biological carbon pump weakened as ocean circulation resumed globally, releasing previously sequestered CO_2 (Galbraith and Jaccard, 2015; Bauska et al., 2016; Jaccard et al., 2016; Anderson et al., 2019) (*high confidence*). Paleoceanographic observations thus suggest a strong sensitivity of the biological carbon pump to climate, with a weaker efficiency in warm climate intervals.

At the time of AR5, the direction of modelled PP in response to increased atmospheric CO_2 concentration and climate warming was unclear (Taucher and Oschlies, 2011; Laufkoetter et al., 2015). This remains the case in the CMIP6 models available at the time of writing. Several interacting processes drive the response of PP to a changing climate and the choice of model parameterisation has a significant effect on projections. Warmer temperatures increase metabolic rates (*high confidence*), including the rate of PP and respiration rate; the latter potentially more rapidly than for PP (Boscolo-Galazzo et al., 2018). At high temperatures however, physiological stress to organisms can affect CO_2 fixation rates (Mathur et al., 2014). Warming also acts to increase stratification which may alleviate seasonal light limitation in high latitudes, thereby extending the phytoplankton growing season (*low confidence*). However, increased stratification also reduces nutrient supply to the upper ocean (Section 9.2.3.3) and would thus result in decreased PP. Phytoplankton populations may also be driven deeper to form sub-surface maxima; there is *low agreement* in the available literature on the potential effects on total PP (Martinez et al., 2016; Agusti et al., 2019). Deposition of anthropogenic airborne nitrogen on the surface ocean increases nitrogen concentration (Kim et al., 2014), but is *unlikely* to be of sufficient magnitude (or sufficiently widespread) to counteract the reduced vertical nutrient supply due to enhanced stratification. Experimental studies have shown that nutrient limitation may reduce the temperature dependence of metabolic rates (Marañón et al., 2018), implying that the dominant effect of warming may be indirect (nutrient supply) rather than direct mechanisms (metabolic rates) (*low confidence*). Enhanced dust input into the ocean from desertification could alleviate iron limitation and result in increased PP (*medium confidence*; Mahowald et al., 2017), that is a similar mechanism as occurred during the last glacial maximum (Albani et al., 2018; Section 5.~~2.~~2.1.3). ~~-~~ At a local scale, large icebergs may be an increasingly important iron source in the future (Duprat et al., 2016), however basin scale nutrient availability will not be affected (*medium confidence*). Alternatively, changes in ocean circulation and increased stratification could result in reduced iron supply to iron-limited regions, decreasing PP. Tagliabue et al. (2014) show that atmospheric CO_2 concentration increases by only 2 ppm if dust deposition is completely shut off, but incorporating light-iron colimitation leads to an increase of 9.9 ppm at low dust deposition (Nickelsen and Oschlies, 2015). Further changes to nutrient availability may occur via alterations to the nitrogen cycle, such as increasing denitrification in oxygen minimum zones or increasing atmospheric nitrogen fixation with increased dust inputs (see Section 5.3.3.2 and SROCC Section 5.2.3.1.2). An additional effect of increased warming is predicted to be changes in phytoplankton community structure towards smaller functional types that are adapted to low nutrient conditions (*medium confidence*), with the exception of possible increases in diatom populations in the Southern Ocean and tropics (Fu et al., 2016). Ocean acidification is also *likely* to reduce the viability of calcareous organisms (Finkel et al., 2010).

Both ocean acidification and a shift toward smaller phytoplankton are expected to reduce PP and carbon export flux (*medium confidence*). These stressors will not change in isolation in the future ocean, and whether multiple stressors will have synergistic, or antagonistic, effects is unclear (Brennan and Collins, 2015; Boyd et al., 2015).

As a result of this complexity, CMIP5 model-simulated PP responses to the RCP8.5 scenario have a wide spread (Laufkötter et al., 2015), from –4.3 to +10 GtC yr^{-1} (–15 to +30% change; median –2 GtC yr^{-1}; –7.2%), with 5 out of 9 models analysed showing a decrease in global PP from 2012 to 2100. The reduction in net PP at low latitudes in 3 of the models is driven solely by nutrient limitation due to increased stratification, whereas in 4 other models there are additional temperature-driven increases in loss processes (grazing, sinking, mortality) which outweigh the higher phytoplankton growth rates (Laufkötter et al., 2015). In the CMIP6 output available thus far, one model predicts a decrease in global mean PP by 2100 (relative to 1850–1900) of 3%, one has no clear trend, and three predict an increase of 3–7% in the SSP5-8.5 scenario (median change +3%, 1.7 GtC yr^{-1}). Observations provide little direct constraint on the modelled responses of PP to climate change, partly due to insufficiently long records (Henson et al., 2016). However, there is some indication of an emergent constraint on changes in tropical PP based-on interannual variability estimated from remote-sensing (Kwiatkowski et al., 2017) – see Section 5.4.6.

As climate change exposes phytoplankton to lower nutrient supply and potentially increased light levels at high latitudes, phytoplankton community structure changes are *likely* to affect the nutrient stoichiometry of organic matter. Biogeochemical models which incorporate variable stoichiometry predict that the phytoplankton C:N ratio will increase by 0.4% and the C:P ratio by 4.3% under RCP8.5 (Kwiatkowski et al., 2018), which means that the amount of carbon stored via the biological carbon pump increases relative to the amount of PP. In a 5 box ocean model with variable stoichiometry, declines in subtropical phosphate supply driven by an increase in ocean temperature of 5°C resulted in a decrease in atmospheric CO_2 concentrations of 60 ppm (Moreno et al., 2018). By overlooking variable organic matter stoichiometry, the fixed stoichiometry models (as used in CMIP5) may underestimate cumulative ocean carbon uptake to 2100 by 0.5–3.5% (2–15 PgC) (Kwiatkowski et al., 2018).

Particulate organic carbon (POC) export flux is projected to decline by 1–12% by 2100 in CMIP5 models run under RCP8.5 (Laufkötter et al., 2016). Similar values are predicted in the 3 CMIP6 models available at the time of writing, with declines of 3–16% (–0.2 GtC yr^{-1} to –1.9 GtC yr^{-1}) by 2100 under the SSP5-8.5 scenario. The mechanisms driving these changes vary widely between models due to differences in parameterisation of particle formation, remineralisation and phytoplankton community structure. Changes to ocean circulation and sea ice in the Southern Ocean by year 2300 are expected to result in global-scale nutrient redistribution and a projected decrease in global POC export flux of 30% (Moore et al., 2018). Exported POC must be transferred from the near-surface to the deep ocean in order to contribute to carbon storage on climatically-relevant timescales. The mechanisms underlying the remineralisation of POC in the water column are myriad, interlinked and difficult to quantify observationally (Boyd et al., 2019). Factors altering the efficiency and functioning of the biological carbon pump include those due to changing circulation, altered microbial, phyto- and zooplankton community structure (Fu et al., 2016) (altering both the magnitude of POC export from the upper ocean and the type of sinking material produced), warming affecting metabolic rates (Cavan et al., 2019a), and changing stoichiometry of organic matter (Kwiatkowski et al., 2018). In addition, a reduction in the viability of calcifying organisms due to ocean acidification may affect the biological carbon pump by reducing the amount of material available to ballast POC (*low confidence;* Matear and Lenton, 2014). Other climate effects such as de-oxygenation and warming could also result in alterations to the magnitude and efficiency of the biological carbon pump via changes in phytoplankton community composition (*medium confidence;* Beman and Carolan, 2013; Gao et al., 2019), which potentially alters the sinking rate, respiration rate and aggregation/fragmentation of sinking particles. In a model experiment under RCP8.5 where POC flux is prescribed to increase with atmospheric CO_2, Matear and Lenton (2014) found that atmospheric CO_2 drops by about 43 ppm by 2100, while enhanced remineralisation of POC and dissolution of particulate inorganic carbon (PIC) could increase atmospheric CO_2 by about 18 ppm by 2100. The combination of the above processes reduced atmospheric CO_2 by 38 ppm by 2100. Higher water temperatures will tend to increase organismal metabolic rates, which would enhance remineralisation (Cavan et al., 2019b). If the organic carbon remineralisation occurs in the near-

surface ocean, surface pCO_2 would increase, creating a positive feedback (*high confidence;* Matsumoto, 2007). Increased remineralisation implies a shoaling of the depth to which organic carbon penetrates the deep ocean, which would also tend to create a positive feedback between remineralisation and atmospheric CO_2 concentration (*high confidence*; Kwon et al., 2009). Under the RCP8.5 scenario, a coupled model study suggests that temperature-dependent remineralisation, together with general ocean warming, could reduce ocean carbon uptake by 0.2 GtC yr^{-1} by the year 2100 (Segschneider and Bendtsen, 2013; Bendtsen et al., 2015). However, the complexity of the mechanisms involved in the remineralisation of POC represent a significant uncertainty in the magnitude and sign of ocean carbon cycle feedback to changes in atmospheric CO_2 and climate (Hülse et al., 2017). Improved model representation (which will require better observational constraints) of the biological carbon pump is required, as the contribution of biological processes to CO_2 uptake is expected to become more significant with continued climate change, due to a combination of decreasing buffer capacity and strong seasonality in the pump at high latitudes resulting in strengthening seasonality in anthropogenic carbon uptake (*medium confidence*; Hauck et al., 2015).

5.4.5 Carbon Cycle Projections in Earth system models

This section summarises future projections of land and ocean carbon sinks, and of atmospheric CO_2, from the latest Earth system models (ESMs). ESMs are the basis for century timescale projections, and for detection and attribution studies (Chapter 3). These models aim to simulate the evolution of the carbon sources and sinks on land and in the ocean, in addition to the physical components of the climate system.

Land-atmosphere and ocean-atmosphere carbon fluxes are sensitive to changes in climate and atmospheric CO_2, for the many reasons outlined in Sections 5.4.2 and 5.4.3. Early attempts to include the carbon cycle as an interactive element within GCM climate models showed the potential for the carbon cycle to accelerate the rate of global warming (Cox et al., 2000; Friedlingstein et al., 2001). The subsequent C^4MIP project compared coupled climate-carbon cycle simulations from six GCM models, highlighting the uncertainties associated with carbon cycle feedbacks (Friedlingstein et al., 2006). By the time of the IPCC AR5 most climate modelling groups had included an interactive carbon cycle, leading to the evolution of climate models into ESMs.

The CMIP5 ESMs discussed in the AR5 produced a wide range of projections of future CO_2 (Friedlingstein et al., 2014) primarily associated with different magnitudes of carbon-climate and carbon-concentration feedbacks (Arora et al., 2013), but also exacerbated by differences in the simulation of the net carbon release from land-use change (Brovkin et al., 2013). A key difference among the CMIP5 models was the extent to which nutrient availability limited the CO_2-fertilisation of plant photosynthesis, with most models assuming no nutrient limitations (Zaehle et al., 2015).

The CMIP6 models considered in this report now include nutrient limitations on vegetation growth, along with many other added processes compared to CMIP5. Table 5.4 summarises characteristics of the land and ocean carbon cycle models used in CMIP6 ESMs (Arora et al., submitted). In CMIP6, most ocean carbon cycle models (8 of 11) track three or more limiting nutrients (most often nitrogen, phosphorus, silicon, iron), and represent two or more phytoplankton types. More than half of the land carbon cycle models (6 of 11) now include an interactive nitrogen cycle, and almost half (5 of 11) represent forest fires. However, even for CMIP6, very few models explicitly represent vegetation dynamics (3 of 11) or permafrost carbon (1 of 11). Relative to CMIP5, we are nevertheless confident that CMIP6 carbon cycle models represent important additional biogeochemical processes and feedbacks.

[START TABLE 5.4 HERE]

Table 5.4: Properties of the CMIP6 Earth system models, focussing on the land and ocean carbon cycle components of these models (Arora et al., submitted).

Modelling group	CSIRO	BCC	CCCma	CESM	CNRM	GFDL	IPSL	JAMSETC	MPI	NorESM2-LM	UK
ESM	ACCESS-ESM1.5	BCC-CSM2-MR	CanESM5	CESM2	CNRM-ESM2-1	GFDL-ESM4	IPSL-CM6A-LR	MIROC-ES2L	MPI-ESM1.2-LR	NorESM2-LM	UKESM1-0-LL
Land carbon/biogeochemistry component											
Model name	CABLE2.4 CASA-CNP	BCC-AVIM2	CLASS-CTEM	CLM5	ISBA-CTRIP	LM4p1	ORCHIDEE (2)	MATSIRO (phys) VISIT-e (BGC)	JSBACH3.2	CLM5	JULES-ES-1.0
Veg C pools	3	3	3	22	6	6	8	3	3	3	3
Dead C pools	6	8	2	7	7	4	3	6	18		4
PFTS	13	16	9	22	16	6	15	13	13	21	13
Fire	No	No	No	Yes	Yes	Yes	No	No	Yes	Yes	No
Dynamic Veg	No	No	No	No	No	Yes	No	No	Yes	No	Yes
Permafrost C			No	Yes		No					
Nitrogen cycle	Yes	No	No	Yes	No	No	No	Yes	Yes	Yes	Yes
Ocean carbon/biogeochemistry component											
Model name	WOMBAT	MOM4_L40	CMOC (biol)	MARBL	PISCESv2-gas	COBALTv2	PISCES-v2	OECO2	HAMOCC6	HAMOCC5.1	MEDUSA-2.1
Phytoplankton	1	0	1	3	2	2	2	2	2	1	2
Zooplankton	1	0	1	1	2	3	2	1	1	1	2
Nutrients	P, Fe	P	N	N, P, Si, Fe	N, P, Si, Fe	N, P, Si, Fe	N, P, Si, Fe	N, P, Fe	N, P, Si, FE	N, P, Si, Fe	N, Si, Fe

[END TABLE 5.4 HERE]

ESMs can be driven by anthropogenic CO_2 emission ('emissions-driven' runs), in which case atmospheric CO_2 concentration is a predicted variable; or by prescribed time-varying atmospheric concentrations ('concentration-driven' runs), in which case land and ocean carbon sinks are still calculated interactively but do not feedback through changes in the atmospheric CO_2 concentration. Concentration-driven runs can be used to diagnose the carbon emissions consistent with a prescribed concentration scenario (see Section 5.5). They also enable individual modelling groups to contribute projections of either the land or ocean carbon sink, without requiring both to be simulated. As emissions-driven runs require both the land and ocean carbon cycles to be modelled interactively, fewer modelling groups carry these out. In this subsection we analyse results from concentration-driven ESM projections. Emissions-driven projections are discussed in Chapter 4 of this report.

5.4.5.1 Evaluation of the contemporary carbon cycle in concentration-driven runs

To have confidence in their projections the models should be compared to as wide an array of observational benchmarks as possible. This is particularly the case for highly-uncertain land carbon cycle feedbacks (Friedlingstein et al., 2003, 2006; Arora et al., 2013; Friedlingstein et al., 2014b). Land models within ESMs should be compared to multiple different datasets of processes such as gross carbon uptake, physical predictions such as leaf area and carbon stocks which influence carbon fluxes and are diagnostic of carbon turnover times, as well as linkages between carbon and water cycles and other aspects of the terrestrial

carbon cycle. To address this, a model benchmarking system, the international land model benchmarking (ILAMB) has been developed (Collier et al., 2018) to provide these multiple orthogonal constraints.

Figure 5.22 shows an overview of an overview set of (Figure 5.23a) land and (Figure 5.23b) ocean benchmarks applied to both the CMIP5 and CMIP6 models from the historical simulation. There is good evidence of an improvement in model performance from CMIP5 (left of thick line in both panels) to CMIP6 (right of thick line in both panels), in both the land and ocean, based on these benchmarks. The mean of the CMIP6 land models outperforms or is performs equivalently to the mean of the CMIP5 land models on all available metrics. [Placeholder: Based on preliminary data from CMIP6 models, it appears that model benchmarking scores have generally improved from the CMIP5 to the CMIP6 generation of models, which is consistent with the models providing a more useful estimate of feedback parameters than the CMIP5 generation of ESMs. Need to include more details on the benchmarking (period of evaluation, etc.) and resolve issues of missing data (grey squares) in many of the comparisons, and inclusion of CMIP5 and CMIP6 ensemble-mean values for ocean models.]

[START FIGURE 5.22 HERE]

Figure 5.22: Overview scores of CMIP5 (left hand side of table) and CMIP6 (right hand side of table) models, for multiple benchmarks against different datasets. (a) Benchmarking of ESM land models, (b) benchmarking of ocean models. Scores are relative to other models within each benchmark row, with positive scores indicating a better agreement with observations. Thick vertical lines separate CMIP5 from CMIP6 models, and individual models from ensemble means.

[END FIGURE 5.22 HERE]

5.4.5.2 Evaluation of historical carbon cycle simulations in concentration-driven runs

This section evaluates concentration-driven historical simulations of changes in land and ocean carbon storage, against observation-based estimates from the Global Carbon Project (Le Quéré et al., 2018a). For each model, common historical land-use changes were prescribed (Jones et al., 2016a).

Figure 5.23 shows global mean, annual mean values from CMIP6 concentration-driven runs for 1850 to 2014. The ocean carbon cycle models reproduce historical carbon uptake well, with the model range for the global ocean carbon sink in 2014 (2.3–2.7 PgC yr^{-1}) clustering around the GCP estimate of 2.56 PgC yr^{-1}. Simulated changes in ocean carbon storage (1850–2014) range from 111 to 163 PgC, with a model mean of 129 ± 19 PgC which is lower than the GCP estimate of 150 PgC (Figure 5.23a).

The land carbon cycle components of historical ESM simulations show a much larger range, with simulated historical changes in land carbon storage (1850–2014) spanning the range from –48 to +32 PgC, compared to the GCP estimate of –12 PgC (Figure 5.23b). This range is due in part to the complications of simulating the difference between carbon uptake by intact ecosystems (e.g. due to CO_2 fertilisation of photosynthesis) and the direct release of carbon due to land-use change (e.g. tropical deforestation). There is *high confidence* that the land continues to dominate the overall uncertainty in the response of the global carbon cycle to climate change.

[START FIGURE 5.23 HERE]

Figure 5.23: CMIP6 ESM concentration-driven historical simulations for 1850 to 2014, compared to observation-based estimates from the Global Carbon Project (GCP). Panel (a) change in ocean carbon storage from 1850 (PgC); (b) change in land carbon storage from 1850 (PgC). Only models that simulate both land and ocean carbon fluxes are shown here.

[END FIGURE 5.23 HERE]

5.4.5.3 Evaluation of latitudinal distribution of simulated carbon in emissions-driven runs

This distinction between the relatively high-fidelity with which the ocean carbon sink is simulated, and the much wider range of simulations of the land carbon sink, is also evident in the zonal distribution of the sinks (Figure 5.24). We compare the ESM simulations to estimates from three atmospheric inversion models: CAMS (Chevallier et al., 2005), CT 2017 (Peters et al., 2007) and MIROC-ATM4 (Saeki and Patra, 2017). The ocean carbon cycle components of CMIP6 ESMs are able to simulate the tropical CO_2 source and mid-latitude CO_2 sink, with relatively small model spread (Figure 5.24a). The CMIP6 ensemble (red wedge) simulates a larger ocean carbon sink at 50°N and a weaker sink in the Southern Ocean, than the inversion estimate, but with some evidence of a reduction in these residual errors compared to CMIP5 (blue wedge). The spread in inversion fluxes arises primarily from differences in the atmospheric CO_2 measurement networks and from transport model uncertainties.

By contrast, the land carbon components of ESMs produce a wider range in the latitudinal distribution of net land carbon uptake (Figure 5.24b). It has been previously noted that AR5 models tended to overestimate land-uptake in the tropics and underestimate uptake in the northern mid-latitudes, compared to inversion estimates. Further, it was hoped that the inclusion of nitrogen-limitations on CO_2-fertilisation within CMIP6 models would significantly reduce this discrepancy (Anav et al., 2013). There is indeed some evidence that the CMIP6 ensemble (red wedge in Figure 5.24b) captures the northern land carbon sink more clearly than CMIP5 (blue wedge in Figure 5.24b), but there remains a tendency for the ESMs to place more of the global land carbon sink in the tropics than the mid-latitudes, compared to the inversion estimates. There is *high confidence* that land carbon cycle models continue to underestimate the Northern Hemisphere land carbon sink, when compared to estimates from atmospheric inversion (Ciais et al., 2019a).

[START FIGURE 5.24 HERE]

Figure 5.24: Comparison of modelled zonal distribution of carbon sinks against atmospheric inversion estimates for 2000–2009, (a) ocean carbon uptake; (b) net land uptake. Positive uptake represents a carbon sink to ocean/land while negative uptake represents a carbon source. The land uptake is taken as Net Biome Productivity (NBP) and so includes net land-use change emissions. The bands show the mean ± 1 standard deviation across the available inversions (black bands, 3 models), CMIP5 ESMs (blue bands, 12 models for the ocean, 12 models for the land), and CMIP6 ESMs (red bands, 11 models for ocean, 10 models for land).

[END FIGURE 5.24 HERE]

5.4.5.4 Coupled Climate-Carbon Cycle Projections

Here we briefly describe results from CMIP6 concentration-driven runs. Concentration-driven runs enable a cleaner comparison of the differences across the carbon cycle components of the ESMs. Figure 5.25 shows results from both the SSP1-2.6 (SSP1, RCP2.6) and the SSP5-8.5 (SSP5, RCP8.5) scenarios, which span a large range in future CO_2 concentrations.

In each panel of Figure 5.25 the wedges represent the model-mean plus and minus one-standard deviation. Ocean and land carbon uptake are shorthand for the net flux from the atmosphere, such that positive uptake implies a carbon sink to the land/ocean and negative uptake means a carbon source or 'efflux' to the atmosphere. The land uptake is equivalent to net biome productivity, and therefore includes any modelled effects of land-use change on land carbon storage. The change in ocean and land carbon storage shown in panels c and d is calculated as the cumulative sum of the uptake fluxes from 2014.

The CMIP6 ESMs agree well on the evolution of the global ocean carbon sink through the 21st century for both SSP1-2.6 and SSP5-8.5. The ocean sink is projected to peak around 2080 at 5.5 ± 0.4 PgC yr^{-1} under SSP5-8.5, and to decline to 0.5 ± 0.3 PgC yr^{-1} by 2100 under SSP1-2.6 (Figure 5.25a). Cumulative ocean carbon uptake from 2014 is projected to reach 355 ± 35 PgC by 2100 under SSP5-8.5, and to saturate at

approximately 140 ± 25 PgC under SSP1-2.6.

Th ensemble mean changes in land and ocean sinks are qualitatively similar, but the land shows much higher interannual variability in carbon uptake (Figure 5.25b) and also a much larger spread in the model projections of changes in land carbon storage (Figure 5.25d). The ensemble-mean land carbon sink is projected to saturate at around 5 ± 3 PgC yr^{-1} under SSP5-8.5, and to decline to less than 0.3 ± 0.8 PgC yr^{-1} by 2100 under SSP1-2.6 (Figure 5.25a). Cumulative land carbon uptake from 2014 is projected to reach 280 ± 130 PgC by 2100 under SSP5-8.5, and to saturate at approximately 160 ± 35 PgC under SSP1-2.6. For comparison, the equivalent figures for the CMIP5 ensemble were 110 ± 170 PgC and 60 ± 90 PgC. Significant uncertainty remains in the future of the global land carbon sink, but there has been a notable reduction in the model spread from CMIP5 to CMIP6.

[START FIGURE 5.25 HERE]

Figure 5.25: Projected evolution of the global land and ocean carbon sinks for 2014 to 2090 in concentration-driven SSP1-2.6 (SSP1, RCP2.6; green) and SSP5-8.5 (SSP5, RCP8.5; purple) CMIP6 ESM runs: (a) net ocean uptake rate (PgC yr^{-1}); (b) net land uptake rate (PgC yr^{-1}); (c) change in ocean carbon store from 2014 (PgC); (d) change in land carbon store from 2014 (PgC). Positive uptake represents a carbon sink to ocean/land, and negative uptake represents a carbon source. Changes in carbon storage are calculated as the cumulative annual uptake fluxes. The land uptake is taken as Net Biome Productivity (NBP) and so includes any modelled net land-use change emissions. Thick lines represent the ensemble mean of the available ESM runs that provided the necessary carbon fluxes (7 ESMs), and the shaded area represents ± one standard deviation about that mean.

[END FIGURE 5.25 HERE]

5.4.5.5 Linear Feedback Analysis

In order to diagnose the causes of the varying time-evolution of carbon sinks, the traditional linear feedback approach is adopted (Friedlingstein et al., 2003), as used previously to analyse C^4MIP (Friedlingstein et al., 2006) and CMIP5 models (Arora et al., 2013). Changes in land carbon storage (ΔC_L) and changes in ocean carbon storage (ΔC_o) are decomposed into contributions arising from warming (ΔT) and increases in CO_2 (ΔCO_2):

$$\Delta C_L = \beta_L \, \Delta CO_2 + \gamma_L \, \Delta T$$

$$\Delta C_o = \beta_o \, \Delta CO_2 + \gamma_o \, \Delta T$$

where β_L (β_o) and γ_L (γ_o) are coefficients that represent the sensitivity of land (ocean) carbon storage to changes in CO_2 and climate respectively.

This quasi-equilibrium framework is known to be dependent on scenario because of the timescales associated with land and ocean carbon uptake. However, it is we retained here for consistency with the AR5, and because it has been used to define a number of emergent constraints on carbon cycle feedbacks (see Section 5.4.6). In order to minimise the confounding effect of the scenario dependence, β and γ values are diagnosed from idealised runs in which a 1% per year increase in atmospheric CO_2 concentration is prescribed, as for AR5 (Arora et al., 2013). Values of β are calculated from 'biogeochemical' runs in which the prescribed CO_2 increases do not affect climate, and these are then used to isolate γ values in fully-coupled runs in which both climate and CO_2 change (Friedlingstein et al., 2003).

Table 5.5 shows the global land and global ocean values of β and γ for each of the CMIP6 ESMs (Arora et al., submitted). Also shown in the last two rows are the ensemble mean and standard deviation across the ensemble, for CMIP6 and CMIP5. In both ensembles, the largest uncertainties are in the sensitivity of land carbon storage to climate change (γ_L) and the sensitivity of land carbon storage to CO_2 (β_L). Emergent

constraints have been suggested for both of these sensitivities (see Section 5.4.6). The more widespread modelling of nitrogen-limitations in CMIP6 was expected to lead to reductions in both of these feedback parameters. There is indeed some evidence for that with γ_L moving from –58 ± 38 PgC °C^{-1} to –33 ± 33 PgC °C^{-1} from CMIP5 to CMIP6, and β_L moving from 0.93 ± 0.49 PgC ppmv^{-1} to 0.89 ± 0.30 PgC ppmv^{-1}. There is no significant change in climate effects on global ocean carbon storage (γ_o) between CMIP5 and CMIP6, but there is the suggestion of a reduction in the value of β_o from CMIP5 to CMIP6 (0.82 ± 0.07 to 0.77 ± 0.06 PgC ppmv^{-1}).

[START TABLE 5.5 HERE]

Table 5.5: Diagnosed global feedback parameters for CMIP6 ESMs based on 4 · CO_2 runs (Arora et al., submitted). The last two rows show the mean and standard deviation cross the CMIP6 and CMIP5 models, respectively.

	Land Feedback Factors		Ocean Feedback Factors	
Model Name	γ_L (Pg C/K)	β_L (Pg C/ppmv)	γ_o (Pg C/K)	β_o (Pg C/ppmv)
ACCESS-ESM1.5	-21.1	0.37	-23.8	0.90
CanESM5	16.0	1.28	-14.7	0.77
CESM2	-21.6	0.90	-10.9	0.71
CNRM-ESM2-1	-83.1	1.36	-9.4	0.70
IPSL-CM6A-LR	-8.7	0.62	-13.0	0.76
MIROC-ES2L	-69.6	1.12	-22.3	0.73
MPI-ESM1.2-LR	-5.2	0.71	-20.1	0.77
NOAA-GFDL-ESM4	-80.1	0.93	-21.7	0.84
NorESM2-LM	-21.0	0.85	-19.6	0.78
UKESM1-0-LL	-38.4	0.75	-14.1	0.75
CMIP6 Model Mean	**-33.3 +/- 33.8**	**0.89 +/- 0.30**	**-16.9 +/- 5.1**	**0.77 +/- 0.06**
CMIP5 Model Mean	**-57.9 +/- 38.2**	**0.93 +/- 0.49**	**-17.3 +/- 3.8**	**0.82 +/- 0.07**

[END TABLE 5.5 HERE]

CMIP6 models show a consistent signal in the geographical patterns of β, which is also consistent with the CMIP5 models assessed in AR5: the land β is driven primarily by the tropical forest regions, with secondary drivers in temperate in boreal forests, while the ocean β is driven primarily in the North Atlantic, Northeast Pacific, and Southern Ocean (Figure 5.26a). In all cases, and in all locations, the sign of β is positive (i.e., it acts as a negative feedback). Spatial patterns of γ (Figure 5.26b) are more differentiated between both models and regions. On the land, the CMIP6 ensemble mean γ has a more complex pattern. In tropical forests, all models show a negative sign of γ in the Amazon region, though some models show positive γ in southeast Asian and/or African tropical forests. In mid-latitudes the ensemble mean shows a negative γ, but without widespread agreement in the sign. In the boreal zone, the ensemble mean is again for a positive γ, due to longer growing seasons, with some regions of model agreement, but also regions with limited agreement in sign due to projected increases in fire and increased respiration. At arctic latitudes, the model ensemble mean projects a positive γ, although the few ESMs that include permafrost feedbacks project a negative γ in this region, so there is not model unanimity of the sign of γ in this region. In the ocean, γ has a negative sign in the North Atlantic and acts to shift the Southern Ocean carbon sink southwards.

[START FIGURE 5.26 HERE]

Figure 5.26: Maps of carbon-concentration and carbon-climate feedback terms as evaluated from CMIP6 ESMs. Shown are the model means from ten CMIP6 ESMs, stippling indicates 80% of the models agree in sign

with the multi-model mean. Also shown are zonal-mean latitude profiles of land (green) and ocean (blue) feedbacks. [To update to include zonal-mean breakdowns based on model criteria (e.g., nutrient-enabled, permafrost carbon-enabled) once there is sufficient data]

[END FIGURE 5.26 HERE]

5.4.6 Emergent constraints to reduce uncertainties in projections

Emergent constraints are based-on relationships between observable aspects of the current or past climate (such as trends or variability), and uncertain aspects of future climate change (such as the strength of particular feedbacks) – relationships which are evident across an ensemble of models. When combined with an observational estimate of the trend or variability in the real climate, such emergent relationships can yield 'emergent constraints' on the future climate change. The term was coined in 2002 (Allen and Ingram, 2002), but the archetypal example is an emergent constraint on snow-albedo feedback (Hall and Qu, 2006). At the time of the AR5, there had been relatively few applications of the technique to constrain carbon cycle sensitivities, but there have been many relevant studies published since (Cox, 2019; Hall et al., 2019). The concept of emergent constraints is explained in more depth in Chapter 1 Section 1.5.4.6. In this subsection we discuss previously published emergent constraints on the carbon cycle in ESMs. To date, these have been derived predominantly from the CMIP5 models.

The simplest type of emergent constraint is a relationship between a past-to-present change and a present-to-future change. For example, a relationship was noted in CMIP5 ESM runs between the simulated CO_2 concentration by 2010, and the projected CO_2 concentration in the future under the RCP8.5 scenario (Friedlingstein et al., 2014b). As the CO_2 concentration in 2010 is known from observations, there is a potential emergent constraint on the future CO_2 concentration under this common scenario (Hoffman et al., 2014), as shown in Figure 5.27a. Such trend-on-trend relationships depend on models being similarly forced (in this case by CO_2 emissions consistent with RCP8.5).

Other emergent constraints assume relationships between short-term variability and long-term sensitivity to forcing, and are often motivated by ideas related to the fluctuation-dissipation theorem (Leith, 1975). These constraints can also be understood as utilizing relationships between the sensitivity of fluxes and the sensitivity of stores. For example, the observed interannual variability in the growth-rate of atmospheric CO_2 is known to be due to variability in land uptake of CO_2 which is itself driven by ENSO climate variability. Interannual variations in CO_2 in response to ENSO therefore reveal the sensitivity of the net atmosphere-land CO_2 flux to temperature. In ESMs this flux sensitivity has been shown to be approximately proportional to the sensitivity of the tropical land carbon store to future warming (γ_{LT}). Since CO_2 and climate records allow the observed flux sensitivity to be estimated, this implies an emergent constraint on γ_{LT}, which was originally reported for C^4MIP models (Cox et al., 2013) and confirmed for CMIP5 models (Wenzel et al., 2014) – see Figure 5.27b. In a similar way, satellite estimates of the variability in ocean productivity constrain projected changes in tropical marine productivity under long-term warming (Kwiatkowski et al., 2017).

Other constraints relate the seasonal cycle (Hall and Qu, 2006), or changes in the seasonal cycle (Wenzel et al., 2016), to the strength of particular feedbacks. A recent carbon cycle example uses the well-documented increase in the amplitude of the seasonal cycle of atmospheric CO_2 as measured on Hawaii and at Point Barrow (Graven et al., 2013) to constrain CO_2–fertilisation of photosynthesis on mid and high-latitude (Wenzel et al., 2016), as shown in Figure 5.27c. Figure 5.27 also shows recent published emergent constraints on increases in high-latitude gross primary productivity derived from satellite records of 'greening' (Winkler et al., 2019), and on the future global ocean carbon sink based-on a strong correlation with current-day carbon uptake by the Southern Ocean (Kessler and Tjiputra, 2016).

[START FIGURE 5.27 HERE]

Figure 5.27: Examples of emergent constraints on the carbon cycle in ESMs, reproduced from previously published

studies: (a) projected global mean atmospheric CO_2 concentration by 2060 under the RCP8.5 emissions scenario against the simulated CO_2 in 2010 (Friedlingstein et al., 2014b; Hoffman et al., 2014); (b) sensitivity of tropical land carbon to warming (γ_{LT}) against the sensitivity of the atmospheric CO_2 growth-rate to tropical temperature variability (Cox et al., 2013; Wenzel et al., 2014); (c) sensitivity of extratropical (30°N–90°N) gross primary production to a doubling of atmospheric CO_2 against the sensitivity of the amplitude of the CO_2 seasonal cycle at Kumkahi, Hawaii to global atmospheric CO_2 concentration (Wenzel et al., 2016); (d) change in high-latitude (30°N–90°N) gross primary production versus trend in high-latitude leaf area index or 'greenness'(Winkler et al., 2019) ; (e) sensitivity of the primary production of the Tropical ocean to climate change versus its sensitivity to ENSO-driven temperature variability (Kwiatkowski et al., 2017); (f) global ocean carbon sink in the 2090s versus the current-day carbon sink in the Southern Ocean. In each case, a red-dot represents a single ESM projection, the grey bar represents the emergent relationship between the y-variable and the x-variable, the blue bar represents the observational estimate of the x-axis variable, and the green bar represents the resulting emergent constraint on the y-axis variable. The thicknesses represent ± one standard error in each case. Figure after (Cox, 2019).

[END FIGURE 5.27 HERE]

5.4.7 Non-CO_2 feedbacks

Sources and sinks of non-CO_2 greenhouse gases such as methane (CH_4) and nitrous oxide (N_2O) respond both directly and indirectly to atmospheric CO_2 concentration and climate change, and thereby give rise to additional biogeochemical feedbacks in the climate system. Many of these feedbacks are only partially understood and are not yet fully-included in ESMs. Nevertheless, the strength of many feedbacks can be estimated in a similar linear framework as for CO_2, based on simulations with standalone models or ESMs of intermediate complexity (Figure 5.28). As for the carbon cycle feedbacks discussed in Section 5.4.5, non-linearities may make these estimates state or scenario dependent.

[START FIGURE 5.28 HERE]

Figure 5.28: An overview of biogeochemical feedbacks in the climate system, based on the framework proposed by (Gregory et al., 2009; Arneth et al., 2010). a) Synthesis of biogeochemical feedbacks from panels b and c. Red (blue) bars correspond to positive (negative) feedbacks increasing (decreasing) radiative forcing at the top of the atmosphere. Bars denote the mean and the error bar represents one standard deviation of the estimates assuming variance between individual components are independent; b) carbon-cycle feedbacks as assessed by CMIP5 (Arora et al., 2013) and CMIP6 (Arora et al., submitted), where dots represent single model estimates, and open (filled) circles are those estimates which do (not) include the representation of a terrestrial nitrogen cycle; c) Estimates of other biogeochemical feedback mechanisms. These feedback metrics have, where possible, been assessed for the RCP8.5 scenario in year 2100, using the radiative forcing equations by with updated by (Etminan et al., 2016). Note the different x-axis scale for this panel. Black dots represent single estimates, and coloured bars denote the simple mean of the dots with no weighting or assessment being made to likelihood of any single estimate. Results in panel c have been compiled from (a) Section 5.4.3.2 (Arneth et al., 2010; Eliseev et al., 2014; Harrison et al., 2018); (b) Section 5.4.3.3 (Schneider von Deimling et al., 2012; Burke et al., 2013; Koven et al., 2015; Gasser et al., 2018; Kleinen and Brovkin, 2018), where the estimates from Burke et al. has been constrained as assessed in their study (c) Section 5.4.7 (Schneider von Deimling et al., 2012, 2015; Turetsky et al., in press, b); (d) Section 5.4.7 (Denisov et al., 2013; Shindell et al., 2013; Stocker et al., 2013a; Zhang et al., 2017); (f) (Xu-Ri et al., 2012; Zaehle, 2013; Stocker et al., 2013; Tian et al., 2019); (g) (Martinez-Rey et al., 2015; Landolfi et al., 2017; Battaglia and Joos, 2018). (h) These feedbacks are assessed in Section 6.3 and the range indicated is the standard deviation of the feedback.

[END FIGURE 5.28 HERE]

CH_4 feedbacks may arise from changing wetland emissions (including rice farming), from new sources related for example to permafrost thaw, and from the response of atmospheric chemistry to climate change.

CH_4 emissions from wetlands generally increase with warming due to enhanced decomposition with higher temperatures, thereby potentially providing a positive CH_4 feedback on climate (Dean et al., 2018). The contribution of wetlands to interannual variability of atmospheric CH_4 is shaped by the different impacts of temperature and precipitation anomalies on wetland emissions (e.g., during El Niños) and therefore the relationship between climate anomalies and the wetland contribution to the CH_4 growth rate is less clear (Pison et al., 2013; Zhang et al., 2018c). There is robust agreement across model simulations that the wetland response to future climate change enhances the CH_4 build up in the atmosphere at decadal to multidecadal timescales, but that the corresponding effect on the methane radiative forcing is low because of i) limited additional CH_4 emissions and ii) the sub-linear dependence of CH_4 radiative forcing on its atmospheric concentration (Gedney, 2004; Volodin, 2008; Ringeval et al., 2011; Denisov et al., 2013; Shindell et al., 2013). Some studies even suggest that the feedback between climate and CH_4 emissions from wetlands is weaker than the simulated effect of rising atmospheric CO_2 on CH_4 emissions feedback due to the effect of increased plant productivity (thus, of larger amount of litter) on methane production in wetlands (Ringeval et al., 2011; Melton et al., 2013). Permafrost thaw and methane emissions from thermokarst lakes and wetlands may further contribute to a positive land-CH_4-climate feedback, but the quantitative understanding of the magnitude and timing of CH_4 release is low (Schneider von Deimling et al., 2012, 2015; Turetsky et al., in press, b). These positive feedbacks will be counteracted by the effect of higher temperatures on atmospheric chemistry, which reduces the lifetime of methane in the atmosphere and therefore provides a negative feedback (see Section 6.3).

Both land and ocean N_2O emissions respond to climate change. Land biosphere models suggest that long-term global warming will be accompanied by enhanced N_2O release from terrestrial ecosystems (*limited evidence, high agreement*) (Xu-Ri et al., 2012; Stocker et al., 2013; Zaehle, 2013; Tian et al., 2019). These models do not account for the potentially strong increases in boreal and arctic ecosystems associated with warming and permafrost thaw (Elberling et al., 2010; Voigt et al., 2017). The response of terrestrial N_2O emissions to CO_2 is dependent on nitrogen availability and is positive in nitrogen-rich ecosystems, such as highly-fertilised fields, although the feedback has not been quantified at large scale (van Groenigen et al., 2011; Butterbach-Bahl et al., 2013; Tian et al., 2019). Climate change will also affect N_2O production in the ocean through changes in productivity, stronger vertical stratification and ocean de-oxygenation (Codispoti, 2010; Freing et al., 2012; Bopp et al., 2013). Model projections under the RCP8.5 scenario suggest ocean N_2O emissions may decrease by 4–12% over the 21st century due to a combination of factors including increased ocean stratification, decreases in ocean productivity, and the impact of increasing atmospheric N_2O abundance on the air-sea flux (Martinez-Rey et al., 2015; Landolfi et al., 2017; Battaglia and Joos, 2018). Ocean N_2O emissions may recover on longer timescales owing to ocean de-oxygenation and long-term increases in remineralisation, leading to a positive correlation of N_2O emission and climate at the timescale of millennia (Battaglia and Joos, 2018b). The magnitude of mutually compensating terrestrial and oceanic N_2O feedbacks combined with the long atmospheric lifetime of N_2O imply that their effect on radiative forcing in the next century will be low, but may become important if the terrestrial emission changes are sustained beyond that time scale (Xu-Ri et al., 2012).

Despite these uncertainties, there is *medium to high confidence* that, at multidecadal and centennial timescales, the combined additional radiative forcing arising from climate-CH_4 and climate-N_2O feedbacks of 0.05 ± 0.02 W m^{-2} °C^{-1} (Figure 5.28) will be small compared to anthropogenic forcing in the 21st century. Nevertheless, these feedbacks will contribute to a decrease of the remaining anthropogenic CO_2 emissions to limit global warming by specific target (Section 5.5).

5.4.8 Possible abrupt changes and tipping points

The utility of the linear feedback framework (Section 5.4.4.1) suggests that large-scale biogeochemical feedbacks are approximately linear in the forcing from changes in CO_2 and climate. Nevertheless, regionally the biosphere is known to be capable of producing abrupt changes or even 'tipping points' (Higgins and Scheiter, 2012; Lasslop et al., 2016) (see Section 1.4.5). The catalogue of possible abrupt changes associated with Earth system feedbacks includes a number related to ecosystems and biogeochemistry (Lenton et al., 2008; Steffen et al., 2018) – including tropical and boreal forest dieback, greening of sub-Saharan Africa,

release of carbon from permafrost, and ocean acidification and deoxygenation (Table 5.6). Some of the proposed abrupt changes are essentially tipping point bifurcations of a system with multiple steady-states. These cases are described as 'irreversible' when crossing the bifurcation point leads to a new steady-state that is not destabilised by merely passing back through the bifurcation point. In addition, for transient climate changes (e.g., for 21st climate projections under anthropogenic forcing) system inertia can lead to the possibility of rate-induced tipping (Ashwin et al., 2012). Chapter 1, Section 1.4.5 describes the concept of bifurcation, noise-induced and rate-dependent tipping points, in more detail. This section focuses on non-linear changes that could have a significant impact on greenhouse gas concentrations to 2100, relative to changes caused directly by anthropogenic emissions (see Section 5.4.9 for longer time scales).

[START TABLE 5.6 HERE]

Table 5.6: Summary of the possible tipping points and abrupt changes in the Earth system.

Tipping point / abrupt change	Key region(s)	Carbon dioxide or methane release in the 21st century	Development timescale	Associated CO_2 or CH_4 rate of change	(Ir)reversibility
Tropical forests dieback	Amazon watershed	< 100 PgC as CO_2 (*high confidence*)	multi-decadal	CO_2: < 0.25 ppm yr^{-1}	unknown
Boreal forests dieback	boreal Eurasia and North America	unquantified, but *likely* small	multi-decadal	unquantified, but *likely* small	*likely* irreversible at multi-decadal scale
Biogenic emissions from permafrost thaw and development of thermokarst lakes	pan-Arctic	up to 9000 Tg of CH_4 (*low confidence*)	multi-decadal	CH_4: ≤ 10 ppb yr^{-1}	*likely* irreversible at centennial timescales
Methane release from clathrates	oceanic shelf	unquantified, but very likely small	multi-millennium	unquantified, but very likely small	likely irreversible at multi-millennium timescales
Oceanic acidification and deoxygenation [placeholder]	Southern Hemisphere mid-latitudes	unquantified	millennium	unquantified	likely irreversible at multi-millennium timescales

[END TABLE 5.6 HERE]

5.4.8.1 Forest dieback

Published examples of abrupt changes involving biogeochemical cycles feedbacks include tropical rain forest dieback (Cox et al., 2004; Jones et al., 2009; Brando et al., 2014; Le Page et al., 2017; Zemp et al., 2017) ,and temperate and boreal forests dieback (Joos et al., 2001; Lucht et al., 2006; Scheffer et al., 2012; Lasslop et al., 2016). Such transitions may be related to (i) large-scale changes in mean climate conditions (Joos et al., 2001; Cox et al., 2004; Lucht et al., 2006; Hirota et al., 2011; Scheffer et al., 2012; Le Page et al., 2017; Zemp et al., 2017) and may be traced to crossing of particular climatic thresholds, (ii) temperature and precipitation extremes (Staver et al., 2011; Higgins and Scheiter, 2012; Scheffer et al., 2012; Pavlov, 2015; Zemp et al., 2017), or (iii) possible intermittency in fire activity (Staver et al., 2011; Higgins and Scheiter, 2012; Lasslop et al., 2016) occurring either due to climate feedbacks or due to human (ignition) forcing. For dieback driven by large-scale changes in mean climate conditions, *confidence is low* because there is disagreement between different simulations. Most ESMs project climate changes which are insufficient to cross the climatic thresholds for tropical forest viability (Huntingford et al., 2013; Boulton et al., 2017). In addition, real forests may be less vulnerable to climate than those modelled in ESMs. This is

because the real world has a much greater plant trait diversity which confers additional resilience (Levine et al., 2016; Sakschewski et al., 2016), and also because of possible acclimation of vegetation to imposed climate changes (Good et al., 2011, 2013; Lloret et al., 2012; Mercado et al., 2018). In the latter case, acclimation is more likely for relatively slow climate changes. In general, forest dieback is more probable under higher-emission scenarios of anthropogenic forcing leading to more prominent climate changes (Lyra et al., 2017) as well as under more intensive land use (Le Page et al., 2017). Emergent constraint approaches have been used to estimate a loss of tropical land carbon due to climate change alone, of around 50 PgC per ^{o}C of tropical warming (Cox et al., 2013; Wenzel et al., 2014). This implies an upper limit to the release of tropical land carbon of <200 PgC over the 21st century (assuming tropical warming of <4^{o}C). However, this is likely to be an overestimate due to the neglect of the compensating effects of CO_2-fertilization. For the RCP8.5 scenario Anadón et al. (2014) estimate that 24% (range 9–39%) of the contemporary American tropical rainforests might be converted to savanna by the late 21st century. Extrapolating this estimate to all tropical forests, and using the estimate of the tropical forest carbon stock (Saatchi et al., 2011), an upper bound for the respective carbon release into the atmosphere is about 100 PgC, which translates to $dCO_2/dt <$ 0.25 ppm yr^{-1}). This estimate becomes smaller if the carbon stored in the remaining savannah grasses is taken into account (Steffen et al., 2018).

Boreal forest dieback is *unlikely* to change the atmospheric perturbation substantially because forest loss at the south is partly compensated by (i) temperate forest invasion into the previous boreal area (ii) boreal forest gain at the north (Friend et al., 2014; Kicklighter et al., 2014; Schaphoff et al., 2016). Tropical and boreal dieback tipping trajectories are slow, associated with a multi-decadal development timescale. Thus, there is a *medium confidence* that forest dieback will not release more than 100 PgC over the 21st century.

5.4.8.2 Biogenic emissions following permafrost thaw

The permafrost region has acted as either a weak carbon sink or source during the last few decades (McGuire et al., 2012; Belshe et al., 2013), but the sources could strengthen considerably under warming. Model projections of CO_2 emissions by 2100 under a high warming scenario have been estimated at 11–199 PgC (Schneider von Deimling et al., 2012; Schaefer et al., 2014; Koven et al., 2015; Schuur et al., 2015; MacDougall and Knutti, 2016; Gasser et al., 2018); and strengthen even further by 2300 (Schneider von Deimling et al., 2012; Schuur et al., 2015; Gasser et al., 2018; McGuire et al., 2018). The uncertainty range is controlled by simulated changes in water table position, wetland extent and the temperature sensitivity of decomposition in organic soils (Schneider von Deimling et al., 2012; Schuur et al., 2015). These emissions also depend on CO_2 pathways (Kleinen and Brovkin, 2018). The uncertainty of the above estimates might be underestimated due to the neglect of emissions during winter (Natali et al., 2014). One CMIP6 ESM (only CESM2 during the SOD preparation) estimates losses up to 27 PgC from the permafrost-containing soils during the 21st century. Because of widespread soil saturation and anoxia in the region, part of the carbon flux from ecosystems to the atmosphere is via production of CH_4, which is a more powerful greenhouse gas. Methane release from permafrost thaw (including thermokarst lakes) has been estimated at 836–2614 Tg CH_4 over the 21st century (Schneider von Deimling et al., 2015), and from all abrupt thaw processes as 9000 Tg CH_4 over the 21st century (Turetsky et al., in press, b). These emissions develop at multi-decadal timescale. The uppermost of these estimates lead to the annual methane release of the order of 100 TgCH_4 yr^{-1}, assuming a CH_4 lifetime in the atmosphere of the order of 10 years and the associated feedback parameter of 1.4 (Holmes, 2018). This would increase the atmospheric methane content by about 500 ppb in one century, which corresponds to the rate of change ≤ 10 ppb yr^{-1}. We currently have *low confidence* in the impact of biogenic emissions from permafrost thaw on the global biogeochemical cycles. However, because soil carbon replenishment in pan-Arctic region is slow, it is *likely* that soil carbon losses in these regions are irreversible at centennial or even at larger timescales. Internal heat production in organic permafrost soils is able to amplify permafrost thawing and accelerate organic matter decomposition, thus, increasing carbon loss and leading to the theoretically possible compost-bomb instability in carbon-rich soils (Koven et al., 2011; Luke and Cox, 2011, Hollesen et al., 2015). Coupled CH_4-climate models show that possible increases in CH_4 lead to similar global patterns of radiative forcing from CH_4, irrespective of where the CH_4 sources are located (Volodin, 2015). Another possible source of CH_4 from the terrestrial cryosphere are relict, shallow, metastable gas hydrates in deeper permafrost (Buldovicz et al., 2018; Chuvilin et al., 2018), which

may have caused recent craters in the Russian North (Arzhanov et al., 2016; Kizyakov et al., 2017, 2018), and which might indicate that the contemporary warming already exceeded the mid-Holocene climate in these regions (Arzhanov and Mokhov, 2017).

Thus, there is *high confidence* that thawing terrestrial permafrost will lead to carbon releases, but *low confidence* in the timing, magnitude and the relative roles of CO_2 versus CH_4 as feedback processes.

5.4.8.3 Methane release from clathrates

The total global clathrate reservoir is estimated to contain 1500–2000 PgC (Archer et al., 2009; Ruppel and Kessler, 2017). Methane release from shelf clathrates is <10 $TgCH_4$ yr^{-1} (Saunois et al., 2016a). Abrupt change is *very unlikely* for the permafrost-embedded subsea clathrates owing to a long response time (Minshull et al., 2016; Malakhova and Eliseev, 2017). Deeper ocean clathrates are *extremely unlikely* to dissociate and release significant methane on a centennial timescale. This makes the 'clathrate gun' hypothesis *extremely unlikely* to be relevant on the timescales we are considering in this report. Early estimates had suggested that the ocean may release 600 $PgCH_4$ in response to 1000 PgC of cumulative emissions from fossil fuels over 10 kyr (Archer et al., 2009; Zeebe, 2013), indicating that this hypothesis would be plausible at multi-millennium and longer time scales (Majorowicz et al., 2014). However, the amount of clathrate that might be destabilised by warming is a small fraction of this, there are long timescales associated with clathrate destabilisation, and much of that CH_4 would likely be oxidised in the process. This leads to estimated fluxes of less than 5 $TgCH_4$ yr^{-1} over the next century (Kretschmer et al., 2015; Saunois et al., 2016b). Thus, there is *medium confidence* that this tipping point is *unlikely* to substantially warm the climate system over the next few centuries.

5.4.8.4 Ocean acidification and de-oxygenation

As seawater pH lowers under accumulating CO_2 in the atmosphere, there is a decrease in the saturation state of calcium carbonate, which in turn alters the marine food web. Because of the slow rate of deep ocean mixing and equilibration with carbonate sediments on the seafloor, there is very limited capacity to reverse ocean acidification by solely decreasing CO_2 emissions or by removing CO_2 from the atmosphere (Section 5.3.3.4). Given the available evidence, ocean acidification will continue to occur during millennia after stabilization of carbon dioxide emissions (Section 5.3). For instance, carbon dioxide removal strategies could lower atmospheric CO_2 by 2100 under RCP4.5 scenario, but would only alleviate surface ocean acidification (Taylor et al., 2015a).

In addition, an ocean de-oxygenation is already documented to be occurring (Section 5.4.3). It is estimated that the global ocean has already lost 2% of the global ocean oxygen content. Model estimates predict a further loss of 2–4% until year 2100 (Bopp et al., 2013; Battaglia and Joos, 2018b). Model studies (Battaglia and Joos, 2018b; Kemena et al., 2019) suggest that ocean de-oxygenation will peak a thousand years after the stabilization of radiative forcing. Following this, the ocean interior would arrive at a new steady-state in oxygen content, closer to pre-industrial conditions only after ten thousand years (SROCC, Chapter 6). There is a *high confidence* that both oceanic acidification and de-oxygenation will continue during the 21st century. For both processes, additional carbon release, however, remains unquantified.

5.4.8.5 Abrupt changes detected in ESM projections

Projecting abrupt changes is intrinsically difficult, because by definition abrupt changes occur in a small region of the parameter and/or forcing space. Fortunately though, many bifurcation-like tipping points exhibit time-series precursors that may be used to detect them (Scheffer et al., 2009). The most commonly used tipping point precursors relate to 'critical slowing down' (Lenton, 2011). These detect the reducing resilience of the current state through fluctuations about that state. Essentially, less resilient systems exhibit longer and larger oscillations about their steady-state, as revealed by the variance and autocorrelation of the

key state variables (such as temperature or CO_2). Through detecting changes in these metrics, it has been possible to identify potential tipping points in many past climate records (Dakos et al., 2008; Lenton et al., 2012; Armstrong McKay and Lenton, 2018). At the time of the AR5 there was, however, no available systematic study of tipping points in ESMs.

An analysis of ESMs since the AR5 has however identified a number of abrupt changes in the CMIP5 ensemble (Drijfhout et al., 2015). The most commonly detected abrupt changes in the CMIP5 archive relate to sea-ice changes, but there also a number of detected changes in the land biosphere especially in that subset of models which included dynamic vegetation. These include abrupt changes in tropical forests and high-latitude greening, permafrost thaw, and vegetation composition change. Thus, there is *medium confidence* that abrupt changes may occur during next several centuries but with only a *limited confidence* for their impact on atmospheric GHG concentrations.

However, we have *high-confidence* that the uncertainty in 21st century GHG concentrations associated with abrupt changes and tipping points, is small compared to the uncertainty associated with future anthropogenic emissions.

5.4.8.6 Knowledge gaps

There are important knowledge gaps for assessing possibility of tipping points, their climatic thresholds, and irreversibility:

- For tropical and boreal feedbacks, there is insufficient knowledge on plant resilience and acclimation to future climate changes;
- For methane release from clathrates, there is very limited knowledge of the location of clathrates and their methane stocks;
- For release of CO_2 and CH_4, there is a limited ability of processed-based large-scale modelling of thermokarst activity in the contemporary ESMs;
- Potential interactions between abrupt changes remain largely unstudied (Cai et al., 2016; Steffen et al., 2018; Turetsky et al., in press, b).

5.4.9 Long term response past 2100

The strength of carbon cycle feedbacks is dependent on the state of the system, the specific scenarios followed, and the timescale of interest. Feedbacks estimated from an idealised 1% CO_2 increase per year experiment may be different from those on longer timescales beyond 2100. Few of the CMIP5-era ESMs have explored these longer timescales. However, experiments with the CESM1 for the period 1850–2300 suggest that both land and ocean carbon-climate feedbacks strengthen in time, land and ocean carbon-concentration feedbacks weaken, and the relative importance of ocean sinks versus land sinks increases. The overall strengthening of carbon-climate feedbacks projected beyond 2100 offsets the declining climate sensitivity to incremental increases of CO_2, leading to an overall strengthening of the carbon cycle gain from one century to the next (Randerson et al., 2015). Experiments with permafrost-enabled models suggest that the magnitude of the permafrost C feedback strengthens considerably over the period 2100-2300 under a high-emissions scenario (Schneider von Deimling et al., 2015; McGuire et al., 2018). It has been estimated that thawing permafrost could release 115–172 PgC of CO_2 and 2.8–7.4 PgCH_4 in the period from 2100 to 2300 under the RCP8.5 scenario' leading to up to a 0.23ºC increase in global temperature. Under RCP2.6, permafrost has been projected to release less than 40 PgC over the same period.

Figure 5.29 shows long-term carbon cycle changes from the present to 2300 under the two SSP scenarios with long-term extensions: SSP5-8.5 and SSP5-3.4-overshoot, for two models [placeholder: Will be updated to include more CMIP6 in the FGD]. Under both emissions scenarios, both models project a reversal of the terrestrial carbon cycle from a sink to a source, however, the reasons for these reversals under high emissions and low/negative emissions are very different. Under the high emissions SSP5-8.5 scenario, climate change is projected to drive terrestrial carbon-climate feedbacks to strengthen beyond the carbon-concentration

feedbacks, and thus drive the land to become a net carbon source. The difference in both timing and magnitude of this transition between the two models, however, highlights the strong degree of uncertainty in this projected transition from sink to source, thus we assess that there is *low confidence* in the likelihood, timing, or strength of the terrestrial system transitioning from a net sink to a net source under such a scenario. We assess with *medium confidence* that the ocean sink strength would weaken but not reverse under such a long-term high-emissions scenario. In the SSP5-3.4-overshoot scenario, both the terrestrial and ocean reservoirs act as transient carbon sources during the overshoot period in which atmospheric CO_2 concentrations are falling, and then revert to near-zero fluxes after stabilization of atmospheric CO_2. Such a transition would be expected – due to declining CO_2 driving outgassing from the ocean and a reduction of carbon-concentration feedbacks on land – with *medium confidence* (see also section 5.6).

The long-term responses of the coupled carbon and climate systems under net-zero CO_2 emissions—the "Zero Emissions Commitment (ZEC)" – are assessed in sections 5.5.1.2 and Chapter 4, Section 4.7.2.

[START FIGURE 5.29 HERE]

Figure 5.29: Trajectories of carbon cycle dynamics for ESMs beyond 2100. Shown are two scenarios, SSP5-8.5 and SSP5-3.4-overshoot, from one ESM (CanESM5) and one EMIC (UVIC-ESCM) for which extensions beyond 2100 are available. [Placeholder: To be updated in the FGD to include more CMIP6 model results] (a) Terrestrial carbon sink dynamics, and (b) Ocean carbon sink dynamics, for over the period 2015–2300.

[END FIGURE 5.29 HERE]

5.4.10 Near-term prediction of ocean and land carbon sinks

The IPCC AR5 (WG1 Chapter 11) assessed near-term climate predictability based on Earth system models initialised from the observed climate state. Since the AR5 there is growing number of prediction systems based on ESMs that include the ocean and land carbon cycle components. Predictability of key physical climate variables (assessed in Chapter 4) provide a platform to establish predictive skill for interannual variations in the strength of the natural carbon sinks in response to internal climate variability. The carbon cycle components are only indirectly initialised with the data assimilative physics and respond to the initialised climate variations (Ilyina et al., submitted). Predictions of variability in the natural carbon sinks represent a major challenge owing to limited data availability. Therefore, this subsection synthesises information on predictability of the land and ocean carbon sinks using both, the idealised potential predictability and the actual predictability skill measures.

Predictability of marine biogeochemical properties is associated with internal variability in the ocean that is largely driven by the processes acting on multi-year to decadal time-scales (McKinley et al., 2017; Li and Ilyina, 2018). Such longer-term memory residing in the ocean enables predictability of the ocean carbon sink. Evidence is accumulating that predictive horizon of the globally integrated air-sea CO_2 fluxes assessed in perfect model studies (Séférian et al., 2018; Spring and Ilyina, submitted) and verified against observations (Ilyina et al., submitted; Li et al., 2019) is up to 6 years (Figure 5.30). There is a potential for longer regional predictability in some regions including the North Atlantic and subpolar Southern Ocean (Li et al., 2016a; Lovenduski et al., 2019b). Progress has been made in understanding the drivers of predictability of the ocean carbon sink. Models suggest that predictability of the air-sea CO_2 flux is related to predictability of the ocean biogeochemical state variables such as DIC and TA (Lovenduski et al., 2019b) and the mixed layer depth (Li et al., 2016a). Furthermore, temperature variations largely control shorter-term predictability of the ocean carbon sink, while longer term predictability is related to non-thermal drivers such as ocean circulation and biology (Li et al., 2019). Although there is a substantial spatial heterogeneity, initialised predictions suggest stronger multi-year variations of the air-sea CO_2 flux and generally tend to

outperform the uninitialised simulations on the global scale (Ilyina et al., submitted; Li et al., 2019). Predictive skill of air-sea CO_2 flux shows a consistent spatial pattern in different models despite a wide range of techniques to assimilate observational information used in prediction systems (Ilyina et al., submitted). ESM-based prediction systems also demonstrate predictability of other marine biogeochemical properties such as for instance net primary production (Séférian et al., 2014; Yeager et al., 2018; Park et al., 2019) and seawater pH (Brady et al., submitted). One caveat associated with the initialised predictions of ocean biogeochemical variables is that the skill is degraded owing to spurious signals in vertical velocities induced by data assimilation (Li et al., 2016a; Park et al., 2018). Predictive skill can also be degraded by errors and gaps in observational datasets used for verification of skill (Ilyina et al., submitted; Li et al., 2019; Yeager et al., 2018).

Seasonal predictability of air-land CO_2 flux up to 6–8 months is driven by the state of ENSO (Zeng et al., 2008; Betts et al., 2018). Fewer land carbon initialised predictions are available from decadal prediction systems, yet they tend to outperform the uninitialised simulations in capturing the major year-to-year variations as indicated by higher correlations with the Global Carbon Budget estimates (Ilyina et al., submitted). There is growing evidence that potential predictive skill of air-land CO_2 flux is maintained at lead year 2 (Ilyina et al., submitted; Lovenduski et al., 2019a) ; this predictability horizon is also supported by perfect model studies (Séférian et al., 2018; Spring and Ilyina, submitted). The origins of this interannual predictability are not yet fully assessed, but seem to be associated with the oscillatory behaviour of ENSO (Séférian et al., 2014) and the predictability of terrestrial ecosystem drivers such as ecosystem respiration and gross primary production (Lovenduski et al., 2019b). The initialization of the physical climate components invokes improvements in climate modulated responses of the land carbon cycle variations that lead to an establishment of a predictive skill of the air-land CO_2 fluxes.

Predictability horizon of variations in atmospheric CO_2 growth are not yet fully assessed. However, predictive skill of the land and ocean carbon sinks show potential to establish predictability of variations in atmospheric CO_2 up to 2 years in advance in the initialised prediction systems (Ilyina et al., submitted ; Figure 5.30 - right panel) with an upper bound of up to 3 years in a perfect model study (Spring and Ilyina, submitted); the skill is limited by the terrestrial carbon sink predictability.

[START FIGURE 5.30 HERE]

Figure 5.30: Predictive skill of the carbon cycle in a multi-model framework. (a) Predictive skill of the CO_2 flux into the ocean; (b) CO_2 flux into the land; (c) variations in the detrended atmospheric CO_2 growth inferred from the global air-sea and air-land CO_2 flux. The predictive skill is quantified as anomaly correlation coefficients of the model simulations assessed against three available references shown by different symbols: (Circles) Global Carbon Budget 2018 (Le Quéré et al., 2018a); (Squares) Reconstruction / assimilation simulation; (Triangles) SOM-FFN observational product (only for air-sea CO_2 flux). The significantly improved predictive skills at 95% level due to initialization, that is the difference between initialised and the uninitialised, are marked with filled dots. Note that the time period available for calculating the correlations varies between the models, being 1995–2005 for IPSL-ESM; 1982–2013 for CESM and MPI-ESM; 1997–2013 for GFDL-ESM.

[END FIGURE 5.30 HERE]

5.5 Remaining Carbon Budgets

Science at the time of the IPCC AR5 established a near-linear relationship between cumulative emissions of CO_2 and the resulting global average surface temperature increase (Allen et al., 2009; Matthews et al., 2009; Meinshausen et al., 2009; Zickfeld et al., 2009; Collins et al., 2013; Stocker et al., 2013;). The amount of global average surface temperature warming per unit of cumulated CO_2 emissions is called the transient climate response to cumulative emissions of carbon dioxide (TCRE). This TCRE relationship is now used to estimate the amount of CO_2 emissions that would be consistent with limiting global average temperature increase to specific levels (Allen et al., 2009; Matthews et al., 2009; Meinshausen et al., 2009; Zickfeld et al., 2009; Matthews et al., 2012; Collins et al., 2013; Stocker et al., 2013; Knutti and Rogelj, 2015; Rogelj et al., 2016; Goodwin et al., 2018; Rogelj et al., 2019). Most of the warming to date has been driven by cumulative emissions of CO_2 (Chapter 7, Figure 7.12 [[Placeholder: check reference]]), but studies highlight that global warming depends on more than the cumulative emissions of CO_2 only (Meinshausen et al., 2009; Collins et al., 2013; Stocker et al., 2013; Rogelj et al., 2015a, 2015b, 2016; Simmons and Matthews, 2016; Mengis et al., 2018; Tokarska and Gillett, 2018). The remainder of CO_2 emissions that would be in line with limiting global warming to a specific temperature threshold (while accounting for all other factors affecting global warming) is referred to as the remaining carbon budget. This section first assesses the TCRE as one of the core concepts underlying the notion of a remaining carbon budget (Section 5.5.1) and then integrates this with the assessment of other contributing factors from across this assessment to provide a consolidated assessment of remaining carbon budgets (Section 5.5.2).

5.5.1 Transient climate response to cumulative emissions of carbon dioxide (TCRE)

5.5.1.1 Contributing physical processes and theoretical frameworks

The processes that translate emissions of CO_2 into a change in global temperature (terrestrial and oceanic carbon uptake, radiative forcing from CO_2, and ocean heat uptake) are governed by complex mechanisms that all evolve in time (Gregory et al., 2009) (Section 5.4). However, since AR5 (Collins et al., 2013; Stocker et al., 2013b) a body of literature has proposed a set of physical mechanisms from which a simple proportional relationship between cumulative emissions of CO_2 and change in global temperature (TCRE) arises.

Studies have focused on two key features of the TCRE relationship: i) why the relationship is nearly constant in time (Goodwin et al., 2015; MacDougall and Friedlingstein, 2015; Williams et al., 2016; Ehlert et al., 2017; Katavouta et al., 2018); and ii) why and under which conditions the relationship is independent of the pathway of CO_2 emissions (MacDougall, 2017; Seshadri, 2017).

There is increased confidence in the near-constancy of TCRE because of studies that have used a variety of methods to examine this relationship: sensitivity studies with Earth system models of Intermediate Complexity (EMICs) (Herrington and Zickfeld, 2014; Ehlert et al., 2017); theory-based equations used to examine Earth system model (ESM) and EMIC output (Goodwin et al., 2015; Williams et al., 2016, 2017d); and simple analytical models that capture aspects of the relationship (MacDougall and Friedlingstein, 2015). These methods vary in the specific approach and processes considered. However, all studies agree that the near-constancy of the TCRE arises from compensation between the diminishing sensitivity of radiative forcing to CO_2 at higher atmospheric concentration (Matthews et al., 2009), and the diminishing ability of the ocean to take up heat and carbon at higher cumulative emissions (Frölicher and Paynter, 2015; Goodwin et al., 2015; Gregory et al., 2015; MacDougall and Friedlingstein, 2015; MacDougall, 2016; Tokarska et al., 2016; Ehlert et al., 2017) (see also Sections 7.2 and 7.3 in Chapter 7 for the latest assessment of CO_2 radiative forcing [[Placeholder: check reference]]). The approach of (Matthews et al., 2009), which has later been further elaborated by Williams et al. (2016), decomposes TCRE into terms of TCR and the airborne fraction of anthropogenic CO_2 emissions over time. These two terms, which can be assessed individually (see Section 5.4 and Chapter 7, respectively), allow one to integrate the scientific evidence assessed in other parts of the report into the assessment of TCRE (Section 5.5.1.3).

The pathway independence of TCRE has been examined by using simple mathematically-tractable models

that capture pathway independence (MacDougall, 2017; Seshadri, 2017). Based on the assumption that the cumulative land fraction is constant, both studies agree that pathway independence is sensitive to the rate of CO_2 emissions, such that pathway independence is expected to breakdown at both very high and very low CO_2 emission rates (MacDougall, 2017; Seshadri, 2017). The studies also agree that no similar relationship analogous to TCRE can be expected for short-lived non-CO_2 forcers, for which the annual emissions are a closer proxy for the implied warming (Collins et al., 2013). MacDougall, (2017) suggests that two additional constraints are required to create pathway independence: first, the transport of heat and carbon into the deep ocean should be governed by the same physical process; and second, the ratio of the net change in the atmospheric carbon pool to the net change in the ocean carbon pool should be close to the ratio of the radiative response of the surface to ocean heat uptake. If these ratios are identical then TCRE would be completely path independent (MacDougall, 2017). If the ratios are close but not identical, TCRE would be only approximately path independent over a wide range of cumulative emissions (MacDougall, 2017).

The land carbon cycle does not appear to play a fundamental role in the origin of the linearity and path-independence of TCRE (Goodwin et al., 2015; MacDougall and Friedlingstein, 2015; Ehlert et al., 2017). However, the land carbon cycle does play an important role in controlling the magnitude of TCRE by modulating the cumulative airborne fraction of carbon (Goodwin et al., 2015; Williams et al., 2016; Katavouta et al., 2018). A recent study also shows how the value of TCRE can depend on the various processes underlying ocean ventilation (Katavouta et al., 2019). Some modelling studies suggest that terrestrial carbon cycle feedbacks (such as the permafrost carbon feedback) have the potential to break both the linearity and pathway independence of TCRE, if such feedbacks significantly contribute carbon to the atmosphere (MacDougall and Friedlingstein, 2015) (Section 5.5.1.2.3).

5.5.1.2 Assessment of TCRE limits

5.5.1.2.1 Sensitivity to amount of cumulative CO_2 emissions

AR5 assessed that the TCRE remains approximately constant for scenarios with increasing cumulative CO_2 emissions up to 2000 PgC (Collins et al., 2013). More recent modelling studies support this finding up to a similar limit (Herrington and Zickfeld, 2014; Steinacher and Joos, 2016) or extend this limit up to at least 3000 PgC (Leduc et al., 2015; Tokarska et al., 2016). Going beyond these upper limits, studies are inconclusive with some suggesting that TCRE will decrease (Leduc et al., 2015) and others indicating that the linearity would still hold (Tokarska et al., 2016). Using an analytical approach, MacDougall and Friedlingstein (2015) quantified a window of constant TCRE – defined as the range in cumulative emissions over which the TCRE remains within 95% of its maximum value – as between 360 to 1560 PgC. However, models with a more sophisticated ocean representation suggest that TCRE could also remain constant for considerably larger quantities of cumulative emissions (Franks et al., 2013; Tokarska et al., 2016).

As cumulative emissions increase, weakening land and ocean carbon sinks tend to increase the airborne fraction of CO_2 emissions (see Section 5.4), but each unit increase in atmospheric CO_2 has a smaller effect on global temperature owing to the logarithmic relationship between carbon dioxide and its radiative forcing (Matthews et al., 2009; Etminan et al., 2016). At high values of cumulative emissions, some models simulate less warming per unit CO_2 emitted, suggesting that the saturation of CO_2 radiative forcing becomes more important than the effect of weakened carbon sinks (Herrington and Zickfeld, 2014; Leduc et al., 2015). Most of the models used to assess the limits of the TCRE, however, do not include the effect of permafrost carbon feedbacks (Section 5.5.1.2.3 and Section 5.4), which would tend to further increase the airborne fraction of emissions at high emissions levels, and could therefore extend the window of linearity to higher total amounts of emissions (MacDougall et al., 2015). Leduc et al. (2016) suggested further that a declining strength of snow and sea-ice feedbacks in a warmer world would also contribute to a smaller TCRE at high amounts of cumulative emissions. On the other hand, Tokarska et al. (2016) suggested that a large decrease in TCRE for high cumulative emissions is only associated with some EMICs; in the four ESMs analysed in their study, the TCRE remained approximately constant up to 5000 PgC, owing to stronger declines in the efficiency of ocean heat uptake in ESMs compared to EMICs. Overall, there is *high agreement* between multiple lines of evidence (*robust evidence*) resulting in *high confidence* that TCRE remains constant for the domain of increasing cumulative CO_2 emissions until roughly 1500 PgC, which has earlier been assessed to

be broadly consistent with warming significantly beyond 2°C (Collins et al., 2013).

5.5.1.2.2 Sensitivity to the rate of CO_2 emissions

Global average temperature increase responds over a timescale of about 10 year following the emission of a 100 PgC pulse of CO_2 (Joos et al., 2013; Ricke and Caldeira, 2014), with a longer timescale associated with larger emission pulses and vice versa for shorter timescales and smaller pulses (Joos et al., 2013; Matthews and Solomon, 2013; Zickfeld and Herrington, 2015). Studies that have calculated the temperature response to CO_2 emission pulses (or instantaneous doubling/quadrupling of atmospheric CO_2) have shown an initial deviation from a linear temperature response to cumulative emissions that is consistent with this decadal response timescale to large emission pulses (Matthews et al., 2009; Gillett et al., 2013; Herrington and Zickfeld, 2014; Leduc et al., 2015). This suggests that the TCRE would also be sensitive to the rate of emissions, though this sensitivity is expected to be relatively small for small changes in emission rates. Studies that have assessed the sensitivity of the TCRE to emission rates have found varying results. Herrington and Zickfeld (2014) and Leduc et al. (2015) found a decrease in TCRE with increasing emission rates in their EMIC experiment, which is consistent with the finding of a longer temperature response timescale for larger CO_2 emission pulses. However, Krasting et al. (2014) found in their ESM experiment that TCRE is highest for low and high emission rates (2 and 25 PgC yr^{-1}) but is lower for current emission rates (between 5–10 PgC yr^{-1}). Ultimately, Tachiiri et al. (2015) found that the uncertainty in TCRE increased in cases where CO_2 concentrations were stabilised (and implied annual CO_2 emissions hence gradually decline), and that TCRE increases under an idealised declining forced CO_2 path (Tachiiri et al., 2019). A robust finding of these studies is that the TCRE would in most cases be expected to increase in ambitious climate mitigation scenarios with decreasing annual emissions rates. This increase in TCRE for annual CO_2 emissions declining towards zero can be the result of unrepresented Earth system processes (see Section 5.5.2.2.4), the zero emissions commitment (ZEC, Chapter 4, Section 4.7.2) or both, and highlights the importance to take these factors into account when using TCRE to estimate CO_2 emissions consistent with a specific maximum warming level. Combined with recent literature on the ZEC (MacDougall et al., submitted) and emissions pathways (Huppmann et al., 2018) and noting the lack of literature that disentangles these various contributions, there is *medium evidence* yet *high agreement* resulting in *medium confidence* that TCRE can be considered constant when applied in the context of emission reduction pathways, provided that ZEC and long-term Earth system feedback are adequately accounted for.

5.5.1.2.3 Reversibility and Earth system feedbacks

There are relatively few studies that have assessed how the TCRE is expected to change in scenarios of declining emissions followed by net negative annual CO_2 emissions. Conceptually, the literature assessed here suggests that the small lag of about a decade between CO_2 emissions and temperature change (Ricke and Caldeira, 2014; Zickfeld and Herrington, 2015) would result in more warming at a given amount of cumulative emissions in a scenario where that emission level is reached via overshoot followed by negative emissions (for example, as is often the case in scenarios that aim to limit radiative forcing in 2100 to 2.6 or 1.9 W/m^2). Zickfeld et al. (2016) showed this to hold across a range of scenarios with positive emissions followed by negative emissions, whereby the TCRE increased by about 10% across the transition from positive to negative emissions as a result of the thermal and carbon inertia of the deep ocean. In an idealised CO_2-concentration driven setting Tachiiri et al. (2019) also reported in increase in TCRE. Exploring pathways with emissions rates and overshoots closer to mitigation pathways considered over the 21st century, a recent emission-driven EMIC experiment showed pathway independence of TCRE (Tokarska et al., 2019b).

Several studies have highlighted that TCRE might increase when annual CO_2 emissions decline towards zero (Krasting et al., 2014; Tachiiri et al., 2015). This increase might be because warming in this case can be the result of a combination of TCRE, ZEC, and other factors, although dedicated studies that try to disentangle this behaviour are currently lacking. Furthermore, on timescales of millennia, warming would not necessarily remain perfectly constant but could both decrease or increase (Frölicher and Paynter, 2015b; Williams et al., 2017b). These additional changes in global mean temperature increase at various timescales are known as the ZEC (Jones et al., 2019; MacDougall et al., submitted) (see also Section 4.7.2) and can impair the use of

TCRE in overshoot scenarios. At time scales of up to a century, a combined assessment of the TCRE and the ZEC is required when considering CO_2 emission evolutions towards zero.

The AR5-assessed range of the TCRE was based in part on the ESMs available at the time, which did not include some potentially important Earth system feedbacks. Since then, a number of studies have assessed the importance of permafrost carbon feedbacks in particular on remaining carbon budgets (MacDougall et al., 2015; MacDougall and Friedlingstein, 2015; Burke et al., 2017; Gasser et al., 2018; Lowe and Bernie, 2018), a development highlighted and assessed in the IPCC Special Report on Global Warming of 1.5°C (Rogelj et al., 2018). MacDougall and Friedlingstein (2015) showed that the TCRE increased by about 15% in a model version that included permafrost carbon feedbacks; while the overall linearity of the TCRE during the 21st century was not affected, they did find that permafrost carbon feedbacks also caused a larger increase in the TCRE on multi-century timescales in response to declining CO_2 emission rates. In addition, other processes that are currently not explicitly considered in ESMs could cause a further increase or decrease of TCRE. These are discussed in detail in Section 5.4, but their quantitative effects on TCRE have not yet been explored by the literature. The *limited evidence* and its *limited agreement* on the overall impact of additional Earth system feedbacks on TCRE results in *low confidence* in the reversibility assessment of TCRE, particularly for time scales beyond centuries.

5.5.1.3 Estimates of TCRE

IPCC AR5 (Collins et al., 2013) assessed TCRE to *likely* fall in the range of 0.8–2.5°C per 1000 PgC for cumulative emissions up to 2000 PgC, based on multiple lines of evidence. These include estimates based on carbon-cycle models (Matthews et al., 2009), EMICs (Zickfeld et al., 2013), ESMs (Gillett et al., 2013), simple carbon-cycle and climate models reflecting uncertainties in forcing, climate sensitivity and observational constraints (Rogelj et al., 2012), or other approaches that use either simple climate modelling approaches (Allen et al., 2009) or observational constraints and attributable warming (Gillett et al., 2013).

Since IPCC AR5, new studies have further expanded the evidence base for estimating the value of TCRE (Goodwin et al., 2015; Steinacher and Joos, 2016; Ehlert et al., 2017; MacDougall et al., 2017; Goodwin et al., 2018; Millar and Friedlingstein, 2018; Tachiiri et al., 2015) (Table 5.7). These studies rely on (i) EMICs (combined with observational constraints) (Tachiiri et al., 2015; Steinacher and Joos, 2016; Ehlert et al., 2017; MacDougall et al., 2017) , (ii) concepts of attributable warming from observations (Millar and Friedlingstein, 2018), or (iii) theoretically derived equations (Goodwin et al., 2015).

A number of studies have endeavoured to partition the uncertainty in the value of TCRE into constituent sources (Matthews et al., 2009; MacDougall et al., 2017; Spafford and MacDougall, submitted; Williams et al., 2017b). The studies use a variety of methods including analysing CMIP5 output (Williams et al., 2017d), conducting perturbed parameter experiments with a single model (MacDougall et al., 2017), and Monte-Carlo methods applied to a simple climate model (Spafford and MacDougall, submitted). All of the studies agree that uncertainty in equilibrium climate sensitivity is amongst the most important contribution to uncertainty in TCRE, with uncertainty in the strength of the land carbon feedback and ocean heat uptake or ventilation having also been identified as crucial to uncertainty in TCRE (MacDougall et al., 2017; Spafford and MacDougall, submitted; Williams et al., 2017b; Katavouta et al., 2019). From theory (Matthews et al., 2009) the uncertainty and spread in transient climate response (TCR) would contribute even more directly to the variation in TCRE.

[START TABLE 5.7 HERE]

Table 5.7: Overview of TCRE estimates. GSAT = Global average surface air temperature increase, SAT = surface air temperature, SST = sea surface temperature

Study	TCRE Range (K EgC^{-1})	Notes
Studies available at the time of IPCC AR5		
(Matthews et al., 2009)	1–2.1	5 to 95% range GSAT C^4MIP model range
(Allen et al., 2009)	1.4–2.5	5 to 95% range Blended global mean surface air and sea-surface temperatures (no infilling of coverage gaps) Simple model
(Zickfeld et al., 2009)	1.5	Best estimate GSAT, EMIC
(Rogelj et al., 2012)	About 1–2	5 to 95% range Mixed definition of global average temperature increase MAGICC model calibrated to C^4MIP model range and 2°C to 4.5°C *likely* equilibrium climate sensitivity
(Zickfeld et al., 2013)	1.4–2.5 mean: 1.9	Model range GSAT
(Gillett et al., 2013)	0.8–2.4	Model range GSAT, CMIP5 ESMs
(Gillett et al., 2013)	0.7–2.0	5 to 95% range Blended global mean surface air and sea-surface temperatures Observationally constrained estimates of historical warming and emissions
IPCC AR5 (Collins et al., 2013)	0.8–2.5	Assessed *likely* range Multiple lines of evidence. Mixed definition of global average temperature increase
Studies published after IPCC AR5		
(Tachiiri et al., 2015)	0.3–2.4	5 to 95% range Blended global mean surface air and sea-surface temperatures JUMP-LCM model perturbed physics ensemble (EMIC)
(Tachiiri et al., 2015)	1.1–1.7	5 to 95% range Blended global mean surface air and sea-surface temperatures Observationally constrained JUMP-LCM perturbed physics ensemble
(Goodwin et al., 2015)	1.1 ± 0.5	Theoretically derived equation for TCRE constrained by surface warming, radiative forcing, and historic ocean and land carbon uptake adopted by IPCC AR5. Assumes no radiative forcing from other sources.
(Steinacher and Joos, 2016)	1.0–2.7 median: 1.7	5 to 95% range GSAT, observationally constrained BERN3D-LPJ EMIC
(MacDougall et al., 2017)	0.9–2.5 mean: 1.7	5 to 95% range GSAT, emulation of 23 CMIP5 ESMs
(Goodwin et al., 2018)	1.8–2.6 mean: 2.2	2-sigma range Efficient model ensemble constrained by several blended SAT and SST records, ocean heat uptake reconstructions and the evaluations of historic ocean and land carbon uptake adopted in IPCC AR5. Estimate evaluated from simulations for the four RCPs (Meinshausen et al., 2011a).
(Millar and Friedlingstein, 2018)	0.9–2.6 best estimate: 1.3	5 to 95% range Blended global mean surface air and sea-surface temperatures (HadCRUT4) (Cowtan and Way, 2014) Detection attribution with observational constraints
(Millar and Friedlingstein, 2018)	best estimate: 1.5	Blended global mean surface air and sea-surface temperatures (Berkeley Earth) Detection attribution with observational constraints
(Millar and Friedlingstein, 2018)	best estimate: 1.2	Blended global mean surface air and sea-surface temperatures (HadCRUT4) (Cowtan and Way, 2014) Detection attribution with observational constraints, with updated historical CO_2 emissions (Le Quéré et al., 2018b)
(Ehlert et al., 2017)	1.2–2.1	Model range GSAT, UVIC EMIC with varying ocean mixing parameters
(Jenkins et al., submitted)	0.8–2.5	90% confidence interval Blended global mean surface air and sea-surface temperatures, average of four datasets as in (Allen et al., 2018) Observationally constrained estimate translating non-CO_2 forcers in CO_2-forcing equivalent emissions
(Matthews et al., submitted)	1.0–2.2 median: 1.5	90% confidence interval Blended global mean surface air and sea-surface temperatures Human-induced warming (Haustein et al., 2017) based on an average of

		three observational datasets with full spatial coverage Observationally constrained estimate using the current non-CO_2 fraction of total anthropogenic forcing
Cross-AR6 lines of evidence		
Carbon-cycle feedback parameters	1.2–2.7 median: 1.8	5 to 95% range GSAT Estimate based on decomposition presented in (Jones and Friedlingstein, submitted) with ranges of carbon cycle feedback parameters from CMIP6 (Arora et al. submitted), see Section 5.4.
Transient Climate Response (TCR) and Airborne Fraction (AF)	1.0–2.2 median: 1.6	5 to 95% range GSAT Estimate based on decomposition presented in (Matthews et al., 2009) from assessed ranges of the transient climate response TCR in Section 7.5 and airborne fraction of 56% +- 8% (1 sigma range) in transient 1% 2xCO_2 runs in C4MIP and CMIP5.
Overall assessment		
IPCC AR6	1.0–2.2	*Likely* range GSAT Based on combination of cross-AR6 lines of evidence

[END TABLE 5.7 HERE]

5.5.1.4 Combined assessment of TCRE

All available evidence provided in the preceding Section 5.5.1 and a cross-chapter assessment of various lines of evidence supports an assessed *likely* TCRE range of 1.0–2.2 K EgC^{-1}. Warming here reflects the globally averaged surface air temperature increase. Forthcoming literature based on simulations from and understanding of the latest version of ESMs as part of the Sixth Phase of the Coupled Model Intercomparison Project (CMIP6) might further inform the robustness of this range. Taking into account the evidence discussing the impact of permafrost and potentially other feedbacks suggests that values at the lower end of the above-mentioned range are less supported. However, given the large uncertainties in projections of these Earth system feedback processes and the limited amount of studies, there is *low confidence* in their precise quantitative impact on TCRE. Further integration of assessments of the transient climate response (TCR) and the projected airborne fraction could allow to further limit the TCRE range in the future. These potential additional lines of evidence might also provide additional information that can inform the shape of the uncertainty distribution surrounding TCRE which is considered normal by this assessment.

5.5.2 Remaining carbon budget assessment

Estimates of remaining carbon budgets consistent with holding global warming below a specific temperature threshold depend on a range of factors which are increasingly being studied and quantified. These factors include (1) well-understood methodological and definitional choices (Friedlingstein et al., 2014a; Rogelj et al., 2016, 2018) (see Sections 5.5.2.1 and Section 5.5.2.2), and (2) a set of contributing factors like historical warming, the TCRE and its limitations, as well as contributions of non-CO_2 climate forcers (Section 5.5.2.2) (MacDougall and Friedlingstein, 2015; Rogelj et al., 2015b, 2015a; MacDougall, 2016; Simmons and Matthews, 2016; Ehlert et al., 2017; Matthews et al., 2017; Millar et al., 2017; Goodwin et al., 2018; Mengis et al., 2018; Pfleiderer et al., 2018; Tokarska and Gillett, 2018; Cain et al., 2019). These contributing factors are integrated in an overarching assessment of remaining carbon budgets for limiting global average warming to levels ranging from 1.5°C to 2.5°C relative to pre-industrial levels provided in Section 5.5.2.3.

5.5.2.1 Framework and earlier approaches

Remaining carbon budgets can be defined in a variety of ways. For example, remaining carbon budgets can be defined as the cumulative emissions at the time when global-mean temperature increase would reach,

exceed, avoid, or peak at a given warming level with a given probability (Rogelj et al., 2016). These definitional choices affect the approach by which remaining carbon budgets are estimated as well as assumptions about the contributions of the various factors listed above (see also Section 5.5.2.2). The choice of remaining carbon budget definition and associate methods for their estimation thus determines the domain in which these estimates can be appropriately used and the questions they can inform. In this report, the remaining carbon budget is defined as the amount of cumulative CO_2 emissions starting today (or at a point in the recent past) that could be emitted while still holding global warming below a specific temperature threshold, consistent with its use in the IPCC Special Report on Global Warming of 1.5°C (Rogelj et al., 2018). Given that the magnitude of some feedbacks are time dependents, the values in this section apply to emissions and warming limited to the 21st century, consistent with recent studies highlighting the usefulness of time-limited carbon budgets (Sanderson, submitted). Irrespective of the exact definition of the remaining carbon budget, the finding that higher cumulative CO_2 emissions lead to higher temperatures implies that annual net CO_2 emissions have to decline to close to zero in order to halt global warming, whether at 1.5°C, 2°C or another level.

Two approaches were used in AR5 to determine carbon budgets (Collins et al., 2013; Stocker et al., 2013; Clarke et al., 2014; IPCC, 2014; Rogelj et al., 2016). Working Group I (WGI) reported Threshold Exceedance Budgets (TEB) that correspond to the amount of cumulative CO_2 emissions at the time a specific temperature threshold is exceeded with a given probability in a particular multi-gas and aerosol emission scenario (Collins et al., 2013; IPCC, 2013; Stocker et al., 2013b). WGI also reported TEBs for the hypothetical case that only CO_2 would be emitted by human activities (Collins et al., 2013; IPCC, 2013; Stocker et al., 2013b). Working Group III (WGIII) used Threshold Avoidance Budgets (TAB) that correspond to the cumulative CO_2 emissions over a given time period of a subset of multi-gas and aerosol emission scenarios in which global-mean temperature increase stays below a specific temperature threshold with at least a given probability (Clarke et al., 2014). The AR5 Synthesis Report used TABs defined until the time of peak warming over the 21st century (IPCC, 2014). Drawbacks have been identified for both TEBs and TABs (Rogelj et al., 2016). TABs provide an estimate of the cumulative CO_2 emissions under pathways that have as a common characteristic that they do not exceed a specific global warming threshold. The actual level of maximum warming can however vary between pathways, leading to an unnecessary and poorly constrained spread in TAB estimates (Rogelj et al., 2016). The TAB approach is hence imprecise and does typically not result in accurate projections of the remaining carbon budget. On the other hand, a drawback of TEBs is that they provide an estimate of the cumulative CO_2 emissions at the time global warming crosses a given threshold of interest in a specific emissions scenario. Because of potential variations in the non-CO_2 warming contribution at that point in time or lags of about a decade in warming (Joos et al., 2013; Ricke and Caldeira, 2014; Zickfeld and Herrington, 2015; Rogelj et al., 2015a, 2016, 2018) TEBs are thus also not providing a precise estimate of the remaining carbon budget for limiting warming to a specific level. More recent approaches provide a solution to the identified limitations of TABs and TEBs.

Since the publication of AR5, several new approaches have been proposed to estimate carbon budgets compatible with limiting warming to specific temperature levels. Most of these approaches indirectly rely on the concept of TCRE (Section 5.5.1), for example, because they estimate modelled cumulative CO_2 emissions until a temperature threshold is crossed and use this budget to infer insights for pathways which attempt to limit warming to below this threshold but would need to follow a difference path (Friedlingstein et al., 2014; Matthews et al., 2017; Millar et al., 2017; Goodwin et al., 2018; Tokarska and Gillett, 2018). In this report, we use the assessment framework as applied in the IPCC Special Report on Global Warming of 1.5°C to estimate remaining carbon budgets compatible with a range of maximum global warming levels (Rogelj et al., 2018). This framework (Rogelj et al., 2019b) builds on the advances in estimating remaining carbon budgets or related quantities that have been published since AR5 (Rogelj et al., 2015a; Haustein et al., 2017; Matthews et al., 2017; Millar et al., 2017; Gasser et al., 2018; Lowe and Bernie, 2018; Tokarska and Gillett, 2018; Nicholls et al. submitted) and linearly combines the assessment of four contributing factors (historical warming, TCRE, non-CO_2 warming contribution, and adjustments due to additional Earth system feedbacks, see Section 5.5.2.2) to estimate remaining carbon budgets from 2020 onwards. Recent studies suggest further changes to this framework by including non-linear adjustments to the TCRE contribution (Nicholls et al., submitted), or including non-CO_2 forcers in different ways by accounting for their different forcing effects (Jenkins et al., submitted; Matthews et al., submitted). Figure 5.31 provides a conceptual

schematic of how the various contributions are combined to assess the remaining carbon budget. Together with estimates of historical CO_2 emissions to date (Section 5.2.1), these remaining carbon budgets provide the overall amount of cumulative CO_2 emissions consistent with limiting global warming to specific levels, although no formal method is available to combine the uncertainty estimates surrounding these values. A comparison with the approach applied in AR5 (Collins et al., 2013; Clarke et al., 2014) is available in the IPCC Special Report on Global Warming of 1.5°C Section 2.2.2 (Rogelj et al., 2018) as well as Box 5.1.

[START FIGURE 5.31 HERE]

Figure 5.31: Illustration of relationship between cumulative emissions of CO_2 and global mean surface air temperature increase (left) and conceptual schematic of the assessment of the remaining carbon budget from its constituting components (right). Historical data in the left-hand panel (thin black line data) shows historical CO_2 emissions as reported in (Friedlingstein et al., 2019) together with the assessed global surface air temperature increase from 1850-1900 as assessed in Chapter 2 (Box 2.3). Orange-brown range with its central line show the human-induced share of historical warming (Haustein et al., 2017). The circle and vertical line show the assessed range of historical human-induced warming for the 2010–2019 period relative to 1850-1900 (Chapter 3). The grey cone shows the assessed range for the transient climate response to cumulative emissions of carbon dioxide (TCRE) assessed to fall *likely* in the 1.0–2.2 °C/EgC range (Section 5.5.1), starting from 2015. The red range and thin red lines within it represent CMIP6 simulations of the SSP5-8.5 scenario, starting from 2015.

[END FIGURE 5.31 HERE]

5.5.2.2 Assessment of individual components

Remaining carbon budgets are estimated through the combination of four components that are estimated separately (Forster et al., 2018; Rogelj et al., 2018). Each component is discussed separately in the sections below.

5.5.2.2.1 TCRE

The first and central component for estimating remaining carbon budgets is the TCRE. Based on the assessment in Section 5.5.1.4, an assessed *likely* range for TCRE of 1.0–2.2°C/1000 PgC is used. The value and uncertainty surrounding TCRE directly affects estimates of the remaining carbon budget (Matthews et al., 2017; Millar and Friedlingstein, 2018; Rogelj et al., 2018). As in IPCC AR5 (Collins et al., 2013), a normal uncertainty distribution with a one-sigma range corresponding to the *likely* range is applied.

5.5.2.2.2 Historical warming

Advances in methods to estimate remaining carbon budgets have shown the importance of applying an as precise as possible estimate of historical warming to date (Millar et al., 2017; Tokarska and Gillett, 2018a). This becomes particularly important when assessing remaining carbon budgets for global warming thresholds that are relatively close to present-day warming, such as a 1.5°C or 2°C threshold (Rogelj et al., 2018). Also the definition of global average temperature by which historical warming is estimated is shown to be important (see Cross-Chapter Box 2.3 on surface temperature metrics in Chapter 2) (Cowtan and Way, 2014; Allen et al., 2018; Pfleiderer et al., 2018; Richardson et al., 2018), as is the correct isolation of human-induced global warming (Haustein et al., 2017; Allen et al., 2018). We here apply an assessed historical warming estimate expressed in global average surface air temperatures (GSAT) of 1.1°C (0.9–1.3°C, *likely* range) between the 1850–1900 and 2010–2019 periods, based on the assessment of human-induced global warming by Chapter 3 (Section 3.3). The application of the GSAT temperature metric is fully consistent with AR5 where carbon budgets were also reported in the same metric (Collins et al., 2013; Stocker et al., 2013b), and recent studies highlight how the use of GSAT enables an easy translation with AR5 (Tokarska et al., 2019a). The use of other historical reference periods (ref. Chapter 1) can result in a different estimated historical warming and thus a changed estimate of the remaining carbon budget.

5.5.2.2.3 Non-CO_2 warming contribution

Projected global average warming of non-CO_2 emissions affects estimates of remaining carbon budgets consistent with limiting warming to specific temperature thresholds by reducing the amount of warming that could still result from CO_2 emissions (Meinshausen et al., 2009; Friedlingstein et al., 2014; Knutti and Rogelj, 2015; Rogelj et al., 2015a, 2016; Williams et al., 2016; Matthews et al., 2017; Williams et al., 2017b; Collins et al., 2018; Mengis et al., 2018; Tokarska and Gillett, 2018). The size of this contribution has been estimated by both implicitly (Meinshausen et al., 2009; Friedlingstein et al., 2014; Rogelj et al., 2016; Matthews et al., 2017; Mengis et al., 2018; Tokarska and Gillett, 2018) and explicitly (Rogelj et al., 2015a; Collins et al., 2018; Rogelj et al., 2018) varying the assumptions of non-CO_2 emissions and associated warming. Internally consistent evolutions of future CO_2 and non-CO_2 emissions allow to derive non-CO_2 warming contributions that reflect societal developments by which global CO_2 emissions are held to within a finite remaining carbon budget (Smith and Mizrahi, 2013; Clarke et al., 2014; Rogelj et al., 2018) – that is, developments in which global CO_2 emissions decline to net zero levels. Integrated pathways (Clarke et al., 2014; Huppmann et al., 2018) allow the assessment of non-CO_2 emission contributions at the time global CO_2 emissions reach net zero levels (Rogelj et al., 2018), and show that the internally consistent evolutions of CO_2 and non-CO_2 forcers in such pathways show a stabilisation or decline in non-CO_2 radiative forcing at and after the time of global CO_2 emissions reaching net zero levels (Huppmann et al., 2018). These emission contributions can subsequently be assessed in terms of their estimated global average temperature outcome with simple climate model and emulator approaches which incorporate synthesised knowledge of climate and carbon-cycle response and uncertainty (Meinshausen et al., 2009; Millar et al., 2017; Gasser et al., 2018; Goodwin et al., 2018; Rogelj et al., 2018; Smith et al., 2018a).Cross Chapter Box 7.1 (emulators) and Section 7.6 provide an assessment of these tools and of how they are used to reflect the assessment and uncertainty in climate (Chapter 7) and carbon-cycle (Section 5.4) response in line with historical observations (Chapters 1–4). Application of these tools suggest a non-CO_2 warming contribution of about 0.1°C from scenarios halting warming to less than 0.5°C of additional warming from today. The assessment of the non-CO_2 warming in stringent mitigation pathways also suggests that in virtually all cases no further non-CO_2 warming is projected after the time CO_2 emissions have reach net zero levels. Additional methods that can estimate the CO_2 equivalence of a given level of non-CO_2 forcing have recently been suggested and are assessed in Chapter 7 Section 7.6, yet their uncertainties and wide-ranging applicability have not yet been explored in the literature.

[Placeholder: Pending updated assessments of Chapters 1–4 and 7.]
[Placeholder: Pending confidence statement based on integrated assessment of Chapters 1–4 and 7 confidence statements.]

5.5.2.2.4 Adjustments due to other not represented feedbacks and potential limitations of TCRE

Recent literature has led to an improved understanding of the limitations and applicability of TCRE (Section 5.5.1.2), which is here reflected in the assessment of remaining carbon budgets. A first aspect affecting the use of TCRE for estimating remaining carbon budgets is whether there is any expected additional warming after a complete cessation of net CO_2 emissions, also referred to as zero emissions commitment (ZEC) of CO_2 emissions. Estimates of the ZEC are assessed in Chapter 4, Section 4.7.2. At present no conclusive evidence is available about the sign of the ZEC and estimates range from slightly negative (i.e. global average temperatures decline slightly after a complete cessation of CO_2 emissions) to slightly positive (Matthews and Caldeira, 2008; Lowe et al., 2009; Frölicher and Joos, 2010; Gillett et al., 2011; Matthews and Zickfeld, 2012; Collins et al., 2013), but in most cases showing that once CO_2 emissions decline to net zero levels, they do not contribute to substantial further warming (Solomon et al., 2010; Matthews and Solomon, 2013; Allen et al., 2018; Smith et al., 2019). Studies that do suggest a higher ZEC identify this only for cumulative CO_2 emissions that lay beyond the range cumulative CO_2 emissions consistent with keeping warming to 1.5°C–2.5°C relative to pre-industrial levels and add to future warming over century to millennial timescales (Frölicher et al., 2014; Ehlert and Zickfeld, 2017), a behaviour resulting from a decline in ocean heat uptake, which increases the proportion of radiative forcing that raises surface temperature (Williams et al., 2017c).

Recently, new, dedicated modelling efforts have focussed on improving our understanding of the ZEC (Jones

et al., 2019b), for which quantitative results are forthcoming. For its integration in the assessment of the remaining carbon budget, the ZEC is considered for a time frame of half a century, as this reflects a policy-relevant time horizon between the time stringent mitigation pathways reach net zero CO_2 emissions and the end of the century (Huppmann et al., 2018; Rogelj et al., 2018). Based on the assessment presented in Section 4.7.2, the central ZEC value for CO_2 is considered zero for the estimation of the remaining carbon budget with a range of ±0.18°C [Placeholder: Authors to double-checked with Section 4.7.2], noting that it might either in- or decrease over time horizons beyond half a century. The diverging evidence on this matter results in an overall *low confidence* in the sign of the ZEC, although based on dedicated experiments with a large set of models there is *medium confidence* that for cumulative CO_2 emissions of 1000 PgC it is of the order of tenths of a degree Celsius following an instantaneous cessation of emissions after a 1% increasing trajectory. Experiments that ramped up and down emissions following a bell-shaped trajectory (MacDougall and Knutti, 2016a) show that when annual CO_2 emissions decline to zero at a pace consistent with those currently assumed in mitigation scenarios (Huppmann et al., 2018; Rogelj et al., 2018), the ZEC will already to a large degree be realised at the time of reaching net zero CO_2 emissions (MacDougall et al., submitted).

As highlighted in Section 5.5.1.2, recent literature has described potential impacts of Earth system feedbacks that have typically not been included in standard ESMs (Schneider von Deimling et al., 2015; MacDougall and Friedlingstein, 2015; Schädel et al., 2016; Burke et al., 2017; Mahowald et al., 2017; Comyn-Platt et al., 2018; Gasser et al., 2018; Lowe and Bernie, 2018), the most important of which is carbon release from thawing permafrost. Due to the long-term and potentially non-linear reinforcing feedbacks (see Section 5.4) this process is anticipated to both increase the value of TCRE and add additional carbon emissions to the atmosphere over timescales of centuries to millennia. The IPCC Special Report on Global Warming of 1.5°C (Rogelj et al., 2018) estimated unrepresented Earth system processes to result in a reduction of remaining carbon budgets of up to 100 $GtCO_2$ over the course of this century, and more thereafter. Here we update this assessment based on the assessment of Earth system feedbacks in Section 5.4 and synthesised in Figure 5.28 by applying the reverse method by (Gregory et al., 2009).

There is *high agreement* across available studies that unrepresented Earth system feedbacks related to permafrost thawing will result in more carbon being released into the atmosphere and hence a reduction in the size of remaining carbon budgets over century timescales. Recent studies indicate that under strong warming scenarios (about 4°C and more of warming by 2100) vegetation dynamics in high-latitudes over timescales beyond centuries might temper if not reverse this effect (Pugh et al., 2018). These various lines of evidence result in *medium confidence* about the direction of the overall effect of these additional processes on estimates of the remaining carbon budget during this century. However, the large range in potential magnitude of permafrost thawing effects in the available literature and the absence of dedicated multi-model intercomparison exercises leads overall to *low confidence* in the quantified magnitude of this effect. The same *low confidence* qualifier is assigned to the precise quantification of the CH_4–lifetime response to climate (Section 5.4). For other not represented Earth system feedbacks very few to no studies are available (*limited evidence*) and both the sign and magnitude of their effect on the remaining carbon budget remain at time uncertain (*low agreement*) resulting in overall *very low confidence* in our current understanding of these feedbacks.

Given the assessed *low confidence* in the understanding and quantification of these additional Earth system feedbacks, their impact on the remaining carbon budget cannot be estimated with high precision and these estimates would only be applicable to remaining carbon budget estimates for this century. We here use the assessment presented in Figure 5.28 to estimate the potential impact of these additional Earth system feedbacks. The permafrost CO_2 climate feedback is estimated to further reduce estimates of the remaining carbon budget by about 75 Gt CO_2 (±50 Gt CO_2, 1 sigma range) per degree of additional warming, while the CH_4-lifetime feedback would result in an increase in remaining carbon budgets by about 35 Gt CO_2 (±8 Gt CO_2, 1 sigma range) per degree of additional warming. All other identified *very low confidence* feedbacks in Figure 5.28 together could result in an additional reduction of about 100 Gt CO_2 per degree of additional warming, but with a very large 1 sigma range of ±100 Gt CO_2. The combined effect of these additional Earth system feedbacks is represented as a reduction of remaining carbon budget by about 135 Gt CO_2 per °C (±135 Gt CO_2, 1 sigma range) of additional warming relative to the recent past (2010–2019). Despite the large uncertainties surrounding the understanding and quantification of the impact of these processes, they

represent identified additional risk factors that scale with additional warming and mostly increase the challenge of limiting warming to specific temperature thresholds.

5.5.2.3 Remaining budget overview

The combination of the four contributions assessed in Sections 5.5.2.2.1-5.5.2.2.4 allows for an overall assessment of the remaining carbon budget in line with different levels of global average warming, as documented in the IPCC Special Report on Global Warming of 1.5°C (Rogelj et al., 2018). The overall assessment of remaining carbon budgets (Table 5.8) reflects the uncertainty in TCRE quantification and provides estimates of the uncertainties surrounding the contributions of each of the respective further components. The *likely* range of TCRE uncertainty results in a +50% to –25% variation around remaining carbon budget estimate reported for the central 50th percentile (Table 5.8). A formal combination of all uncertainties is not possible because they are not independent and no estimates of the correlation between them are available in the literature. There is *robust evidence* supporting the concept of TCRE as well as the *high confidence* in the range of historical human-induced warming. Combined with the assessed uncertainties in the Earth system's response to non-CO_2 emissions and less well-established quantification of some of the effect of non-linear Earth system feedbacks, this leads to *medium confidence* being assigned to the assessed remaining carbon budget estimates while noting the identified and assessed uncertainties and potential variations. The reported values are applicable to warming and cumulative emissions over the 21st century. For climate stabilisation beyond the 21st century this confidence would decline to *very low confidence* due to uncertainties in Earth system feedbacks and the ZEC.

[START TABLE 5.8 HERE]

Table 5.8: The assessed remaining carbon budget and corresponding uncertainties. Assessed estimates are provided for additional human-induced warming expressed as global average surface air temperature since the recent past (2010–2019), which amounted to 1.1°C ± 0.2°C relative to the 1850–1900 period.

Additional warming since 2010-2019 (°C)*(1)	Approx. warming since 1850-1900 (°C)*(1)	Remaining carbon budget*(2)			Key uncertainties and variations						
		Percentiles of TCRE*(3)			Earth-system feedbacks *(4)	Non-CO_2 scenario variation* (5)	Non-CO_2 forcing and response uncertainty	TCRE distribution uncertainty*(7)	Historical temperature uncertainty*(1)	Zero Emissions Commitment (ZEC)*(8)	Recent emissions uncertainty*(9)
		33rd ($GtCO_2$)	*50th ($GtCO_2$)*	*67th ($GtCO_2$)*	*($GtCO_2$)*	*($GtCO_2$)*	*($GtCO_2$)*	*($GtCO_2$)*	*($GtCO_2$)*	*($GtCO_2$)*	*($GtCO_2$)*
0.2	1.3	140	90	50							
0.3	1.4	320	240	180	Already included in left-hand table						
0.4	1.5	500	390	310							
0.5	1.6	670	540	440		±250	-400 to +200 TBC*(6)	+60 to +110 $GtCO_2$ per °C of additional warming	±450	±410	±20
0.6	1.7	850	690	570	Reduce 135 $GtCO_2$ per °C of additional warming						TBC
0.7	1.8	1030	840	700							
0.8	1.9	1210	990	830							
0.9	2.0	1390	1140	960							
1.0	2.1	1570	1290	1090							
1.1	2.2	1740	1440	1220							
1.2	2.3	1920	1590	1350							
1.3	2.4	2100	1740	1480							
1.4	2.5	2280	1890	1610							

*(1) Human-induced global surface air temperature increase between 1850-1900 and 2010-2019 is assessed at 0.9-1.3°C (*likely* range; Chapter 3) with a central estimate of 1.1°C.

*(2) Historical CO2 emissions since the middle of the 1850-1900 reference period (mid-1875) until and including 2019 are estimated at 2120 $GtCO_2$ (±15% one standard deviation range) until end 2014. Since 1 January 2015, an additional 210 $GtCO_2$ has been emitted until the end of 2019 (Friedlingstein et al., 2019).
*(3) TCRE: transient climate response to cumulative emissions of carbon, assessed to fall *likely* between 1.0-2.2 °C/EgC, considering a normal distribution consistent with AR5 (Stocker et al., 2013b). Values are rounded to the nearest 10 $GtCO_2$.
*(4) Earth system feedbacks include CO_2 released by permafrost thawing as shown in Figure 5.28, and discussed in Section 5.5.2.2.4. This uncertainty contribution is included in the left-hand part of the table. The 135 $GtCO_2$ reduction per °C of additional warming comes with a ±100% one standard deviation range.
*(5) Variations due to different scenario assumptions related to the future evolution of non-CO_2 emissions in mitigation scenarios reaching net zero CO_2 emissions (Huppmann et al., 2018; Rogelj et al., 2018).
*(6) Remaining carbon budget variation due to geophysical uncertainty in forcing and temperature response of non-CO_2 emissions. Currently still based on (Forster et al., 2018; Rogelj et al., 2018).
*(7) The distribution of TCRE is not precisely defined. Here the influence of assuming a lognormal with a 1.0-2.2 °C/EgC central 66% range instead of a normal distribution with a 0.6 °C/EgC 1-sigma range centred around 1.6°C is shown.
*(8) The variation due to the ZEC is estimated for a central TCRE value of 1.6 °C/EgC and a 1-sigma ZEC range of 0.18°C
*(9) Historical emissions uncertainty reflects the uncertainty in historical emissions since 1 January 2015.

[END TABLE 5.8 HERE]

[START BOX 5.1 HERE]

BOX 5.1: Methodological advancements in estimating the remaining carbon budget since IPCC AR5

Several methodological advancements since IPCC Fifth Assessment Report (AR5) (Collins et al., 2013; IPCC, 2013; Clarke et al., 2014; IPCC, 2014; Stocker et al., 2013) have resulted in an updated and strengthened assessment of remaining carbon budgets in Chapter 2 of the IPCC Special Report on Global Warming of 1.5°C (SR1.5) (Rogelj et al., 2018) and the here presented Working Group 1 contribution to the IPCC's Sixth Assessment (AR6). Earlier methods and approaches are described in Section 5.5.2.1. Here, we clarify the key methodological advancements that underpin this cycle's assessment of the remaining carbon budget and put them in context of the state of the science at the time of the AR5.

IPCC AR5 did not apply a single methodology for estimating and discussing the remaining carbon budget in line with limiting warming to various temperature limits throughout its full report (see Section 5.5.2.1). Since then, however, strengths and weaknesses of various approaches have been more clearly articulated in the literature (Rogelj et al., 2016), resulting in a new consolidated framework applied in SR1.5 (Rogelj et al., 2018, 2019b). The SR1.5 remaining carbon budget framework that is also applied here incorporates methodological advancements in three dimensions.

First, the post-AR5 literature presented improved methods to deal with model uncertainties that accumulate over the historical time period (Millar et al., 2017; Tokarska and Gillett, 2018b). These studies identified that large uncertainties exist in historical, diagnosed emissions in coupled Earth system models, and provide methods to limit the impact of this weakness on estimates of the remaining carbon budget. The application of these new methods is reflected in the fact that the remaining carbon budget is expressed relative to a recent reference period instead of from pre-industrial (Tokarska et al., 2019a) – while estimates of the full carbon budget since pre-industrial can be obtained by adding estimates of historical CO_2 emissions (Section 5.2) to the estimates of the remaining carbon budget. This methodological re-adjustment results an upward revision of remaining carbon budget estimates of the order of 300 $GtCO_2$ compared to AR5.

At the time of the AR5, limited evidence was available informing the specific contributions of CO_2 and non-CO_2 forcers to future warming and therewith the remaining carbon budget consistent with a given temperature threshold. However, disentangling these contributions is necessary to determine how much warming can still be assigned to CO_2. Coupled model simulations of the Fifth phase of the Coupled Model Intercomparison Project (CMIP5) (Taylor et al., 2012) provided global mean surface air temperature (GSAT) projections for the representative concentration pathways (Meinshausen et al., 2011a), which were used to determine carbon budgets while taking into account non-CO_2 forcers (Stocker et al., 2013b). Their use came with two recognised limitations for which since solutions have been presented: first, the model spread of the CMIP5 ensemble represents an ensemble of opportunity with limited statistical value (Tebaldi and Knutti, 2007); and second, the evolution of non-CO_2 emissions as a function of cumulative CO_2 emissions can differ markedly between high and low emissions pathways (Meinshausen et al., 2011a; Rogelj et al., 2016;

Friedlingstein et al., 2014; Matthews et al., 2017). Solutions to these two earlier limitations represent the second and third methodological improvement compared to AR5.

The reliance on an ensemble of opportunity is avoided by methodologically separating the assessment of future warming contributions of non-CO_2 emissions from the spread in TCRE. This facilitates the explicit representation of TCRE uncertainty by a formal distribution, in this case a normal distribution with a 1.0–2.2 °C EgC^{-1} 1–sigma range. The estimation of the effect of this methodological advance is limited in precision but of the order of 100–250 $GtCO_2$, estimated from a direct comparison of the frequency distribution of CMIP5 models used in AR5 and the normal TCRE distribution applied here. Finally, a more direct estimation of the warming contribution of non-CO_2 emissions, consistent with pathways that bring global CO_2 emissions down to net zero, is the last methodological improvement. Instead of deriving this contribution implicitly from the CMIP ensemble, dedicated and vetted climate emulators (Meinshausen et al., 2011b; Schwarber et al., 2018; Smith et al., 2018a) that are representative of the combined AR6 assessment [Placeholder: Cross Chapter box on Emulators – now in Chapter 7] are used to estimate the non-CO_2 contribution across a wide variety of stringent mitigation scenarios (Huppmann et al., 2018). The relative effect of this advance is not calculable from AR5 data.

Carbon budgets in AR5 were all expressed as a function of GSAT. The same temperature metric is applied here.

All methodological improvements combined result in remaining carbon budgets that are about 300 $GtCO_2$ increased compared to those assessed by the methods available at the time of the AR5.

[END BOX 5.1 HERE]

5.6 Biogeochemical implications of Carbon Dioxide Removal and Solar Radiation Modification

5.6.1 Introduction

Carbon Dioxide Removal (CDR) refers to anthropogenic activities that seek to remove CO_2 from the atmosphere and durably store it in geological, terrestrial or ocean reservoirs, or in products (SR1.5 glossary, IPCC, 2018). CO_2 is removed from the atmosphere by enhancing biological or geochemical carbon sinks or by direct capture of CO_2 from air and storage. Solar Radiation Modification (SRM), on the other hand, refers to the intentional, planetary-scale modification of the Earth's shortwave radiative budget with the aim of reducing warming (SR1.5 glossary, IPCC, 2018). While some radiation modification measures, such as cirrus cloud thinning aim at enhancing outgoing long-wave radiation, SRM is used in this report to refer to all direct interventions on the planetary radiation budget. SRM does not fall within the IPCC definitions of mitigation and adaptation (SR1.5 glossary; IPCC, 2018). CDR and SRM are considered as 'geoengineering' in some of the literature but are considered separately in this report.

This section assesses the implications of CDR and SRM for biogeochemical cycles. CDR has received growing interest as an important mitigation option in emission scenarios consistent with meeting the Paris climate goals (AR5; , IPCC, 2018). The climate effects of CDR and SRM are assessed in Chapter 4, and a detailed assessment of the socio-economic dimensions of these options is presented in AR6 WGIII, Chapters 7 and 12.

5.6.2 Biogeochemical responses to Carbon Dioxide Removal (CDR)

The scope of this section is to assess the general and methods-specific effects of CDR on the global carbon cycle and other biogeochemical cycles. The focus is on Earth system feedbacks that either amplify or reduce carbon sequestration potentials of specific CDR methods, and determine their effectiveness in reducing atmospheric CO_2. Effects of CDR methods on climate are also assessed. Global carbon sequestration potentials of CDR methods are briefly discussed, but a comprehensive assessment is left to the AR6

Working Group III report (Chapters 7 and 12), as these potentials depend on socio-economic factors (e.g. availability of land, carbon pricing), consideration of which is beyond the scope of this report. The assessment emphasises literature published since AR5. The IPCC Special Reports on the global warming of 1.5 degrees (SR1.5, IPCC, 2018) and on climate change and land (SRCCL) assessed CDR potentials and side effects but did not address the effects of CDR on carbon and other biogeochemical cycles in detail.

Considering the carbon cycle processes that result in CO_2 removal, CDR methods are here divided into four major categories: (1) enhanced net biological uptake and storage by land ecosystems, (2) enhanced net biological uptake and storage in the ocean, (3) enhanced geochemical processes on land and in the ocean, (4) direct air capture by technological (chemical) processes with carbon storage. CDR methods commonly discussed in the literature are summarised in Table 5.9.

Other CDR options have been suggested, but there is insufficient literature for an assessment. These include biomass burial, ocean downwelling, removal of CO_2 from seawater with storage, and cloud alkalinisation (Keller et al., 2018b).

[START TABLE 5.9 HERE]

Table 5.9: Carbon Dioxide Removal methods

Category	Methods	Nature of CO_2 Removal Process / Storage Form	Description
Enhanced biological production and storage on land (or geologically)	Afforestation, reforestation and forest management	Biological / Organic	Store carbon in trees and soils by planting, restoring or managing forests
	Agricultural soil management	Biological / Organic	Use agricultural management practices to improve soil carbon storage
	Biochar	Biological / Organic	Pyrolyse terrestrial biomass to form biochar and add to soils
	Bioenergy with carbon capture and storage (BECCS)	Biological / Inorganic	Capture and storage of CO_2 produced by burning of bioenergy crops
	Wetland restoration	Biological / Organic	Store carbon in soil by creating or restoring wetlands and restoring peatlands
Enhanced biological production and storage in ocean	Ocean fertilisation	Biological / organic	Fertilise upper ocean with micro (Fe) and macronutrients (N, P) to increase phytoplankton photosynthesis and biomass and deep ocean carbon storage through the biological pump
	Artificial ocean upwelling	Biological / organic	Pump nutrient rich deep ocean water to the surface
	Blue carbon management	Biological / organic	Manage coastal ecosystems to increase Net Primary Production and store carbon in sediments
Enhanced geochemical processes on land and in ocean	Enhanced weathering	Geochemical / inorganic	Spread alkaline minerals on land to chemically remove atmospheric CO_2 in reactions that form solid minerals (carbonates and silicates) that are stored in soils or in the ocean
	Ocean alkalinisation	Geochemical / inorganic	Increased CO_2 uptake via increased alkalinity by deposition of alkaline minerals (e.g. olivine).
Technological (chemical)	Direct air capture with carbon storage (DACCS)	Technological / inorganic	Direct removal of CO_2 from air through chemical adsorption, absorption or mineralization, and storage underground, in deep ocean or in long-lasting usable materials

[END TABLE 5.9 HERE]

5.6.2.1 Global carbon cycle responses to CDR

This subsection assesses evidence about the response of the global carbon cycle to CDR from idealised model simulations which assume that CO_2 is removed from the atmosphere directly and stored permanently in the geologic reservoir, which is analogous to direct air capture with carbon storage (DACCS; Table 5.9). The carbon cycle response to specific CDR methods is discussed in Section 5.6.2.2.2.

Although our understanding of the climate-carbon cycle response to CDR has evolved since AR5, a limited number of modelling studies exists (Cao and Caldeira, 2010; Vichi et al., 2013; Tokarska and Zickfeld, 2015; Jones et al., 2016b). We assess results from two types of model simulations: idealised 'pulse removal' simulations, whereby a specified amount of CO_2 is removed instantly from the atmosphere, and scenario simulations, whereby CO_2 emissions and removals follow a plausible trajectory. The assessment is based on a review of the literature since AR5 and results from the Carbon Dioxide Removal Model Intercomparison Project (CDR-MIP) (Keller et al., 2018b) and the Scenario Model Intercomparison Project (ScenarioMIP) (O'Neill et al., 2018), which include pulse removal and scenario simulations, respectively. This section assesses three aspects of the climate-carbon cycle response to CDR: the time-dependent behaviour of CO_2 fluxes in scenarios with CDR, the effectiveness of CDR in drawing down atmospheric CO_2 and the symmetry of the carbon cycle response to positive and negative CO_2 emissions.

[START BOX 5.2 HERE]

BOX 5.2: Carbon cycle response to CO_2 removal from the atmosphere

During the Industrial Era, CO_2 emitted by human activities such as fossil-fuel combustion and land-use change, has been redistributed between atmosphere, land, ocean and geological carbon reservoirs due to carbon cycle processes (Figure 1b of Box 5.2). Over the past decade (2008–2017) 44% of the emitted CO_2 remained in the atmosphere, 24% was taken up by the ocean and 29% by the terrestrial biosphere (Le Quéré et al., 2018b) (see Section 5.2.1.5). When CDR is applied during periods of positive CO_2 emissions and is smaller in magnitude than these emissions (*net positive* emissions), it acts to counteract these emissions, reducing their magnitude (Figure 1c of Box 5.2). The excess CO_2 in the atmosphere is partly taken up by the land and the ocean, as in the case of Industrial Era emissions without CDR. When CDR exceeds CO_2 emissions (net removal of CO_2 from the atmosphere or *net negative* emissions) and atmospheric CO_2 declines, land and ocean carbon reservoirs initially continue to take up CO_2 from the atmosphere. After some time lag, which is determined by the magnitude of negative emissions and the emission scenarios prior to application of CDR, land and ocean carbon reservoirs will begin to release CO_2 to the atmosphere (Figure 1d of Box 5.2).

[START BOX 5.2, FIGURE 1 HERE]

Box 5.2, Figure 1: Schematic representation of carbon fluxes between atmosphere, land, ocean and geological reservoirs for (a) an unperturbed Earth system; and changes in carbon fluxes for (b) an Earth system perturbed by fossil fuel CO_2 emissions, (c) an Earth system in which fossil fuel CO_2 emissions are partially offset by CDR, (d) an Earth system in which CDR exceeds CO_2 emissions from fossil fuels ("net negative emissions"). Carbon fluxes depicted in (a) (solid and dashed black lines) also occur in (b)-(d). The question mark in the land to ocean carbon flux perturbation in (c) and (d) indicates that the effect of CDR on this flux is unknown. Adapted from (Keller et al., 2018b).

[END BOX 5.2, FIGURE 1 HERE]

[END BOX 5.2 HERE]

5.6.2.1.1 Carbon cycle response over time in scenarios with CDR

Idealised "pulse" removal Earth system model simulations are useful to understanding the carbon cycle to CDR. Figure 5.32 illustrates the response of atmospheric CO_2 and land and ocean carbon sinks for an instantaneous removal applied from i) a state of the Earth system in equilibrium with a given atmospheric CO_2 concentration, and ii) a 'transient' state, that is a state of the Earth that is not in equilibrium with an evolving atmospheric CO_2 concentration. When CO_2 is removed from the atmosphere from a state of equilibrium (Figure 5.32, blue line), the atmospheric CO_2 concentration declines rapidly at first and then rebounds (Collins et al., 2013). The atmospheric CO_2 rebound is due to CO_2 release by the terrestrial biosphere and the ocean in response to declining atmospheric CO_2 levels (Cao and Caldeira, 2010). For the example shown in Figure 5.32, 100 years after the instantaneous CO_2 removal, 40% of the removed CO_2 remains out of the atmosphere, whereas 60% is replaced by CO_2 outgassing from land and ocean sinks. When CO_2 is removed from a state not in equilibrium with a given atmospheric CO_2 concentration ('transient' state) (Figure 5.32, red line), atmospheric CO_2 continues to decline after the instantaneous CO_2 removal. The reason for this continued decline is that the terrestrial biosphere and the ocean lag the decline in atmospheric CO_2 and continue to take up carbon for decades (land; Figure 5.32b) to centuries (ocean; Figure 5.32c) (Tokarska and Zickfeld, 2015; Jones et al., 2016b; Zickfeld et al., 2016). The carbon cycle response is therefore a combination of the responses to the emission scenario prior to the instantaneous removal and the removal itself, which is relevant for quantifying the effectiveness of CDR in reducing atmospheric CO_2 (Section 5.6.2.1.2).

[START FIGURE 5.32 HERE]

Figure 5.32: Idealised model simulations to illustrate carbon cycle response to instantaneous CO_2 removal from the atmosphere. (a) Atmospheric CO_2 concentration, (b) change in land carbon reservoir, (c) change in ocean carbon reservoir. Results are shown for simulations with the UVic ESCM model of intermediate complexity (Eby et al., 2009) with 100 GtC instantaneously removed from the atmosphere and stored in a permanent reservoir. The 'pulse' removal is applied from a model state in equilibrium with an atmospheric CO_2 concentration of 420 ppm (blue lines), and a 'transient' state, attained with atmospheric CO_2 concentration increasing at 1% yr^{-1} from pre-industrial levels until reaching a CO_2 concentration of 420 ppm (red lines). Changes in land and ocean carbon reservoirs are calculated relative to the time immediately prior to the instantaneous CO_2 removal.

[END FIGURE 5.32 HERE]

Since AR5, studies with Earth system models have explored the land and ocean carbon sink response to scenarios (e.g. RCP2.6) with CO_2 emissions gradually declining during the 21st century. As CDR and other mitigation activities are ramped up, CO_2 emissions in these scenarios reach net zero and, as removals exceed emissions, become net negative. Studies exploring the carbon sink response in such scenarios suggest that when net CO_2 emissions are positive, but start to decline, the land and ocean carbon sinks begin to weaken and take up less CO_2 (compare land and ocean sink in panels (a) and (b) of Figure 5.33) (Tokarska and Zickfeld, 2015; Jones et al., 2016b;). During the first decades after CO_2 emissions become net negative, both the ocean and land carbon sinks continue to take up CO_2, albeit at a lower rate (Figure 5.33c). For the land carbon sink, the sink-to-source transition occurs decades to a few centuries after CO_2 emissions become net negative. The ocean remains a sink of CO_2 for centuries after emissions become net negative (Figure 5.33d). This sink-to-source transition lags the time CO_2 emissions become net negative as carbon sinks respond much later to the prior atmospheric CO_2 concentration and continue to take up CO_2 for decades to centuries (Tokarska and Zickfeld, 2015; Jones et al., 2016b; Zickfeld et al., 2016). While the general response is robust across models, the magnitude of the CO_2 fluxes and the timing of the sink-to-source transition vary between models, particularly for the land sink. For instance, the land sink-to-source transition in the four models examined in Jones et al. (2016b) occurs between years 2000–2050 and 2250–2300 under RCP2.6. These

uncertainties reflect the large spread in simulated terrestrial carbon cycle responses under positive CO_2 emissions associated with differences in model representations of system processes (Section 5.4). Due to *limited evidence* and *limited agreement* between models there is *low confidence* in the strength and timing in the sink-to-source transition in scenarios with net negative emissions.

[Placeholder: This section will be expanded based on analysis of CMIP6 simulations. It is planned to repeat the analysis of Jones et al. (2016) for SSP1-2.6 and SSP5-3.4OS scenarios and their long-term extensions. Such analysis will allow to investigate the time and scenario dependence of the carbon cycle response to CDR. It is expected that the sink-to-source transition will occur with a longer lag relative to the time emissions become net negative in SSP5-3.4OS than in SSP1-2.6.]

[START FIGURE 5.33 HERE]

Figure 5.33: Carbon flux components during different stages of ESM simulations driven by RCP2.6. (a) Large positive CO_2 emissions, (b) Small net positive CO_2 emissions, (c) Net negative CO_2 emissions (short-term response), (d) Net negative CO_2 emissions (long-term response). Fossil fuel and land use emissions as well as emissions from negative emission technologies are from the RCP2.6 scenario. Due to small differences between the compatible CO_2 emissions diagnosed from the ESMs and the emissions in RCP2.6, emissions and land and ocean carbon fluxes over each 50-year period do not balance precisely. Modified from (Jones et al., 2016a).

[END FIGURE 5.33 HERE]

5.6.2.1.2 Effectiveness of CDR

It is well known that the response of land and ocean carbon sinks is sensitive to the level of atmospheric CO_2 and climate change and differs under different future scenarios (Section 5.4). It is therefore important to establish to what extent the effectiveness of CDR – here defined as the reduction in atmospheric CO_2 per unit CO_2 removed – is dependent on the climate scenario from which it is applied. Different metrics have been proposed to quantify the effectiveness of CDR (Tokarska and Zickfeld, 2015; Jones et al., 2016b; Zickfeld et al., 2016). One is the airborne fraction of cumulative CO_2 emissions (AF), defined in the same way as for positive emissions (i.e. as the ratio of change in atmospheric CO_2 at a given point in time to the cumulative emissions up to that time), with its use extended to periods of declining and net negative CO_2 emissions. This metric, however, has not proven to be useful to quantify the effectiveness of CDR in simulations where CDR is applied from a transient state, as it measures the carbon cycle response to CDR as well as to the prior increase in atmospheric CO_2 concentration (Tokarska and Zickfeld, 2015; Jones et al., 2016b) (Section 5.6.2.1.1). Therefore, an alternative metric has been proposed: the airborne fraction of the perturbation relative to a reference scenario (Tokarska and Zickfeld, 2015; Jones et al., 2016b), dubbed the 'perturbation airborne fraction' (PAF) (Jones et al., 2016b). The advantage of this metric is that it separates the response to a positive or negative emission perturbation from the response to atmospheric CO_2 prior to the point in time the perturbation is applied. A disadvantage is that the PAF cannot be calculated from a single model simulation but requires a reference simulation relative to which the effect of the perturbation can be evaluated.

In scenario simulations and idealised model simulations with pulse CO_2 removals applied from an equilibrium state, the effectiveness of CDR is found to be rather insensitive to the rate and amount of CDR (Tokarska and Zickfeld, 2015; Jones et al., 2016b), but to be strongly dependent on the emission scenario from which CDR is applied (Jones et al., 2016b) (Figure 5.34). The effectiveness of CDR is larger in scenarios with higher background atmospheric CO_2 concentration, due to state dependencies and climate-carbon cycle feedbacks that lead to a weaker overall response to CO_2 removal (Zickfeld et al., submitted). Based on the agreement between studies we assess with *medium confidence* that the effectiveness of CDR is largely independent on the rate and magnitude of removal and is larger at higher background atmospheric CO_2 concentrations. However, it should be noted that the larger effectiveness of CDR at higher background CO_2 levels does not translate into a larger effectiveness in terms of temperature response, because the global surface air temperature response per unit change in atmospheric CO_2 is smaller at high background CO_2 (due

to the dependence of the radiative forcing on the logarithm of the CO_2 concentration perturbation). Due to these two opposing effects, the 'cooling effectiveness' of CDR is approximately independent of the background level of CO_2 (Zickfeld et al., submitted) (*high confidence*), consistent with the approximate proportionality of warming to cumulative CO_2 emissions (Section 5.5).

[Will be expanded when results of CDR-MIP simulations become available].

[START FIGURE 5.34 HERE]

Figure 5.34: Effectiveness of CDR. (a) Perturbation airborne fraction (PAF) for model simulations where CDR is applied from four RCPs (shown on the horizontal axis in terms of their cumulative CO_2 emissions over 2020–2099). Symbols indicate results for four CDR scenarios, which differ in terms of the magnitude and rate of CDR (see Jones et al. (2016b) for details). Results are based on simulations with the Hadley Centre Simple Climate-Carbon Model and are shown for the year 2100. Data from Jones et al. (2016b). (b) Airborne fraction of cumulative emissions (AF) for idealised model simulations with CDR applied instantly (pulse removals) from climate states in equilibrium with different atmospheric CO_2 concentration levels (1 to 4 times the pre-industrial atmospheric CO_2 concentration; shown on the horizontal axis). The airborne fraction is calculated 100 years after pulse removal. Symbols indicate results for different magnitudes of pulse removals (triangles: –100 PgC; squares: –500 PgC; circles: –1000 PgC). Based on simulations with the UVic ESCM model of intermediate complexity. Data from Zickfeld et al. (2019). [Placeholder: Will be supplemented with results from CDR-MIP simulations].

[END FIGURE 5.34 HERE]

5.6.2.1.3 Symmetry of carbon cycle response to positive and negative CO2 emissions

It is commonly assumed that climate-carbon cycle response to a negative CO_2 emission is equal in magnitude and opposite in sign to the response to an equivalent positive CO_2 emission, meaning that the climate-carbon cycle response is symmetric. Establishing the symmetry in the response is important to determining the extent to which an emission of CO_2 into the atmosphere can be offset by a negative emission of the same magnitude. Symmetry in the response would also allow to apply the wealth of insights gained about carbon cycle responses and feedbacks under positive CO_2 emissions (Section 5.4) to quantify the effectiveness of CDR. This subsection assesses the symmetry in the coupled climate-carbon cycle response to positive and negative CO_2 emission pulses of the same magnitude released from different climate states. Simulations with an Earth system model of intermediate complexity suggest that the response is approximately symmetric for pulse emissions/removals of ±100 PgC, but becomes increasingly asymmetric for larger pulse emissions/removals (Zickfeld et al., submitted). This asymmetry is illustrated in Figure 5.35a, which shows that the fraction of CO_2 remaining in the atmosphere after an emission is larger than the fraction of CO_2 remaining out of the atmosphere after a removal. In other words, an emission of CO_2 into the atmosphere is more effective at raising atmospheric CO_2 than an equivalent CO_2 removal is at lowering it, particularly for larger emissions/removals. This asymmetry in the atmospheric CO_2 response originates from asymmetries in the land and ocean carbon cycle response (Figure 5.35b,c) due to state-dependencies and nonlinearities (Zickfeld et al., submitted). Given limited evidence, there is *low confidence* in the sign and magnitude of the asymmetry in the response to positive and negative CO_2 emissions [Placeholder: confidence statement to be revised when results from CDR-MIP pulse simulations become available].

[Placeholder for assessment based on results of CDR-MIP simulations with positive and negative 100 PgC emission pulses released from a climate state in equilibrium with the pre-industrial atmospheric CO_2 concentration (Keller et al., 2018b).]

[START FIGURE 5.35 HERE]

Figure 5.35: Changes in carbon reservoirs (atmosphere, ocean, land) as a fraction of cumulative CO_2 emissions (equivalent to CO_2 pulse size) 100 years after the pulse emission/removal (±100 PgC, ±500 PgC, ±1000

PgC) for simulations initialised from different equilibrium states (1 to 4 times the pre-industrial atmospheric CO_2 concentration). Changes in carbon reservoirs are positive (i.e. uptake) for positive CO_2 pulses and negative (i.e. outgassing) for negative CO_2 pulses. (a) Atmospheric carbon burden change fraction, (b) ocean carbon reservoir change fraction, (c) land carbon reservoir change fraction. From (Zickfeld et al., submitted). [Placeholder: Will be updated based on results from CDR-MIP simulations.]

[END FIGURE 5.35 HERE]

5.6.2.2 Effects of specific CDR methods on biogeochemical cycles and climate

5.6.2.2.1 Land-based biological CDR methods

Land biological processes are the main drivers of CO_2 exchange between the land and the atmosphere. CO_2 is removed by gross primary production (GPP) and returned to the atmosphere mainly by autotrophic and heterotrophic respiration, but also by deforestation and disturbances like fire. As long as GPP is greater than these three sources, global land will act as a net sink, as is the case today (Section 5.2.1.4). Biological CDR methods seek to take deliberate measures to increase the difference between GPP and the CO_2 sources leading to increased carbon storage on land.

CO_2 sequestration rates via forest restoration, reforestation and afforestation depend on climate, biodiversity, forest age and are highest for young, diverse, productive ecosystems, but decrease as forest matures, usually after several decades to a few centuries. The above-ground carbon pool in forests is vulnerable, subject to droughts, fires, insects, diseases and other disturbances. Thus, the management of forests for carbon sequestration may be considered a temporary solution while fossils fuels are phased out (Houghton et al., 2015). Primary forests are generally more resilient as carbon stocks than modified natural forests or plantations, as their higher biodiversity, the genetic variability within species and the large size of natural forest ecosystems make them less susceptible to pests and fires (Thompson et al., 2009). Restoring degraded tropical forests is thus the most effective approach to maintain carbon stocks from depletion and sustaining CO_2 sequestration rates (Kurz et al., 2016; Naudts et al., 2016; Griscom et al., 2017; Yousefpour et al., 2018; Maxwell et al. 2019). Pugh et al. (2019) estimate that global forests will accumulate an additional 69 (44–131) PgC in live biomass if natural disturbances, wood harvest and reforestation continue at rates comparable to those during 1981–2010. The global sequestration potential of forestation is uncertain, varying substantially with the amount of land available to this practice. A recent study by Bastin et al. (2019) estimate that 9 Mkm^2 of previously forested area are available for reforestation, which, if allowed to mature to a similar state of protect areas, could store 205 PgC. Other authors, however, suggest that these figures are overestimated by a factor of 5 (Veldman et al., 2015). Furthermore, afforestation of native grasslands, savannas, and open-canopy woodlands may lead to the undesirable loss of these existing natural ecosystems, that support large amounts of biodiversity, carbon storage and other ecosystem services (Veldman et al., 2015; Bastin et al., 2019). Dynamic global vegetation models (DGVMs) suggest different mechanisms that would favour higher sequestration potentials, including carbon-climate-vegetation feedbacks such as the CO_2 fertilisation effect on forest productivity, soil carbon enrichment due to enhanced litter input or the northward shift of the tree-line in future climate projection (Bathiany et al., 2010; Sonntag et al., 2015; Boysen et al., 2017; Harper et al., 2018). There is, however, *low confidence* in the net direction of these feedbacks on global mean temperature; afforestation, particularly high latitudes, would lead to changes albedo and evapotranspiration, potentially resulting in a positive climate feedback and amplifying warming (Pearson et al., 2013; Zhang et al., 2013a). Afforestation and reforestation affect the hydrological cycle through increased transpiration, which will lead to suppressed runoff and especially in dry areas impact water supply (Farley et al., 2005; Smith et al., 2016; Mengis et al., 2019). The impact on N_2O emissions is not well understood and can both increase or decrease the fluxes (*low confidence*) (Benanti et al., 2014; Chen et al., 2019; McDaniel et al., 2019). Forestation will enhance the formation of biogenic volatile organic compounds, but the magnitude is less certain (Krause et al., 2017). Afforestation would decrease biodiversity if for example native species are replaced by monocultures (*high confidence*) (Smith et al., 2018b). On the other hand, biodiversity can be improved in cases where forests are introduced into land areas with degraded soils or intensive monocultures, or where native species are introduced into managed land (*medium confidence*) (Smith et al., 2018b).

Methods to increase soil carbon content include the restoration of marginal or degraded land (Paustian et al., 2016; Smith, 2016) and improved agricultural practices, including selection of appropriate varieties or species with greater root mass, selection of crop rotation cycles that improve C sequestration, increasing the amount of crop residues, using cover crops which prevent periods of bare soil (Paustian et al., 2016), applying optimised grazing (Henderson et al., 2015), planting cover crops in fallow periods (Griscom et al., 2017; Poeplau and Don, 2015), selecting cultivars with deeper roots (Kell, 2011) or higher yields (Burney et al., 2010), optimizing residue management (Wilhelm et al., 2004), employing low-tillage, avoiding grassland conversion, covering crops, using alley cropping, and cropland nutrient management (Fargione et al., 2018). The carbon sequestration potential of soil carbon sequestration methods is substantial (*medium confidence* for any ecosystem), with *high confidence* on the sign and magnitude of carbon sequestration of grassland restoration (Guo and Gifford, 2002; Don et al., 2011; Poeplau et al., 2011; Li et al., 2018; Sanderman et al., 2018). Several of these methods would not only to (Yang et al., 2018) increase carbon input and storage in soil, but to hamper environmental risks such as N_2O emissions and nutrient leaching, and improve soil fertility and biological activity (*medium confidence*) (David, & Drinkwater, 2006; Fornara et al., 2011; Paustian et al., 2016; Tonitto). However, if improved soil C sequestration practices involve higher fertilisation rates, enhanced N_2O emissions are possible (Gu et al., 2017). Deployment of soil carbon sequestration methods will in most cases increase biodiversity (*medium confidence*) (Smith et al., 2018b).

Biochar is produced by burning biomass at high temperatures under anoxic conditions (pyrolysis) and can, when added to soils, increase soil carbon stocks and fertility for decades to centuries (Woolf et al., 2010; Lehmann et al., 2015). Sequestration potentials depend on the biomass feedstock source and the residence time, in turn determined by the feedstock type and the applied pyrolysis temperature. Use of biochar can improve soil productivity, reduce nutrient losses (*medium confidence*) (Woolf et al., 2010) and diminish soil N_2O emissions (*medium confidence*) (Cayuela et al., 2014; Kammann et al., 2017). Effects of biochar addition on soil CH_4 dynamics are less well understood (Jeffery et al., 2017). Application of biochar also has a potential to enhance fertiliser nitrogen use efficiency and improve the bioavailability of phosphorus (*low confidence*) (Clough et al., 2013; Shen et al., 2016; Liu et al., 2017).

Enhanced production of biofuels from bioenergy crops, combined with carbon capture and storage (BECCS) has been considered one of the most important CDR methods for limiting global warming under 2°C (Anderson and Peters, 2016). Sequestration potentials from BECCS depend strongly on the feedstock, climate and management practices (Beringer et al., 2011; Kato & Yamagata, 2014; Heck et al., 2016; Smith et al., 2016; Krause et al., 2017), and have been studied by DGVMs. If marginal land is replaced by woody bioenergy plants, DGVMs simulate increases in net carbon uptake enriching soil carbon (Don et al., 2012; Smith et al., 2012b; Kraxner et al., 2013; Heck et al., 2016; Boysen et al., 2017). On the other hand, if carbon-rich ecosystems are replaced by herbaceous bioenergy plants, DGVMs simulate depletion of soil-carbon stocks and reductions in the sink capacity of standing forests (Elshout et al., 2015; Boysen et al., 2017b, 2017a; Richards et al,. 2017; Harper et al., 2018; Heck et al., 2018; Vaughan et al., 2018). Moreover, carbon losses along the biomass transport, conversion and capture chain could reduce the overall CDR potential of BECCS to 50 to >90% of the initially sequestered carbon (Humpenöder et al., 2014; Creutzig et al., 2015; Vaughan & Gough, 2016; Krause et al., 2017; Fuss et al., 2018; Harper et al., 2018; Heck et al., 2018). Furthermore, BECCS may not be carbon negative in the next decades. Lifecycle analysis indicate that some bioenergy crops may initially emit more CO_2 than fossil fuels (Sterman et al., 2018), and carbon capture and storage (CCS) technology has been demonstrated but is not commercially ready yet to be scaled (Vaughan and Gough, 2016), while leakage and uncertain permanence of CCS could substantially diminish the anticipated CDR goal (Scott et al., 2015; Vaughan et al., 2018). BECCS has moderate potential to sequester C (*medium confidence)* but has several adverse side effects (*low confidence*), such as threatening water supply in dry areas or soil nutrient deficiency (Farley et al., 2005; Smith et al., 2016). Deployment of BECCS would decrease biodiversity and require large land areas, competing with food security (Anderson and Peters, 2016; Smith et al., 2018b) (*medium confidence*).

Wetlands are less extensive than forests, croplands and grazing lands, yet per unit area they hold a high carbon stock. Wetland restoration relies on back-conversion or build of high-carbon-density soils, essentially through flooding (Griscom et al., 2017; Leifeld et al., 2019). High water level is a prerequisite for restoring, (i.e., returning a drained and/or degraded peatland back to its natural state of a CO_2 sink), but restoration

results in enhanced CH_4 emissions which are similar or higher than the pre-drainage fluxes (*medium confidence*) (Koskinen et al., 2016; Wilson et al., 2016; Renou-Wilson et al., 2019;). Restored wetlands can act as buffer zones which provide infiltration and nutrient retention function and offer protection to water quality (Daneshvar et al., 2017; Lundin et al., 2017). Particularly in nutrient-loaded agricultural catchments wetlands can have a significant role in improving water quality. Wetland restoration can recover much of the original biodiversity (Meli et al., 2014).

[START TABLE 5.10 HERE]

Table 5.10: Characteristics of specific CDR methods: global CDR potential, time scale of C storage, factors that affect C storage timescale, termination effects.

Method	CDR potential PgC yr^{-1}	Time scale of C storage	Factors that affect C storage time scale	Termination effects
Afforestation, reforestation and forest management	0.5–2.8 (SRCCL technical potential)	Decades to centuries	Fires, pests, extreme weather	None
Soil carbon sequestration	0.11–2.3 (SRCCL technical potential)	Decades to centuries	Soil management	None
Biochar	1.0–1.8 (SRCCL technical potential)	Decades to centuries	Fire	None
BECCS	0.1–3.0 (SRCCL technical potential)	Potentially permanent	Leakage	None
Wetland restoration	0.19–0.67 (Griscom et al., 2017)	Decades to centuries	Wetland drainage	None
Ocean fertilisation	0.32–12 (Fuss et al., 2018)	Centuries to millennia	Ocean stratification and circulation	Unknown
Artificial ocean upwelling	0.9–4.3 (Oschlies, 2010; Keller et al., 2014)	Centuries to millennia	Ocean circulation; DIC content of upwelled waters	Causes subsequent warming beyond temperatures experienced if AOUpw not started (Keller et al., 2014)
Restoration of vegetated coastal ecosystems (‘blue carbon’)	No cost limits: 0.17–0.29 (0.23); cost effective: ~0.05 (Griscom et al., 2017b; National Academies of Sciences and Medicine, 2019)	Decades to centuries if functional integrity of ecosystem maintained	Anthropogenic disturbance of coastal vegetation	Risk of CO_2 release under climate change impacts
Enhanced weathering - terrestrial	0.05–26 (Fuss et al., 2018) - Low agreement on technical potential	Centuries to millennia for carbonates, permanent for silicates		
Ocean alkalinisation	<27 (González and Ilyina, 2016; Sonntag et al.,	10,000 to 100,000 years	Ocean stratification and circulation	Higher rates of warming and acidification than if alkalinisation not begun

	2018)			(González et al., 2018)
Direct air carbon capture and storage (DACCS)	0.14–1.4 (Fuss et al., 2018)	Permanent	Leakage	

[END TABLE 5.10 HERE]

5.6.2.2.2 Ocean-based biological CDR methods

Both ocean biological and physical processes drive the CO_2 exchange between the ocean and atmosphere. However, the ocean physical processes that remove CO_2 from the atmosphere, such as large-scale circulation and mixing, cannot be feasibly altered, so ocean CDR methods focus on increasing the productivity of ocean ecosystems, and subsequent sequestration of carbon.

Artificial ocean upwelling (AOUpw) brings nutrient-rich water to the ocean surface to alleviate nutrient limitation of (near-)surface phytoplankton growth and thus boost primary production and subsequent ocean CO_2 uptake. For AOUpw to be effective at increasing ocean carbon storage, the increased primary production has to result in increased transfer of organic carbon into the deep ocean. AOUpw also returns previously-sequestered dissolved inorganic carbon to the surface ocean, thus increasing surface water pCO2 and decreasing (or potentially negating) atmospheric CO_2 drawdown stimulated by the additional nutrient input. In model simulations (Oschlies, 2010; Keller et al., 2014) where AOUpw is applied continuously and at the largest feasible scales, cumulative atmospheric CO_2 removal is up to 4.3 PgC yr^{-1} during the first decade, and decreases afterwards to 0.9 to 1.5 PgC yr^{-1} (average), with 50–80% of this removal resulting from cooling-induced enhancement of the terrestrial carbon sink (Keller et al., 2014). AOUpw is *likely* to have widespread side effects (Figure 5.36).

Ocean fertilisation (OF) aims to boost primary production and subsequently organic carbon export by seeding the ocean surface with nutrients, typically in iron-limited areas such as the Southern Ocean or North Pacific. Iron fertilisation experiments have been inconclusive on whether deep-sea carbon sequestration is enhanced (Boyd et al., 2007; Yoon et al., 2018), with only one observing an increase in the biological pump below 1000 m (Smetacek et al., 2012), suggesting that the effectiveness of ocean fertilisation is low (*medium confidence*). Model simulations (Oschlies et al., 2010; Keller et al., 2014) suggest that if ocean fertilisation is applied continuously under a high CO_2 emission scenarios, CO_2 sequestration rates are initially between 2 and 4 PgC yr^{-1}, but then decrease to 0.4 to 1 PgC yr^{-1} (average) after the initial decade. Increased productivity in the fertilised areas is *likely* to result in decreased productivity in unfertilised regions (Oschlies, 2010). The carbonate counter pump could also potentially reduce iron fertilisation-induced C sequestration by 6–32% (Salter et al., 2014). Upon fertilisation termination, up to a third of the sequestered carbon may be returned to the atmosphere within a century (Robinson et al., 2014). Ocean iron fertilization is prohibited by the London Protocol, unless constituting legitimate scientific research authorised under permit (Dixon et al., 2014).

The carbon sequestration potential of ocean fertilisation and artificial ocean upwelling is low to moderate (*high confidence*), but both have a multitude of negative side effects (*high confidence)* (Figure 5.36). Stimulating ocean productivity may increase biological production of N_2O. Sinking of associated organic carbon and remineralisation in the mid-water decreases oxygen concentration and, if sufficient to induce suboxia, increases methane production (Lampitt et al., 2008). Additionally, both AOUpw and OF would enhance surface ocean acidification and perturb marine ecosystems via reorganisation of community structure (*high confidence)* (Oschlies, 2010; Williamson et al., 2012a).

Restoration of vegetated coastal ecosystems (sometimes referred to as 'blue carbon') refers to the potential for increasing carbon sequestration by plant growth and burial of organic carbon in the soil of coastal wetlands (including salt marshes and mangroves) and seagrass ecosystems. Wider usage of the term blue carbon occurs in the literature, for example including seaweeds (macroalgae), shelf sea sediments and open ocean carbon exchanges; however, such systems are less amenable to management, with many uncertainties relating to the permanence of their carbon stores (Windham-Myers et al., 2018; Lovelock and Duarte,

2019); SROCC Section 5.5.1.1 [Placeholder: add reference link].

Coastal wetlands and seagrass meadows are among the most productive ecosystems per unit area, with a global annual sequestration rate estimated to be 0.08–0.23 PgC yr^{-1} (Mcleod et al., 2011). These rates could be reduced in future, since these habitats are vulnerable to changing conditions, such as temperature, salinity, sediment supply, storm severity and continued coastal development (National Academies of Sciences and Medicine, 2019; Bindoff et al., 2019). Although sea level rise might lead to greater carbon sequestration in coastal wetlands (Rogers et al., 2019), increases in the frequency and intensity of marine heatwaves pose a more immediate threat to the integrity of coastal carbon stocks (Smale et al., 2019). Blue carbon restoration seeks to increase the rate of carbon sequestration, with the potential to provide additional global CO_2 sequestration of 0.17–0.29 PgC yr^{-1} by 2030 (Griscom et al., 2017). These estimates are not cost-constrained and assume that nearly all coastal ecosystems can be restored to their natural extents. Such action would be challenging, because of on-going use of coastal land for human settlement, conversion to agriculture and aquaculture, shoreline hardening and port development. More realistic potential values for cost-effective restoration of wetlands and seagrass meadows are around 0.04–0.05 PgC yr^{-1} (National Academies of Sciences and Medicine, 2019)(Griscom et al., 2017).

Biogeochemical factors affecting reliable quantification of the climatic benefits of coastal vegetation include the variable production of CH_4 and N_2O by such ecosystems (Adams et al., 2012; Rosentreter et al., 2018; Keller, 2019;), uncertainties regarding the provenance of the carbon that they accumulate (Macreadie et al., 2019), and the release of CO_2 by biogenic carbonate formation in seagrass ecosystems (Kennedy et al., 2019). Whilst coastal habitat restoration potentially provides significant mitigation of national emissions for some countries (Taillardat et al., 2018), the global sequestration potential of blue carbon approaches is relatively low (*medium confidence*). Nevertheless, effective conservation measures that avoid habitat loss would help maintain the integrity of existing carbon stores, and the maintenance and restoration of coastal wetlands and seagrass meadows can greatly assist climate change adaptation, for example in preventing coastal erosion, providing storm protection, biodiversity benefits and many other valuable ecosystem services (*high confidence*) (SROCC Chapter 5.5.1.1 and 5.5.1.2.2).

5.6.2.2.3 Geochemical and chemical CDR methods

Enhanced weathering (EW) is based on naturally occurring weathering process in which Mg- and/or Ca-rich rock minerals are decomposed and reacts with the elevated CO_2 environment of soil pores, at the same time dissolved CO_2 is converted to bicarbonate which is then leached to surface waters and ultimately to the ocean. Weathering is accelerated by spreading grinded rocks on for example managed croplands which will increase the reactive surface area and accelerate the rate of weathering (Taylor et al., 2015b). For enhanced weathering the carbon sequestration potential is higher and the time scale of C storage is longer than those of most land-based methods (*high confidence*). Enhanced weathering has several potential side-effects which can be both beneficial and adverse (*low confidence*). EW increases the alkalinity and pH of natural waters, helps dampen ocean acidification and increases ocean carbon uptake (Beerling et al., 2018). The dissolution of minerals is likely to stimulate biological productivity of croplands (Hartmann et al., 2013; Beerling et al., 2018), but can also liberate toxic trace metals (such as Ni, Cr, Cu) into soil or water bodies (Keller et al., 2018a; Strefler et al., 2018). As another negative side effect, EW can contribute to freshwater salinization which is due to increased salt inputs and accelerated chemical weathering and cation exchange in watersheds. Also, EW can cause adverse implications for availability of high quality drinking water and toxicity of metals and ammonia (*medium confidence*) (Kaushal et al., 2018). The mining of minerals causes adverse impacts on biodiversity without careful restoration. The spreading of minerals on land can have both beneficial and adverse impacts on biodiversity, depending on whether the minerals are spread at low or high rates, respectively (Smith et al., 2018b).

Ocean alkalinisation, via the deposition of alkaline minerals (e.g. olivine) or their dissociation products (e.g. quicklime) at the ocean surface, can increase surface total alkalinity and thus increase CO_2 uptake and storage. Modelling studies suggest that massive additions of alkalinity (114 Pmol by the end of the century) during high CO_2 emission scenarios could increase ocean uptake by up to 27 PgC yr^{-1} by the end of the century, and permanently keep it there (100 ka residence time; Renforth & Henderson, 2017) even if

additions were stopped (González et al., 2016; Feng et al., 2017; Sonntag et al., 2018). Enhanced ocean carbon uptake rapidly stops upon termination of ocean alkalinisation (González et al., 2018). If olivine is deposited, the associated addition of iron and silicic acid is predicted to enhance primary production (Köhler et al., 2013; Hauck et al., 2016). The carbon sequestration potential of ocean alkalinisation is high (*high confidence*). Ocean alkalinisation has both positive and negative side effects on the marine ecosystem, most of which are poorly understood or quantified. Ocean alkalinisation decreases surface ocean acidification (*high confidence*), but also releases toxic trace metals from deposited minerals and perturbs marine ecosystem community structure (*low confidence)*.

Direct air capture with carbon storage is a combination of two techniques, direct air capture of CO_2 (DAC) and carbon storage. DAC entails the flow of large amounts of air through a filter that separates carbon dioxide from air, producing a concentrated CO_2 gas stream. The CO_2 stream then may be either stored geologically as a high-pressure gas or sequestered by a mineral carbonation process. DACCS (DAC with carbon capture and storage) has significant requirements of water and energy, and carbon storage has additional energy requirements. Storage is potentially permanent in both pressurised gas form and mineral form. The main risks and side effects of DACCS are largely related to the high pressure at which CO_2 is stored in geologic formations. The conversion of CO_2 captured by BECCS/DACCS to ocean alkalinity and subsequent storage in the ocean has been proposed (Rau, 2014) and carries with it the same potential feedbacks and side effects as ocean alkalinisation.

[START FIGURE 5.36 HERE]

Figure 5.36: Characteristics of CDR methods. The left hand side of the figure shows ranges of technical sequestration potentials of CDR methods, grouped according to the time scale of C storage. The right hand side shows Earth system feedbacks that deployment of a given CDR method would have on carbon sequestration and climate, along with biogeochemical, biophysical, and other side effects of that method. For Earth system feedbacks, the colours indicate whether the feedbacks strengthen or weaken C sequestration and the climate cooling effect of a given CDR method. For biogeochemical and biophysical side effects the colours indicate whether the deployment of a CDR method increases or decreases the magnitude of the effect, whereas for other side effects the colour indicates whether deployment of a CDR method is adverse or beneficial.

[END FIGURE 5.36 HERE]

5.6.3 Biogeochemical response to Solar Radiation Modification (SRM)

This section assesses the possible impacts of SRM on the biosphere and global biogeochemical cycles, calling on published modelling studies such as GeoMIP (Kravitz et al., 2011). The physical climate response to SRM is assessed in detail in Chapter 4 (Section 4.6.3)

5.6.3.1 Impact of SRM relative to an elevated CO_2 climate state

Relative to a high-CO_2 world without SRM, SRM is expected to affect biogeochemical cycles through changes in sunlight, climate (e.g. temperature, precipitation, soil moisture, ocean circulation), and atmospheric chemistry (e.g. ozone) (Cao, 2018). Net SRM effects on biogeochemical cycles, relative to a world without SRM, depend on the change of individual factors, and interactions among them.

SRM-mediated sunlight change directly affects biogeochemical cycles. Stratospheric aerosol injection acts to reduce the sunlight reaching the Earth's surface, but also increases the fraction of sunlight that is diffuse. These changes in the quantity and quality of the sunlight have opposing effects on the photosynthesis of land plants. On their own, reductions in photosynthetic active radiation (PAR) will reduce photosynthesis. However, diffuse light is more effective than direct light in accessing the light-limited leaves within plant

canopies, leading to the so-called 'diffuse-radiation' fertilisation effect (Mercado et al., 2009). The balance between the negative impacts of reducing PAR and the positive impacts of increasing diffuse fraction differ between models (Kalidindi et al., 2015; Xia et al., 2016) and across different ecosystems. For the moderately small changes in surface PAR implied by SRM, diffuse-radiation fertilisation is *likely* to overcome the reduction in total PAR, at least for dense canopies with high leaf area index (Ito, 2017). The change in direct and diffuse radiation could also depend on the height of the additional sulphate aerosol layer in the stratosphere, which would affect vegetation response (Krishna-Pillai Sukumara-Pillai et al., 2019).

SRM-mediated cooling further affects biogeochemcial cycles. An example of multi-model simulated global GPP and NPP response to SRM that directly reduces sunlight is illustrated in Figure 5.37. Relative to a high-CO_2 world, SRM-induced cooling will decrease NPP at high latitudes because of reduced length of the growing season (Glienke et al., 2015; Dagon and Schrag, 2019). At low latitudes, the NPP response to SRM-induced cooling is sensitive to the effect of nitrogen limitation. SRM-induced cooling increases NPP in models without the nitrogen cycle because of reduced heat stress. In models with the nitrogen cycle, SRM-induced cooling reduces NPP because of reduction in nitrogen mineralisation and reduced nitrogen availability (Glienke et al., 2015). SRM-induced changes in the hydrological cycle, including changes in evapotranspiration, precipitation, and soil moisture, also pose strong constraints on vegetation response (Dagon and Schrag, 2019). In addition, SRM would cauese changes in troposhere and surface ozone concentrations with the response strongly sensitive to SRM approaches, which has important implication for vegetation response (Xia et al., 2017). Due to the highly idealised nature of these modeling studies and complex interplays between SRM-induced changes in direct and diffuse sunlight, temperature, the coupling of water-carbon-nitrogen cycles, and atmospheric chemistry, there is *low confidence* in how different SRM approaches would affect the terrestrial biosphere.

[START FIGURE 5.37 HERE]

Figure 5.37: [Placeholder: From (Glienke et al., 2015). Global mean values for NPP averaged over land (colored with numbers above), R_a (grey) and GPP (total) for all models of the three experiments abrupt $4 \cdot CO_2$, G1, and piControl. The number in the top left corner is the global average of NPP determined from MODIS data. Abrupt $4 \cdot CO_2$ is an experiment with an abrupt quadrupling of atmospheric CO_2 and G1 is a GEOMIP experiment in which a decrease in the solar constant offsets the global radiative forcing of $4 \cdot CO_2$.]

[END FIGURE 5.37 HERE]

Relative to a high-CO_2 world without SRM, stratospheric aerosol injection increases crop yields at the global scale largely due to dimished heat stress (Pongratz et al., 2012). Direct reduction of sunlight is found to have little impact on rice production in China but could increase maize production (Xia et al., 2014), and it is found that SRM would reduce the yield of groundnut in large parts of India (Yang et al., 2016). Based on the response of crop yields to the eruption of Mount Pinatubo (as a surrogate of stratospehric aerosol injection), stratospheric aerosol injection would attenuate little of the global agricultural damage from climate change because of compensating effects of cooling and reduced light availability (Proctor et al., 2018). Overall, there is *low confidence* in the effect of SRM on crop yields.

There is *high confidence* that SRM would not mitigate CO_2-induced ocean acidification (AR5); SRM could even accelerate deep-ocean acidification as a result of ocean circulation change (Tjiputra et al., 2016; Lauvset et al., 2017). SRM-induced cooling through marine cloud brightening has different effects on ocean NPP in different regions due to changes in temperature and ocean stratification and circulation (Partanen et al., 2016). Reduced sunlight would have a substantial effect on local ocean NPP where light availability is the main limiting factor for phytoplankton growth (Partanen et al., 2016) (*low confidence*).

5.6.3.2 Impact of elevated CO_2 and SRM relative to an unpertubed climate state

Based on available evidence, SRM with elevated CO_2 would increase global mean net primary productivity and carbon storage on land, relative to an unperturbed climate mainly because of CO_2 fertilisation of photosynthesis (*medium confidence*). However, the amount of increase is highly uncertain depending on the extent to which CO_2 fertilisation of land plants is limited by other constraints, such as nutrient and water availability. SRM with elevated CO_2 would have negative impacts on ocean ecosystems relative to unpertubed climate mainly due to CO_2-induced ocean acidification (*high confidence*), with poorly-known consequences for the biological carbon pump and the ocean carbon sink.

5.6.3.3 Impact of SRM on atmospheric CO_2 burden

Compared to a scenario of unmitigated anthropogenic emissions, SRM reduces the burden of atmospheric CO_2 by enhancing global land and ocean sinks. SRM acts to cool the planet relative to unmitigated climate change, which reduces plant and soil respiration, and also reduces the negative impacts of warming on ocean carbon uptake. Cao and Jiang (2017) reported that if SRM is used to limit global warming below 2°C, SRM would reduce atmospheric burden of CO_2 by about by 47 PgC in 2100. Keith et al. (2017) reported that if SRM was used to hold radiative forcing at current level under RCP8.5, SRM may reduce atmospheric CO_2 by about 100 PgC. However, Tjiputra et al. (2016) reported a much smaller reduction of atmospheric CO_2 in response to SRM probably because of the inclusion of the nitrogen cycle that leads to a weaker terrestrial carbon sink. Alternatively, SRM could also increases allowable CO_2 emission for a specific CO_2 concentration scenario as a result of enhanced terrestrial and ocean CO_2 uptake (Plazzotta et al., 2019).

5.6.3.4 Impacts of SRM termination

A hypothetical, sudden and sustained termination of SRM causes a rapid increase in global warming that poses great risks to biodiversity (Jones et al., 2013a; McCusker et al., 2014; Trisos et al., 2018) (Section 4.6.3). A sudden and sustained termination of SRM also weakens carbon sinks, accelerating atmospheric CO_2 accumulation and inducing further warming (Matthews and Caldeira, 2007; Tjiputra et al., 2016; Plazzotta et al., 2019). A sudden termination of SRM would also cause a rapid return of ocean NPP to a high-CO_2 world without SRM (Lauvset et al., 2017). However, a scenario with gradual phase-out of SRM under emission reduction could avoid the large negative effect of sudden SRM termination (Keith and MacMartin, 2015; Tilmes et al., 2016). Climate policy could also prevent sudden SRM termination and a termination shock might be much less likely (Parker and Irvine, 2018; Rabitz, 2019).

5.7 Knowledge Gaps

In carrying out the assessment presented in the chapter, several knowledge gaps have been identified. If these knowledge gaps are adequately addressed in the future, it will improve the level of confidence of key statements in this assessment. All these knowledge gaps have been duly considered in the assessment and associated confidence levels presented in this chapter. Their listing in this section does not weaken any of the statements found in other parts of the chapter.

Contemporary GHG Trends and Attribution

Two key aspects of assessing the magnitude and trends of the land CO_2 sink through terrestrial models require development. Firstly, further constraining the flux from land use, land use change and forestry. Improving model resolution and including representations of land management, such as forestry, grazing and cropland management, which covers three quarters of the ice-free land surface; remote sensing observations can provide additional constraints. Secondly, better representing the variability and trends in the transport of carbon through the land to ocean continuum (land-freshwater bodies-rivers-coastal zones-open ocean), which

has implications for the strength of the land and ocean CO_2 sinks.

Data gaps in space and time for ocean CO_2 and biogeochemical observations in the surface as well as at depths are one of the main obstacles to advancing our knowledge of and reducing the biases and uncertainties in air-sea fluxes and inventory changes. Better observational coverage is an essential avenue to providing improved global constraints on the variability and trends of ocean CO_2 uptakes, particularly to resolve the spatial and seasonal cycle biases in sampling. This applies particularly to the Arctic and the Southern Hemisphere oceans, which account for most of the uncertainty in global estimates of the ocean CO_2 uptake. Emerging observational networks like autonomous platforms and remote sensing observations in addition to the shipboard precise full-depth observations can contribute to addressing these limitations. Attributing the drivers of the variability remains a challenge.

There is good understanding on the source attribution of the observed CH_4 trends in the atmosphere, but uncertainties remain for some of the anthropogenic sources and reducing these uncertainties can improve the design of effective mitigation strategies. In addition, wetlands are the single largest source term in the global CH_4 budget, and proportionally have the largest uncertainty; a reduction of these uncertainties will help understand the potential future CH_4-climate feedback. This may also apply to the permafrost stocks of methane.

Progress has been made in quantifying land and ocean N_2O sources, and large remaining uncertainties in the magnitude and underlying process contributions can be the subject of targeted further research. It is clear that anthropogenic N_2O emissions have increased. Improvements in the currently weak quantitative understanding of the processes leading to large inter annual variations of the atmospheric growth rate of N_2O can improve the attribution of the recent increase in the growth rate to underlying causes.

The integration of how human activities and natural processes are modifying all main GHGs (CO_2, CH_4, N_2O) concurrently and where trade-offs exist is an area where research can further support mitigation efforts.

Ocean Acidification and De-oxygenation

Better sampling and focussed research in the interplay between carbonate chemistry and a variety of biogeochemical and physical processes including eutrophication and freshwater inflow, has the potential to significantly increase our understanding and confidence in ocean acidification, particularly in subpolar and coastal regions. Resolving fine-scale temporal and spatial variability and processes that are not captured by models today, can allow model simulations to better project important future changes in marine biogeochemistry such as acidification. Further research can also significantly improve the quantification of the sign and magnitude of many feedbacks within the marine ecosystem. Confidence in future projections can be further strengthened by dedicated efforts to better understand the impact of differences between prescribed concentrations and emissions driven models on the variability, trends and feedbacks on ocean acidification.

Improving our understanding of changes in water mass ventilation and further constraining its evolution can further inform future trends in ocean acidification and de-oxygenation in the ocean interior as it in part provides the link between these two processes. Many Earth system models project a global decline in the oxygen content of the ocean in the future. Persistent uncertainties for the subtropical oceans where the major oxygen-depleted environments exist can be further reduced, for example, by focussing research on improving our understanding of future ocean de-oxygenation in the subsurface tropical ocean and its relation to a consistent compensation in the trends and variability between oxygen saturation due to warming and decreasing apparent oxygen utilisation as a result of increased ventilation. Determining the threshold of oxygen concentration at which nitrous oxide (N_2O) production turns into consumption could result in a strengthened understanding of ocean emissions; N_2O is produced in hypoxic areas, mediated by bacteria.

Biogeochemical Feedbacks on Climate Change

Improving our understanding of changes in land carbon storage remains key to reducing the uncertainty in

carbon cycle projections. Models differ in the treatments of CO_2-fertilisation, nutrient-limitations, and the net effect of land-use change. The challenge is to better constrain the land carbon components of ESMs with observations, including using the findings of emergent constraint and process-based studies to focus on model evaluation and development. The understanding of the role and importance of limiting nutrients in the biospheric carbon responses to increasing CO_2, can be further improved through the development and evaluation of coupled carbon-nitrogen-phosphorus land cycle models, which remains a challenge to date.

In order to strengthen the confidence in carbon cycle feedbacks projections, models may also need to include soil microbial and mineral stabilisation processes, large-scale and fine-scale permafrost carbon processes, the growth and mortality dynamics of individual trees, plant trait competition and more explicit representation of disturbance processes. For each of these, better global-scale observational constraints would provide a necessary evidence base for testing emerging modelling approaches that include each of these processes.

Model projections of changes in ocean carbon fluxes and storage agree better than for land. However, improving understanding of the processes (e.g., dynamic nutrient stoichiometry or explicit representation of plankton functional types) affecting the efficiency, climate sensitivity and emerging feedbacks in the ocean carbon cycle via the biological carbon pump can contribute to resolving the uncertainty in the magnitude and sign of projections of future global ocean primary production by 2100 (noting that this is not the primary driver of the ocean sink).

The assessment of risks associated with tipping points in the Earth system is based largely on paleo climate data, for which the rates of change are much slower than expected in the next 100 years and which thus potentially provides only a conservative proxy. New conceptual models, analyses, and ESM runs can help improve our understanding of how tipping point risks vary with the rate of change of climate and CO_2 emissions.

Remaining Carbon Budget to Climate Stabilization

Important areas remain for advancing the more precise estimation of the carbon budgets. These include a better understanding of both the sign and magnitude of a possible Zero Emissions Commitment (ZEC). The ZEC impacts estimates of carbon budgets derived from the TCRE, but not TCRE itself. ZEC is particularly relevant once global CO_2 emissions decline towards net zero.

A better and more broadly supported understanding of the potential magnitude of permafrost thawing feedbacks and their effect on TCRE would allow more precise remaining carbon budget estimates and at longer timescales. There are also other currently not represented Earth system feedbacks that could affect the TCRE and a better quantification can also contribute to a further improved understanding of the remaining carbon budget until peak warming and beyond.

Another important avenue for further interdisciplinary advance is the development of translation tools that allow the easy and internally consistent integration of radiative forcing and other assessments in the estimation of non-CO_2 warming for remaining carbon budgets.

Carbon Dioxide Removal and Solar Radiation Modification

There is still *low confidence* regarding global CO_2 sequestration potentials of specific land- and ocean-based Carbon Dioxide Removal (CDR) methods. Large-scale and long-term experiments or assessments that involve independent verification are needed to demonstrate that these methods are regionally feasible, they present an actual and verifiable negative regional carbon balance, and have no negative unintended consequences. More realistic scenarios of deployment will help to assess their mitigation capacity.

Assessment of the global carbon cycle response to CDR is based on a limited number of modelling studies. Simulations with Earth system Models and the exploration of a broader range of scenarios will increase confidence in the assessment, particularly with regard to the effectiveness of CDR in reducing atmospheric CO_2 and the asymmetry in the climate-carbon cycle response to CO_2 emissions and removals. A common

limitation of existing studies is the assumption of idealised CDR deployment, without specification of the CDR method or at rates far beyond the magnitudes considered practically feasible, or in socioeconomic mitigation pathways. Explicit representation of CDR processes in Earth system models will advance our understanding of the carbon cycle response and Earth system feedbacks associated with these methods.

Key uncertainties in the assessment of the effects of Solar Radiation Modification (SRM) on the carbon cycle are related to the response of terrestrial and marine ecosystems and associated carbon storage. Several of these uncertainties are in common with the assessment of the land and ocean carbon cycle response to CO_2 increase and warming, such as the impact of ocean acidification on the biological carbon pump and the impact of nutrient limitation on soil respiration and land carbon storage.

Frequently Asked Questions

FAQ 5.1: Is the rate at which nature removes carbon from the atmosphere slowing down?

For decades, nature has removed about half of the carbon dioxide (CO_2) that human activities have emitted to the atmosphere by increasing the amount of carbon stored in vegetation, soils and oceans. This removal of CO_2 has thus roughly halved the rate at which atmospheric CO_2 concentrations have increased, and therefore slowed down global warming. There is as yet no observable evidence that this natural removal is slowing down or that the processes underlying this removal are changing.

Since CO_2 concentrations in the atmosphere have been measured, commencing in 1958, only about half of yearly emissions from the combustion of fossil fuels and land-use change (for example, deforestation) have remained in the atmosphere. Natural carbon sinks, processes on land and oceans that remove CO_2 from the atmosphere, have removed the other half of the emissions.

The key land process that removes CO_2 from the atmosphere is plant photosynthesis, which for most plants increases as the concentration of atmospheric CO_2 rises, due to what is known as the CO_2 fertilisation effect. In cold regions, longer growing seasons due to global warming also contribute to increased land CO_2 uptake.

A large part of the CO_2 captured by photosynthesis is lost back to the atmosphere through respiration or natural disturbances (such as fires and wind throw). Human activities (for instance, de- and reforestation, land degradation, nitrogen deposition, air pollution) also influence the net removal of carbon by the land biosphere. The net balance between removals by photosynthesis and losses is the carbon sequestered which we call the net land carbon sink.

The processes involved in how much carbon is ultimately sequestered is affected by climate factors, and so as climate changes, the amount of carbon sequestered will change too. Regionally, extreme temperatures and droughts tend to reduce the land sink, a process that is for instance, often observed during El Niño years, a periodic climate event during which parts of the Earth's surface have well above average temperatures. The natural land sink varies strongly from year to year, making it challenging to detect long-term trends.

In the ocean, the CO_2 uptake is driven by several factors: the difference in CO_2 concentration between the atmosphere and the surface ocean (approximately the upper 50 m but change seasonally), the chemical capacity of seawater to take up CO_2 (or buffering capacity), wind speeds at the ocean surface, and the use of CO_2 in photosynthesis by phytoplankton. All these processes are known to be dependent on temperature, with a tendency to weaken ocean uptake under warmer conditions. The CO_2-enrich surface ocean water is transported to the deep ocean in specific zones around the globe (such as the Northern Atlantic and the Southern Ocean), effectively storing the CO_2 away from the atmosphere for many decades to centuries.

Remarkably, both the land and ocean sinks have been growing largely proportional to the increase in CO_2 emissions. This has made the airborne fraction, the fraction of yearly CO_2 emissions staying in the atmosphere, to remain on average unchanged over the last six decades despite continuously increasing CO_2 emissions from human activities. There is currently no evidence that the land or ocean sink are slowing down.

The fact that both the land and ocean sink respond to excess anthropogenic CO_2 in the atmosphere, suggests that the absolute amount of CO_2 removed by the land and ocean will vary in proportion to future anthropogenic emissions. This implies that if countries manage to strongly reduce global CO_2 emissions or reach net zero or negative emission levels, these sinks will become smaller. Regardless the future trajectory of emissions from human activities, the ocean sink will become smaller in the future because the buffer capacity to continue uptake CO_2 will diminish at the same time the warming of the ocean will further reduce its capacity to remove CO_2. For the land sink, model simulations suggest that if emissions are not reduced sufficiently to cap warming at 2°C, the combined effect of reduced the CO_2 fertilisation effect and climate change is likely to weaken the land sink in the second half of this century. In summary, CO_2 sinks will change in the future and understanding the magnitude of change will be important to design mitigation

pathways.

[START FAQ 5.1, FIGURE 1 HERE]

FAQ 5.1, Figure 1: Overview of the global carbon budget and the fraction of CO_2 remaining in atmosphere, land and ocean from 1960 to 2019. Estimates are derived from atmospheric observations, process-based models, data-driven ocean flux products, and atmospheric inversions (Le Quéré et al., 2018a). Dots denote yearly values, lines are the seven years running mean.

[END FAQ 5.1, FIGURE 1 HERE]

FAQ 5.2: Can thawing permafrost on land or under the ocean substantially increase global temperatures?

Carbon released as carbon dioxide (CO_2) or methane (CH_4) as a result of increased rates of decomposition in thawing permafrost soils may add an additional amount of warming, that is significant enough that it should be considered in carbon estimates, but does not appear to be a process that will lead to runaway warming. Warming of frozen sediments beneath the ocean and deeper on land appears to be a weaker potential source of greenhouse gases.

Across Arctic ecosystems, where deep soils remain frozen throughout the year, there are enormous amounts of carbon in accumulated soil organic matter: more than twice the amount of CO_2 that is currently in the atmosphere. This carbon has built up over thousands of years, through the growth of plants that become thick organic litter layers when they die, which then can be buried into deeper, permanently-frozen soil layers, where the cold conditions slow the rate of their decomposition for as long as the soils remain frozen. These processes have led permafrost soils to act as carbon sinks historically, but experiments have shown that, by warming these ecosystems, the carbon in these soils will begin to decompose rapidly and return to the atmosphere as either CO_2 or CH_4, which are both important greenhouse gases. Climate models project that much of the near-surface permafrost (<3m depth) throughout the Arctic would thaw under moderate (2–3°C) to high amounts (more than 4°C) of global warming, and thus the carbon stored in this ecosystem is at risk.

Thawing of permafrost carbon has already been observed to have begun due to the rapid warming experienced in the Arctic, where air temperatures have increased twice as fast as the global average. With this thawing there are measurements showing very old carbon frozen for thousands of years being emitted to the atmosphere and transported into waterways. There are many processes that can speed up the loss of carbon from these northern ecosystems. Melting of massive blocks of ice in the soils can cause the landscape to sink and erode. Ponds and lakes that are common in some Arctic ecosystems can expand and move across the landscape. Thick surface organic layers can dry out in warmer summers and catch fire, leading to further permafrost thaw. Some processes may partially offset carbon losses: warming also releases nutrients during decomposition to increase soil fertility, and warmer and longer growing seasons favour plants to grow and store carbon, which is being observed in some regions of tundra.

While these processes are complex, they are beginning to be included in models that represent the climate and the carbon cycle in an interactive manner. The projections from these models show a wide range in the estimated strength of a carbon-climate self-reinforcing loop, of approximately 20 ± 13 PgC as CO_2 per °C global temperature change, and also provide some clear insights. Firstly, this extra warming is strong enough that it must be included to estimate the total amount of emissions permitted to stabilise the climate at a given level. However, it is not so strong that they would lead to warming that is greater than the warming from fossil fuel burning. Finally, emissions of greenhouse gases from permafrost are projected to be higher under high emissions scenarios.

In addition to carbon within permafrost soils, concern has been raised about carbon frozen in sediments deep below the soils of permafrost ecosystems or frozen in ocean sediments, known as methane hydrates or clathrates, which are methane molecules locked within a cage of ice molecules. Hydrates are stable at low temperatures and high pressures, conditions that are found below permafrost and in ocean sediments. As global warming affects both the permafrost and the oceans, there are concerns this warming could destabilise hydrates, releasing methane into the atmosphere and significantly exacerbating climate change.

The global marine hydrate reserve is currently estimated at 2000 PgC, which is smaller than initially thought. Global warming takes millennia to penetrate into the deep ocean and reach these hydrates, so the hydrate that could be destabilised during a century timescale is a small fraction of the total estimated marine hydrate reserve. Finally, even when methane is released from hydrates, most of it is expected to be either consumed or oxidised to carbon dioxide in the ocean before reaching the atmosphere. The most complete modelling of these processes to date suggests a release of less than 5 $TgCH_4\ yr^{-1}$ over the next century, which is less than 2% of current anthropogenic methane emissions.

[START FAQ 5.2, FIGURE 1 HERE]

FAQ 5.2, Figure 1: [Figure Placeholder: Schematic of the processes that affect permafrost thawing (what speeds up or slows down the release of GHG emissions.)]

[END FAQ 5.2, FIGURE 1 HERE]

FAQ 5.3: Can negative emissions reverse climate change?

Negative emissions refer to the deliberate removal of carbon dioxide (CO_2) from the atmosphere. If deliberate CO_2 removal exceeds anthropogenic CO_2 release, emissions are said to be net negative. The effect of negative emissions on atmospheric CO_2 depends on the balance between anthropogenic CO_2 releases, deliberate removals and removals by natural carbon sinks. Generally, net negative emissions result in a decline in atmospheric CO_2. However, because of the delayed reaction of many climate system components such as vegetation, soils, the deep ocean, ice sheets, a decline in atmospheric CO_2 would not result in immediate attenuation of climate changes. While some parts of the Earth's climate system such as surface air temperature would follow a decline in atmospheric CO_2 quite rapidly, others would take decades to millennia to react.

Negative emissions refer to removal of carbon dioxide (CO_2) from the atmosphere by deliberate human activities; that means, in addition to the removal that would occur naturally. The term negative emissions is often used as synonymous with carbon dioxide removal (CDR). Negative emissions can compensate release of CO_2 into the atmosphere by human activities. They could be achieved by strengthening marine and/or terrestrial CO_2 sequestration or by removing CO_2 directly from the atmosphere. If negative emissions are greater than anthropogenic CO_2 releases, emissions are said to be *net* negative.

In the absence of negative emissions, the CO_2 concentration in the atmosphere (a measure of the amount of CO_2 in the atmosphere) results from a balance between anthropogenic CO_2 release and removal by natural processes on land and in the ocean (natural 'carbon sinks'). If CO_2 release exceeds removal by carbon sinks, the CO_2 concentration in the atmosphere would increase; if CO_2 release equals removal the, atmospheric CO_2 concentration would stabilise; and if CO_2 removal exceeds release, the CO_2 concentration would decline. This applies in the same way to <u>*net*</u> emissions (that is the sum of anthropogenic releases and deliberate removals)

If the CO_2 concentration in the atmosphere starts to go down, the Earth's climate would respond to this change. Some parts of the climate system have a delayed reaction to a change in CO_2 in the atmosphere and a decline in atmospheric CO_2 through net negative emissions would therefore not imply a simultaneous attenuation of climate change. Recent studies have shown that surface air temperature starts to decline within a few years following a decline in atmospheric CO_2. Other components of the climate system, however, such as vegetation, soils, the deep ocean, ice sheets, take decades to millennia to react to the decline in atmospheric CO_2. For these components, net negative emissions would not result in an immediate attenuation of changes caused by CO_2. For instance, warming, acidification and oxygen loss of the deep ocean would take centuries to reverse following a decline in the atmospheric CO_2 concentration. Sea level rise due to warming and expansion of seawater would continue for centuries even if large amounts of negative emissions would be implemented.

A class of future scenarios that is receiving increasing attention, particularly in the context of ambitious climate goals, such as the 1.5°C and 2°C goals included in the Paris Agreement, are so-called 'overshoot' scenarios. In these scenarios slow emission reductions in the near term are compensated by net negative CO_2 emissions in the later part of this century, which results in a temporary breach or "overshoot" of a specific temperature level. Due to the delayed reaction of several climate system components it follows that the temporary breach of a temperature goal level would result in additional climate changes (compared to a scenario that reaches the goal level without overshoot) that would take decades to many centuries to reverse, with longer reversal times for scenarios with larger overshoot.

In conclusion, negative emissions can only reverse climate change to a limited degree. Some parts of the Earth's climate system such as surface air temperature would follow a decline in atmospheric CO_2 within a few years, while others such as sea level rise would take multiple centuries to reverse.

[START FAQ 5.3, FIGURE 1 HERE]

FAQ 5.3, Figure 1: [Figure suggestion – Time series of responses of climate system components with short to long response time scales (short term would include things like surface air temperature, long term would be warming, acidification and oxygen loss of the deep ocean, sea level etc.).]

[END FAQ 5.3, FIGURE 1 HERE]

FAQ 5.4: What is the remaining carbon budget?

The remaining carbon budget is to the total net amount of carbon dioxide emission that can still be emitted by human activities, while managing to keep global warming below a specific maximum temperature threshold. Several choices and value judgments have to be made before it can be unambiguously estimated. When combined with all CO_2 emissions that have been emitted to date, also a total carbon budget compatible with a specific temperature limit can be defined.

The term remaining carbon budget is used to describe the total net amount of carbon dioxide that human activities would still be allowed to release into the atmosphere while keeping global warming to a specific temperature threshold, like 1.5°C or 2°C relative to pre-industrial levels. Underlying the concept of a remaining carbon budget is our understanding that global warming is roughly linearly proportional to the total net amount of carbon dioxide emissions – also referred to as cumulative carbon dioxide emissions – that are released into the atmosphere by human activities. This characteristic only holds true for carbon dioxide, because of the specific way carbon dioxide behaves in the Earth system. The concept of a remaining carbon budgets comes with some direct implications. It means that to halt global warming, global emissions of carbon dioxide need to be reduced to net zero levels. It also means that if emissions are not reduced in the next decade, deeper and faster reductions in carbon dioxide emissions are required thereafter.

The size of the remaining carbon budget can be estimates but is conditional on a set of choices. These choices include the global warming level that is chosen as a limit (for example, 1.5°C or 2°C relative to pre-industrial levels), the probability with which we want to ensure that warming is held below that limit (for example, a 50%, 66% or higher probability), and how successful we are in limiting emissions of other non-CO_2 forcing agents that affect the climate, such as methane or nitrous oxide. These choices can be informed by science but ultimately represent subjective value judgments. Once they have been made, knowledge about how much our planet has already warmed to date, of the amount of warming per cumulative tonne of CO_2, and about the amount of warming that is still expected once global net CO_2 emissions are brought down to zero can be combined to estimate how much of a carbon budget remains for a given temperature target.

The remaining carbon budget by definitions starts from today, but warming is also caused by historical emissions which are estimated by looking at the historical carbon budget. The historical carbon budget describes all past and present sources and sinks of CO_2. It thus describes how the CO_2 emissions that were emitted by human activities have redistributed across the various reservoirs of the Earth system. These are the ocean, the land biosphere, and the atmosphere, into which CO_2 emissions were released to start with. Whatever amount of carbon dioxide emissions that is not taken up by the ocean or the land biosphere results in an increase of atmospheric CO_2 concentrations, and therewith further drives global warming. CO_2 taken up by the ocean is not harmless, because it results in changing the chemistry of the ocean water, reducing its alkalinity. This process is known as ocean acidification. The study of the historical carbon budget teaches us that of the about 2440 billion tonnes of CO_2 that were released into the atmosphere by human activities between 1750 and 2017, about a quarter was absorbed by the ocean, and about a third by the land biosphere. About 40% of these emissions remains currently in the atmosphere. Adding these historical CO_2 emissions to estimates of remaining carbon budgets allows one to estimate the total budget consistent with a specific temperature goal.

[START FAQ 5.4, FIGURE 1 HERE]

FAQ 5.4, Figure 1: [Figure idea: visual combining the historical carbon budget, with straight lines going down from today's emissions to zero, and in line with the remaining carbon budget for 1.5°C or 2°C – coloured and labelled differently to make the difference clear.]

[END FAQ 5.4, FIGURE 1 HERE]

References

Abatzoglou, J. T., Williams, A. P., and Barbero, R. (2019). Global emergence of anthropogenic climate change in fire weather indices. *Geophys. Res. Lett.* 46, 326–336. doi:10.1029/2018GL080959.

Achat, D. L., Augusto, L., Gallet-Budynek, A., and Loustau, D. (2016). Future challenges in coupled C–N–P cycle models for terrestrial ecosystems under global change: a review. *Biogeochemistry* 131, 173–202. doi:10.1007/s10533-016-0274-9.

Adams, C. A., Andrews, J. E., and Jickells, T. (2012). Nitrous oxide and methane fluxes vs. carbon, nitrogen and phosphorous burial in new intertidal and saltmarsh sediments. *Sci. Total Environ.* 434, 240–251. doi:10.1016/j.scitotenv.2011.11.058.

Agusti, S., Lubián, L. M., Moreno-Ostos, E., Estrada, M., and Duarte, C. M. (2019). Projected changes in photosynthetic picoplankton in a warmer subtropical ocean. *Front. Mar. Sci.* 5. doi:10.3389/fmars.2018.00506.

Ahlstrom, A., Raupach, M. R., Schurgers, G., Smith, B., Arneth, A., Jung, M., et al. (2015). The dominant role of semi-arid ecosystems in the trend and variability of the land CO2 sink. *Science* 348, 895–899. doi:10.1126/science.aaa1668.

Ainsworth, E. A., and Long, S. P. (2005). What have we learned from 15 years of free-air CO2 enrichment (FACE)? A meta-analytic review of the responses of photosynthesis, canopy properties and plant production to rising CO2. *New Phytol.* 165, 351–372. doi:10.1111/j.1469-8137.2004.01224.x.

Albani, S., Balkanski, Y., Mahowald, N., Winckler, G., Maggi, V., and Delmonte, B. (2018). Aerosol-climate interactions during the last glacial maximum. *Curr. Clim. Chang. Reports* 4, 99–114. doi:10.1007/s40641-018-0100-7.

Allen, G. H., and Pavelsky, T. M. (2018). Global extent of rivers and streams. *Science* 361, 585–588. doi:10.1126/science.aat0636.

Allen, M. R., Dube, O. P., Solecki, W., Aragón-Durand, F., Cramer, W., Humphreys, S., et al. (2018). "Framing and Context," in *Global Warming of 1.5°C. An IPCC Special Report on the impacts of global warming of 1.5°C above pre-industrial levels and related global greenhouse gas emission pathways, in the context of strengthening the global response to the threat of climate change,* eds. V. Masson-Delmotte, P. Zhai, H.-O. Pörtner, D. Roberts, J. Skea, P. R. Shukla, et al. (In Press).

Allen, M. R., Frame, D. J., Huntingford, C., Jones, C. D., Lowe, J. A., Meinshausen, M., et al. (2009). Warming caused by cumulative carbon emissions towards the trillionth tonne. *Nature* 458, 1163–1166. doi:10.1038/nature08019.

Allen, M. R., and Ingram, W. J. (2002). Constraints on future changes in climate and the hydrologic cycle. *Nature* 419, 228–232. doi:10.1038/nature01092.

Anadón, J. D., Sala, O. E., and Maestre, F. T. (2014). Climate change will increase savannas at the expense of forests and treeless vegetation in tropical and subtropical Americas. *J. Ecol.* 102, 1363–1373. doi:10.1111/1365-2745.12325.

Anagnostou, E., John, E. H., Edgar, K. M., Foster, G. L., Ridgwell, A., Inglis, G. N., et al. (2016). Changing atmospheric CO2 concentration was the primary driver of early Cenozoic climate. *Nature* 533, 380–384. doi:10.1038/nature17423.

Anav, A., Friedlingstein, P., Beer, C., Ciais, P., Harper, A., Jones, C., et al. (2015). Spatiotemporal patterns of terrestrial gross primary production: A review. *Rev. Geophys.* doi:10.1002/2015RG000483.

Anav, A., Friedlingstein, P., Kidston, M., Bopp, L., Ciais, P., Cox, P., et al. (2013). Evaluating the Land and Ocean Components of the Global Carbon Cycle in the CMIP5 Earth System Models. *J. Clim.* 26, 6801–6843. doi:10.1175/JCLI-D-12-00417.1.

Andela, N., Morton, D. C., Giglio, L., Chen, Y., Van Der Werf, G. R., Kasibhatla, P. S., et al. (2017). A human-driven decline in global burned area. *Science* 1356, 1356–1362. doi:10.1126/science.aal4108.

Andela, N., and Van Der Werf, G. R. (2014). Recent trends in African fires driven by cropland expansion and El Niño to la Niña transition. *Nat. Clim. Chang.* doi:10.1038/nclimate2313.

Anderson, K., and Peters, G. (2016). The trouble with negative emissions. *Science* 354, 182 LP – 183. doi:10.1126/science.aah4567.

Anderson, L. G., Ek, J., Ericson, Y., Humborg, C., Semiletov, I., Sundbom, M., et al. (2017). Export of calcium carbonate corrosive waters from the East Siberian Sea. *Biogeosciences* 14, 1811–1823. doi:10.5194/bg-14-1811-2017.

Anderson, R. F., Sachs, J. P., Fleisher, M. Q., Allen, K. A., Yu, J., Koutavas, A., et al. (2019). Deep-Sea Oxygen Depletion and Ocean Carbon Sequestration During the Last Ice Age. *Global Biogeochem. Cycles* 33, 301–317. doi:10.1029/2018GB006049.

Andrew, R. M. (2018). Global CO2 emissions from cement production. *Earth Syst. Sci. Data* 10, 195–217. doi:10.5194/essd-10-195-2018.

Aragão, L. E. O. C., Anderson, L. O., Fonseca, M. G., Rosan, T. M., Vedovato, L. B., Wagner, F. H., et al. (2018). 21st Century drought-related fires counteract the decline of Amazon deforestation carbon emissions. *Nat. Commun.* 9, 536. doi:10.1038/s41467-017-02771-y.

Araujo, M., Noriega, C., and Lefèvre, N. (2014). Nutrients and carbon fluxes in the estuaries of major rivers flowing into the tropical Atlantic. *Front. Mar. Sci.* 1. doi:10.3389/fmars.2014.00010.

Araujo, M., Noriega, C., Medeiros, C., Lefèvre, N., Ibánhez, J. S. P., Flores Montes, M., et al. (2019). On the variability in the CO2 system and water productivity in the western tropical Atlantic off North and Northeast Brazil. *J. Mar. Syst.* 189, 62–77. doi:10.1016/j.jmarsys.2018.09.008.

Archer, D., Buffett, B., and Brovkin, V. (2009). Ocean methane hydrates as a slow tipping point in the global carbon cycle. *Proc. Natl. Acad. Sci.* 106, 20596–20601. doi:10.1073/pnas.0800885105.

Archer, D., Kheshgi, H., and Maier-Reimer, E. (1998). Dynamics of fossil fuel CO2 neutralization by marine CaCO3. *Global Biogeochem. Cycles* 12, 259–276. doi:10.1029/98GB00744.

Arévalo-Martínez, D. L., Kock, A., Löscher, C. R., Schmitz, R. A., and Bange, H. W. (2015). Massive nitrous oxide emissions from the tropical South Pacific Ocean. *Nat. Geosci.* 8, 530–533. doi:10.1038/ngeo2469.

Armstrong McKay, D. I., and Lenton, T. M. (2018). Reduced carbon cycle resilience across the Paleocene--Eocene Thermal Maximum. *Clim. Past* 14, 1515–1527. doi:10.5194/cp-14-1515-2018.

Arneth, A., Harrison, S. P., Zaehle, S., Tsigaridis, K., Menon, S., Bartlein, P. J., et al. (2010). Terrestrial biogeochemical feedbacks in the climate system. *Nat. Geosci.* 3, 525–532. doi:10.1038/ngeo905.

Arneth, A., Sitch, S., Pongratz, J., Stocker, B. D., Ciais, P., Poulter, B., et al. (2017). Historical carbon dioxide emissions caused by land-use changes are possibly larger than assumed. *Nat. Geosci.* 10, 79–84. doi:10.1038/ngeo2882.

Arora, V. K., Boer, G. J., Friedlingstein, P., Eby, M., Jones, C. D., Christian, J. R., et al. (2013). Carbon–concentration and carbon–climate feedbacks in CMIP5 Earth system models. *J. Clim.* 26, 5289–5314. doi:10.1175/JCLI-D-12-00494.1.

Arora, V. K., Katavouta, A., Williams, R. G., Jones, C. D., Brovkin, V., Schwinger, J., et al. (submitted). Carbon-concentration and carbon-climate feedbacks in CMIP6 models, and their comparison to CMIP5 models. *Biogeosciences Discuss.* (submitted). doi:10.5194/bg-2019-473.

Arora, V. K., and Melton, J. R. (2018). Reduction in global area burned and wildfire emissions since 1930s enhances carbon uptake by land. *Nat. Commun.* 9, 1326. doi:10.1038/s41467-018-03838-0.

Arzhanov, M. M., and Mokhov, I. I. (2017). Stability of continental relic methane hydrates for the holocene climatic optimum and for contemporary conditions. *Dokl. Earth Sci.* 476, 1163–1167. doi:10.1134/S1028334X17100026.

Arzhanov, M. M., Mokhov, I. I., and Denisov, S. N. (2016). Impact of regional climatic change on the stability of relic gas hydrates. *Dokl. Earth Sci.* 468, 616–618. doi:10.1134/S1028334X1606009X.

Ashwin, P., Wieczorek, S., Vitolo, R., and Cox, P. (2012). Tipping points in open systems: bifurcation, noise-induced and rate-dependent examples in the climate system. *Philos. Trans. R. Soc. A Math. Phys. Eng. Sci.* 370, 1166–1184. doi:10.1098/rsta.2011.0306.

Aumont, O., and Bopp, L. (2006). Globalizing results from ocean in situ iron fertilization studies. *Global Biogeochem. Cycles* 20, GB2017. doi:10.1029/2005GB002591.

Aumont, O., Ethé, C., Tagliabue, A., Bopp, L., and Gehlen, M. (2015). PISCES-v2: an ocean biogeochemical model for carbon and ecosystem studies. *Geosci. Model Dev.* 8, 2465–2513. doi:10.5194/gmd-8-2465-2015.

Azetsu-Scott, K., Clarke, A., Falkner, K., Hamilton, J., Jones, E. P., Lee, C., et al. (2010). Calcium carbonate saturation states in the waters of the Canadian Arctic Archipelago and the Labrador Sea. *J. Geophys. Res.* 115, C11021. doi:10.1029/2009JC005917.

Babbin, A. R., Bianchi, D., Jayakumar, A., and Ward, B. B. (2015). Rapid nitrous oxide cycling in the suboxic ocean. *Science* 348, 1127–1129. doi:10.1126/science.aaa8380.

Babila, T. L., Penman, D. E., Hönisch, B., Kelly, D. C., Bralower, T. J., Rosenthal, Y., et al. (2018). Capturing the global signature of surface ocean acidification during the Paleocene–Eocene Thermal Maximum. *Philos. Trans. R. Soc. A Math. Phys. Eng. Sci.* 376, 20170072. doi:10.1098/rsta.2017.0072.

Bacastow, R. B., Adams, J. A., Keeling, C. D., Moss, D. J., Whorf, T. P., and Wong, C. S. (1980). Atmospheric carbon dioxide, the Southern oscillation, and the weak 1975 El Nino. *Science* 210, 66–68. doi:10.1126/science.210.4465.66.

Baig, S., Medlyn, B. E., Mercado, L. M., and Zaehle, S. (2015). Does the growth response of woody plants to elevated CO2increase with temperature? A model-oriented meta-analysis. *Glob. Chang. Biol.* 21, 4303–4319. doi:10.1111/gcb.12962.

Bakker, D. C. E., Pfeil, B., Landa, C. S., Metzl, N., O'Brien, K. M., Olsen, A., et al. (2016). A multi-decade record of high-quality fCO2 data in version 3 of the Surface Ocean CO2 Atlas (SOCAT). *Earth Syst. Sci. Data* 8, 383–413. doi:10.5194/essd-8-383-2016.

Ballantyne, A. P., Alden, C. B., Miller, J. B., Tans, P. P., and White, J. W. C. (2012). Increase in observed net carbon dioxide uptake by land and oceans during the past 50 years. *Nature* 488, 70–72. doi:10.1038/nature11299.

Ballantyne, A., Smith, W., Anderegg, W., Kauppi, P., Sarmiento, J., Tans, P., et al. (2017). Accelerating net terrestrial carbon uptake during the warming hiatus due to reduced respiration. *Nat. Clim. Chang.* 7, 148–152. doi:10.1038/nclimate3204.

Bândă, N., Krol, M., van Weele, M., van Noije, T., Le Sager, P., and Röckmann, T. (2016). Can we explain the observed methane variability after the Mount Pinatubo eruption? *Atmos. Chem. Phys.* 16, 195–214. doi:10.5194/acp-16-195-2016.

Barker, S. (2002). Foraminiferal Calcification Response to Glacial-Interglacial Changes in Atmospheric CO2. *Science* 297, 833–836. doi:10.1126/science.1072815.

Barker, S., Higgins, J. A., and Elderfield, H. (2003). The future of the carbon cycle: review, calcification response, ballast and feedback on atmospheric CO2. *Philos. Trans. R. Soc. London. Ser. A Math. Phys. Eng. Sci.* 361, 1977–1999. doi:10.1098/rsta.2003.1238.

Bastin, J.-F., Finegold, Y., Garcia, C., Mollicone, D., Rezende, M., Routh, D., et al. (2019). The global tree restoration potential. *Science* 365, 76 LP – 79. doi:10.1126/science.aax0848.

Bastos, A., Friedlingstein, P., Sitch, S., Chen, C., Mialon, A., Wigneron, J.-P., et al. (2018). Impact of the 2015/2016 El Niño terrestrial carbon cycle constrained by bottom-up and top-down approaches. *Philos. Trans. R. Soc. B Biol. Sci.* 373, 1–11. doi:10.1098/rstb.2017.0304.

Bastos, A., Janssens, I. A., Gouveia, C. M., Trigo, R. M., Ciais, P., Chevallier, F., et al. (2016). European land CO2 sink influenced by NAO and East-Atlantic Pattern coupling. *Nat. Commun.* 7, 10315. doi:10.1038/ncomms10315.

Bastos, A., O'Sullivan, M., Ciais, P., Makowski, D., Sitch, S., Friedlingstein, P., et al. (submitted). Source of uncertainty in regional and global terrestrial CO2-exchange estimates. *Global Biogeochem. Cycles* (submitted).

Bates, N. R., Astor, Y. M. A., Church, M. J., Currie, K., Dore, J. E., Gonaález-Dávila, M., et al. (2014). A time-series view of changing ocean chemistry due to ocean uptake of anthropogenic CO2 and ocean acidification. *Oceanography* 27, 126–141. doi:10.5670/oceanog.2014.16.

Bates, N. R., Mathis, J. T., and Cooper, L. W. (2009). Ocean acidification and biologically induced seasonality of carbonate mineral saturation states in the western Arctic Ocean. *J. Geophys. Res.* 114, C11007. doi:10.1029/2008JC004862.

Bathiany, S., Claussen, M., Brovkin, V., Raddatz, T., and Gayler, V. (2010). Combined biogeophysical and biogeochemical effects of large-scale forest cover changes in the MPI earth system model. *Biogeosciences* 7, 1383–1399. doi:10.5194/bg-7-1383-2010.

Batjes, N. H. (2016). Harmonized soil property values for broad-scale modelling (WISE30sec) with estimates of global soil carbon stocks. *Geoderma* 269, 61–68. doi:10.1016/j.geoderma.2016.01.034.

Battaglia, G., and Joos, F. (2018a). Hazards of decreasing marine oxygen: the near-term and millennial-scale benefits of meeting the Paris climate targets. *Earth Syst. Dyn.* 9, 797–816. doi:10.5194/esd-9-797-2018.

Battaglia, G., and Joos, F. (2018b). Marine N2O emissions from nitrification and denitrification constrained by modern observations and projected in multimillennial global warming simulations. *Global Biogeochem. Cycles* 32, 92–121. doi:10.1002/2017GB005671.

Bauska, T. K., Baggenstos, D., Brook, E. J., Mix, A. C., Marcott, S. A., Petrenko, V. V., et al. (2016). Carbon isotopes characterize rapid changes in atmospheric carbon dioxide during the last deglaciation. *Proc. Natl. Acad. Sci.* 113, 3465–3470. doi:10.1073/pnas.1513868113.

Beaufort, L., Probert, I., de Garidel-Thoron, T., Bendif, E. M., Ruiz-Pino, D., Metzl, N., et al. (2011). Sensitivity of coccolithophores to carbonate chemistry and ocean acidification. *Nature* 476, 80–83. doi:10.1038/nature10295.

Beaulieu, J. J., DelSontro, T., and Downing, J. A. (2019). Eutrophication will increase methane emissions from lakes and impoundments during the 21st century. *Nat. Commun.* 10, 1375. doi:10.1038/s41467-019-09100-5.

Beerling, D. J., Leake, J. R., Long, S. P., Scholes, J. D., Ton, J., Nelson, P. N., et al. (2018). Farming with crops and rocks to address global climate, food and soil security. *Nat. Plants* 4, 138–147. doi:10.1038/s41477-018-0108-y.

Belshe, E. F., Schuur, E. A. G., and Bolker, B. M. (2013). Tundra ecosystems observed to be CO2 sources due to differential amplification of the carbon cycle. *Ecol. Lett.* 16, 1307–1315. doi:10.1111/ele.12164.

Beman, J. M., and Carolan, M. T. (2013). Deoxygenation alters bacterial diversity and community composition in the ocean's largest oxygen minimum zone. *Nat. Commun.* 4, 2705. Available at: https://doi.org/10.1038/ncomms3705.

Benanti, G., Saunders, M., Tobin, B., and Osborne, B. (2014). Contrasting impacts of afforestation on nitrous oxide and methane emissions. *Agric. For. Meteorol.* 198–199, 82–93. doi:10.1016/j.agrformet.2014.07.014.

Bendtsen, J., Hilligsøe, K. M., Hansen, J. L. S., and Richardson, K. (2015). Analysis of remineralisation, lability, temperature sensitivity and structural composition of organic matter from the upper ocean. *Prog. Oceanogr.* 130, 125–145. doi:10.1016/j.pocean.2014.10.009.

Bennedsen, M., Hillebrand, E., and Jan Koopman, S. (2019). Trend analysis of the airborne fraction and sink rate of anthropogenically released CO2. *Biogeosciences* 16, 3651–3663. doi:10.5194/bg-16-3651-2019.

Beringer, T., Lucht, W., and Schaphoff, S. (2011). Bioenergy production potential of global biomass plantations under environmental and agricultural constraints. *GCB Bioenergy* 3, 299–312. doi:10.1111/j.1757-1707.2010.01088.x.

Bernardello, R., Marinov, I., Palter, J. B., Sarmiento, J. L., Galbraith, E. D., and Slater, R. D. (2014). Response of the ocean natural carbon storage to projected twenty-first-century climate change. *J. Clim.* 27, 2033–2053. doi:10.1175/JCLI-D-13-00343.1.

Berthet, S., Séférian, R., Bricaud, C., Chevallier, M., Voldoire, A., and Ethé, C. (2019). Evaluation of an Online Grid-Coarsening Algorithm in a Global Eddy-Admitting Ocean Biogeochemical Model. *J. Adv. Model. Earth Syst.* 11, 1759–1783. doi:10.1029/2019MS001644.

Betts, R. A., Jones, C. D., Knight, J. R., Keeling, R. F., Kennedy, J. J., Wiltshire, A. J., et al. (2018). A successful prediction of the record CO2 rise associated with the 2015/2016 El Niño. *Philos. Trans. R. Soc. B Biol. Sci.* 373, 20170301. doi:10.1098/rstb.2017.0301.

BGR (2017). BGR Energy Study 2017 - Data and Developments Concerning German and Global Energy Supplies. Hannover.

Bianchi, D., Dunne, J. P., Sarmiento, J. L., and Galbraith, E. D. (2012). Data-based estimates of suboxia, denitrification, and N 2 O production in the ocean and their sensitivities to dissolved O 2. *Global Biogeochem. Cycles* 26, GB2009. doi:10.1029/2011GB004209.

Bindoff, N.L., W.W.L. Cheung, J.G. Kairo, J. Arístegui, V.A. Guinder, R. Hallberg, N. Hilmi, N. Jiao, M.S. Karim, L. Levin, S. O'Donoghue, S.R. Purca Cuicapusa, B. Rinkevich, T. Suga, A. Tagliabue, and P. W. (2019). "Changing Ocean, Marine Ecosystems, and Dependent Communities," in *IPCC Special Report on the Ocean and Cryosphere in a Changing Climate*, ed. N. M. W. H.-O. Pörtner, D.C. Roberts, V. Masson-Delmotte, P. Zhai, M. Tignor, E. Poloczanska, K. Mintenbeck, A. Alegría, M. Nicolai, A. Okem, J. Petzold, B. Rama.

Bock, M., Schmitt, J., Beck, J., Seth, B., Chappellaz, J., and Fischer, H. (2017). Glacial/interglacial wetland, biomass burning, and geologic methane emissions constrained by dual stable isotopic CH 4 ice core records. *Proc. Natl. Acad. Sci.* 114, E5778–E5786. doi:10.1073/pnas.1613883114.

Bock, M., Schmitt, J., Möller, L., Spahni, R., Blunier, T., and Fischer, H. (2010). Hydrogen isotopes preclude marine hydrate CH4 emissions at the onset of Dansgaard-Oeschger events. *Science* 328, 1686–9. doi:10.1126/science.1187651.

Boden, T. A., Marland, G., and Andres, R. J. (2017). Global, Regional, and National Fossil-Fuel CO2 Emissions. *Oak Ridge*.

Bopp, L., Resplandy, L., Orr, J. C., Doney, S. C., Dunne, J. P., Gehlen, M., et al. (2013). Multiple stressors of ocean ecosystems in the 21st century: projections with CMIP5 models. *Biogeosciences* 10, 6225–6245. doi:10.5194/bg-10-6225-2013.

Bopp, L., Resplandy, L., Untersee, A., Le Mezo, P., and Kageyama, M. (2017). Ocean (de)oxygenation from the Last Glacial Maximum to the twenty-first century: insights from Earth System models. *Philos. Trans. R. Soc. A Math. Phys. Eng. Sci.* 375, 20160323. doi:10.1098/rsta.2016.0323.

Borges, A. V., and Abril, G. (2011). "Carbon Dioxide and Methane Dynamics in Estuaries," in *Treatise on Estuarine and Coastal Science* (Elsevier), 119–161. doi:10.1016/B978-0-12-374711-2.00504-0.

Boscolo-Galazzo, F., Crichton, K. A., Barker, S., and Pearson, P. N. (2018). Temperature dependency of metabolic rates in the upper ocean: A positive feedback to global climate change? *Glob. Planet. Change* 170, 201–212. doi:10.1016/j.gloplacha.2018.08.017.

Boulton, C. A., Booth, B. B. B., and Good, P. (2017). Exploring uncertainty of Amazon dieback in a perturbed parameter Earth system ensemble. *Glob. Chang. Biol.* 23, 5032–5044. doi:10.1111/gcb.13733.

Bouwman, L., Daniel, J. S., Davidson, E. A., de Klein, C., Holland, E., Ju, X., et al. (2013). *Drawing down N2O to protect climate and the ozone layer. A UNEP Synthesis report*. United Nations Environment Programme (UNEP).

Bowen, G. J., and Zachos, J. C. (2010). Rapid carbon sequestration at the termination of the Paleocene–Eocene Thermal Maximum. *Nat. Geosci.* 3, 866–869. doi:10.1038/ngeo1014.

Bowman, D. M. J. S., Williamson, G. J., Abatzoglou, J. T., Kolden, C. A., Cochrane, M. A., and Smith, A. M. S. (2017). Human exposure and sensitivity to globally extreme wildfire events. *Nat. Ecol. Evol.* doi:10.1038/s41559-016-0058.

Boyd, P. W., Claustre, H., Levy, M., Siegel, D. A., and Weber, T. (2019). Multi-faceted particle pumps drive carbon sequestration in the ocean. *Nature* 568, 327–335. doi:10.1038/s41586-019-1098-2.

Boyd, P. W., Jickells, T., Law, C. S., Blain, S., Boyle, E. A., Buesseler, K. O., et al. (2007). Mesoscale Iron Enrichment Experiments 1993-2005: Synthesis and Future Directions. *Science* 315, 612–617. doi:10.1126/science.1131669.

Boyd, P. W., Lennartz, S. T., Glover, D. M., and Doney, S. C. (2015). Biological ramifications of climate-change-mediated oceanic multi-stressors. *Nat. Clim. Chang.* 5, 71–79. doi:10.1038/nclimate2441.

Boysen, L. R., Lucht, W., and Gerten, D. (2017a). Trade-offs for food production, nature conservation and climate limit the terrestrial carbon dioxide removal potential. *Glob. Chang. Biol.* 23, 4303–4317. doi:10.1111/gcb.13745.

Boysen, L. R., Lucht, W., Gerten, D., Heck, V., Lenton, T. M., and Schellnhuber, H. J. (2017b). The limits to global-warming mitigation by terrestrial carbon removal. *Earth's Futur.* 5, 463–474. doi:10.1002/2016EF000469.

BP (2018). BP Statistical Review of World Energy June 2018. Available at: https://www.bp.com/content/dam/bp/%0Aen/corporate/pdf/energy-economics/statistical-review/%0Abp-stats-review-2018-full-report.pdf.

Brady, R., Lovenduski, N., Yeager, S., Long, M., and Lindsay, K. (submitted). Skillful multiyear predictions of ocean acidification in the California Current System. *Nat. Commun.* (submitted). Available at: https://eartharxiv.org/3m2h7/.

Bralower, T. J., Kump, L. R., Self-Trail, J. M., Robinson, M. M., Lyons, S., Babila, T., et al. (2018). Evidence for shelf acidification during the onset of the Paleocene-Eocene thermal maximum. *Paleoceanogr. Paleoclimatology* 33, 1408–1426. doi:10.1029/2018PA003382.

Brando, P. M., Balch, J. K., Nepstad, D. C., Morton, D. C., Putz, F. E., Coe, M. T., et al. (2014a). Abrupt increases in Amazonian tree mortality due to drought{\textendash}fire interactions. *Proc. Natl. Acad. Sci.* 111, 6347–6352. doi:10.1073/pnas.1305499111.

Brando, P. M., Balch, J. K., Nepstad, D. C., Morton, D. C., Putz, F. E., Coe, M. T., et al. (2014b). Abrupt increases in Amazonian tree mortality due to drought{\textendash}fire interactions. *Proc. Natl. Acad. Sci.* 111, 6347–6352. doi:10.1073/pnas.1305499111.

Breitburg, D., Levin, L. A., Oschlies, A., Grégoire, M., Chavez, F. P., Conley, D. J., et al. (2018). Declining oxygen in the global ocean and coastal waters. *Science* 359, eaam7240. doi:10.1126/science.aam7240.

Brennan, G., and Collins, S. (2015). Growth responses of a green alga to multiple environmental drivers. *Nat. Clim. Chang.* 5, 892–897. doi:10.1038/nclimate2682.

Brienen, R. J. W., Gloor, E., Clerici, S., Newton, R., Arppe, L., Boom, A., et al. (2017). Tree height strongly affects estimates of water-use efficiency responses to climate and CO2 using isotopes. *Nat. Commun.* 8, 288. doi:10.1038/s41467-017-00225-z.

Brienen, R. J. W., Phillips, O. L., Feldpausch, T. R., Gloor, E., Baker, T. R., Lloyd, J., et al. (2015). Long-term decline of the Amazon carbon sink. *Nature* 519, 344–348. doi:10.1038/nature14283.

Broucek, J. (2014). Production of Methane Emissions from Ruminant Husbandry: A Review. *J. Environ. Prot. (Irvine,. Calif).* 05, 1482–1493. doi:10.4236/jep.2014.515141.

Brovkin, V., Boysen, L., Arora, V. K., Boisier, J. P., Cadule, P., Chini, L., et al. (2013). Effect of anthropogenic land-use and land-cover changes on climate and land carbon storage in CMIP5 projections for the twenty-first century. *J. Clim.* 26, 6859–6881. doi:10.1175/JCLI-D-12-00623.1.

Brovkin, V., Brücher, T., Kleinen, T., Zaehle, S., Joos, F., Roth, R., et al. (2016). Comparative carbon cycle dynamics of the present and last interglacial. *Quat. Sci. Rev.* 137, 15–32. doi:10.1016/j.quascirev.2016.01.028.

Brovkin, V., Ganopolski, A., Archer, D., and Munhoven, G. (2012). Glacial CO2 cycle as a succession of key physical and biogeochemical processes. *Clim. Past* 8, 251–264. doi:10.5194/cp-8-251-2012.

Browman, H. I. (2016). Applying organized scepticism to ocean acidification research. *ICES J. Mar. Sci. J. du Cons.* 73, 529.1-536. doi:10.1093/icesjms/fsw010.

Brown, M. S., Munro, D. R., Feehan, C. J., Sweeney, C., Ducklow, H. W., and Schofield, O. M. (2019). Enhanced oceanic CO2 uptake along the rapidly changing West Antarctic Peninsula. *Nat. Clim. Chang.* 9, 678–683. doi:10.1038/s41558-019-0552-3.

Buchanan, P. J., Matear, R. J., Lenton, A., Phipps, S. J., Chase, Z., and Etheridge, D. M. (2016). The simulated climate of the Last Glacial Maximum and insights into the global marine carbon cycle. *Clim. Past* 12, 2271–2295. doi:10.5194/cp-12-2271-2016.

Buermann, W., Forkel, M., O'Sullivan, M., Sitch, S., Friedlingstein, P., Haverd, V., et al. (2018). Widespread seasonal compensation effects of spring warming on northern plant productivity. *Nature* 562, 110–114. doi:10.1038/s41586-018-0555-7.

Buitenhuis, E. T., Rivkin, R. B., Sailley, S., and Le Quéré, C. (2010). Biogeochemical fluxes through microzooplankton. *Global Biogeochem. Cycles* 24, GB4015. doi:10.1029/2009GB003601.

Buitenhuis, E. T., Suntharalingam, P., and Le Quéré, C. (2018). Constraints on global oceanic emissions of N2O from observations and models. *Biogeosciences* 15, 2161–2175. doi:10.5194/bg-15-2161-2018.

Buldovicz, S. N., Khilimonyuk, V. Z., Bychkov, A. Y., Ospennikov, E. N., Vorobyev, S. A., Gunar, A. Y., et al. (2018). Cryovolcanism on the Earth: prigin of a spectacular crater in the Yamal peninsula (Russia). *Sci. Rep.* 8, 13534. doi:10.1038/s41598-018-31858-9.

Burke, E. J., Chadburn, S. E., and Ekici, A. (2017a). A vertical representation of soil carbon in the JULES land surface scheme (vn4.3_permafrost) with a focus on permafrost regions. *Geosci. Model Dev.* 10, 959–975. doi:10.5194/gmd-10-959-2017.

Burke, E. J., Ekici, A., Huang, Y., Chadburn, S. E., Huntingford, C., Ciais, P., et al. (2017b). Quantifying uncertainties of permafrost carbon–climate feedbacks. *Biogeosciences* 14, 3051–3066. doi:10.5194/bg-14-3051-2017.

Burke, E. J., Jones, C. D., and Koven, C. D. (2013). Estimating the permafrost-carbon climate response in the CMIP5 climate models using a simplified approach. *J. Clim.* 26, 4897–4909. doi:10.1175/JCLI-D-12-00550.1.

Burney, J. A., Davis, S. J., and Lobell, D. B. (2010). Greenhouse gas mitigation by agricultural intensification. *Proc. Natl. Acad. Sci.* 107, 12052–12057. doi:10.1073/pnas.0914216107.

Butterbach-Bahl, K., Baggs, E. M., Dannenmann, M., Kiese, R., and Zechmeister-Boltenstern, S. (2013). Nitrous oxide emissions from soils: how well do we understand the processes and their controls? *Philos. Trans. R. Soc. B Biol. Sci.* 368, 20130122–20130122. doi:10.1098/rstb.2013.0122.

Byrne, R. H., Mecking, S., Feely, R. A., and Liu, X. (2010). Direct observations of basin-wide acidification of the North Pacific Ocean. *Geophys. Res. Lett.* 37, L02601. doi:10.1029/2009GL040999.

Cai, W.-J., Hu, X., Huang, W.-J., Murrell, M. C., Lehrter, J. C., Lohrenz, S. E., et al. (2011). Acidification of subsurface coastal waters enhanced by eutrophication. *Nat. Geosci.* 4, 766–770. doi:10.1038/ngeo1297.

Cai, W.-J., Huang, W.-J., Luther, G. W., Pierrot, D., Li, M., Testa, J., et al. (2017). Redox reactions and weak buffering capacity lead to acidification in the Chesapeake Bay. *Nat. Commun.* 8, 369. doi:10.1038/s41467-017-00417-7.

Cai, Y., Lenton, T. M., and Lontzek, T. S. (2016). Risk of multiple interacting tipping points should encourage rapid CO2 emission reduction. *Nat. Clim. Chang.* 6, 520. Available at: https://doi.org/10.1038/nclimate2964.

Cain, M., Lynch, J., Allen, M. R., Fuglestvedt, J. S., Frame, D. J., and Macey, A. H. (2019). Improved calculation of warming-equivalent emissions for short-lived climate pollutants. *npj Clim. Atmos. Sci.* 2. doi:10.1038/s41612-019-0086-4.

Campbell, J. E., Berry, J. A., Seibt, U., Smith, S. J., Montzka, S. A., Launois, T., et al. (2017). Large historical growth in global terrestrial gross primary production. *Nature* 544, 84–87. doi:10.1038/nature22030.

Cao, L. (2018). The effects of solar radiation management on the carbon cycle. *Curr. Clim. Chang. Reports*.

Cao, L., and Caldeira, K. (2010). Atmospheric carbon dioxide removal: long-term consequences and commitment. *Environ. Res. Lett.* 5, 024011. doi:10.1088/1748-9326/5/2/024011.

Cao, L., and Jiang, J. (2017). Simulated effect of carbon cycle feedback on climate response to solar geoengineering. *Geophys. Res. Lett.* 44, 12,484-12,491. doi:10.1002/2017GL076546.

Cao, L., Zhang, H., Zheng, M., and Wang, S. (2014). Response of ocean acidification to a gradual increase and decrease of atmospheric CO2. *Environ. Res. Lett.* 9, 024012. doi:10.1088/1748-9326/9/2/024012.

Carstensen, J., Andersen, J. H., Gustafsson, B. G., and Conley, D. J. (2014). Deoxygenation of the Baltic Sea during the last century. *Proc. Natl. Acad. Sci.* 111, 5628–5633. doi:10.1073/pnas.1323156111.

Carstensen, J., and Duarte, C. M. (2019). Drivers of pH variability in coastal ecosystems. *Environ. Sci. Technol.* 53, 4020–4029. doi:10.1021/acs.est.8b03655.

Cartapanis, O., Galbraith, E. D., Bianchi, D., and Jaccard, S. L. (2018). Carbon burial in deep-sea sediment and implications for oceanic inventories of carbon and alkalinity over the last glacial cycle. *Clim. Past* 14, 1819–1850. doi:10.5194/cp-14-1819-2018.

Carter, B. R., Feely, R. A., Mecking, S., Cross, J. N., Macdonald, A. M., Siedlecki, S. A., et al. (2017). Two decades of Pacific anthropogenic carbon storage and ocean acidification along Global Ocean Ship-based Hydrographic Investigations Program sections P16 and P02. *Global Biogeochem. Cycles* 31, 306–327. doi:10.1002/2016GB005485.

Carter, B. R., Feely, R. A., Wanninkhof, R., Kouketsu, S., Sonnerup, R. E., Pardo, P. C., et al. (2019). Pacific anthropogenic carbon between 1991 and 2017. *Global Biogeochem. Cycles* 33, 597–617. doi:10.1029/2018GB006154.

Cavan, E. L., Henson, S. A., and Boyd, P. W. (2019a). The sensitivity of subsurface microbes to ocean warming accentuates future declines in particulate carbon export. *Front. Ecol. Evol.* 6. doi:10.3389/fevo.2018.00230.

Cavan, E. L., Henson, S. A., and Boyd, P. W. (2019b). The Sensitivity of Subsurface Microbes to Ocean Warming Accentuates Future Declines in Particulate Carbon Export. *Front. Ecol. Evol.* 6. doi:10.3389/fevo.2018.00230.

Cayuela, M. L., van Zwieten, L., Singh, B. P., Jeffery, S., Roig, A., and Sánchez-Monedero, M. A. (2014). Biochar's role in mitigating soil nitrous oxide emissions: A review and meta-analysis. *Agric. Ecosyst. Environ.* 191, 5–16. doi:10.1016/j.agee.2013.10.009.

Chan, F., Barth, J., Kroeker, K., Lubchenco, J., and Menge, B. (2019). The dynamics and impact of ocean acidification and hypoxia: insights from sustained investigations in the northern California current large marine ecosystem. *Oceanography* 32, 62–71. doi:10.5670/oceanog.2019.312.

Chandra, N., Patra, P. K., Bisht, J. S. H., Ito, A., Morimoto, S., Janssens-Maenhout, G., et al. (submitted). Dominance of anthropogenic emissions on the global methane growth rate during 1988-2016. (submitted).

Chavez, F. P., Bertrand, A., Guevara-Carrasco, R., Soler, P., and Csirke, J. (2008). The northern Humboldt Current System: Brief history, present status and a view towards the future. *Prog. Oceanogr.* 79, 95–105. doi:10.1016/j.pocean.2008.10.012.

Chen, C.-C., Gong, G.-C., and Shiah, F.-K. (2007). Hypoxia in the East China Sea: One of the largest coastal low-oxygen areas in the world. *Mar. Environ. Res.* 64, 399–408. doi:10.1016/j.marenvres.2007.01.007.

Chen, C.-T. A., and Borges, A. V. (2009). Reconciling opposing views on carbon cycling in the coastal ocean: Continental shelves as sinks and near-shore ecosystems as sources of atmospheric CO2. *Deep Sea Res. Part II Top. Stud. Oceanogr.* 56, 578–590. doi:10.1016/j.dsr2.2009.01.001.

Chen, C.-T. A., Lui, H.-K., Hsieh, C.-H., Yanagi, T., Kosugi, N., Ishii, M., et al. (2017). Deep oceans may acidify faster than anticipated due to global warming. *Nat. Clim. Chang.* 7, 890–894. doi:10.1038/s41558-017-0003-y.

Chen, P., Zhou, M., Wang, S., Luo, W., Peng, T., Zhu, B., et al. (2019). Effects of afforestation on soil CH4 and N2O fluxes in a subtropical karst landscape. *Sci. Total Environ.*, 135974. doi:https://doi.org/10.1016/j.scitotenv.2019.135974.

Cheng, L., Zhang, L., Wang, Y.-P., Canadell, J. G., Chiew, F. H. S., Beringer, J., et al. (2017). Recent increases in terrestrial carbon uptake at little cost to the water cycle. *Nat. Commun.* 8, 110. doi:10.1038/s41467-017-00114-5.

Chevallier, F., Fisher, M., Peylin, P., Serrar, S., Bousquet, P., Bréon, F.-M., et al. (2005). Inferring CO2 sources and sinks from satellite observations: Method and application to TOVS data. *J. Geophys. Res.* 110, D24309. doi:10.1029/2005JD006390.

Chierici, M., and Fransson, A. (2009). Calcium carbonate saturation in the surface water of the Arctic Ocean: undersaturation in freshwater influenced shelves. *Biogeosciences* 6, 2421–2431. doi:10.5194/bg-6-2421-2009.

Chu, S. N., Wang, Z. A., Doney, S. C., Lawson, G. L., and Hoering, K. A. (2016). Changes in anthropogenic carbon storage in the Northeast Pacific in the last decade. *J. Geophys. Res. Ocean.* 121, 4618–4632. doi:10.1002/2016JC011775.

Chuvilin, E., Bukhanov, B., Davletshina, D., Grebenkin, S., and Istomin, V. (2018). Dissociation and self-preservation of gas hydrates in permafrost. *Geosciences* 8, 431. doi:10.3390/geosciences8120431.

Ciais, P., Sabine, C., Bala, G., Bopp, L., Brovkin, V., Canadell, J., et al. (2013). "Carbon and Other Biogeochemical Cycles," in *Climate Change 2013: The Physical Science Basis. Contribution of Working Group I to the Fifth Assessment Report of the Intergovernmental Panel on Climate Change*, eds. T. F. Stocker, D. Qin, G.-K. Plattner, M. Tignor, S. K. Allen, J. Boschung, et al. (Cambridge, United Kingdom and New York, NY, USA: Cambridge University Press). Available at: http://www.ipcc.ch/report/ar5/wg1/.

Ciais, P., Tagliabue, A., Cuntz, M., Bopp, L., Scholze, M., Hoffmann, G., et al. (2012). Large inert carbon pool in the terrestrial biosphere during the Last Glacial Maximum. *Nat. Geosci.* 5, 74–79. doi:10.1038/ngeo1324.

Ciais, P., Tan, J., Wang, X., Roedenbeck, C., Chevallier, F., Piao, S.-L., et al. (2019a). Five decades of northern land carbon uptake revealed by the interhemispheric CO2 gradient. *Nature* 568, 221–225. doi:10.1038/s41586-019-1078-6.

Ciais, P., Tan, J., Wang, X., Roedenbeck, C., Chevallier, F., Piao, S.-L., et al. (2019b). Five decades of northern land carbon uptake revealed by the interhemispheric CO2 gradient. *Nature* 568, 221–225. doi:10.1038/s41586-019-1078-6.

Claret, M., Galbraith, E. D., Palter, J. B., Bianchi, D., Fennel, K., Gilbert, D., et al. (2018). Rapid coastal deoxygenation due to ocean circulation shift in the northwest Atlantic. *Nat. Clim. Chang.* 8, 868–872. doi:10.1038/s41558-018-0263-1.

Clarke, L., Jiang, K., Akimoto, K., Babiker, M., Blanford, G., Fisher-Vanden, K., et al. (2014). "Assessing transformation pathways," in *Climate Change 2014: Mitigation of Climate Change. Contribution of Working Group III to the Fifth Assessment Report of the Intergovernmental Panel on Climate Change*, eds. O. Edenhofer, R. Pichs-Madruga, Y. Sokona, E. Farahani, S. Kadner, K. Seyboth, et al. (Cambridge, United Kingdom and New York, NY, USA: Cambridge University Press), 413–510.

Claustre, H., Johnson, K. S., and Takeshita, Y. (2020). Observing the global ccean with biogeochemical-argo. *Ann. Rev. Mar. Sci.* 12. doi:10.1146/annurev-marine-010419-010956.

Clement, D., and Gruber, N. (2018). The eMLR(C*) method to determine decadal changes in the global ocean storage of anthropogenic CO2. *Global Biogeochem. Cycles* 32, 654–679. doi:10.1002/2017GB005819.

Clough, T., Condron, L., Kammann, C., and Müller, C. (2013). A review of biochar and soil nitrogen dynamics. *Agronomy* 3, 275–293. doi:10.3390/agronomy3020275.

Codispoti, L. A. (2007). An oceanic fixed nitrogen sink exceeding 400 Tg N a−1 vs the concept of homeostasis in the fixed-nitrogen inventory. *Biogeosciences* 4, 233–253. doi:10.5194/bg-4-233-2007.

Codispoti, L. A. (2010). Interesting Times for Marine N2O. *Science* 327, 1339–1340. doi:10.1126/science.1184945.

Collier, N., Hoffman, F. M., Lawrence, D. M., Keppel-Aleks, G., Koven, C. D., Riley, W. J., et al. (2018). The International Land Model Benchmarking (ILAMB) system: design, theory, and implementation. *J. Adv. Model. Earth Syst.* 10, 2731–2754. doi:10.1029/2018MS001354.

Collins, M., Knutti, R., Arblaster, J., Dufresne, J.-L. J.-L., Fichefet, T., Friedlingstein, P., et al. (2013). "Long-term Climate Change: Projections, Commitments and Irreversibility," in *Climate Change 2013: The Physical Science Basis. Contribution of Working Group I to the Fifth Assessment Report of the Intergovernmental Panel on Climate Change*, eds. T. F. Stocker, D. Qin, G.-K. Plattner, M. Tignor, S. K. Allen, J. Boschung, et al. (Cambridge, United Kingdom and New York, NY, USA: Cambridge University Press), 1029–1136. doi:10.1017/CBO9781107415324.024.

Collins, W. J., Webber, C. P., Cox, P. M., Huntingford, C., Lowe, J., Sitch, S., et al. (2018). Increased importance of methane reduction for a 1.5 degree target. *Environ. Res. Lett.* 13, 054003. doi:10.1088/1748-9326/aab89c.

Comyn-Platt, E., Hayman, G., Huntingford, C., Chadburn, S. E., Burke, E. J., Harper, A. B., et al. (2018). Carbon budgets for 1.5 and 2°C targets lowered by natural wetland and permafrost feedbacks. *Nat. Geosci.* 11, 568–573. doi:10.1038/s41561-018-0174-9.

Conrad, C. J., and Lovenduski, N. S. (2015). Climate-driven variability in the Southern Ocean carbonate system. *J. Clim.* 28, 5335–5350. doi:10.1175/JCLI-D-14-00481.1.

Conway, T. J., Tans, P. P., Waterman, L. S., Thoning, K. W., Kitzis, D. R., Masarie, K. A., et al. (1994). Evidence for interannual variability of the carbon cycle from the National Oceanic and Atmospheric Administration/Climate monitoring and diagnostics laboratory global air sampling network. *J. Geophys. Res.* 99, 22831. doi:10.1029/94JD01951.

Cotovicz Jr., L. C., Knoppers, B. A., Brandini, N., Costa Santos, S. J., and Abril, G. (2015). A strong CO2 sink enhanced by eutrophication in a tropical coastal embayment (Guanabara Bay, Rio de Janeiro, Brazil). *Biogeosciences* 12, 6125–6146. doi:10.5194/bg-12-6125-2015.

Cotovicz, L. C., Knoppers, B. A., Brandini, N., Poirier, D., Costa Santos, S. J., Cordeiro, R. C., et al. (2018). Predominance of phytoplankton-derived dissolved and particulate organic carbon in a highly eutrophic tropical coastal embayment (Guanabara Bay, Rio de Janeiro, Brazil). *Biogeochemistry* 137, 1–14. doi:10.1007/s10533-017-0405-y.

Covey, K. R., and Megonigal, J. P. (2019). Methane production and emissions in trees and forests. *New Phytol.* 222, 35–51. doi:10.1111/nph.15624.

Cowtan, K., and Way, R. G. (2014). Coverage bias in the HadCRUT4 temperature series and its impact on recent temperature trends. *Q. J. R. Meteorol. Soc.* 140, 1935–1944. doi:10.1002/qj.2297.

Cox, P. M. (2019). Emergent constraints on climate-carbon cycle feedbacks. *Curr. Clim. Chang. Reports* 5, 275–281. doi:10.1007/s40641-019-00141-y.

Cox, P. M., Betts, R. A., Collins, M., Harris, P. P., Huntingford, C., and Jones, C. D. (2004). Amazonian forest dieback under climate-carbon cycle projections for the 21st century. *Theor. Appl. Climatol.* 78, 137–156. doi:10.1007/s00704-004-0049-4.

Cox, P. M., Betts, R. A., Jones, C. D., Spall, S. A., and Totterdell, I. J. (2000). Acceleration of global warming due to carbon-cycle feedbacks in a coupled climate model. *Nature* 408, 184–187. doi:10.1038/35041539.

Cox, P. M., Pearson, D., Booth, B. B., Friedlingstein, P., Huntingford, C., Jones, C. D., et al. (2013). Sensitivity of tropical carbon to climate change constrained by carbon dioxide variability. *Nature* 494, 341–344. doi:10.1038/nature11882.

Crain, C. M., Kroeker, K., and Halpern, B. S. (2008). Interactive and cumulative effects of multiple human stressors in marine systems. *Ecol. Lett.* 11, 1304–1315. doi:10.1111/j.1461-0248.2008.01253.x.

Creutzig, F., Ravindranath, N. H., Berndes, G., Bolwig, S., Bright, R., Cherubini, F., et al. (2015). Bioenergy and climate change mitigation: an assessment. *GCB Bioenergy* 7, 916–944. doi:10.1111/gcbb.12205.

Crichton, K. A., Bouttes, N., Roche, D. M., Chappellaz, J., and Krinner, G. (2016). Permafrost carbon as a missing link to explain CO2 changes during the last deglaciation. *Nat. Geosci.* 9, 683–686. doi:10.1038/ngeo2793.

Crowley, J. W., Katz, R. F., Huybers, P., Langmuir, C. H., and Park, S.-H. (2015). Glacial cycles drive variations in the production of oceanic crust. *Science* 347, 1237–1240. doi:10.1126/science.1261508.

Cui, Y., Kump, L. R., Ridgwell, A. J., Charles, A. J., Junium, C. K., Diefendorf, A. F., et al. (2011). Slow release of fossil carbon during the Paleocene–Eocene Thermal Maximum. *Nat. Geosci.* 4, 481–485. doi:10.1038/ngeo1179.

D'Olivo, J. P., McCulloch, M. T., Eggins, S. M., and Trotter, J. (2015). Coral records of reef-water pH across the central Great Barrier Reef, Australia: assessing the influence of river runoff on inshore reefs. *Biogeosciences* 12, 1223–1236. doi:10.5194/bg-12-1223-2015.

Dagon, K., and Schrag, D. P. (2019). Quantifying the effects of solar geoengineering on vegetation. *Clim. Change* 153, 235–251. doi:10.1007/s10584-019-02387-9.

Dakos, V., Scheffer, M., van Nes, E. H., Brovkin, V., Petoukhov, V., and Held, H. (2008). Slowing down as an early warning signal for abrupt climate change. *Proc. Natl. Acad. Sci.* 105, 14308–14312. doi:10.1073/pnas.0802430105.

Dalsøren, S. B., Myhre, C. L., Myhre, G., Gomez-Pelaez, A. J., Søvde, O. A., Isaksen, I. S. A., et al. (2016). Atmospheric methane evolution the last 40 years. *Atmos. Chem. Phys.* 16, 3099–3126. doi:10.5194/acp-16-3099-2016.

Daneshvar, F., Nejadhashemi, A. P., Adhikari, U., Elahi, B., Abouali, M., Herman, M. R., et al. (2017). Evaluating the significance of wetland restoration scenarios on phosphorus removal. *J. Environ. Manage.* 192, 184–196. doi:10.1016/j.jenvman.2017.01.059.

Davidson, E. A. (2009). The contribution of manure and fertilizer nitrogen to atmospheric nitrous oxide since 1860. *Nat. Geosci.* 2, 659–662. doi:10.1038/ngeo608.

De Kauwe, M. G., Medlyn, B. E., Zaehle, S., Walker, A. P., Dietze, M. C., Hickler, T., et al. (2013). Forest water use and water use efficiency at elevated CO2 : a model-data intercomparison at two contrasting temperate forest FACE sites. *Glob. Chang. Biol.* 19, 1759–1779. doi:10.1111/gcb.12164.

De Kauwe, M. G., Medlyn, B. E., Zaehle, S., Walker, A. P., Dietze, M. C., Wang, Y.-P., et al. (2014). Where does the carbon go? A model-data intercomparison of vegetation carbon allocation and turnover processes at two temperate forest free-air CO2 enrichment sites. *New Phytol.* 203, 883–899. doi:10.1111/nph.12847.

De Klein, C., Novoa, S., Ogle, A., Smith, P., Rochette, P., Wirth, T., et al. (2006). "Agriculture, Forestry and Other Land Use (Volume 4); N2O Emissions from Managed Soils, and CO2 Emissions from Lime and Urea Application (Chapter 11)," in *2006 IPCC Guidelines for National Greenhouse Gas Inventories*, 11.1-11.54. Available at: https://www.ipcc-nggip.iges.or.jp/public/2006gl/pdf/4_Volume4/V4_11_Ch11_N2O&CO2.pdf.

de Vries, W., Solberg, S., Dobbertin, M., Sterba, H., Laubhann, D., van Oijen, M., et al. (2009). The impact of nitrogen deposition on carbon sequestration by European forests and heathlands. *For. Ecol. Manage.* 258, 1814–1823. doi:10.1016/j.foreco.2009.02.034.

Dean, J. F., Middelburg, J. J., Röckmann, T., Aerts, R., Blauw, L. G., Egger, M., et al. (2018). Methane feedbacks to the global climate system in a warmer world. *Rev. Geophys.* 56, 207–250. doi:10.1002/2017RG000559.

DeConto, R. M., Galeotti, S., Pagani, M., Tracy, D., Schaefer, K., Zhang, T., et al. (2012). Past extreme warming events linked to massive carbon release from thawing permafrost. *Nature* 484, 87–91. doi:10.1038/nature10929.

DeConto, R. M., Pollard, D., Wilson, P. A., Pälike, H., Lear, C. H., and Pagani, M. (2008). Thresholds for Cenozoic bipolar glaciation. *Nature* 455, 652–656. doi:10.1038/nature07337.

Deemer, B. R., Harrison, J. A., Li, S., Beaulieu, J. J., DelSontro, T., Barros, N., et al. (2016). Greenhouse gas emissions from reservoir water surfaces: a new global synthesis. *Bioscience* 66, 949–964. doi:10.1093/biosci/biw117.

Denisov, S. N., Eliseev, A. V., and Mokhov, I. I. (2013). Climate change in IAP RAS global model taking account of interaction with methane cycle under anthropogenic scenarios of RCP family. *Russ. Meteorol. Hydrol.* 38, 741–749. doi:10.3103/S1068373913110034.

Denvil-Sommer, A., Gehlen, M., Vrac, M., and Mejia, C. (2019). LSCE-FFNN-v1: a two-step neural network model for the reconstruction of surface ocean p CO 2 over the global ocean. *Geosci. Model Dev.* 12, 2091–2105. doi:10.5194/gmd-12-2091-2019.

Deutsch, C., Berelson, W., Thunell, R., Weber, T., Tems, C., McManus, J., et al. (2014). Centennial changes in North Pacific anoxia linked to tropical trade winds. *Science* 345, 665–668. doi:10.1126/science.1252332.

Devaraju, N., Bala, G., Caldeira, K., and Nemani, R. (2016). A model based investigation of the relative importance of CO2-fertilization, climate warming, nitrogen deposition and land use change on the global terrestrial carbon uptake in the historical period. *Clim. Dyn.* doi:10.1007/s00382-015-2830-8.

Devaraju, N., Bala, G., and Modak, A. (2015). Effects of large-scale deforestation on precipitation in the monsoon regions: Remote versus local effects. *Proc. Natl. Acad. Sci.* 112, 3257–3262. doi:10.1073/pnas.1423439112.

DEVARAJU, N., BALA, G., and NEMANI, R. (2015). Modelling the influence of land-use changes on biophysical and biochemical interactions at regional and global scales. *Plant. Cell Environ.* 38, 1931–1946. doi:10.1111/pce.12488.

DeVries, T., Holzer, M., and Primeau, F. (2017). Recent increase in oceanic carbon uptake driven by weaker upper-ocean overturning. *Nature* 542, 215–218. doi:10.1038/nature21068.

DeVries, T., Le Quéré, C., Andrews, O., Berthet, S., Hauck, J., Ilyina, T., et al. (2019). Decadal trends in the ocean carbon sink. *Proc. Natl. Acad. Sci. U. S. A.* 116, 11646–11651. doi:10.1073/pnas.1900371116.

Dickson, A. J., Cohen, A. S., and Coe, A. L. (2012). Seawater oxygenation during the Paleocene-Eocene Thermal Maximum. *Geology* 40, 639–642. doi:10.1130/G32977.1.

Dixon, T., Garrett, J., and Kleverlaan, E. (2014). Update on the London protocol - Developments on transboundary CCS and on geoengineering. in *Energy Procedia* (Elsevier), 6623–6628. doi:10.1016/j.egypro.2014.11.698.

Djakovac, T., Supić, N., Bernardi Aubry, F., Degobbis, D., and Giani, M. (2015). Mechanisms of hypoxia frequency changes in the northern Adriatic Sea during the period 1972–2012. *J. Mar. Syst.* 141, 179–189. doi:10.1016/j.jmarsys.2014.08.001.

Dlugokencky, E. J. (2003). Atmospheric methane levels off: Temporary pause or a new steady-state? *Geophys. Res. Lett.* 30, 1992. doi:10.1029/2003GL018126.

Dlugokencky, E. J., Lang, P. M., Crotwell, A. M., Mund, J. W., Crotwell, M. J., and Thoning, K. W. Atmospheric methane dry air mole fractions. *NOAA ERSL Carbon Cycle Coorperative Glob. Air Sampl. Netw.* Available at: ftp://aftp.cmdl.noaa.gov/data/trace_gases/ch4/flask/surface/ [Accessed August 1, 2018].

Dlugokencky, E. J., Nisbet, E. G., Fisher, R., and Lowry, D. (2011). Global atmospheric methane: budget, changes and dangers. *Philos. Trans. R. Soc. A Math. Phys. Eng. Sci.* 369, 2058–2072. doi:10.1098/rsta.2010.0341.

Dlugokencky, E., and Tans, P. (2019). Trends in atmospheric carbon dioxide. Available at: www.esrl.noaa.gov/gmd/ccgg/trends/global.html [Accessed March 25, 2019].

Don, A., Osborne, B., Hastings, A., Skiba, U., Carter, M. S., Drewer, J., et al. (2012). Land-use change to bioenergy production in Europe: implications for the greenhouse gas balance and soil carbon. *GCB Bioenergy* 4, 372–391. doi:10.1111/j.1757-1707.2011.01116.x.

Don, A., Schumacher, J., and Freibauer, A. (2011). Impact of tropical land-use change on soil organic carbon stocks – a meta-analysis. *Glob. Chang. Biol.* 17, 1658–1670. doi:10.1111/j.1365-2486.2010.02336.x.

Doney, S. C., Lima, I., Feely, R. A., Glover, D. M., Lindsay, K., Mahowald, N., et al. (2009). Mechanisms governing interannual variability in upper-ocean inorganic carbon system and air–sea CO2 fluxes: Physical climate and atmospheric dust. *Deep Sea Res. Part II Top. Stud. Oceanogr.* 56, 640–655. doi:10.1016/j.dsr2.2008.12.006.

Dore, J. E., Lukas, R., Sadler, D. W., Church, M. J., and Karl, D. M. (2009). Physical and biogeochemical modulation of ocean acidification in the central North Pacific. *Proc. Natl. Acad. Sci.* 106, 12235–12240. doi:10.1073/pnas.0906044106.

Drake, J. E., Gallet-Budynek, A., Hofmockel, K. S., Bernhardt, E. S., Billings, S. A., Jackson, R. B., et al. (2011). Increases in the flux of carbon belowground stimulate nitrogen uptake and sustain the long-term enhancement of forest productivity under elevated CO2. *Ecol. Lett.* 14, 349–357. doi:10.1111/j.1461-0248.2011.01593.x.

Drake, J. E., Macdonald, C. A., Tjoelker, M. G., Reich, P. B., Singh, B. K., Anderson, I. C., et al. (2018). Three years of soil respiration in a mature eucalypt woodland exposed to atmospheric CO2 enrichment. *Biogeochemistry* 139, 85–101. doi:10.1007/s10533-018-0457-7.

Drijfhout, S., Bathiany, S., Beaulieu, C., Brovkin, V., Claussen, M., Huntingford, C., et al. (2015). Catalogue of abrupt shifts in Intergovernmental panel on climate change climate models. *Proc. Natl. Acad. Sci.* 112, E5777–E5786. doi:10.1073/pnas.1511451112.

Du, C., Wang, X., Zhang, M., Jing, J., and Gao, Y. (2019). Effects of elevated CO2 on plant C-N-P stoichiometry in terrestrial ecosystems: A meta-analysis. *Sci. Total Environ.* 650, 697–708. doi:10.1016/j.scitotenv.2018.09.051.

Duarte, C. M., Hendriks, I. E., Moore, T. S., Olsen, Y. S., Steckbauer, A., Ramajo, L., et al. (2013). Is ocean acidification an open-ocean Syndrome? understanding anthropogenic impacts on seawater pH. *Estuaries and Coasts* 36, 221–236. doi:10.1007/s12237-013-9594-3.

Dunkley Jones, T., Lunt, D. J., Schmidt, D. N., Ridgwell, A., Sluijs, A., Valdes, P. J., et al. (2013). Climate model and proxy data constraints on ocean warming across the Paleocene–Eocene Thermal Maximum. *Earth-Science Rev.* 125, 123–145. doi:10.1016/j.earscirev.2013.07.004.

Dupont, S., Dorey, N., and Thorndyke, M. (2010). What meta-analysis can tell us about vulnerability of marine biodiversity to ocean acidification? *Estuar. Coast. Shelf Sci.* 89, 182–185. doi:10.1016/j.ecss.2010.06.013.

Duprat, L. P. A. M., Bigg, G. R., and Wilton, D. J. (2016). Enhanced Southern Ocean marine productivity due to fertilization by giant icebergs. *Nat. Geosci.* 9, 219.

Dürr, H. H., Laruelle, G. G., Kempen, C. M., Slomp, C. P., Meybeck, M., and Middelkoop, H. (2011). Worldwide typology of nearshore coastal systems: defining the estuarine filter of river inputs to the oceans. *Estuaries and Coasts* 34, 441–458. doi:10.1007/s12237-011-9381-y.

Earl, N., and Simmonds, I. (2018). Spatial and temporal variability and trends in 2001–2016 global fire activity. *J. Geophys. Res. Atmos.* doi:10.1002/2017JD027749.

Eby, M., Zickfeld, K., Montenegro, A., Archer, D., Meissner, K. J., and Weaver, A. J. (2009). Lifetime of anthropogenic climate change: Millennial time scales of potential CO2 and surface temperature perturbations. *J. Clim.* 22, 2501–2511. doi:10.1175/2008JCLI2554.1.

Ehlert, D., and Zickfeld, K. (2017). What determines the warming commitment after cessation of CO2 emissions? *Environ. Res. Lett.* 12, 015002. doi:10.1088/1748-9326/aa564a.

Ehlert, D., Zickfeld, K., Eby, M., and Gillett, N. (2017). The sensitivity of the proportionality between temperature change and cumulative CO2 emissions to ocean mixing. *J. Clim.* 30, 2921–2935. doi:10.1175/JCLI-D-16-0247.1.

Elberling, B., Christiansen, H. H., and Hansen, B. U. (2010). High nitrous oxide production from thawing permafrost. *Nat. Geosci.* 3, 332–335. doi:10.1038/ngeo803.

Eliseev, A. V., Mokhov, I. I., and Chernokulsky, A. V. (2014). Influence of ground and peat fires on CO2 emissions into the atmosphere. *Dokl. Earth Sci.* 459, 1565–1569. doi:10.1134/S1028334X14120034.

Elkins, J. W., Dlugokencky, E., Hall, B., Dutton, G., Nance, D., and Mondeel, D. J. (2018). Combined Nitrous Oxide data from the NOAA/ESRL Global Monitoring Division. *Earth Syst. Res. Lab. (ESRL), Natl. Ocean. Atmos. Adm.* Available at: https://www.esrl.noaa.gov/gmd/hats/combined/N2O.html [Accessed January 24, 2019].

Elshout, P. M. F., van Zelm, R., Balkovic, J., Obersteiner, M., Schmid, E., Skalsky, R., et al. (2015). Greenhouse-gas payback times for crop-based biofuels. *Nat. Clim. Chang.* 5, 604–610. doi:10.1038/nclimate2642.

Elsig, J., Schmitt, J., Leuenberger, D., Schneider, R., Eyer, M., Leuenberger, M., et al. (2009). Stable isotope constraints on Holocene carbon cycle changes from an Antarctic ice core. *Nature* 461, 507–510. doi:10.1038/nature08393.

Emerson, S., and Hedges, J. I. (1988). Processes controlling the organic carbon content of open ocean sediments. *Paleoceanography* 3, 621–634. doi:10.1029/PA003i005p00621.

Erb, K.-H., Kastner, T., Plutzar, C., Bais, A. L. S., Carvalhais, N., Fetzel, T., et al. (2018). Unexpectedly large impact of forest management and grazing on global vegetation biomass. *Nature* 553, 73–76. doi:10.1038/nature25138.

Etiope, G., Ciotoli, G., Schwietzke, S., and Schoell, M. (2019). Gridded maps of geological methane emissions and their isotopic signature. *Earth Syst. Sci. Data* 11, 1–22. doi:10.5194/essd-11-1-2019.

Etminan, M., Myhre, G., Highwood, E. J., and Shine, K. P. (2016). Radiative forcing of carbon dioxide, methane, and nitrous oxide: A significant revision of the methane radiative forcing. *Geophys. Res. Lett.* 43, 12,614-12,623. doi:10.1002/2016GL071930.

Fan, L., Wigneron, J.-P., Ciais, P., Chave, J., Brandt, M., Fensholt, R., et al. (2019). Satellite-observed pantropical carbon dynamics. *Nat. Plants*. doi:10.1038/s41477-019-0478-9.

Fang, Y., Michalak, A. M., Schwalm, C. R., Huntzinger, D. N., Berry, J. A., Ciais, P., et al. (2017). Global land carbon sink response to temperature and precipitation varies with ENSO phase. *Environ. Res. Lett.* 12, 064007. doi:10.1088/1748-9326/aa6e8e.

Fargione, J. E., Bassett, S., Boucher, T., Bridgham, S. D., Conant, R. T., Cook-Patton, S. C., et al. (2018). Natural climate solutions for the United States. *Sci. Adv.* 4, eaat1869. doi:10.1126/sciadv.aat1869.

Farías, L., Besoain, V., and García-Loyola, S. (2015). Presence of nitrous oxide hotspots in the coastal upwelling area off central Chile: an analysis of temporal variability based on ten years of a biogeochemical time series. *Environ. Res. Lett.* 10, 044017. doi:10.1088/1748-9326/10/4/044017.

Farley, K. A., Jobbagy, E. G., and Jackson, R. B. (2005). Effects of afforestation on water yield: a global synthesis with implications for policy. *Glob. Chang. Biol.* 11, 1565–1576. doi:10.1111/j.1365-2486.2005.01011.x.

Farrior, C. E., Rodriguez-Iturbe, I., Dybzinski, R., Levin, S. A., and Pacala, S. W. (2015). Decreased water limitation under elevated CO2 amplifies potential for forest carbon sinks. *Proc. Natl. Acad. Sci.* 112, 7213–7218. doi:10.1073/pnas.1506262112.

Fatichi, S., Pappas, C., Zscheischler, J., and Leuzinger, S. (2019). Modelling carbon sources and sinks in terrestrial vegetation. *New Phytol.* 221, 652–668. doi:10.1111/nph.15451.

Fay, A. R., and McKinley, G. A. (2014). Global open-ocean biomes: mean and temporal variability. *Earth Syst. Sci. Data* 6, 273–284. doi:10.5194/essd-6-273-2014.

Feely, R. A., Alin, S. R., Carter, B., Bednaršek, N., Hales, B., Chan, F., et al. (2016). Chemical and biological impacts of ocean acidification along the west coast of North America. *Estuar. Coast. Shelf Sci.* 183, 260–270. doi:10.1016/j.ecss.2016.08.043.

Feely, R. A., Alin, S. R., Newton, J., Sabine, C. L., Warner, M., Devol, A., et al. (2010). The combined effects of ocean acidification, mixing, and respiration on pH and carbonate saturation in an urbanized estuary. *Estuar. Coast. Shelf Sci.* 88, 442–449. doi:10.1016/j.ecss.2010.05.004.

Feely, R. A., Okazaki, R. R., Cai, W.-J., Bednaršek, N., Alin, S. R., Byrne, R. H., et al. (2018). The combined effects of acidification and hypoxia on pH and aragonite saturation in the coastal waters of the California current ecosystem and the northern Gulf of Mexico. *Cont. Shelf Res.* 152, 50–60. doi:10.1016/j.csr.2017.11.002.

Feely, R. A., Sabine, C. L., Hernandez-Ayon, J. M., Ianson, D., and Hales, B. (2008). Evidence for upwelling of corrosive "acidified" water onto the continental shelf. *Science* 320, 1490–1492. doi:10.1126/science.1155676.

Feng, E. Y., Koeve, W., Keller, D. P., and Oschlies, A. (2017). Model-based assessment of the CO2 sequestration potential of coastal ocean alkalinization. *Earth's Futur.* 5, 1252–1266. doi:10.1002/2017EF000659.

Feng, J., Chen, C., Zhang, Y., Song, Z., Deng, A., Zheng, C., et al. (2013). Impacts of cropping practices on yield-scaled greenhouse gas emissions from rice fields in China: A meta-analysis. *Agric. Ecosyst. Environ.* 164, 220–228. doi:10.1016/j.agee.2012.10.009.

Fennel, K., Alin, S., Barbero, L., Evans, W., Bourgeois, T., Cooley, S., et al. (2019). Carbon cycling in the North American coastal ocean: a synthesis. *Biogeosciences* 16, 1281–1304. doi:10.5194/bg-16-1281-2019.

Fennel, K., and Testa, J. M. (2019). Biogeochemical controls on coastal hypoxia. *Ann. Rev. Mar. Sci.* 11, 105–130. doi:10.1146/annurev-marine-010318-095138.

Fernández-Martínez, M., Sardans, J., Chevallier, F., Ciais, P., Obersteiner, M., Vicca, S., et al. (2019). Global trends in carbon sinks and their relationships with CO2 and temperature. *Nat. Clim. Chang.* 9, 73–79. doi:10.1038/s41558-018-0367-7.

Ferrari, R., Jansen, M. F., Adkins, J. F., Burke, A., Stewart, A. L., and Thompson, A. F. (2014). Antarctic sea ice control on ocean circulation in present and glacial climates. *Proc. Natl. Acad. Sci.* 111, 8753–8758. doi:10.1073/pnas.1323922111.

Ferretti, D. F. (2005). Unexpected changes to the global methane budget over the past 2000 years. *Science* 309, 1714–1717. doi:10.1126/science.1115193.

Ferretti, D. F., Miller, J. B., White, J. W. C., Etheridge, D. M., Lassey, K. R., Lowe, D. C., et al. (2005). Unexpected changes to the global methane budget over the past 2000 years. *Science* 309, 1714–7. doi:10.1126/science.1115193.

Field, R. D., van der Werf, G. R., Fanin, T., Fetzer, E. J., Fuller, R., Jethva, H., et al. (2016). Indonesian fire activity and smoke pollution in 2015 show persistent nonlinear sensitivity to El Niño-induced drought. *Proc. Natl. Acad. Sci.* 113, 9204–9209. doi:10.1073/pnas.1524888113.

Finkel, Z. V., Beardall, J., Flynn, K. J., Quigg, A., Rees, T. A. V., and Raven, J. A. (2010). Phytoplankton in a changing world: cell size and elemental stoichiometry. *J. Plankton Res.* 32, 119–137. doi:10.1093/plankt/fbp098.

Finzi, A. C., Norby, R. J., Calfapietra, C., Gallet-Budynek, A., Gielen, B., Holmes, W. E., et al. (2007). Increases in nitrogen uptake rather than nitrogen-use efficiency support higher rates of temperate forest productivity under elevated CO2. *Proc. Natl. Acad. Sci.* 104, 14014–14019. doi:10.1073/pnas.0706518104.

Fischer, H., Meissner, K. J., Mix, A. C., Abram, N. J., Austermann, J., Brovkin, V., et al. (2018). Paleoclimate constraints on the impact of 2°C anthropogenic warming and beyond. *Nat. Geosci.* 11, 474–485. doi:10.1038/s41561-018-0146-0.

Fischer, H., Schmitt, J., Bock, M., Seth, B., Joos, F., Spahni, R., et al. (2019). N 2 O changes from the Last Glacial Maximum to the preindustrial – Part 1: Quantitative reconstruction of terrestrial and marine emissions using N 2 O stable isotopes in ice cores. *Biogeosciences* 16, 3997–4021. doi:10.5194/bg-16-3997-2019.

Fleischer, K., Rammig, A., De Kauwe, M. G., Walker, A. P., Domingues, T. F., Fuchslueger, L., et al. (2019). Amazon forest response to CO2 fertilization dependent on plant phosphorus acquisition. *Nat. Geosci.* 12, 736–741. doi:10.1038/s41561-019-0404-9.

Fleming, E. L., Jackman, C. H., Stolarski, R. S., and Douglass, A. R. (2011). A model study of the impact of source gas changes on the stratosphere for 1850–2100. *Atmos. Chem. Phys.* 11, 8515–8541. doi:10.5194/acp-11-8515-2011.

Forkel, M., Andela, N., P Harrison, S., Lasslop, G., Van Marle, M., Chuvieco, E., et al. (2019a). Emergent relationships with respect to burned area in global satellite observations and fire-enabled vegetation models. *Biogeosciences*. doi:10.5194/bg-16-57-2019.

Forkel, M., Carvalhais, N., Rodenbeck, C., Keeling, R., Heimann, M., Thonicke, K., et al. (2016). Enhanced seasonal CO2 exchange caused by amplified plant productivity in northern ecosystems. *Science* 351, 696–699. doi:10.1126/science.aac4971.

Forkel, M., Dorigo, W., Lasslop, G., Chuvieco, E., Hantson, S., Heil, A., et al. (2019b). Recent global and regional trends in burned area and their compensating environmental controls. *Environ. Res. Commun.* doi:10.1088/2515-7620/ab25d2.

Fornara, D. A., Steinbeiss, S., McNamara, N. P., Gleixner, G., Oakley, S., Poulton, P. R., et al. (2011). Increases in soil organic carbon sequestration can reduce the global warming potential of long-term liming to permanent grassland. *Glob. Chang. Biol.* 17, 1925–1934. doi:10.1111/j.1365-2486.2010.02328.x.

Forster, P., Huppmann, D., Kriegler, E., Mundaca, L., Smith, C., Rogelj, J., et al. (2018). "Mitigation Pathways Compatible with 1.5°C in the Context of Sustainable Development Supplementary Material," in *Global Warming of 1.5°C. An IPCC Special Report on the impacts of global warming of 1.5°C above pre-industrial levels and related global greenhouse gas emission pathways, in the context of strengthening the global response to the threat of climate change,* eds. V. Masson-Delmotte, P. Zhai, H.-O. Pörtner, D. Roberts, J. Skea, P. R. Shukla, et al. Available at: https://www.ipcc.ch/sr15.

Forzieri, G., Alkama, R., Miralles, D. G., and Cescatti, A. (2017). Satellites reveal contrasting responses of regional climate to the widespread greening of Earth. *Science* 356, 1180–1184. doi:10.1126/science.aal1727.

Foster, G. L., Royer, D. L., and Lunt, D. J. (2017). Future climate forcing potentially without precedent in the last 420 million years. *Nat. Commun.* 8, 14845. doi:10.1038/ncomms14845.

Fowell, S. E., Foster, G. L., Ries, J. B., Castillo, K. D., de la Vega, E., Tyrrell, T., et al. (2018). Historical trends in pH and carbonate biogeochemistry on the belize mesoamerican barrier reef system. *Geophys. Res. Lett.* 45, 3228–3237. doi:10.1002/2017GL076496.

Frank, D. C., Poulter, B., Saurer, M., Esper, J., Huntingford, C., Helle, G., et al. (2015). Water-use efficiency and transpiration across European forests during the Anthropocene. *Nat. Clim. Chang.* 5, 579–583. doi:10.1038/nclimate2614.

Franks, P. J., Adams, M. A., Amthor, J. S., Barbour, M. M., Berry, J. A., Ellsworth, D. S., et al. (2013). Sensitivity of plants to changing atmospheric CO2 concentration: from the geological past to the next century. *New Phytol.* 197, 1077–1094. doi:10.1111/nph.12104.

Freing, A., Wallace, D. W. R., and Bange, H. W. (2012). Global oceanic production of nitrous oxide. *Philos. Trans. R. Soc. B Biol. Sci.* 367, 1245–1255. doi:10.1098/rstb.2011.0360.

Friedlingstein, P., Andrew, R. M., Rogelj, J., Peters, G. P., Canadell, J. G., Knutti, R., et al. (2014a). Persistent growth of CO2 emissions and implications for reaching climate targets. *Nat. Geosci.* 7, 709–715. doi:10.1038/ngeo2248.

Friedlingstein, P., Bopp, L., Ciais, P., Dufresne, J., Fairhead, L., LeTreut, H., et al. (2001). Positive feedback between future climate change and the carbon cycle. *Geophys. Res. Lett.* 28, 1543–1546. doi:10.1029/2000GL012015.

Friedlingstein, P., Cox, P., Betts, R., Bopp, L., von Bloh, W., Brovkin, V., et al. (2006). Climate–Carbon Cycle Feedback Analysis: Results from the C 4 MIP Model Intercomparison. *J. Clim.* 19, 3337–3353. doi:10.1175/JCLI3800.1.

Friedlingstein, P., Dufresne, J.-L., Cox, P. M., and Rayner, P. (2003). How positive is the feedback between climate change and the carbon cycle? *Tellus B* 55, 692–700. doi:10.1034/j.1600-0889.2003.01461.x.

Friedlingstein, P., Jones, M. W., O'Sullivan, M., Andrew, R. M., Hauck, J., Peters, G. P., et al. (2019). Global Carbon Budget 2019. *Earth Syst. Sci. Data* 11, 1783–1838. doi:10.5194/essd-11-1783-2019.

Friedlingstein, P., Meinshausen, M., Arora, V. K., Jones, C. D., Anav, A., Liddicoat, S. K., et al. (2014b). Uncertainties in CMIP5 climate projections due to carbon cycle feedbacks. *J. Clim.* 27, 511–526. doi:10.1175/JCLI-D-12-00579.1.

Friend, A. D., Lucht, W., Rademacher, T. T., Keribin, R., Betts, R., Cadule, P., et al. (2014). Carbon residence time dominates uncertainty in terrestrial vegetation responses to future climate and atmospheric CO2. *Proc. Natl. Acad. Sci.* 111, 3280–3285. doi:10.1073/pnas.1222477110.

Frölicher, T. L., and Joos, F. (2010). Reversible and irreversible impacts of greenhouse gas emissions in multi-century projections with the NCAR global coupled carbon cycle-climate model. *Clim. Dyn.* 35, 1439–1459. doi:10.1007/s00382-009-0727-0.

Frölicher, T. L., Joos, F., Raible, C. C., and Sarmiento, J. L. (2013). Atmospheric CO2 response to volcanic eruptions: The role of ENSO, season, and variability. *Global Biogeochem. Cycles* 27, 239–251. doi:10.1002/gbc.20028.

Frölicher, T. L., and Paynter, D. J. (2015a). Extending the relationship between global warming and cumulative carbon emissions to multi-millennial timescales. *Environ. Res. Lett.* 10, 075002. doi:10.1088/1748-9326/10/7/075002.

Frölicher, T. L., and Paynter, D. J. (2015b). Extending the relationship between global warming and cumulative carbon emissions to multi-millennial timescales. *Environ. Res. Lett.* 10, 075002. doi:10.1088/1748-9326/10/7/075002.

Frölicher, T. L., Sarmiento, J. L., Paynter, D. J., Dunne, J. P., Krasting, J. P., and Winton, M. (2015). Dominance of the Southern Ocean in anthropogenic carbon and heat uptake in CMIP5 models. *J. Clim.* 28, 862–886. doi:10.1175/JCLI-D-14-00117.1.

Frölicher, T. L., Winton, M., and Sarmiento, J. L. (2014). Continued global warming after CO2 emissions stoppage. *Nat. Clim. Chang.* 4, 40–44. doi:10.1038/nclimate2060.

Frolking, S., and Roulet, N. T. (2007). Holocene radiative forcing impact of northern peatland carbon accumulation and methane emissions. *Glob. Chang. Biol.* 13, 1079–1088. doi:10.1111/j.1365-2486.2007.01339.x.

Fu, W., Randerson, J. T., and Moore, J. K. (2016). Climate change impacts on net primary production (NPP) and export production (EP) regulated by increasing stratification and phytoplankton community structure in the CMIP5 models. *Biogeosciences* 13, 5151–5170. doi:10.5194/bg-13-5151-2016.

Fuss, S., Lamb, W. F., Callaghan, M. W., Hilaire, J., Creutzig, F., Amann, T., et al. (2018). Negative emissions—Part 2: Costs, potentials and side effects. *Environ. Res. Lett.* 13, 063002. doi:10.1088/1748-9326/aabf9f.

Galbraith, E. D., and Eggleston, S. (2017). A lower limit to atmospheric CO2 concentrations over the past 800,000 years. *Nat. Geosci.* 10, 295–298. doi:10.1038/ngeo2914.

Galbraith, E. D., and Jaccard, S. L. (2015). Deglacial weakening of the oceanic soft tissue pump: global constraints from sedimentary nitrogen isotopes and oxygenation proxies. *Quat. Sci. Rev.* 109, 38–48. doi:10.1016/j.quascirev.2014.11.012.

Galbraith, E. D., and Kienast, M. (2013). The acceleration of oceanic denitrification during deglacial warming. *Nat. Geosci.* 6, 579–584. doi:10.1038/ngeo1832.

Galbraith, E. D., and Skinner, L. C. (2020). The biological pump during the Last Glacial Maximum. *Ann. Rev. Mar. Sci.* 12, 559–586. doi:10.1146/annurev-marine-010419-010906.

Gangstø, R., Joos, F., and Gehlen, M. (2011). Sensitivity of pelagic calcification to ocean acidification. *Biogeosciences* 8, 433–458. doi:10.5194/bg-8-433-2011.

Ganopolski, A., and Brovkin, V. (2017). Simulation of climate, ice sheets and CO2 evolution during the last four glacial cycles with an Earth system model of intermediate complexity. *Clim. Past* 13, 1695–1716. doi:10.5194/cp-13-1695-2017.

Gao, K., Beardall, J., Häder, D.-P., Hall-Spencer, J. M., Gao, G., and Hutchins, D. A. (2019). Effects of Ocean Acidification on marine photosynthetic organisms under the concurrent influences of warming, UV radiation, and deoxygenation. *Front. Mar. Sci.* 6. doi:10.3389/fmars.2019.00322.

Gasser, T., Kechiar, M., Ciais, P., Burke, E. J., Kleinen, T., Zhu, D., et al. (2018). Path-dependent reductions in CO2 emission budgets caused by permafrost carbon release. *Nat. Geosci.* 11, 830–835. doi:10.1038/s41561-018-0227-0.

Gattuso, J.-P., Frankignoulle, M., and Wollast, R. (1998). Carbon and carbonate metabolism in coastal aquatic ecosystems. *Annu. Rev. Ecol. Syst.* 29, 405–434. doi:10.1146/annurev.ecolsys.29.1.405.

Gattuso, J.-P., Magnan, A., Billé, R., Cheung, W. W. L., Howes, E. L., Joos, F., et al. (2015). Contrasting futures for ocean and society from different anthropogenic CO2 emissions scenarios. *Science* 349, aac4722. doi:10.1126/science.aac4722.

Gauthier, S., Bernier, P., Kuuluvainen, T., Shvidenko, A. Z., and Schepaschenko, D. G. (2015). Boreal forest health and global change. *Science* 349, 819 LP – 822. doi:10.1126/science.aaa9092.

Gedney, N. (2004). Climate feedback from wetland methane emissions. *Geophys. Res. Lett.* 31, L20503. doi:10.1029/2004GL020919.

Genesio, L., Miglietta, F., Lugato, E., Baronti, S., Pieri, M., and Vaccari, F. P. (2012). Surface albedo following biochar application in durum wheat. *Environ. Res. Lett.* 7, 014025. doi:10.1088/1748-9326/7/1/014025.

Gerber, J. S., Carlson, K. M., Makowski, D., Mueller, N. D., Garcia de Cortazar-Atauri, I., Havlík, P., et al. (2016). Spatially explicit estimates of N2O emissions from croplands suggest climate mitigation opportunities from improved fertilizer management. *Glob. Chang. Biol.* 22, 3383–3394. doi:10.1111/gcb.13341.

Ghosh, A., Patra, P. K., Ishijima, K., Umezawa, T., Ito, A., Etheridge, D. M., et al. (2015). Variations in global methane sources and sinks during 1910–2010. *Atmos. Chem. Phys.* 15, 2595–2612. doi:10.5194/acp-15-2595-2015.

Giglio, L., Randerson, J. T., and Van Der Werf, G. R. (2013). Analysis of daily, monthly, and annual burned area using the fourth-generation global fire emissions database (GFED4). *J. Geophys. Res. Biogeosciences*. doi:10.1002/jgrg.20042.

Gillett, N. P., Arora, V. K., Matthews, D., and Allen, M. R. (2013). Constraining the ratio of global warming to cumulative CO2 emissions using CMIP5 simulations*. *J. Clim.* 26, 6844–6858. doi:10.1175/JCLI-D-12-00476.1.

Gillett, N. P., Arora, V. K., Zickfeld, K., Marshall, S. J., and Merryfield, W. J. (2011). Ongoing climate change following a complete cessation of carbon dioxide emissions. *Nat. Geosci.* 4, 83–87. doi:10.1038/ngeo1047.

Gitz, V., and Ciais, P. (2003). Amplifying effects of land-use change on future atmospheric CO2 levels. *Global Biogeochem. Cycles* 17, 1–15. doi:10.1029/2002GB001963.

Glienke, S., Irvine, P. J., and Lawrence, M. G. (2015). The impact of geoengineering on vegetation in experiment G1 of the GeoMIP. *J. Geophys. Res. Atmos.* 120, 10,196-10,213. doi:10.1002/2015JD024202.

Gloege, L., McKinley, G. A., Landschützer, P., Fay, A. R., Frölicher, T. L., Fyfe, J. C., et al. (submitted). Quantifying errors in observationally-based estimates of ocean carbon sink variability. *Proc. Natl. Acad. Sci.* (submitted).

Gloor, E., Wilson, C., Chipperfield, M. P., Chevallier, F., Buermann, W., Boesch, H., et al. (2018). Tropical land carbon cycle responses to 2015/16 El Niño as recorded by atmospheric greenhouse gas and remote sensing data. *Philos. Trans. R. Soc. B Biol. Sci.* doi:10.1098/rstb.2017.0302.

Gloor, M., Sarmiento, J. L., and Gruber, N. (2010). What can be learned about carbon cycle climate feedbacks from the CO2 airborne fraction? *Atmos. Chem. Phys.* 10, 7739–7751. doi:10.5194/acp-10-7739-2010.

Goll, D. S., Winkler, A. J., Raddatz, T., Dong, N., Prentice, I. C., Ciais, P., et al. (2017). Carbon–nitrogen interactions in idealized simulations with JSBACH (version 3.10). *Geosci. Model Dev.* 10, 2009–2030. doi:10.5194/gmd-10-2009-2017.

González-Dávila, M., Santana-Casiano, J. M., Rueda, M. J., and Llinás, O. (2010). The water column distribution of carbonate system variables at the ESTOC site from 1995 to 2004. *Biogeosciences* 7, 3067–3081. doi:10.5194/bg-7-3067-2010.

González, M. F., and Ilyina, T. (2016). Impacts of artificial ocean alkalinization on the carbon cycle and climate in Earth system simulations. *Geophys. Res. Lett.* 43, 6493–6502. doi:10.1002/2016GL068576.

González, M. F., Ilyina, T., Sonntag, S., and Schmidt, H. (2018). Enhanced rates of regional warming and ocean acidification after termination of large-scale ocean alkalinization. *Geophys. Res. Lett.* 45, 7120–7129. doi:10.1029/2018GL077847.

González, M. F. T. (2016). Impacts of artificial ocean alkalinization on the carbon cycle and climate in Earth system simulations. *Geophys. Res. Lett.* 43, 6493.

Good, P., Jones, C., Lowe, J., Betts, R., Booth, B., and Huntingford, C. (2011). Quantifying environmental drivers of future tropical forest extent. *J. Clim.* 24, 1337–1349. doi:10.1175/2010JCLI3865.1.

Good, P., Jones, C., Lowe, J., Betts, R., and Gedney, N. (2013). Comparing tropical forest projections from two denerations of Hadley Centre Earth System Models, HadGEM2-ES and HadCM3LC. *J. Clim.* 26, 495–511. doi:10.1175/JCLI-D-11-00366.1.

Goodkin, N. F., Wang, B.-S., You, C.-F., Hughen, K. A., Grumet-Prouty, N., Bates, N. R., et al. (2015). Ocean circulation and biogeochemistry moderate interannual and decadal surface water pH changes in the Sargasso Sea. *Geophys. Res. Lett.* 42, 4931–4939. doi:10.1002/2015GL064431.

Goodwin, P., Katavouta, A., Roussenov, V. M., Foster, G. L., Rohling, E. J., and Williams, R. G. (2018). Pathways to 1.5 °C and 2 °C warming based on observational and geological constraints. *Nat. Geosci.* 11, 102–107. doi:10.1038/s41561-017-0054-8.

Goodwin, P., Williams, R. G., and Ridgwell, A. (2015). Sensitivity of climate to cumulative carbon emissions due to compensation of ocean heat and carbon uptake. *Nat. Geosci.* 8, 29–34. doi:10.1038/ngeo2304.

Goris, N., Tjiputra, J. F., Olsen, A., Schwinger, J., Lauvset, S. K., and Jeansson, E. (2018). Constraining projection-based estimates of the future North Atlantic carbon uptake. *J. Clim.* 31, 3959–3978. doi:10.1175/JCLI-D-17-0564.1.

Gottschalk, J., Battaglia, G., Fischer, H., Frölicher, T. L., Jaccard, S. L., Jeltsch-Thömmes, A., et al. (2019). Mechanisms of millennial-scale atmospheric CO2 change in numerical model simulations. *Quat. Sci. Rev.* 220, 30–74. doi:10.1016/j.quascirev.2019.05.013.

Gottschalk, J., Skinner, L. C., Lippold, J., Vogel, H., Frank, N., Jaccard, S. L., et al. (2016). Biological and physical controls in the Southern Ocean on past millennial-scale atmospheric CO2 changes. *Nat. Commun.* 7, 11539. doi:10.1038/ncomms11539.

Govindasamy, B., Thompson, S., Duffy, P. B., Caldeira, K., and Delire, C. (2002). Impact of geoengineering schemes on the terrestrial biosphere. *Geophys. Res. Lett.* 29, 18-1-18–4. doi:10.1029/2002GL015911.

Graham, L. A., Belisle, S. L., and Rieger, P. (2009). Nitrous oxide emissions from light duty vehicles. *Atmos. Environ.* 43, 2031–2044. doi:10.1016/j.atmosenv.2009.01.002.

Grandy, A. S., Salam, D. S., Wickings, K., McDaniel, M. D., Culman, S. W., and Snapp, S. S. (2013). Soil respiration and litter decomposition responses to nitrogen fertilization rate in no-till corn systems. *Agric. Ecosyst. Environ.* 179, 35–40. doi:10.1016/j.agee.2013.04.020.

Grassi, G., House, J., Kurz, W. A., Cescatti, A., Houghton, R. A., Peters, G. P., et al. (2018). Reconciling global-model estimates and country reporting of anthropogenic forest CO2 sinks. *Nat. Clim. Chang.* 8, 914–920. doi:10.1038/s41558-018-0283-x.

Graven, H., Allison, C. E., Etheridge, D. M., Hammer, S., Keeling, R. F., Levin, I., et al. (2017). Compiled records of carbon isotopes in atmospheric CO2 for historical simulations in CMIP6. *Geosci. Model Dev.* 10, 4405–4417. doi:10.5194/gmd-10-4405-2017.

Graven, H. D., Keeling, R. F., Piper, S. C., Patra, P. K., Stephens, B. B., Wofsy, S. C., et al. (2013). Enhanced seasonal exchange of CO2 by northern ecosystems since 1960. *Science* 341, 1085–1089. doi:10.1126/science.1239207.

Gray, A. R., Johnson, K. S., Bushinsky, S. M., Riser, S. C., Russell, J. L., Talley, L. D., et al. (2018). Autonomous biogeochemical Ffoats detect significant carbon dioxide outgassing in the high-latitude Southern Ocean. *Geophys. Res. Lett.* 45, 9049–9057. doi:10.1029/2018GL078013.

Gregor, L., Kok, S., and Monteiro, P. M. S. (2018). Interannual drivers of the seasonal cycle of CO2 in the Southern Ocean. *Biogeosciences* 15, 2361–2378. doi:10.5194/bg-15-2361-2018.

Gregor, L., Lebehot, A. D., Kok, S., and Scheel Monteiro, P. M. (2019). A comparative assessment of the uncertainties of global surface ocean CO2; estimates using a machine-learning ensemble (CSIR-ML6 version 2019a) - have we hit the wall? *Geosci. Model Dev.* 12, 5113–5136. doi:10.5194/gmd-12-5113-2019.

Gregory, J. M., Andrews, T., and Good, P. (2015). The inconstancy of the transient climate response parameter under increasing CO2. *Philos. Trans. R. Soc. A Math. Phys. Eng. Sci.* 373, 20140417. doi:10.1098/rsta.2014.0417.

Gregory, J. M., Jones, C. D., Cadule, P., and Friedlingstein, P. (2009). Quantifying Carbon Cycle Feedbacks. *J. Clim.* 22, 5232–5250. doi:10.1175/2009JCLI2949.1.

Grimm, R., Notz, D., Glud, R. N., Rysgaard, S., and Six, K. D. (2016). Assessment of the sea-ice carbon pump: Insights from a three-dimensional ocean-sea-ice-biogeochemical model (MPIOM/HAMOCC). *Elem. Sci. Anthr.* 4, 000136. doi:10.12952/journal.elementa.000136.

Griscom, B. W., Adams, J., Ellis, P. W., Houghton, R. A., Lomax, G., Miteva, D. A., et al. (2017). Natural climate solutions. *Proc. Natl. Acad. Sci.* 114, 11645–11650. doi:10.1073/pnas.1710465114.

Gruber, N. (2011). Warming up, turning sour, losing breath: ocean biogeochemistry under global change. *Philos. Trans. R. Soc. A Math. Phys. Eng. Sci.* 369, 1980–1996. doi:10.1098/rsta.2011.0003.

Gruber, N., Clement, D., Carter, B. R., Feely, R. A., van Heuven, S., Hoppema, M., et al. (2019a). The oceanic sink for anthropogenic CO2 from 1994 to 2007. *Science* 363, 1193–1199. doi:10.1126/science.aau5153.

Gruber, N., and Galloway, J. N. (2008). An Earth-system perspective of the global nitrogen cycle. *Nature* 451, 293–296. doi:10.1038/nature06592.

Gruber, N., Landschützer, P., and Lovenduski, N. S. (2019b). The variable Southern Ocean carbon sink. *Ann. Rev. Mar. Sci.* 11, 159–186. doi:10.1146/annurev-marine-121916-063407.

Gu, J., Yuan, M., Liu, J., Hao, Y., Zhou, Y., Qu, D., et al. (2017). Trade-off between soil organic carbon sequestration and nitrous oxide emissions from winter wheat-summer maize rotations: Implications of a 25-year fertilization experiment in Northwestern China. *Sci. Total Environ.* 595, 371–379. doi:10.1016/j.scitotenv.2017.03.280.

Guanter, L., Zhang, Y., Jung, M., Joiner, J., Voigt, M., Berry, J. A., et al. (2014). Global and time-resolved monitoring of crop photosynthesis with chlorophyll fluorescence. *Proc. Natl. Acad. Sci.* 111, E1327–E1333. doi:10.1073/pnas.1320008111.

Guenet, B., Camino-Serrano, M., Ciais, P., Tifafi, M., Maignan, F., Soong, J. L., et al. (2018). Impact of priming on global soil carbon stocks. *Glob. Chang. Biol.* 24, 1873–1883. doi:10.1111/gcb.14069.

Guimberteau, M., Zhu, D., Maignan, F., Huang, Y., Yue, C., Dantec-Nédélec, S., et al. (2018). ORCHIDEE-MICT (v8.4.1), a land surface model for the high latitudes: model description and validation. *Geosci. Model Dev.* 11, 121–163. doi:10.5194/gmd-11-121-2018.

Guo, L. B., and Gifford, R. M. (2002). Soil carbon stocks and land use change: a meta analysis. *Glob. Chang. Biol.* 8, 345–360. doi:10.1046/j.1354-1013.2002.00486.x.

Gupta, G. V. M., Sudheesh, V., Sudharma, K. V, Saravanane, N., Dhanya, V., Dhanya, K. R., et al. (2016). Evolution to decay of upwelling and associated biogeochemistry over the southeastern Arabian Sea shelf. *J. Geophys. Res. Biogeosciences* 121, 159–175. doi:10.1002/2015JG003163.

Gutjahr, M., Ridgwell, A., Sexton, P. F., Anagnostou, E., Pearson, P. N., Pälike, H., et al. (2017). Very large release of mostly volcanic carbon during the Paleocene–Eocene Thermal Maximum. *Nature* 548, 573–577. doi:10.1038/nature23646.

Hadi, A., Inubushi, K., Purnomo, E., Razie, F., Yamakawa, K., and Tsuruta, H. (2000). Effect of land-use changes on nitrous oxide (N2O) emission from tropical peatlands. *Chemosph. - Glob. Chang. Sci.* 2, 347–358. doi:10.1016/S1465-9972(00)00030-1.

Hahn, J., Brandt, P., Schmidtko, S., and Krahmann, G. (2017). Decadal oxygen change in the eastern tropical North Atlantic. *Ocean Sci.* 13, 551–576. doi:10.5194/os-13-551-2017.

Hain, M. P., Sigman, D. M., and Haug, G. H. (2010). Carbon dioxide effects of Antarctic stratification, North Atlantic Intermediate Water formation, and subantarctic nutrient drawdown during the last ice age: Diagnosis and synthesis in a geochemical box model. *Global Biogeochem. Cycles* 24, GB4023. doi:10.1029/2010GB003790.

Hajima, T., Tachiiri, K., Ito, A., and Kawamiya, M. (2014). Uncertainty of concentration–terrestrial carbon feedback in Earth System Models*. *J. Clim.* 27, 3425–3445. doi:10.1175/JCLI-D-13-00177.1.

Hall, A., Cox, P., Huntingford, C., and Klein, S. (2019). Progressing emergent constraints on future climate change. *Nat. Clim. Chang.* 9, 269–278. doi:10.1038/s41558-019-0436-6.

Hall, A., and Qu, X. (2006). Using the current seasonal cycle to constrain snow albedo feedback in future climate change. *Geophys. Res. Lett.* 33, L03502. doi:10.1029/2005GL025127.
Hall, B. D., Dutton, G. S., and Elkins, J. W. (2007). The NOAA nitrous oxide standard scale for atmospheric observations. *J. Geophys. Res.* 112, D09305. doi:10.1029/2006JD007954.
Hansis, E., Davis, S. J., and Pongratz, J. (2015). Relevance of methodological choices for accounting of land use change carbon fluxes. *Global Biogeochem. Cycles* 29, 1230–1246. doi:10.1002/2014GB004997.
Harper, A. B., Powell, T., Cox, P. M., House, J., Huntingford, C., Lenton, T. M., et al. (2018). Land-use emissions play a critical role in land-based mitigation for Paris climate targets. *Nat. Commun.* 9, 2938. doi:10.1038/s41467-018-05340-z.
Harris, I., Jones, P. D., Osborn, T. J., and Lister, D. H. (2014). Updated high-resolution grids of monthly climatic observations - the CRU TS3.10 Dataset. *Int. J. Climatol.* 34, 623–642. doi:10.1002/joc.3711.
Harrison, S. P., Bartlein, P. J., Brovkin, V., Houweling, S., Kloster, S., and Prentice, I. C. (2018). The biomass burning contribution to climate–carbon-cycle feedback. *Earth Syst. Dyn.* 9, 663–677. doi:10.5194/esd-9-663-2018.
Hartmann, J., West, A. J., Renforth, P., Köhler, P., De La Rocha, C. L., Wolf-Gladrow, D. A., et al. (2013). Enhanced chemical weathering as a geoengineering strategy to reduce atmospheric carbon dioxide, supply nutrients, and mitigate ocean acidification. *Rev. Geophys.* 51, 113–149. doi:10.1002/rog.20004.
Hauck, J., Hoppema, M., Bellerby, R. G. J., Völker, C., and Wolf-Gladrow, D. (2010). Data-based estimation of anthropogenic carbon and acidification in the Weddell Sea on a decadal timescale. *J. Geophys. Res.* 115, C03004. doi:10.1029/2009JC005479.
Hauck, J., Köhler, P., Wolf-Gladrow, D., and Völker, C. (2016). Iron fertilisation and century-scale effects of open ocean dissolution of olivine in a simulated CO2 removal experiment. *Environ. Res. Lett.* 11, 024007. doi:10.1088/1748-9326/11/2/024007.
Hauck, J., Lenton, A., Langlais, C., and Matear, R. (2018). The fate of carbon and nutrients exported out of the Southern Ocean. *Global Biogeochem. Cycles* 32, 1556–1573. doi:10.1029/2018GB005977.
Hauck, J., and Völker, C. (2015). Rising atmospheric CO2 leads to large impact of biology on Southern Ocean CO2 uptake via changes of the Revelle factor. *Geophys. Res. Lett.* 42, 1459–1464. doi:10.1002/2015GL063070.
Hauck, J., Völker, C., Wolf-Gladrow, D. A., Laufkötter, C., Vogt, M., Aumont, O., et al. (2015). On the Southern Ocean CO2 uptake and the role of the biological carbon pump in the 21st century. *Global Biogeochem. Cycles* 29, 1451–1470. doi:10.1002/2015GB005140.
Hauri, C., Friedrich, T., and Timmermann, A. (2016). Abrupt onset and prolongation of aragonite undersaturation events in the Southern Ocean. *Nat. Clim. Chang.* 6, 172–176. doi:10.1038/nclimate2844.
Hauri, C., Gruber, N., Vogt, M., Doney, S. C., Feely, R. A., Lachkar, Z., et al. (2013). Spatiotemporal variability and long-term trends of ocean acidification in the California Current System. *Biogeosciences* 10, 193–216. doi:10.5194/bg-10-193-2013.
Haustein, K., Allen, M. R., Forster, P. M., Otto, F. E. L., Mitchell, D. M., Matthews, H. D., et al. (2017). A real-time Global Warming Index. *Sci. Rep.* 7, 15417. doi:10.1038/s41598-017-14828-5.
He, Y., Trumbore, S. E., Torn, M. S., Harden, J. W., Vaughn, L. J. S., Allison, S. D., et al. (2016). Radiocarbon constraints imply reduced carbon uptake by soils during the 21st century. *Science* 353, 1419 LP – 1424. doi:10.1126/science.aad4273.
Heck, V., Gerten, D., Lucht, W., and Boysen, L. R. (2016). Is extensive terrestrial carbon dioxide removal a 'green' form of geoengineering? A global modelling study. *Glob. Planet. Change* 137, 123–130. doi:10.1016/j.gloplacha.2015.12.008.
Heck, V., Gerten, D., Lucht, W., and Popp, A. (2018). Biomass-based negative emissions difficult to reconcile with planetary boundaries. *Nat. Clim. Chang.* 8, 151–155. doi:10.1038/s41558-017-0064-y.
Heinze, C. (2004). Simulating oceanic CaCO 3 export production in the greenhouse. *Geophys. Res. Lett.* 31, L16308. doi:10.1029/2004GL020613.
Heland, J., and Schäfer, K. (1998). Determination of major combustion products in aircraft exhausts by FTIR emission spectroscopy. *Atmos. Environ.* 32, 3067–3072. doi:10.1016/S1352-2310(97)00395-6.
Helm, K. P., Bindoff, N. L., and Church, J. A. (2011). Observed decreases in oxygen content of the global ocean. *Geophys. Res. Lett.* 38, L23602. doi:10.1029/2011GL049513.
Henderson, B. B., Gerber, P. J., Hilinski, T. E., Falcucci, A., Ojima, D. S., Salvatore, M., et al. (2015). Greenhouse gas mitigation potential of the world's grazing lands: Modeling soil carbon and nitrogen fluxes of mitigation practices. *Agric. Ecosyst. Environ.* 207, 91–100. doi:10.1016/j.agee.2015.03.029.
Henson, S. A., Beaulieu, C., and Lampitt, R. (2016). Observing climate change trends in ocean biogeochemistry: when and where. *Glob. Chang. Biol.* 22, 1561–1571. doi:10.1111/gcb.13152.

Herrero, M., Henderson, B., Havlík, P., Thornton, P. K., Conant, R. T., Smith, P., et al. (2016). Greenhouse gas mitigation potentials in the livestock sector. *Nat. Clim. Chang.* 6, 452–461. doi:10.1038/nclimate2925.

Herrington, T., and Zickfeld, K. (2014). Path independence of climate and carbon cycle response over a broad range of cumulative carbon emissions. *Earth Syst. Dyn.* 5, 409–422. doi:10.5194/esd-5-409-2014.

Higgins, S. I., and Scheiter, S. (2012). Atmospheric CO2 forces abrupt vegetation shifts locally, but not globally. *Nature* 488, 209–212. doi:10.1038/nature11238.

Hirota, M., Holmgren, M., Van Nes, E. H., and Scheffer, M. (2011). Global resilience of tropical forest and savanna to critical transitions. *Science* 334, 232–235. doi:10.1126/science.1210657.

Hoffman, F. M., Randerson, J. T., Arora, V. K., Bao, Q., Cadule, P., Ji, D., et al. (2014). Causes and implications of persistent atmospheric carbon dioxide biases in Earth System Models. *J. Geophys. Res. Biogeosciences* 119, 141–162. doi:10.1002/2013JG002381.

Hoffmann, S. S., McManus, J. F., and Swank, E. (2018). Evidence for stable Holocene basin-scale overturning circulation despite variable currents along the deep Western Boundary of the North Atlantic Ocean. *Geophys. Res. Lett.* 45, 13,427-13,436. doi:10.1029/2018GL080187.

Hofmann, E. E., Cahill, B., Fennel, K., Friedrichs, M. A. M. M., Hyde, K., Lee, C., et al. (2011a). Modeling the dynamics of continental shelf carbon. *Ann. Rev. Mar. Sci.* 3, 93–122. doi:10.1146/annurev-marine-120709-142740.

Hofmann, G. E., Smith, J. E., Johnson, K. S., Send, U., Levin, L. A., Micheli, F., et al. (2011b). High-frequency dynamics of ocean pH: a multi-ecosystem comparison. *PLoS One* 6, e28983. doi:10.1371/journal.pone.0028983.

Hofmann, M., and Schellnhuber, H.-J. (2009). Oceanic acidification affects marine carbon pump and triggers extended marine oxygen holes. *Proc. Natl. Acad. Sci.* 106, 3017–3022. doi:10.1073/pnas.0813384106.

Holden, Z. A., Swanson, A., Luce, C. H., Jolly, W. M., Maneta, M., Oyler, J. W., et al. (2018). Decreasing fire season precipitation increased recent western US forest wildfire activity. *Proc. Natl. Acad. Sci. U. S. A.* doi:10.1073/pnas.1802316115.

Hollesen, J., Matthiesen, H., Møller, A. B., and Elberling, B. (2015). Permafrost thawing in organic Arctic soils accelerated by ground heat production. *Nat. Clim. Chang.* 5, 574–578. doi:10.1038/nclimate2590.

Holmes, C. D. (2018). Methane feedback on atmospheric chemistry: methods, models, and mechanisms. *J. Adv. Model. Earth Syst.* 10, 1087–1099. doi:10.1002/2017MS001196.

Hönisch, B., and Hemming, N. G. (2005). Surface ocean pH response to variations in pCO2 through two full glacial cycles. *Earth Planet. Sci. Lett.* 236, 305–314. doi:10.1016/j.epsl.2005.04.027.

Honisch, B., Ridgwell, A., Schmidt, D. N., Thomas, E., Gibbs, S. J., Sluijs, A., et al. (2012). The geological record of ocean acidification. *Science* 335, 1058–1063. doi:10.1126/science.1208277.

Hoogakker, B. A. A., Elderfield, H., Schmiedl, G., McCave, I. N., and Rickaby, R. E. M. (2015). Glacial–interglacial changes in bottom-water oxygen content on the Portuguese margin. *Nat. Geosci.* 8, 40–43. doi:10.1038/ngeo2317.

Hoogakker, B. A. A., Lu, Z., Umling, N., Jones, L., Zhou, X., Rickaby, R. E. M., et al. (2018). Glacial expansion of oxygen-depleted seawater in the eastern tropical Pacific. *Nature* 562, 410–413. doi:10.1038/s41586-018-0589-x.

Hoppe, C. J. M., Hassler, C. S., Payne, C. D., Tortell, P. D., Rost, B., and Trimborn, S. (2013). Iron limitation modulates ocean acidification effects on Southern Ocean phytoplankton communities. *PLoS One* 8, e79890. doi:10.1371/journal.pone.0079890.

Houghton, R. A. (2013). Keeping management effects separate from environmental effects in terrestrial carbon accounting. *Glob. Chang. Biol.* 19, 2609–2612. doi:10.1111/gcb.12233.

Houghton, R. A., Byers, B., and Nassikas, A. A. (2015). A role for tropical forests in stabilizing atmospheric CO2. *Nat. Clim. Chang.* 5, 1022–1023. doi:10.1038/nclimate2869.

Houghton, R. A., and Nassikas, A. A. (2017). Global and regional fluxes of carbon from land use and land cover change 1850-2015. *Global Biogeochem. Cycles* 31, 456–472. doi:10.1002/2016GB005546.

Houweling, S., Baker, D., Basu, S., Boesch, H., Butz, A., Chevallier, F., et al. (2015). An intercomparison of inverse models for estimating sources and sinks of CO2 using GOSAT measurements. *J. Geophys. Res. Atmos.* 120, 5253–5266. doi:10.1002/2014JD022962.

Hovenden, M. J., Leuzinger, S., Newton, P. C. D., Fletcher, A., Fatichi, S., Lüscher, A., et al. (2019). Globally consistent influences of seasonal precipitation limit grassland biomass response to elevated CO2. *Nat. Plants* 5, 167–173. doi:10.1038/s41477-018-0356-x.

Hristov, A. N., Oh, J., Firkins, J. L., Dijkstra, J., Kebreab, E., Waghorn, G., et al. (2013a). SPECIAL TOPICS — Mitigation of methane and nitrous oxide emissions from animal operations: I. A review of enteric methane mitigation options1. *J. Anim. Sci.* 91, 5045–5069. doi:10.2527/jas.2013-6583.

Hristov, A. N., Oh, J., Lee, C., Meinen, R., Montes, F., Ott, T., et al. (2013b). *Mitigation of greenhouse gas emissions in livestock production – A review of technical options for non-CO2 emissions.* , ed. H. P. S. Gerber, Pierre J.; Henderson, Benjamin; Makkar Food and Agriculture Organization of the United Nations Available at: https://books.google.co.za/books?id=iSXinQEACAAJ.

Hu, M., Chen, D., and Dahlgren, R. A. (2016). Modeling nitrous oxide emission from rivers: a global assessment. *Glob. Chang. Biol.* 22, 3566–3582. doi:10.1111/gcb.13351.

Huang, M., Piao, S., Ciais, P., Peñuelas, J., Wang, X., Keenan, T. F., et al. (2019). Air temperature optima of vegetation productivity across global biomes. *Nat. Ecol. Evol.* 3, 772–779. doi:10.1038/s41559-019-0838-x.

Hugelius, G., Strauss, J., Zubrzycki, S., Harden, J. W., Schuur, E. A. G., Ping, C.-L., et al. (2014). Estimated stocks of circumpolar permafrost carbon with quantified uncertainty ranges and identified data gaps. *Biogeosciences* 11, 6573–6593. doi:10.5194/bg-11-6573-2014.

Hülse, D., Arndt, S., Wilson, J. D., Munhoven, G., and Ridgwell, A. (2017). Understanding the causes and consequences of past marine carbon cycling variability through models. *Earth-Science Rev.* 171, 349–382. doi:10.1016/j.earscirev.2017.06.004.

Humpenöder, F., Popp, A., Dietrich, J. P., Klein, D., Lotze-Campen, H., Bonsch, M., et al. (2014). Investigating afforestation and bioenergy CCS as climate change mitigation strategies. *Environ. Res. Lett.* 9, 064029. doi:10.1088/1748-9326/9/6/064029.

Humphrey, V., Zscheischler, J., Ciais, P., Gudmundsson, L., Sitch, S., and Seneviratne, S. I. (2018). Sensitivity of atmospheric CO2 growth rate to observed changes in terrestrial water storage. *Nature* 560, 628–631. doi:10.1038/s41586-018-0424-4.

Hungate, B. A., Dijkstra, P., Wu, Z., Duval, B. D., Day, F. P., Johnson, D. W., et al. (2013). Cumulative response of ecosystem carbon and nitrogen stocks to chronic CO2 exposure in a subtropical oak woodland. *New Phytol.* 200, 753–766. doi:10.1111/nph.12333.

Huntingford, C., Atkin, O. K., Martinez-de la Torre, A., Mercado, L. M., Heskel, M. A., Harper, A. B., et al. (2017). Implications of improved representations of plant respiration in a changing climate. *Nat. Commun.* 8, 1602. doi:10.1038/s41467-017-01774-z.

Huntingford, C., Zelazowski, P., Galbraith, D., Mercado, L. M., Sitch, S., Fisher, R., et al. (2013). Simulated resilience of tropical rainforests to CO2-induced climate change. *Nat. Geosci.* 6, 268–273. doi:10.1038/ngeo1741.

Huntzinger, D. N., Michalak, A. M., Schwalm, C., Ciais, P., King, A. W., Fang, Y., et al. (2017). Uncertainty in the response of terrestrial carbon sink to environmental drivers undermines carbon-climate feedback predictions. *Sci. Rep.* 7, 4765. doi:10.1038/s41598-017-03818-2.

Huppmann, D., Rogelj, J., Kriegler, E., Krey, V., and Riahi, K. (2018). A new scenario resource for integrated 1.5 °C research. *Nat. Clim. Chang.* 8, 1027–1030. doi:10.1038/s41558-018-0317-4.

Hurd, C. L., Lenton, A., Tilbrook, B., and Boyd, P. W. (2018). Current understanding and challenges for oceans in a higher-CO2 world. *Nat. Clim. Chang.* 8, 686–694. doi:10.1038/s41558-018-0211-0.

Hurteau, M. D., Liang, S., Westerling, A. L., and Wiedinmyer, C. (2019). Vegetation-fire feedback reduces projected area burned under climate change. *Sci. Rep.* 9, 2838. doi:10.1038/s41598-019-39284-1.

Huybers, P., and Langmuir, C. H. (2017). Delayed CO2 emissions from mid-ocean ridge volcanism as a possible cause of late-Pleistocene glacial cycles. *Earth Planet. Sci. Lett.* 457, 238–249. doi:10.1016/j.epsl.2016.09.021.

IEA (2017). *CO2 emissions from fuel combustion*. International Energy Agency/Organisation for Economic Cooperation and Development, Paris.

Iida, Y., Kojima, A., Takatani, Y., Nakano, T., Sugimoto, H., Midorikawa, T., et al. (2015). Trends in pCO2 and sea–air CO2 flux over the global open oceans for the last two decades. *J. Oceanogr.* 71, 637–661. doi:10.1007/s10872-015-0306-4.

Ilyina, T., Li, H., Spring, A., Müller, W. A., Bopp, L., Chikamoto, M., et al. (submitted). Predictable variations in the carbon sinks and atmospheric CO2 growth in a multi-model framework. *Science* (submitted).

IPCC (2013). "Summary for Policymakers," in *Climate Change 2013: The Physical Science Basis. Contribution of Working Group I to the Fifth Assessment Report of the Intergovernmental Panel on Climate Change*, eds. T. F. Stocker, D. Qin, G.-K. Plattner, M. Tignor, S. K. Allen, J. Boschung, et al. (Cambridge, United Kingdom and New York, NY, USA: Cambridge University Press), 1–29.

IPCC (2014). Climate Change 2014: Synthesis Report. Contribution of Working Groups I, II and III to the Fifth Assessment Report of the Intergovernmental Panel on Climate Change. , eds. Core Writing Team, R. K. Pachauri, and L. A. Meyer Cambridge, United Kingdom and New York, NY, USA: Cambridge University Press.

IPCC (2018a). "Annex I: Glossary [Matthews, J.B.R. (ed.)]," in *Global Warming of 1.5°C. An IPCC Special Report on the impacts of global warming of 1.5°C above pre-industrial levels and related global greenhouse gas emission*

pathways, in the context of strengthening the global response to the threat of climate change, eds. V. Masson-Delmotte, P. Zhai, H.-O. Pörtner, D. Roberts, J. Skea, P. R. Shukla, et al. (In Press).

IPCC (2018b). Global Warming of 1.5°C. An IPCC Special Report on the impacts of global warming of 1.5°C above pre-industrial levels and related global greenhouse gas emission pathways, in the context of strengthening the global response to the threat of climate change,. , eds. V. Masson-Delmotte, P. Zhai, H.-O. Pörtner, D. Roberts, J. Skea, P. R. Shukla, et al. In Press.

IPCC (2018c). "Summary for Policymakers," in *Global Warming of 1.5°C. An IPCC Special Report on the impacts of global warming of 1.5°C above pre-industrial levels and related global greenhouse gas emission pathways, in the context of strengthening the global response to the threat of climate change,* eds. V. Masson-Delmotte, P. Zhai, H.-O. Pörtner, D. Roberts, J. Skea, P. R. Shukla, et al. (World Meteorological Organization, Geneva, Switzerland), 32. Available at: https://www.ipcc.ch/sr15/chapter/spm/.

IPCC (2019). "Summary for Policymakers," in *IPCC Special Report on the Ocean and Cryosphere in a Changing Climate*, eds. H.-O. Pörtner, D. C. Roberts, V. Masson-Delmotte, P. Zhai, M. Tignor, E. Poloczanska, et al., In press.

Ishidoya, S., Aoki, S., Goto, D., Nakazawa, T., Taguchi, S., and Patra, P. (2012). Time and space variations of the O2/N2 ratio in the troposphere over Japan and estimation of the global CO2 budget for the period 2000–2010. *Tellus B Chem. Phys. Meteorol.* 64, 18964. doi:10.3402/tellusb.v64i0.18964.

Ishii, M., Kosugi, N., Sasano, D., Saito, S., Midorikawa, T., and Inoue, H. Y. (2011). Ocean acidification off the south coast of Japan: A result from time series observations of CO2 parameters from 1994 to 2008. *J. Geophys. Res.* 116, C06022. doi:10.1029/2010JC006831.

Ishii, M., Rodgers, K. B., Inoue, H. Y., Toyama, K., Sasano, D., Kosugi, N., et al. (submitted). Ocean acidification from below in the tropical Pacific. *Global Biogeochem. Cycles* (submitted).

Ishijima, K., Nakazawa, T., and Aoki, S. (2009). Variations of atmospheric nitrous oxide concentration in the northern and western Pacific. *Tellus B Chem. Phys. Meteorol.* 61, 408–415. doi:10.1111/j.1600-0889.2008.00406.x.

Ishijima, K., Sugawara, S., Kawamura, K., Hashida, G., Morimoto, S., Murayama, S., et al. (2007). Temporal variations of the atmospheric nitrous oxide concentration and its δ15N and δ18O for the latter half of the 20th century reconstructed from firn air analyses. *J. Geophys. Res.* 112, D03305. doi:10.1029/2006JD007208.

Ito, A. (2017). Solar radiation management and ecosystem functional responses. *Clim. Change* 142, 53–66. doi:10.1007/s10584-017-1930-3.

Ito, T., Bracco, A., Deutsch, C., Frenzel, H., Long, M., and Takano, Y. (2015). Sustained growth of the Southern Ocean carbon storage in a warming climate. *Geophys. Res. Lett.* 42, 4516–4522. doi:10.1002/2015GL064320.

Ito, T., Minobe, S., Long, M. C., and Deutsch, C. (2017). Upper ocean O 2 trends: 1958-2015. *Geophys. Res. Lett.* 44, 4214–4223. doi:10.1002/2017GL073613.

Jaccard, S., Galbraith, E., Frölicher, T., and Gruber, N. (2014). Ocean (de)oxygenation across the last deglaciation: insights for the future. *Oceanography* 27, 26–35. doi:10.5670/oceanog.2014.05.

Jaccard, S. L., and Galbraith, E. D. (2012). Large climate-driven changes of oceanic oxygen concentrations during the last deglaciation. *Nat. Geosci.* 5, 151–156. doi:10.1038/ngeo1352.

Jaccard, S. L., Galbraith, E. D., Martínez-García, A., and Anderson, R. F. (2016). Covariation of deep Southern Ocean oxygenation and atmospheric CO2 through the last ice age. *Nature* 530, 207–210. doi:10.1038/nature16514.

Jaccard, S. L., Galbraith, E. D., Sigman, D. M., Haug, G. H., Francois, R., Pedersen, T. F., et al. (2009). Subarctic Pacific evidence for a glacial deepening of the oceanic respired carbon pool. *Earth Planet. Sci. Lett.* 277, 156–165. doi:10.1016/j.epsl.2008.10.017.

Jackson, R. B., Canadell, J. G., Le Quéré, C., Andrew, R. M., Korsbakken, J. I., Peters, G. P., et al. (2016). Reaching peak emissions. *Nat. Clim. Chang.* 6, 7–10. doi:10.1038/nclimate2892.

Jackson, R. B., Lajtha, K., Crow, S. E., Hugelius, G., Kramer, M. G., and Piñeiro, G. (2017). The ecology of soil carbon: pools, vulnerabilities, and biotic and abiotic controls. *Annu. Rev. Ecol. Evol. Syst.* 48, 419–445. doi:10.1146/annurev-ecolsys-112414-054234.

Janssens-Maenhout, G., Crippa, M., Guizzardi, D., Muntean, M., Schaaf, E., Dentener, F., et al. (2019). EDGAR v4.3.2 Global atlas of the three major greenhouse gas emissions for the period 1970-2012. *Earth Syst. Sci. Data* 11, 959–1002. doi:10.5194/essd-11-959-2019.

Jeffery, S., Verheijen, F. G. A., Kammann, C., and Abalos, D. (2016). Biochar effects on methane emissions from soils: A meta-analysis. *Soil Biol. Biochem.* 101, 251–258. doi:10.1016/j.soilbio.2016.07.021.

Jeffrey, L. C., Reithmaier, G., Sippo, J. Z., Johnston, S. G., Tait, D. R., Harada, Y., et al. (2019). Are methane emissions from mangrove stems a cryptic carbon loss pathway? Insights from a catastrophic forest mortality. *New Phytol.* 224, 146–154. doi:10.1111/nph.15995.

Jeltsch-Thömmes, A., Battaglia, G., Cartapanis, O., Jaccard, S. L., and Joos, F. (2019). Low terrestrial carbon storage at the Last Glacial Maximum: constraints from multi-proxy data. *Clim. Past* 15, 849–879. doi:10.5194/cp-15-849-2019.

Jenkins, S., Cain, M., Friedlingstein, P., Gillett, N., and Allen, M. R. (submitted). Quantifying non-CO2 contributions to remaining carbon budgets. *Nature* (submitted).

Ji, Q., Altabet, M. A., Bange, H. W., Graco, M. I., Ma, X., Arévalo-Martínez, D. L., et al. (2019). Investigating the effect of El Niño on nitrous oxide distribution in the eastern tropical South Pacific. *Biogeosciences* 16, 2079–2093. doi:10.5194/bg-16-2079-2019.

Ji, Q., Babbin, A. R., Jayakumar, A., Oleynik, S., and Ward, B. B. (2015). Nitrous oxide production by nitrification and denitrification in the Eastern Tropical South Pacific oxygen minimum zone. *Geophys. Res. Lett.* 42, 10,755-10,764. doi:10.1002/2015GL066853.

Jiang, M., Medlyn, B., Drake, J. E., and Duursma, R. A. (submitted). The fate of carbon in a mature forest under carbon dioxide enrichment. *Nature* (submitted).

Jiang, Y., van Groenigen, K. J., Huang, S., Hungate, B. A., van Kessel, C., Hu, S., et al. (2017). Higher yields and lower methane emissions with new rice cultivars. *Glob. Chang. Biol.* 23, 4728–4738. doi:10.1111/gcb.13737.

Jickells, T. D., Buitenhuis, E., Altieri, K., Baker, A. R., Capone, D., Duce, R. A., et al. (2017). A reevaluation of the magnitude and impacts of anthropogenic atmospheric nitrogen inputs on the ocean. *Global Biogeochem. Cycles* 31, 289–305. doi:10.1002/2016GB005586.

Jin, X., and Gruber, N. (2003). Offsetting the radiative benefit of ocean iron fertilization by enhancing N 2 O emissions. *Geophys. Res. Lett.* 30, 2249. doi:10.1029/2003GL018458.

Jin, Y., Goulden, M. L., Faivre, N., Veraverbeke, S., Sun, F., Hall, A., et al. (2015). Identification of two distinct fire regimes in Southern California: implications for economic impact and future change. *Environ. Res. Lett.* 10, 94005. doi:10.1088/1748-9326/10/9/094005.

Joiner, J., Yoshida, Y., Zhang, Y., Duveiller, G., Jung, M., Lyapustin, A., et al. (2018). Estimation of terrestrial global gross primary production (GPP) with satellite data-driven models and eddy covariance flux data. *Remote Sens.* 10, 1346. doi:10.3390/rs10091346.

Jolly, W. M., Cochrane, M. A., Freeborn, P. H., Holden, Z. A., Brown, T. J., Williamson, G. J., et al. (2015). Climate-induced variations in global wildfire danger from 1979 to 2013. *Nat. Commun.* doi:10.1038/ncomms8537.

Jones, A., Haywood, J. M., Alterskjaer, K., Boucher, O., Cole, J. N. S., Curry, C. L., et al. (2013a). The impact of abrupt suspension of solar radiation management (termination effect) in experiment G2 of the Geoengineering Model Intercomparison Project (GeoMIP). *J. Geophys. Res. Atmos.* 118, 9743–9752. doi:10.1002/jgrd.50762.

Jones, C. D., Arora, V., Friedlingstein, P., Bopp, L., Brovkin, V., Dunne, J., et al. (2016a). C4MIP - The Coupled Climate–Carbon Cycle Model Intercomparison Project: experimental protocol for CMIP6. *Geosci. Model Dev.* 9, 2853–2880. doi:10.5194/gmd-9-2853-2016.

Jones, C. D., Ciais, P., Davis, S. J., Friedlingstein, P., Gasser, T., Peters, G. P., et al. (2016b). Simulating the earth system response to negative emissions. *Environ. Res. Lett.* 11, 095012. doi:10.1088/1748-9326/11/9/095012.

Jones, C. D., and Friedlingstein, P. (submitted). Quantifying process-level uncertainty contributions to TCRE and Carbon Budgets for meeting Paris Agreement climate targets. *Environ. Res. Lett.* (submitted).

Jones, C. D., Frölicher, T. L., Koven, C., MacDougall, A. H., Matthews, H. D., Zickfeld, K., et al. (2019a). The Zero Emissions Commitment Model Intercomparison Project (ZECMIP) contribution to C4MIP: quantifying committed climate changes following zero carbon emissions. *Geosci. Model Dev.* 12, 4375–4385. doi:10.5194/gmd-12-4375-2019.

Jones, C. D., Frölicher, T. L., Koven, C., MacDougall, A. H., Matthews, H. D., Zickfeld, K., et al. (2019b). The Zero Emissions Commitment Model Intercomparison Project (ZECMIP) contribution to C4MIP: quantifying committed climate changes following zero carbon emissions. *Geosci. Model Dev.* 12, 4375–4385. doi:10.5194/gmd-12-4375-2019.

Jones, C., Lowe, J., Liddicoat, S., and Betts, R. (2009). Committed terrestrial ecosystem changes due to climate change. *Nat. Geosci.* 2, 484–487. doi:10.1038/ngeo555.

Jones, C., Robertson, E., Arora, V., Friedlingstein, P., Shevliakova, E., Bopp, L., et al. (2013b). Twenty-First-Century Compatible CO2 Emissions and Airborne Fraction Simulated by CMIP5 Earth System Models under Four Representative Concentration Pathways. *J. Clim.* 26, 4398–4413. doi:10.1175/JCLI-D-12-00554.1.

Jones, S. D., Le Quéré, C., Rödenbeck, C., Manning, A. C., and Olsen, A. (2015). A statistical gap-filling method to interpolate global monthly surface ocean carbon dioxide data. *J. Adv. Model. Earth Syst.* 7, 1554–1575. doi:10.1002/2014MS000416.

Joos, F., Prentice, I. C., Sitch, S., Meyer, R., Hooss, G., Plattner, G.-K., et al. (2001). Global warming feedbacks on terrestrial carbon uptake under the Intergovernmental Panel on Climate Change (IPCC) emission scenarios. *Global Biogeochem. Cycles* 15, 891–907. doi:10.1029/2000GB001375.

Joos, F., Roth, R., Fuglestvedt, J. S., Peters, G. P., Enting, I. G., von Bloh, W., et al. (2013). Carbon dioxide and climate impulse response functions for the computation of greenhouse gas metrics: a multi-model analysis. *Atmos. Chem. Phys.* 13, 2793–2825. doi:10.5194/acp-13-2793-2013.

Joos, F., and Spahni, R. (2008). Rates of change in natural and anthropogenic radiative forcing over the past 20,000 years. *Proc. Natl. Acad. Sci.* 105, 1425–1430. doi:10.1073/pnas.0707386105.

Jung, M., Reichstein, M., Schwalm, C. R., Huntingford, C., Sitch, S., Ahlström, A., et al. (2017). Compensatory water effects link yearly global land CO2 sink changes to temperature. *Nature* 541, 516–520. doi:10.1038/nature20780.

Junium, C. K., Dickson, A. J., and Uveges, B. T. (2018). Perturbation to the nitrogen cycle during rapid Early Eocene global warming. *Nat. Commun.* 9, 3186. doi:10.1038/s41467-018-05486-w.

Kalidindi, S., Bala, G., Modak, A., and Caldeira, K. (2015). Modeling of solar radiation management: a comparison of simulations using reduced solar constant and stratospheric sulphate aerosols. *Clim. Dyn.* 44, 2909–2925. doi:10.1007/s00382-014-2240-3.

Kammann, C., Ippoloto, J., Hagemann, N., Borchard, N., Cayuela, M. L., Estavillo, J. M., et al. (2017). Biochar as a tool to reduce the agricultural greenhouse-gas burden - knows, unknows and future research needs. *J. Environ. Eng. Landsc. Manag.* 25, 114–139. doi:10.3846/16486897.2017.1319375.

Karhu, K., Mattila, T., Bergström, I., and Regina, K. (2011). Biochar addition to agricultural soil increased CH4 uptake and water holding capacity – Results from a short-term pilot field study. *Agric. Ecosyst. Environ.* 140, 309–313. doi:https://doi.org/10.1016/j.agee.2010.12.005.

Katavouta, A., Williams, R. G., and Goodwin, P. (2019). The effect of ocean ventilation on the Transient Climate Response to Emissions. *J. Clim.* 32, 5085–5105. doi:10.1175/JCLI-D-18-0829.1.

Katavouta, A., Williams, R. G., Goodwin, P., and Roussenov, V. (2018). Reconciling atmospheric and oceanic views of the Transient Climate Response to Emissions. *Geophys. Res. Lett.* 45, 6205–6214. doi:10.1029/2018GL077849.

Kato, E., and Yamagata, Y. (2014). BECCS capability of dedicated bioenergy crops under a future land-use scenario targeting net negative carbon emissions. *Earth's Futur.* 2, 421–439. doi:10.1002/2014EF000249.

Kattge, J., and Knorr, W. (2007). Temperature acclimation in a biochemical model of photosynthesis: a reanalysis of data from 36 species. *Plant. Cell Environ.* 30, 1176–1190. doi:10.1111/j.1365-3040.2007.01690.x.

Kaushal, S. S., Likens, G. E., Pace, M. L., Utz, R. M., Haq, S., Gorman, J., et al. (2018). Freshwater salinization syndrome on a continental scale. *Proc. Natl. Acad. Sci.* 115, E574–E583. doi:10.1073/pnas.1711234115.

Kawahata, H., Fujita, K., Iguchi, A., Inoue, M., Iwasaki, S., Kuroyanagi, A., et al. (2019). Perspective on the response of marine calcifiers to global warming and ocean acidification—Behavior of corals and foraminifera in a high CO2 world "hot house." *Prog. Earth Planet. Sci.* 6, 5. doi:10.1186/s40645-018-0239-9.

Keeling, C. D. (1960). The concentration and isotopic abundances of carbon dioxide in the atmosphere. *Tellus* XII, 200–203.

Keeling, C. D., Whorf, T. P., Wahlen, M., and van der Plicht, J. (2001). Exchanges of atmospheric CO2, and 13CO2, with the terrestrial biosphere and oceans from 1978 to 2000. Available at: https://escholarship.org/uc/item/09v319r9.

Keeling, R. F., Graven, H. D., Welp, L. R., Resplandy, L., Bi, J., Piper, S. C., et al. (2017). Atmospheric evidence for a global secular increase in carbon isotopic discrimination of land photosynthesis. *Proc. Natl. Acad. Sci.* 114, 10361–10366. doi:10.1073/pnas.1619240114.

Keeling, R. F., and Manning, A. C. (2014). "5.15 - Studies of Recent Changes in Atmospheric O2 Content," in *Treatise on Geochemistry (Second Edition)*, eds. H. D. Holland and K. K. Turekian (Oxford: Elsevier), 385–404. doi:https://doi.org/10.1016/B978-0-08-095975-7.00420-4.

Keenan, T. F., Prentice, I. C., Canadell, J. G., Williams, C. A., Wang, H., Raupach, M., et al. (2016). Recent pause in the growth rate of atmospheric CO2 due to enhanced terrestrial carbon uptake. *Nat. Commun.* 7, 13428. doi:10.1038/ncomms13428.

Keith, D. W., and MacMartin, D. G. (2015). A temporary, moderate and responsive scenario for solar geoengineering. *Nat. Clim. Chang.* 5, 201–206. doi:10.1038/nclimate2493.

Keith, D. W., Wagner, G., and Zabel, C. L. (2017). Solar geoengineering reduces atmospheric carbon burden. *Nat. Clim. Chang.* 7, 617–619. doi:10.1038/nclimate3376.

Kell, D. B. (2011). Breeding crop plants with deep roots: their role in sustainable carbon, nutrient and water sequestration. *Ann. Bot.* 108, 407–418. doi:10.1093/aob/mcr175.

Keller, D. P., Feng, E. Y., and Oschlies, A. (2014). Potential climate engineering effectiveness and side effects during a high carbon dioxide-emission scenario. *Nat. Commun.* 5, 3304. doi:10.1038/ncomms4304.

Keller, D. P., Lenton, A., Littleton, E. W., Oschlies, A., Scott, V., and Vaughan, N. E. (2018a). The effects of carbon dioxide removal on the carbon cycle. *Curr. Clim. Chang. Reports* 4, 250–265. doi:10.1007/s40641-018-0104-3.

Keller, D. P., Lenton, A., Scott, V., Vaughan, N. E., Bauer, N., Ji, D., et al. (2018b). The Carbon Dioxide Removal Model Intercomparison Project (CDRMIP): rationale and experimental protocol for CMIP6. *Geosci. Model Dev.* 11, 1133–1160. doi:10.5194/gmd-11-1133-2018.

Keller, J. (2019). "Greenhouse gases," in *A Blue Carbon Primer, The State of Coastal Wetland Carbon Science, Practice and Policy*, eds. L. Windham-Myers, S. Crooks, and Troxler (Taylor and Francis Group/CRC Press), 93–106.

Kelly, J. W. G., Duursma, R. A., Atwell, B. J., Tissue, D. T., and Medlyn, B. E. (2016). Drought × CO2 interactions in trees: a test of the low-intercellular CO2 concentration (C i) mechanism. *New Phytol.* 209, 1600–1612. doi:10.1111/nph.13715.

Kemena, T. P., Landolfi, A., Oschlies, A., Wallmann, K., and Dale, A. W. (2019). Ocean phosphorus inventory: large uncertainties in future projections on millennial timescales and their consequences for ocean deoxygenation. *Earth Syst. Dynam.* 10, 539–553. doi:10.5194/esd-10-539-2019.

Kennedy, H., Fourqueran, J., and Papadimitriou, S. (2019). "The calcium carbonate cycle in seagrass ecosystems," in *A Blue Carbon Primer. The State of Coastal Wetland Carbon Science, Practice and Policy*, eds. L. Windham-Myers, S. Crooks, and T. Troxler (Taylor and Francis Group./CRC Press), 107–119.

Kessler, A., and Tjiputra, J. (2016). The Southern Ocean as a constraint to reduce uncertainty in future ocean carbon sinks. *Earth Syst. Dyn.* 7, 295–312. doi:10.5194/esd-7-295-2016.

Kicklighter, D. W., Cai, Y., Zhuang, Q., Parfenova, E. I., Paltsev, S., Sokolov, A. P., et al. (2014). Potential influence of climate-induced vegetation shifts on future land use and associated land carbon fluxes in Northern Eurasia. *Environ. Res. Lett.* 9, 35004. doi:10.1088/1748-9326/9/3/035004.

Kim, I.-N., Lee, K., Gruber, N., Karl, D. M., Bullister, J. L., Yang, S., et al. (2014). Increasing anthropogenic nitrogen in the North Pacific Ocean. *Science* 346, 1102–1106. doi:10.1126/science.1258396.

Kirschke, S., Bousquet, P., Ciais, P., Saunois, M., Canadell, J. G., Dlugokencky, E. J., et al. (2013). Three decades of global methane sources and sinks. *Nat. Geosci.* 6, 813–823. doi:10.1038/ngeo1955.

Kizyakov, A., Khomutov, A., Zimin, M., Khairullin, R., Babkina, E., Dvornikov, Y., et al. (2018). Microrelief associated with gas emission craters: remote-sensing and field-based study. *Remote Sens.* 10, 677. doi:10.3390/rs10050677.

Kizyakov, A., Zimin, M., Sonyushkin, A., Dvornikov, Y., Khomutov, A., and Leibman, M. (2017). Comparison of gas emission crater geomorphodynamics on Yamal and Gydan Peninsulas (Russia), based on repeat very-high-resolution stereopairs. *Remote Sens.* 9, 1023. doi:10.3390/rs9101023.

Kleinen, T., and Brovkin, V. (2018). Pathway-dependent fate of permafrost region carbon. *Environ. Res. Lett.* 13, 094001. doi:10.1088/1748-9326/aad824.

Kleinen, T., Brovkin, V., and Munhoven, G. (2016). Modelled interglacial carbon cycle dynamics during the Holocene, the Eemian and Marine Isotope Stage (MIS) 11. *Clim. Past* 12, 2145–2160. doi:10.5194/cp-12-2145-2016.

Kluber, L. A., Miller, J. O., Ducey, T. F., Hunt, P. G., Lang, M., and S. Ro, K. (2014). Multistate assessment of wetland restoration on CO2 and N2O emissions and soil bacterial communities. *Appl. Soil Ecol.* 76, 87–94. doi:10.1016/j.apsoil.2013.12.014.

Knauer, J., Zaehle, S., Reichstein, M., Medlyn, B. E., Forkel, M., Hagemann, S., et al. (2017). The response of ecosystem water-use efficiency to rising atmospheric CO2 concentrations: sensitivity and large-scale biogeochemical implications. *New Phytol.* 213, 1654–1666. doi:10.1111/nph.14288.

Knutti, R., and Rogelj, J. (2015). The legacy of our CO2 emissions: a clash of scientific facts, politics and ethics. *Clim. Change* 133, 361–373. doi:10.1007/s10584-015-1340-3.

Kock, A., Arévalo-Martínez, D. L., Löscher, C. R., and Bange, H. W. (2016). Extreme N2O accumulation in the coastal oxygen minimum zone off Peru. *Biogeosciences* 13, 827–840. doi:10.5194/bg-13-827-2016.

Kock, A., Schafstall, J., Dengler, M., Brandt, P., and Bange, H. W. (2012). Sea-to-air and diapycnal nitrous oxide fluxes in the eastern tropical North Atlantic Ocean. *Biogeosciences* 9, 957–964. doi:10.5194/bg-9-957-2012.

Köhler, P., Abrams, J. F., Völker, C., Hauck, J., and Wolf-Gladrow, D. A. (2013). Geoengineering impact of open ocean dissolution of olivine on atmospheric CO2, surface ocean pH and marine biology. *Environ. Res. Lett.* 8, 014009. doi:10.1088/1748-9326/8/1/014009.

Köhler, P., Knorr, G., and Bard, E. (2014). Permafrost thawing as a possible source of abrupt carbon release at the onset of the Bølling/Allerød. *Nat. Commun.* 5, 5520. doi:10.1038/ncomms6520.

Köhler, P., Nehrbass-Ahles, C., Schmitt, J., Stocker, T. F., and Fischer, H. (2017). A 156 kyr smoothed history of the atmospheric greenhouse gases CO2, CH4, and N2O and their radiative forcing. *Earth Syst. Sci. Data* 9, 363–387. doi:10.5194/essd-9-363-2017.

Kolby Smith, W., Reed, S. C., Cleveland, C. C., Ballantyne, A. P., Anderegg, W. R. L., Wieder, W. R., et al. (2016). Large divergence of satellite and Earth system model estimates of global terrestrial CO2 fertilization. *Nat. Clim. Chang.* 6, 306–310. doi:10.1038/nclimate2879.

Kondo, M., Ichii, K., Patra, P. K., Poulter, B., Calle, L., Koven, C., et al. (2018). Plant regrowth as a driver of recent enhancement of terrestrial CO2 Uptake. *Geophys. Res. Lett.* 45, 4820–4830. doi:10.1029/2018GL077633.

Koven, C. D., Chambers, J. Q., Georgiou, K., Knox, R., Negron-Juarez, R., Riley, W. J., et al. (2015a). Controls on terrestrial carbon feedbacks by productivity versus turnover in the CMIP5 Earth System Models. *Biogeosciences* 12, 5211–5228. doi:10.5194/bg-12-5211-2015.

Koven, C. D., Hugelius, G., Lawrence, D. M., and Wieder, W. R. (2017). Higher climatological temperature sensitivity of soil carbon in cold than warm climates. *Nat. Clim. Chang.* 7, 817–822. doi:10.1038/nclimate3421.

Koven, C. D., Lawrence, D. M., and Riley, W. J. (2015b). Permafrost carbon−climate feedback is sensitive to deep soil carbon decomposability but not deep soil nitrogen dynamics. *Proc. Natl. Acad. Sci.* 112, 201415123. doi:10.1073/pnas.1415123112.

Koven, C. D., Ringeval, B., Friedlingstein, P., Ciais, P., Cadule, P., Khvorostyanov, D., et al. (2011). Permafrost carbon-climate feedbacks accelerate global warming. *Proc. Natl. Acad. Sci.* 108, 14769–14774. doi:10.1073/pnas.1103910108.

Koven, C. D., Schuur, E. A. G., Schädel, C., Bohn, T. J., Burke, E. J., Chen, G., et al. (2015c). A simplified, data-constrained approach to estimate the permafrost carbon–climate feedback. *Philos. Trans. R. Soc. A Math. Phys. Eng. Sci.* 373, 20140423. doi:10.1098/rsta.2014.0423.

Krasting, J. P., Dunne, J. P., Shevliakova, E., and Stouffer, R. J. (2014). Trajectory sensitivity of the transient climate response to cumulative carbon emissions. *Geophys. Res. Lett.* 41, 2520–2527. doi:10.1002/2013GL059141.

Krause, A., Pugh, T. A. M., Bayer, A. D., Doelman, J. C., Humpenöder, F., Anthoni, P., et al. (2017). Global consequences of afforestation and bioenergy cultivation on ecosystem service indicators. *Biogeosciences* 14, 4829–4850. doi:10.5194/bg-14-4829-2017.

Kravitz, B., Robock, A., Boucher, O., Schmidt, H., Taylor, K. E., Stenchikov, G., et al. (2011). The Geoengineering Model Intercomparison Project (GeoMIP). *Atmos. Sci. Lett.* 12, 162–167. doi:10.1002/asl.316.

Kraxner, F., Nordström, E.-M., Havlík, P., Gusti, M., Mosnier, A., Frank, S., et al. (2013). Global bioenergy scenarios – Future forest development, land-use implications, and trade-offs. *Biomass and Bioenergy* 57, 86–96. doi:10.1016/j.biombioe.2013.02.003.

Kretschmer, K., Biastoch, A., Rüpke, L., and Burwicz, E. (2015). Modeling the fate of methane hydrates under global warming. *Global Biogeochem. Cycles* 29, 610–625. doi:10.1002/2014GB005011.

Krishna-Pillai Sukumara-Pillai, K., Bala, G., Cao, L., Duan, L., and Caldeira, K. (2019). Climate system response to stratospheric sulfate aerosols: sensitivity to altitude of aerosol layer. *Earth Syst. Dyn. Discuss.* 2019, 1–30. doi:10.5194/esd-2019-21.

Kroeker, K. J., Kordas, R. L., Crim, R., Hendriks, I. E., Ramajo, L., Singh, G. S., et al. (2013). Impacts of ocean acidification on marine organisms: quantifying sensitivities and interaction with warming. *Glob. Chang. Biol.* 19, 1884–1896. doi:10.1111/gcb.12179.

Kubota, K., Yokoyama, Y., Ishikawa, T., Suzuki, A., and Ishii, M. (2017). Rapid decline in pH of coral calcification fluid due to incorporation of anthropogenic CO2. *Sci. Rep.* 7, 7694. doi:10.1038/s41598-017-07680-0.

Kumarathunge, D. P., Medlyn, B. E., Drake, J. E., Tjoelker, M. G., Aspinwall, M. J., Battaglia, M., et al. (2019). Acclimation and adaptation components of the temperature dependence of plant photosynthesis at the global scale. *New Phytol.* 222, 768–784. doi:10.1111/nph.15668.

Kurz, W. A., Smyth, C., and LemprièreT.C (2016). Climate change mitigation through forest sector activities: principles, potential and priorities 1 - ProQuest. *Unasylva* 67, 61.

Kuypers, M. M. M., Lavik, G., Woebken, D., Schmid, M., Fuchs, B. M., Amann, R., et al. (2005). From The Cover: Massive nitrogen loss from the Benguela upwelling system through anaerobic ammonium oxidation. *Proc. Natl. Acad. Sci.* 102, 6478–6483. doi:10.1073/pnas.0502088102.

Kwiatkowski, L., Aumont, O., Bopp, L., and Ciais, P. (2018). The impact of variable phytoplankton stoichiometry on projections of primary production, food quality, and carbon uptake in the global ocean. *Global Biogeochem. Cycles* 32, 516–528. doi:10.1002/2017GB005799.

Kwiatkowski, L., Bopp, L., Aumont, O., Ciais, P., Cox, P. M., Laufkötter, C., et al. (2017). Emergent constraints on projections of declining primary production in the tropical oceans. *Nat. Clim. Chang.* 7, 355–358. doi:10.1038/nclimate3265.

Kwiatkowski, L., and Orr, J. C. (2018). Diverging seasonal extremes for ocean acidification during the twenty-first century. *Nat. Clim. Chang.* 8, 141–145. doi:10.1038/s41558-017-0054-0.

Kwon, E. Y., Primeau, F., and Sarmiento, J. L. (2009). The impact of remineralization depth on the air–sea carbon balance. *Nat. Geosci.* 2, 630–635. doi:10.1038/ngeo612.

Lampitt, R. ., Achterberg, E. ., Anderson, T. ., Hughes, J. ., Iglesias-Rodriguez, M. ., Kelly-Gerreyn, B. ., et al. (2008). Ocean fertilization: a potential means of geoengineering? *Philos. Trans. R. Soc. A Math. Phys. Eng. Sci.* 366, 3919–3945. doi:10.1098/rsta.2008.0139.

Landolfi, A., Somes, C. J., Koeve, W., Zamora, L. M., and Oschlies, A. (2017). Oceanic nitrogen cycling and N 2 O flux perturbations in the Anthropocene. *Global Biogeochem. Cycles* 31, 1236–1255. doi:10.1002/2017GB005633.

Landschützer, P., Gruber, N., and Bakker, D. C. E. (2016). Decadal variations and trends of the global ocean carbon sink. *Global Biogeochem. Cycles* 30, 1396–1417. doi:10.1002/2015GB005359.

Landschützer, P., Gruber, N., Bakker, D. C. E., and Schuster, U. (2014). Recent variability of the global ocean carbon sink. *Global Biogeochem. Cycles* 28, 927–949. doi:10.1002/2014GB004853.

Landschützer, P., Gruber, N., Bakker, D. C. E., Stemmler, I., and Six, K. D. (2018). Strengthening seasonal marine CO2 variations due to increasing atmospheric CO2. *Nat. Clim. Chang.* 8, 146–150. doi:10.1038/s41558-017-0057-x.

Landschützer, P., Gruber, N., Haumann, F. A., Rödenbeck, C., Bakker, D. C. E., van Heuven, S., et al. (2015). The reinvigoration of the Southern Ocean carbon sink. *Science* 349, 1221–1224. doi:10.1126/science.aab2620.

Laruelle, G. G., Cai, W.-J., Hu, X., Gruber, N., Mackenzie, F. T., and Regnier, P. (2018). Continental shelves as a variable but increasing global sink for atmospheric carbon dioxide. *Nat. Commun.* 9, 454. doi:10.1038/s41467-017-02738-z.

Laruelle, G. G., Landschützer, P., Gruber, N., Tison, J.-L., Delille, B., and Regnier, P. (2017). Global high-resolution monthly CO2 climatology for the coastal ocean derived from neural network interpolation. *Biogeosciences* 14, 4545–4561. doi:10.5194/bg-14-4545-2017.

Laruelle, G. G., Lauerwald, R., Pfeil, B., and Regnier, P. (2014). Regionalized global budget of the CO2 exchange at the air-water interface in continental shelf seas. *Global Biogeochem. Cycles* 28, 1199–1214. doi:10.1002/2014GB004832.

Lasslop, G., Brovkin, V., Reick, C. H., Bathiany, S., and Kloster, S. (2016). Multiple stable states of tree cover in a global land surface model due to a fire-vegetation feedback. *Geophys. Res. Lett.* 43, 6324–6331. doi:10.1002/2016GL069365.

Laufkötter, C., Vogt, M., Gruber, N., Aita-Noguchi, M., Aumont, O., Bopp, L., et al. (2015). Drivers and uncertainties of future global marine primary production in marine ecosystem models. *Biogeosciences* 12, 6955–6984. doi:10.5194/bg-12-6955-2015.

Laufkötter, C., Vogt, M., Gruber, N., Aumont, O., Bopp, L., Doney, S. C., et al. (2016). Projected decreases in future marine export production: the role of the carbon flux through the upper ocean ecosystem. *Biogeosciences* 13, 4023–4047. doi:10.5194/bg-13-4023-2016.

Laurent, A., Fennel, K., Cai, W.-J., Huang, W.-J., Barbero, L., and Wanninkhof, R. (2017). Eutrophication-induced acidification of coastal waters in the northern Gulf of Mexico: Insights into origin and processes from a coupled physical-biogeochemical model. *Geophys. Res. Lett.* 44, 946–956. doi:10.1002/2016GL071881.

Lauvset, S. K., Carter, B. R., Perez, F. F., Jiang, L. -Q., Feely, R. A., Velo, A., et al. (2020). Processes driving global interior ocean pH distribution. *Global Biogeochem. Cycles*, 2019GB006229. doi:10.1029/2019GB006229.

Lauvset, S. K., Key, R. M., Olsen, A., van Heuven, S., Velo, A., Lin, X., et al. (2016). A new global interior ocean mapped climatology: the 1° × 1° GLODAP version 2. *Earth Syst. Sci. Data* 8, 325–340. doi:10.5194/essd-8-325-2016.

Lauvset, S. K., Tjiputra, J., and Muri, H. (2017). Climate engineering and the ocean: effects on biogeochemistry and primary production. *Biogeosciences* 14, 5675–5691. doi:10.5194/bg-14-5675-2017.

Lavergne, A., Graven, H., De Kauwe, M. G., Keenan, T. F., Medlyn, B. E., and Prentice, I. C. (2019). Observed and modelled historical trends in the water-use efficiency of plants and ecosystems. *Glob. Chang. Biol.*, gcb.14634. doi:10.1111/gcb.14634.

Law, R. M., Ziehn, T., Matear, R. J., Lenton, A., Chamberlain, M. A., Stevens, L. E., et al. (2017). The carbon cycle in the Australian Community Climate and Earth System Simulator (ACCESS-ESM1) – Part 1: Model description and pre-industrial simulation. *Geosci. Model Dev.* 10, 2567–2590. doi:10.5194/gmd-10-2567-2017.

Le Page, Y., Morton, D., Hartin, C., Bond-Lamberty, B., Pereira, J. M. C., Hurtt, G., et al. (2017). Synergy between land use and climate change increases future fire risk in Amazon forests. *Earth Syst. Dyn.* 8, 1237–1246. doi:10.5194/esd-8-1237-2017.

Le Quéré, C., Andrew, R. M., Friedlingstein, P., Sitch, S., Hauck, J., Pongratz, J., et al. (2018a). Global Carbon Budget 2018. *Earth Syst. Sci. Data* 10, 2141–2194. doi:10.5194/essd-10-2141-2018.

Le Quéré, C., Andrew, R. M., Friedlingstein, P., Sitch, S., Pongratz, J., Manning, A. C., et al. (2018b). Global Carbon Budget 2017. *Earth Syst. Sci. Data* 10, 405–448. doi:10.5194/essd-10-405-2018.

Le Quéré, C., Takahashi, T., Buitenhuis, E. T., Rödenbeck, C., and Sutherland, S. C. (2010). Impact of climate change and variability on the global oceanic sink of CO2. *Global Biogeochem. Cycles* 24, GB4007. doi:10.1029/2009GB003599.

Lebehot, A. D., Halloran, P. R., Watson, A. J., McNeall, D., Ford, D. A., Landschützer, P., et al. (2019). Reconciling observation and model trends in North Atlantic surface CO2. *Global Biogeochem. Cycles* 33, 1204–1222. doi:10.1029/2019GB006186.

Leduc, M., Matthews, H. D., and de Elía, R. (2015). Quantifying the limits of a linear temperature response to cumulative CO2 emissions. *J. Clim.* 28, 9955–9968. doi:10.1175/JCLI-D-14-00500.1.

Leduc, M., Matthews, H. D., and de Elía, R. (2016). Regional estimates of the transient climate response to cumulative CO2 emissions. *Nat. Clim. Chang.* 6, 474–478. doi:10.1038/nclimate2913.

Lee, K., Tong, L. T., Millero, F. J., Sabine, C. L., Dickson, A. G., Goyet, C., et al. (2006). Global relationships of total alkalinity with salinity and temperature in surface waters of the world's oceans. *Geophys. Res. Lett.* 33. doi:10.1029/2006GL027207.

Lee, S.-J., Ryu, I.-S., Kim, B.-M., and Moon, S.-H. (2011). A review of the current application of N2O emission reduction in CDM projects. *Int. J. Greenh. Gas Control* 5, 167–176. doi:10.1016/j.ijggc.2010.07.001.

Lehmann, C. E. R., Anderson, T. M., Sankaran, M., Higgins, S. I., Archibald, S., Hoffmann, W. A., et al. (2014). Savanna vegetation-fire-climate relationships differ among continents. *Science* 343, 548 LP – 552. doi:10.1126/science.1247355.

Lehmann, J., Abiven, S., Kleber, M., Pan, G., Singh, B. P., Sohi, S., et al. (2015). "Persistence of biochar in soil," in *Biochar for Environmental Management: Science, Technology and Implementation*, eds. J. Lehmann and S. Joseph (London, UK), 233--80. doi:https://doi.org/10.4324/9780203762264.

Leifeld, J., Wüst-Galley, C., and Page, S. (2019). Intact and managed peatland soils as a source and sink of GHGs from 1850 to 2100. *Nat. Clim. Chang.* 9, 945–947. doi:10.1038/s41558-019-0615-5.

Leith, C. E. (1975). Climate response and fluctuation dissipation. *J. Atmos. Sci.* 32, 2022–2026. doi:10.1175/1520-0469(1975)032<2022:CRAFD>2.0.CO;2.

Lenton, A., Tilbrook, B., Law, R. M., Bakker, D., Doney, S. C., Gruber, N., et al. (2013). Sea–air CO2 fluxes in the Southern Ocean for the period 1990-2009. *Biogeosciences* 10, 4037–4054. doi:10.5194/bg-10-4037-2013.

Lenton, T. M. (2011). Early warning of climate tipping points. *Nat. Clim. Chang.* 1, 201–209. doi:10.1038/nclimate1143.

Lenton, T. M., Held, H., Kriegler, E., Hall, J. W., Lucht, W., Rahmstorf, S., et al. (2008). Tipping elements in the Earth's climate system. *Proc. Natl. Acad. Sci.* 105, 1786–1793. doi:10.1073/pnas.0705414105.

Lenton, T. M., Livina, V. N., Dakos, V., van Nes, E. H., and Scheffer, M. (2012). Early warning of climate tipping points from critical slowing down: comparing methods to improve robustness. *Philos. Trans. R. Soc. A Math. Phys. Eng. Sci.* 370, 1185–1204. doi:10.1098/rsta.2011.0304.

Levin, I., Naegler, T., Kromer, B., Diehl, M., Francey, R., Gomez-Pelaez, A., et al. (2010). Observations and modelling of the global distribution and long-term trend of atmospheric 14 CO2. *Tellus B Chem. Phys. Meteorol.* 62, 26–46. doi:10.1111/j.1600-0889.2009.00446.x.

Levin, L. A. (2018). Manifestation, drivers, and emergence of open ocean deoxygenation. *Ann. Rev. Mar. Sci.* 10, 229–260. doi:10.1146/annurev-marine-121916-063359.

Levine, N. M., Zhang, K., Longo, M., Baccini, A., Phillips, O. L., Lewis, S. L., et al. (2016). Ecosystem heterogeneity determines the ecological resilience of the Amazon to climate change. *Proc. Natl. Acad. Sci.* 113, 793–797. doi:10.1073/pnas.1511344112.

Li, H., and Ilyina, T. (2018). Current and future decadal trends in the oceanic carbon uptake are dominated by internal variability. *Geophys. Res. Lett.* 45, 916–925. doi:10.1002/2017GL075370.

Li, H., Ilyina, T., Müller, W. A., and Landschützer, P. (2019). Predicting the variable ocean carbon sink. *Sci. Adv.* 5, eaav6471. doi:10.1126/sciadv.aav6471.

Li, H., Ilyina, T., Müller, W. A., and Sienz, F. (2016a). Decadal predictions of the North Atlantic CO2 uptake. *Nat. Commun.* 7, 11076. doi:10.1038/ncomms11076.

Li, M., Lee, Y. J., Testa, J. M., Li, Y., Ni, W., Kemp, W. M., et al. (2016b). What drives interannual variability of hypoxia in Chesapeake Bay: Climate forcing versus nutrient loading? *Geophys. Res. Lett.* 43, 2127–2134. doi:10.1002/2015GL067334.

Li, W., Ciais, P., Guenet, B., Peng, S., Chang, J., Chaplot, V., et al. (2018). Temporal response of soil organic carbon after grassland-related land-use change. *Glob. Chang. Biol.* 24, 4731–4746. doi:10.1111/gcb.14328.

Li, W., Ciais, P., Wang, Y., Peng, S., Broquet, G., Ballantyne, A. P., et al. (2016c). Reducing uncertainties in decadal variability of the global carbon budget with multiple datasets. *Proc. Natl. Acad. Sci.* 113, 13104–13108. doi:10.1073/pnas.1603956113.

Lilly, L. E., Send, U., Lankhorst, M., Martz, T. R., Feely, R. A., Sutton, A. J., et al. (2019). Biogeochemical anomalies at two Southern California Current system moorings during the 2014–2016 warm anomaly-El Niño sequence. *J. Geophys. Res. Ocean.* 124, 6886–6903. doi:10.1029/2019JC015255.

Lippold, J., Gutjahr, M., Blaser, P., Christner, E., de Carvalho Ferreira, M. L., Mulitza, S., et al. (2016). Deep water provenance and dynamics of the (de)glacial Atlantic meridional overturning circulation. *Earth Planet. Sci. Lett.* 445, 68–78. doi:10.1016/j.epsl.2016.04.013.

Liu, C., Wang, H., Tang, X., Guan, Z., Reid, B. J., Rajapaksha, A. U., et al. (2016). Biochar increased water holding capacity but accelerated organic carbon leaching from a sloping farmland soil in China. *Environ. Sci. Pollut. Res.* 23, 995–1006. doi:10.1007/s11356-015-4885-9.

Liu, J., Bowman, K. W., Schimel, D. S., Parazoo, N. C., Jiang, Z., Lee, M., et al. (2017a). Contrasting carbon cycle responses of the tropical continents to the 2015-2016 El Nino. *Science* 358. doi:10.1126/science.aam5690.

Liu, X., Dunne, J. P., Stock, C. A., Harrison, M. J., Adcroft, A., and Resplandy, L. (2019a). Simulating water residence time in the coastal ocean: a global perspective. *Geophys. Res. Lett.* 46, 13910–13919. doi:10.1029/2019GL085097.

Liu, Y., Peng, Z., Zhou, R., Song, S., Liu, W., You, C.-F., et al. (2015). Acceleration of modern acidification in the South China Sea driven by anthropogenic CO2. *Sci. Rep.* 4, 5148. doi:10.1038/srep05148.

Liu, Y., Piao, S., Gasser, T., Ciais, P., Yang, H., Wang, H., et al. (2019b). Field-experiment constraints on the enhancement of the terrestrial carbon sink by CO2 fertilization. *Nat. Geosci.* 12, 809–814. doi:10.1038/s41561-019-0436-1.

Liu, Z., He, T., Cao, T., Yang, T., Meng, J., and Chen, W. (2017b). Effects of biochar application on nitrogen leaching, ammonia volatilization and nitrogen use efficiency in two distinct soils. *J. soil Sci. plant Nutr.* 17, 515–528. doi:10.4067/S0718-95162017005000037.

Lloret, F., Escudero, A., Iriondo, J. M., Martínez-Vilalta, J., and Valladares, F. (2012). Extreme climatic events and vegetation: the role of stabilizing processes. *Glob. Chang. Biol.* 18, 797–805. doi:10.1111/j.1365-2486.2011.02624.x.

Lloyd, J., and Farquhar, G. D. (2008). Effects of rising temperatures and [CO2] on the physiology of tropical forest trees. *Philos. Trans. R. Soc. B Biol. Sci.* 363, 1811–1817. doi:10.1098/rstb.2007.0032.

Lombardozzi, D. L., Bonan, G. B., Smith, N. G., Dukes, J. S., and Fisher, R. A. (2015). Temperature acclimation of photosynthesis and respiration: A key uncertainty in the carbon cycle-climate feedback. *Geophys. Res. Lett.* 42, 8624–8631. doi:10.1002/2015GL065934.

Loulergue, L., Schilt, A., Spahni, R., Masson-Delmotte, V., Blunier, T., Lemieux, B., et al. (2008). Orbital and millennial-scale features of atmospheric CH4 over the past 800,000 years. *Nature* 453, 383–386. doi:10.1038/nature06950.

Lovelock, C. E., and Duarte, C. M. (2019). Dimensions of Blue Carbon and emerging perspectives. *Biol. Lett.* 15, 20180781. doi:10.1098/rsbl.2018.0781.

Lovenduski, N. S., Bonan, G. B., Yeager, S. G., Lindsay, K., and Lombardozzi, D. L. (2019a). High predictability of terrestrial carbon fluxes from an initialized decadal prediction system. *Environ. Res. Lett.* 14, 124074. doi:10.1088/1748-9326/ab5c55.

Lovenduski, N. S., Yeager, S. G., Lindsay, K., and Long, M. C. (2019b). Predicting near-term variability in ocean carbon uptake. *Earth Syst. Dyn.* 10, 45–57. doi:10.5194/esd-10-45-2019.

Lowe, A. T., Bos, J., and Ruesink, J. (2019). Ecosystem metabolism drives pH variability and modulates long-term ocean acidification in the Northeast Pacific coastal ocean. *Sci. Rep.* 9, 963. doi:10.1038/s41598-018-37764-4.

Lowe, J. A., and Bernie, D. (2018). The impact of Earth system feedbacks on carbon budgets and climate response. *Philos. Trans. R. Soc. A Math. Phys. Eng. Sci.* 376, 20170263. doi:10.1098/rsta.2017.0263.

Lowe, J. A., Huntingford, C., Raper, S. C. B., Jones, C. D., Liddicoat, S. K., and Gohar, L. K. (2009). How difficult is it to recover from dangerous levels of global warming? *Environ. Res. Lett.* 4, 014012. doi:10.1088/1748-9326/4/1/014012.

Lucht, W., Schaphoff, S., Erbrecht, T., Heyder, U., and Cramer, W. (2006). Terrestrial vegetation redistribution and carbon balance under climate change. *Carbon Balance Manag.* 1, 6. doi:10.1186/1750-0680-1-6.

Łukawska-Matuszewska, K., Graca, B., Brocławik, O., and Zalewska, T. (2019). The impact of declining oxygen conditions on pyrite accumulation in shelf sediments (Baltic Sea). *Biogeochemistry* 142, 209–230. doi:10.1007/s10533-018-0530-2.

Luke, C. M., and Cox, P. M. (2011). Soil carbon and climate change: from the Jenkinson effect to the compost-bomb instability. *Eur. J. Soil Sci.* 62, 5–12. doi:10.1111/j.1365-2389.2010.01312.x.

Lund, D. C., Asimow, P. D., Farley, K. A., Rooney, T. O., Seeley, E., Jackson, E. W., et al. (2016). Enhanced East Pacific Rise hydrothermal activity during the last two glacial terminations. *Science* 351, 478–482. doi:10.1126/science.aad4296.

Lundin, L., Nilsson, T., Jordan, S., Lode, E., and Strömgren, M. (2017). Impacts of rewetting on peat, hydrology and water chemical composition over 15 years in two finished peat extraction areas in Sweden. *Wetl. Ecol. Manag.* 25, 405–419. doi:10.1007/s11273-016-9524-9.

Luo, Y., Ahlström, A., Allison, S. D., Batjes, N. H., Brovkin, V., Carvalhais, N., et al. (2016). Toward more realistic projections of soil carbon dynamics by Earth system models. *Global Biogeochem. Cycles* 30, 40–56. doi:10.1002/2015GB005239.

Lüthi, D., Le Floch, M., Bereiter, B., Blunier, T., Barnola, J.-M., Siegenthaler, U., et al. (2008). High-resolution carbon dioxide concentration record 650,000–800,000 years before present. *Nature* 453, 379–382. doi:10.1038/nature06949.

Luyssaert, S., Jammet, M., Stoy, P. C., Estel, S., Pongratz, J., Ceschia, E., et al. (2014). Land management and land-cover change have impacts of similar magnitude on surface temperature. *Nat. Clim. Chang.* 4, 389–393. doi:10.1038/nclimate2196.

Lyra, A., Imbach, P., Rodriguez, D., Chou, S. C., Georgiou, S., and Garofolo, L. (2017). Projections of climate change impacts on central America tropical rainforest. *Clim. Change* 141, 93–105. doi:10.1007/s10584-016-1790-2.

M. Koskinen, L. Maanavilja, M. Nieminen, K. Minkkinen, E. S. . T. (2016). High methane emissions from restored Norway spruce swamps in southern Finland over one growing season. *Mires Peat* 17, 1–13. doi:10.19189/MaP.2015.OMB.202.

Maavara, T., Lauerwald, R., Laruelle, G. G., Akbarzadeh, Z., Bouskill, N. J., Van Cappellen, P., et al. (2019). Nitrous oxide emissions from inland waters: Are IPCC estimates too high? *Glob. Chang. Biol.* 25, 473–488. doi:10.1111/gcb.14504.

MacDougall, A. H. (2016). The Transient Response to Cumulative CO2 Emissions: a Review. *Curr. Clim. Chang. Reports* 2, 39–47. doi:10.1007/s40641-015-0030-6.

MacDougall, A. H. (2017). The oceanic origin of path-independent carbon budgets. *Sci. Rep.* 7, 10373. doi:10.1038/s41598-017-10557-x.

MacDougall, A. H., and Friedlingstein, P. (2015). The origin and limits of the near proportionality between climate warming and cumulative CO2 emissions. *J. Clim.* 28, 4217–4230. doi:10.1175/JCLI-D-14-00036.1.

MacDougall, A. H., Frölicher, T. L., Jones, C. D., and et al. (submitted). Is there warming in the pipeline? A multi-model analysis of the zero emission commitment from CO2. *Biogeosciences Discuss.* (submitted).

MacDougall, A. H., and Knutti, R. (2016a). Enhancement of non-CO2 radiative forcing via intensified carbon cycle feedbacks. *Geophys. Res. Lett.* 43, 5833–5840. doi:10.1002/2016GL068964.

MacDougall, A. H., and Knutti, R. (2016b). Projecting the release of carbon from permafrost soils using a perturbed parameter ensemble modelling approach. *Biogeosciences* 13, 2123–2136. doi:10.5194/bg-13-2123-2016.

MacDougall, A. H., Swart, N. C., and Knutti, R. (2017). The uncertainty in the transient climate response to cumulative CO2 emissions arising from the uncertainty in physical climate parameters. *J. Clim.* 30, 813–827. doi:10.1175/JCLI-D-16-0205.1.

MacDougall, A. H., Zickfeld, K., Knutti, R., and Matthews, H. D. (2015). Sensitivity of carbon budgets to permafrost carbon feedbacks and non-CO2 forcings. *Environ. Res. Lett.* 10, 125003. doi:10.1088/1748-9326/10/12/125003.

MacFarling Meure, C., Etheridge, D., Trudinger, C., Steele, P., Langenfelds, R., van Ommen, T., et al. (2006). Law Dome CO2 , CH4 and N2O ice core records extended to 2000 years BP. *Geophys. Res. Lett.* 33, L14810. doi:10.1029/2006GL026152.

Mack, M. C., Bret-Harte, M. S., Hollingsworth, T. N., Jandt, R. R., Schuur, E. A. G., Shaver, G. R., et al. (2011). Carbon loss from an unprecedented Arctic tundra wildfire. *Nature* 475, 489–492. doi:10.1038/nature10283.

Macreadie, P. I., Anton, A., Raven, J. A., Beaumont, N., Connolly, R. M., Friess, D. A., et al. (2019). The future of Blue Carbon science. *Nat. Commun.* 10, 3998. doi:10.1038/s41467-019-11693-w.

Madhupratap, M., Kumar, S. P., Bhattathiri, P. M. A., Kumar, M. D., Raghukumar, S., Nair, K. K. C., et al. (1996). Mechanism of the biological response to winter cooling in the northeastern Arabian Sea. *Nature* 384, 549–552. doi:10.1038/384549a0.

Mahowald, N., Kohfeld, K., Hansson, M., Balkanski, Y., Harrison, S. P., Prentice, I. C., et al. (1999). Dust sources and deposition during the last glacial maximum and current climate: A comparison of model results with paleodata from ice cores and marine sediments. *J. Geophys. Res. Atmos.* 104, 15895–15916. doi:10.1029/1999JD900084.

Mahowald, N. M., Scanza, R., Brahney, J., Goodale, C. L., Hess, P. G., Moore, J. K., et al. (2017). Aerosol deposition impacts on land and ocean carbon cycles. *Curr. Clim. Chang. Reports* 3, 16–31. doi:10.1007/s40641-017-0056-z.

Majorowicz, J., Grasby, S. E., Safanda, J., and Beauchamp, B. (2014). Gas hydrate contribution to Late Permian global warming. *Earth Planet. Sci. Lett.* 393, 243–253. doi:10.1016/j.epsl.2014.03.003.

Malakhova, V. V., and Eliseev, A. V. (2017). The role of heat transfer time scale in the evolution of the subsea permafrost and associated methane hydrates stability zone during glacial cycles. *Glob. Planet. Change* 157, 18–25. doi:10.1016/j.gloplacha.2017.08.007.

Malhi, Y., Rowland, L., Aragão, L. E. O. C., and Fisher, R. A. (2018). New insights into the variability of the tropical land carbon cycle from the El Niño of 2015/2016. *Philos. Trans. R. Soc. B Biol. Sci.* 373, 20170298. doi:10.1098/rstb.2017.0298.

Manizza, M., Keeling, R. F., and Nevison, C. D. (2012). On the processes controlling the seasonal cycles of the air–sea fluxes of O2 and N2O: A modelling study. *Tellus B Chem. Phys. Meteorol.* 64, 18429. doi:10.3402/tellusb.v64i0.18429.

Mao, J., Ribes, A., Yan, B., Shi, X., Thornton, P. E., Séférian, R., et al. (2016). Human-induced greening of the northern extratropical land surface. *Nat. Clim. Chang.* 6, 959–963. doi:10.1038/nclimate3056.

Marañón, E., Lorenzo, M. P., Cermeño, P., and Mouriño-Carballido, B. (2018). Nutrient limitation suppresses the temperature dependence of phytoplankton metabolic rates. *ISME J.* 12, 1836–1845. doi:10.1038/s41396-018-0105-1.

Marcott, S. A., Bauska, T. K., Buizert, C., Steig, E. J., Rosen, J. L., Cuffey, K. M., et al. (2014). Centennial-scale changes in the global carbon cycle during the last deglaciation. *Nature* 514, 616–619. doi:10.1038/nature13799.

Martínez-Botí, M. A., Foster, G. L., Chalk, T. B., Rohling, E. J., Sexton, P. F., Lunt, D. J., et al. (2015a). Plio-Pleistocene climate sensitivity evaluated using high-resolution CO2 records. *Nature* 518, 49–54. doi:10.1038/nature14145.

Martínez-Botí, M. A., Marino, G., Foster, G. L., Ziveri, P., Henehan, M. J., Rae, J. W. B., et al. (2015b). Boron isotope evidence for oceanic carbon dioxide leakage during the last deglaciation. *Nature* 518, 219–222. doi:10.1038/nature14155.

Martinez-Garcia, A., Sigman, D. M., Ren, H., Anderson, R. F., Straub, M., Hodell, D. A., et al. (2014). Iron Fertilization of the Subantarctic Ocean During the Last Ice Age. *Science* 343, 1347–1350. doi:10.1126/science.1246848.

Martinez-Rey, J., Bopp, L., Gehlen, M., Tagliabue, A., and Gruber, N. (2015). Projections of oceanic N₂O emissions in the 21st century using the IPSL Earth system model. *Biogeosciences* 12, 4133–4148. doi:10.5194/bg-12-4133-2015.

Martinez, E., Raitsos, D. E., and Antoine, D. (2016). Warmer, deeper, and greener mixed layers in the North Atlantic subpolar gyre over the last 50 years. *Glob. Chang. Biol.* 22, 604–612. doi:10.1111/gcb.13100.

Mastrotheodoros, T., Pappas, C., Molnar, P., Burlando, P., Keenan, T. F., Gentine, P., et al. (2017). Linking plant functional trait plasticity and the large increase in forest water use efficiency. *J. Geophys. Res. Biogeosciences* 122, 2393–2408. doi:10.1002/2017JG003890.

Matear, R. J., and Lenton, A. (2014). Quantifying the impact of ocean acidification on our future climate. *Biogeosciences* 11, 3965–3983. doi:10.5194/bg-11-3965-2014.

Matear, R. J., and Lenton, A. (2018). Carbon–climate feedbacks accelerate ocean acidification. *Biogeosciences* 15, 1721–1732. doi:10.5194/bg-15-1721-2018.

Mathesius, S., Hofmann, M., Caldeira, K., and Schellnhuber, H. J. (2015). Long-term response of oceans to CO2 removal from the atmosphere. *Nat. Clim. Chang.* 5, 1107–1113. doi:10.1038/nclimate2729.

Mathur, S., Agrawal, D., and Jajoo, A. (2014). Photosynthesis: Response to high temperature stress. *J. Photochem. Photobiol. B Biol.* 137, 116–126. doi:10.1016/j.jphotobiol.2014.01.010.

Matsumoto, K. (2007). Biology-mediated temperature control on atmospheric pCO2 and ocean biogeochemistry. *Geophys. Res. Lett.* 34, L20605. doi:10.1029/2007GL031301.

Matsumoto, K., Tokos, K., Chikamoto, M., and Ridgwell, A. (2010). Characterizing post-industrial changes in the ocean carbon cycle in an Earth system model. *Tellus B Chem. Phys. Meteorol.* 62, 296–313. doi:10.1111/j.1600-0889.2010.00461.x.

Matthews, H. D., and Caldeira, K. (2007). Transient climate carbon simulations of planetary geoengineering. *Proc. Natl. Acad. Sci.* 104, 9949–9954. doi:10.1073/pnas.0700419104.

Matthews, H. D., and Caldeira, K. (2008). Stabilizing climate requires near-zero emissions. *Geophys. Res. Lett.* 35, L04705. doi:10.1029/2007GL032388.

Matthews, H. D., Gillett, N. P., Stott, P. A., and Zickfeld, K. (2009). The proportionality of global warming to cumulative carbon emissions. *Nature* 459, 829–832. doi:10.1038/nature08047.

Matthews, H. D., Landry, J.-S., Partanen, A.-I., Allen, M., Eby, M., Forster, P. M., et al. (2017). Estimating carbon budgets for ambitious climate targets. *Curr. Clim. Chang. Reports* 3, 69–77. doi:10.1007/s40641-017-0055-0.

Matthews, H. D., and Solomon, S. (2013). Irreversible does not mean unavoidable. *Science* 340, 438–439. doi:10.1126/science.1236372.

Matthews, H. D., Solomon, S., and Pierrehumbert, R. (2012). Cumulative carbon as a policy framework for achieving climate stabilization. *Philos. Trans. R. Soc. A Math. Phys. Eng. Sci.* 370, 4365–4379. doi:10.1098/rsta.2012.0064.

Matthews, H. D., Tokarska, K. B., Rogelj, J., Forster, P. M., Haustein, K., Smith, Christopher J. MacDougall, A. H., et al. (submitted). A new framework for understanding and quantifying uncertainties in the remaining carbon budget. *Nature* (submitted).

Matthews, H. D., and Zickfeld, K. (2012). Climate response to zeroed emissions of greenhouse gases and aerosols. *Nat. Clim. Chang.* 2, 338–341. doi:10.1038/nclimate1424.

Mauritsen, T., Bader, J., Becker, T., Behrens, J., Bittner, M., Brokopf, R., et al. (2019). Developments in the MPI-M Earth system model version 1.2 (MPI-ESM1.2) and its response to increasing CO2. *J. Adv. Model. Earth Syst.* 11, 998–1038. doi:10.1029/2018MS001400.

McCormack, C. G., Born, W., Irvine, P. J., Achterberg, E. P., Amano, T., Ardron, J., et al. (2016). Key impacts of climate engineering on biodiversity and ecosystems, with priorities for future research. *J. Integr. Environ. Sci.* 13, 1–26. doi:10.1080/1943815X.2016.1159578.

McCusker, K. E., Armour, K. C., Bitz, C. M., and Battisti, D. S. (2014). Rapid and extensive warming following cessation of solar radiation management. *Environ. Res. Lett.* 9. doi:10.1088/1748-9326/9/2/024005.

McDaniel, M. D., Saha, D., Dumont, M. G., Hernández, M., and Adams, M. A. (2019). The effect of land-use change on soil CH4 and N2O fluxes: a global meta-analysis. *Ecosystems* 22, 1424–1443. doi:10.1007/s10021-019-00347-z.

McGuire, A. D., Christensen, T. R., Hayes, D., Heroult, A., Euskirchen, E., Kimball, J. S., et al. (2012). An assessment of the carbon balance of Arctic tundra: comparisons among observations, process models, and atmospheric inversions. *Biogeosciences* 9, 3185–3204. doi:10.5194/bg-9-3185-2012.

McGuire, A. D., Koven, C., Lawrence, D. M., Clein, J. S., Xia, J., Beer, C., et al. (2016). Variability in the sensitivity among model simulations of permafrost and carbon dynamics in the permafrost region between 1960 and 2009. *Global Biogeochem. Cycles* 30, 1015–1037. doi:10.1002/2016GB005405.

McGuire, A. D., Lawrence, D. M., Koven, C., Clein, J. S., Burke, E., Chen, G., et al. (2018). Dependence of the evolution of carbon dynamics in the northern permafrost region on the trajectory of climate change. *Proc. Natl. Acad. Sci.* 115, 3882–3887. doi:10.1073/pnas.1719903115.

McInerney, F. A., and Wing, S. L. (2011). The Paleocene-Eocene thermal maximum: a perturbation of carbon cycle, climate, and biosphere with implications for the future. *Annu. Rev. Earth Planet. Sci.* 39, 489–516. doi:10.1146/annurev-earth-040610-133431.

McKinley, G. A., Fay, A. R., Gloege, L., and Lovenduski, N. S. (submitted). External forcing explains recent decadal variability of the ocean carbon sink. *AGU Adv.* (submitted).

McKinley, G. A., Fay, A. R., Lovenduski, N. S., and Pilcher, D. J. (2017). Natural variability and anthropogenic Trends in the ocean carbon sink. *Ann. Rev. Mar. Sci.* doi:10.1146/annurev-marine-010816-060529.

McLaughlin, K., Nezlin, N. P., Weisberg, S. B., Dickson, A. G., Booth, J. A., Cash, C. L., et al. (2017). An evaluation of potentiometric pH sensors in coastal monitoring applications. *Limnol. Oceanogr. Methods* 15, 679–689. doi:10.1002/lom3.10191.

Mcleod, E., Chmura, G. L., Bouillon, S., Salm, R., Björk, M., Duarte, C. M., et al. (2011). A blueprint for blue carbon: toward an improved understanding of the role of vegetated coastal habitats in sequestering CO2. *Front. Ecol. Environ.* 9, 552–560. doi:10.1890/110004.

McManus, J. F., Francois, R., Gherardi, J.-M., Keigwin, L. D., and Brown-Leger, S. (2004). Collapse and rapid resumption of Atlantic meridional circulation linked to deglacial climate changes. *Nature* 428, 834–837. doi:10.1038/nature02494.

McNorton, J., Wilson, C., Gloor, M., Parker, R. J., Boesch, H., Feng, W., et al. (2018). Attribution of recent increases in atmospheric methane through 3-D inverse modelling. *Atmos. Chem. Phys.* 18, 18149–18168. doi:10.5194/acp-18-18149-2018.

Medlyn, B. E., De Kauwe, M. G., Zaehle, S., Walker, A. P., Duursma, R. A., Luus, K., et al. (2016). Using models to guide field experiments: a priori predictions for the CO2 response of a nutrient- and water-limited native Eucalypt woodland. *Glob. Chang. Biol.* 22, 2834–2851. doi:10.1111/gcb.13268.

Medlyn, B. E., Zaehle, S., De Kauwe, M. G., Walker, A. P., Dietze, M. C., Hanson, P. J., et al. (2015). Using ecosystem experiments to improve vegetation models. *Nat. Clim. Chang.* 5, 528–534. doi:10.1038/nclimate2621.

Meier, I. C., Finzi, A. C., and Phillips, R. P. (2017). Root exudates increase N availability by stimulating microbial turnover of fast-cycling N pools. *Soil Biol. Biochem.* 106, 119–128. doi:10.1016/j.soilbio.2016.12.004.

Meinshausen, M., Meinshausen, N., Hare, W., Raper, S. C. B., Frieler, K., Knutti, R., et al. (2009). Greenhouse-gas emission targets for limiting global warming to 2°C. *Nature* 458, 1158–1162. doi:10.1038/nature08017.

Meinshausen, M., Smith, S. J., Calvin, K., Daniel, J. S., Kainuma, M. L. T., Lamarque, J.-F., et al. (2011a). The RCP greenhouse gas concentrations and their extensions from 1765 to 2300. *Clim. Change* 109, 213–241. doi:10.1007/s10584-011-0156-z.

Meinshausen, M., Wigley, T. M. L., and Raper, S. C. B. (2011b). Emulating atmosphere-ocean and carbon cycle models with a simpler model, MAGICC6 – Part 2: Applications. *Atmos. Chem. Phys.* 11, 1457–1471. doi:10.5194/acp-11-1457-2011.

Meli, P., Rey Benayas, J. M., Balvanera, P., and Martínez Ramos, M. (2014). Restoration enhances wetland biodiversity and ecosystem service supply, but results are context-dependent: a meta-analysis. *PLoS One* 9, e93507–e93507. doi:10.1371/journal.pone.0093507.

Melillo, J. M., Butler, S., Johnson, J., Mohan, J., Steudler, P., Lux, H., et al. (2011). Soil warming, carbon-nitrogen interactions, and forest carbon budgets. *Proc. Natl. Acad. Sci.* 108, 9508–9512. doi:10.1073/pnas.1018189108.

Melillo, J. M., Frey, S. D., DeAngelis, K. M., Werner, W. J., Bernard, M. J., Bowles, F. P., et al. (2017). Long-term pattern and magnitude of soil carbon feedback to the climate system in a warming world. *Science* 358, 101–105. doi:10.1126/science.aan2874.

Melton, J. R., Wania, R., Hodson, E. L., Poulter, B., Ringeval, B., Spahni, R., et al. (2013). Present state of global wetland extent and wetland methane modelling: conclusions from a model inter-comparison project (WETCHIMP). *Biogeosciences* 10, 753–788. doi:10.5194/bg-10-753-2013.

Mengis, N., Keller, D. P., Rickels, W., Quaas, M., and Oschlies, A. (2019). Climate engineering–induced changes in correlations between Earth system variables—implications for appropriate indicator selection. *Clim. Change* 153, 305–322. doi:10.1007/s10584-019-02389-7.

Mengis, N., Partanen, A.-I., Jalbert, J., and Matthews, H. D. (2018). 1.5 °C carbon budget dependent on carbon cycle uncertainty and future non-CO2 forcing. *Sci. Rep.* 8, 5831. doi:10.1038/s41598-018-24241-1.

Menviel, L., and Joos, F. (2012). Toward explaining the Holocene carbon dioxide and carbon isotope records: Results from transient ocean carbon cycle-climate simulations. *Paleoceanography* 27, PA1207. doi:10.1029/2011PA002224.

Mercado, L. M., Bellouin, N., Sitch, S., Boucher, O., Huntingford, C., Wild, M., et al. (2009). Impact of changes in diffuse radiation on the global land carbon sink. *Nature* 458, 1014–1017. doi:10.1038/nature07949.

Mercado, L. M., Medlyn, B. E., Huntingford, C., Oliver, R. J., Clark, D. B., Sitch, S., et al. (2018). Large sensitivity in land carbon storage due to geographical and temporal variation in the thermal response of photosynthetic capacity. *New Phytol.* 218, 1462–1477. doi:10.1111/nph.15100.

Merlivat, L., Boutin, J., Antoine, D., Beaumont, L., Golbol, M., and Vellucci, V. (2018). Increase of dissolved inorganic carbon and decrease in pH in near-surface waters in the Mediterranean Sea during the past two decades. *Biogeosciences* 15, 5653–5662. doi:10.5194/bg-15-5653-2018.

Meyerholt, J., Sickel, K., and Zaehle, S. (submitted). Ensemble projections elucidate effects of uncertainty in terrestrial nitrogen limitation on future carbon uptake. *Glob. Chang. Biol.* (submitted).

Midorikawa, T., Ishii, M., Saito, S., Sasano, D., Kosugi, N., Motoi, T., et al. (2010). Decreasing pH trend estimated from 25-yr time series of carbonate parameters in the western North Pacific. *Tellus B Chem. Phys. Meteorol.* 62, 649–659. doi:10.1111/j.1600-0889.2010.00474.x.

Millar, R. J., and Friedlingstein, P. (2018). The utility of the historical record for assessing the transient climate response to cumulative emissions. *Philos. Trans. R. Soc. A Math. Phys. Eng. Sci.* 376, 20160449. doi:10.1098/rsta.2016.0449.

Millar, R. J., Fuglestvedt, J. S., Friedlingstein, P., Rogelj, J., Grubb, M. J., Matthews, H. D., et al. (2017). Emission budgets and pathways consistent with limiting warming to 1.5 °C. *Nat. Geosci.* 10, 741–747. doi:10.1038/ngeo3031.

Miller, S. M., Michalak, A. M., Detmers, R. G., Hasekamp, O. P., Bruhwiler, L. M. P., and Schwietzke, S. (2019). China's coal mine methane regulations have not curbed growing emissions. *Nat. Commun.* 10, 303. doi:10.1038/s41467-018-07891-7.

Millero, F., Woosley, R., DiTrolio, B., and Waters, J. (2009). Effect of Ocean Acidification on the Speciation of Metals in Seawater. *Oceanography* 22, 72–85. doi:10.5670/oceanog.2009.98.

Minschwaner, K., Salawitch, R. J., and McElroy, M. B. (1993). Absorption of solar radiation by O2 : Implications for O3 and lifetimes of N2O, CFCl3, and CF2Cl2. *J. Geophys. Res.* 98, 10543. doi:10.1029/93JD00223.

Minshull, T. A., Marín-Moreno, H., Armstrong McKay, D. I., and Wilson, P. A. (2016). Mechanistic insights into a hydrate contribution to the Paleocene-Eocene carbon cycle perturbation from coupled thermohydraulic simulations. *Geophys. Res. Lett.* 43, 8637–8644. doi:10.1002/2016GL069676.

Moffitt, S. E., Hill, T. M., Roopnarine, P. D., and Kennett, J. P. (2015). Response of seafloor ecosystems to abrupt global climate change. *Proc. Natl. Acad. Sci.* 112, 4684–4689. doi:10.1073/pnas.1417130112.

Molari, M., Guilini, K., Lott, C., Weber, M., de Beer, D., Meyer, S., et al. (2018). CO2 leakage alters biogeochemical and ecological functions of submarine sands. *Sci. Adv.* 4, eaao2040. doi:10.1126/sciadv.aao2040.

Mongwe, N. P., Chang, N., and Monteiro, P. M. S. (2016). The seasonal cycle as a mode to diagnose biases in modelled CO2 fluxes in the Southern Ocean. *Ocean Model.* 106, 90–103. doi:10.1016/j.ocemod.2016.09.006.

Mongwe, N. P., Vichi, M., and Monteiro, P. M. S. (2018). The seasonal cycle of pCO2 and CO2 fluxes in the Southern Ocean: diagnosing anomalies in CMIP5 Earth system models. *Biogeosciences* 15, 2851–2872. doi:10.5194/bg-15-2851-2018.

Monnin, E. (2001). Atmospheric CO2 Concentrations over the Last Glacial Termination. *Science* 291, 112–114. doi:10.1126/science.291.5501.112.

Moore, J. K., Fu, W., Primeau, F., Britten, G. L., Lindsay, K., Long, M., et al. (2018). Sustained climate warming drives declining marine biological productivity. *Science* 359, 1139–1143. doi:10.1126/science.aao6379.

Mora, C., Wei, C.-L., Rollo, A., Amaro, T., Baco, A. R., Billett, D., et al. (2013). Biotic and human vulnerability to projected changes in ocean biogeochemistry over the 21st Century. *PLoS Biol.* 11, e1001682. doi:10.1371/journal.pbio.1001682.

Moreno, A. R., Hagstrom, G. I., Primeau, F. W., Levin, S. A., and Martiny, A. C. (2018). Marine phytoplankton stoichiometry mediates nonlinear interactions between nutrient supply, temperature, and atmospheric CO2. *Biogeosciences* 15, 2761–2779. doi:10.5194/bg-15-2761-2018.

Murata, A., and Saito, S. (2012). Decadal changes in the CaCO3 saturation state along 179°E in the Pacific Ocean. *Geophys. Res. Lett.* 39, L12604. doi:10.1029/2012GL052297.

Murray, R. H., Erler, D. V, and Eyre, B. D. (2015). Nitrous oxide fluxes in estuarine environments: response to global change. *Glob. Chang. Biol.* 21, 3219–3245. doi:10.1111/gcb.12923.

Nakano, H., Ishii, M., Rodgers, K. B., Tsujino, H., and Yamanaka, G. (2015). Anthropogenic CO2 uptake, transport, storage, and dynamical controls in the ocean imposed by the meridional overturning circulation: A modeling study. *Global Biogeochem. Cycles* 29, 1706–1724. doi:10.1002/2015GB005128.

Nakazawa, T., Morimoto, S., Aoki, S., and Tanaka, M. (1997). Temporal and spatial variations of the carbon isotopic ratio of atmospheric carbon dioxide in the western Pacific region. *J. Geophys. Res. Atmos.* 102, 1271–1285. doi:10.1029/96JD02720.

Naqvi, S. W. A., Bange, H. W., Farías, L., Monteiro, P. M. S., Scranton, M. I., and Zhang, J. (2010). Marine hypoxia/anoxia as a source of CH_4 and N_2O. *Biogeosciences* 7, 2159–2190. doi:10.5194/bg-7-2159-2010.

Natali, S. M., Schuur, E. A. G., Webb, E. E., Pries, C. E. H., and Crummer, K. G. (2014). Permafrost degradation stimulates carbon loss from experimentally warmed tundra. *Ecology* 95, 602–608. doi:10.1890/13-0602.1.

Natchimuthu, S., Wallin, M. B., Klemedtsson, L., and Bastviken, D. (2017). Spatio-temporal patterns of stream methane and carbon dioxide emissions in a hemiboreal catchment in Southwest Sweden. *Sci. Rep.* 7, 39729. doi:10.1038/srep39729.

National Academies of Sciences and Medicine, E. (2019). *Negative Emissions Technologies and Reliable Sequestration*. Washington, D.C.: National Academies Press doi:10.17226/25259.

Naudts, K., Chen, Y., McGrath, M. J., Ryder, J., Valade, A., Otto, J., et al. (2016). Europes forest management did not mitigate climate warming. *Science* 351, 597–600. doi:10.1126/science.aad7270.

Naus, S., Montzka, S. A., Pandey, S., Basu, S., Dlugokencky, E. J., and Krol, M. (2019). Constraints and biases in a tropospheric two-box model of OH. *Atmos. Chem. Phys.* 19, 407–424. doi:10.5194/acp-19-407-2019.

Negrete-García, G., Lovenduski, N. S., Hauri, C., Krumhardt, K. M., and Lauvset, S. K. (2019). Sudden emergence of a shallow aragonite saturation horizon in the Southern Ocean. *Nat. Clim. Chang.* 9, 313–317. doi:10.1038/s41558-019-0418-8.

Nevison, C. D., Dlugokencky, E., Dutton, G., Elkins, J. W., Fraser, P., Hall, B., et al. (2011). Exploring causes of interannual variability in the seasonal cycles of tropospheric nitrous oxide. *Atmos. Chem. Phys.* 11, 3713–3730. doi:10.5194/acp-11-3713-2011.

Nevison, C. D., Lueker, T. J., and Weiss, R. F. (2004). Quantifying the nitrous oxide source from coastal upwelling. *Global Biogeochem. Cycles* 18, GB1018. doi:10.1029/2003GB002110.

Nevison, C. D., Mahowald, N. M., Weiss, R. F., and Prinn, R. G. (2007). Interannual and seasonal variability in atmospheric N2O. *Global Biogeochem. Cycles* 21, GB3017. doi:10.1029/2006GB002755.

Ni, X., and Groffman, P. M. (2018). Declines in methane uptake in forest soils. *Proc. Natl. Acad. Sci.* 115, 8587–8590. doi:10.1073/pnas.1807377115.

Nicely, J. M., Canty, T. P., Manyin, M., Oman, L. D., Salawitch, R. J., Steenrod, S. D., et al. (2018). Changes in global tropospheric OH expected as a result of climate change over the last several decades. *J. Geophys. Res. Atmos.* 123, 10,774-10,795. doi:10.1029/2018JD028388.

Nicholls, Z. R. J., Gieseke, R., Lewis, J., Nauels, A., and Meinshausen, M. (submitted). A bias correction for the remaining carbon budget assessment framework. *Environ. Res. Lett.* (submitted).

Nichols, J. E., and Peteet, D. M. (2019). Rapid expansion of northern peatlands and doubled estimate of carbon storage. *Nat. Geosci.* 12, 917–921. doi:10.1038/s41561-019-0454-z.

Nickelsen, L., and Oschlies, A. (2015). Enhanced sensitivity of oceanic CO2 uptake to dust deposition by iron-light colimitation. *Geophys. Res. Lett.* 42, 492–499. doi:10.1002/2014GL062969.

Nisbet, E. G., Dlugokencky, E. J., Manning, M. R., Lowry, D., Fisher, R. E., France, J. L., et al. (2016). Rising atmospheric methane: 2007-2014 growth and isotopic shift. *Global Biogeochem. Cycles* 30, 1356–1370. doi:10.1002/2016GB005406.

Nisbet, E. G., Manning, M. R., Dlugokencky, E. J., Fisher, R. E., Lowry, D., Michel, S. E., et al. (2019). Very strong atmospheric methane growth in the 4 years 2014–2017: implications for the Paris Agreement. *Global Biogeochem. Cycles* 33, 2018GB006009. doi:10.1029/2018GB006009.

Nitzbon, J., Westermann, S., Langer, M., Martin, L., Strauss, J., LaboorS, et al. (submitted). Collapse or conservation: Response of cold ice-rich permafrost in northeast Siberia to a warming climate. *Nat. Commun.* (submitted).

Norby, R. J., De Kauwe, M. G., Domingues, T. F., Duursma, R. A., Ellsworth, D. S., Goll, D. S., et al. (2016). Model-data synthesis for the next generation of forest free-air CO2 enrichment (FACE) experiments. *New Phytol.* 209, 17–28. doi:10.1111/nph.13593.

Norby, R. J., Warren, J. M., Iversen, C. M., Medlyn, B. E., and McMurtrie, R. E. (2010). CO2 enhancement of forest productivity constrained by limited nitrogen availability. *Proc. Natl. Acad. Sci.* 107, 19368–19373. doi:10.1073/pnas.1006463107.

Noriega, C., and Araujo, M. (2014). Carbon dioxide emissions from estuaries of northern and northeastern Brazil. *Sci. Rep.* 4, 6164. doi:10.1038/srep06164.

Noriega, C. E. D., Araujo, M., and Lefèvre, N. (2013). Spatial and temporal variability of the CO2 fluxes in a tropical, highly urbanized estuary. *Estuaries and Coasts* 36, 1054–1072. doi:10.1007/s12237-013-9608-1.

O'Neill, B. C., Tebaldi, C., van Vuuren, D. P., Eyring, V., Friedlingstein, P., Hurtt, G., et al. (2016). The Scenario Model Intercomparison Project (ScenarioMIP) for CMIP6. *Geosci. Model Dev.* 9, 3461–3482. doi:10.5194/gmd-9-3461-2016.

O'Sullivan, M., Spracklen, D. V, Batterman, S., Arnold, S. R., Gloor, M., and Buermann, W. (2019). Have synergies between nitrogen deposition and atmospheric CO2 driven the recent enhancement of the terrestrial carbon sink? *Global Biogeochem. Cycles* 33, 163–180. doi:10.1029/2018GB005922.

Obermeier, W. A., Lehnert, L. W., Kammann, C. I., Müller, C., Grünhage, L., Luterbacher, J., et al. (2017). Reduced CO2 fertilization effect in temperate C3 grasslands under more extreme weather conditions. *Nat. Clim. Chang.* 7, 137–141. doi:10.1038/nclimate3191.

Oka, E., Qiu, B., Takatani, Y., Enyo, K., Sasano, D., Kosugi, N., et al. (2015). Decadal variability of Subtropical Mode Water subduction and its impact on biogeochemistry. *J. Oceanogr.* 71, 389–400. doi:10.1007/s10872-015-0300-x.

Oka, E., Yamada, K., Sasano, D., Enyo, K., Nakano, T., and Ishii, M. (2019). Remotely forced decadal physical and biogeochemical variability of North Pacific Subtropical Mode Water over the last 40 years. *Geophys. Res. Lett.* 46, 1555–1561. doi:10.1029/2018GL081330.

Olsen, A., Key, R. M., van Heuven, S., Lauvset, S. K., Velo, A., Lin, X., et al. (2016). The Global Ocean Data Analysis Project version 2 (GLODAPv2) – an internally consistent data product for the world ocean. *Earth Syst. Sci. Data* 8, 297–323. doi:10.5194/essd-8-297-2016.

Ono, H., Kosugi, N., Toyama, K., Tsujino, H., Kojima, A., Enyo, K., et al. (2019). Acceleration of ocean acidification in the Western North Pacific. *Geophys. Res. Lett.* 46, 13161–13169. doi:10.1029/2019GL085121.

Oo, A. Z., Sudo, S., Inubushi, K., Mano, M., Yamamoto, A., Ono, K., et al. (2018). Methane and nitrous oxide emissions from conventional and modified rice cultivation systems in South India. *Agric. Ecosyst. Environ.* 252, 148–158. doi:10.1016/j.agee.2017.10.014.

Oschlies, A. (2010). Climate engineering by artificial ocean upwelling: channelling the sorcerer's apprentice. *Geophys. Res. Lett.* 37.

Oschlies, A., Brandt, P., Stramma, L., and Schmidtko, S. (2018). Drivers and mechanisms of ocean deoxygenation. *Nat. Geosci.* 11, 467–473. doi:10.1038/s41561-018-0152-2.

Oschlies, A., Koeve, W., Rickels, W., and Rehdanz, K. (2010a). Side effects and accounting aspects of hypothetical large-scale Southern Ocean iron fertilization. *Biogeosciences* 7, 4017–4035. doi:10.5194/bg-7-4017-2010.

Oschlies, A., Pahlow, M., Yool, A., and Matear, R. J. (2010b). Climate engineering by artificial ocean upwelling: Channelling the sorcerer's apprentice. *Geophys. Res. Lett.* 37, L04701. doi:10.1029/2009GL041961.

Pälike, C., Delaney, M. L., and Zachos, J. C. (2014). Deep-sea redox across the Paleocene-Eocene thermal maximum. *Geochemistry, Geophys. Geosystems* 15, 1038–1053. doi:10.1002/2013GC005074.

Palmer, P. I., Feng, L., Baker, D., Chevallier, F., Bösch, H., and Somkuti, P. (2019). Net carbon emissions from African biosphere dominate pan-tropical atmospheric CO2 signal. *Nat. Commun.* doi:10.1038/s41467-019-11097-w.

Panchuk, K., Ridgwell, A., and Kump, L. R. (2008). Sedimentary response to Paleocene-Eocene Thermal Maximum carbon release: A model-data comparison. *Geology* 36, 315. doi:10.1130/G24474A.1.

Pandey, S., Gautam, R., Houweling, S., Van Der Gon, H. D., Sadavarte, P., Borsdorff, T., et al. (2019). Satellite observations reveal extreme methane leakage from a natural gas well blowout. *Proc. Natl. Acad. Sci. U. S. A.* 116, 26376–26381. doi:10.1073/pnas.1908712116.

Pangala, S. R., Enrich-Prast, A., Basso, L. S., Peixoto, R. B., Bastviken, D., Hornibrook, E. R. C., et al. (2017). Large emissions from floodplain trees close the Amazon methane budget. *Nature* 552, 230–234. doi:10.1038/nature24639.

Parekh, P., Dutkiewicz, S., Follows, M. J., and Ito, T. (2006). Atmospheric carbon dioxide in a less dusty world. *Geophys. Res. Lett.* 33, L03610. doi:10.1029/2005GL025098.

Park, J.-Y., Stock, C. A., Dunne, J. P., Yang, X., and Rosati, A. (2019). Seasonal to multiannual marine ecosystem prediction with a global Earth system model. *Science* 365, 284–288. doi:10.1126/science.aav6634.

Park, J.-Y., Stock, C. A., Yang, X., Dunne, J. P., Rosati, A., John, J., et al. (2018). Modeling global ocean biogeochemistry with physical data assimilation: a pragmatic solution to the Equatorial instability. *J. Adv. Model. Earth Syst.* 10, 891–906. doi:10.1002/2017MS001223.

Park, S., Croteau, P., Boering, K. A., Etheridge, D. M., Ferretti, D., Fraser, P. J., et al. (2012). Trends and seasonal cycles in the isotopic composition of nitrous oxide since 1940. *Nat. Geosci.* 5, 261–265. doi:10.1038/ngeo1421.

Parker, A., and Irvine, P. J. (2018). The risk of termination shock from solar geoengineering. *Earth's Futur.* 6, 456–467. doi:10.1002/2017EF000735.

Partanen, A.-I., Keller, D. P., Korhonen, H., and Matthews, H. D. (2016). Impacts of sea spray geoengineering on ocean biogeochemistry. *Geophys. Res. Lett.* 43, 7600–7608. doi:10.1002/2016GL070111.

Patra, P. K., Krol, M. C., Montzka, S. A., Arnold, T., Atlas, E. L., Lintner, B. R., et al. (2014). Observational evidence for interhemispheric hydroxyl-radical parity. *Nature* 513, 219–223. doi:10.1038/nature13721.

Patra, P. K., Saeki, T., Dlugokencky, E. J., Ishijima, K., Umezawa, T., Ito, A., et al. (2016). Regional methane emission estimation based on observed atmospheric concentrations (2002-2012). *J. Meteorol. Soc. Japan. Ser. II* 94, 91–113. doi:10.2151/jmsj.2016-006.

Pau, S., Detto, M., Kim, Y., and Still, C. J. (2018). Tropical forest temperature thresholds for gross primary productivity. *Ecosphere* 9, e02311. doi:10.1002/ecs2.2311.

Paulmier, A., and Ruiz-Pino, D. (2009). Oxygen minimum zones (OMZs) in the modern ocean. *Prog. Oceanogr.* 80, 113–128. doi:10.1016/j.pocean.2008.08.001.

Paustian, K., Larson, E., Kent, J., Marx, E., and Swan, A. (2019). Soil C Sequestration as a Biological Negative Emission Strategy. *Front. Clim.* 1, 8. doi:10.3389/fclim.2019.00008.

Paustian, K., Lehmann, J., Ogle, S., Reay, D., Robertson, G. P., and Smith, P. (2016). Climate-smart soils. *Nature* 532, 49–57. doi:10.1038/nature17174.

Pavlov, I. N. (2015). Biotic and abiotic factors as causes of coniferous forests dieback in Siberia and Far East. *Contemp. Probl. Ecol.* 8, 440–456. doi:10.1134/S1995425515040125.

Pearson, R. G., Phillips, S. J., Loranty, M. M., Beck, P. S. A., Damoulas, T., Knight, S. J., et al. (2013). Shifts in Arctic vegetation and associated feedbacks under climate change. *Nat. Clim. Chang.* 3, 673–677. doi:10.1038/nclimate1858.

Pelejero, C. (2005). Preindustrial to modern interdecadal variability in coral reef pH. *Science* 309, 2204–2207. doi:10.1126/science.1113692.

Peng, S., Piao, S., Bousquet, P., Ciais, P., Li, B., Lin, X., et al. (2016). Inventory of anthropogenic methane emissions in mainland China from 1980 to 2010. *Atmos. Chem. Phys.* 16, 14545–14562. doi:10.5194/acp-16-14545-2016.

Penman, D. E., Hönisch, B., Zeebe, R. E., Thomas, E., and Zachos, J. C. (2014). Rapid and sustained surface ocean acidification during the Paleocene-Eocene Thermal Maximum. *Paleoceanography* 29, 357–369. doi:10.1002/2014PA002621.

Pépin, L., Raynaud, D., Barnola, J.-M., and Loutre, M. F. (2001). Hemispheric roles of climate forcings during glacial-interglacial transitions as deduced from the Vostok record and LLN-2D model experiments. *J. Geophys. Res. Atmos.* 106, 31885–31892. doi:10.1029/2001JD900117.

Pérez-Ramírez, J., Kapteijn, F., Schöffel, K., and Moulijn, J. . (2003). Formation and control of N2O in nitric acid production. *Appl. Catal. B Environ.* 44, 117–151. doi:10.1016/S0926-3373(03)00026-2.

Perez, F. F., Fontela, M., García-Ibáñez, M. I., Mercier, H., Velo, A., Lherminier, P., et al. (2018). Meridional overturning circulation conveys fast acidification to the deep Atlantic Ocean. *Nature* 554, 515–518. doi:10.1038/nature25493.

Pérez, F. F., Mercier, H., Vázquez-Rodríguez, M., Lherminier, P., Velo, A., Pardo, P. C., et al. (2013). Atlantic Ocean CO2 uptake reduced by weakening of the meridional overturning circulation. *Nat. Geosci.* 6, 146–152. doi:10.1038/ngeo1680.

Peters, G. P., Marland, G., Le Quéré, C., Boden, T., Canadell, J. G., and Raupach, M. R. (2012). Rapid growth in CO2 emissions after the 2008–2009 global financial crisis. *Nat. Clim. Chang.* 2, 2–4. doi:10.1038/nclimate1332.

Peters, W., Jacobson, A. R., Sweeney, C., Andrews, A. E., Conway, T. J., Masarie, K., et al. (2007). An atmospheric perspective on North American carbon dioxide exchange: CarbonTracker. *Proc. Natl. Acad. Sci.* 104, 18925–18930. doi:10.1073/pnas.0708986104.

Peterson, C. D., Lisiecki, L. E., and Stern, J. V. (2014). Deglacial whole-ocean δ13C change estimated from 480 benthic foraminiferal records. *Paleoceanography* 29, 549–563. doi:10.1002/2013PA002552.

Petit, J. R., Jouzel, J., Raynaud, D., Barkov, N. I., Barnola, J.-M., Basile, I., et al. (1999). Climate and atmospheric history of the past 420,000 years from the Vostok ice core, Antarctica. *Nature* 399, 429–436. doi:10.1038/20859.

Petrenko, V. V, Smith, A. M., Schaefer, H., Riedel, K., Brook, E., Baggenstos, D., et al. (2017). Minimal geological methane emissions during the Younger Dryas–Preboreal abrupt warming event. *Nature* 548, 443–446. doi:10.1038/nature23316.

Peylin, P., Law, R. M., Gurney, K. R., Chevallier, F., Jacobson, A. R., Maki, T., et al. (2013). Global atmospheric carbon budget: results from an ensemble of atmospheric CO2 inversions. *Biogeosciences* 10, 6699–6720. doi:10.5194/bg-10-6699-2013.

Pfleiderer, P., Schleussner, C.-F., Mengel, M., and Rogelj, J. (2018). Global mean temperature indicators linked to warming levels avoiding climate risks. *Environ. Res. Lett.* 13, 064015. doi:10.1088/1748-9326/aac319.

Pham-Duc, B., Prigent, C., Aires, F., and Papa, F. (2017). Comparisons of global terrestrial surface water datasets over 15 years. *J. Hydrometeorol.* 18, 993–1007. doi:10.1175/JHM-D-16-0206.1.

Piao, S., Huang, M., Liu, Z., Wang, X., Ciais, P., Canadell, J. G., et al. (2018a). Lower land-use emissions responsible for increased net land carbon sink during the slow warming period. *Nat. Geosci.* 11, 739–743. doi:10.1038/s41561-018-0204-7.

Piao, S., Liu, Z., Wang, T., Peng, S., Ciais, P., Huang, M., et al. (2017). Weakening temperature control on the interannual variations of spring carbon uptake across northern lands. *Nat. Clim. Chang.* 7, 359–363. doi:10.1038/nclimate3277.

Piao, S., Liu, Z., Wang, Y., Ciais, P., Yao, Y., Peng, S., et al. (2018b). On the causes of trends in the seasonal amplitude of atmospheric CO2. *Glob. Chang. Biol.* 24, 608–616. doi:10.1111/gcb.13909.

Piao, S., Sitch, S., Ciais, P., Friedlingstein, P., Peylin, P., Wang, X., et al. (2013). Evaluation of terrestrial carbon cycle models for their response to climate variability and to CO2 trends. *Glob. Chang. Biol.* 19, 2117–2132. doi:10.1111/gcb.12187.

Pison, I., Ringeval, B., Bousquet, P., Prigent, C., and Papa, F. (2013). Stable atmospheric methane in the 2000s: key-role of emissions from natural wetlands. *Atmos. Chem. Phys.* 13, 11609–11623. doi:10.5194/acp-13-11609-2013.

Plazzotta, M., Séférian, R., and Douville, H. (2019). Impact of solar radiation modification on allowable CO2 emissions: what can we learn from multimodel simulations? *Earth's Futur.* 7, 664–676. doi:10.1029/2019EF001165.

Poeplau, C., and Don, A. (2015). Carbon sequestration in agricultural soils via cultivation of cover crops – A meta-analysis. *Agric. Ecosyst. Environ.* 200, 33–41. doi:10.1016/j.agee.2014.10.024.

Poeplau, C., Don, A., Vesterdal, L., Leifeld, J., Van Wesemael, B. A. S., Schumacher, J., et al. (2011). Temporal dynamics of soil organic carbon after land-use change in the temperate zone – carbon response functions as a model approach. *Glob. Chang. Biol.* 17, 2415–2427. doi:10.1111/j.1365-2486.2011.02408.x.

Pongratz, J., Dolman, H., Don, A., Erb, K.-H., Fuchs, R., Herold, M., et al. (2018). Models meet data: Challenges and opportunities in implementing land management in Earth system models. *Glob. Chang. Biol.* 24, 1470–1487. doi:10.1111/gcb.13988.

Pongratz, J., Lobell, D. B., Cao, L., and Caldeira, K. (2012). Crop yields in a geoengineered climate. *Nat. Clim. Chang.* 2, 101–105. doi:10.1038/nclimate1373.

Pongratz, J., Reick, C. H., Houghton, R. A., and House, J. I. (2014). Terminology as a key uncertainty in net land use and land cover change carbon flux estimates. *Earth Syst. Dyn.* 5, 177–195. doi:10.5194/esd-5-177-2014.

Pongratz, J., Reick, C. H., Raddatz, T., and Claussen, M. (2010). Biogeophysical versus biogeochemical climate response to historical anthropogenic land cover change. *Geophys. Res. Lett.* 37, L08702. doi:10.1029/2010GL043010.

Poulter, B., Bousquet, P., Canadell, J. G., Ciais, P., Peregon, A., Saunois, M., et al. (2017). Global wetland contribution to 2000–2012 atmospheric methane growth rate dynamics. *Environ. Res. Lett.* 12, 094013. doi:10.1088/1748-9326/aa8391.

Poulter, B., Frank, D., Ciais, P., Myneni, R. B., Andela, N., Bi, J., et al. (2014). Contribution of semi-arid ecosystems to interannual variability of the global carbon cycle. *Nature* 509, 600–603. doi:10.1038/nature13376.

Praetorius, S. K., Mix, A. C., Walczak, M. H., Wolhowe, M. D., Addison, J. A., and Prahl, F. G. (2015). North Pacific deglacial hypoxic events linked to abrupt ocean warming. *Nature* 527, 362–366. doi:10.1038/nature15753.

Prather, M. J., Hsu, J., DeLuca, N. M., Jackman, C. H., Oman, L. D., Douglass, A. R., et al. (2015). Measuring and modeling the lifetime of nitrous oxide including its variability. *J. Geophys. Res. Atmos.* 120, 5693–5705. doi:10.1002/2015JD023267.

Prinn, R. G., Weiss, R. F., Fraser, P. J., Simmonds, P. G., Cunnold, D. M., Alyea, F. N., et al. (2000). A history of chemically and radiatively important gases in air deduced from ALE/GAGE/AGAGE. *J. Geophys. Res. Atmos.* 105, 17751–17792. doi:10.1029/2000JD900141.

Prinn, R. G., Weiss, R. F., Krummel, P. B., O'Doherty, S., Fraser, P. J., Muhle, J., et al. (2016). The ALE / GAGE AGAGE Network.

Proctor, J., Hsiang, S., Burney, J., Burke, M., and Schlenker, W. (2018). Estimating global agricultural effects of geoengineering using volcanic eruptions. *Nature* 560, 480–483. doi:10.1038/s41586-018-0417-3.

Prokopiou, M., Martinerie, P., Sapart, C. J., Witrant, E., Monteil, G., Ishijima, K., et al. (2017). Constraining N2O emissions since 1940 using firn air isotope measurements in both hemispheres. *Atmos. Chem. Phys.* 17, 4539–4564. doi:10.5194/acp-17-4539-2017.

Prokopiou, M., Sapart, C. J., Rosen, J., Sperlich, P., Blunier, T., Brook, E., et al. (2018). Changes in the isotopic signature of atmospheric nitrous oxide and its global average source during the last three Millennia. *J. Geophys. Res. Atmos.* 123, 10,757-10,773. doi:10.1029/2018JD029008.

Pugh, T. A. M., Jones, C. D., Huntingford, C., Burton, C., Arneth, A., Brovkin, V., et al. (2018). A large committed long-term sink of carbon due to vegetation dynamics. *Earth's Futur.* 6, 1413–1432. doi:10.1029/2018EF000935.

Pugh, T. A. M., Lindeskog, M., Smith, B., Poulter, B., Arneth, A., Haverd, V., et al. (2019). Role of forest regrowth in global carbon sink dynamics. *Proc. Natl. Acad. Sci.* 116, 4382–4387. doi:10.1073/pnas.1810512116.

Qi, D., Chen, L., Chen, B., Gao, Z., Zhong, W., Feely, R. A., et al. (2017). Increase in acidifying water in the western Arctic Ocean. *Nat. Clim. Chang.* 7, 195–199. doi:10.1038/nclimate3228.

Qian, W., Dai, M., Xu, M., Kao, S., Du, C., Liu, J., et al. (2017). Non-local drivers of the summer hypoxia in the East China Sea off the Changjiang Estuary. *Estuar. Coast. Shelf Sci.* 198, 393–399. doi:10.1016/j.ecss.2016.08.032.

Rabalais, N., Cai, W.-J., Carstensen, J., Conley, D., Fry, B., Hu, X., et al. (2014). Eutrophication-driven deoxygenation in the coastal ocean. *Oceanography* 27, 172–183. doi:10.5670/oceanog.2014.21.

Rabitz, F. (2019). Governing the termination problem in solar radiation management. *Env. Polit.* 28, 502–522. doi:10.1080/09644016.2018.1519879.

Rae, J. W. B., Burke, A., Robinson, L. F., Adkins, J. F., Chen, T., Cole, C., et al. (2018). CO2 storage and release in the deep Southern Ocean on millennial to centennial timescales. *Nature* 562, 569–573. doi:10.1038/s41586-018-0614-0.

Rafter, P. A., Carriquiry, J. D., Herguera, J., Hain, M. P., Solomon, E. A., and Southon, J. R. (2019). Anomalous >2000 year old surface ocean radiocarbon age as evidence for deglacial geologic carbon release. *Geophys. Res. Lett.*, 2019GL085102. doi:10.1029/2019GL085102.

Randerson, J. T., Lindsay, K., Munoz, E., Fu, W., Moore, J. K., Hoffman, F. M., et al. (2015). Multicentury changes in ocean and land contributions to the climate-carbon feedback. *Global Biogeochem. Cycles* 29, 744–759. doi:10.1002/2014GB005079.

Rau, G. H. (2014). "Enhancing the Ocean's Role in CO2 Mitigation," in *Global Environmental Change*, ed. B. Freedman (Dordrecht: Springer Netherlands), 817–824. doi:10.1007/978-94-007-5784-4_54.

Raupach, M. R., Gloor, M., Sarmiento, J. L., Canadell, J. G., Frölicher, T. L., Gasser, T., et al. (2014). The declining uptake rate of atmospheric CO2 by land and ocean sinks. *Biogeosciences* 11, 3453–3475. doi:10.5194/bg-11-3453-2014.

Ravishankara, A. R., Daniel, J. S., and Portmann, R. W. (2009). Nitrous Oxide (N2O): The Dominant Ozone-Depleting Substance Emitted in the 21st Century. *Science* 326, 123–125. doi:10.1126/science.1176985.

Raynaud, D., Barnola, J.-M., Souchez, R., Lorrain, R., Petit, J.-R., Duval, P., et al. (2005). The record for marine isotopic stage 11. *Nature* 436, 39–40. doi:10.1038/43639b.

Rayner, P. J., Stavert, A., Scholze, M., Ahlström, A., Allison, C. E., and Law, R. M. (2015). Recent changes in the global and regional carbon cycle: analysis of first-order diagnostics. *Biogeosciences* 12, 835–844. doi:10.5194/bg-12-835-2015.

Regnier, P., Friedlingstein, P., Ciais, P., Mackenzie, F. T., Gruber, N., Janssens, I. A., et al. (2013). Anthropogenic perturbation of the carbon fluxes from land to ocean. *Nat. Geosci.* 6, 597–607. doi:10.1038/ngeo1830.

Reich, P. B., and Hobbie, S. E. (2013). Decade-long soil nitrogen constraint on the CO2 fertilization of plant biomass. *Nat. Clim. Chang.* 3, 278–282. doi:10.1038/nclimate1694.

Reich, P. B., Hobbie, S. E., and Lee, T. D. (2014). Plant growth enhancement by elevated CO2 eliminated by joint water and nitrogen limitation. *Nat. Geosci.* 7, 920–924. doi:10.1038/ngeo2284.

Reich, P. B., Hobbie, S. E., Lee, T. D., and Pastore, M. A. (2018). Unexpected reversal of C3 versus C4 grass response to elevated CO2 during a 20-year field experiment. *Science* 360, 317–320. doi:10.1126/science.aas9313.

Renforth, P., and Henderson, G. (2017). Assessing ocean alkalinity for carbon sequestration. *Rev. Geophys.* 55, 636–674. doi:10.1002/2016RG000533.

Renou-Wilson, F., Moser, G., Fallon, D., Farrell, C. A., Müller, C., and Wilson, D. (2019). Rewetting degraded peatlands for climate and biodiversity benefits: Results from two raised bogs. *Ecol. Eng.* 127, 547–560. doi:https://doi.org/10.1016/j.ecoleng.2018.02.014.

Resplandy, L., Keeling, R. F., Rödenbeck, C., Stephens, B. B., Khatiwala, S., Rodgers, K. B., et al. (2018). Revision of global carbon fluxes based on a reassessment of oceanic and riverine carbon transport. *Nat. Geosci.* 11, 504–509. doi:10.1038/s41561-018-0151-3.

Reuter, M., Buchwitz, M., Hilker, M., Heymann, J., Bovensmann, H., Burr Ows, J. P., et al. (2017). How much CO2 is taken up by the European terrestrial biosphere? *Bull. Am. Meteorol. Soc.* doi:10.1175/BAMS-D-15-00310.1.

Revelle, R., and Suess, H. E. (1957). Carbon dioxide exchange between atmosphere and ocean and the question of an increase of atmospheric CO2 during the past decades. *Tellus* 9, 18–27. doi:10.1111/j.2153-3490.1957.tb01849.x.

Rheuban, J. E., Doney, S. C., McCorkle, D. C., and Jakuba, R. W. (2019). Quantifying the effects of nutrient enrichment and freshwater mixing on coastal ocean acidification. *J. Geophys. Res. Ocean.* n/a, 2019JC015556. doi:10.1029/2019JC015556.

Rice, A. L., Butenhoff, C. L., Teama, D. G., Röger, F. H., Khalil, M. A. K., and Rasmussen, R. A. (2016). Atmospheric methane isotopic record favors fossil sources flat in 1980s and 1990s with recent increase. *Proc. Natl. Acad. Sci.* 113, 10791–10796. doi:10.1073/pnas.1522923113.

Richardson, M., Cowtan, K., and Millar, R. J. (2018). Global temperature definition affects achievement of long-term climate goals. *Environ. Res. Lett.* 13, 054004. doi:10.1088/1748-9326/aab305.

Ricke, K. L., and Caldeira, K. (2014). Maximum warming occurs about one decade after a carbon dioxide emission. *Environ. Res. Lett.* 9, 124002. doi:10.1088/1748-9326/9/12/124002.

Ridgwell, A., and Schmidt, D. N. (2010). Past constraints on the vulnerability of marine calcifiers to massive carbon dioxide release. *Nat. Geosci.* 3, 196–200. doi:10.1038/ngeo755.

Ridgwell, A., Zondervan, I., Hargreaves, J. C., Bijma, J., and Lenton, T. M. (2007). Assessing the potential long-term increase of oceanic fossil fuel CO2 uptake due to CO2-calcification feedback. *Biogeosciences* 4, 481–492. doi:10.5194/bg-4-481-2007.

Rigby, M., Montzka, S. A., Prinn, R. G., White, J. W. C., Young, D., O'Doherty, S., et al. (2017). Role of atmospheric oxidation in recent methane growth. *Proc. Natl. Acad. Sci. U. S. A.* 114, 5373–5377. doi:10.1073/pnas.1616426114.

Ringeval, B., Friedlingstein, P., Koven, C., Ciais, P., de Noblet-Ducoudré, N., Decharme, B., et al. (2011). Climate-CH4 feedback from wetlands and its interaction with the climate-CO2 feedback. *Biogeosciences* 8, 2137–2157. doi:10.5194/bg-8-2137-2011.

Ríos, A. F., Resplandy, L., García-Ibáñez, M. I., Fajar, N. M., Velo, A., Padin, X. A., et al. (2015). Decadal acidification in the water masses of the Atlantic Ocean. *Proc. Natl. Acad. Sci.* 112, 9950–9955. doi:10.1073/pnas.1504613112.

Robbins, L. L., and Lisle, J. T. (2018). Regional acidification trends in Florida shellfish estuaries: a 20+ year look at pH, oxygen, temperature, and salinity. *Estuaries and Coasts* 41, 1268–1281. doi:10.1007/s12237-017-0353-8.

Robinson, C. (2019). Microbial respiration, the engine of ocean deoxygenation. *Front. Mar. Sci.* 5, 533. doi:10.3389/fmars.2018.00533.

Robinson, J., Popova, E. E., Yool, A., Srokosz, M., Lampitt, R. S., and Blundell, J. R. (2014). How deep is deep enough? Ocean iron fertilization and carbon sequestration in the Southern Ocean. *Geophys. Res. Lett.* 41, 2489–2495. doi:10.1002/2013GL058799.

Robinson, S. A. (2011). Shallow-water carbonate record of the Paleocene-Eocene Thermal Maximum from a Pacific Ocean guyot. *Geology* 39, 51–54. doi:10.1130/G31422.1.

Rödenbeck, C., Bakker, D. C. E., Gruber, N., Iida, Y., Jacobson, A. R., Jones, S., et al. (2015). Data-based estimates of the ocean carbon sink variability – first results of the Surface Ocean pCO2 Mapping intercomparison (SOCOM). *Biogeosciences* 12, 7251–7278. doi:10.5194/bg-12-7251-2015.

Rödenbeck, C., Bakker, D. C. E., Metzl, N., Olsen, A., Sabine, C., Cassar, N., et al. (2014). Interannual sea–air CO2 flux variability from an observation-driven ocean mixed-layer scheme. *Biogeosciences* 11, 4599–4613. doi:10.5194/bg-11-4599-2014.

Rödenbeck, C., Houweling, S., Gloor, M., and Heimann, M. (2003). CO_2 flux history 1982–2001 inferred from atmospheric data using a global inversion of atmospheric transport. *Atmos. Chem. Phys.* 3, 1919–1964. doi:10.5194/acp-3-1919-2003.

Rödenbeck, C., Keeling, R. F., Bakker, D. C. E., Metzl, N., Olsen, A., Sabine, C., et al. (2013). Global surface-ocean pCO2 and sea–air CO2 flux variability from an observation-driven ocean mixed-layer. *Ocean Sci.* 9, 193–216. doi:10.5194/os-9-193-2013.

Rödenbeck, C., Zaehle, S., Keeling, R., and Heimann, M. (2018). History of El Niño impacts on the global carbon cycle 1957–2017: a quantification from atmospheric CO2 data. *Philos. Trans. R. Soc. B Biol. Sci.* 373, 20170303. doi:10.1098/rstb.2017.0303.

Rodgers, K. B., Sarmiento, J. L., Aumont, O., Crevoisier, C., de Boyer Montégut, C., and Metzl, N. (2008). A wintertime uptake window for anthropogenic CO2 in the North Pacific. *Global Biogeochem. Cycles* 22, GB2020. doi:10.1029/2006GB002920.

Rogelj, J., Forster, P. M., Kriegler, E., Smith, C. J., and Séférian, R. (2019a). Estimating and tracking the remaining carbon budget for stringent climate targets. *Nature* 571, 335–342. doi:10.1038/s41586-019-1368-z.

Rogelj, J., Forster, P. M., Kriegler, E., Smith, C. J., and Séférian, R. (2019b). Estimating and tracking the remaining carbon budget for stringent climate targets. *Nature* 571, 335–342. doi:10.1038/s41586-019-1368-z.

Rogelj, J., Meinshausen, M., and Knutti, R. (2012). Global warming under old and new scenarios using IPCC climate sensitivity range estimates. *Nat. Clim. Chang.* 2, 248–253. doi:10.1038/nclimate1385.

Rogelj, J., Meinshausen, M., Schaeffer, M., Knutti, R., and Riahi, K. (2015a). Impact of short-lived non-CO2 mitigation on carbon budgets for stabilizing global warming. *Environ. Res. Lett.* 10, 075001. doi:10.1088/1748-9326/10/7/075001.

Rogelj, J., Reisinger, A., McCollum, D. L., Knutti, R., Riahi, K., and Meinshausen, M. (2015b). Mitigation choices impact carbon budget size compatible with low temperature goals. *Environ. Res. Lett.* 10, 075003. doi:10.1088/1748-9326/10/7/075003.

Rogelj, J., Schaeffer, M., Friedlingstein, P., Gillett, N. P., van Vuuren, D. P., Riahi, K., et al. (2016). Differences between carbon budget estimates unravelled. *Nat. Clim. Chang.* 6, 245–252. doi:10.1038/nclimate2868.

Rogelj, J., Shindell, D., Jiang, K., Fifita, S., Forster, P., Ginzburg, V., et al. (2018). "Mitigation Pathways Compatible with 1.5°C in the Context of Sustainable Development," in *Global Warming of 1.5°C. An IPCC Special Report on the impacts of global warming of 1.5°C above pre-industrial levels and related global greenhouse gas emission pathways, in the context of strengthening the global response to the threat of climate change,* eds. V. Masson-Delmotte, P. Zhai, H.-O. Pörtner, D. Roberts, J. Skea, P. R. Shukla, et al. (In Press).

Rogers, K., Kelleway, J. J., Saintilan, N., Megonigal, J. P., Adams, J. B., Holmquist, J. R., et al. (2019). Wetland carbon storage controlled by millennial-scale variation in relative sea-level rise. *Nature* 567, 91–95. doi:10.1038/s41586-019-0951-7.

Ronge, T. A., Tiedemann, R., Lamy, F., Köhler, P., Alloway, B. V., De Pol-Holz, R., et al. (2016). Radiocarbon constraints on the extent and evolution of the South Pacific glacial carbon pool. *Nat. Commun.* 7, 11487. doi:10.1038/ncomms11487.

Roobaert, A., Laruelle, G. G., Landschützer, P., Gruber, N., Chou, L., and Regnier, P. (2019). The spatiotemporal dynamics of the sources and sinks of CO2 in the global coastal ocean. *Global Biogeochem. Cycles* n/a, 2019GB006239. doi:10.1029/2019GB006239.

Rosentreter, J. A., Maher, D. T., Erler, D. V., Murray, R. H., and Eyre, B. D. (2018). Methane emissions partially offset "blue carbon" burial in mangroves. *Sci. Adv.* 4, eaao4985. doi:10.1126/sciadv.aao4985.

Roth, R., and Joos, F. (2012). Model limits on the role of volcanic carbon emissions in regulating glacial–interglacial CO2 variations. *Earth Planet. Sci. Lett.* 329–330, 141–149. doi:10.1016/j.epsl.2012.02.019.

Ruddiman, W. F., Fuller, D. Q., Kutzbach, J. E., Tzedakis, P. C., Kaplan, J. O., Ellis, E. C., et al. (2016). Late Holocene climate: Natural or anthropogenic? *Rev. Geophys.* 54, 93–118. doi:10.1002/2015RG000503.

Ruppel, C. D., and Kessler, J. D. (2017). The interaction of climate change and methane hydrates. *Rev. Geophys.* 55, 126–168. doi:10.1002/2016RG000534.

Rysgaard, S., Søgaard, D. H., Cooper, M., Pućko, M., Lennert, K., Papakyriakou, T. N., et al. (2013). Ikaite crystal distribution in winter sea ice and implications for CO2 system dynamics. *Cryosph.* 7, 707–718. doi:10.5194/tc-7-707-2013.

Saatchi, S. S., Harris, N. L., Brown, S., Lefsky, M., Mitchard, E. T. A., Salas, W., et al. (2011). Benchmark map of forest carbon stocks in tropical regions across three continents. *Proc. Natl. Acad. Sci.* 108, 9899–9904. doi:10.1073/pnas.1019576108.

Sabine, C. L. (2004). The oceanic sink for anthropogenic CO2. *Science* 305, 367–371. doi:10.1126/science.1097403.

Saeki, T., and Patra, P. K. (2017). Implications of overestimated anthropogenic CO2 emissions on East Asian and global land CO2 flux inversion. *Geosci. Lett.* 4, 9. doi:10.1186/s40562-017-0074-7.

Saikawa, E., Prinn, R. G., Dlugokencky, E., Ishijima, K., Dutton, G. S., Hall, B. D., et al. (2014). Global and regional emissions estimates for N2O. *Atmos. Chem. Phys.* 14, 4617–4641. doi:10.5194/acp-14-4617-2014.

Sakaguchi, K., Zeng, X., Leung, L., and Shao, P. (2016). Influence of dynamic vegetation on carbon-nitrogen cycle feedback in the Community Land Model (CLM4). *Environ. Res. Lett.* 11, 124029. doi:10.1088/1748-9326/aa51d9.

Sakschewski, B., von Bloh, W., Boit, A., Poorter, L., Peña-Claros, M., Heinke, J., et al. (2016). Resilience of Amazon forests emerges from plant trait diversity. *Nat. Clim. Chang.* 6, 1032–1036. doi:10.1038/nclimate3109.

Sallée, J.-B., Matear, R. J., Rintoul, S. R., and Lenton, A. (2012). Localized subduction of anthropogenic carbon dioxide in the Southern Hemisphere oceans. *Nat. Geosci.* 5, 579–584. doi:10.1038/ngeo1523.

Salter, I., Schiebel, R., Ziveri, P., Movellan, A., Lampitt, R., and Wolff, G. A. (2014). Carbonate counter pump stimulated by natural iron fertilization in the Polar Frontal Zone. *Nat. Geosci.* 7, 885–889. doi:10.1038/ngeo2285.

Sanderman, J., Hengl, T., and Fiske, G. J. (2018). Correction for Sanderman et al., Soil carbon debt of 12,000 years of human land use. *Proc. Natl. Acad. Sci.* 115, E1700–E1700. doi:10.1073/pnas.1800925115.

Sanderson, B. M. (submitted). Time-limited carbon budgets for risk-framing in climate policy. *Sci. Adv.* (submitted).

Sarmiento, J. L., Gloor, M., Gruber, N., Beaulieu, C., Jacobson, A. R., Mikaloff Fletcher, S. E., et al. (2010). Trends and regional distributions of land and ocean carbon sinks. *Biogeosciences* 7, 2351–2367. doi:10.5194/bg-7-2351-2010.

Sarmiento, J. L., and Gruber, N. (2006). *Ocean Biogeochemical Dynamics*. Princenton, NJ, USA: Princenton University Press.

Sarnthein, M., Schneider, B., and Grootes, P. M. (2013). Peak glacial 14C ventilation ages suggest major draw-down of carbon into the abyssal ocean. *Clim. Past* 9, 2595–2614. doi:10.5194/cp-9-2595-2013.

Sasano, D., Takatani, Y., Kosugi, N., Nakano, T., Midorikawa, T., and Ishii, M. (2015). Multidecadal trends of oxygen and their controlling factors in the western North Pacific. *Global Biogeochem. Cycles* 29, 935–956. doi:10.1002/2014GB005065.

Sasano, D., Takatani, Y., Kosugi, N., Nakano, T., Midorikawa, T., and Ishii, M. (2018). Decline and Bidecadal Oscillations of Dissolved Oxygen in the Oyashio Region and Their Propagation to the Western North Pacific. *Global Biogeochem. Cycles* 32, 909–931. doi:10.1029/2017GB005876.

Sasse, T. P., McNeil, B. I., Matear, R. J., and Lenton, A. (2015). Quantifying the influence of CO2 seasonality on future aragonite undersaturation onset. *Biogeosciences* 12, 6017–6031. doi:10.5194/bg-12-6017-2015.

Saunders, K. M., Roberts, S. J., Perren, B., Butz, C., Sime, L., Davies, S., et al. (2018). Holocene dynamics of the Southern Hemisphere westerly winds and possible links to CO2 outgassing. *Nat. Geosci.* 11, 650–655. doi:10.1038/s41561-018-0186-5.

Saunois, M., Bousquet, P., Poulter, B., Peregon, A., Ciais, P., Canadell, J. G., et al. (2016a). The global methane budget 2000–2012. *Earth Syst. Sci. Data* 8, 697–751. doi:10.5194/essd-8-697-2016.

Saunois, M., Bousquet, P., Poulter, B., Peregon, A., Ciais, P., Canadell, J. G., et al. (2017). Variability and quasi-decadal changes in the methane budget over the period 2000–2012. *Atmos. Chem. Phys.* 17, 11135–11161. doi:10.5194/acp-17-11135-2017.

Saunois, M., Jackson, R. B., Bousquet, P., Poulter, B., and Canadell, J. G. (2016b). The growing role of methane in anthropogenic climate change. *Environ. Res. Lett.* 11, 120207. doi:10.1088/1748-9326/11/12/120207.

Saunois, M., Stavert, A. R., Poulter, B., Bousquet, P., Canadell, J. G., Jackson, R. B., et al. (2019). The Global Methane Budget 2000–2017. *Earth Syst. Sci. Data Discuss.* doi:https://doi.org/10.5194/essd-2019-128.

Schädel, C., Bader, M. K.-F., Schuur, E. A. G., Biasi, C., Bracho, R., Čapek, P., et al. (2016). Potential carbon emissions dominated by carbon dioxide from thawed permafrost soils. *Nat. Clim. Chang.* 6, 950–953. doi:10.1038/nclimate3054.

Schädel, C., Schuur, E. A. G., Bracho, R., Elberling, B., Knoblauch, C., Lee, H., et al. (2014). Circumpolar assessment of permafrost C quality and its vulnerability over time using long-term incubation data. *Glob. Chang. Biol.* 20, 641–652. doi:10.1111/gcb.12417.

Schaefer, H., Fletcher, S. E. M., Veidt, C., Lassey, K. R., Brailsford, G. W., Bromley, T. M., et al. (2016). A 21st-century shift from fossil-fuel to biogenic methane emissions indicated by 13CH4. *Science* 352, 80–84. doi:10.1126/science.aad2705.

Schaefer, K., Lantuit, H., Romanovsky, V. E., Schuur, E. A. G., and Witt, R. (2014). The impact of the permafrost carbon feedback on global climate. *Environ. Res. Lett.* 9, 85003. doi:10.1088/1748-9326/9/8/085003.

Schaphoff, S., Reyer, C. P. O., Schepaschenko, D., Gerten, D., and Shvidenko, A. (2016). Tamm Review: Observed and projected climate change impacts on Russia's forests and its carbon balance. *For. Ecol. Manage.* 361, 432–444. doi:10.1016/j.foreco.2015.11.043.

Scheffer, M., Bascompte, J., Brock, W. A., Brovkin, V., Carpenter, S. R., Dakos, V., et al. (2009). Early-warning signals for critical transitions. *Nature* 461, 53–59. doi:10.1038/nature08227.

Scheffer, M., Hirota, M., Holmgren, M., Van Nes, E. H., and Chapin, F. S. (2012). Thresholds for boreal biome transitions. *Proc. Natl. Acad. Sci.* 109, 21384–21389. doi:10.1073/pnas.1219844110.

Schilt, A., Baumgartner, M., Blunier, T., Schwander, J., Spahni, R., Fischer, H., et al. (2010a). Glacial–interglacial and millennial-scale variations in the atmospheric nitrous oxide concentration during the last 800,000 years. *Quat. Sci. Rev.* 29, 182–192. doi:10.1016/j.quascirev.2009.03.011.

Schilt, A., Baumgartner, M., Schwander, J., Buiron, D., Capron, E., Chappellaz, J., et al. (2010b). Atmospheric nitrous oxide during the last 140,000years. *Earth Planet. Sci. Lett.* 300, 33–43. doi:10.1016/j.epsl.2010.09.027.

Schilt, A., Brook, E. J., Bauska, T. K., Baggenstos, D., Fischer, H., Joos, F., et al. (2014). Isotopic constraints on marine and terrestrial N2O emissions during the last deglaciation. *Nature* 516, 234–237. doi:10.1038/nature13971.

Schimel, D., Stephens, B. B., and Fisher, J. B. (2015). Effect of increasing CO2 on the terrestrial carbon cycle. *Proc. Natl. Acad. Sci. U. S. A.* 112, 436–441. doi:10.1073/pnas.1407302112.

Schlesinger, W. H. (2013). An estimate of the global sink for nitrous oxide in soils. *Glob. Chang. Biol.* 19, 2929–2931. doi:10.1111/gcb.12239.

Schlunegger, S., Rodgers, K. B., Sarmiento, J. L., Frölicher, T. L., Dunne, J. P., Ishii, M., et al. (2019). Emergence of anthropogenic signals in the ocean carbon cycle. *Nat. Clim. Chang.* 9, 719–725. doi:10.1038/s41558-019-0553-2.

Schmidt, M. W. I., Torn, M. S., Abiven, S., Dittmar, T., Guggenberger, G., Janssens, I. A., et al. (2011). Persistence of soil organic matter as an ecosystem property. *Nature* 478, 49–56. doi:10.1038/nature10386.

Schmidtko, S., Stramma, L., and Visbeck, M. (2017). Decline in global oceanic oxygen content during the past five decades. *Nature* 542, 335–339. doi:10.1038/nature21399.

Schmitt, J., Schneider, R., Elsig, J., Leuenberger, D., Lourantou, A., Chappellaz, J., et al. (2012). Carbon Isotope Constraints on the Deglacial CO2 Rise from Ice Cores. *Science* 336, 711–714. doi:10.1126/science.1217161.

Schmittner, A., Oschlies, A., Matthews, H. D., and Galbraith, E. D. (2008). Future changes in climate, ocean circulation, ecosystems, and biogeochemical cycling simulated for a business-as-usual CO2 emission scenario until year 4000 AD. *Global Biogeochem. Cycles* 22, GB1013. doi:10.1029/2007GB002953.

Schneider von Deimling, T., Grosse, G., Strauss, J., Schirrmeister, L., Morgenstern, A., Schaphoff, S., et al. (2015). Observation-based modelling of permafrost carbon fluxes with accounting for deep carbon deposits and thermokarst activity. *Biogeosciences* 12, 3469–3488. doi:10.5194/bg-12-3469-2015.

Schneider von Deimling, T., Meinshausen, M., Levermann, A., Huber, V., Frieler, K., Lawrence, D. M., et al. (2012). Estimating the near-surface permafrost-carbon feedback on global warming. *Biogeosciences* 9, 649–665. doi:10.5194/bg-9-649-2012.

Schuur, E. A. G., McGuire, A. D., Schädel, C., Grosse, G., Harden, J. W., Hayes, D. J., et al. (2015). Climate change and the permafrost carbon feedback. *Nature* 520, 171–179. doi:10.1038/nature14338.

Schuur, E. A. G., Vogel, J. G., Crummer, K. G., Lee, H., Sickman, J. O., and Osterkamp, T. E. (2009). The effect of permafrost thaw on old carbon release and net carbon exchange from tundra. *Nature* 459, 556–559. doi:10.1038/nature08031.

Schwarber, A. K., Smith, S. J., Hartin, C. A., Vega-Westhoff, B. A., and Sriver, R. (2018). Evaluating Climate Emulation: Unit Testing of Simple Climate Models. *Earth Syst. Dyn. Discuss.*, 1–13. doi:10.5194/esd-2018-63.

Schwietzke, S., Sherwood, O. A., Bruhwiler, L. M. P., Miller, J. B., Etiope, G., Dlugokencky, E. J., et al. (2016). Upward revision of global fossil fuel methane emissions based on isotope database. *Nature* 538, 88–91. doi:10.1038/nature19797.

Schwinger, J., Goris, N., Tjiputra, J. F., Kriest, I., Bentsen, M., Bethke, I., et al. (2016). Evaluation of NorESM-OC (versions 1 and 1.2), the ocean carbon-cycle stand-alone configuration of the Norwegian Earth System Model (NorESM1). *Geosci. Model Dev.* 9, 2589–2622. doi:10.5194/gmd-9-2589-2016.

Schwinger, J., Tjiputra, J. F., Heinze, C., Bopp, L., Christian, J. R., Gehlen, M., et al. (2014). Nonlinearity of Ocean Carbon Cycle Feedbacks in CMIP5 Earth System Models. *J. Clim.* 27, 3869–3888. doi:10.1175/JCLI-D-13-00452.1.

Scott, V., Haszeldine, R. S., Tett, S. F. B., and Oschlies, A. (2015). Fossil fuels in a trillion tonne world. *Nat. Clim. Chang.* 5, 419–423. doi:10.1038/nclimate2578.

Séférian, R., Berthet, S., and Chevallier, M. (2018). Assessing the decadal predictability of land and ocean carbon uptake. *Geophys. Res. Lett.* 45, 2455–2466. doi:10.1002/2017GL076092.

Séférian, R., Bopp, L., Gehlen, M., Swingedouw, D., Mignot, J., Guilyardi, E., et al. (2014). Multiyear predictability of tropical marine productivity. *Proc. Natl. Acad. Sci.* 111, 11646–11651. doi:10.1073/pnas.1315855111.

Segschneider, J., and Bendtsen, J. (2013). Temperature-dependent remineralization in a warming ocean increases surface pCO2 through changes in marine ecosystem composition. *Global Biogeochem. Cycles* 27, 1214–1225. doi:10.1002/2013GB004684.

Seitzinger, S. P., Kroeze, C., and Styles, R. V (2000). Global distribution of N2O emissions from aquatic systems: natural emissions and anthropogenic effects. *Chemosph. - Glob. Chang. Sci.* 2, 267–279. doi:10.1016/S1465-9972(00)00015-5.

Semiletov, I., Pipko, I., Gustafsson, Ö., Anderson, L. G., Sergienko, V., Pugach, S., et al. (2016). Acidification of East Siberian Arctic Shelf waters through addition of freshwater and terrestrial carbon. *Nat. Geosci.* 9, 361–365. doi:10.1038/ngeo2695.

Seshadri, A. K. (2017). Origin of path independence between cumulative CO2 emissions and global warming. *Clim. Dyn.* 49, 3383–3401. doi:10.1007/s00382-016-3519-3.

Shakhova, N., Semiletov, I., Gustafsson, O., Sergienko, V., Lobkovsky, L., Dudarev, O., et al. (2017). Current rates and mechanisms of subsea permafrost degradation in the East Siberian Arctic Shelf. *Nat. Commun.* 8, 15872. doi:10.1038/ncomms15872.

Shakhova, N., Semiletov, I., Salyuk, A., Yusupov, V., Kosmach, D., and Gustafsson, O. (2010). Extensive methane venting to the atmosphere from sediments of the East Siberian Arctic shelf. *Science* 327, 1246–1250. doi:10.1126/science.1182221.

Shakun, J. D., Clark, P. U., He, F., Marcott, S. A., Mix, A. C., Liu, Z., et al. (2012). Global warming preceded by increasing carbon dioxide concentrations during the last deglaciation. *Nature* 484, 49–54. doi:10.1038/nature10915.

Shcherbak, I., Millar, N., and Robertson, G. P. (2014). Global metaanalysis of the nonlinear response of soil nitrous oxide (N2O) emissions to fertilizer nitrogen. *Proc. Natl. Acad. Sci.* 111, 9199–9204. doi:10.1073/pnas.1322434111.

Shen, Q., Hedley, M., Camps Arbestain, M., and Kirschbaum, M. U. . (2016). Can biochar increase the bioavailability of phosphorus? *J. soil Sci. plant Nutr.* 16. doi:10.4067/S0718-95162016005000022.

Shilong Piao, Xuhui Wang, Kai Wang, Xiangyi Li, Ana Bastos, Josep G. Canadell, Philippe Ciais, Pierre Friedlingstein, S. S. (2019). Interannual variation of global carbon cycle: issues and perspectives. *Glob. Chang. Biol.*

Shindell, D. T., Pechony, O., Voulgarakis, A., Faluvegi, G., Nazarenko, L., Lamarque, J.-F., et al. (2013). Interactive ozone and methane chemistry in GISS-E2 historical and future climate simulations. *Atmos. Chem. Phys.* 13, 2653–2689. doi:10.5194/acp-13-2653-2013.

Shinjo, R., Asami, R., Huang, K.-F., You, C.-F., and Iryu, Y. (2013). Ocean acidification trend in the tropical North Pacific since the mid-20th century reconstructed from a coral archive. *Mar. Geol.* 342, 58–64. doi:10.1016/j.margeo.2013.06.002.

Siegenthaler, U., Stocker, T. F., Monnin, E., Lüthi, D., Schwander, J., Stauffer, B., et al. (2005). EPICA Dome C carbon dioxide concentrations from 650 to 391 kyr BP. *PANGEA*. doi:10.1594/PANGAEA.728136.

Sigman, D. M., and Boyle, E. A. (2000). Glacial/interglacial variations in atmospheric carbon dioxide. *Nature* 407, 859–869. doi:10.1038/35038000.

Sigman, D. M., Hain, M. P., and Haug, G. H. (2010). The polar ocean and glacial cycles in atmospheric CO2 concentration. *Nature* 466, 47–55. doi:10.1038/nature09149.

Sigman, D. M., Jaccard, S. L., and Haug, G. H. (2004). Polar ocean stratification in a cold climate. *Nature* 428, 59–63. doi:10.1038/nature02357.

Simmons, C. T., and Matthews, H. D. (2016). Assessing the implications of human land-use change for the transient climate response to cumulative carbon emissions. *Environ. Res. Lett.* 11, 035001. doi:10.1088/1748-9326/11/3/035001.

Simpson, I. J., Sulbaek Andersen, M. P., Meinardi, S., Bruhwiler, L., Blake, N. J., Helmig, D., et al. (2012). Long-term decline of global atmospheric ethane concentrations and implications for methane. *Nature* 488, 490–494. doi:10.1038/nature11342.

Sitch, S., Friedlingstein, P., Gruber, N., Jones, S. D., Murray-Tortarolo, G., Ahlström, A., et al. (2015). Recent trends and drivers of regional sources and sinks of carbon dioxide. *Biogeosciences* 12, 653–679. doi:10.5194/bg-12-653-2015.

Skinner, L. C., Fallon, S., Waelbroeck, C., Michel, E., and Barker, S. (2010). Ventilation of the Deep Southern Ocean and Deglacial CO2 Rise. *Science* 328, 1147–1151. doi:10.1126/science.1183627.

Skinner, L. C., Primeau, F., Freeman, E., de la Fuente, M., Goodwin, P. A., Gottschalk, J., et al. (2017). Radiocarbon constraints on the glacial ocean circulation and its impact on atmospheric CO2. *Nat. Commun.* 8, 16010. doi:10.1038/ncomms16010.

Sluijs, A., Schouten, S., Pagani, M., Woltering, M., Brinkhuis, H., Damsté, J. S. S., et al. (2006). Subtropical Arctic Ocean temperatures during the Paleocene/Eocene thermal maximum. *Nature* 441, 610–613. doi:10.1038/nature04668.

Smale, D. A., Wernberg, T., Oliver, E. C. J., Thomsen, M., Harvey, B. P., Straub, S. C., et al. (2019). Marine heatwaves threaten global biodiversity and the provision of ecosystem services. *Nat. Clim. Chang.* 9, 306–312. doi:10.1038/s41558-019-0412-1.

Smetacek, V., Klaas, C., Strass, V. H., Assmy, P., Montresor, M., Cisewski, B., et al. (2012). Deep carbon export from a Southern Ocean iron-fertilized diatom bloom. *Nature* 487, 313–319. doi:10.1038/nature11229.

Smith, C. J., Forster, P. M., Allen, M., Fuglestvedt, J., Millar, R. J., Rogelj, J., et al. (2019). Current fossil fuel infrastructure does not yet commit us to 1.5 °C warming. *Nat. Commun.* 10, 101. doi:10.1038/s41467-018-07999-w.

Smith, C. J., Forster, P. M., Allen, M., Leach, N., Millar, R. J., Passerello, G. A., et al. (2018a). FAIR v1.3: a simple emissions-based impulse response and carbon cycle model. *Geosci. Model Dev.* 11, 2273–2297. doi:10.5194/gmd-11-2273-2018.

Smith, D. R., Townsend, T. J., Choy, A. W. K., Hardy, I. C. W., and Sjögersten, S. (2012a). Short-term soil carbon sink potential of oil palm plantations. *GCB Bioenergy* 4, 588–596. doi:10.1111/j.1757-1707.2012.01168.x.

Smith, N. G., and Dukes, J. S. (2013). Plant respiration and photosynthesis in global-scale models: incorporating acclimation to temperature and CO2. *Glob. Chang. Biol.* 19, 45–63. doi:10.1111/j.1365-2486.2012.02797.x.

Smith, N. G., Malyshev, S. L., Shevliakova, E., Kattge, J., and Dukes, J. S. (2015). Foliar temperature acclimation reduces simulated carbon sensitivity to climate. *Nat. Clim. Chang.* 6, 407. Available at: https://doi.org/10.1038/nclimate2878.

Smith, P. (2016). Soil carbon sequestration and biochar as negative emission technologies. *Glob. Chang. Biol.* 22, 1315–1324. doi:10.1111/gcb.13178.

Smith, P., Davis, S. J., Creutzig, F., Fuss, S., Minx, J., Gabrielle, B., et al. (2016). Biophysical and economic limits to negative CO2 emissions. *Nat. Clim. Chang.* 6, 42–50. doi:10.1038/nclimate2870.

Smith, P., Price, J., Molotoks, A., Warren, R., and Malhi, Y. (2018b). Impacts on terrestrial biodiversity of moving from a 2°C to a 1.5°C target. *Philos. Trans. R. Soc. A Math. Eng. Sci.* 376, 20160456. doi:10.1098/rsta.2016.0456.

Smith, S. J., and Mizrahi, A. (2013). Near-term climate mitigation by short-lived forcers. *Proc. Natl. Acad. Sci.* 110, 14202–14206. doi:10.1073/pnas.1308470110.

Smith, W. K., Zhao, M., and Running, S. W. (2012b). Global bioenergy capacity as constrained by observed biospheric productivity rates. *Bioscience* 62, 911–922. doi:10.1525/bio.2012.62.10.11.

Snider, D. M., Venkiteswaran, J. J., Schiff, S. L., and Spoelstra, J. (2015). From the ground up: global nitrous oxide sources are constrained by stable isotope values. *PLoS One* 10, e0118954. doi:10.1371/journal.pone.0118954.

Solomon, S., Daniel, J. S., Sanford, T. J., Murphy, D. M., Plattner, G.-K., Knutti, R., et al. (2010). Persistence of climate changes due to a range of greenhouse gases. *Proc. Natl. Acad. Sci.* 107, 18354–18359. doi:10.1073/pnas.1006282107.

Somes, C. J., Schmittner, A., Muglia, J., and Oschlies, A. (2017). A three-dimensional model of the marine nitrogen cycle during the last glacial maximum constrained by sedimentary isotopes. *Front. Mar. Sci.* 4. doi:10.3389/fmars.2017.00108.

Song, J., Wan, S., Piao, S., Knapp, A. K., Classen, A. T., Vicca, S., et al. (2019). A meta-analysis of 1,119 manipulative experiments on terrestrial carbon-cycling responses to global change. *Nat. Ecol. Evol.* 3, 1309–1320. doi:10.1038/s41559-019-0958-3.

Sonntag, S., Ferrer González, M., Ilyina, T., Kracher, D., Nabel, J. E. M. S., Niemeier, U., et al. (2018). Quantifying and comparing effects of climate engineering methods on the Earth system. *Earth's Futur.* 6, 149–168. doi:10.1002/2017EF000620.

Sonntag, S., Pongratz, J., Reick, C., and Schmidt, H. (2015). Carbon sequestration potential and climatic effects of reforestation in an Earth system model. in, 13707.

Søren, R., Bendtsen, J., Delille, B., Dieckmann, G. S., Glud, R. N., Kennedy, H., et al. (2011). Sea ice contribution to the air–sea CO2 exchange in the Arctic and Southern Oceans. *Tellus B Chem. Phys. Meteorol.* 63, 823–830. doi:10.1111/j.1600-0889.2011.00571.x.

Spafford, L., and MacDougall, A. H. Quantifying the probability distribution function of the Transient Climate Response to Cumulative CO 2 Emissions. *Environ. Res. Lett.*

Spafford, L., and MacDougall, A. H. (submitted). Quantifying the probability distribution function of the Transient Climate Response to Cumulative CO2 Emissions. *Environ. Res. Lett.* (submitted).

Spring, A., and Ilyina, T. (submitted). Predictability Horizons in the Global Carbon Cycle inferred from a perfect-model framework. *Geophys. Res. Lett.* (submitted).

Statistics division. Food and Agriculture Organization of the United Nations (2018). *FAO*. Available at: http://www.fao.org/faostat/en/.

Staver, A. C., Archibald, S., and Levin, S. A. (2011). The global extent and determinants of savanna and forest as alternative biome states. *Science* 334, 230–232. doi:10.1126/science.1210465.

Steele, L. P., Dlugokencky, E. J., Lang, P. M., Tans, P. P., Martin, R. C., and Masarie, K. A. (1992). Slowing down of the global accumulation of atmospheric methane during the 1980s. *Nature* 358, 313–316. doi:10.1038/358313a0.

Steffen, W., Rockström, J., Richardson, K., Lenton, T. M., Folke, C., Liverman, D., et al. (2018). Trajectories of the Earth System in the Anthropocene. *Proc. Natl. Acad. Sci.* 115, 8252–8259. doi:10.1073/pnas.1810141115.

Steinacher, M., and Joos, F. (2016). Transient Earth system responses to cumulative carbon dioxide emissions: linearities, uncertainties, and probabilities in an observation-constrained model ensemble. *Biogeosciences* 13, 1071–1103. doi:10.5194/bg-13-1071-2016.

Sterman, J. D., Siegel, L., and Rooney-Varga, J. N. (2018). Does replacing coal with wood lower CO2 emissions? Dynamic lifecycle analysis of wood bioenergy. *Environ. Res. Lett.* 13, 15007. doi:10.1088/1748-9326/aaa512.

Stern, D. I., and Kaufmann, R. K. (1996). Estimates of global anthropogenic methane emissions 1860–1993. *Chemosphere* 33, 159–176. doi:10.1016/0045-6535(96)00157-9.

Stevenson, D. S., Zhao, A., and Naik, V. (2019). Trends in global tropospheric hydroxyl radical and methane lifetime since 1850 from AerChemMIP. *ACPD*.

Stocker, B. D., and Joos, F. (2015). Quantifying differences in land use emission estimates implied by definition discrepancies. *Earth Syst. Dyn.* 6, 731–744. doi:10.5194/esd-6-731-2015.

Stocker, B. D., Roth, R., Joos, F., Spahni, R., Steinacher, M., Zaehle, S., et al. (2013a). Multiple greenhouse-gas feedbacks from the land biosphere under future climate change scenarios. *Nat. Clim. Chang.* 3, 666–672. doi:10.1038/nclimate1864.

Stocker, B. D., Yu, Z., Massa, C., and Joos, F. (2017). Holocene peatland and ice-core data constraints on the timing and magnitude of CO2 emissions from past land use. *Proc. Natl. Acad. Sci.* 114, 1492–1497. doi:10.1073/pnas.1613889114.

Stocker, T. F., Qin, D., Plattner, G.-K., Alexander, L. V, Allen, S. K., Bindoff, N. L., et al. (2013b). "Technical Summary," in *Climate Change 2013: The Physical Science Basis. Contribution of Working Group I to the Fifth Assessment Report of the Intergovernmental Panel on Climate Change*, eds. T. F. Stocker, D. Qin, G.-K. Plattner, M. Tignor, S. K. Allen, A. Boschung, et al. (Cambridge, United Kingdom and New York, NY, USA: Cambridge University Press), 33–115.

Stott, L. D., Harazin, K. M., and Quintana Krupinski, N. B. (2019a). Hydrothermal carbon release to the ocean and atmosphere from the eastern equatorial Pacific during the last glacial termination. *Environ. Res. Lett.* 14, 025007. doi:10.1088/1748-9326/aafe28.

Stott, L., Davy, B., Shao, J., Coffin, R., Pecher, I., Neil, H., et al. (2019b). CO2 release from pockmarks on the chatham rise-bounty trough at the glacial termination. *Paleoceanogr. Paleoclimatology*, 2019PA003674. doi:10.1029/2019PA003674.

Stramma, L., Johnson, G. C., Sprintall, J., and Mohrholz, V. (2008). Expanding oxygen-minimum zones in the tropical oceans. *Science* 320, 655–658. doi:10.1126/science.1153847.

Strauss, J., Schirrmeister, L., Grosse, G., Fortier, D., Hugelius, G., Knoblauch, C., et al. (2017). Deep Yedoma permafrost: A synthesis of depositional characteristics and carbon vulnerability. *Earth-Science Rev.* 172, 75–86. doi:10.1016/j.earscirev.2017.07.007.

Strefler, J., Amann, T., Bauer, N., Kriegler, E., and Hartmann, J. (2018). Potential and costs of carbon dioxide removal by enhanced weathering of rocks. *Environ. Res. Lett.* 13, 34010. doi:10.1088/1748-9326/aaa9c4.

Studer, A. S., Sigman, D. M., Martínez-García, A., Thöle, L. M., Michel, E., Jaccard, S. L., et al. (2018). Increased nutrient supply to the Southern Ocean during the Holocene and its implications for the pre-industrial atmospheric CO2 rise. *Nat. Geosci.* 11, 756–760. doi:10.1038/s41561-018-0191-8.

Suess, H. E. (1955). Radiocarbon Concentration in Modern Wood. *Science* 122, 415–417. doi:10.1126/science.122.3166.415-a.

Sulman, B. N., Phillips, R. P., Oishi, A. C., Shevliakova, E., and Pacala, S. W. (2014). Microbe-driven turnover offsets mineral-mediated storage of soil carbon under elevated CO2. *Nat. Clim. Chang.* 4, 1099–1102. doi:10.1038/nclimate2436.

Sulman, B. N., Shevliakova, E., Brzostek, E. R., Kivlin, S. N., Malyshev, S., Menge, D. N. L., et al. (2019). Diverse mycorrhizal associations enhance terrestrial C storage in a global model. *Global Biogeochem. Cycles* 33, 501–523. doi:10.1029/2018GB005973.

Suntharalingam, P., Buitenhuis, E., Le Quéré, C., Dentener, F., Nevison, C., Butler, J. H., et al. (2012). Quantifying the impact of anthropogenic nitrogen deposition on oceanic nitrous oxide. *Geophys. Res. Lett.* 39, L07605. doi:10.1029/2011GL050778.

Suntharalingam, P., Zamora, L. M., Bange, H. W., Bikkina, S., Buitenhuis, E., Kanakidou, M., et al. (2019). Anthropogenic nitrogen inputs and impacts on oceanic N2O fluxes in the northern Indian Ocean: The need for an integrated observation and modelling approach. *Deep Sea Res. Part II Top. Stud. Oceanogr.* 166, 104–113. doi:10.1016/j.dsr2.2019.03.007.

Suthhof, A., Ittekkot, V., and Gaye-Haake, B. (2001). Millennial-scale oscillation of denitrification intensity in the Arabian Sea during the Late Quaternary and its potential influence on atmospheric N 2 O and global climate. *Global Biogeochem. Cycles* 15, 637–649. doi:10.1029/2000GB001337.

Sutton, A. J., Feely, R. A., Sabine, C. L., McPhaden, M. J., Takahashi, T., Chavez, F. P., et al. (2014). Natural variability and anthropogenic change in equatorial Pacific surface ocean pCO2 and pH. *Global Biogeochem. Cycles* 28, 131–145. doi:10.1002/2013GB004679.

Sutton, A. J., Sabine, C. L., Feely, R. A., Cai, W.-J., Cronin, M. F., McPhaden, M. J., et al. (2016). Using present-day observations to detect when anthropogenic change forces surface ocean carbonate chemistry outside preindustrial bounds. *Biogeosciences* 13, 5065–5083. doi:10.5194/bg-13-5065-2016.

Tachiiri, K., Hajima, T., and Kawamiya, M. (2015). Increase of uncertainty in transient climate response to cumulative carbon emissions after stabilization of atmospheric CO2 concentration. *Environ. Res. Lett.* 10, 125018. doi:10.1088/1748-9326/10/12/125018.

Tachiiri, K., Hajima, T., and Kawamiya, M. (2019). Increase of the transient climate response to cumulative carbon emissions with decreasing CO2 concentration scenarios. *Environ. Res. Lett.* doi:10.1088/1748-9326/ab57d3.

Tagliabue, A., Aumont, O., and Bopp, L. (2014). The impact of different external sources of iron on the global carbon cycle. *Geophys. Res. Lett.* 41, 920–926. doi:10.1002/2013GL059059.

Taillardat, P., Friess, D. A., and Lupascu, M. (2018). Mangrove blue carbon strategies for climate change mitigation are most effective at the national scale. *Biol. Lett.* 14, 20180251. doi:10.1098/rsbl.2018.0251.

Takata, K., Patra, P. K., Kotani, A., Mori, J., Belikov, D., Ichii, K., et al. (2017). Reconciliation of top-down and bottom-up CO2 fluxes in Siberian larch forest. *Environ. Res. Lett.* 12. doi:10.1088/1748-9326/aa926d.

Takatani, Y., Enyo, K., Iida, Y., Kojima, A., Nakano, T., Sasano, D., et al. (2014). Relationships between total alkalinity in surface water and sea surface dynamic height in the Pacific Ocean. *J. Geophys. Res. Ocean.* 119, 2806–2814. doi:10.1002/2013JC009739.

Takatani, Y., Sasano, D., Nakano, T., Midorikawa, T., and Ishii, M. (2012). Decrease of dissolved oxygen after the mid-1980s in the western North Pacific subtropical gyre along the 137°E repeat section. *Global Biogeochem. Cycles* 26, GB2013. doi:10.1029/2011GB004227.

Takeshita, Y., Frieder, C. A., Martz, T. R., Ballard, J. R., Feely, R. A., Kram, S., et al. (2015). Including high-frequency variability in coastal ocean acidification projections. *Biogeosciences* 12, 5853–5870. doi:10.5194/bg-12-5853-2015.

Talhelm, A. F., Pregitzer, K. S., Kubiske, M. E., Zak, D. R., Campany, C. E., Burton, A. J., et al. (2014). Elevated carbon dioxide and ozone alter productivity and ecosystem carbon content in northern temperate forests. *Glob. Chang. Biol.* 20, 2492–2504. doi:10.1111/gcb.12564.

Tan, Z.-H., Zeng, J., Zhang, Y.-J., Slot, M., Gamo, M., Hirano, T., et al. (2017). Optimum air temperature for tropical forest photosynthesis: mechanisms involved and implications for climate warming. *Environ. Res. Lett.* 12, 054022. doi:10.1088/1748-9326/aa6f97.

Tanhua, T., Hoppema, M., Jones, E. M., Stöven, T., Hauck, J., Dávila, M. G., et al. (2017). Temporal changes in ventilation and the carbonate system in the Atlantic sector of the Southern Ocean. *Deep Sea Res. Part II Top. Stud. Oceanogr.* 138, 26–38. doi:10.1016/j.dsr2.2016.10.004.

Taucher, J., and Oschlies, A. (2011). Can we predict the direction of marine primary production change under global warming? *Geophys. Res. Lett.* 38, L02603. doi:10.1029/2010GL045934.

Taylor, K. E., Stouffer, R. J., and Meehl, G. A. (2012). An Overview of CMIP5 and the Experiment Design. *Bull. Am. Meteorol. Soc.* 93, 485–498. doi:10.1175/BAMS-D-11-00094.1.

Taylor, L. L., Quirk, J., Thorley, R. M. S., Kharecha, P. A., Hansen, J., Ridgwell, A., et al. (2015a). Enhanced weathering strategies for stabilizing climate and averting ocean acidification. *Nat. Clim. Chang.* 6, 402.

Taylor, L. L., Quirk, J., Thorley, R. M. S., Kharecha, P. A., Hansen, J., Ridgwell, A., et al. (2015b). Enhanced weathering strategies for stabilizing climate and averting ocean acidification. *Nat. Clim. Chang.* 6, 402. Available at: https://doi.org/10.1038/nclimate2882.

Tebaldi, C., and Knutti, R. (2007). The use of the multi-model ensemble in probabilistic climate projections. *Philos. Trans. R. Soc. A Math. Phys. Eng. Sci.* 365, 2053–2075. doi:10.1098/rsta.2007.2076.

Teckentrup, L., Harrison, S. P., Hantson, S., Heil, A., Melton, J. R., Forrest, M., et al. (2019). Response of simulated burned area to historical changes in environmental and anthropogenic factors: a comparison of seven fire models. *Biogeosciences* 16, 3883–3910. doi:10.5194/bg-16-3883-2019.

Terrer, C., Vicca, S., Hungate, B. A., Phillips, R. P., and Prentice, I. C. (2016). Mycorrhizal association as a primary control of the CO2 fertilization effect. *Science* 353, 72–74. doi:10.1126/science.aaf4610.

Terrer, C., Vicca, S., Stocker, B. D., Hungate, B. A., Phillips, R. P., Reich, P. B., et al. (2018). Ecosystem responses to elevated CO2 governed by plant-soil interactions and the cost of nitrogen acquisition. *New Phytol.* 217, 507–522. doi:10.1111/nph.14872.

Thomas, E. (2007). "Cenozoic mass extinctions in the deep sea: What perturbs the largest habitat on Earth?," in *Special Paper 424: Large Ecosystem Perturbations: Causes and Consequences*, eds. S. Monechi, R. Coccioni, and M. R. Rampino (Geological Society of America), 1–23. doi:10.1130/2007.2424(01).

Thomas, R. Q., Brookshire, E. N. J., and Gerber, S. (2015). Nitrogen limitation on land: how can it occur in Earth system models? *Glob. Chang. Biol.* 21, 1777–1793. doi:10.1111/gcb.12813.

Thomas, R. T., Prentice, I. C., Graven, H., Ciais, P., Fisher, J. B., Hayes, D. J., et al. (2016). Increased light-use efficiency in northern terrestrial ecosystems indicated by CO2 and greening observations. *Geophys. Res. Lett.* doi:10.1002/2016GL070710.

Thompson, I., Mackey, B., Mcnulty, S., and Mosseler, A. (2009). Forest Resilience, Biodiversity, and Climate Change. A Synthesis of the Biodiversity/Resilience/Stability Relationship in Forest Ecosystems. Secretariat of the Convention on Biological Diversity, Montreal.

Thompson, R. L., Dlugokencky, E., Chevallier, F., Ciais, P., Dutton, G., Elkins, J. W., et al. (2013). Interannual variability in tropospheric nitrous oxide. *Geophys. Res. Lett.* 40, 4426–4431. doi:10.1002/grl.50721.

Thompson, R. L., Lassaletta, L., Patra, P. K., Wilson, C., Wells, K. C., Gressent, A., et al. (2019). Acceleration of global N2O emissions seen from two decades of atmospheric inversion. *Nat. Clim. Chang.* 9, 993–998. doi:10.1038/s41558-019-0613-7.

Thompson, R. L., Nisbet, E. G., Pisso, I., Stohl, A., Blake, D., Dlugokencky, E. J., et al. (2018). Variability in Atmospheric Methane From Fossil Fuel and Microbial Sources Over the Last Three Decades. *Geophys. Res. Lett.* 45, 11,499–11,508. doi:10.1029/2018GL078127.

Thornton, B. F., Wik, M., and Crill, P. M. (2016). Double-counting challenges the accuracy of high-latitude methane inventories. *Geophys. Res. Lett.* 43, 12,569-12,577. doi:10.1002/2016GL071772.

Thornton, P. E., Doney, S. C., Lindsay, K., Moore, J. K., Mahowald, N., Randerson, J. T., et al. (2009). Carbon-nitrogen interactions regulate climate-carbon cycle feedbacks: results from an atmosphere-ocean general circulation model. *Biogeosciences* 6, 2099–2120. doi:10.5194/bg-6-2099-2009.

Thurner, M., Beer, C., Ciais, P., Friend, A. D., Ito, A., Kleidon, A., et al. (2017). Evaluation of climate-related carbon turnover processes in global vegetation models for boreal and temperate forests. *Glob. Chang. Biol.* 23, 3076–3091. doi:10.1111/gcb.13660.

Tian, H., Davidson, E. A., Canadell, J. G., Thompson, R. L., Suntharalingam, P., and Etal. (submitted, a). Recent patterns and trends of global nitrous oxide sources and sinks. *Nature* (submitted).

Tian, H., Xu, R., Canadell, J. G., Thompson, R. L., Winiwarter, W., Parvadha Suntharalingam, et al. (submitted, b). A comprehensive global nitrous oxide budget reveals lack of mitigation. *Nature* (submitted).

Tian, H., Yang, J., Xu, R., Lu, C., Canadell, J. G., Davidson, E. A., et al. (2019). Global soil nitrous oxide emissions since the preindustrial era estimated by an ensemble of terrestrial biosphere models: Magnitude, attribution, and uncertainty. *Glob. Chang. Biol.* 25, 640–659. doi:10.1111/gcb.14514.

Tilmes, S., Sanderson, B. M., and O'Neill, B. C. (2016). Climate impacts of geoengineering in a delayed mitigation scenario. *Geophys. Res. Lett.* 43, 8222–8229. doi:10.1002/2016GL070122.

Tjiputra, J. F., Grini, A., and Lee, H. (2016). Impact of idealized future stratospheric aerosol injection on the large-scale ocean and land carbon cycles. *J. Geophys. Res. Biogeosciences* 121, 2–27. doi:10.1002/2015JG003045.

Todd-Brown, K. E. O., Randerson, J. T., Post, W. M., Hoffman, F. M., Tarnocai, C., Schuur, E. A. G., et al. (2013). Causes of variation in soil carbon simulations from CMIP5 Earth system models and comparison with observations. *Biogeosciences* 10, 1717–1736. doi:10.5194/bg-10-1717-2013.

Tohjima, Y., Mukai, H., Machida, T., Hoshina, Y., and Nakaoka, S.-I. (2019). Global carbon budgets estimated from atmospheric O_2/N_2 andCO_2 observations in the western Pacific region over a 15-year period. *Atmos. Chem. Phys.* 19, 9269–9285. doi:10.5194/acp-19-9269-2019.

Tokarska, K. B., and Gillett, N. P. (2018a). Cumulative carbon emissions budgets consistent with 1.5 °C global warming. *Nat. Clim. Chang.* 8, 296–299. doi:10.1038/s41558-018-0118-9.

Tokarska, K. B., and Gillett, N. P. (2018b). Cumulative carbon emissions budgets consistent with 1.5 °C global warming. *Nat. Clim. Chang.* 8, 296–299. doi:10.1038/s41558-018-0118-9.

Tokarska, K. B., Gillett, N. P., Arora, V. K., Lee, W. G., and Zickfeld, K. (2018). The influence of non-CO2 forcings on cumulative carbon emissions budgets. *Environ. Res. Lett.* 13, 034039. doi:10.1088/1748-9326/aaafdd.

Tokarska, K. B., Gillett, N. P., Weaver, A. J., Arora, V. K., and Eby, M. (2016). The climate response to five trillion tonnes of carbon. *Nat. Clim. Chang.* 6, 851–855. doi:10.1038/nclimate3036.

Tokarska, K. B., Schleussner, C.-F., Rogelj, J., Stolpe, M. B., Matthews, H. D., Pfleiderer, P., et al. (2019a). Recommended temperature metrics for carbon budget estimates, model evaluation and climate policy. *Nat. Geosci.* 12, 964–971. doi:10.1038/s41561-019-0493-5.

Tokarska, K. B., and Zickfeld, K. (2015). The effectiveness of net negative carbon dioxide emissions in reversing anthropogenic climate change. *Environ. Res. Lett.* 10, 094013. doi:10.1088/1748-9326/10/9/094013.

Tokarska, K. B., Zickfeld, K., and Rogelj, J. (2019b). Path independence of carbon budgets when meeting a stringent global mean temperature target after an overshoot. *Earth's Futur.*, 2019EF001312. doi:10.1029/2019EF001312.

Tonitto, C., David, M. B., and Drinkwater, L. E. (2006). Replacing bare fallows with cover crops in fertilizer-intensive cropping systems: A meta-analysis of crop yield and N dynamics. *Agric. Ecosyst. Environ.* 112, 58–72. doi:10.1016/j.agee.2005.07.003.

Toyama, K., Rodgers, K. B., Blanke, B., Iudicone, D., Ishii, M., Aumont, O., et al. (2017). Large reemergence of anthropogenic carbon into the ocean's surface mixed layer sustained by the ocean's overturning circulation. *J. Clim.* 30, 8615–8631. doi:10.1175/JCLI-D-16-0725.1.

Treat, C. C., Kleinen, T., Broothaerts, N., Dalton, A. S., Dommain, R., Douglas, T. A., et al. (2019). Widespread global peatland establishment and persistence over the last 130,000 y. *Proc. Natl. Acad. Sci.* 116, 4822–4827. doi:10.1073/pnas.1813305116.

Trimmer, M., Chronopoulou, P.-M., Maanoja, S. T., Upstill-Goddard, R. C., Kitidis, V., and Purdy, K. J. (2016). Nitrous oxide as a function of oxygen and archaeal gene abundance in the North Pacific. *Nat. Commun.* 7, 13451. doi:10.1038/ncomms13451.

Trisos, C. H., Amatulli, G., Gurevitch, J., Robock, A., Xia, L., and Zambri, B. (2018). Potentially dangerous consequences for biodiversity of solar geoengineering implementation and termination. *Nat. Ecol. Evol.* 2, 475–482. doi:10.1038/s41559-017-0431-0.

Tubiello, F. N., Salvatore, M., Rossi, S., Ferrara, A., Fitton, N., and Smith, P. (2013). The FAOSTAT database of greenhouse gas emissions from agriculture. *Environ. Res. Lett.* 8, 015009. doi:10.1088/1748-9326/8/1/015009.

Turco, M., Llasat, M.-C., von Hardenberg, J., and Provenzale, A. (2014). Climate change impacts on wildfires in a Mediterranean environment. *Clim. Change* 125, 369–380. doi:10.1007/s10584-014-1183-3.

Turco, M., Rosa-Cánovas, J. J., Bedia, J., Jerez, S., Montávez, J. P., Llasat, M. C., et al. (2018). Exacerbated fires in Mediterranean Europe due to anthropogenic warming projected with non-stationary climate-fire models. *Nat. Commun.* doi:10.1038/s41467-018-06358-z.

Turetsky, M., Abbott, B., Jones, M., Walter Anthony, K. M., Olefeldt, D., Schuur, E. A. G., et al. (in press, a). Carbon release through abrupt permafrost thaw. *Nat. Geosci.* (in press).

Turetsky, M. R., Abbot, B., Jones, M., Walter Anthony, K., Olefeldt, D., Schuur, E. A. G., et al. (in press, b). Abrupt thaw amplifies the permafrost carbon feedback through upland erosion and methane hotspots. *Nat. Geosci.* (in press).

Turi, G., Lachkar, Z., Gruber, N., and Münnich, M. (2016). Climatic modulation of recent trends in ocean acidification in the California Current System. *Environ. Res. Lett.* 11, 014007. doi:10.1088/1748-9326/11/1/014007.

Turnbull, J. C., Mikaloff Fletcher, S. E., Ansell, I., Brailsford, G. W., Moss, R. C., Norris, M. W., et al. (2017). Sixty years of radiocarbon dioxide measurements at Wellington, New Zealand: 1954–2014. *Atmos. Chem. Phys.* 17, 14771–14784. doi:10.5194/acp-17-14771-2017.

Turner, A. J., Frankenberg, C., Wennberg, P. O., and Jacob, D. J. (2017). Ambiguity in the causes for decadal trends in atmospheric methane and hydroxyl. *Proc. Natl. Acad. Sci.* 114, 5367–5372.

Turner, S. K. (2018). Constraints on the onset duration of the Paleocene–Eocene Thermal Maximum. *Philos. Trans. R. Soc. A Math. Phys. Eng. Sci.* 376, 20170082. doi:10.1098/rsta.2017.0082.

Tyrrell, T., and Lucas, M. I. (2002). Geochemical evidence of denitrification in the Benguela upwelling system. *Cont. Shelf Res.* 22, 2497–2511. doi:10.1016/S0278-4343(02)00077-8.

Ukkola, A. M., Prentice, I. C., Keenan, T. F., van Dijk, A. I. J. M., Viney, N. R., Myneni, R. B., et al. (2016). Reduced streamflow in water-stressed climates consistent with CO2 effects on vegetation. *Nat. Clim. Chang.* 6, 75–78. doi:10.1038/nclimate2831.

van der Sleen, P., Groenendijk, P., Vlam, M., Anten, N. P. R., Boom, A., Bongers, F., et al. (2015). No growth stimulation of tropical trees by 150 years of CO2 fertilization but water-use efficiency increased. *Nat. Geosci.* 8, 24–28. doi:10.1038/ngeo2313.

van der Werf, G. R., Randerson, J. T., Giglio, L., van Leeuwen, T. T., Chen, Y., Rogers, B. M., et al. (2017). Global fire emissions estimates during 1997–2016. *Earth Syst. Sci. Data* 9, 697–720. doi:10.5194/essd-9-697-2017.

van Gestel, N., Shi, Z., van Groenigen, K. J., Osenberg, C. W., Andresen, L. C., Dukes, J. S., et al. (2018). Predicting soil carbon loss with warming. *Nature* 554, E4–E5. doi:10.1038/nature25745.

van Groenigen, K. J., Osenberg, C. W., and Hungate, B. A. (2011). Increased soil emissions of potent greenhouse gases under increased atmospheric CO2. *Nature* 475, 214–216. doi:10.1038/nature10176.

van Groenigen, K. J., Osenberg, C. W., Terrer, C., Carrillo, Y., Dijkstra, F. A., Heath, J., et al. (2017). Faster turnover of new soil carbon inputs under increased atmospheric CO2. *Glob. Chang. Biol.* 23, 4420–4429. doi:10.1111/gcb.13752.

Vargas, C. A., Contreras, P. Y., Pérez, C. A., Sobarzo, M., Saldías, G. S., and Salisbury, J. (2016). Influences of riverine and upwelling waters on the coastal carbonate system off Central Chile and their ocean acidification implications. *J. Geophys. Res. Biogeosciences* 121, 1468–1483. doi:10.1002/2015JG003213.

Varney, R., Chadburn, S. E., Friedlingstein, P., Burke, E. J., Koven, C. D., Hugelius, G., et al. (submitted). A spatial emergent constraint on the sensitivity of soil carbon turnover time to global warming. *Nat. Clim. Chang.* (submitted).

Vaughan, N. E., and Gough, C. (2016). Expert assessment concludes negative emissions scenarios may not deliver. *Environ. Res. Lett.* 11, 095003. doi:10.1088/1748-9326/11/9/095003.

Vaughan, N. E., Gough, C., Mander, S., Littleton, E. W., Welfle, A., Gernaat, D. E. H. J., et al. (2018). Evaluating the use of biomass energy with carbon capture and storage in low emission scenarios. *Environ. Res. Lett.* 13, 044014. doi:10.1088/1748-9326/aaaa02.

Veldman, J. W., Overbeck, G. E., Negreiros, D., Mahy, G., Le Stradic, S., Fernandes, G. W., et al. (2015). Where tree planting and forest expansion are bad for biodiversity and ecosystem services. *Bioscience* 65, 1011–1018. doi:10.1093/biosci/biv118.

Veraverbeke, S., Rogers, B. M., Goulden, M. L., Jandt, R. R., Miller, C. E., Wiggins, E. B., et al. (2017). Lightning as a major driver of recent large fire years in North American boreal forests. *Nat. Clim. Chang.* doi:10.1038/nclimate3329.

Verheijen, F. G. A., Zhuravel, A., Silva, F. C., Amaro, A., Ben-Hur, M., and Keizer, J. J. (2019). The influence of biochar particle size and concentration on bulk density and maximum water holding capacity of sandy vs sandy loam soil in a column experiment. *Geoderma* 347, 194–202. doi:https://doi.org/10.1016/j.geoderma.2019.03.044.

Vichi, M., Navarra, A., and Fogli, P. G. (2013). Adjustment of the natural ocean carbon cycle to negative emission rates. *Clim. Change* 118, 105–118. doi:10.1007/s10584-012-0677-0.

Vitousek, P. M., Porder, S., Houlton, B. Z., and Chadwick, O. a (2010). Terrestrial phosphorus limitation: mechanisms, implications, and nitrogen–phosphorus interactions. *Ecol. Appl.* 20, 5–15. doi:10.1890/08-0127.1.

Voigt, C., Marushchak, M. E., Lamprecht, R. E., Jackowicz-Korczyński, M., Lindgren, A., Mastepanov, M., et al. (2017). Increased nitrous oxide emissions from Arctic peatlands after permafrost thaw. *Proc. Natl. Acad. Sci.* 114, 6238–6243. doi:10.1073/pnas.1702902114.

Volodin, E. M. (2008). Methane cycle in the INM RAS climate model. *Izv. Atmos. Ocean. Phys.* 44, 153–159. doi:10.1134/S0001433808020023.

Volodin, E. M. (2015). Influence of methane sources in Northern Hemisphere high latitudes on the interhemispheric asymmetry of its atmospheric concentration and climate. *Izv. Atmos. Ocean. Phys.* 51, 251–258. doi:10.1134/S0001433815030123.

Voss, M., Bange, H. W., Dippner, J. W., Middelburg, J. J., Montoya, J. P., and Ward, B. (2013). The marine nitrogen cycle: recent discoveries, uncertainties and the potential relevance of climate change. *Philos. Trans. R. Soc. B Biol. Sci.* 368, 20130121. doi:10.1098/rstb.2013.0121.

Wagner-Riddle, C., Congreves, K. A., Abalos, D., Berg, A. A., Brown, S. E., Ambadan, J. T., et al. (2017). Globally important nitrous oxide emissions from croplands induced by freeze–thaw cycles. *Nat. Geosci.* 10, 279–283. doi:10.1038/ngeo2907.

Wakita, M., Nagano, A., Fujiki, T., and Watanabe, S. (2017). Slow acidification of the winter mixed layer in the subarctic western North Pacific. *J. Geophys. Res. Ocean.* 122, 6923–6935. doi:10.1002/2017JC013002.

Walker, A. P., De Kauwe, M. G., Medlyn, B. E., Zaehle, S., Iversen, C. M., Asao, S., et al. (2019). Decadal biomass increment in early secondary succession woody ecosystems is increased by CO2 enrichment. *Nat. Commun.* 10, 454. doi:10.1038/s41467-019-08348-1.

Walker, A. P., Zaehle, S., Medlyn, B. E., De Kauwe, M. G., Asao, S., Hickler, T., et al. (2015). Predicting long-term carbon sequestration in response to CO2 enrichment: How and why do current ecosystem models differ? *Global Biogeochem. Cycles* 29, 476–495. doi:10.1002/2014GB004995.

Wallace, R. B., Baumann, H., Grear, J. S., Aller, R. C., and Gobler, C. J. (2014). Coastal ocean acidification: The other eutrophication problem. *Estuar. Coast. Shelf Sci.* 148, 1–13. doi:10.1016/j.ecss.2014.05.027.

Wallmann, K., Schneider, B., and Sarnthein, M. (2016). Effects of eustatic sea-level change, ocean dynamics, and nutrient utilization on atmospheric pCO2 and seawater composition over the last 130 000 years: a model study. *Clim. Past* 12, 339–375. doi:10.5194/cp-12-339-2016.

Wang, L., Huang, J., Luo, Y., and Zhao, Z. (2016a). Narrowing the spread in CMIP5 model projections of air-sea CO2 fluxes. *Sci. Rep.* 6, 37548. doi:10.1038/srep37548.

Wang, W., Ciais, P., Nemani, R. R., Canadell, J. G., Piao, S., Sitch, S., et al. (2013). Variations in atmospheric CO2 growth rates coupled with tropical temperature. *Proc. Natl. Acad. Sci.* 110, 13061–13066. doi:10.1073/pnas.1219683110.

Wang, X., Piao, S., Ciais, P., Friedlingstein, P., Myneni, R. B., Cox, P., et al. (2014). A two-fold increase of carbon cycle sensitivity to tropical temperature variations. *Nature* 506, 212–215. doi:10.1038/nature12915.

Wang, Y., Hendy, I., and Napier, T. J. (2017). Climate and anthropogenic controls of coastal deoxygenation on interannual to centennial timescales. *Geophys. Res. Lett.* 44, 11,528-11,536. doi:10.1002/2017GL075443.

Wang, Y. P., Jiang, J., Chen-Charpentier, B., Agusto, F. B., Hastings, A., Hoffman, F., et al. (2016b). Responses of two nonlinear microbial models to warming and increased carbon input. *Biogeosciences* 13, 887–902. doi:10.5194/bg-13-887-2016.

Wanninkhof, R., Doney, S. C., Bullister, J. L., Levine, N. M., Warner, M., and Gruber, N. (2010). Detecting anthropogenic CO2 changes in the interior Atlantic Ocean between 1989 and 2005. *J. Geophys. Res.* 115, C11028. doi:10.1029/2010JC006251.

Ward, N. D., Bianchi, T. S., Medeiros, P. M., Seidel, M., Richey, J. E., Keil, R. G., et al. (2017). Where carbon goes when water flows: carbon cycling across the aquatic continuum. *Front. Mar. Sci.* 4. doi:10.3389/fmars.2017.00007.

Wårlind, D., Smith, B., Hickler, T., and Arneth, A. (2014). Nitrogen feedbacks increase future terrestrial ecosystem carbon uptake in an individual-based dynamic vegetation model. *Biogeosciences* 11, 6131–6146. doi:10.5194/bg-11-6131-2014.

Webb, J. R., Hayes, N. M., Simpson, G. L., Leavitt, P. R., Baulch, H. M., and Finlay, K. (2019). Widespread nitrous oxide undersaturation in farm waterbodies creates an unexpected greenhouse gas sink. *Proc. Natl. Acad. Sci.*, 201820389. doi:10.1073/pnas.1820389116.

Wei, G., McCulloch, M. T., Mortimer, G., Deng, W., and Xie, L. (2009). Evidence for ocean acidification in the Great Barrier Reef of Australia. *Geochim. Cosmochim. Acta* 73, 2332–2346. doi:10.1016/j.gca.2009.02.009.

Wei, G., Wang, Z., Ke, T., Liu, Y., Deng, W., Chen, X., et al. (2015). Decadal variability in seawater pH in the West Pacific: Evidence from coral δ1 B records. *J. Geophys. Res. Ocean.* 120, 7166–7181. doi:10.1002/2015JC011066.

Welch, B., Gauci, V., and Sayer, E. J. (2019). Tree stem bases are sources of CH4 and N2O in a tropical forest on upland soil during the dry to wet season transition. *Glob. Chang. Biol.* 25, 361–372. doi:10.1111/gcb.14498.

Wenzel, S., Cox, P. M., Eyring, V., and Friedlingstein, P. (2014). Emergent constraints on climate-carbon cycle feedbacks in the CMIP5 Earth system models. *J. Geophys. Res. Biogeosciences* 119, 794–807. doi:10.1002/2013JG002591.

Wenzel, S., Cox, P. M., Eyring, V., and Friedlingstein, P. (2016). Projected land photosynthesis constrained by changes in the seasonal cycle of atmospheric CO2. *Nature* 538, 499–501. doi:10.1038/nature19772.

Werner, C., Butterbach-Bahl, K., Haas, E., Hickler, T., and Kiese, R. (2007). A global inventory of N2O emissions from tropical rainforest soils using a detailed biogeochemical model. *Global Biogeochem. Cycles* 21, GB3010. doi:10.1029/2006GB002909.

Wieder, W. R., Bonan, G. B., and Allison, S. D. (2013). Global soil carbon projections are improved by modelling microbial processes. *Nat. Clim. Chang.* 3, 909–912. doi:10.1038/nclimate1951.

Wieder, W. R., Cleveland, C. C., Smith, W. K., and Todd-Brown, K. (2015). Future productivity and carbon storage limited by terrestrial nutrient availability. *Nat. Geosci.* 8, 441–444. doi:10.1038/ngeo2413.

Wieder, W. R., Hartman, M. D., Sulman, B. N., Wang, Y.-P., Koven, C. D., and Bonan, G. B. (2018). Carbon cycle confidence and uncertainty: Exploring variation among soil biogeochemical models. *Glob. Chang. Biol.* 24, 1563–1579. doi:10.1111/gcb.13979.

Wieder, W. R., Lawrence, D. M., Fisher, R. A., Bonan, G. B., Cheng, S. J., Goodale, C. L., et al. (2019). Beyond static benchmarking: using experimental manipulations to evaluate land model assumptions. *Global Biogeochem. Cycles* 33, 1289–1309. doi:10.1029/2018GB006141.

Wiesen, P., Kleffmann, J., Kurtenbach, R., and Becker, K. H. (1994). Nitrous oxide and methane emissions from aero engines. *Geophys. Res. Lett.* 21, 2027–2030. doi:10.1029/94GL01709.

Wiesen, P., Kleffmann, J., Kurtenbach, R., and Becker, K. H. (1996). Emission of nitrous oxide and methane from aero engines: monitoring by tunable diode laser spectroscopy. *Infrared Phys. Technol.* 37, 75–81. doi:10.1016/S1350-4495(97)80763-3.

Wik, M., Thornton, B. F., Bastviken, D., Uhlbäck, J., and Crill, P. M. (2016a). Biased sampling of methane release from northern lakes: A problem for extrapolation. *Geophys. Res. Lett.* 43, 1256–1262. doi:10.1002/2015GL066501.

Wik, M., Varner, R. K., Anthony, K. W., MacIntyre, S., and Bastviken, D. (2016b). Climate-sensitive northern lakes and ponds are critical components of methane release. *Nat. Geosci.* 9, 99–105. doi:10.1038/ngeo2578.

Wilhelm, W. W., Johnson, J. M. F., Hatfield, J. L., Voorhees, W. B., and Linden, D. R. (2004). Crop and Soil Productivity Response to Corn Residue Removal. *Agron. J.* 96, 1–17. doi:10.2134/agronj2004.1000.

Williams, N. L., Feely, R. A., Sabine, C. L., Dickson, A. G., Swift, J. H., Talley, L. D., et al. (2015). Quantifying anthropogenic carbon inventory changes in the Pacific sector of the Southern Ocean. *Mar. Chem.* 174, 147–160. doi:10.1016/j.marchem.2015.06.015.

Williams, N. L., Juranek, L. W., Feely, R. A., Johnson, K. S., Sarmiento, J. L., Talley, L. D., et al. (2017a). Calculating surface ocean pCO2 from biogeochemical Argo floats equipped with pH: An uncertainty analysis. *Global Biogeochem. Cycles* 31, 591–604. doi:10.1002/2016GB005541.

Williams, R. G., Goodwin, P., Roussenov, V. M., and Bopp, L. (2016). A framework to understand the transient climate response to emissions. *Environ. Res. Lett.* 11, 015003. doi:10.1088/1748-9326/11/1/015003.

Williams, R. G., Roussenov, V., Frölicher, T. L., and Goodwin, P. (2017b). Drivers of continued surface warming after cessation of carbon emissions. *Geophys. Res. Lett.* 44, 10,633-10,642. doi:10.1002/2017GL075080.

Williams, R. G., Roussenov, V., Frölicher, T. L., and Goodwin, P. (2017c). Drivers of Continued Surface Warming After Cessation of Carbon Emissions. *Geophys. Res. Lett.* 44, 10,633-10,642. doi:10.1002/2017GL075080.

Williams, R. G., Roussenov, V., Goodwin, P., Resplandy, L., Bopp, L., Williams, R. G., et al. (2017d). Sensitivity of global warming to carbon emissions: effects of heat and carbon uptake in a suite of Earth System Models. *J. Clim.* 30, 9343–9363. doi:10.1175/JCLI-D-16-0468.1.

Williams, R. G., Roussenov, V., Goodwin, P., Resplandy, L., Bopp, L., Williams, R. G., et al. (2017e). Sensitivity of Global Warming to Carbon Emissions: Effects of Heat and Carbon Uptake in a Suite of Earth System Models. *J. Clim.* 30, 9343–9363. doi:10.1175/JCLI-D-16-0468.1.

Williams, R., Katavouta, A., and Goodwin, P. (2019). Carbon-cycle feedbacks operating in the climate system. *Curr. Clim. Chang. Reports*. doi:10.1007/s40641-019-00144-9.

Williamson, P., & Bodle, R. (2016). Update on climate geoengineering in relation to the convention on biological diversity: potential impacts and regulatory framework. Montreal.

Williamson, P., Wallace, D. W. R., Law, C. S., Boyd, P. W., Collos, Y., Croot, P., et al. (2012a). Ocean fertilization for geoengineering: A review of effectiveness, environmental impacts and emerging governance. *Process Saf. Environ. Prot.* 90, 475–488. doi:10.1016/j.psep.2012.10.007.

Williamson, P., Wallace, D. W. R., Law, C. S., Boyd, P. W., Collos, Y., Croot, P., et al. (2012b). Ocean fertilization for geoengineering: A review of effectiveness, environmental impacts and emerging governance. *Process Saf. Environ. Prot.* 90, 475–488. doi:10.1016/j.psep.2012.10.007.

Wilson, D., Blain, D., Couwenberg, J., Evans, C.D., Murdiyarso, D., Page, S.E., Renou-Wilson, F., Rieley, J.O., Sirin, A., Strack, M. & Tuittila, E.-S. (2016). Greenhouse gas emission factors associated with rewetting of organic soils. *Mires Peat* 17, 1–28. doi:10.19189/MaP.2016.OMB.222.

Windham-Myers, L., Crooks, S., and Troxler, T. (2018). *A Blue Carbon Primer: The State of Coastal Wetland Carbon Science, Practice and Policy*. Taylor & Francis Group/CRC Press.

Winguth, A. M. E., Thomas, E., and Winguth, C. (2012). Global decline in ocean ventilation, oxygenation, and productivity during the Paleocene-Eocene Thermal Maximum: Implications for the benthic extinction. *Geology* 40, 263–266. doi:10.1130/G32529.1.

Winiwarter, W., Höglund-Isaksson, L., Klimont, Z., Schöpp, W., and Amann, M. (2018). Technical opportunities to reduce global anthropogenic emissions of nitrous oxide. *Environ. Res. Lett.* 13, 014011. doi:10.1088/1748-9326/aa9ec9.

Winkler, A. J., Myneni, R. B., Alexandrov, G. A., and Brovkin, V. (2019). Earth system models underestimate carbon fixation by plants in the high latitudes. *Nat. Commun.* 10, 885. doi:10.1038/s41467-019-08633-z.

Wolf, J., Asrar, G. R., and West, T. O. (2017). Revised methane emissions factors and spatially distributed annual carbon fluxes for global livestock. *Carbon Balance Manag.* 12, 16. doi:10.1186/s13021-017-0084-y.

Wolter, K., and Timlin, M. S. (1998). Measuring the strength of ENSO events: How does 1997/98 rank? *Weather* 53, 315–324. doi:10.1002/j.1477-8696.1998.tb06408.x.

Woolf, D., Amonette, J. E., Street-Perrott, F. A., Lehmann, J., and Joseph, S. (2010). Sustainable biochar to mitigate global climate change. *Nat. Commun.* 1, 56. doi:10.1038/ncomms1053.

Woosley, R. J., Millero, F. J., and Wanninkhof, R. (2016). Rapid anthropogenic changes in CO2 and pH in the Atlantic Ocean: 2003-2014. *Global Biogeochem. Cycles* 30, 70–90. doi:10.1002/2015GB005248.

Worden, J. R., Bloom, A. A., Pandey, S., Jiang, Z., Worden, H. M., Walker, T. W., et al. (2017). Reduced biomass burning emissions reconcile conflicting estimates of the post-2006 atmospheric methane budget. *Nat. Commun.* 8, 2227. doi:10.1038/s41467-017-02246-0.

Wu, H. C., Dissard, D., Douville, E., Blamart, D., Bordier, L., Tribollet, A., et al. (2018). Surface ocean pH variations since 1689 CE and recent ocean acidification in the tropical South Pacific. *Nat. Commun.* 9, 2543. doi:10.1038/s41467-018-04922-1.

Xia, L., Nowack, P. J., Tilmes, S., and Robock, A. (2017). Impacts of stratospheric sulfate geoengineering on tropospheric ozone. *Atmos. Chem. Phys.* 17, 11913–11928. doi:10.5194/acp-17-11913-2017.

Xia, L., Robock, A., Cole, J., Curry, C. L., Ji, D., Jones, A., et al. (2014). Solar radiation management impacts on agriculture in China: A case study in the Geoengineering Model Intercomparison Project (GeoMIP). *J. Geophys. Res. Atmos.* 119, 8695–8711. doi:10.1002/2013JD020630.

Xia, L., Robock, A., Tilmes, S., and Neely III, R. R. (2016). Stratospheric sulfate geoengineering could enhance the terrestrial photosynthesis rate. *Atmos. Chem. Phys.* 16, 1479–1489. doi:10.5194/acp-16-1479-2016.

Xu-Ri, Prentice, I. C., Spahni, R., and Niu, H. S. (2012). Modelling terrestrial nitrous oxide emissions and implications for climate feedback. *New Phytol.* 196, 472–488. doi:10.1111/j.1469-8137.2012.04269.x.

Yamamoto-Kawai, M., McLaughlin, F. A., Carmack, E. C., Nishino, S., and Shimada, K. (2009). Aragonite undersaturation in the Arctic ocean: effects of ocean acidification and sea ice melt. *Science* 326, 1098–1100. doi:10.1126/science.1174190.

Yamamoto, A., Abe-Ouchi, A., Ohgaito, R., Ito, A., and Oka, A. (2019). Glacial CO2 decrease and deep-water deoxygenation by iron fertilization from glaciogenic dust. *Clim. Past* 15, 981–996. doi:10.5194/cp-15-981-2019.

Yamamoto, A., Abe-Ouchi, A., and Yamanaka, Y. (2018). Long-term response of oceanic carbon uptake to global warming via physical and biological pumps. *Biogeosciences* 15, 4163–4180. doi:10.5194/bg-15-4163-2018.

Yang, G., Peng, Y., Marushchak, M. E., Chen, Y., Wang, G., Li, F., et al. (2018). Magnitude and pathways of increased nitrous oxide emissions from uplands following permafrost thaw. *Environ. Sci. Technol.* 52, 9162–9169. doi:10.1021/acs.est.8b02271.

Yang, H., Dobbie, S., Ramirez-Villegas, J., Feng, K., Challinor, A. J., Chen, B., et al. (2016). Potential negative consequences of geoengineering on crop production: A study of Indian groundnut. *Geophys. Res. Lett.* 43, 11,711-786,795. doi:10.1002/2016GL071209.

Yao, W., Paytan, A., and Wortmann, U. G. (2018). Large-scale ocean deoxygenation during the Paleocene-Eocene Thermal Maximum. *Science* 361, 804–806. doi:10.1126/science.aar8658.

Yeager, S. G., Danabasoglu, G., Rosenbloom, N. A., Strand, W., Bates, S. C., Meehl, G. A., et al. (2018). Predicting near-term changes in the Earth system: a large ensemble of initialized decadal prediction simulations using the community Earth system model. *Bull. Am. Meteorol. Soc.* 99, 1867–1886. doi:10.1175/BAMS-D-17-0098.1.

Yousefpour, R., Nabel, J. E. M. S., and Pongratz, J. (2019). Simulating growth-based harvest adaptive to future climate change. *Biogeosciences* 16, 241–254. doi:10.5194/bg-16-241-2019.

Yu, J., Broecker, W. S., Elderfield, H., Jin, Z., McManus, J., and Zhang, F. (2010a). Loss of carbon from the Deep Sea since the last glacial maximum. *Science* 330, 1084–1087. doi:10.1126/science.1193221.

Yu, L., Huang, Y., Sun, F., and Sun, W. (2017). A synthesis of soil carbon and nitrogen recovery after wetland restoration and creation in the United States. *Sci. Rep.* 7, 7966. doi:10.1038/s41598-017-08511-y.

Yu, Z., Loisel, J., Brosseau, D. P., Beilman, D. W., and Hunt, S. J. (2010b). Global peatland dynamics since the Last Glacial Maximum. *Geophys. Res. Lett.* 37, LI3402. doi:10.1029/2010GL043584.

Yue, X., and Unger, N. (2018). Fire air pollution reduces global terrestrial productivity. *Nat. Commun.* doi:10.1038/s41467-018-07921-4.

Zachos, J. C. (2005). Rapid acidification of the ocean during the Paleocene-Eocene Thermal Maximum. *Science* 308, 1611–1615. doi:10.1126/science.1109004.

Zaehle, S. (2013). Terrestrial nitrogen-carbon cycle interactions at the global scale. *Philos. Trans. R. Soc. B Biol. Sci.* 368, 20130125–20130125. doi:10.1098/rstb.2013.0125.

Zaehle, S., Ciais, P., Friend, A. D., and Prieur, V. (2011). Carbon benefits of anthropogenic reactive nitrogen offset by nitrous oxide emissions. *Nat. Geosci.* 4, 601–605. doi:10.1038/ngeo1207.

Zaehle, S., Friedlingstein, P., and Friend, A. D. (2010). Terrestrial nitrogen feedbacks may accelerate future climate change. *Geophys. Res. Lett.* 37, L01401. doi:10.1029/2009GL041345.

Zaehle, S., Jones, C. D., Houlton, B., Lamarque, J.-F., and Robertson, E. (2015). Nitrogen availability reduces CMIP5 projections of twenty-first-century land carbon uptake*. *J. Clim.* 28, 2494–2511. doi:10.1175/JCLI-D-13-00776.1.

Zaehle, S., Medlyn, B. E., De Kauwe, M. G., Walker, A. P., Dietze, M. C., Hickler, T., et al. (2014). Evaluation of 11 terrestrial carbon-nitrogen cycle models against observations from two temperate free-air CO2 Enrichment studies. *New Phytol.* 202, 803–822. doi:10.1111/nph.12697.

Zamora, L. M., Oschlies, A., Bange, H. W., Huebert, K. B., Craig, J. D., Kock, A., et al. (2012). Nitrous oxide dynamics in low oxygen regions of the Pacific: insights from the MEMENTO database. *Biogeosciences* 9, 5007–5022. doi:10.5194/bg-9-5007-2012.

Zeebe, R. E. (2013). What caused the long duration of the Paleocene-Eocene Thermal Maximum? *Paleoceanography* 28, 440–452. doi:10.1002/palo.20039.

Zeebe, R. E., Ridgwell, A., and Zachos, J. C. (2016). Anthropogenic carbon release rate unprecedented during the past 66 million years. *Nat. Geosci.* 9, 325–329. doi:10.1038/ngeo2681.

Zeebe, R. E., and Zachos, J. C. (2013). Long-term legacy of massive carbon input to the Earth system: Anthropocene versus Eocene. *Philos. Trans. R. Soc. A Math. Phys. Eng. Sci.* 371, 20120006–20120006. doi:10.1098/rsta.2012.0006.

Zeebe, R. E., Zachos, J. C., and Dickens, G. R. (2009). Carbon dioxide forcing alone insufficient to explain Paleocene–Eocene Thermal Maximum warming. *Nat. Geosci.* 2, 576–580. doi:10.1038/ngeo578.

Zemp, D. C., Schleussner, C.-F., Barbosa, H. M. J., Hirota, M., Montade, V., Sampaio, G., et al. (2017). Self-amplified Amazon forest loss due to vegetation-atmosphere feedbacks. *Nat. Commun.* 8, 14681. doi:10.1038/ncomms14681.

Zeng, J., Nojiri, Y., Nakaoka, S., Nakajima, H., and Shirai, T. (2015). Surface ocean CO2 in 1990-2011 modelled using a feed-forward neural network. *Geosci. Data J.* 2, 47–51. doi:10.1002/gdj3.26.

Zeng, N., Yoon, J.-H., Vintzileos, A., Collatz, G. J., Kalnay, E., Mariotti, A., et al. (2008). Dynamical prediction of terrestrial ecosystems and the global carbon cycle: A 25-year hindcast experiment. *Global Biogeochem. Cycles* 22, n/a-n/a. doi:10.1029/2008GB003183.

Zhang, H., and Cao, L. (2016). Simulated effect of calcification feedback on atmospheric CO2 and ocean acidification. *Sci. Rep.* 6, 20284. doi:10.1038/srep20284.

Zhang, Q., Wang, Y. P., Matear, R. J., Pitman, A. J., and Dai, Y. J. (2014). Nitrogen and phosphorous limitations significantly reduce future allowable CO2 emissions. *Geophys. Res. Lett.* 41, 632–637. doi:10.1002/2013GL058352.

Zhang, W., Miller, P. A., Smith, B., Wania, R., Koenigk, T., and Döscher, R. (2013a). Tundra shrubification and tree-line advance amplify arctic climate warming: results from an individual-based dynamic vegetation model. *Environ. Res. Lett.* 8, 34023. doi:10.1088/1748-9326/8/3/034023.

Zhang, X., Wang, Y.-P., Peng, S., Rayner, P. J., Ciais, P., Silver, J. D., et al. (2018a). Dominant regions and drivers of the variability of the global land carbon sink across timescales. *Glob. Chang. Biol.* 24, 3954–3968. doi:10.1111/gcb.14275.

Zhang, Y. G., Pagani, M., Liu, Z., Bohaty, S. M., and DeConto, R. (2013b). A 40-million-year history of atmospheric CO2. *Philos. Trans. R. Soc. A Math. Phys. Eng. Sci.* 371, 20130096–20130096. doi:10.1098/rsta.2013.0096.

Zhang, Y., Hu, X., Zou, J., Zhang, D., Chen, W., Liu, Y., et al. (2018b). Response of surface albedo and soil carbon dioxide fluxes to biochar amendment in farmland. *J. Soils Sediments* 18, 1590–1601. doi:10.1007/s11368-017-1889-8.

Zhang, Z., Zimmermann, N. E., Calle, L., Hurtt, G., Chatterjee, A., and Poulter, B. (2018c). Enhanced response of global wetland methane emissions to the 2015–2016 El Niño-Southern Oscillation event. *Environ. Res. Lett.* 13, 074009. doi:10.1088/1748-9326/aac939.

Zhang, Z., Zimmermann, N. E., Stenke, A., Li, X., Hodson, E. L., Zhu, G., et al. (2017). Emerging role of wetland methane emissions in driving 21st century climate change. *Proc. Natl. Acad. Sci.* 114, 9647–9652. doi:10.1073/pnas.1618765114.

Zhao, M., and Running, S. W. (2010). Drought-induced reduction in global terrestrial net primary production from 2000 through 2009. *Science* 329, 940–943. doi:10.1126/science.1192666.

Zhao, Y., Saunois, M., Bousquet, P., Lin, X., Hegglin, M. I., Canadell, J. G., et al. (2019). Inter-model comparison of global hydroxyl radical (OH) distributions and their impact on atmospheric methane over the 2000-2016 period. *Atmos. Chem. Phys. Discuss.* 2019, 1–47. doi:10.5194/acp-2019-281.

Zheng, Y., Fang, Z., Fan, T., Liu, Z., Wang, Z., Li, Q., et al. (2019). Operation of the boreal peatland methane cycle across the past 16 k.y. *Geology*. doi:10.1130/G46709.1.

Zhou, F., Shang, Z., Zeng, Z., Piao, S., Ciais, P., Raymond, P. A., et al. (2015). New model for capturing the variations of fertilizer-induced emission factors of N 2 O. *Global Biogeochem. Cycles* 29, 885–897. doi:10.1002/2014GB005046.

Zhou, X., Thomas, E., Rickaby, R. E. M., Winguth, A. M. E., and Lu, Z. (2014). I/Ca evidence for upper ocean deoxygenation during the PETM. *Paleoceanography* 29, 964–975. doi:10.1002/2014PA002702.

Zhu, Z., Piao, S., Myneni, R. B., Huang, M., Zeng, Z., Canadell, J. G., et al. (2016). Greening of the Earth and its drivers. *Nat. Clim. Chang.* 6, 791–795. doi:10.1038/nclimate3004.

Zickfeld, K., Azevedo, D., and Matthews, H. D. (submitted). Asymmetry in the climate-carbon cycle response to positive and negative CO2 emissions. (submitted).

Zickfeld, K., Eby, M., Matthews, H. D., and Weaver, A. J. (2009). Setting cumulative emissions targets to reduce the risk of dangerous climate change. *Proc. Natl. Acad. Sci.* 106, 16129–16134. doi:10.1073/pnas.0805800106.

Zickfeld, K., Eby, M., Weaver, A. J., Alexander, K., Crespin, E., Edwards, N. R., et al. (2013). Long-term climate change commitment and reversibility: An EMIC intercomparison. *J. Clim.* 26, 5782–5809. doi:10.1175/JCLI-D-12-00584.1.

Zickfeld, K., and Herrington, T. (2015). The time lag between a carbon dioxide emission and maximum warming increases with the size of the emission. *Environ. Res. Lett.* 10, 031001. doi:10.1088/1748-9326/10/3/031001.

Zickfeld, K., MacDougall, A. H., and Matthews, H. D. (2016). On the proportionality between global temperature change and cumulative CO2 emissions during periods of net negative CO2 emissions. *Environ. Res. Lett.* 11, 055006. doi:10.1088/1748-9326/11/5/055006.

Ziegler, M., Diz, P., Hall, I. R., and Zahn, R. (2013). Millennial-scale changes in atmospheric CO2 levels linked to the Southern Ocean carbon isotope gradient and dust flux. *Nat. Geosci.* 6, 457–461. doi:10.1038/ngeo1782.

5.A Appendix Chapter 5

5.A.1 [Placeholder: Display to be updated, and reference link to be created.]

Summary of the mean air-sea CO2 flux (PgC yr-1) integrated over the global oceans (negative to the ocean)

	Mean	1σ	90% C.I.	Mean	1σ	90% C.I.	Mean	1σ	90% C.I.	Mean	1σ	90% C.I.	Mean	1σ	90% C.I.	Mean	1σ	90% C.I.	
	1990-1999			1994-2007			2000-2009			2005-2014			2007-2016			2009-2018			Data source
Global Ocean BGC Models	**-1.95**	**±0.29**	**±0.48**	**-2.05**	**±0.28**	**±0.47**	**-2.17**	**±0.29**	**±0.48**	**-2.37**	**±0.31**	**±0.52**	**-2.45**	**±0.32**	**±0.52**	**-2.51**	**±0.33**	**±0.54**	
CESM-ETH	-1.73	±0.16		-1.80	±0.23		-1.90	±0.22		-2.06	±0.08		-2.13	±0.16		-2.18	±0.14		Global Carbon Budget 2019 v1.0
CSIRO	-2.41	±0.17		-2.52	±0.26		-2.66	±0.26		-2.95	±0.16		-3.04	±0.19		-3.13	±0.18		Global Carbon Budget 2019 v1.0
MITgcm-REcoM2	-1.93	±0.12		-2.07	±0.18		-2.18	±0.20		-2.38	±0.14		-2.46	±0.15		-2.52	±0.19		Global Carbon Budget 2019 v1.0
MPIOM-HAMOCC	-1.67	±0.11		-1.80	±0.20		-1.94	±0.17		-2.11	±0.18		-2.17	±0.17		-2.23	±0.16		Global Carbon Budget 2019 v1.0
NEMO-PISCES (CNRM)	-1.82	±0.16		-1.81	±0.13		-1.88	±0.17		-2.11	±0.18		-2.24	±0.19		-2.31	±0.14		Global Carbon Budget 2019 v1.0
NEMO-PlankTOM5	-2.17	±0.18		-2.17	±0.20		-2.24	±0.20		-2.51	±0.17		-2.59	±0.15		-2.64	±0.13		Global Carbon Budget 2019 v1.0
NorESM-OC	-2.39	±0.12		-2.48	±0.17		-2.61	±0.14		-2.77	±0.14		-2.85	±0.18		-2.91	±0.17		Global Carbon Budget 2019 v1.0
MOM6-COBALT (Princeton)	-1.74	±0.14		-1.86	±0.24		-1.98	±0.26		-2.21	±0.11		-2.28	±0.15		-2.35	±0.14		Global Carbon Budget 2019 v1.0
NEMO-PISCES (IPSL)	-1.74	±0.13		-1.97	±0.17		-2.11	±0.09		-2.25	±0.09		-2.32	±0.13		-2.34	±0.12		Global Carbon Budget 2019 v1.0
pCO2_Observation-Based Empirical Models	**-1.37**	**±0.16**	**±0.26**	**-1.35**	**±0.16**	**±0.26**	**-1.44**	**±0.19**	**±0.31**	**-1.70**	**±0.21**	**±0.35**	**-1.81**	**±0.22**	**±0.36**				
MPI_SOMFFN (Landschützer et al., 2014)	-1.17	±0.23		-1.11	±0.24		-1.25	±0.33		-1.63	±0.17		-1.74	0.147					From L. Gregor on 20191206
JENA_MLS (Rödenbeck et al., 2014)	-1.36	±0.30		-1.21	±0.25		-1.24	±0.28		-1.43	±0.22		-1.53	0.251					From L. Gregor on 20191206
CMEMS_FFNN (Denvil-Sommer et al., 2019)	-1.19	±0.06		-1.23	±0.13		-1.30	±0.15		-1.50	±0.12		-1.62	0.203					
JMA_MLR (Iida et al., 2015)	-1.56	±0.18		-1.41	±0.13		-1.41	±0.15		-1.57	±0.14		-1.70	0.275					From L. Gregor on 20191206
NIES_NN (Zeng et al., 2014)	-1.39	±0.09		-1.49	±0.22		-1.69	±0.27		-1.92	±0.13		-1.97	0.117					From L. Gregor on 20191206
UEA_SI (Jones et al. 2015)	-1.56	±0.14		-1.54	±0.16		-1.66	±0.19		-1.96	±0.18		-2.12	0.293					From L. Gregor on 20191206
CSIR_ML6 (Gregor et al., 2019)	-1.34	±0.10		-1.42	±0.18		-1.54	±0.22		-1.86	±0.20		-2.01	0.268					From L. Gregor on 20191206
Atmospheric CO2 and O2/N2	**-1.94**	**±0.62**	**±1.02**				**-2.52**	**±0.57**	**±0.94**				**-2.60**	**±0.57**	**±0.94**				
Keeling and Manning, 2014	-1.94	±0.62					-2.72	±0.60											Description in the paper
Tohjima et al., 2019							-2.31	±0.97					-2.60	±0.57					Figure in the paper (numerical values from PI)
Ocean Carbon Inversion Model	**-1.25**	**±0.32**	**±0.53**				**-2.41**	**±0.12**	**±0.20**										
DeVries et al. 2017	-1.25	±0.32					-2.41	±0.12											Description in the paper
Ocean Carbon Inventory Change				**-2.23**	**±0.19**	**±0.31**													
Gruber et al., 2019				-2.23	±0.19														Accounted for loss of nat. ocean CO2 (-0.38 +/- 0.115 PgC yr-1)
				-2.62	±0.15														Anthropogenic carbon inventory change
Atmospheric CO2 Inversions							**-1.61**	**±0.13**	**±0.22**				**-1.98**	**±0.29**	**±0.48**				
Chevallier et al., 2005 (CAMS)							-1.62	±0.24					-2.13	±0.22					from Prabir on 20190913
Rödenbeck et al., 2003 (Jena)							-1.74	±0.34					-2.16	±0.31					from Naveen on 20191201
Saeki and Patra, 2017 (MIROC)							-1.48	±0.35					-1.65	±0.18					from Naveen on 20191129

Method	Earth system feedbacks on CO_2 sequestration potential and temperature	Biogeochemical and biophysical effects	Side effects on water quantity and quality, food supply, biodiversity (BD)
Afforestation, reforestation and forest management	Weakens ocean C sequestration through decreased [CO_2] (Keller et al. 2018; Sonntag et al., 2018); decrease in albedo due to afforestation weakens the effect of CO_2 removal on surface air temperature (Sonntag et al. 2018); may shift the location of the Intertropical Convergence Zone and hence precipitation in the monsoon regions (Devaraju et al., 2015)	VOC emissions** (Krause et al., 2017), decreased and increased surface temperature, in tropics and boreal region, respectively, due to changes in reflectivity, evapotranspiration and surface roughness*** (Fuss et al., 2018; Griscom et al., 2017; Pongratz et al., 2010; Jackson et al., 2008; Bright et al., 2015; Devaraju et al., 2015)	Threatened water supply in dry areas (Farley et al., 2005; (Mengis et al., 2019)**; affects food supply through competition for land (Smith et al., 2018)***; decreased BD if not adopted wisely*, increased BD if monocultures are replaced by native species** (Smith et al., 2018; Williamson & Bodle, 2016)
Soil carbon sequestration	Weakens ocean C sequestration through decreased [CO_2] (Keller et al. 2018)	Decreased N_2O emissions, depending on fertilization, land-use, use of cover crops* (Smith et al., 2016; Gu et al., 2017)	Reduced nutrient losses**, increased biological activity** (Fornara et al., 2011; Paustian et al., 2016; Tonitto et al., 2006; (Fuss et al., 2018b; Smith, 2016), improved soil water holding capacity**(Paustian et al., 2019), no impact or increased BD, depending on method** (Paustian et al., 2016; Smith et al., 2018)
Biochar	Weakens ocean C sequestration through decreased [CO_2] (Keller et al. 2018)	Reduced N_2O emissions* (Cayuela et al., 2014; Kammann, C., 2017), local warming related to darkened surface* (Genesio et al., 2012; Zhang et al., 2018b)	Improved soil fertility and productivity**, reduced nutrient losses**, enhanced fertilizer N use efficiency* (Clough et al., 2013; Liu et al., 2017; Shen et al., 2016, Woolf et al., 2010); improved soil water holding capacity** (Karhu et al., 2011; Verheijen et al., 2019; C. Liu et al., 2016), decreased BD* (Smith et al., 2018b)
BECCS	Weakens ocean C sequestration through decreased [CO_2] (Keller et al. 2018)	Increased N_2O emissions related to land-use or if fertilized* (Creutzig et al., 2015; Smith et al., 2016); local warming due to decreased albedo depending on the type of bioenergy crop* (Smith et al., 2016); VOC emissions (Krause et al., 2017)	Threatened water supply** (Farley et al., 2005; Smith et al., 2016); competition for land*** (Smith et al., 2019); soil nutrient deficiency; decreased BD** (Smith et al., 2018b); see DACCS for storage-related side effects
Wetland restoration		Enhanced CH_4 emission*** (Wilson et al., 2016; Renou-Wilson et al., 2019)	Increased nutrient infiltration and retention to increase water quality** (Daneshvar et al., 2017; Kluber et al., 2014; Lundin et al., 2017); protection from fire, increased BD*** (Meli et al., 2014; Smith et al., 2018)
Ocean fertilisation	Decreased productivity in unfertilised regions** (Oschlies, 2010); carbonate counter pump could decrease C sequestration* (Salter et al., 2014)	Enhanced ocean acidification**; Increased suboxic zone extent in fertilised areas**; Shrinkage of suboxic zones outside fertilised areas* (Keller et al., 2014); Increased production of	Perturbation to marine ecosystems via reorganisation of community structure, including possibly toxic algal blooms** (Oschlies et al., 2010a; Williamson et al., 2012b)

		N2O* (Jin and Gruber, 2003)	
Artificial ocean upwelling	Cooling effect**; increases terrestrial C storage** (Oschlies et al., 2010b; Keller et al., 2014)	Enhanced ocean acidification**; Increased suboxic zone extent in fertilised areas**; Alters ocean temperature, salinity, circulation***; Alters Earth's heat and water budget** (Keller et al., 2014)	Perturbation to marine ecosystems via reorganisation of community structure, including possibly toxic algal blooms** (Oschlies et al., 2010a; Williamson et al., 2012b)
Restoration of vegetated coastal ecosystems ('blue carbon')		Emission of CH_4 and N_2O, and biogenic calcification may partly offset benefits* (Rosentreter et al., 2018; Keller, 2019; Kennedy et al., 2019)	Provision of very wide range of ecosystem services (biodiversity support ; recreation and tourism; fishery habitats; improved water quality, and flood and erosion protection)*** (Bindoff et al. 2019)
Enhanced weathering - terrestrial	Will initially reduce the ocean CO_2 sequestration, but after enough weathering products are transported into ocean to increase alkalinity, will increase ocean CO_2 sequestration (Keller et al., 2018a)	.	Soil fertilisation and stimulated biological production*** (Hartmann et al., 2013); can liberate toxic trace metals into soil or water bodies** (Keller et al., 2018a); can decrease drinking water quality by causing freshwater salinization** (Kaushal et al., 2018); increases alkalinity and pH of natural waters, helps dampen ocean acidification, increases ocean carbon uptake** (Beerling et al., 2018); decreased or increased BD* (Smith et al., 2018b)
Ocean alkalinisation	Enhanced primary production through addition of iron and silicic acid from olivine dissolution* (Köhler et al., 2013) (Hauck et al., 2016); Lowers terrestrial carbon storage** (González and Ilyina, 2016(Sonntag et al., 2018))	Decreased ocean acidification (surface waters only)**; Decreased de-oxygenation* (González, 2016)	Release of toxic trace metals from deposited minerals* (Hartmann et al., 2013) Perturbation to marine ecosystems via reorganisation of community structure** (González and Ilyina, 2016; González et al., 2018)
Direct air carbon capture and storage (DACCS)			Pollution of drinking water; seismic activity (Fuss et al., 2018); Perturbation of marine ecosystems through leakage of CO_2 from submarine storage (Molari et al., 2018)

Figures

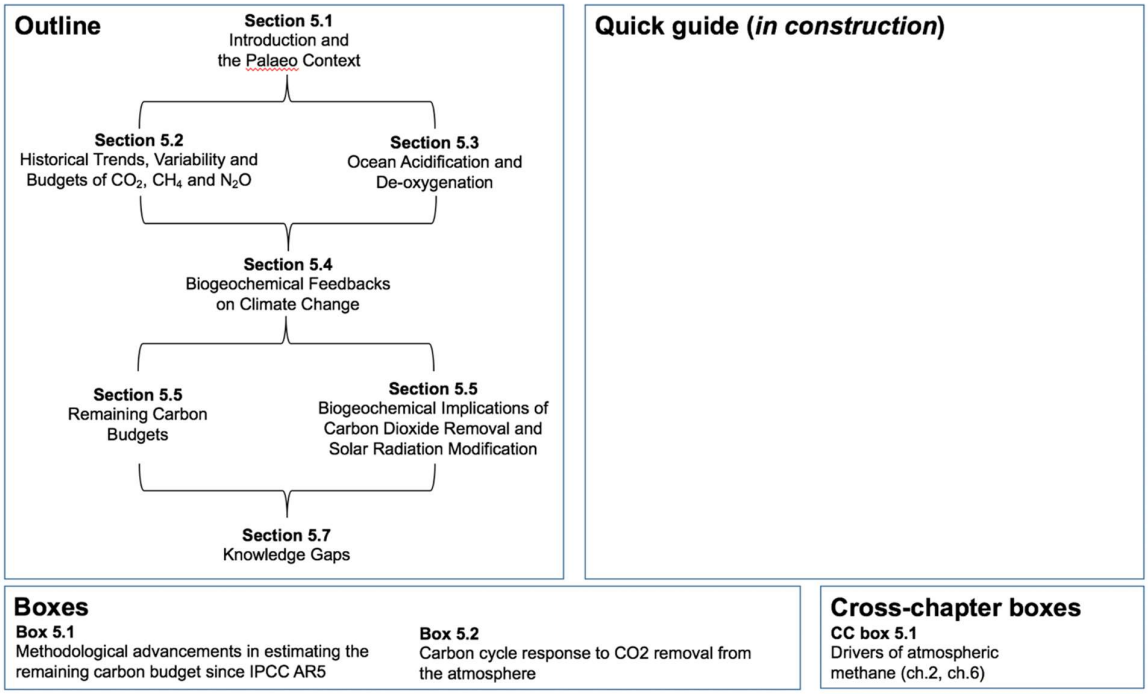

Figure 5.0: Chapter overview figure. [Placeholder: This Figure numbering will be changed to 5.1 for the FGD]

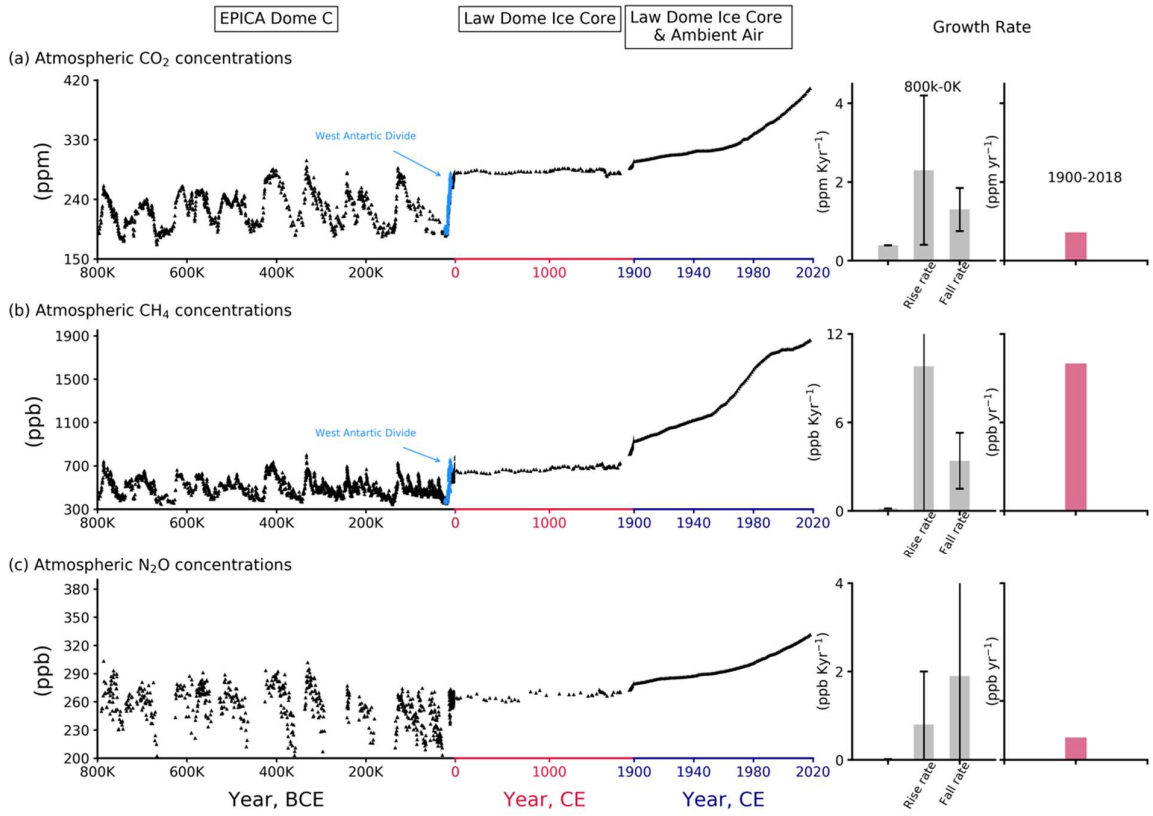

Figure 5.1: Atmospheric concentrations of CO_2, CH_4 and N_2O in air bubbles and clathrate crystals in ice cores, dated period from 800,000 BCE to 1990 CE (note the variable x-axis range and tick mark intervals for the 3 columns). Ice core data is over-plotted by atmospheric observations from 1958 to present for CO_2, from 1984 for CH_4 and from 1994 for N_2O. The linear growth rates for different time periods (800,000–0 BCE, 0–1900 CE and 1900–2017 CE) are given in each panel. For the BCE period, mean rise and fall rates are calculated for the individual slopes between the peaks and troughs, which are given in the panels in left column. The data for BCE period are used from the Vostok, EPICA, Dome C and WAIS ice cores (Petit et al., 1999; Monnin, 2001; Pépin et al., 2001; Raynaud et al., 2005; Siegenthaler et al., 2005; Loulergue et al., 2008; Lüthi et al., 2008; Schilt et al., 2010a). The data after 0–yr CE are taken mainly from Law Dome ice core analysis (MacFarling Meure et al., 2006). The surface observations for all species are taken from NOAA cooperative research network (Dlugokencky and Tans, 2019), where ALT, MLO and SPO stand for Alert (Canada), Mauna Loa Observatory, and South Pole Observatory, respectively. BCE = Before Current Era, CE = Current Era.

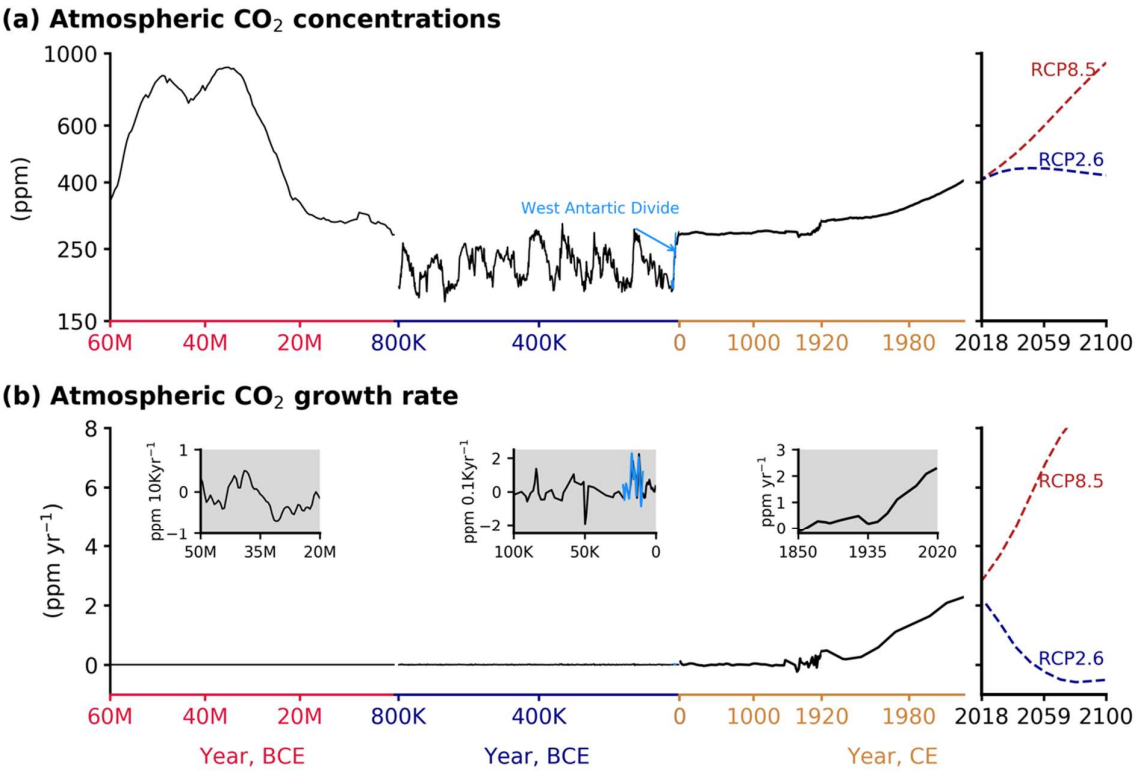

Figure 5.2: CO_2 concentrations (a) and growth rates (b) for the past 60 million years to 2100 using RCP2.6 and RCP8.5. Concentrations data as in Figure 5.1 and data prior to 800 Kyr from (Foster et al., 2017). Inserts in (b) shows growth rates at the scale of the sampling resolution.

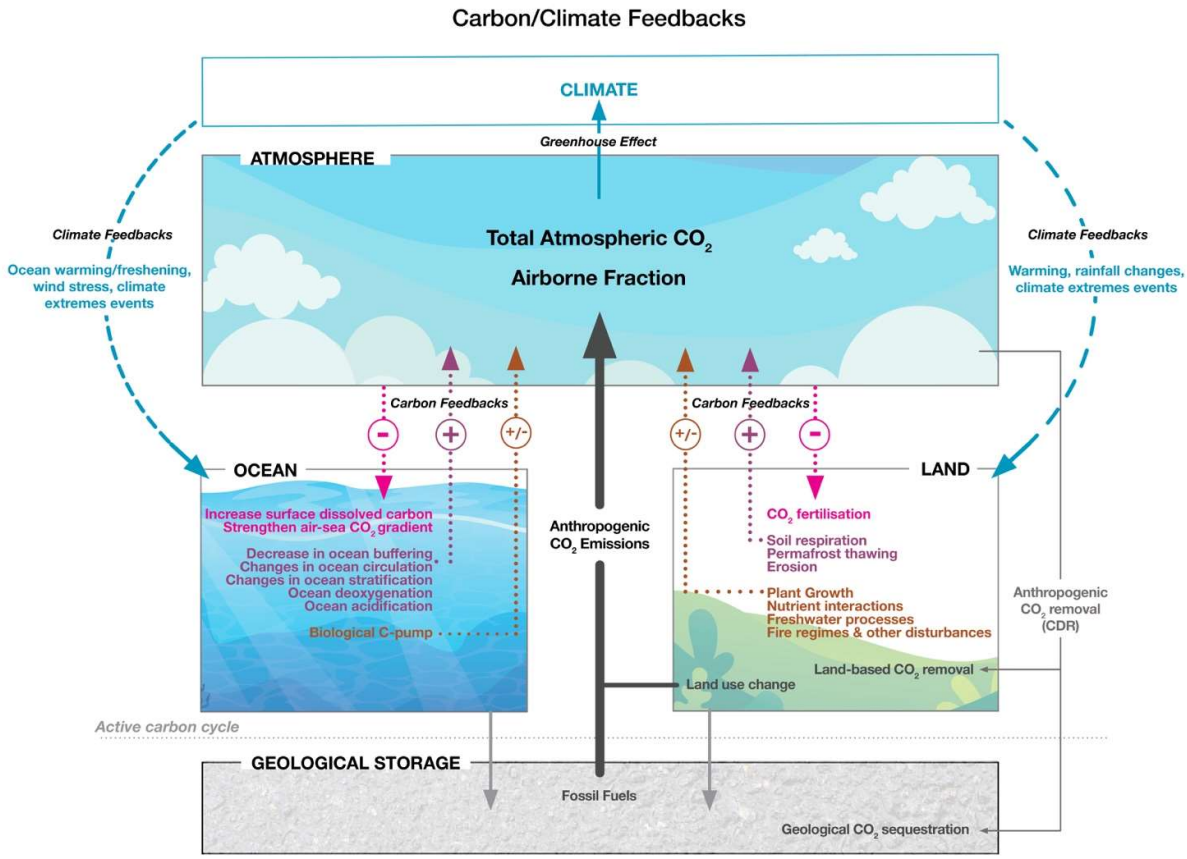

Figure 5.3: Schematic summarizing the key compartments, processes and pathways that govern historical and future carbon concentration and carbon–climate feedbacks through both terrestrial and ocean systems. Central to this is the influence of both carbon (dotted arrows) and climate (dashed arrows) feedbacks on the evolution of the GHG burden in the atmosphere and the airborne fraction of anthropogenic CO2, which drives the Earth's energy imbalance that is partitioned between the ocean (93%) and the terrestrial residual (7%). The ocean dominates the heat feedback in respect of the excess heat from increasing atmospheric CO2. The airborne fraction that drives this historical climate forcing (about 44%) is largely regulated by the negative feedback of ocean (22%) and terrestrial (29%) sinks that partition anthropogenic CO2 (black arrows) in ocean and terrestrial domains (magenta) and result in negative feedbacks (magenta)(partition excludes the estimated imbalance of 0.5 PgC: see Table 5.1). Positive feedback processes (purple arrows) although mostly weak in the historical period, are likely to strengthen in the coming decades and are influenced by both carbon and climate forcing simultaneously (purple). Additional biosphere processes have been included that have an, as yet uncertain feedback bias, especially at regional and global scales (brown arrows). Although this schematic is built around CO2, the dominant GHG, some of the same processes also influence the fluxes of CH4 and N2O from the terrestrial and ocean systems. Those are noted as they contribute to the total radiative forcing.

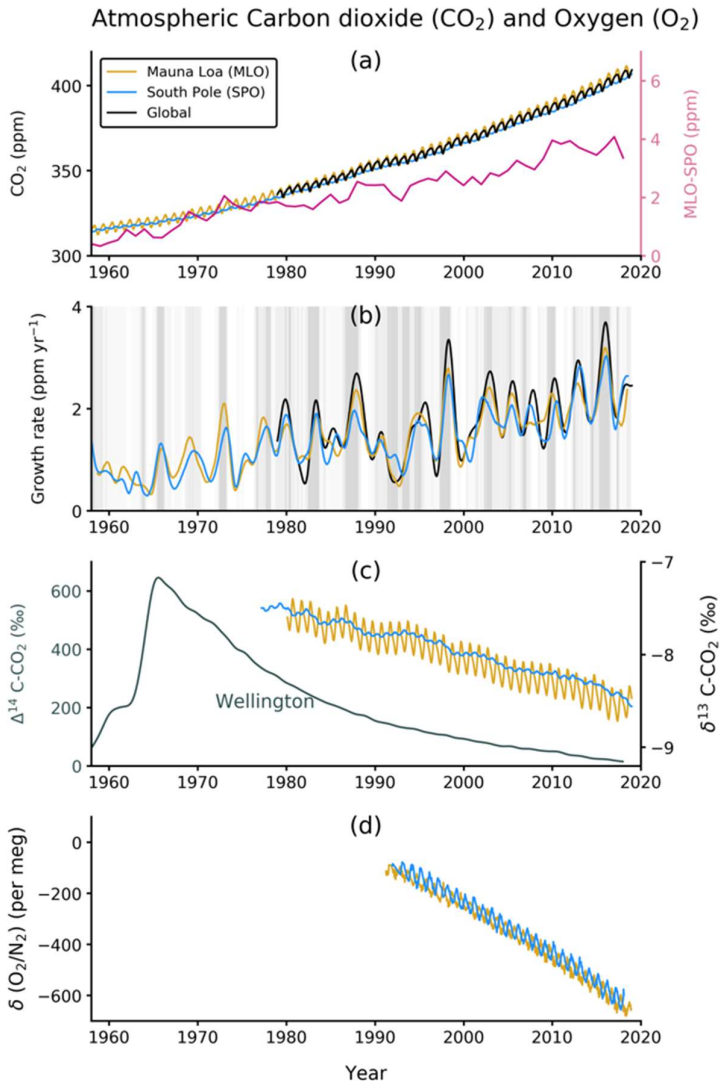

Figure 5.4: Time series of CO_2 concentrations and related measurements in ambient air (a: concentration time series and MLO-SPO difference, b: growth rates, c: ^{14}C and ^{13}C isotopes, and d: O_2/N_2 ratio). The data for Mauna Loa Observatory (MLO) and South Pole Observatory (SPO) are taken from the Scripps Institution of Oceanography (SIO)/University of California, San Diego (Keeling et al., 2001) except for the $\Delta^{14}C$-CO_2 (panel c, left y-axis). The global mean CO_2 and growth rate are taken from NOAA cooperative network (as in Chapter 2). The $\delta(O_2/N2)$ are expressed in per meg units (= $(FF/M)\times10^6$, where FF = moles of O_2 consumed by fossil-fuel burning, M = 3.706×10^{19}, total number of O_2 molecules in the atmosphere; http://scrippso2.ucsd.edu/units-and-terms). The $^{14}CO_2$ time series at Wellington, New Zealand (BHD) is provided by GNS Science and NIWA (Turnbull et al., 2017). The multivariate ENSO index (MEI) is shown as the shaded background in panel (b).

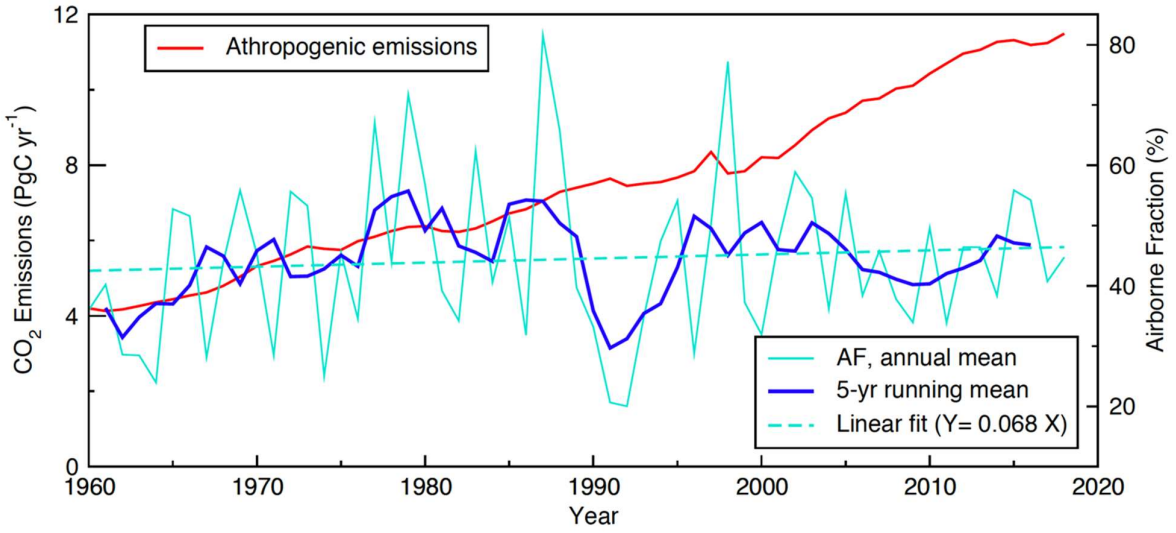

Figure 5.5: Airborne fraction and anthropogenic (fossil fuel and land use change) CO_2 emissions. Data as in carbon budget (Section 5.2.1.5).

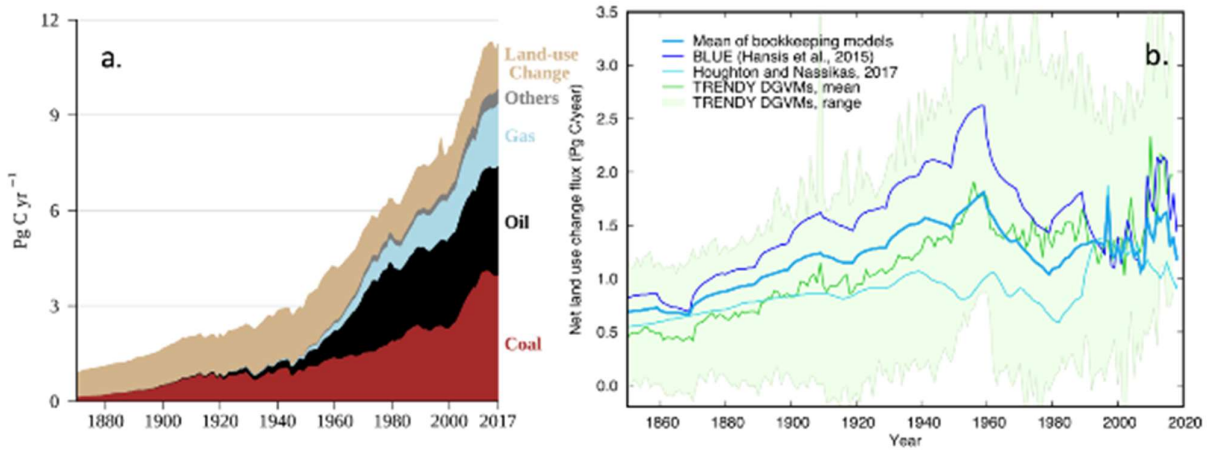

Figure 5.6: Global anthropogenic CO_2 emissions: A) Historical trends of anthropogenic CO_2 emission for the period 1870 to 2016. Data sources: (Boden et al., 2017; IEA, 2017; Andrew, 2018; BP, 2018; Le Quéré et al., 2018a). B) The net land use change CO_2 flux (PgC yr^{-1}) as estimated by two bookkeeping models and 16 dynamic global vegetation models (DGVM) for the global annual carbon budget 2018 (Le Quéré et al., 2018a). The two bookkeeping models are from Hansis et al., 2015 and Houghton and Nassikas, 2017 both updated to 2018; their average is used as to determine the net land use change flux in the annual global carbon budget. The DGVM estimates are the result of differencing a simulation with and one without land use changes run under observed historical climate and CO_2, following the TRENDY v7 protocol; they are used to provide an uncertainty range to the bookkeeping estimates (Friedlingstein et al., 2019). All estimates are unsmoothed annual data. Note that the estimates differ in process comprehensiveness of the models and in definition of flux components included in the net land use change flux.

(a)

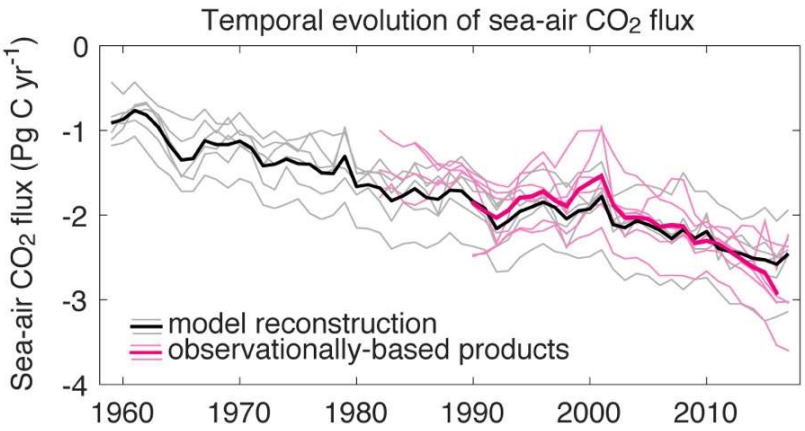

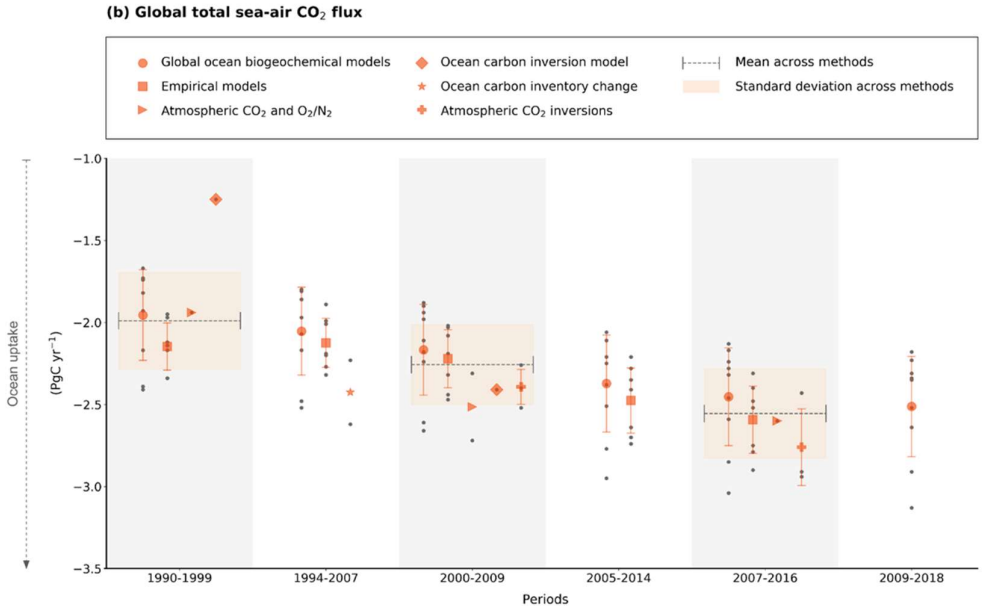

Figure 5.7: (a): Temporal evolution of the globally-integrated sea-air CO_2 flux as reconstructed by (grey/black) ocean physical and biogeochemical models forced with observed atmospheric history (Doney et al., 2009; Buitenhuis et al., 2010; Schwinger et al., 2016; Hauck et al., 2018; Berthet et al., 2019), and (blue) observationally-based products that represent spatial and temporal variability in the flux from sparse observations of surface ocean pCO_2 (Rödenbeck et al., 2013; Iida et al., 2015; Zeng et al., 2015; Landschützer et al., 2016; Denvil-Sommer et al., 2019; Gregor et al., 2019). Thick lines represent the multi-model mean. Observationally-based products have been corrected differences in spatial coverage, as in (McKinley et al., submitted). (b): Mean decadal constraints for global ocean air-sea CO_2 fluxes using quasi-independent lines of evidence or methods for the period 1990–2018 (See supporting Table SM5.1 for magnitudes, uncertainties and published sources). (References as above but including: (Rödenbeck et al., 2003; Chevallier et al., 2005; Keeling and Manning, 2014; Aumont et al., 2015; Jones et al., 2015; Saeki and Patra, 2017; DeVries et al., 2017; Law et al., 2017; Gregor et al., 2018; Mauritsen et al., 2019; Tohjima et al., 2019; Friedlingstein et al., 2019; Gruber et al., 2019a; Liu et al., 2019a). The fluxes from both empirical models and atmospheric inversions have been corrected for the river fluxes (0.78 PgC yr^{-1}) based on the estimate from Resplandy et al. (2018).

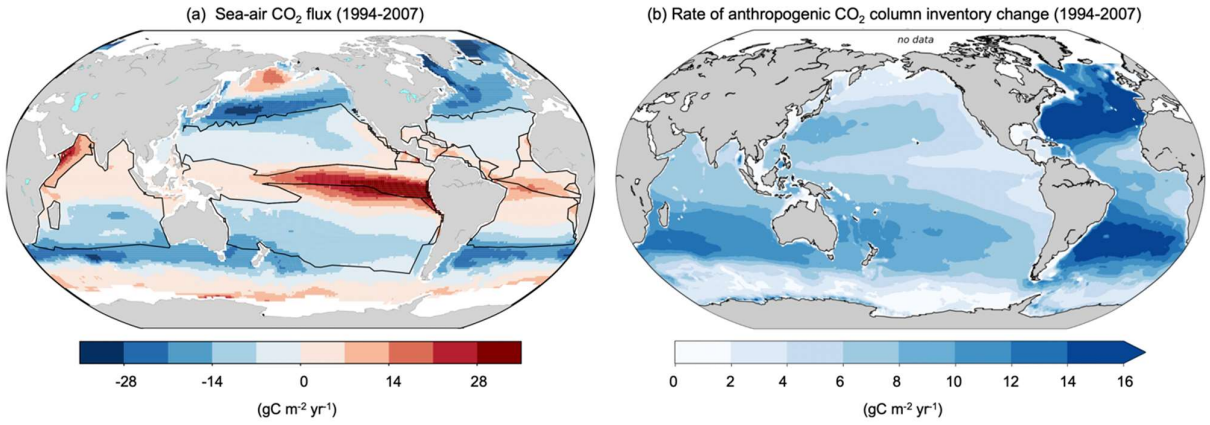

Figure 5.8: A comparative assessment of the spatial characteristics of the mean multi-decadal (1994–2007) (a) ocean air-sea CO_2 fluxes derived from the ensemble observation-based product CSIR-ML6 (Gregor et al., 2019) using SOCATv5 observational data set (Bakker et al., 2016). Black contours characterise the biomes defined by Fay and McKinley, (2014) and adjusted by Gregor et al. (2019) and (b) the storage fluxes of CO_2 in the ocean (Gruber et al., 2019a).

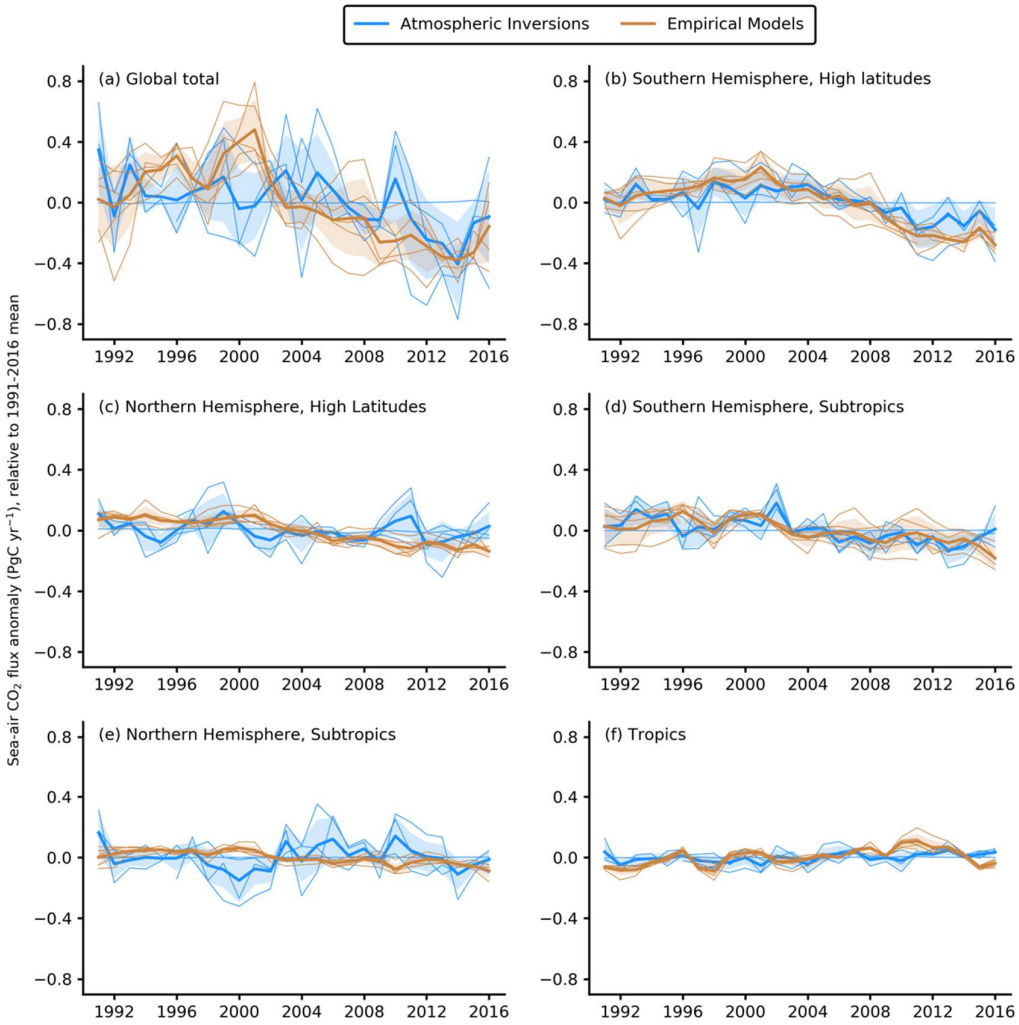

Figure 5.9: A comparative assessment of the contribution made by 5 regional ocean biomes (b-f) to the temporal variability and empirical model spread characteristics of the global air-sea CO_2 fluxes for the period 1990–2016 using both the ensemble observation-based product CSIR-ML6 (Gregor et al., 2019) using SOCATv5 observational data set (Bakker et al., 2016) and an atmospheric inversion model (Friedlingstein et al, 2019).

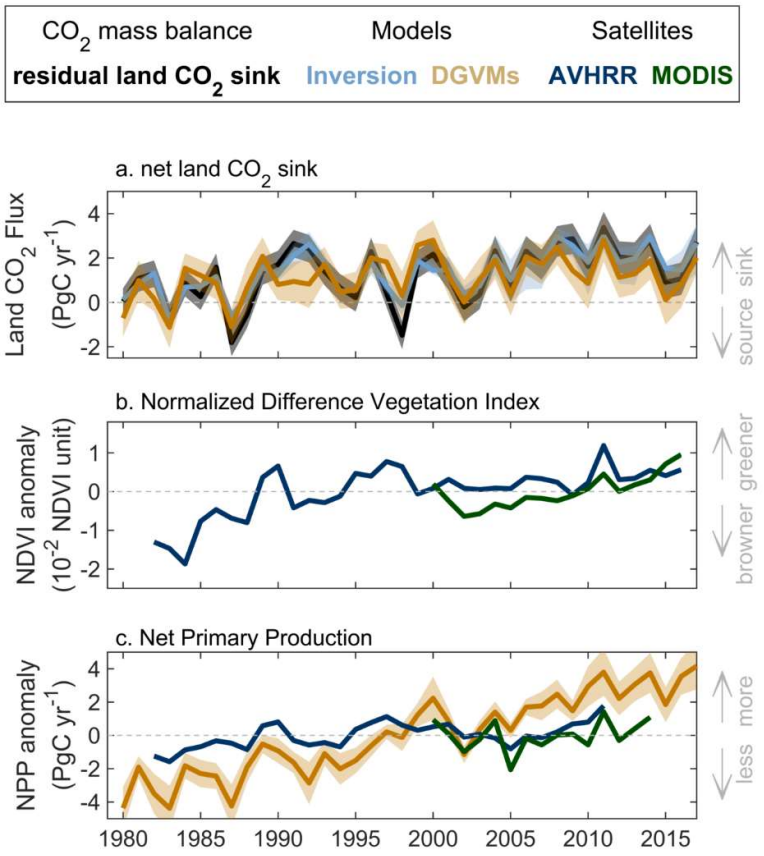

Figure 5.10: Change of net land CO_2 sink, Normalised Difference Vegetation Index (NDVI) and net primary production (NPP) during 1980–2017. **a**. Residual net land CO_2 sink is estimated from the global CO_2 mass balance with fossil fuel emission minus atmospheric CO_2 growth rate and ocean sink. Inversions indicate the net land CO_2 sink estimated by an ensemble of four atmospheric inversions (Le Quéré et al., 2018a). DGVMs indicate the mean net land CO_2 sink estimated by 16 Dynamic Global Vegetation Models driven by climate change, rising atmospheric CO_2, land use change and nitrogen deposition change (for carbon-nitrogen models). The positive CO_2 sink indicates net CO_2 uptake from the atmosphere. **b**. The anomaly of global area-weighted NDVI observed by AVHRR and MODIS satellite sensors. AVHRR data are available during 1982–2016 and MODIS data are available during 2000–2016. **c**. NPP based on the two satellite-based datasets having the temporal coverage of 1982–2011 for AVHRR NPP (Kolby Smith et al., 2016) and 2000-2014 for MODIS NPP (Zhao and Running, 2010). NPP from DGVMs is the ensemble mean global NPP estimated by the same 16 DGVMs that provide the net land CO_2 sink estimates. Shaded area indicates 1–σ inter-model spread except for atmospheric inversions, whose ranges were used due to limited number of models.

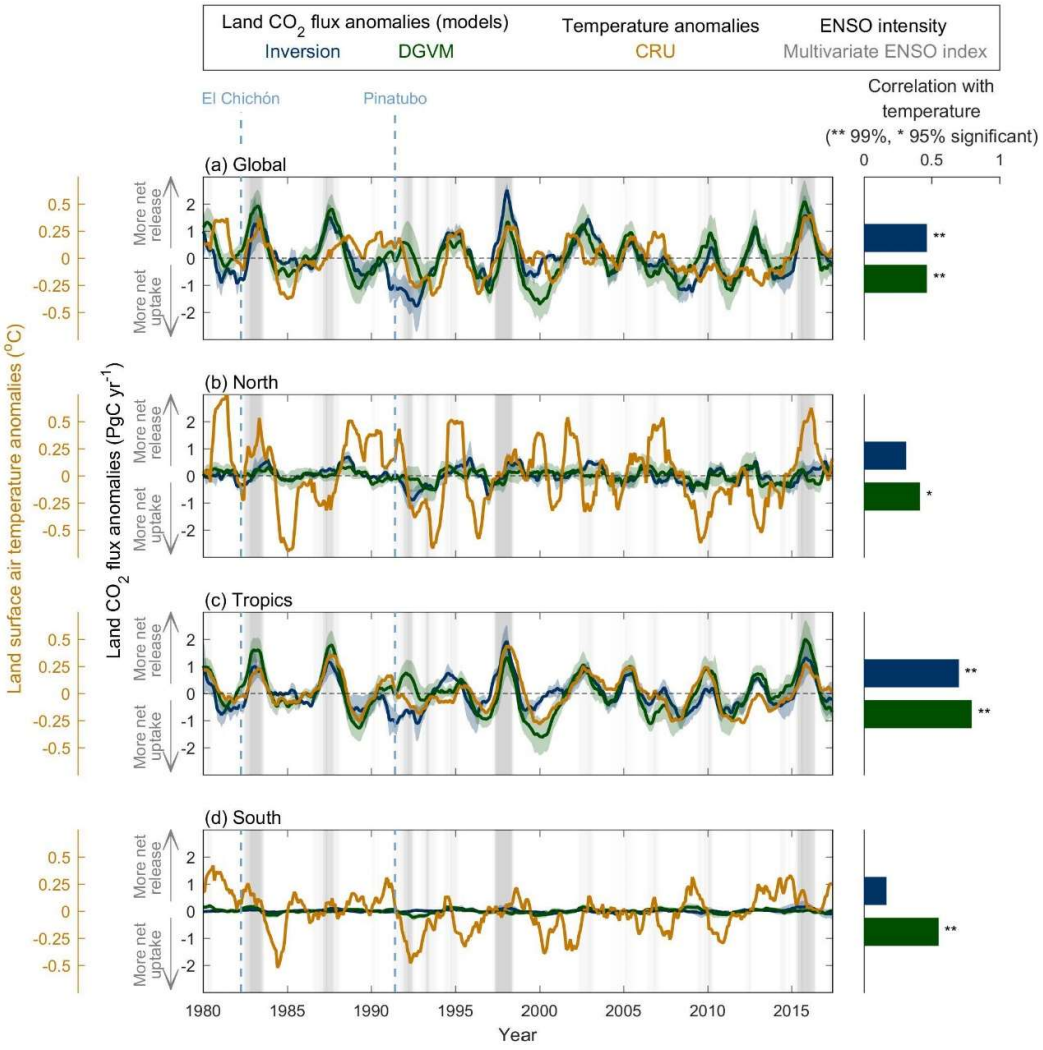

Figure 5.11: Interannual variation in detrended anomalies of net land CO_2 sink and land surface air temperature (T) at the globe or at the latitudinal bands during 1980–2017, and corresponding correlation coefficient between net land CO_2 sink anomalies and temperature anomalies. Net land CO_2 sink is estimated by four atmospheric inversions (blue) and fifteen Dynamic Global Vegetation Models (DGVMs) (green), respectively (Le Quéré et al., 2018a). Solid blue and green lines show model mean detrended anomalies of net land CO_2 sink. The ensemble mean of DGVMs is bounded by the 1–σ inter-model spread in each large latitude band (North 30°N–90°N, Tropics 30°S–30°N, South 90°S–30°S) and the globe. The ensemble mean of atmospheric inversions is bounded by model spread. For each latitudinal band, the anomalies of net land CO_2 sink and temperature (orange) were obtained by removing the long-term trend and seasonal cycle. 12-month running mean was taken to reduce high-frequency noise. Years on the horizontal axis indicate January of this year as the sixth month in the moving 12-month window. The bars in the right panels show correlation coefficients between net land CO_2 sink anomalies and temperature anomalies for each region. Two asterisks indicate $P<0.01$, and one indicates $P<0.05$. Grey shaded area shows the intensity of El Niño-Southern Oscillation (ENSO) as defined by the multivariate ENSO index (MEI). Two volcanic eruptions (El Chichón eruption and Pinatubo eruption) are indicated with light blue dashed lines. Temperature data are from Climatic Research Unit (CRU), University of East Anglia (Harris et al., 2014).

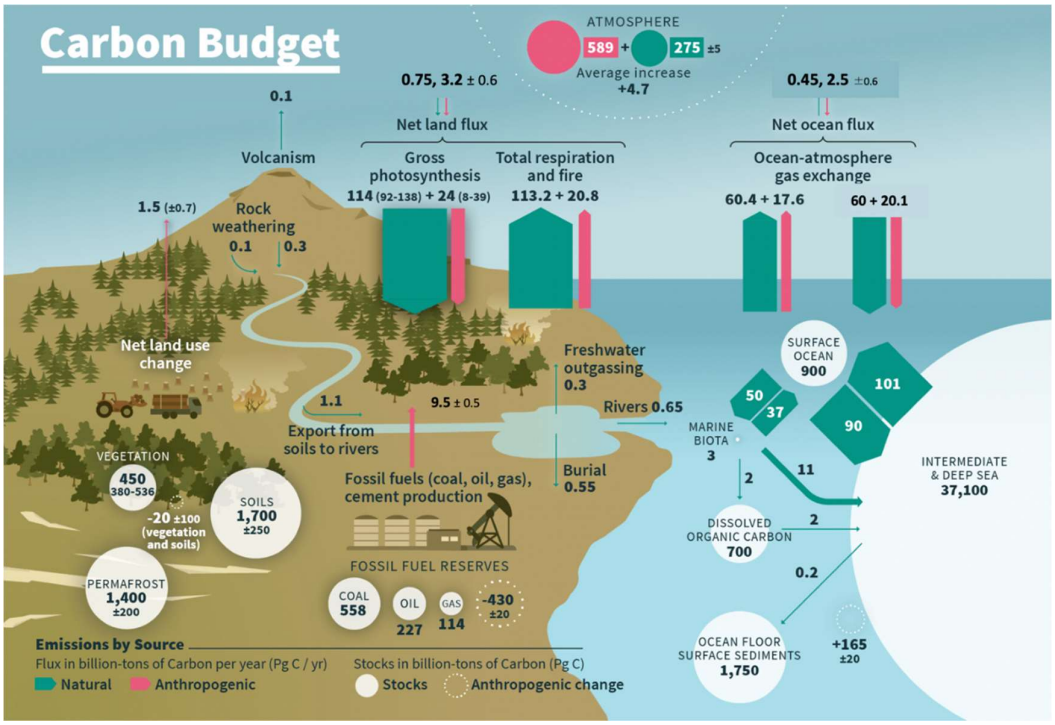

Figure 5.12: The global carbon cycle. Blue arrows represent annual carbon exchange fluxes (in PgC yr^{-1}) associated with the natural carbon cycle estimated for the time prior to the Industrial Era, around 1750. Pink arrows represent anthropogenic fluxes averaged over the period 2008–2017. The rate of carbon accumulation in the atmosphere is equal to net land-use change emissions plus fossil fuel emissions, minus land and ocean sinks (plus a small budget imbalance, Table 5.1). Numbers in white circles represent pre-industrial carbon stocks in PgC. Fossil fuel reserves are those stocks that are currently recoverable using commercially viable existing technologies. Numbers in dashed circles represent anthropogenic changes to these stocks (cumulative anthropogenic fluxes) since 1750. Anthropogenic net fluxes are reproduced from (Friedlingstein et al., 2019) The relative change of *Gross photosynthesis* since pre-industrial times is estimated as the range of observation-based of 31 ± 3 % (Campbell et al., 2017) and land-model of 19 ± 12% (Sitch et al., 2015) estimates. This is used to estimate the pre-industrial *Gross photosynthesis*, assuming a present-day range of 116–175 PgC yr^{-1} (Joiner et al., 2018). The corresponding emissions by *Total respiration and fire* are those required to match the *Net land flux*, exclusive of net land-use change emissions which are accounted for separately. The cumulative change of anthropogenic carbon in the terrestrial reservoir is the sum of carbon cumulatively lost by net land use change emissions, and net carbon accumulated since 1750 in response to environmental drivers (warming, rising CO_2, nitrogen deposition) (Le Quéré et al., 2018a).The change in *Ocean-atmosphere gas exchange* (red arrows of ocean atmosphere gas exchange) is estimated from the difference in atmospheric partial pressure of CO_2 since 1750 (Sarmiento and Gruber, 2006). Individual gross fluxes and their changes since the beginning of the Industrial Era have typical uncertainties of more than 20%, while their differences (*Net ocean flux*) are determined from independent measurements with a much higher accuracy. Therefore, to achieve an overall balance, the values of the more uncertain gross fluxes have been adjusted so that their difference matches the and *Net ocean flux* estimate. The sediment storage is a sum of 150 PgC of the organic carbon in the mixed layer (Emerson and Hedges, 1988) and 1600 PgC of the deep-sea $CaCO_3$ sediments available to neutralie fossil fuel CO_2 (Archer et al., 1998). Note that the mass balance of the two ocean carbon stocks *Surface ocean* and *Intermediate and deep ocean* includes a yearly accumulation of anthropogenic carbon (not shown). Fossil fuel reserves are from (BGR, 2017). Permafrost region stores are from (Hugelius et al., 2014; Strauss et al., 2017) and soil carbon stocks outside of permafrost region from (Batjes, 2016; Jackson et al., 2017) Biomass stocks (range of seven estimates) are from (Erb et al., 2018). Fluxes from volcanic eruptions, rock weathering (removal of atmospheric CO_2 in weathering reactions and chemical weathering of C contained in rocks) export of carbon from soils to rivers, burial of carbon in freshwater lakes and reservoirs, estuaries and coastal ecosystems, and transport of carbon by rivers to the open ocean are all assumed to be pre-industrial fluxes and are sourced from (Regnier et al., 2013).

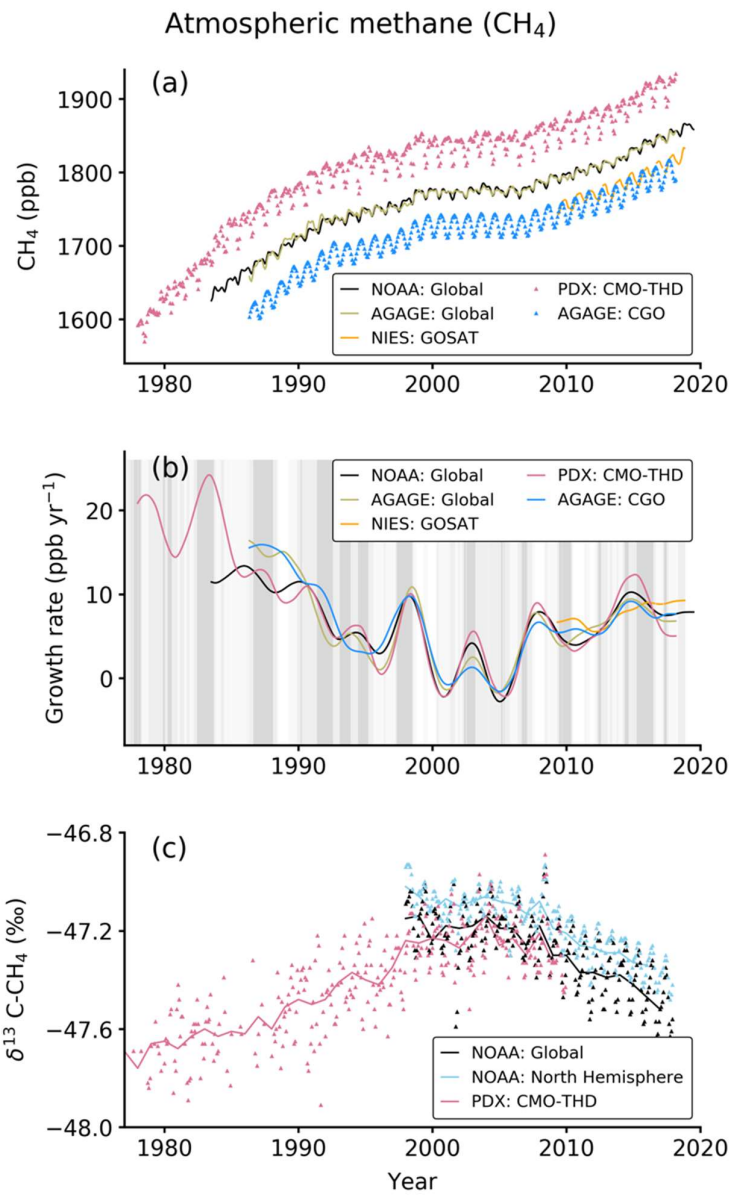

Figure 5.13: Time series of CH_4 dry-air mole fraction (in ppb; panel a), growth rate (ppb yr^{-1}; panel b) and $\delta^{13}C$ (panel c) from selected site networks operated by NOAA (www.esrl.noaa.gov/gmd/ccgg/trends_ch4/), AGAGE (https://agage.mit.edu/data/agage-data) and PDX (Portland State University; (Rice et al., 2016)). To maintain clarity, data from many other measurement networks are not included here. Global mean values of XCH_4 (total-column), retrieved from radiation spectra measured by the Greenhouse gases Observation SATellite (GOSAT; www.gosat.nies.go.jp/en/recent-global-ch4.html) are shown in panels a and b. Cape Grim Observatory (CGO) and Trinidad Head (THD) data are taken from the AGAGE network, NOAA global and northern hemispheric (NH) means for $\delta^{13}C$ are calculated from 10 and 6 sites, respectively. The PDX data adjusted to NH (period: 1977–1996) are merged with THD (period: 1997–2018) for CH_4 concentration and growth rate analysis, and PDX and NOAA NH means of $\delta^{13}C$ data are used for joint interpretation of long-term trends analysis. The multivariate ENSO index (MEI) is shown in panel b (the shading indicates the period and strength of the El Nino).

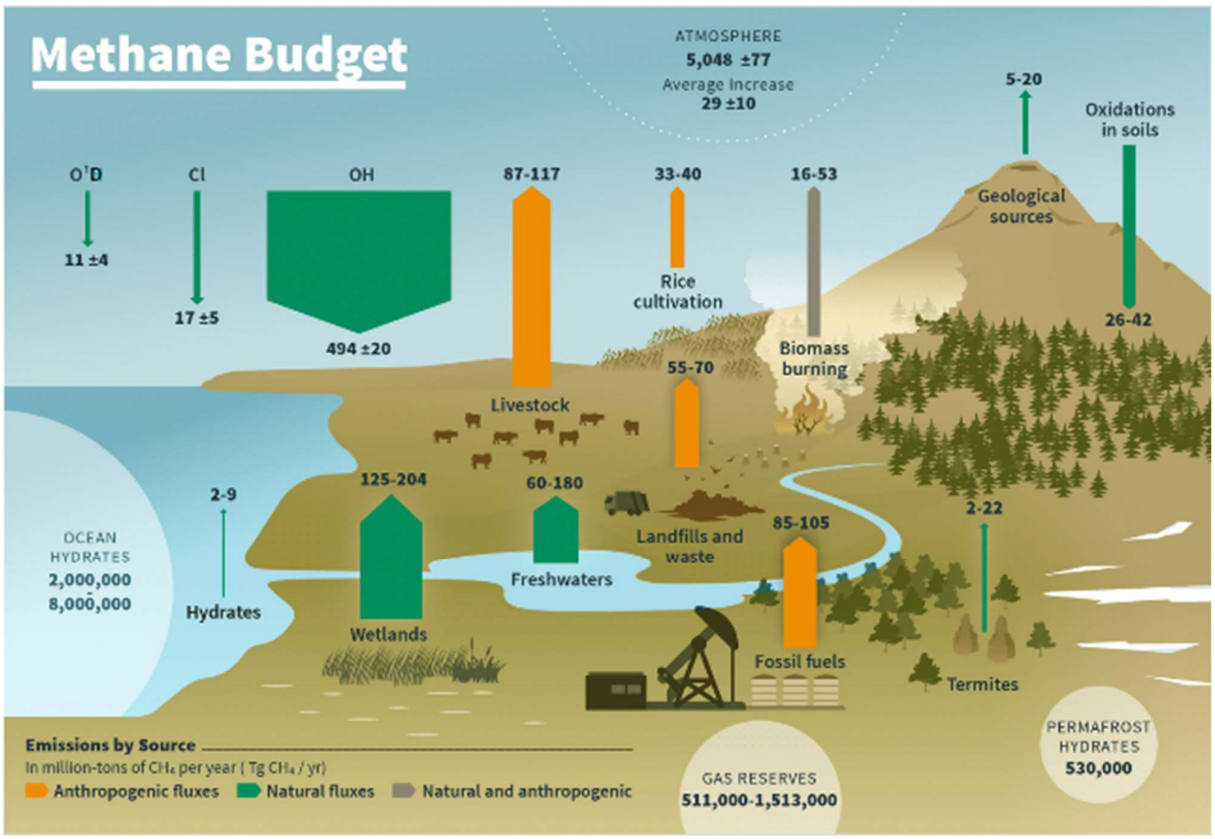

Figure 5.14: Schematic diagram of major sources and sinks of CH_4 for the decade 2010–2017 (in Tg CH_4). Values and data sources as in Table 5.2.

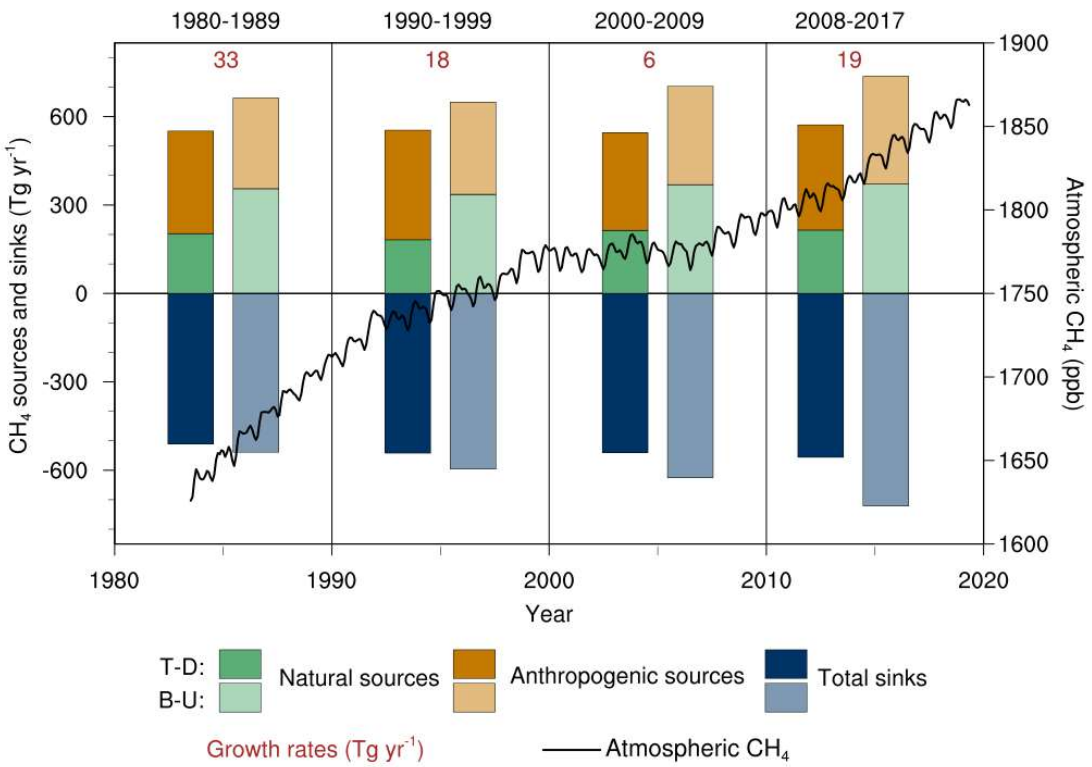

Cross-Chapter Box 5.1, Figure 1: Methane budget estimates for four decades from top-down (darker colour, left; labelled T-D) and bottom-up (lighter colour, right; labelled B-U) analyses (plotted on the left y axis). Sources are positive and sinks are negative. The black line (plotted on the right y axis) represents observed global monthly mean atmospheric CH4 in dry-air mole fractions for 1983–2019 (www.esrl.noaa.gov/gmd/ccgg/trends_ch4; Dlugokencky et al. 2019). The bottom-up total sinks are inferred from global mass balance, i.e., source minus growth in atmospheric CH4 abundance, and are given as the numbers under the top x-axis for different decades.

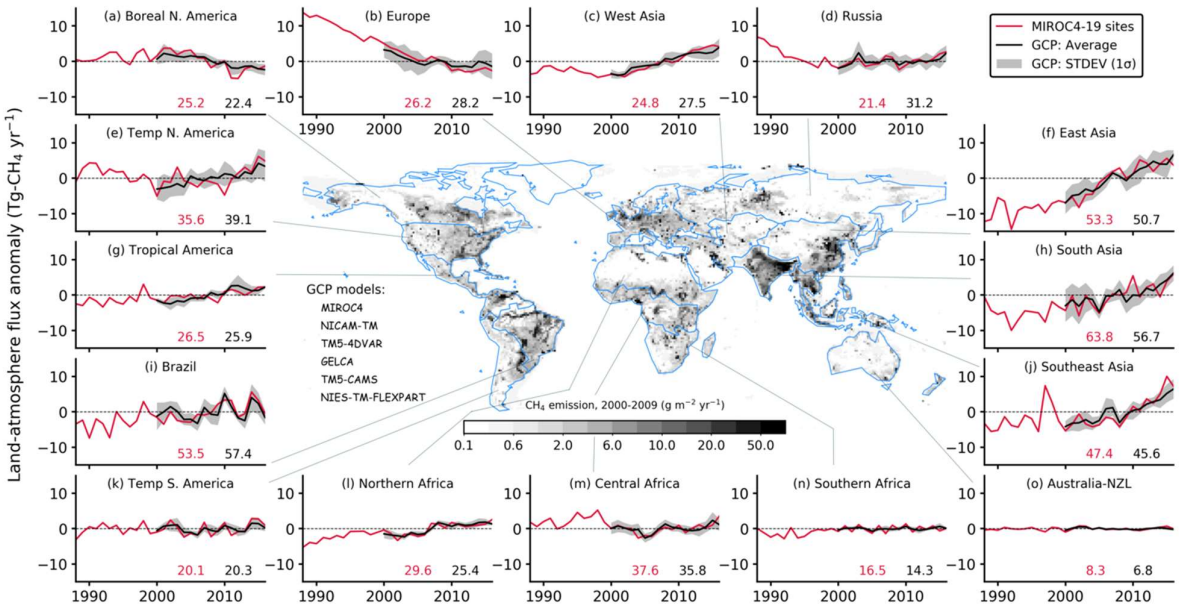

Cross-Box 5.1, Figure 2: Anomalies in regional CH4 emissions during 1988–2016, and a representative CH4 emission map are shown. Results for 2000–2016 are shown for 6 inversion models that participated in GCP-CH4 budget assessment (Saunois et al., 2019), and results for 1988–1999 are available from only one inversion using 19 sites only (Chandra et al., submitted). A long-term mean value, as indicated within each panel separately for the GCP average and MIROC4-19 sites, is subtracted from the annual-mean time series for the calculation of anomalies for each region.

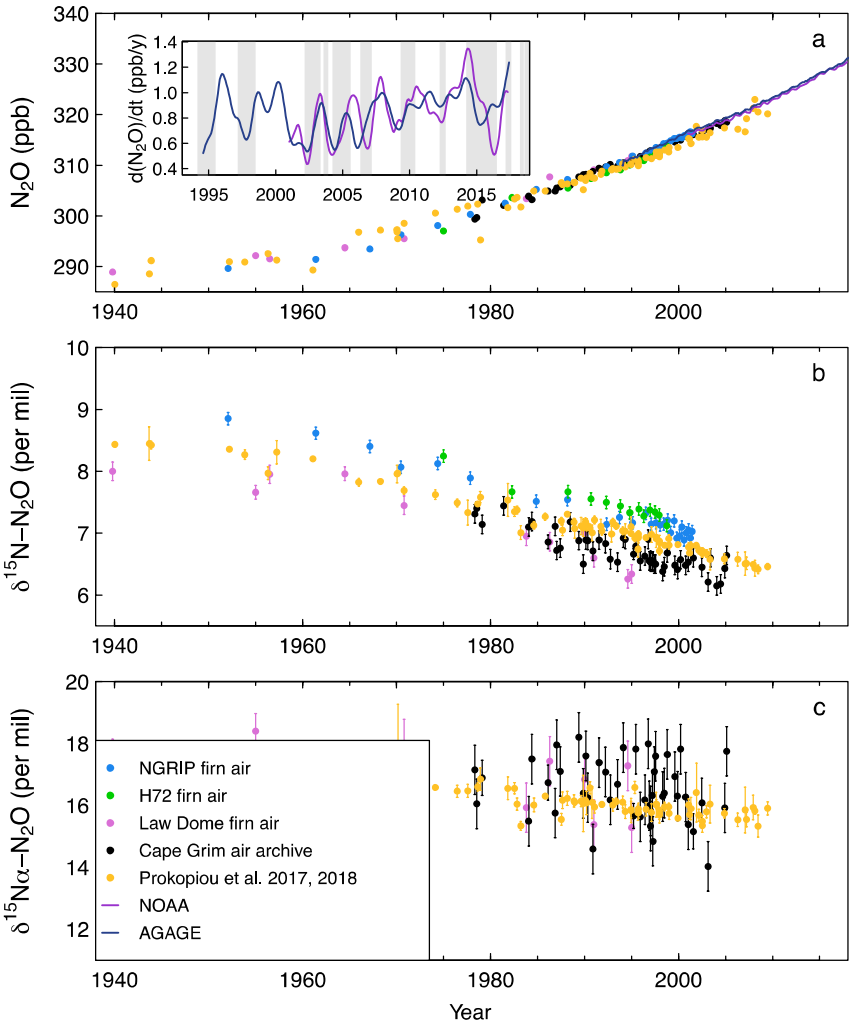

Figure 5.15: (a) Atmospheric N_2O abundance (parts per billion, ppb) and growth rate (ppb yr^{-1}), (b) δ15N of atmospheric N_2O, and (c) alpha-site $^{15}N–N_2O$, based on direct atmospheric measurements in the AGAGE and NOAA (Prinn et al., 2000, 2016; Hall et al., 2007; Elkins et al., 2018) networks, archived air samples from Cape Grim, Australia (Park et al., 2012), and firn air from NGRIP Greenland and H72 Antarctica (Ishijima et al., 2007), Law Dome Antarctica (Park et al., 2012), and NEEM Greenland (Prokopiou et al., 2017). Grey shading in (a) are times of positive values of the multivariate ENSO index, indicating El Niño conditions (Wolter and Timlin, 1998).

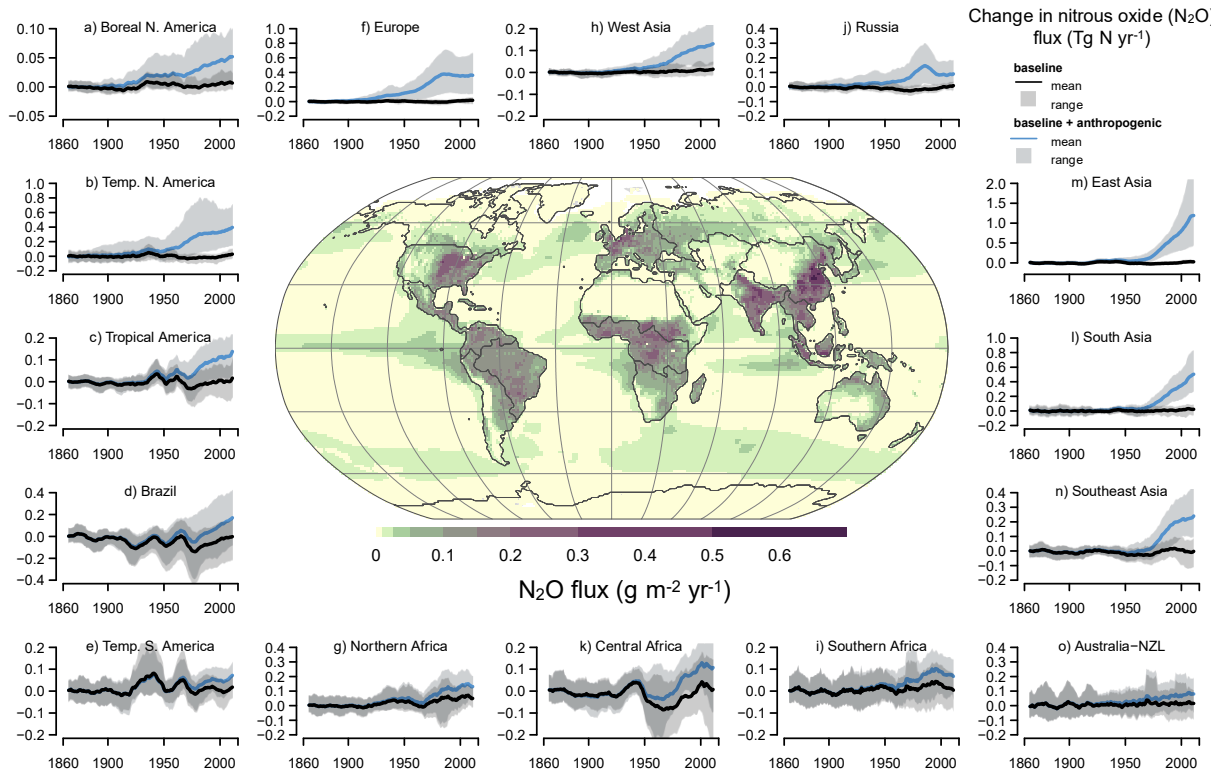

Figure 5.16: Decadal mean N_2O emissions for 2007–2016 based on the N_2O Model Intercomparison Project (NMIP) ensemble of terrestrial biosphere models (Tian et al., 2019) and three ocean biogeochemical models (Landolfi et al., 2017; Battaglia and Joos, 2018a; Buitenhuis et al., 2018), as well as the change in N_2O emissions from terrestrial soils (natural and agriculture) simulated from the (Tian et al., 2019). The effect of anthropogenic nitrogen additions (atmospheric deposition, manure addition, fertiliser use and land-use) is evaluated against the background flux driven by changes in atmospheric CO_2 concentration, and climate change

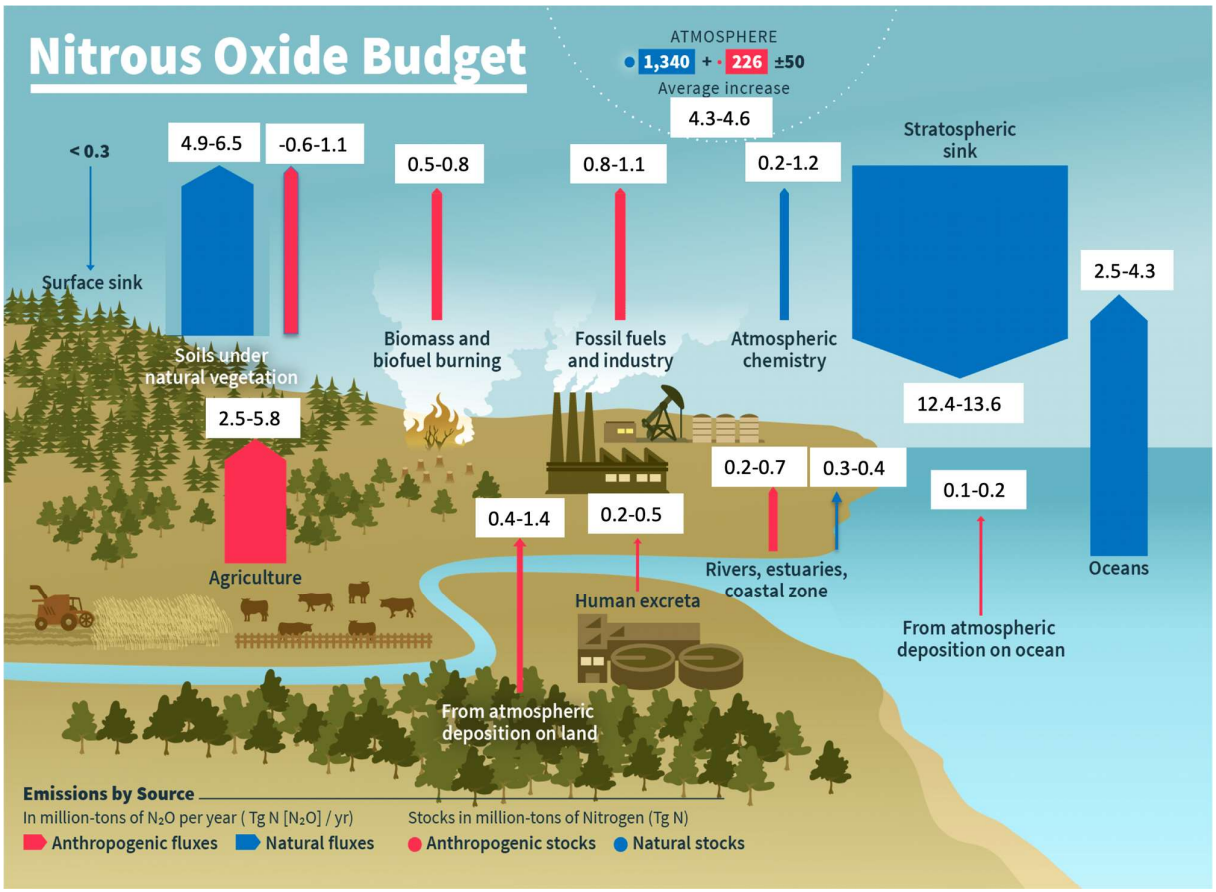

Figure 5.17: Global nitrous oxide (N_2O) budget for the period 2007–2016. Annual nitrous oxide fluxes ($TgN_2O–N\ yr^{-1}$), as described in Table 5.3, and the atmospheric nitrous oxide pools ($TgN_2O–N$)

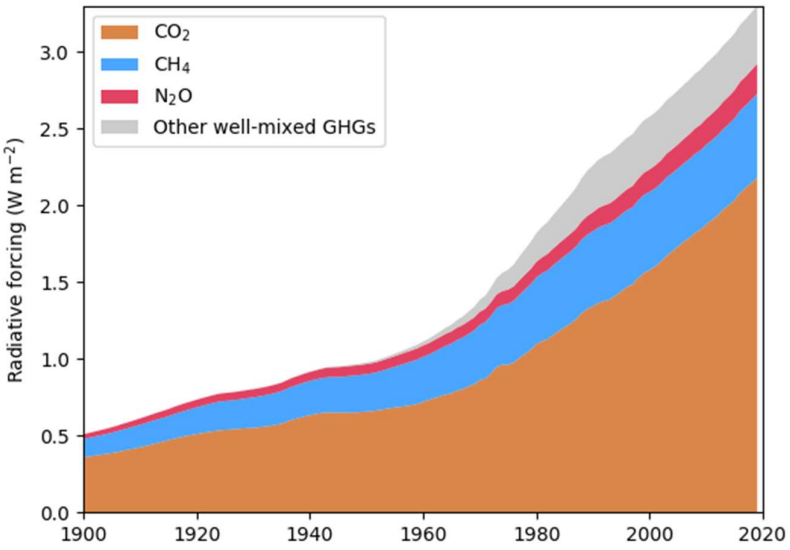

Figure 5.18: Effective Radiative forcing by long-lived GHGs since 1900 (values relative to 1750, as a reference of the pre-industrial Era). All data are taken from Chapter 7, Annex Climate Table (simplified from Figure 2.10).

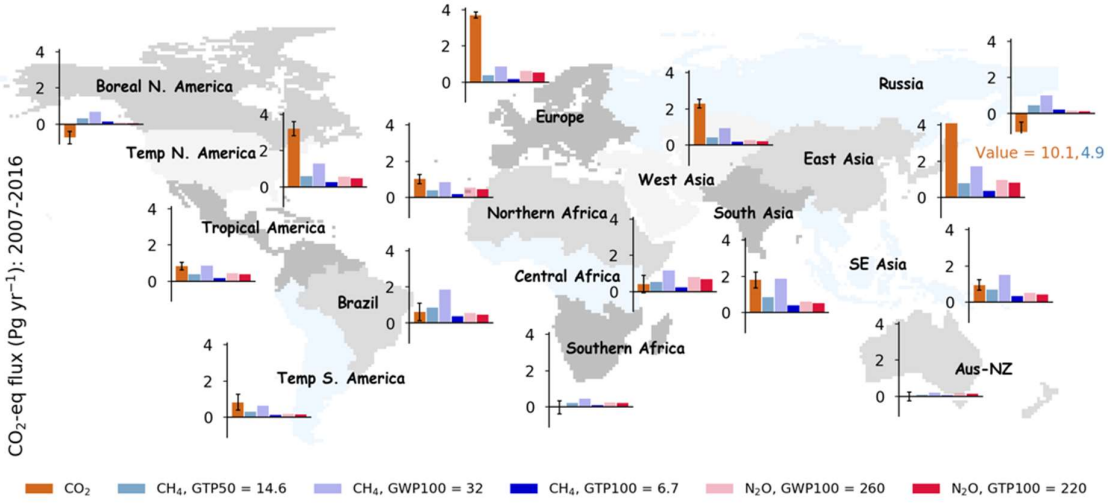

Figure 5.19: Regional attribution of global fluxes of CO_2, CH_4 and N_2O derived from their concentrations, measured globally. The fluxes include anthropogenic sources and sinks, and natural fluxes that result from responses to anthropogenic GHGs and climate forcing (feedbacks) as in the three budgets shown in Sections 5.2.1.5, 5.2.2.5, and 5.2.3.5. The CH_4 and N_2O emissions are weighted by their global warming potential (GWP) and global temperature-change potential (GTP) over 100-year and 50-year time horizon (GTP and GWP values from Table 7.2). Fluxes are shown as the mean from of the inverse models as available from the global carbon project (Le Quéré et al., 2018a; Saunois et al., 2019; Thompson et al., 2019b).

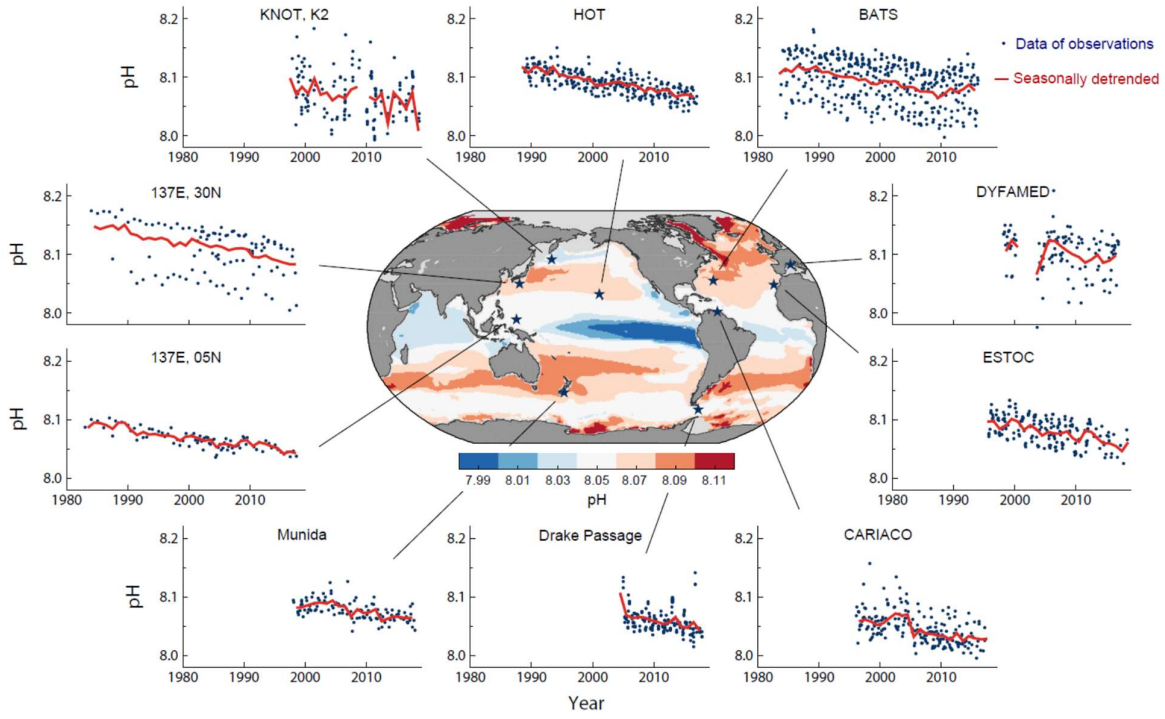

Figure 5.20: Annual mean pH distributions in the year 2017 evaluated from surface pCO_2^{sea} (Iida et al., 2015) and total alkalinity (Lee et al., 2006; Takatani et al., 2014), and time-series of pH in surface layer at various sites of the oceans showing the trends of ocean acidification (Dore et al., 2009; González-Dávila et al., 2010; Midorikawa et al., 2010; Ishii et al., 2011; Bates et al., 2014).

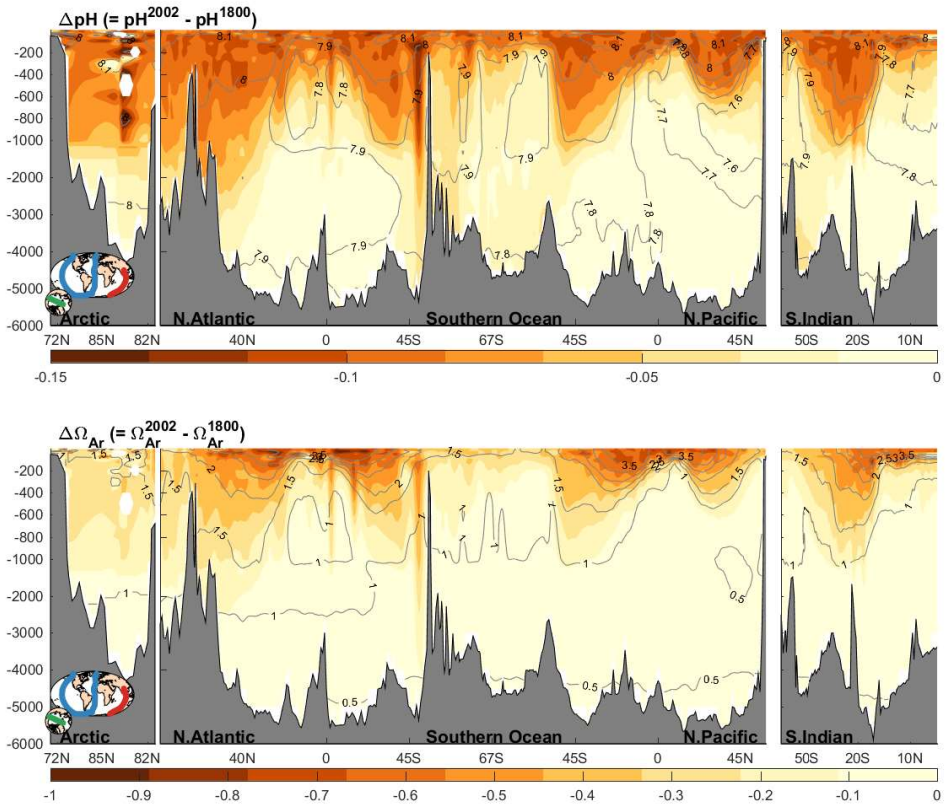

Figure 5.21: Vertical sections of the changes in (a) pH and (b) Ω_{arag} between the years 1800 and 2002 due to anthropogenic CO_2 invasion (colour) and of their contemporary values in 2002 (contour line) in the Arctic, Atlantic, Southern, Pacific and Indian Oceans (left to right) (Lauvset et al., submitted).

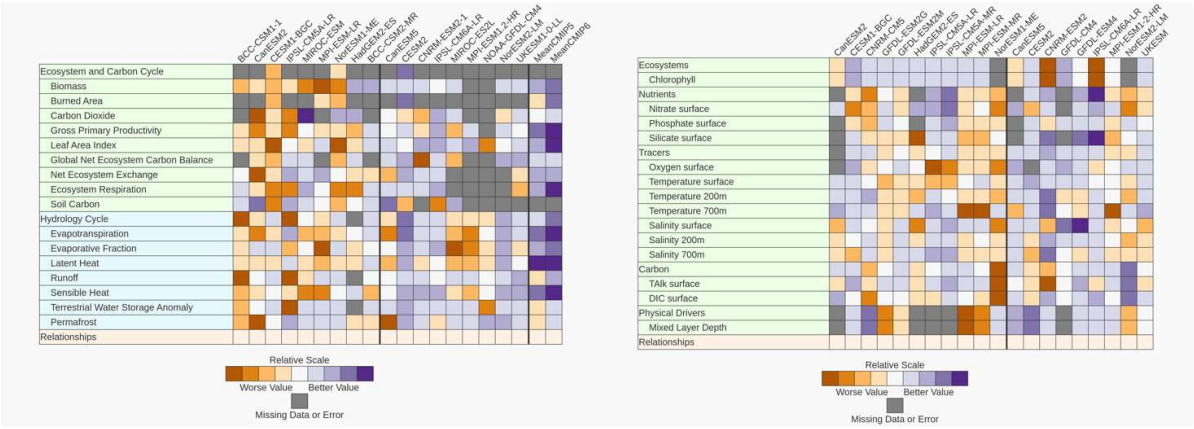

(a) Land Model Benchmarking Scores **(b) Ocean Model Benchmarking Scores**

Figure 5.22: Overview scores of CMIP5 (left hand side of table) and CMIP6 (right hand side of table) models, for multiple benchmarks against different datasets. (a) Benchmarking of ESM land models, (b) benchmarking of ocean models. Scores are relative to other models within each benchmark row, with positive scores indicating a better agreement with observations. Thick vertical lines separate CMIP5 from CMIP6 models, and individual models from ensemble means.

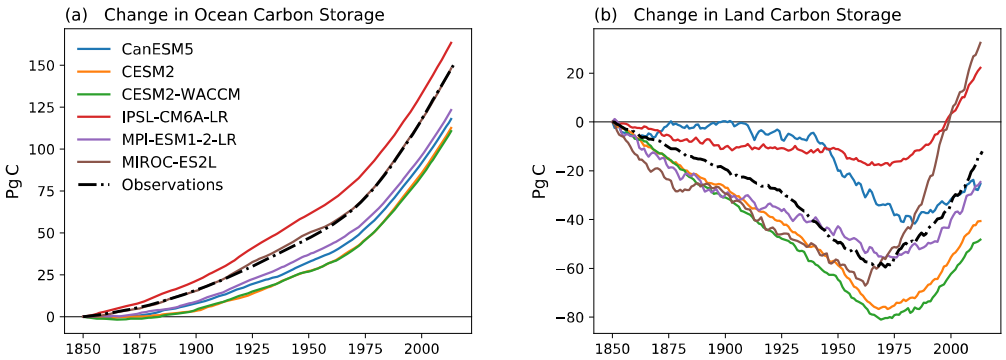

Figure 5.23: CMIP6 ESM concentration-driven historical simulations for 1850 to 2014, compared to observation-based estimates from the Global Carbon Project (GCP). Panel (a) change in ocean carbon storage from 1850 (PgC); (b) change in land carbon storage from 1850 (PgC). Only models that simulate both land and ocean carbon fluxes are shown here.

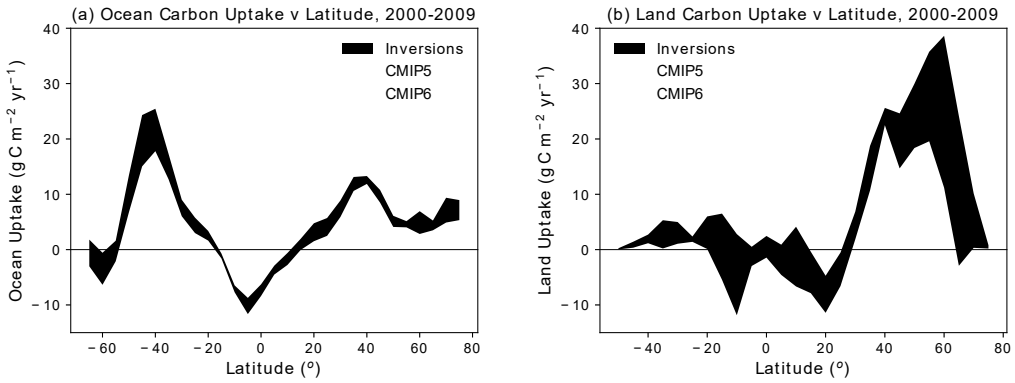

Figure 5.24: Comparison of modelled zonal distribution of carbon sinks against atmospheric inversion estimates for 2000–2009, (a) ocean carbon uptake; (b) net land uptake. Positive uptake represents a carbon sink to ocean/land while negative uptake represents a carbon source. The land uptake is taken as Net Biome Productivity (NBP) and so includes net land-use change emissions. The bands show the mean ± 1 standard deviation across the available inversions (black bands, 3 models), CMIP5 ESMs (blue bands, 12 models for the ocean, 12 models for the land), and CMIP6 ESMs (red bands, 11 models for ocean, 10 models for land).

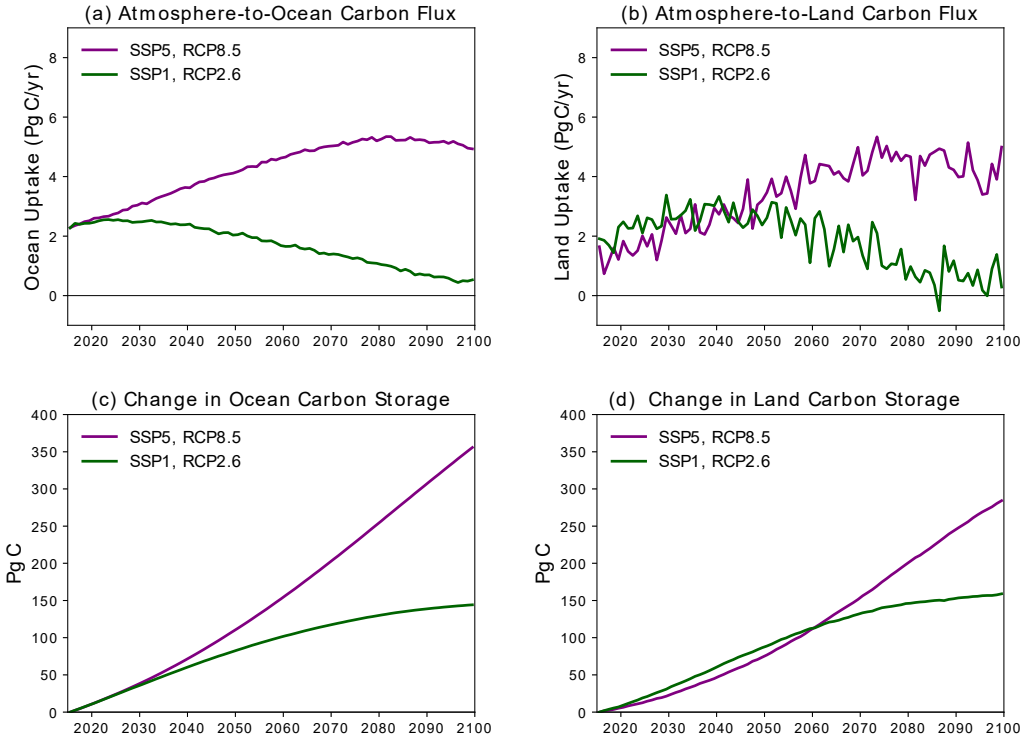

Figure 5.25: Projected evolution of the global land and ocean carbon sinks for 2014 to 2090 in concentration-driven SSP1-2.6 (SSP1, RCP2.6; green) and SSP5-8.5 (SSP5, RCP8.5; purple) CMIP6 ESM runs: (a) net ocean uptake rate (PgC yr^{-1}); (b) net land uptake rate (PgC yr^{-1}); (c) change in ocean carbon store from 2014 (PgC); (d) change in land carbon store from 2014 (PgC). Positive uptake represents a carbon sink to ocean/land, and negative uptake represents a carbon source. Changes in carbon storage are calculated as the cumulative annual uptake fluxes. The land uptake is taken as Net Biome Productivity (NBP) and so includes any modelled net land-use change emissions. Thick lines represent the ensemble mean of the available ESM runs that provided the necessary carbon fluxes (7 ESMs), and the shaded area represents ± one standard deviation about that mean.

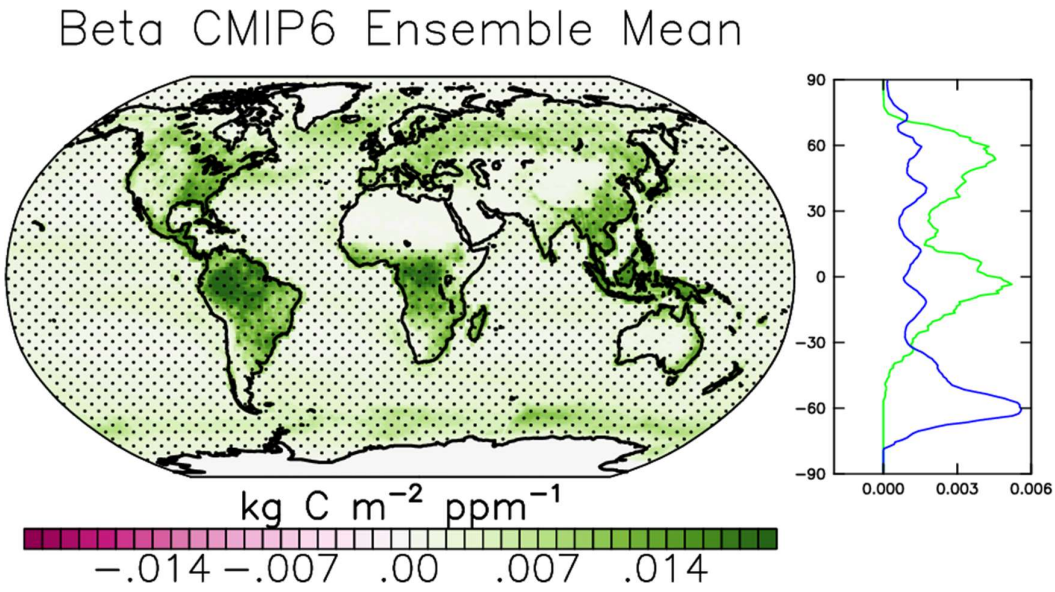

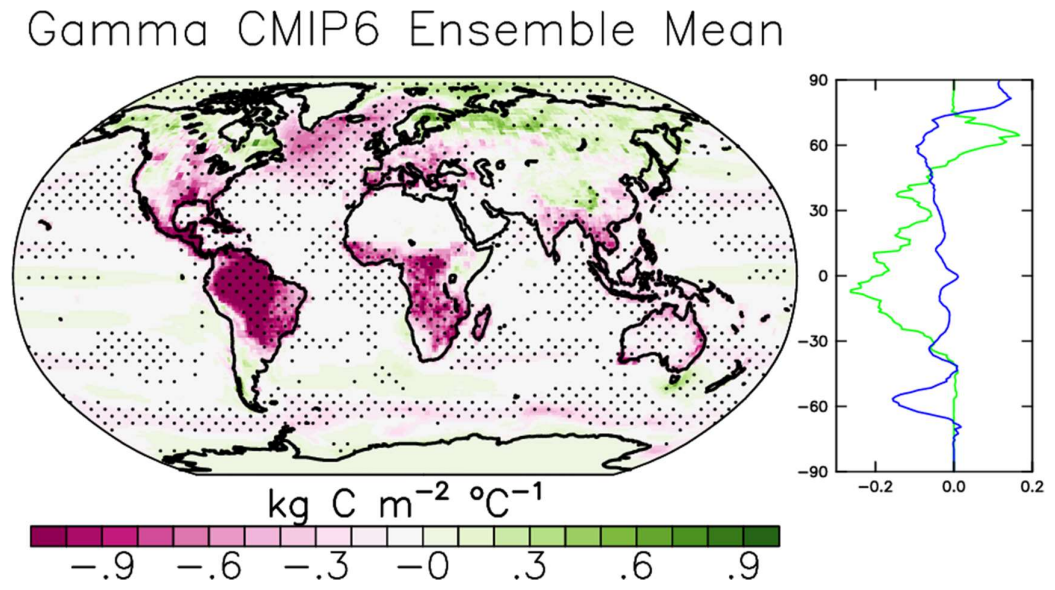

Figure 5.26: Maps of carbon-concentration and carbon-climate feedback terms as evaluated from CMIP6 ESMs. Shown are the model means from ten CMIP6 ESMs, stippling indicates 80% of the models agree in sign with the multi-model mean. Also shown are zonal-mean latitude profiles of land (green) and ocean (blue) feedbacks. [To update to include zonal-mean breakdowns based on model criteria (e.g., nutrient-enabled, permafrost carbon-enabled) once there is sufficient data]

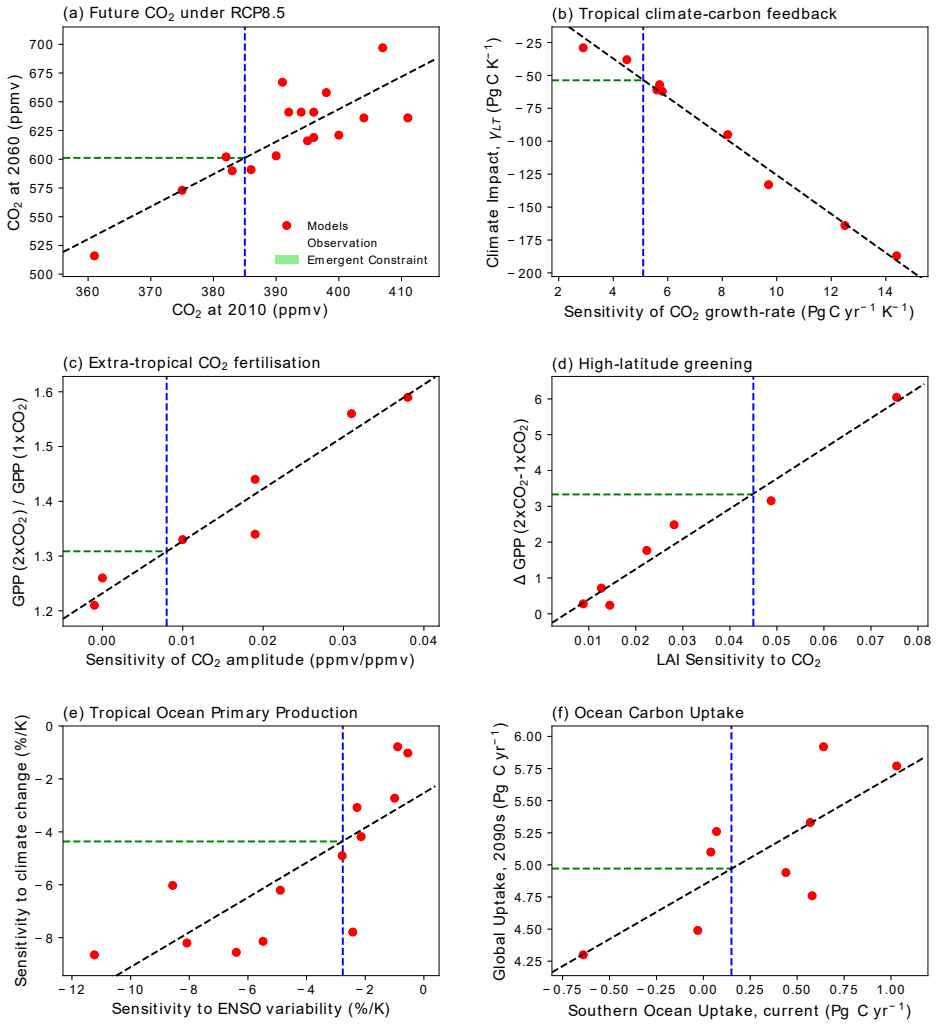

Figure 5.27: Examples of emergent constraints on the carbon cycle in ESMs, reproduced from previously published studies: (a) projected global mean atmospheric CO_2 concentration by 2060 under the RCP8.5 emissions scenario against the simulated CO_2 in 2010 (Friedlingstein et al., 2014b; Hoffman et al., 2014); (b) sensitivity of tropical land carbon to warming (γ_{LT}) against the sensitivity of the atmospheric CO_2 growth-rate to tropical temperature variability (Cox et al., 2013; Wenzel et al., 2014); (c) sensitivity of extratropical (30ºN–90ºN) gross primary production to a doubling of atmospheric CO_2 against the sensitivity of the amplitude of the CO_2 seasonal cycle at Kumkahi, Hawaii to global atmospheric CO_2 concentration (Wenzel et al., 2016); (d) change in high-latitude (30ºN–90ºN) gross primary production versus trend in high-latitude leaf area index or 'greenness'(Winkler et al., 2019) ; (e) sensitivity of the primary production of the Tropical ocean to climate change versus its sensitivity to ENSO-driven temperature variability (Kwiatkowski et al., 2017); (f) global ocean carbon sink in the 2090s versus the current-day carbon sink in the Southern Ocean. In each case, a red-dot represents a single ESM projection, the grey bar represents the emergent relationship between the y-variable and the x-variable, the blue bar represents the observational estimate of the x-axis variable, and the green bar represents the resulting emergent constraint on the y-axis variable. The thicknesses represent ± one standard error in each case. Figure after (Cox, 2019).

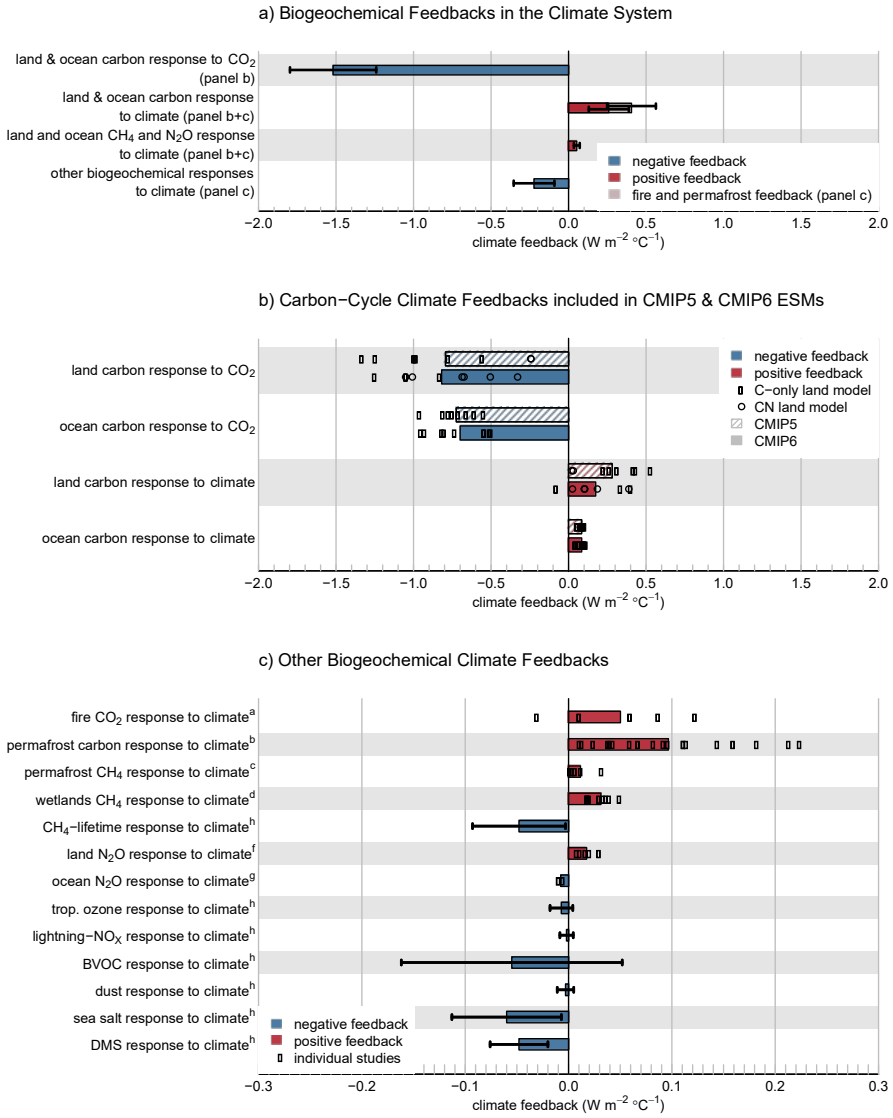

Figure 5.28: An overview of biogeochemical feedbacks in the climate system, based on the framework proposed by (Gregory et al., 2009; Arneth et al., 2010). a) Synthesis of biogeochemical feedbacks from panels b and c. Red (blue) bars correspond to positive (negative) feedbacks increasing (decreasing) radiative forcing at the top of the atmosphere. Bars denote the mean and the error bar represents one standard deviation of the estimates assuming variance between individual components are independent; b) carbon-cycle feedbacks as assessed by CMIP5 (Arora et al., 2013) and CMIP6 (Arora et al., submitted), where dots represent single model estimates, and open (filled) circles are those estimates which do (not) include the representation of a terrestrial nitrogen cycle; c) Estimates of other biogeochemical feedback mechanisms. These feedback metrics have, where possible, been assessed for the RCP8.5 scenario in year 2100, using the radiative forcing equations by with updated by (Etminan et al., 2016). Note the different x-axis scale for this panel. Black dots represent single estimates, and coloured bars denote the simple mean of the dots with no weighting or assessment being made to likelihood of any single estimate. Results in panel c have been compiled from (a) Section 5.4.3.2 (Arneth et al., 2010; Eliseev et al., 2014; Harrison et al., 2018); (b) Section 5.4.3.3 (Schneider von Deimling et al., 2012; Burke et al., 2013; Koven et al., 2015; Gasser et al., 2018; Kleinen and Brovkin, 2018), where the estimates from Burke et al. has been constrained as assessed in their study (c) Section 5.4.7 (Schneider von Deimling et al., 2012, 2015; Turetsky et al., submitted); (d) Section 5.4.7 (Denisov et al., 2013; Shindell et al., 2013; Stocker et al., 2013a; Zhang et al., 2017); (f) (Xu‐Ri et al., 2012; Zaehle, 2013; Stocker et al., 2013; Tian et al., 2019); (g) (Martinez-Rey et al., 2015; Landolfi et al., 2017; Battaglia and Joos, 2018). (h) These feedbacks are assessed in

Section 6.3 and the range indicated is the standard deviation of the feedback.

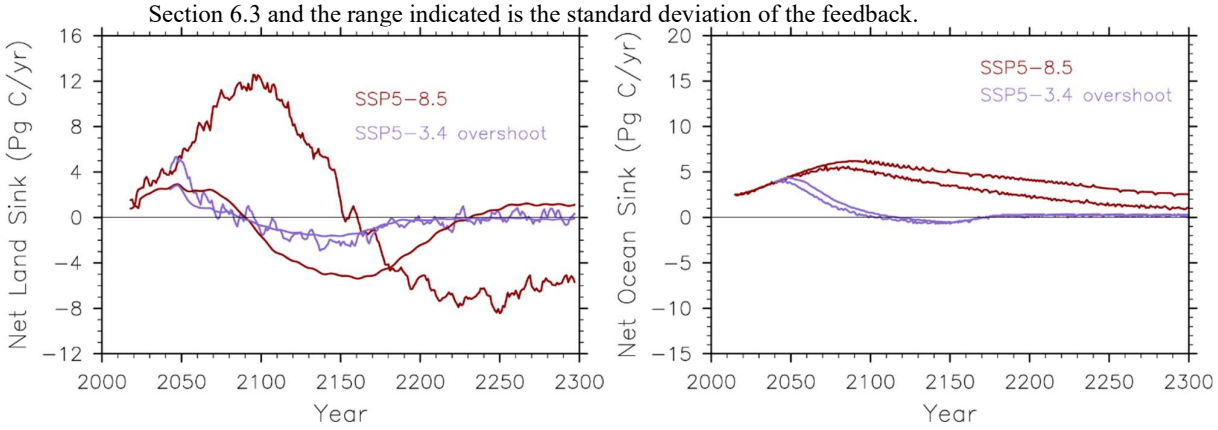

Figure 5.29: Trajectories of carbon cycle dynamics for ESMs beyond 2100. Shown are two scenarios, SSP5-8.5 and SSP5-3.4-overshoot, from one ESM (CanESM5) and one EMIC (UVIC-ESCM) for which extensions beyond 2100 are available. [Placeholder: To be updated in the FGD to include more CMIP6 model results] (a) Terrestrial carbon sink dynamics, and (b) Ocean carbon sink dynamics, for over the period 2015–2300.

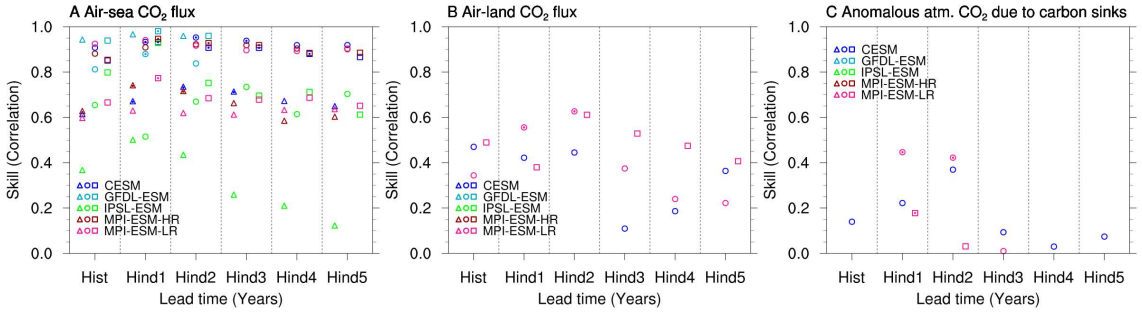

Figure 5.30: Predictive skill of the carbon cycle in a multi-model framework. (a) Predictive skill of the CO_2 flux into the ocean; (b) CO_2 flux into the land; (c) variations in the detrended atmospheric CO_2 growth inferred from the global air-sea and air-land CO_2 flux. The predictive skill is quantified as anomaly correlation coefficients of the model simulations assessed against three available references shown by different symbols: (Circles) Global Carbon Budget 2018 (Le Quéré et al., 2018a); (Squares) Reconstruction / assimilation simulation; (Triangles) SOM-FFN observational product (only for air-sea CO_2 flux). The significantly improved predictive skills at 95% level due to initialization, i.e. the difference between initialised and the uninitialised, are marked with filled dots. Note that the time period available for calculating the correlations varies between the models, being 1995–2005 for IPSL-ESM; 1982–2013 for CESM and MPI-ESM; 1997–2013 for GFDL-ESM.

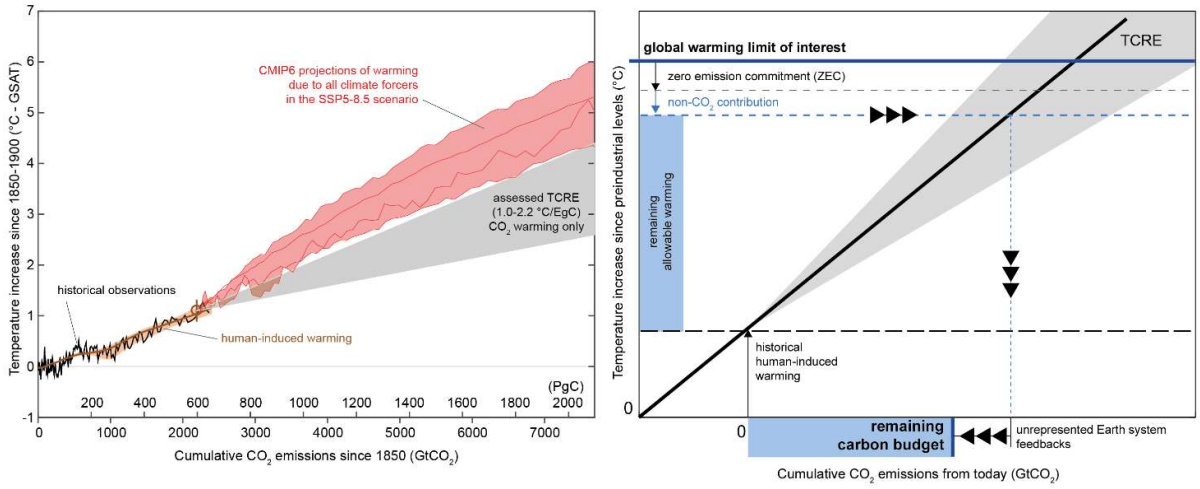

Figure 5.31: Illustration of relationship between cumulative emissions of CO_2 and global mean surface air temperature increase (left) and conceptual schematic of the assessment of the remaining carbon budget from its constituting components (right). Historical data in the left-hand panel (thin black line data) shows historical CO_2 emissions as reported in (Friedlingstein et al., 2019) together with the assessed global surface air temperature increase from 1850-1900 as assessed in Chapter 2 (Box 2.3). Orange-brown range with its central line show the human-induced share of historical warming (Haustein et al., 2017). The circle and vertical line show the assessed range of historical human-induced warming for the 2010–2019 period relative to 1850-1900 (Chapter 3). The grey cone shows the assessed range for the transient climate response to cumulative emissions of carbon dioxide (TCRE) assessed to fall *likely* in the 1.0–2.2 °C/EgC range (Section 5.5.1), starting from 2015. The red range and thin red lines within it represent CMIP6 simulations of the SSP5-8.5 scenario, starting from 2015.

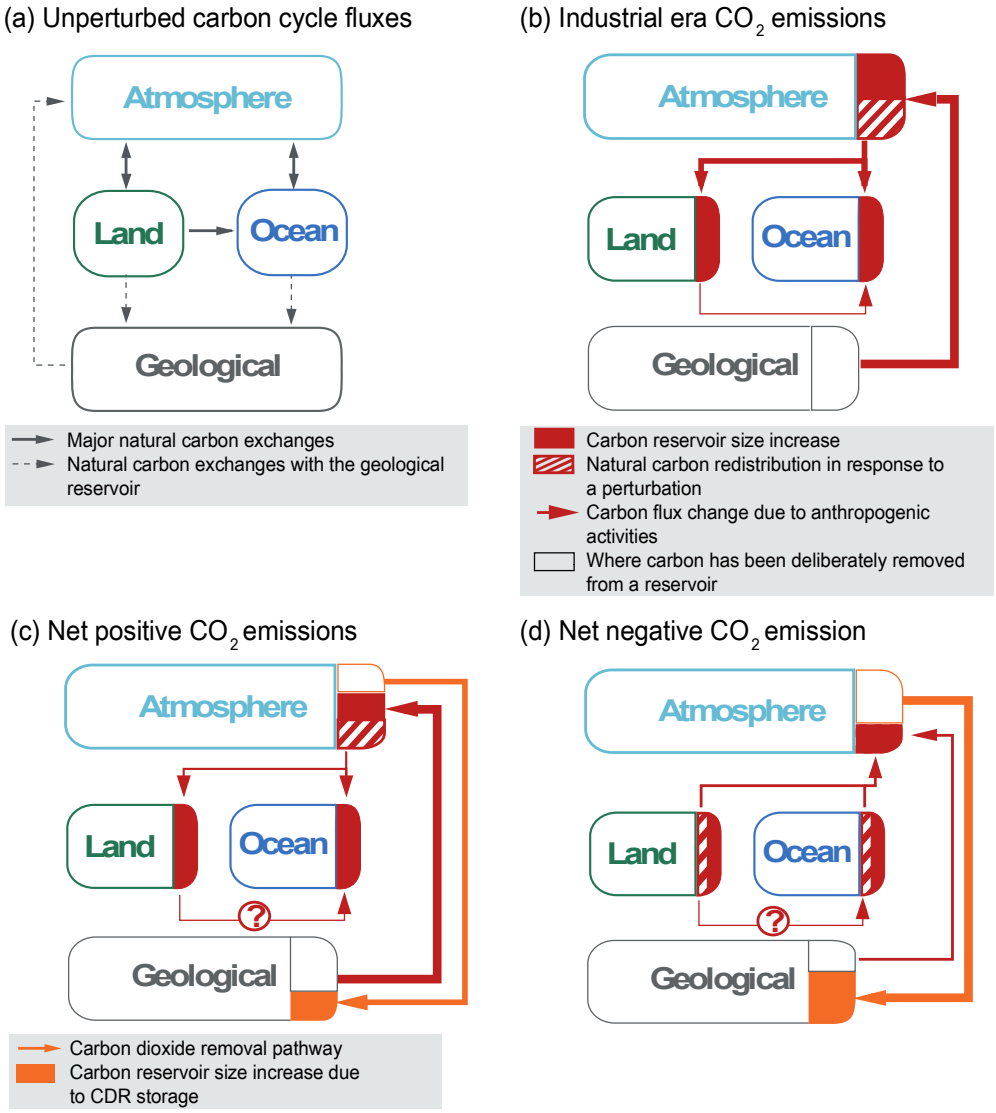

Box 5.2, Figure 1: Schematic representation of carbon fluxes between atmosphere, land, ocean and geological reservoirs for (a) an unperturbed Earth system; and changes in carbon fluxes for (b) an Earth system perturbed by fossil fuel CO_2 emissions, (c) an Earth system in which fossil fuel CO_2 emissions are partially offset by CDR, (d) an Earth system in which CDR exceeds CO_2 emissions from fossil fuels ("net negative emissions"). Carbon fluxes depicted in (a) (solid and dashed black lines) also occur in (b)-(d). The question mark in the land to ocean carbon flux perturbation in (c) and (d) indicates that the effect of CDR on this flux is unknown. Adapted from (Keller et al., 2018).

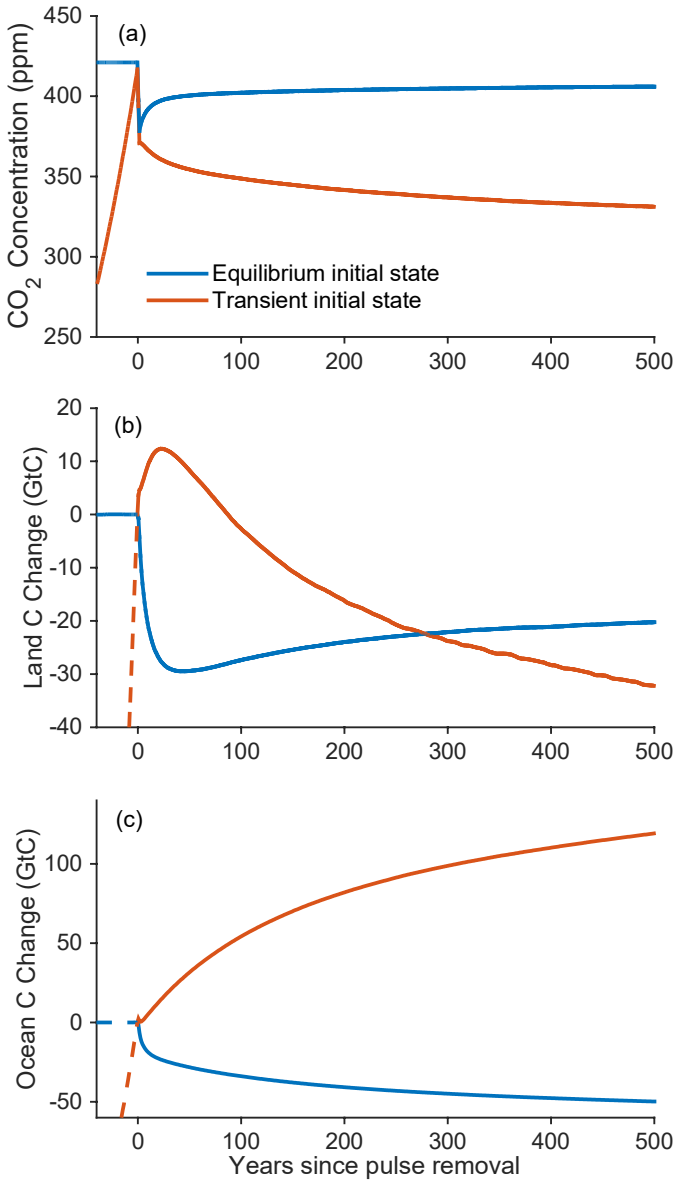

Figure 5.32: Idealised model simulations to illustrate carbon cycle response to instantaneous CO_2 removal from the atmosphere. (a) Atmospheric CO_2 concentration, (b) change in land carbon reservoir, (c) change in ocean carbon reservoir. Results are shown for simulations with the UVic ESCM model of intermediate complexity (Eby et al., 2009) with 100 GtC instantaneously removed from the atmosphere and stored in a permanent reservoir. The 'pulse' removal is applied from a model state in equilibrium with an atmospheric CO_2 concentration of 420 ppm (blue lines), and a 'transient' state, attained with atmospheric CO_2 concentration increasing at 1% yr^{-1} from pre-industrial levels until reaching a CO_2 concentration of 420 ppm (red lines). Changes in land and ocean carbon reservoirs are calculated relative to the time immediately prior to the instantaneous CO_2 removal.

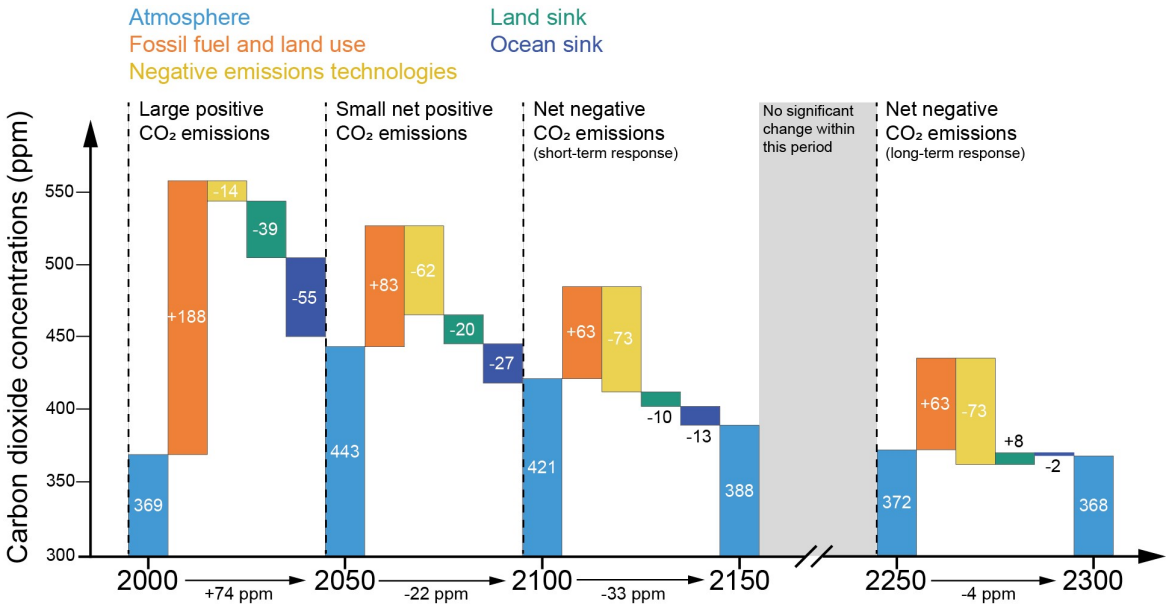

Figure 5.33: Carbon flux components during different stages of ESM simulations driven by RCP2.6. (a) Large positive CO_2 emissions, (b) Small net positive CO_2 emissions, (c) Net negative CO_2 emissions (short-term response), (d) Net negative CO_2 emissions (long-term response). Fossil fuel and land use emissions as well as emissions from negative emission technologies are from the RCP2.6 scenario. Due to small differences between the compatible CO_2 emissions diagnosed from the ESMs and the emissions in RCP2.6, emissions and land and ocean carbon fluxes over each 50-year period do not balance precisely. Modified from (Jones et al., 2016a).

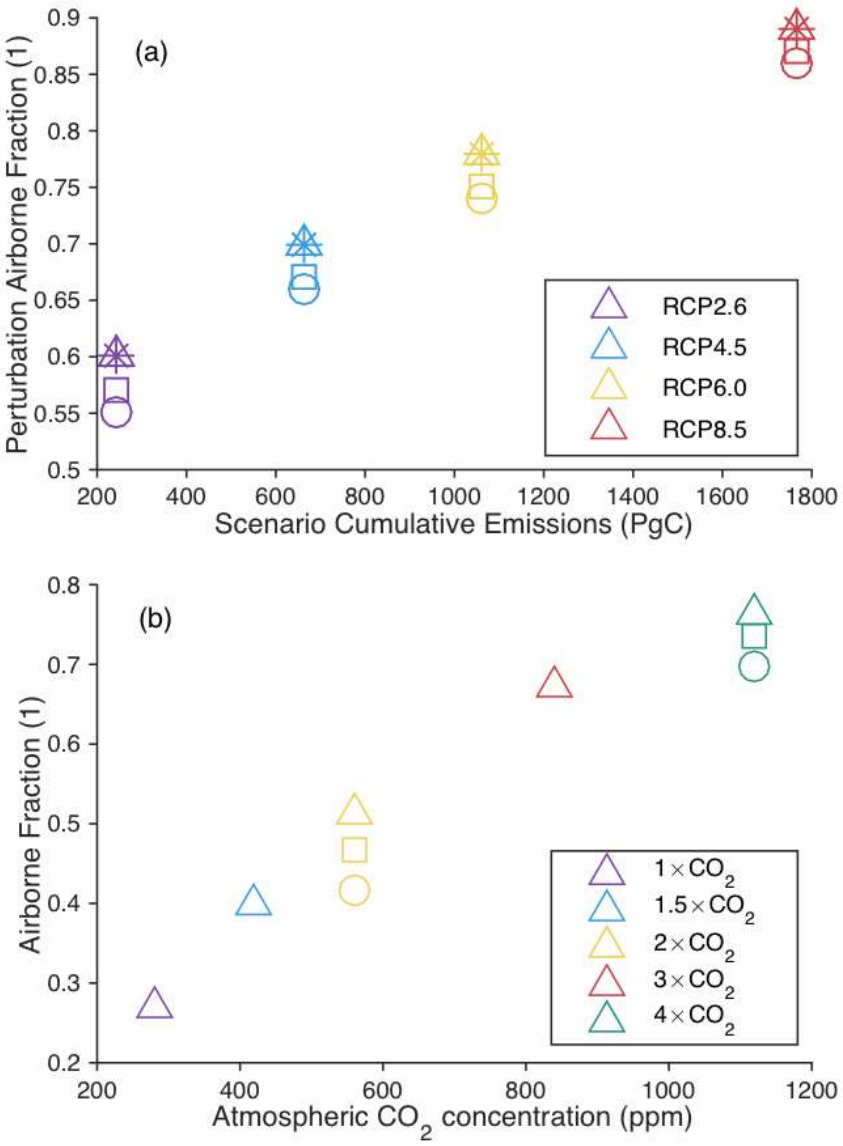

Figure 5.34: Effectiveness of CDR. (a) Perturbation airborne fraction (PAF) for model simulations where CDR is applied from four RCPs (shown on the horizontal axis in terms of their cumulative CO_2 emissions over 2020–2099). Symbols indicate results for four CDR scenarios, which differ in terms of the magnitude and rate of CDR (see Jones et al. (2016b) for details). Results are based on simulations with the Hadley Centre Simple Climate-Carbon Model and are shown for the year 2100. Data from Jones et al. (2016b). (b) Airborne fraction of cumulative emissions (AF) for idealised model simulations with CDR applied instantly (pulse removals) from climate states in equilibrium with different atmospheric CO_2 concentration levels (1 to 4 times the pre-industrial atmospheric CO_2 concentration; shown on the horizontal axis). The airborne fraction is calculated 100 years after pulse removal. Symbols indicate results for different magnitudes of pulse removals (triangles: –100 PgC; squares: –500 PgC; circles: –1000 PgC). Based on simulations with the UVic ESCM model of intermediate complexity. Data from Zickfeld et al. (2019). [Placeholder: Will be supplemented with results from CDR-MIP simulations].

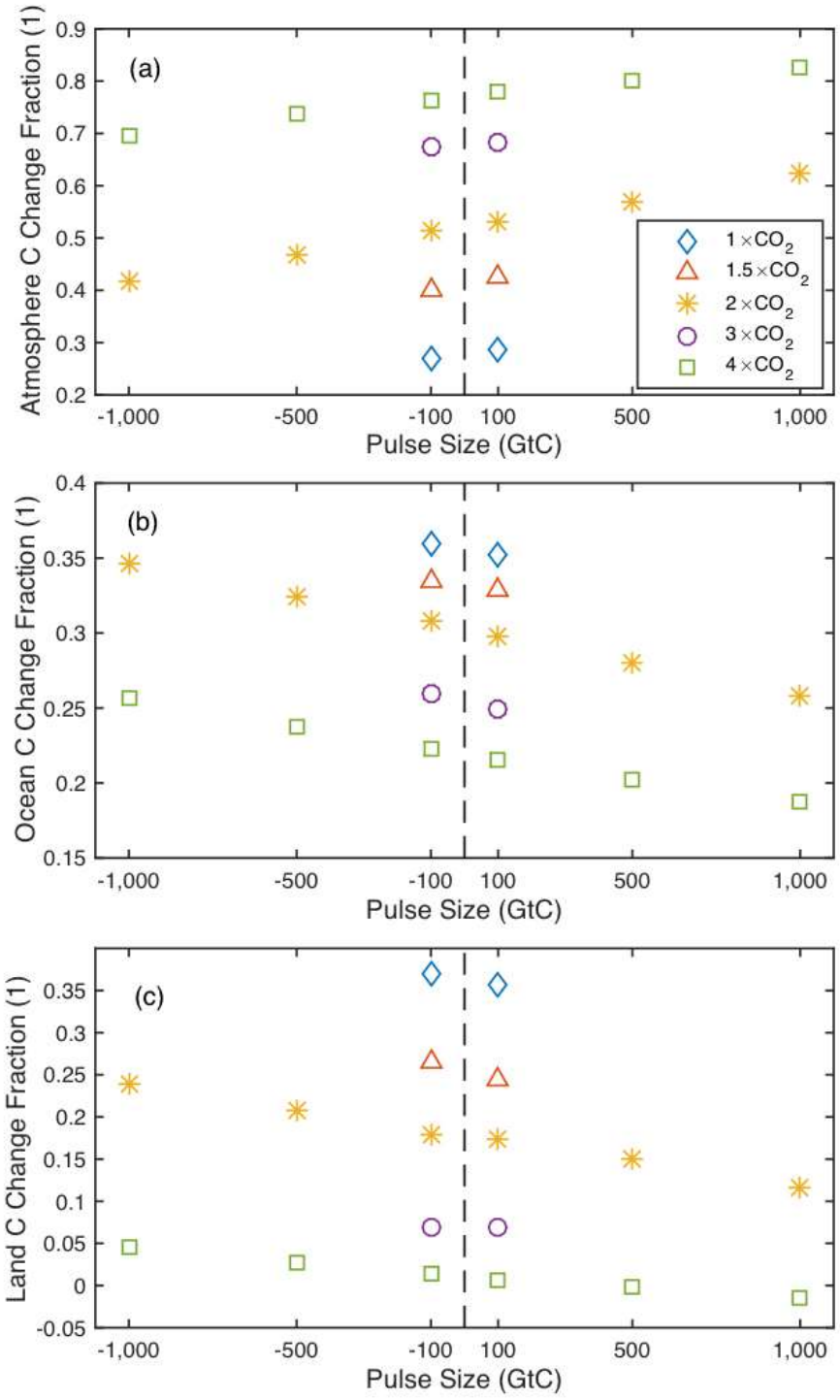

Figure 5.35: Changes in carbon reservoirs (atmosphere, ocean, land) as a fraction of cumulative CO_2 emissions (equivalent to CO_2 pulse size) 100 years after the pulse emission/removal (±100 PgC, ±500 PgC, ±1000 PgC) for simulations initialised from different equilibrium states (1 to 4 times the pre-industrial atmospheric CO_2 concentration). Changes in carbon reservoirs are positive (i.e. uptake) for positive CO_2 pulses and negative (i.e. outgassing) for negative CO_2 pulses. (a) Atmospheric carbon burden change fraction, (b) ocean carbon reservoir change fraction, (c) land carbon reservoir change fraction. From (Zickfeld et al., submitted). [Placeholder: Will be updated based on results from CDR-MIP simulations.]

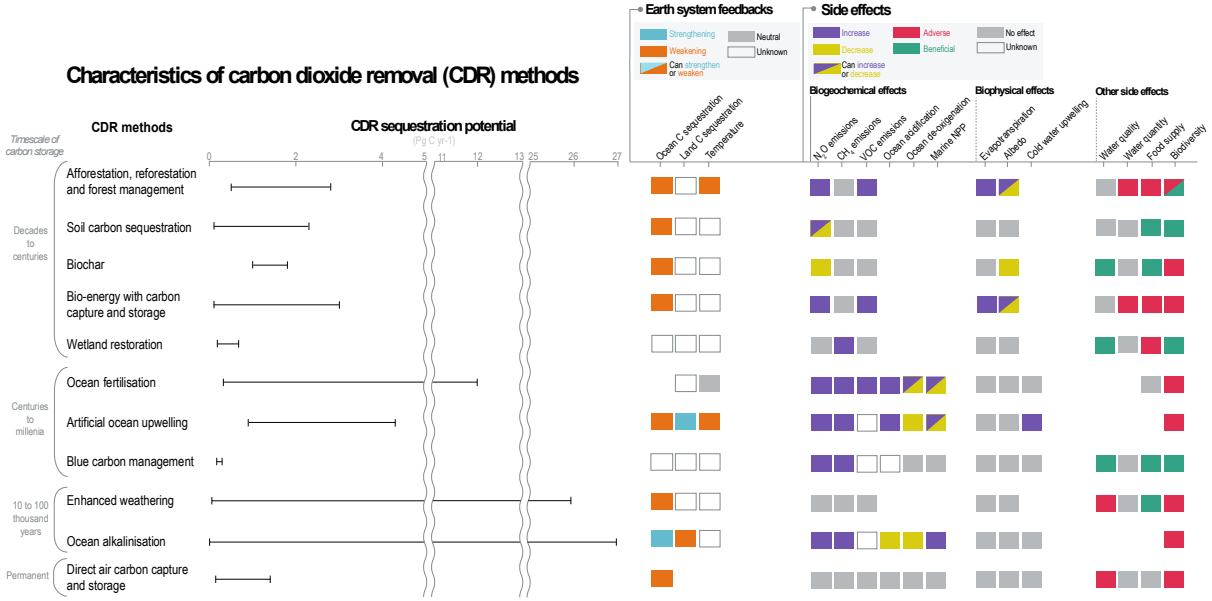

Figure 5.36: Characteristics of CDR methods. The left hand side of the figure shows ranges of technical sequestration potentials of CDR methods, grouped according to the time scale of C storage. The right hand side shows Earth system feedbacks that deployment of a given CDR method would have on carbon sequestration and climate, along with biogeochemical, biophysical, and other side effects of that method. For Earth system feedbacks, the colours indicate whether the feedbacks strengthen or weaken C sequestration and the climate cooling effect of a given CDR method. For biogeochemical and biophysical side effects the colours indicate whether the deployment of a CDR method increases or decreases the magnitude of the effect, whereas for other side effects the colour indicates whether deployment of a CDR method is adverse or beneficial.

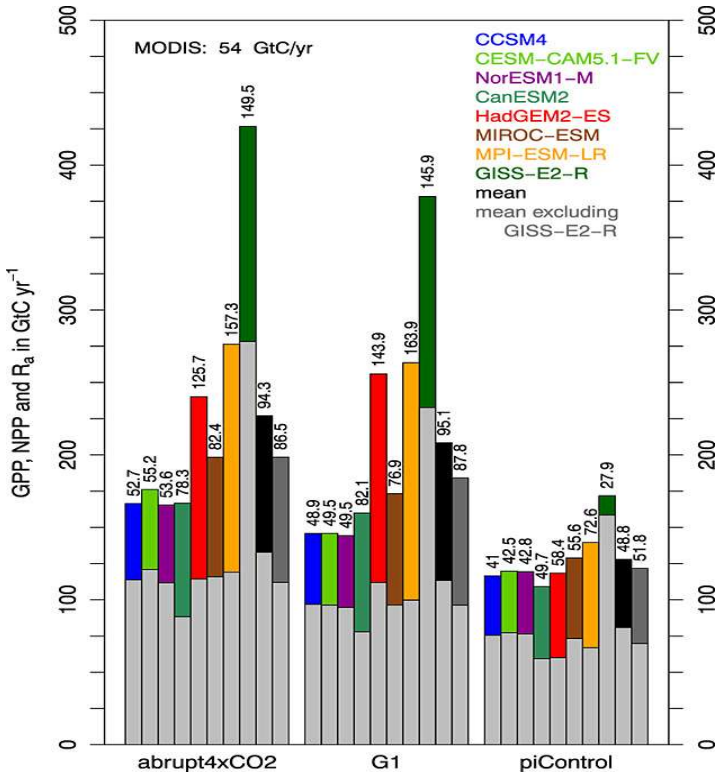

Figure 5.37: [Placeholder: From (Glienke et al., 2015). Global mean values for NPP averaged over land (colored with numbers above), R_a (grey) and GPP (total) for all models of the three experiments abrupt $4 \cdot CO_2$, G1, and piControl. The number in the top left corner is the global average of NPP determined from MODIS data. Abrupt $4 \cdot CO_2$ is an experiment with an abrupt quadrupling of atmospheric CO_2 and G1 is a GEOMIP experiment in which a decrease in the solar constant offsets the global radiative forcing of $4 \cdot CO_2$.]

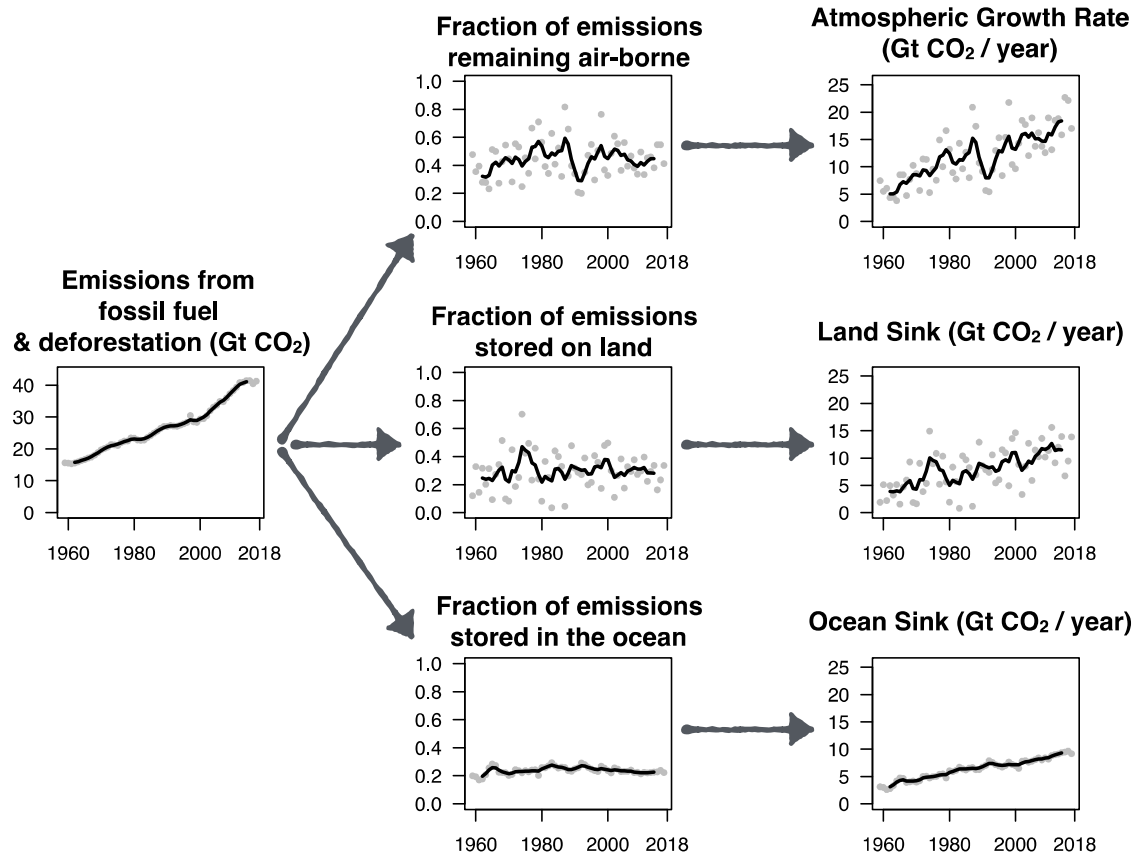

FAQ 5.1, Figure 1: Overview of the global carbon budget and the fraction of CO_2 remaining in atmosphere, land and ocean from 1960 to 2019. Estimates are derived from atmospheric observations, process-based models, data-driven ocean flux products, and atmospheric inversions (Le Quéré et al., 2018a). Dots denote yearly values, lines are the seven years running mean.

FAQ 5.2, Figure 1: [Figure Placeholder: Schematic of the processes that affect permafrost thawing (what speeds up or slows down the release of GHG emissions.)]

FAQ 5.3, Figure 1: [Figure suggestion – Time series of responses of climate system components with short to long response time scales (short term would include things like surface air temperature, long term would be warming, acidification and oxygen loss of the deep ocean, sea level etc.).]

FAQ 5.4, Figure 1: [Figure idea: visual combining the historical carbon budget, with straight lines going down from today's emissions to zero, and in line with the remaining carbon budget for 1.5°C or 2°C – coloured and labelled differently to make the difference clear.]